

# Estimating Properties of Subsurface Layers from GPR Spectral Attributes

Z. L. Huang<sup>1,2</sup> and J. Z. Zhang<sup>1</sup>

<sup>1</sup>College of Marine Geosciences, Ocean University of China, China

<sup>2</sup>School of Information Science and Technology, Xiamen University, China

**Abstract**— Based on the different influence of the geometric and the electric parameters of subsurface layers on the ground penetrating radar (GPR) frequency spectra, we use the different spectral attributes to estimate the different parameters of subsurface layers. For a three-layer model, the frequency of the first extreme point on the amplitude spectrum of GPR response to the model is equal to the inverse of double temporal thickness of the middle layer, and the period of the notches on the amplitude spectrum is equal to the inverse of the thickness. So the temporal thickness of the middle layer can be estimated from the frequency of the first extreme point on the amplitude spectrum, or from the period of the notches. The extreme value frequencies on the phase spectrum depend only on the depth and the thickness of the middle layer. When the thickness has already been obtained, the temporal depth can be estimated using only the extreme value positions of the phase spectrum. When the thickness and the depth of the middle layer are fixed, the permittivities of the three layers and the conductivity of the middle layer can be estimated from only the phase spectrum. In consequence, we propose a step-by-step GPR inversion method for the estimation of thicknesses, depths, permittivities and conductivities of subsurface layers.

## 1. INTRODUCTION

Nowadays, GPR has been applied in the civil engineering and geophysics for the characterization of subsurface structures [1–4]. In this paper, we focus on layered media concerning which a lot of work has been done. For example, Kao et al. created a new multi-layer model to estimate thickness and dielectric constants of highway pavement [5]. Huang et al. used parameter calibration method to estimate permittivity and thickness of pavement [6]. Patriarca et al. established an objective function in the frequency domain with the Green's function for the inversion of thickness and electric parameters [7]. The existing methods need a good prior information for a starting model. Here we present a new method which estimates properties of subsurface layers from spectral attributes.

## 2. METHOD

Consider a model containing several layers and each layer is assumed to be linear, homogeneous and isotropic. When the incident wave is normal to the interface, the reflection coefficient  $r$  and transmission coefficient  $\tau$  can be expressed as

$$r_{mn} = (\hat{\eta}_n - \hat{\eta}_m) / (\hat{\eta}_n + \hat{\eta}_m) \quad (1)$$

$$\tau_{mn} = 2\hat{\eta}_n / (\hat{\eta}_n + \hat{\eta}_m) \quad (2)$$

where the subscript indicates different medium, thus  $r_{12}$  would be the reflection coefficient of the interface between medium 1 and medium 2.  $\hat{\eta}$  is the intrinsic impedance of the medium and is given by

$$\hat{\eta} = \sqrt{\frac{j\omega\mu}{\sigma + j\omega\varepsilon}} \quad (3)$$

where  $\omega$  is the angular frequency.  $\varepsilon$ ,  $\sigma$ , and  $\mu$  are permittivity, electric conductivity and magnetic permeability of the medium respectively.

Under the assumption that the multiple reflections between different interfaces could be neglected, we define a generalized reflection coefficient  $\tilde{r}$  at each interface as the ratio of electric intensity of reflection wave and radar emission wave. The generalized reflection coefficient of the  $i$ -th interface is

$$\tilde{r}_{i,i+1} = r_{i,i+1} \prod_{k=0}^{i-1} (1 - r_{k,k+1}^2) \prod_{k=1}^i e^{-2\alpha_k d_k} \quad (4)$$

where  $d$  is the layer thickness and  $\alpha$  is the attenuation coefficient. The generalized reflection coefficient is a function of both medium electric properties and travel distance. Set the zero-time point at the surface of ground, every two adjacent reflectors would form a coefficient pair, as shown in Fig. 1, which can be expressed as

$$r(t) = \tilde{r}_{12}\delta(t - t_0) + \tilde{r}_{23}\delta(t - t_0 - T) \tag{5}$$

where  $\tilde{r}_{12}$  is the top generalized reflection coefficient,  $\tilde{r}_{23}$  is the base generalized reflection coefficient. The Fourier transform of (5) is

$$r(f) = [2r_e \cos(\pi fT) + i2r_o \sin(\pi fT)] \exp[-i2\pi f(t_0 + T/2)] \tag{6}$$

where  $r_e = (\tilde{r}_{12} + \tilde{r}_{23})/2$  and  $r_o = (\tilde{r}_{12} - \tilde{r}_{23})/2$  are the even component and the odd part of the reflection coefficient pair, as illustrated in Fig. 1. Consider the squared amplitude spectrum of reflection coefficient pair.

$$|r(f)|^2 = 4r_e^2 + 2(r_e^2 - r_o^2) [1 + \cos(2\pi fT)] \tag{7}$$

The solution to the equation  $d|r(f)|^2/df = 0$  is

$$f = \frac{n - 1}{2T}, \quad n = 1, 2, \dots \tag{8}$$

where  $f$  represents the frequency of the extreme points on the squared amplitude spectrum. Let  $\Delta f = f(n + 1) - f(n - 1)$  be the frequency difference between two adjacent extreme points of the spectrum. It's easy to conclude that

$$\Delta f = 1/T \tag{9}$$

Therefore,  $\Delta f$  is a constant and depends only on  $T$ . Conversely,  $T$  can be determined from  $\Delta f$ . It must be pointed out that frequency difference might disappear within the band selected by the interpreter if  $T$  is too small. For such situation, one should find the frequency  $f_p$  of the first extreme point of the squared amplitude spectrum, and then estimate  $T$  using (8) by setting  $n = 2$ , i.e.,  $T = 1/(2f_p)$ .

The phase spectrum,  $\theta(f)$ , of reflection coefficient pair can be expressed as

$$\theta(f) = \arctan[\tan(\pi fT)r_o/r_e] - 2\pi ft_0 - \pi fT \tag{10}$$

where

$$\frac{r_o}{r_e} = \frac{r_{12} - r_{23}(1 - r_{12})e^{(-2\alpha_2 d_2)}}{r_{12} + r_{23}(1 - r_{12})e^{(-2\alpha_2 d_2)}} \tag{11}$$

The phase spectrum of reflection coefficient pair relates to  $t_0$ ,  $T$  and  $r_o/r_e$ . In Equation (11), when the medium is good dielectric, the intrinsic impedance becomes  $\hat{\eta} \approx \sqrt{\mu/\epsilon}$  and the attenuation constant becomes  $\alpha = 0.5\sigma\sqrt{\mu/\epsilon}$ , thus  $r_{12}$  and  $r_{23}$  are decided by the permittivities, which are  $\epsilon_1$ ,  $\epsilon_2$  and  $\epsilon_3$ , of the three layers. Attenuation coefficient  $\alpha_2$  is determined by permittivity  $\epsilon_2$  and conductivity  $\sigma_2$  of the second layer.  $d_2$  is determined by  $T$  and  $\epsilon_2$ . Therefore  $r_o/r_e$  could be considered to be irrelevant to frequency  $f$ . Fig. 2 shows the phase spectrum curves of a coefficient pair regarding to different  $r_o/r_e$ , where  $t_0$  and  $T$  stay unchanged. It can be seen that  $r_o/r_e$  does

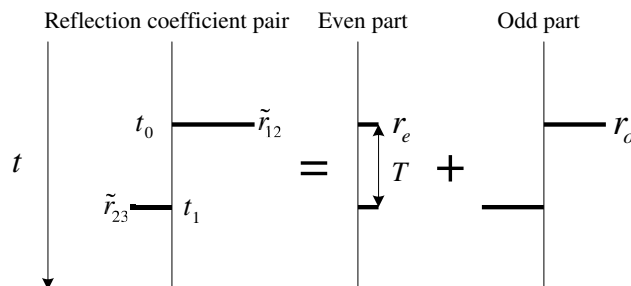


Figure 1: Decomposition of reflection coefficient pair.

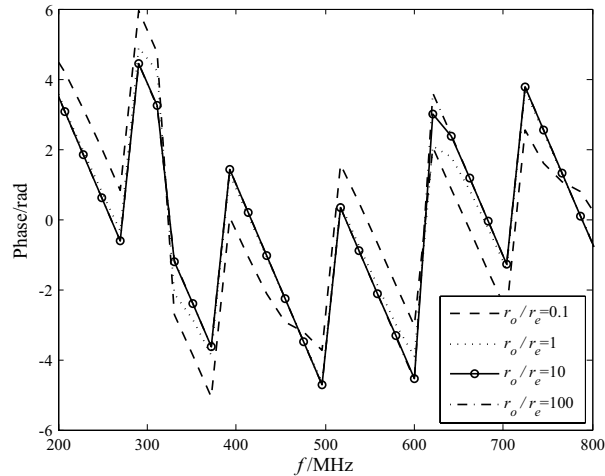


Figure 2: Phase spectrum for different values of  $r_o/r_e$ .

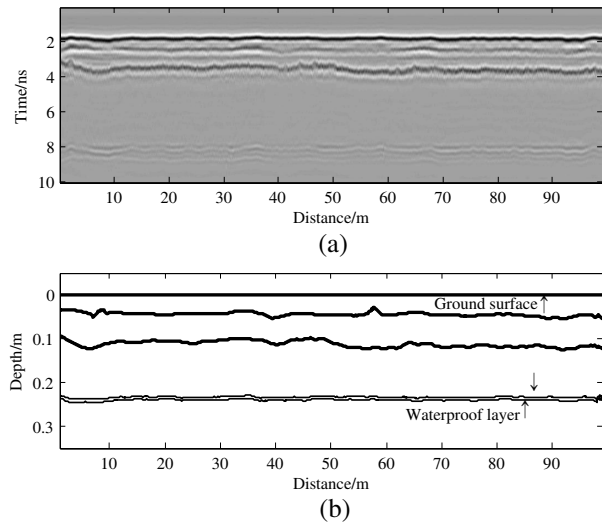


Figure 3: (a) Original GPR data profile. (b) Inversion result of the GPR data, notice the thin layer has been inverted.

not change the extreme value frequencies of the phase spectrum curves. Therefore, the extreme value frequencies of a phase spectrum curve depend only on  $t_0$  and  $T$ . When  $T$  has already been calculated, it's possible to estimate  $t_0$  from only this feature of the extreme value positions of the phase spectrum curve. We estimate  $t_0$  by using the modified Stochastic Hill-Climbing algorithm (SHC) to find the solution that minimizes the error between the extreme value positions of the observed phase spectrum curve and the calculated one, where  $T$  is taken the value calculated using Equation (9) and each of the other parameters is taken a random value in its available range for calculation of the phase spectrum curve.  $t_0$  is updated iteratively and other parameters are fixed in solving this minimizing problem. When  $T$  and  $t_0$  are fixed, the phase spectrum of reflection coefficient pair can be completely described by  $r_o/r_e$ . So after  $T$  and  $t_0$  are obtained,  $\varepsilon_1$ ,  $\varepsilon_2$ ,  $\varepsilon_3$  and  $\sigma_2$  can be estimated by minimizing the error between observed phase spectrum and calculated one using the SHC algorithm. At last, along with  $t_0$ ,  $T$ ,  $\varepsilon_1$ ,  $\varepsilon_2$  and  $\varepsilon_3$  and  $\sigma_2$ ,  $\sigma_1$  and  $\sigma_3$  are calculated by minimizing the error between the observed spectrum and calculated one using the SHC algorithm. What is mentioned above fits for a model with three layers. Actually, the subsurface may consist of more than three layers. Before implementation of the inversion method, each segment of the time domain GPR data that corresponds to a three-layer model must be truncated from original data. Since some layers may be too thin to be identified in time domain, the time domain data is then transformed into time-frequency ( $t$ - $f$ ) domain using the generalized  $S$ -transform (GST) [8], due to its high resolution for subsurface layers. The layer interfaces can be roughly identified from the  $t$ - $f$  amplitude spectrum of GPR data. The inversion is then carried out within each window which contains three layers (two interfaces).

### 3. EXAMPLE

The real GPR data are collected from GPR survey of a road. The asphalt pavement consists of three layers of which the thickness is designed to be 0.04 m, 0.06 m and 0.1 m, respectively. There is a thin waterproof layer beneath the asphalt layer. The emitting frequency of the GPR is 2 GHz. 1024 samples are recorded within 10 ns for each trace. Based on the  $t$ - $f$  analysis result, we divide the signal with three time windows of different length for inversion. The first window covers the air-ground surface and the first underground asphalt interface; the second window contains only the second asphalt interface while the last window includes the waterproof layer. Then the inversion is carried out within each window which contains two interfaces at most. The inverted interfaces are shown in Fig. 3. The average thickness of the three layers above the waterproof layer are 0.0442 m, 0.0736 m, and 0.1216 m, respectively. The average thickness of waterproof estimated is 0.0088 m, which is less than 1/5 wavelength of emitting wave. The resulting permittivities of the layers are, from top to bottom, 3.7, 5.4, 12, 9.3, and 13.2, respectively. The conductivities of the layers are 0.013, 0.02, 0.018, and 0.01 respectively.

#### 4. CONCLUSION

Based on the different influence of geometric and electric parameters of subsurface media on the spectrum of reflection coefficients, we propose a method for the estimation of thicknesses, depths, permittivities and conductivities of subsurface layers. The method estimates individual parameter or several parameters at a time according to different attributes of the GPR spectra. The unique influences of thickness and depth on the spectrum makes it possible for us to give values close to the true ones in each step. This new method is practicable to a thin layer. The inversion is carried out for a segment of GPR data delimited by a time-window, which corresponds to three layers. The time-windows can be divided according to the combined GPR data and its  $t$ - $f$  map.

#### ACKNOWLEDGMENT

This work was supported by the National Natural Science Foundation of China (Grant Nos. 41074077, 40774065).

#### REFERENCES

1. Shao, W. B., A. Bouzerdoum, S. L. Phung, L. J. Su, B. Indraratna, and C. Rujikiatkamjorn, "Automatic classification of ground-penetrating-radar signals for railway-ballast assessment," *IEEE Trans. Geosci. Remote Sensing*, Vol. 49, No. 10, 3961–3971, 2011.
2. Huang, Y. Q., J. Z. Zhang, and Q. H. Liu, "Three-dimensional GPR ray tracing based on wavefront expansion with irregular cells," *IEEE Trans. Geosci. Remote Sensing*, Vol. 49, No. 2, 679–687, 2011.
3. Zhang, J. Z., Y. Q. Huang, L. P. Song, and Q. H. Liu, "Fast and accurate 3-D ray tracing using bilinear traveltime interpolation and the wave front group marching," *Geophys. J. Int.*, Vol. 184, 1327–1340, 2011.
4. Huang, Y. Q., Y. H. Liu, Q. H. Liu, and J. Z. Zhang, "Improved 3-D GPR detection by nufft combined with mpd method," *Progress In Electromagnetics Research*, Vol. 103, 185–199, 2010.
5. Kao, C. P., J. Li, Y. Wang, H. C. Xing, and C. R. Liu, "Measurement of layer thickness and permittivity using a new multilayer model from GPR data," *IEEE Trans. Geosci. Remote Sensing*, Vol. 45, 2463–2470, 2007.
6. Huang, C. L. and S. Yi, "A new GPR calibration method for high accuracy thickness and permittivity measurement of multi-layered pavement," *Proc. of the Tenth Intl. Conf. on GPR*, 627–630, 2004.
7. Patriarca, C., S. Lambot, M. R. Mahmoudzadeh, J. Minet, and E. Slob, "Reconstruction of sub-wavelength fractures and physical properties of masonry media using full-waveform inversion of proximal penetrating radar," *Journal of Appl. Geophys.*, Vol. 74, 26–37, 2011.
8. Stockwell, R. G., L. Mansinha, and R. P. Lowe. "Localization of the complex spectrum: The  $s$  transform," *IEEE Trans. on Signal Processing*, Vol. 44, No. 4. 998–1001, 1996.

# Identification of Subsurface Thin Layers Using Cepstrum of GPR Data

Z. L. Huang<sup>1,2</sup> and J. Z. Zhang<sup>1</sup>

<sup>1</sup>College of Marine Geosciences, Ocean University of China, China

<sup>2</sup>School of Information Science and Technology, Xiamen University, China

**Abstract**— A new method using pseudo-cepstrum to distinguish thin layers from ground penetrating radar (GPR) survey data is presented in this paper. The cepstrum here does not apply natural logarithmic operation on the spectrum. First, spectrum of the reflection coefficients series is estimated, using a Gaussian window to restrict the analysis band. It is found that the real part of the spectrum can be represented by cosine functions, while the image part can be represented by sine functions with reverse sign and same quefencies. The quefencies of the real part spectrum are the positions of the reflection coefficients. However, the cepstrum of a thin layer would look the same as that of a single-interface reflection. In order to tell the difference between these two situations, we calculate the real part pseudo-cepstrum of the reflection coefficient series and the peaks of the gamnitude cepstrum would indicate either a single-interface reflection or a thin layer reflection. According to the peak quefencies of the cepstrum, the Gaussian window used before is forward-shifted and applied on the spectrum to obtain the image part of a forward-shifted spectrum. Then, the image part is backward shifted and added with the former real part of the spectrum. If the peak turns out to be the result of a single-interface reflection, the adding would make the quefency component disappear on the gamnitude cepstrum of the sum. The residual would still be strong if the peak is a result of a thin layer reflection.

## 1. INTRODUCTION

The concept of cepstrum was invented by Boget, et al. in 1963 [1]. The cepstrum is defined as the Fourier transform of the natural logarithm of the Fourier transform of the signal. To distinguish this new domain from time, several new terms had also been invented. Frequency is transformed to quefency, magnitude to gamnitude, phase to saphe, filtering to liftering, even analysis to alany-sis [2]. Cepstral analysis has been widely used in the areas of audio processing [3] and radar signal processing [4]. GPR has been widely used in the geophysics and civil engineering, and lots of work has been done concerning its modeling and inversion [5–7]. In this paper, cepstrum is employed to identify subsurface thin layer from GPR data. A brief review of cepstrum and the concepts of the real (image) part pseudo-cepsttum are given in Section 2. The modeling of the layered media is explained in Section 3. The details of the new method for identifying thin layers are presented in Section 4.

## 2. DEFINITION OF REAL (IMAGE) PART PSEUDO-CEPSTRUM

Let  $g(f)$  be the Fourier transform of a time-domain signal  $g(t)$ , the complex cepstrum  $\tilde{g}(\tilde{f})$  is defined as

$$\tilde{g}(\tilde{f}) = FT [\ln g(f)] = FT \left\{ \ln \left[ |g(f)| e^{j\phi(f)} \right] \right\} = FT [\ln |g(f)|] + FT [j\phi(f)] \quad (1)$$

where  $FT$  denotes the Fourier transform.  $FT[\ln |g(f)|]$  is called the real cepstrum of the signal. If logarithmic operation is not involved, the complex cepstrum becomes a pseudo-cepstrum which is defined as

$$\hat{g}(\hat{f}) = FT [g(f)] \quad (2)$$

We introduce another kind of cepstrum. Instead of performing Fourier transform on the logarithm of the spectrum, we directly calculate the spectrum of the real and image part of the complex spectrum. Thus the results are called the real and the image part pseudo-cepstra, respectively, which are given by

$$\hat{g}_{\text{Re}}(\hat{f}) = FT \{ \text{Re} [g(f)] \} \quad (3)$$

$$\hat{g}_{\text{Im}}(\hat{f}) = FT \{ \text{Im} [g(f)] \} \quad (4)$$

### 3. MODEL OF LAYERED MEDIA

Consider a thin layer as shown in Fig. 1, the top and the base reflection coefficients are  $r_1$  and  $r_2$  respectively. The time thickness of the thin layer is  $T$ . Time sample at the top reflector is  $t_1$ . Locate the zero-time point at the ground surface which is represented by the dash line in Fig. 1, the reflection coefficient pair of the thin layer is expressed as

$$r(t) = r_1\delta(t - t_1) + r_2\delta(t - t_1 - T) \quad (5)$$

The Fourier transform of (5) is

$$r(f) = [r_1 \exp(j\pi f T) + r_2 \exp(-j\pi f T)] \exp[-j2\pi f (t_1 + T/2)] \quad (6)$$

Applying trigonometric identities on (6), the real and imaginary parts of the complex spectrum  $r(f)$  are

$$r_{\text{Re}}(f) = r_1 \cos(2\pi t_1 f) + r_2 \cos[2\pi (t_1 + T) f] \quad (7)$$

$$r_{\text{Im}}(f) = -r_1 \sin(2\pi t_1 f) - r_2 \sin[2\pi (t_1 + T) f] \quad (8)$$

Therefore  $r(f)$  can be expressed as

$$r(f) = [r_1 \cos(2\pi t_1 f) + r_2 \cos(2\pi (t_1 + T) f)] - j[r_1 \sin(2\pi t_1 f) + r_2 \sin(2\pi (t_1 + T) f)] \quad (9)$$

Notice that the quefrequency of each cos and sin function which is a function of frequency  $f$ , is the time sampling point. The GPR signal  $s(t)$  received by the antenna can be represented as the convolution of radar emission wave  $w(t)$  and the reflectivity series  $r(t)$ , i.e.,

$$s(t) = w(t) * r(t) + n(t) \quad (10)$$

where  $n(t)$  is the noise. Performing Fourier transform on both sides of (10) yields

$$s(f) = w(f)r(f) + n(f) \quad (11)$$

where  $s(f)$ ,  $w(f)$  and  $n(f)$  are the spectrum of received signal, radar emission wave and noise respectively. If emission wave  $w(t)$  has already been obtained, the reflection coefficient series can be estimated by divide both sides of (11) with  $w(f)$ . In practice, the analysis band is limited, thus the spectrum of the estimated reflection coefficient series is

$$r'(f) = [r(f) + n(f)/w(f)] \cdot \text{win}(f) = \{[r_{\text{Re}}(f) + nw_{\text{Re}}(f)] + j[r_{\text{Im}}(f) + nw_{\text{Im}}(f)]\} \cdot \text{win}(f) \quad (12)$$

where  $\text{win}(f)$  is a real-value Gaussian window,  $nw_{\text{Re}}(f)$  and  $nw_{\text{Im}}(f)$  are the real and image part of  $n(f)/w(f)$  respectively. The real and image part pseudo-cepstrum of the estimated reflection coefficient series are

$$\hat{r}'_{\text{Re}}(\hat{f}) = FT \{[r_{\text{Re}}(f) + nw_{\text{Re}}(f)] \cdot \text{win}(f)\} \quad (13)$$

$$\hat{r}'_{\text{Im}}(\hat{f}) = FT \{[r_{\text{Im}}(f) + nw_{\text{Im}}(f)] \cdot \text{win}(f)\} \quad (14)$$

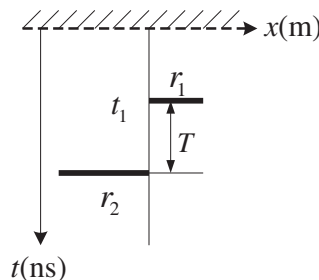


Figure 1: The model of a thin layer.

#### 4. IDENTIFICATION OF THIN LAYER

It's obvious that quefrequencies of the real (or image) part of the spectrum of the reflection coefficient series are the time sampling points and their magnitude depends on the coefficients. However, if the positions of the two coefficients are close, there is a thin layer, it would be impossible to tell the difference between the real (or image) part pseudo-cepstrum from a thin layer and that from a single interface, as shown in Fig. 2. The model contains a thin layer at 15 ns and a single reflector at 25 ns. The synthetic signal is added with 10 dB noise and the real part pseudo-cepstrum of the estimated reflection coefficient series is taken in this case. In order to decide whether the peak of the real part pseudo-cepstrum is caused by a thin layer, we present a new method which consists of the following steps:

i. Restrict the analysis band with a Gaussian window  $win(f)$  and obtain the real part of the spectrum of the estimated reflection coefficient series, i.e.,

$$\text{Re} [\hat{r}'(f)] = \{r_1 \cos(2\pi t_1 f) + r_2 \cos[2\pi(t_1 + T)f] + nw_{\text{Re}}(f)\} \cdot win(f) \quad (15)$$

ii. Calculate the real part pseudo-cepstrum of the coefficient series, i.e.,  $\hat{r}'_{\text{Re}}(\hat{f})$ . To find out whether the peak at  $t_p = 15$  ns represents a thin layer, for example, we calculate image part of the spectrum of the estimated reflection coefficient series  $\text{Im}[\hat{r}'(f)]''$  with another Gaussian window  $win''(f)$ , i.e.,

$$\text{Im}[\hat{r}'(f)]'' = [r_{\text{Im}}(f) + nw_{\text{Im}}(f)] \cdot win''(f) \quad (16)$$

The second Gaussian window  $win''(f)$  is obtained by forward-shifting  $win(f)$ , i.e.,

$$win''(f) = win(f - (4n + 1)/4t_p) \quad (17)$$

where  $n$  is an integer which is assigned as 3 in this case.

iii. Backward-shift  $\text{Im}[\hat{r}'(f)]''$  with the same offset to obtain a new image part of the spectrum of the estimated reflection coefficient series, i.e.,

$$\text{Im}[\hat{r}'(f + (4n + 1)/4t_p)]'' = \left\{ -r_1 \sin \left[ 2\pi t_1 f + \frac{\pi(4n + 1)t_1}{2t_p} \right] - r_2 \sin \left[ 2\pi(t_1 + T)f + \frac{\pi(4n + 1)(t_1 + T)}{2t_p} \right] + nw_{\text{Im}} \left[ f + \frac{(4n + 1)}{4t_p} \right] \right\} \cdot win(f) \quad (18)$$

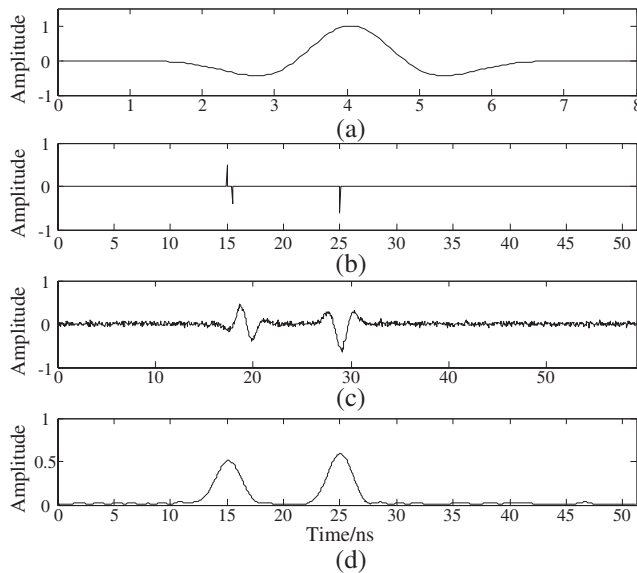


Figure 2: (a) The wavelet used as the emission wave. (b) Reflection coefficient series. (c) The synthetic signal added with 10 dB noise. (d) The real part pseudo-cepstrum of the coefficient series.

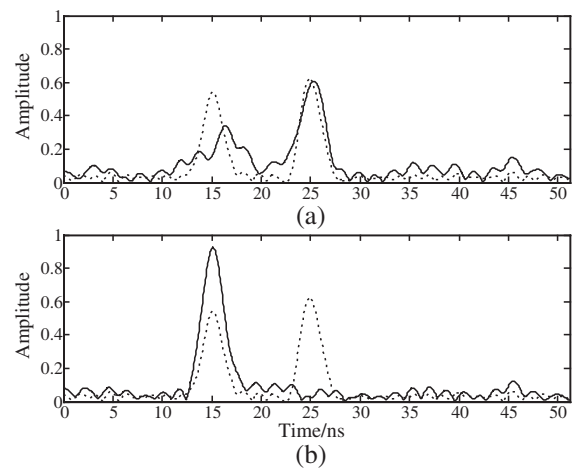


Figure 3: The dot line is the real part pseudo-cepstrum of the estimated reflection coefficient series. The solid lines are the pseudo-cepstra of the sums  $IR_s(f, t_p)$  corresponding to different window shift offsets  $t_p$ . (a)  $t_p = 15$  ns. (b)  $t_p = 25$  ns.

iv. Add (18) with (15) and calculate pseudo-cepstrum of the sum which is denoted as  $IR_s(f, t_p)$ . The disappearance of the peak would indicate the reflection from a single-interface, while strong residuals would be left if the peak represents the reflection from a thin layer. Applying the method twice with different  $t_p$ , i.e.,  $t_p$  is assigned to 15 ns for the first time and 25 ns for the second time. The results are illustrated in Fig. 3. Apparently, the outcomes of the two operations are different. The component of the single-interface reflection disappears on the pseudo-cepstrum of the sum at 25 ns. Comparatively, the residuals of the thin layer component are still obvious around 15 ns due to the existence of a second reflection coefficient at 15.5 ns.

## 5. CONCLUSION

The peak quefrency of the real part pseudo-cepstrum of the reflection coefficient series would indicate either a single-interface or a thin layer reflection. In order to tell the difference between the two situations, the real part of the spectrum of the reflection coefficient series is added with the image part of a shifted spectrum of the reflection coefficient series, and the pseudo-cepstrum of the sum  $IR_s(f, t_p)$  is calculated. The energy of the peak quefrency would disappear on the pseudo-cepstrum of the sum, if it indicates a single-interface reflection, while strong residuals would still be left if the peak quefrency indicates a thin layer. The noise would be left in either situation, thus filtering is always recommended before applying the method.

## ACKNOWLEDGMENT

This work was supported by the National Natural Science Foundation of China (Grant No. 41074077, 40774065).

## REFERENCES

1. Bogert, B. P., M. Healy, and J. W. Tukey, "The quefrency analysis of time series for echoes: Cepstrum, pseudo-autocovariance, cross-cepstrum, and saphe cracking," *Proceedings of the Symposium on Time Series Analysis*, 209–243, Wiley, 1963.
2. Hall, M., "Predicting bed thickness with cepstral decomposition," *The Leading Edge*, Vol. 25, No. 2, 199–204, 2006.
3. Zhang, W. Q., H. Liang., Y. Deng., J. Liu, and M. T. Johnson, "Time-frequency cepstral features and heteroscedastic linear discriminant analysis for language recognition," *IEEE Trans. Audio, Speech, Lang. Process.*, Vol. 19, No. 2, 266–276, 2011.
4. Reddy, T. S. and G. R. Reddy, "MST radar signal processing using cepstral thresholding," *IEEE Trans. Geosci. Remote Sens.*, Vol. 48, No. 6, 2704–2710, 2010.
5. Huang, Y. Q., J. Z. Zhang, and Q. H. Liu, "Three-dimensional GPR ray tracing based on wavefront expansion with irregular cells," *IEEE Trans. Geosci. Remote Sensing*, Vol. 49, No. 2, 679–687, 2011.
6. Huang, Y., Y. Liu, Q. H. Liu, and J. Zhang, "Improved 3-D GPR detection by nufft combined with MPD method," *Progress In Electromagnetics Research*, Vol. 103, 185–199, 2010.
7. Zhang, J. Z., Y. Q. Huang, L. P. Song, and Q. H. Liu, "Fast and accurate 3-D ray tracing using bilinear traveltime interpolation and the wave front group marching," *Geophys. J. Int.*, Vol. 184, 1327–1340, 2011.

# Design and Implementation of Bandgap References Voltage Circuit for SOC Module Applications

Min-Chin Lee, Chi-Jing Hu, and Wen-Shiang Jung  
Orient Institute of Technology, New Taipei City, Taiwan

**Abstract**— This paper proposes a low power bandgap reference voltage circuit with low temperature coefficient and independent of supply voltage for applications to power management of SOC module. The circuit provides an output reference voltage close to the bandgap voltage having a low output resistance and allows resistive loading. This proposed circuit is design and implemented using the TSMC 0.18  $\mu\text{m}$  1P6M CMOS process. Based on simulated results, the chip size is  $0.502 \times 0.583 \text{ mm}^2$  with power dissipation about 0.1 mW, and the operation temperature range from  $-40^\circ\text{C} \sim 85^\circ\text{C}$  with temperature coefficient about 25.53 ppm/ $^\circ\text{C}$ . The chip supply voltage can from 1.3 to 1.8 V with PSRR about 70 dB, and its output reference voltage can stable at 1.12 V. The variation of output reference voltage under five different corners at  $25^\circ\text{C}$  is about 4.218 mV under 1.8 V supply voltage.

## 1. INTRODUCTION

All kinds of portable electronic products in the current market have an orientation toward light, slim and small. They have both a variety of applications and long operation time. Thus a high-efficiency power management module is necessary such as low-power switching power converter or low dropout regulator to integrate with mixed-mode signal circuit into a single chip to achieve the different kinds of low-power applications [1]. Traditionally, bandgap reference voltage (BGRV) circuits are design and implemented using PMOS-input operational amplifier and resistors architecture because this OPA has wider range of input common-mode voltage and modulate the temperature coefficient of circuits [2, 3]. In this paper, we design a Negative Impedance Converter (NIC) current conveyor and current mirrors to convert the proportional to absolute temperature (PTAT) voltage into a current using a MOSFET. The current is converted back to a voltage by using the functional inverse of the MOSFET  $v$ - $i$  characteristics [4]. This makes the voltage gain linear and temperature independent. It does not use an operational amplifier and dissipates low power of 0.1 mW. And no resistors are used in its design and hence it can be fabricated in any digital CMOS technology. Therefore it is suitable for power management circuits of SOC module or low power wireless receiver applications.

## 2. ARCHITECTURE AND CIRCUIT DESIGN

This proposed bandgap reference voltage core circuit is design and implemented using Negative Impedance Converter (NIC) architecture as a current conveyor and reduces the power consumption of whole circuits [4, 5]. Figure 1 shows the core circuit of low-power bandgap reference voltage circuit. Transistors  $M_1$ ,  $M_2$ ,  $M_3$  and  $M_4$  forms a NIC circuit. Vertical substrate PNP transistors  $Q_1$  and  $Q_2$  are biased by currents in the ratio of 10 : 1 and their junction areas are in the ratio of 1 : 10. Thus, their voltage drop are  $V_{BE1}$  and  $V_{BE2}$  connected to  $M_3$  and  $M_4$  source nodes ( $R$ ,  $S$ ) between which the potential difference ( $V_{BE1} - V_{BE2} = V_{PTAT}$ ) is developed. Assuming a gain of  $A_i$  for current mirror ( $M_3, M_4$ ) and the threshold voltages of current mirror ( $M_1, M_2$ ) can be ignored. Then,

$$V_{PTAT} = V_{ON1} - V_{ON2} = \sqrt{\frac{I}{k}} - \sqrt{\frac{A_i I}{nk}} \quad (1)$$

And the output reference voltage of the proposed bandgap reference voltage circuit is shown below,

$$V_{BG} = V_{BE} + \left( \frac{\sqrt{\frac{m}{r}} - \frac{1}{\sqrt{n}}}{\alpha} \right) V_{PTAT} \quad (2)$$

where  $m$  is the current gain of mirror ( $M_3, M_5$ ),  $n$  is the ratio between ( $M_1, M_2$ ) and  $r$  is the ratio between ( $M_1, M_6$ ).

The start up circuit of this low power bandgap reference voltage circuit-NIC is composed of  $MS_1$ ,  $MS_2$  and  $MS_3$  as shown in Figure 2. We used a inverter ( $MS_1, MS_2$ ) that is temporarily closed (due to inverter input is low voltage and  $V_{S1}$  is high voltage) at power ON,  $MS_1$  turn ON,

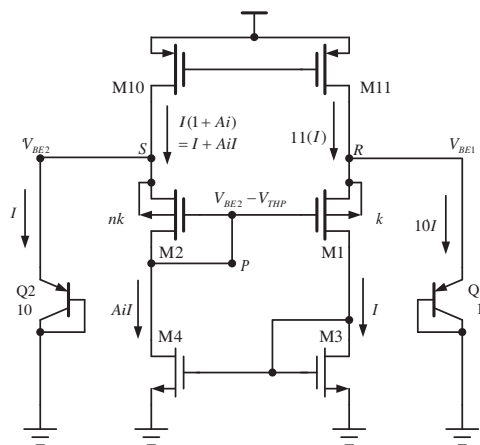


Figure 1: Proposed BGRV core circuit.

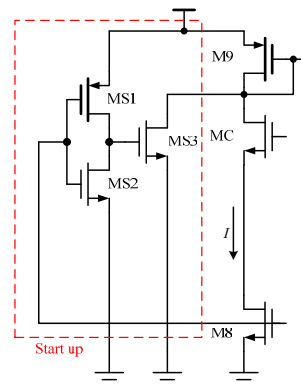


Figure 2: NIC start up circuit.

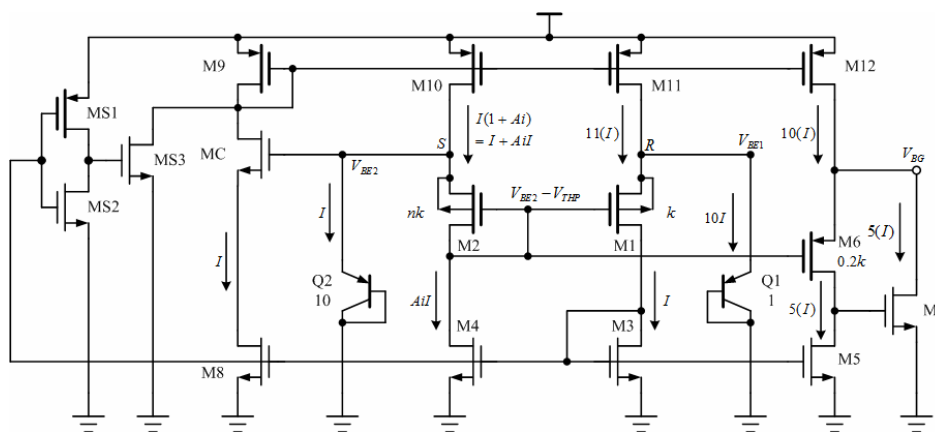


Figure 3: Proposed low power bandgap reference voltage (BGRV) circuit.

thus forcing the gate of the  $MS_3$  to a high voltage causing a current to flow  $M_9$ , then the core circuit of BGRV circuit start-up [6]. When the low power BGRV circuit operated normally, thus forcing the gate of the  $MS_2$  to a high voltage,  $MS_2$  turn ON, thus forcing the gate of the  $MS_3$  to a low voltage,  $MS_3$  turn OFF causing a current to vanish just turn OFF the start up circuit.

The output circuit configuration of the low power BGRV circuit formed by the transistors  $M_{12}$ ,  $M_5$ ,  $M_6$  and  $M_7$  is a super-source-follower circuit as shown in Figure 3. The output of source follower  $M_7$  through  $M_6$  to input of  $M_7$  forms a negative feedback, thus reduces the output impedance,  $R_{out} \approx \frac{1}{g_{m6} + g_{m6}} \left( \frac{1}{g_{m7} r_{o6}} \right)$  [7]. This gives a low output impedance for the bandgap output reference voltage source that is capable of driving resistive loads.

After summarizing the analysis of all component circuits, the full circuit and layout of the proposed low power bandgap reference voltage circuit are shown in Figures 3 and 4. And the chip size is about  $0.502 \times 0.583 \text{ mm}^2$  [8, 9].

### 3. SIMULATION RESULT

By using TSMC  $0.18 \mu\text{m}$  CMOS 1P6M process to simulate the designed BGRV circuit, the result of pre- and post-sim under five different corners are shown below. Figure 5 shows the transient response of reference output voltage  $V_{BG}$  of BGRV circuit can stable at  $1.12 \text{ V}$  within  $100 \mu\text{s}$  steadily under five different corners when supply power ON. Figures 6(a) and (b) show the reference output voltage variation is about  $22 \text{ mV}$  (pre-sim) and  $0.9 \text{ mV}$  (post-sim) that as a function of range of input voltage from  $1.3 \text{ V}$  to  $1.8 \text{ V}$  under different corners, and reference output voltage  $V_{BG}$  of BGRV circuit about  $1.12 \text{ V}$ .

Figures 7(a) and (b) show the temperature coefficient of circuit about  $23.53 \text{ ppm}/^\circ\text{C}$  (Pre-sim) and  $30.1 \text{ ppm}/^\circ\text{C}$  (post-sim) under the TT corner which operation temperature from  $-40^\circ\text{C} \sim 85^\circ\text{C}$ . And the variation of output reference voltage under five different corners at  $25^\circ\text{C}$  is about

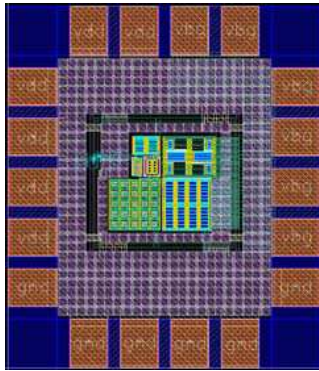


Figure 4: Layout of BGRV circuit.

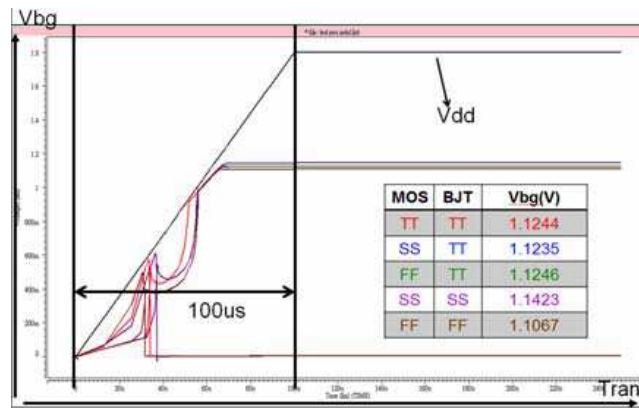
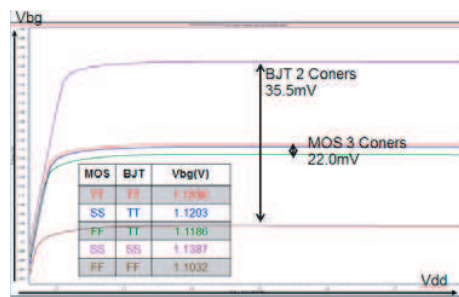
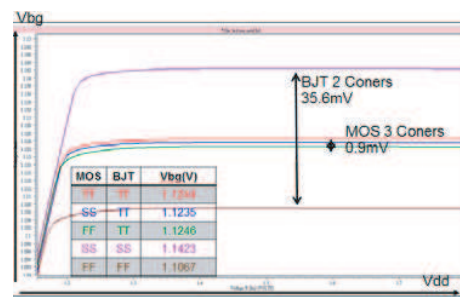


Figure 5: Transient response of BGRV circuit (Post-sim).

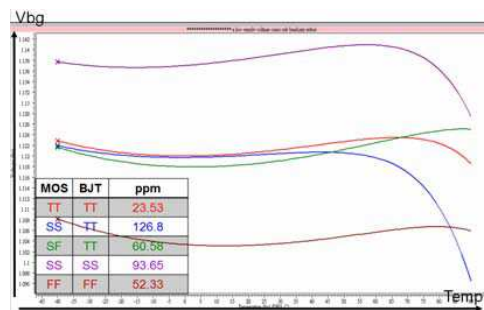


(a)

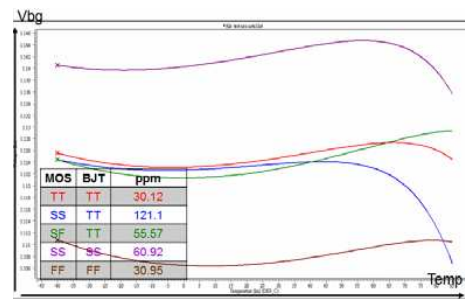


(b)

Figure 6: Reference output voltage variation for (a) Pre-sim and (b) Post-sim.



(a)



(b)

Figure 7: Temperature coefficient of BGRV circuit for (a) Pre-sim and (b) Post-sim.

Table 1: Corner case simulation.

Spec.	MOS TT	MOS SS	MOS FF	BJT SS	BJT FF
Supply Voltage (V)	1.35 to 1.8				
Temperature Coefficient (ppm/°C)	30.12	121.1	55.57	60.92	30.95
Output Voltage(V)	1.1244	1.1235	1.1246	1.1423	1.1067

4.218 mV supply voltage operated at 1.8 V.

Figures 8(a) and (b) show the Power Supply Reject Ratio (PSRR) of output reference voltage of this chip is about 68.8 dB (pre-sim) and 70 dB (post-sim), respectively.

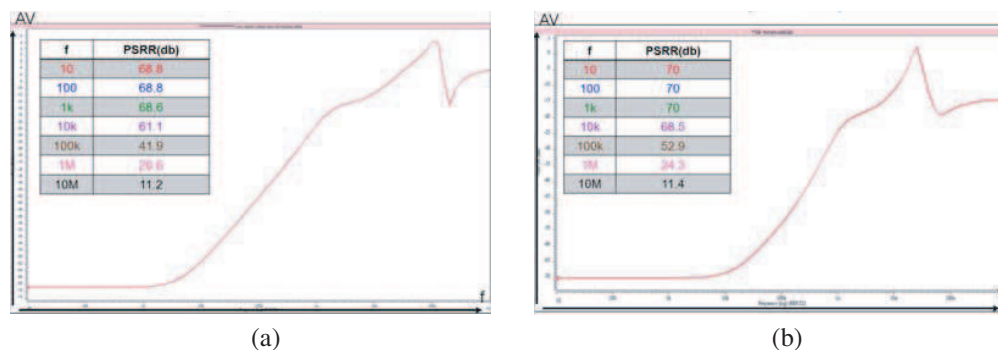


Figure 8: PSRR of BGRV circuit for (a) Pre-sim and (b) Post-sim.

#### 4. CONCLUSIONS

Based on the aforementioned discussions, we can conclude that the implemented low power bandgap reference voltage circuit has the chip size  $0.502 \times 0.583 \text{ mm}^2$  and power dissipation about 0.1 mW. The chip supply voltage can from 1.3 to 1.8 V with PSRR about 70 dB, and its output reference voltage can stable at 1.12 V. The temperature coefficient of circuit about  $23.53 \sim 30.1 \text{ ppm}/^\circ\text{C}$  under the TT corner which operation temperature from  $-40^\circ\text{C} \sim 85^\circ\text{C}$ . And the variation of output reference voltage under five different corners at  $25^\circ\text{C}$  is about 4.218 mV under 1.8 V supply voltage. Finally, Table 1 shows a corner case simulation result about the temperature coefficient and output reference voltage of proposed bandgap reference voltage circuit.

#### ACKNOWLEDGMENT

The authors would like to thank the Chip Implementation Center (CIC) of the National Science Council, Taiwan, R.O.C., for supporting chip manufacturing.

#### REFERENCES

1. Leung, K. N., P. K. T. Mok, and S. K. Lau, "A low-voltage CMOS low-dropout regulator with enhanced loop response," *IEEE International Symposium on Circuits and System*, Vol. 1, 385–388, May 2004.
2. Holberg, A., *CMOS Analog Circuit Design*, McGraw-Hill, 2004.
3. Razavi, B., *Design of Analog CMOS Integrated Circuits*, International Edition, McGraw-Hill, 2001.
4. Brennan, R. L., T. R. Viswanathan, and J. V. Hanson, "The CMOS negative impedance converter," *IEEE J. Solid-State Circuits*, Vol. 5, 1272–1275, Oct. 1988.
5. Becker-Gomez, A., T. Lakshmi Viswanathan, and T. R. Viswanathan, "A low supply voltage CMOS sub-bandgap reference," *IEEE Transactions on Circuits and Systems II: Express Briefs*, Vol. 55, No. 7, 609–613, Jul. 2008.
6. Boni, A., "OP-amps and startup circuits for CMOS bandgap references with near 1-V supply," *IEEE J. Solid-State Circuits*, Vol. 37, No. 10, 1339–1343, Oct. 2002.
7. Gray, P. R., P. J. Hurst, S. H. Lewis, and R. G. Meyer, *Analysis and Design of Analog Integrated Circuits*, John Willy & Sons, Inc., 2003.
8. Huang, H.-Y., "Lab for analog integrated circuits design," 2003.
9. Huang, H.-Y., "Analysis of mixed-signal IC layout," 2006.

# Spatial Interpolation for Mapping Geoclimatic Factor $K$ in South Africa

M. O. Asiyó and T. J. O. Afullo

Department of Electrical, Electronic and Computer Engineering  
University of KwaZulu-Natal, King George V Ave., Durban 4041, South Africa

**Abstract**— A deep fading prediction technique is the most important element of practically all methods for estimating multipath outage probability on terrestrial microwave line-of-sight links (LOS). Most of these techniques are based on empirical fits of Rayleigh-type distributions to the fading data for individual countries and are characterized in terms of climatic conditions. ITU-R provides a global method for predicting the percentage of time that a certain fade depth is exceeded in the average worst month. Apart from link variables, the ITU-R method, has additional variable the geoclimatic factor  $K$ . This variable takes into account the variability of climate and terrain. It is recommended that the geoclimatic factor  $K$  be obtained from fading data in the vicinity links of the planned link if such data exist. However, since in most cases such data is not available, prediction methods based on refractivity gradient statistics are recommended. In this paper, geoclimatic factor  $K$  derived from radiosonde data for five locations in South Africa are used to estimate and map the values for all the regions in South Africa. Three spatial interpolation techniques: Kriging, Inverse Distance Weighting and Thin-Plate Spline are used in estimating the geoclimatic factor in places where data is not observable. Statistical assessment of these methods is done by calculating the mean absolute error (MAE) and the root mean square error (RMSE) between a set of control points and the interpolated results. The best performing method estimated values is used to map the seasonal geoclimatic factor  $K$  for the entire study region. The estimated values of geoclimatic factor will improve accuracy in predicting multipath outage in LOS links in the region.

## 1. INTRODUCTION

Spatial interpolation techniques have been applied in varied fields of study to create a continuous surface data for informed decisions. It has found applications in climatology [1, 2], in electromagnetic field estimation [3, 4], in radioactive contamination [5], aerospace engineering [6], in optics [7], among others. The challenge is always the choice of the best interpolation method to be used and the best performance analysis criteria [3, 8]. In this study we employ three mostly used techniques: Inverse distance weighting (IDW), Kriging and Thin-plate spline.

There is no single preferred method for data interpolation. Choice of method depends on actual data, level of accuracy required, the time and/or computer resources available, quality of secondary information, data variance, grid size or resolution and surface type [3, 8]. In this study, we describe three methods: kriging, thin-plate spline and inverse distance weighting. Techniques that produce smooth surfaces include various approaches that may combine regression analyses and distance-based weighting averages. The key difference among the methods is the criteria used in weight values in relation to distance [1].

## 2. SPATIAL INTERPOLATION TECHNIQUES

Spatially continuous data or spatially continuous surfaces over a region of interest are needed by scientists to make acceptable analyses. However, such data are usually not available and often very difficult and costly to obtain. Additionally, environmental data collected from the field are usually from point sources. Therefore, the values of an attribute at unsampled points need to be estimated in order to generate spatially continuous data. Spatial interpolation techniques provide tools for estimating the values of unobserved variable at unsampled sites using data from point observables [8].

### 2.1. Kriging

There are very many types of kriging, but here we discuss the so called *ordinary kriging*. Kriging uses linear combination of values at observable points to estimate values at un-observable points. It is popular because it is an exact interpolator, i.e., the predictor for an input that has already been observed equals the observed output. The predicted value  $Z_{po}$  is given by Eq. (1) where  $Z_{oi}$

are the observable values and  $\kappa_i$  are the Kriging weights [4, 5]:

$$Z_{po} = \sum_i^N \kappa_i \cdot Z_{oi} \quad (1)$$

with the constraint that;

$$\sum_i^N \kappa_i = 1 \quad (2)$$

Kriging assumes that the closer the input data are, the more positively correlated are their outputs. Kriging is modelled through a covariance process that is second-order stationary, which implies that the first two statistical moments (the means and the covariance) are constant [4, 6]. Kriging is modelled through a semi-variogram. Semi-variogram is a mathematical function that indicates the spatial autocorrelation in observations measured at sample points or locations. It is represented in a graph that shows the semi-variance in measure with distance between the sampled locations. It characterizes the spatial continuity or smoothness of a set of data [9]. From the semi-variance cloud graph, we develop a model that describes the variability of the measure with location. The model developed also acts as a prediction tool for estimating the value of a measure at an un-observed position or location. Some of the commonly used semi-variogram models include; spherical, exponential and Gaussian.

## 2.2. Thin Plate Spline

Thin-plate spline is a deterministic interpolation technique with a local stochastic component that represents two dimensional curves on three dimensional surfaces [1]. The thin-plate spline derives its name from the physical situation of bending of a thin surface. It minimizes the bending energy of a thin plate clamped at data points [7]. It is flexible on how closely they fit the data points. Thin-plate spline function can vary from a surface that exactly interpolates data, to an increasing smooth function and in some cases a plane depending on the user defined smoothing parameter. Its accuracy, therefore depends on its smoothing parameter, hence the important aspect of thin-plate splines is on how to optimize this smoothing parameter [2]. A thin plate spline can be represented by the model [2]:

$$z_i = g(x_{1i}, \dots, x_{di}) + \epsilon_i \quad i = 1, \dots, n \quad (3)$$

where  $n$  is the number of data samples,  $g$  is the slowly varying continuous function and  $\epsilon_i$  is the realization of the random variable  $\epsilon$ . The function  $g$  is assumed to be a continuous long range variable in the process measured by  $z_i$ , with independent zero mean and a variance  $\sigma^2$ . The task in thin plate splines interpolation is to find the process  $g$  by a suitable continuous function. A thin plate smoothing spline is produced by minimizing the optimization problem (4) [7]:

$$\frac{1}{n} \sum_{i=1}^n (z_i - f_i)^2 + \omega J_m^d(f) \quad (4)$$

over functions  $f \in \Gamma$ , where  $\Gamma$  is a space of functions of  $m$ -derivatives in  $d$ -dimensions,  $\omega$  is a fixed smoothing parameter and  $J_m^d$  is a measure of roughness of the function  $f$  in terms of  $m$ th order partial derivatives.  $f_i$  are values of the fitted function at the  $i$ th data point. The smoothing parameter is calculated by minimizing the generalized cross validation (GCV).

## 2.3. Inverse Distance Weighting

Like other spatial interpolation technique, Inverse Distance Weighting (IDW) is used in data analysis to estimate a set of observations related with a set of sampled points or places to a set of un-sampled points or places where observations are not available [10]. The inverse distance weighting or inverse distance weighted (IDW) method estimates the values of an attribute at un-sampled points using a linear addition of values at sampled points weighted by an inverse function of the distance from the point of interest to the sampled points [3]:

$$Z'(x_o) = \sum_{i=1}^n \lambda_i Z(x_i) \quad (5)$$

where  $Z'$  is the estimated value of an attribute at the point of interest  $x_o$ ,  $Z$  is the observed value of the sampled point  $x_i$ ,  $\lambda_i$  is the weight allocated to the sample point and,  $n$  represents the number of sampled points used for approximation. The weighting bias can be represented by (6), where  $d_i$  is the distance between  $x_o$  and  $x_i$ ,  $p$  is a power parameter, and  $n$  is as defined previously [3]:

$$\lambda_i = \frac{\frac{1}{(d_i)^p}}{\sum_{i=1}^n \frac{1}{(d_i)^p}} \quad (6)$$

with the constraint that,

$$\sum_{i=1}^n \lambda_i = 1 \quad (7)$$

### 3. METHODOLOGY

#### 3.1. Data Collection and Processing

Seasonal geoclimatic factor is derived from three year radiosonde data for five regions in South Africa. The three year radiosonde soundings is taken twice per day and were reported after every ten seconds, which gives a fairly good height resolutions. The estimation of geoclimatic factor is for five regions in South Africa is not shown here, but the reader is referred to [11] for details. The sounding data processing, analysis and representation was carried out using PAST version 2.16 (July 2012) and MATLAB version 2010a. PAST is a free software tool distributed under GNU/GPL licence. It is a data analysis package that includes common statistical, plotting and modelling functions. Interpolation of data was done using PAST and plotting of contours was done in MATLAB.

#### 3.2. Error Analysis

There are very many measures of fit for error analysis, in our study, we have applied the mean absolute error (MAE) and the root mean squared error (RMSE). RMSE provides measure of error but is sensitive to outliers as it places a lot of weight to large errors whereas MAE is less sensitive to extreme values. However, they are among the best measures of performance of a model because they summarize the mean different in units of predicted and observed values [8].

Control sites where discrete data exists are used in performance analysis by removing these observed values from data to be processed and then using interpolation techniques to predict these observed values (i.e., cross validation). Error calculation is then done using (8) and (9). The method that gives the minimum values of error is assumed to be the best performing method.  $P_i$  is the predicted value and  $O_i$  is the observed value at various control sites, and  $n$  is the number of control sites. The control points are chosen randomly for large data points, however, where data points are few, all points become control points.

$$RMSE = \frac{1}{n} \sum_{i=1}^n (P_i - O_i)^2 \quad (8)$$

$$MAE = \frac{1}{n} \sum_{i=1}^n |P_i - O_i| \quad (9)$$

### 4. RESULTS AND DISCUSSION

The interpolation process was carried out using Inverse distance weighting, Thin-plate spline and ordinary Kriging. Three models of variogram were used in Kriging: Spherical, Exponential and Gaussian. It should be noted that the algorithms calculate the raster layer, considering all pixels within the rectangle defined by the latitudes and longitudes and may at times fall out of the intended South African region. It is therefore important for one to know the longitudes and latitudes for the region/place of interest.

Table 1 shows the measures of fit carried out. From the interpolation results, it was found that the lowest MAE and RMSE is recorded by Inverse distance weighting method for all the seasons. Hence we can conclude that IDW is the best performing method in this study. This is then followed by Kriging. Kriging performance is influenced by the variogram model used. For our data set, the exponential model has the lowest error among the three variogram models, followed by spherical model. At some points the error between the exponential model and spherical model is negligible.

The Gaussian model fit seems to be the worst performing kriging model. The worst performing techniques is Thin-plate spline. The performance of Thin-plate spline can be attributed to the nature of our data. Thin-plate spline works well with data sets with gently varying surfaces (data sets having low variance). Some contours show geoclimatic factor to be zero, which cannot be the case. These points are far away from the discrete data points, hence the influence of the discrete data points tends to zero, giving this abnormality. Figure 1 shows the contour maps for seasonal geoclimatic factor for February, May, August and November using Inverse Distance Weighting technique. Contour maps for other methods are not shown here but their error analysis is given in Table 1.

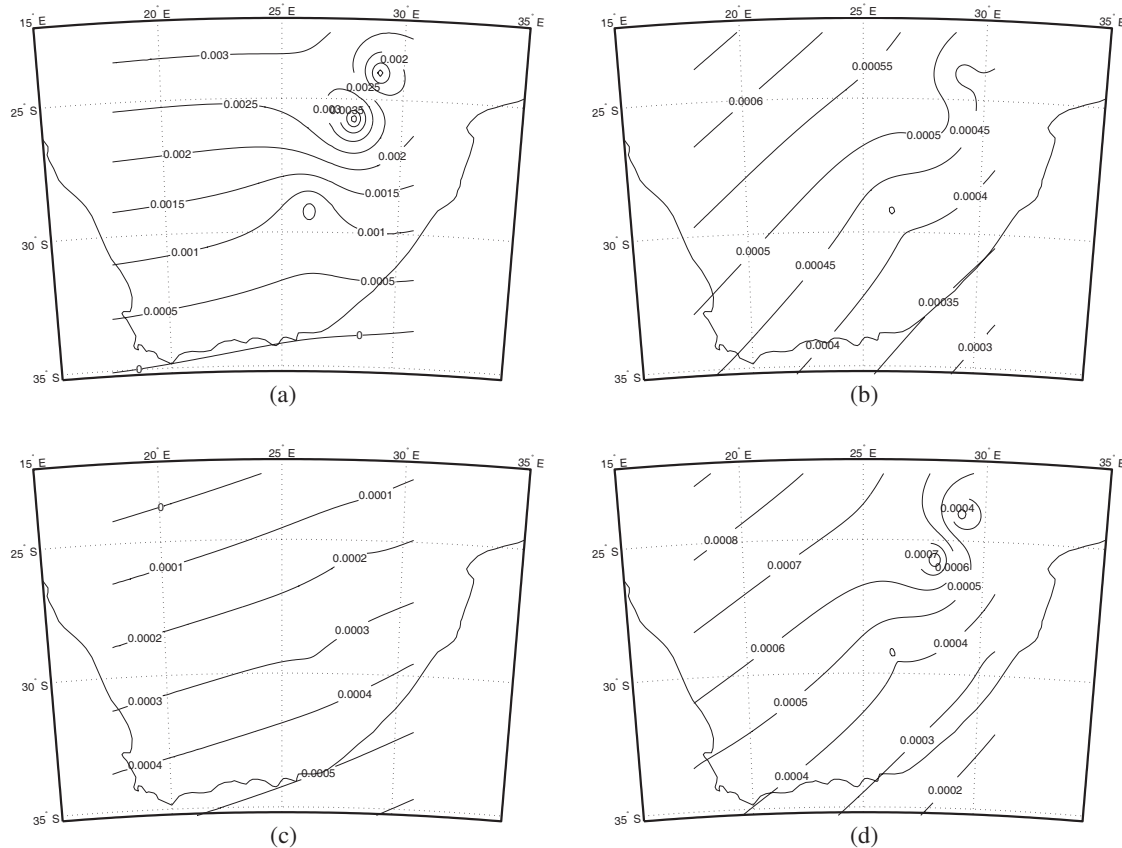


Figure 1: Contour maps for geoclimatic factor  $k$  for South Africa using Inverse Distance Weighting for (a) February, (b) May, (c) August and (d) November.

Table 1: Error analysis applied to interpolation techniques.

Measure of fit	IDW	Spline	Kriging			
			Spherical	Exponential	Gaussian	
Feb.	RMSE	$1.59 \times 10^{-3}$	$5.58 \times 10^{-3}$	$2.36 \times 10^{-3}$	$2.28 \times 10^{-3}$	$2.45 \times 10^{-3}$
	MAE	$1.16 \times 10^{-3}$	$5.37 \times 10^{-3}$	$1.81 \times 10^{-3}$	$1.73 \times 10^{-3}$	$1.92 \times 10^{-3}$
May	RMSE	$5.10 \times 10^{-5}$	$2.04 \times 10^{-4}$	$7.69 \times 10^{-5}$	$7.44 \times 10^{-5}$	$8.13 \times 10^{-5}$
	MAE	$4.04 \times 10^{-5}$	$1.96 \times 10^{-4}$	$6.28 \times 10^{-5}$	$6.06 \times 10^{-5}$	$6.82 \times 10^{-5}$
Aug.	RMSE	$1.68 \times 10^{-5}$	$8.95 \times 10^{-5}$	$2.60 \times 10^{-5}$	$2.60 \times 10^{-5}$	$3.36 \times 10^{-5}$
	MAE	$1.41 \times 10^{-5}$	$7.98 \times 10^{-5}$	$2.35 \times 10^{-5}$	$2.40 \times 10^{-5}$	$3.19 \times 10^{-5}$
Nov.	RMSE	$2.29 \times 10^{-4}$	$6.48 \times 10^{-4}$	$3.32 \times 10^{-4}$	$3.23 \times 10^{-4}$	$3.40 \times 10^{-4}$
	MAE	$1.64 \times 10^{-4}$	$5.84 \times 10^{-4}$	$2.38 \times 10^{-4}$	$2.33 \times 10^{-4}$	$2.47 \times 10^{-4}$

## 5. CONCLUSION

In this submission, it can be concluded that Inverse distance weighting gives the best performance in interpolating the geoclimatic factor  $K$ . Geoclimatic factor depend on the variability of the atmosphere specifically temperature, pressure and relative humidity. If we assume that regions close to each other tend to exhibit the same climatic conditions, then, we can ascertain that IDW is the best method for interpolating the geoclimatic factor. However, it is also known that the geoclimatic factor also depends on the topology of the area in addition to climatic conditions, hence more study need to be done on this by incorporating fading data of given regions to the climatic conditions for a more decisive conclusion on the distribution of this factor in the region of study. It can be shown that different techniques used in evaluation give different results making it a must to choose the best technique which gives the minimum error of performance. The best technique can further be optimized for better accuracy. The IDW here can be optimized by adjusting the power parameter and the search radius.

## REFERENCES

1. Hartkanp, A. D., K. De Beurs, A. Stein, and J. W. White, "Interpolation techniques on climate change," *International Maize and Wheat Improvement Centre*, Netherlands, 1999.
2. Hancock, P. A. and M. F. Hutchison, "Spatial interpolation of large climate data sets using bivariate thin plate smoothing splines," *Environmental Modelling and Software*, Vol. 21, 1684–1694, 2006.
3. Azpurua, M. and K. D. Ramos, "A comparison of spatial interpolation methods for estimation of average electromagnetic field magnitude," *Progress In Electromagnetics Research M*, Vol. 14, 135–145, September 2010.
4. Triantafyllis, J, I. O. A. Odeh, and A. B. McBratney, "Five geostatistical models to predict soil salinity from electromagnetic induction data across irrigated cotton," *Soil Science Society AM. J.*, Vol. 65, 869–878, June 2001.
5. Savelieva, E., "Using ordinary kriging to model radioactive contamination data," *Applied GIS*, Vol. 1, No. 2, 1–10, Mornash University Press, 2005.
6. Simpson, T. W, T. M. Mauery, J. J. Korte, and F. Mistree, "Kriging models for global approximation in simulation-based multidisciplinary design optimization," *AIAA Journal*, Vol. 39, No. 12, 2233–2241, December 2001.
7. Simpson, T. W., "Efficient thin plate spline interpolator and its applications to adaptive optics," MS.c. Thesis, Johannes Kepler University, Linz, Austria, August 2010.
8. Jin, L. and A. D. Heap, "A review of comparative studies of spatial interpolation methods in environmental sciences: Performance and impact factors," *Ecological Informatics*, Vol. 6, 228–241, December 2011.
9. Gunes, H., H. E. Cekli, and U. Rist, "Data enhancement, smoothing, reconstruction and optimization by kriging interpolation," *Proceedings of the 2008 Winter Simulation Conference*, 379–386, 2008.
10. Lystad, S. L, T. G. Hayton, A. K. Marsh, and T. Tjelta, "Interpolation of clear air parameters observed at non-regular observation locations," *Proceedings of URSI CLIMPARA Commission F Open Symposium on Climatic Parameters in Radiowave Propagation Predictions*, Ottawa, Canada, April 27–29, 1998.
11. Asiyo, M. O. and T. J. O. Afullo, "Statistical estimation of fade depth and outage probability due to multipath propagation in Southern Africa," *Progress In Electromagnetics Research B*, Vol. 46, 251–274, 2013.

# Non-parametric and Parametric Modelling and Characterization of the Effective Earth Radius Factor for South Africa

A. M. Nyete and T. J. O. Afullo

Department of Electrical, Electronic and Computer Engineering  
University of Kwa-Zulu Natal, South Africa

**Abstract**— The effective earth radius factor ( $k$ -factor) is an important parameter in the planning and design of both terrestrial microwave and UHF/VHF line-of-sight links. It is for this reason that the structure and variations in the effective earth radius factor in the first 200 m of the atmosphere is critical to radio link planners and optimization engineers alike. The atmospheric composition changes from time to time, place to place and even with height and hence the need for accurate determination and prediction of the  $k$ -factor. The four thirds ( $4/3$ ) value given for the median  $k$ -factor in average temperate climate should only be used for gross planning but where data is available, the actual values of the same should be determined. This will ensure well designed links with minimum outage experienced due to  $k$ -factor related problems, i.e., diffraction ( $k$ -type) fading and thus avoiding expensive reverse engineering and optimization procedures. In this presentation, three years radiosonde measurements data sourced from the South African Weather Service (SAWS) has been processed and only  $k$ -factor statistics for the first 200 m above ground level considered for further analysis. Both non-parametric and parametric methods have been used to model solutions for the distribution characteristics of the  $k$ -factor across seven locations in South Africa. For the non-parametric approach, the kernel density estimate has been used. The so-called ‘curve-fitting’ method (Gaussian distribution modelling) has been used for the parametric technique. The Integral of Squared Error (ISE) has been applied to optimize the solutions in both cases. Using the foregoing procedures, both median ( $k_{50\%}$ ) and  $k$ -factor values exceeded 99.9% of the time ( $k_e$ ) have been determined. From the results, the kernel estimates are found to out-perform the curve-fitting method in terms of the ISE. Also, we observe that both techniques give very close values and so the error performance may be the only key performance indicator between both. The Rectangular kernel is observed to produce superior ISE performance in five out of the seven locations considered. It thus comes out as the more favourable kernel compared to the other three kernels used, i.e., Gaussian, Triangular and Epanechnikov kernel. It is also observed that with the optimum choice of the window width or bandwidth,  $h$ , there is little to choose from in terms of the kernel function,  $K(k)$ . Finally, we draw comparisons between the measured, curve-fitting and kernel values of the  $k$ -factor obtained.

## 1. INTRODUCTION

Clear air research advances in the recent past has been vigorous in South Africa. Palmer and Baker [1–4] have developed a cumulative distribution model for predicting the effective earth radius factor for South Africa. Afullo et al. [5–10] have also reported on the refractivity and  $k$ -factor statistics for Maun in Botswana and Durban in South Africa. For Botswana, they found the all year median value of the  $k$ -factor to be 1.1 and that of the effective value to be 0.61 for 0–200 m height range and 0.7 for the 0–500 m range. They also found median and effective  $k$ -factor values of 1.21 and 0.5 respectively for Durban, 0–500 m height range. Most recently, Fulgence [11] has also worked on refractivity and  $k$ -factor ranges for Central Africa; particularly in Rwanda and Tanzania. Also, in Nigeria, there has been a continued campaign for the determination of refractivity and refractivity gradient statistics mainly within the first 300 m of the atmosphere [12, 13].

## 2. ATMOSPHERIC RADIO REFRACTION

Electromagnetic waves propagating in the atmosphere do not travel in straight line but are bent (refracted) either towards or away from the earth’s surface depending on the value refractive index. The refractive index,  $n$ , is defined as the ratio of the ratio of the velocity of the propagation of an electromagnetic wave in a vacuum to that of the velocity in a medium. It is given by [10]:

$$n = \frac{c}{v} = \sqrt{\mu\varepsilon} = 1 + N \times 10^{-6} \quad (1)$$

where  $c$  is the speed of a radio wave in a vacuum (free space),  $v$  is the speed of a radio wave in air,  $\mu$  is the relative permeability,  $\varepsilon$  is the relative permittivity,  $N$  is the radio refractivity and  $n$  is the refractive index.

The radio refractivity changes with height above ground level. Its vertical gradient is particularly of great importance in the determination of the point  $k$ -factor statistics. The following equation is used to calculate the  $k$ -factor [2]:

$$k = \left[ 1 + \left( \frac{dN}{dh} \right) / 50\pi \right]^{-1} \quad (2)$$

where  $k$  is the effective earth radius factor and  $\frac{dN}{dh}$  is the vertical refractivity gradient.

### 3. PARAMETRIC AND NON-PARAMETRIC DATA TECHNIQUES

Parametric methods of data modelling are described by quantities commonly referred to as parameters which normally give a brief summary of the data structure. Of the many parameters used, the mean, median, standard deviation and variance always feature at the top. Such methods are therefore based on distributional assumptions of the data characteristics. The curve-fitting approach adopted in this paper, therefore falls in this category of data modelling.

On the other hand, non-parametric techniques make no assumptions as to the basic form of the variable under study. Of these, the two most common ones are the histograms and kernel density estimates. The kernel method performs better than the histogram and was actually introduced to counter the limitations associated with histograms. With kernel density estimation, a ‘bump’ is placed on each data point. The shape of this bump is determined by the kernel function,  $K(k)$  and the overall data distribution is determined by the choice of the bandwidth,  $h$ . A very small value of  $h$  will result in estimates that are spiky in nature and difficult to interpret while a very big choice will result in over-smoothed estimates which will obscure fine details of the data structure, e.g., bi-modality.

### 4. MODELLING AND CHARACTERIZATION

Two different approaches were adopted for the task, i.e., the curve-fitting method and the kernel density estimation.

#### 4.1. Curve-fitting Method

Previous work on the effective earth radius factor for Botswana by Afullo et al. [9] revealed that the distribution of the  $k$ -factor is bell-shaped, centred almost on a median value,  $u_k$ . From this observation, Afullo and Odedina [10] later developed an algorithm for modelling the probability density function (pdf) of the  $k$ -factor. They proposed the following pdf,  $f(k)$  [10],

$$f(k) = Ae^{-\alpha(k-\mu_k)^2} \quad (3)$$

They found that the relationship between  $A$  and  $\alpha$  is that of a normal (Gaussian) distribution. Using the algorithm in [10] and radiosonde data measurements obtained from South African Weather Service (SAWS), three-year Gaussian distribution models of the  $k$ -factor for seven locations in South Africa have been developed.

#### 4.2. Kernel Density Estimation

Kernel density estimate of a variable  $k$  is given by [14, 15]:

$$f(k) = \frac{1}{nh} \sum_{i=1}^n K\left(\frac{k - X_i}{n}\right) \quad (4)$$

where  $h$  is the window width, bandwidth or smoothing parameter (depends on literature),  $n$  is the number of samples and  $X_i$  is the  $i$ th observation. Optimal kernel models are only possible when the value of the  $h$  chosen is such that the error performance (typically the Integral Squared Error, ISE) is at the minimum. The ISE is given by [6]:

$$\text{ISE} = \int_{-\infty}^{\infty} [f(k) - f^*(k)]^2 dk \quad (5)$$

Optimal bandwidth determination has been a subject of great research, but no single plug-in method will give the optimum value of  $h$ . Thus all the formulae for computing the optimum value of the

window width will only give an estimate of the optimum  $h$  to start with. Several iterations may be the only sure way to get the global minimum error, thus the optimum value of  $h$ . Silverman’s rule-of-thumb gives a good starting point for optimizing  $h$ . This rule is based on a Gaussian distribution assumption and is summarized by the following expression [14]:

$$h = (4/3n)^{0.2} * \sigma \tag{6}$$

where  $n$  is the number of samples and  $\sigma$  is a robust estimate of the sample standard deviation. The kernels used in this presentation and their efficiencies are shown in Table 1 below [6, 17].

Table 1: Kernels used and their efficiencies.

Kernel	Kernel function, $K(k)$	Efficiency (%)
Epanechnikov	$K(k) = \begin{cases} \frac{3}{4\sqrt{5}}(1 - \frac{1}{5}k^2), & -\sqrt{5} \leq k \leq \sqrt{5} \\ 0, & \text{elsewhere} \end{cases}$	100
Triangular	$K(k) = \begin{cases} \frac{15}{16}(1 -  k ), & -1 \leq k \leq 1 \\ 0, & \text{elsewhere} \end{cases}$	98.6
Gaussian	$K(k) = \frac{1}{\sqrt{2\pi}} e^{-\frac{k^2}{2}}, -\infty < k < \infty$	95.1
Rectangular	$K(k) = \begin{cases} \frac{1}{2}, & -1 \leq k \leq 1 \\ 0, & \text{elsewhere} \end{cases}$	93

### 5. RESULTS AND DISCUSSIONS

Results for the curve-fitting and kernel methods are presented. Figures 1–7 show the curve-fitting plots for the seven locations. Due to space considerations, only the kernel that produces the

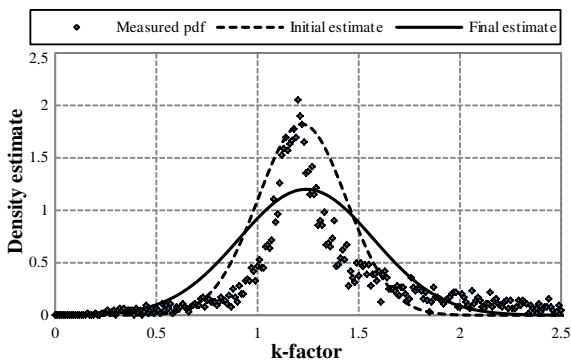


Figure 1: Bloemfontein Gaussian curve-fitting estimate, 200 m a.g.l.

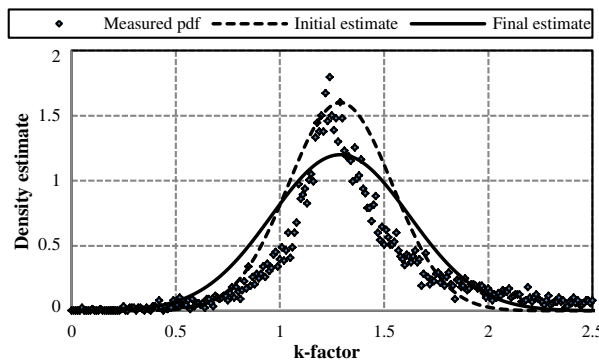


Figure 2: Cape Town Gaussian curve-fitting estimate, 200 m a.g.l.

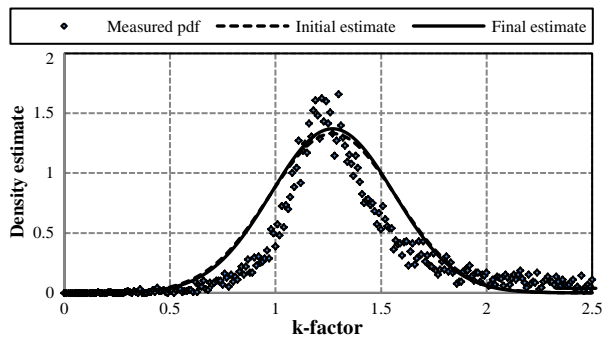


Figure 3: Durban Gaussian curve-fitting estimate, 200 m a.g.l.

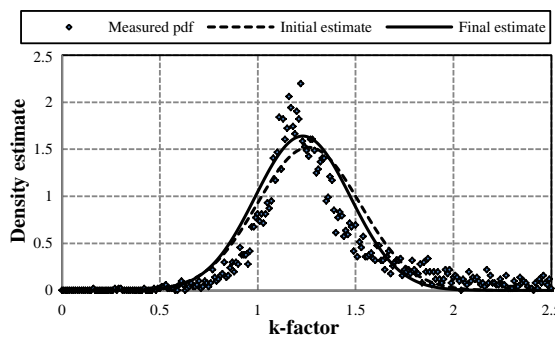


Figure 4: Polokwane Gaussian curve-fitting estimate, 200 m a.g.l.

best ISE performance for each location is plotted in this presentation. These plots are presented in Figures 8–14. Table 2 shows the Gaussian distribution models of the  $k$ -factor for the seven locations. From the results in Table 2, the curve-fitting median  $k$ -factor for Bloemfontein is found to be 1.24, while it is 1.29 and 1.27 for Cape Town and Durban respectively. It is found to be 1.23 for Polokwane, 1.19 for Pretoria, 1.17 for Uppington and 1.20 for Bethlehem. A tabulation of the curve-fitting parameter  $A$ , median  $k$ -factor,  $\mu_k$  and ISE values for the curve-fitting method are presented in Table 3.

From this table, Bethlehem is found to produce the worst error performance for the curve-fitting method while Durban is the best. The initial estimate is the first estimate obtained using values from the measured pdf. The final estimate represents the best estimate in that it is the one where minimum error is achieved. Kernel results of the median  $k$ -factor,  $h$  and ISE values are presented in Table 4. The kernel median  $k$ -factor is seen to vary between 1.21 to 1.22 for Bloemfontein, 1.26 to 1.27 for Cape Town, 1.25 to 1.26 for Durban, 1.25 to 1.26 for Polokwane, 1.20 to 1.21 for Pretoria,

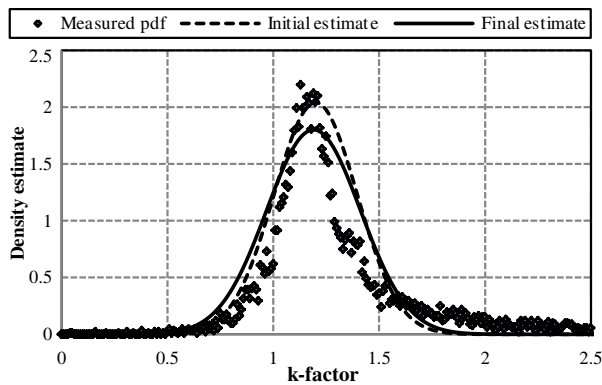


Figure 5: Pretoria Gaussian curve-fitting estimate, 200 m a.g.l.

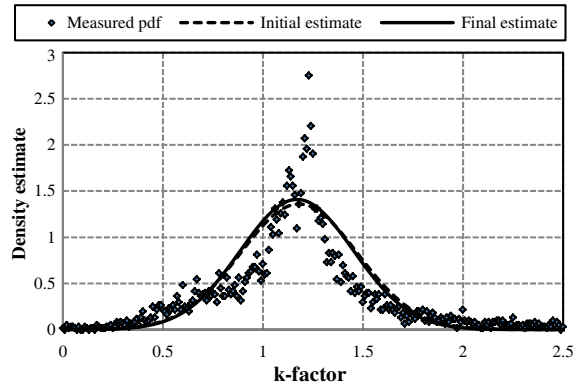


Figure 6: Uppington Gaussian curve-fitting estimate, 200 m a.g.l.

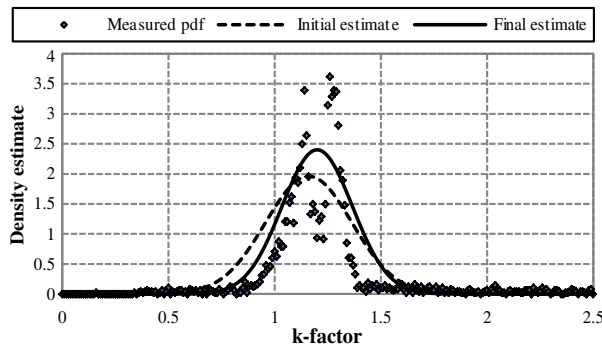


Figure 7: Bethlehem Gaussian curve-fitting estimate, 200 m a.g.l.

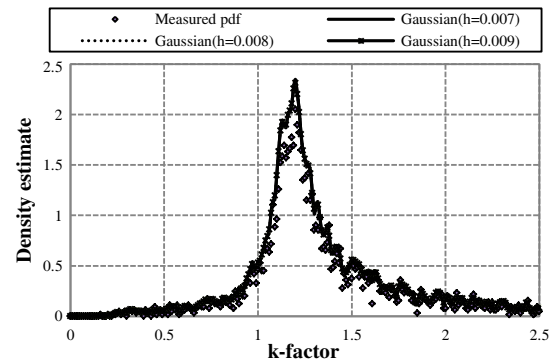


Figure 8: Bloemfontein Gaussian kernel density estimate, 200 m a.g.l.

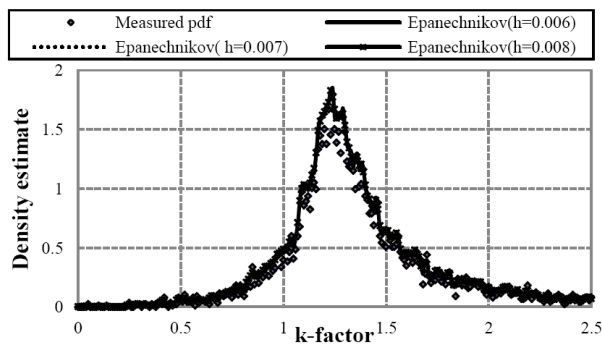


Figure 9: Cape Town Epanechnikov kernel density estimate, 200 m a.g.l.

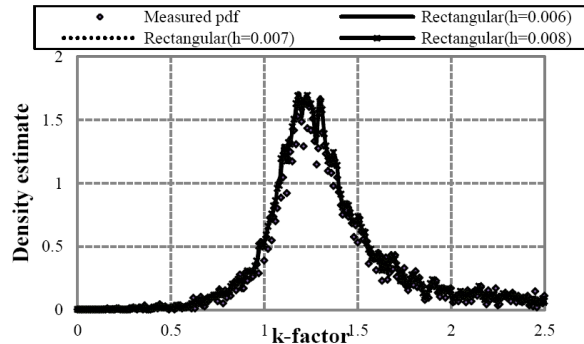


Figure 10: Durban rectangular kernel density estimate, 200 m a.g.l.

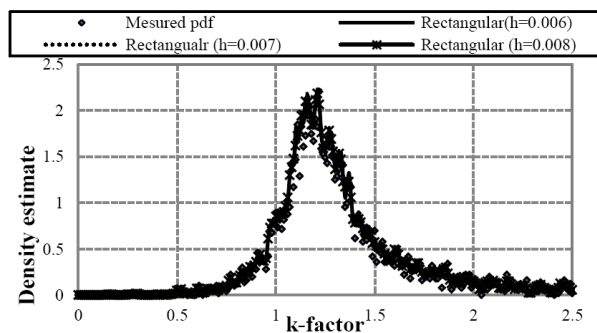


Figure 11: Polokwane rectangular kernel density estimate, 200 m a.g.l.

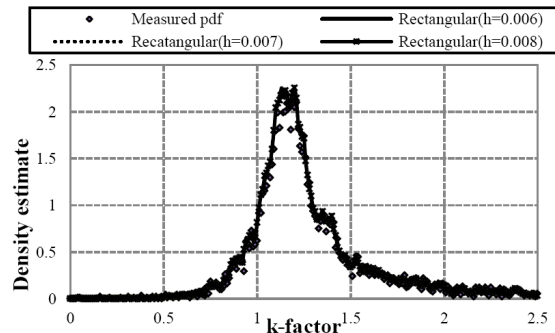


Figure 12: Pretoria-rectangular kernel density estimate, 200 m a.g.l.

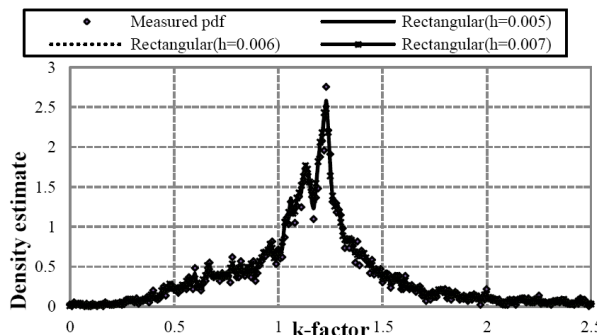


Figure 13: Upington rectangular kernel density estimate, 200 m a.g.l.

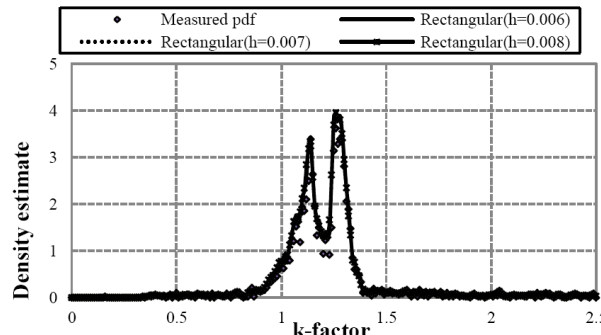


Figure 14: Bethlehem rectangular kernel density estimate, 200 m a.g.l.

Table 2: Three-year curve-fitting distribution models.

Location	Gaussian distribution Model
Bloemfontein	$1.2e^{-4.53(k-1.24)^2}$
Cape Town	$1.2e^{-4.53(k-1.29)^2}$
Durban	$1.37e^{-5.90(k-1.27)^2}$
Polokwane	$1.64e^{-8.45(k-1.23)^2}$
Pretoria	$1.8e^{-10.18(k-1.19)^2}$
Upington	$1.41e^{-6.25(k-1.17)^2}$
Bethlehem	$2.4e^{-18.10(k-1.20)^2}$

Table 3: Three-year curve-fitting parameters and ISE values.

Location	Initial estimates from measurements			Final estimates from curve fitting		
	$u_k$	$A$	ISE	$u_k$	$A$	ISE
Bloemfontein	1.22	1.82	0.23	1.24	1.2	0.19
Cape Town	1.29	1.60	0.13	1.29	1.2	0.11
Durban	1.27	1.33	0.102	1.27	1.37	0.101
Polokwane	1.26	1.52	0.11	1.23	1.64	0.09
Pretoria	1.20	2.04	0.14	1.19	1.8	0.13
Upington	1.18	1.36	0.14	1.17	1.41	0.13
Bethlehem	1.16	1.96	0.46	1.20	2.4	0.38

Table 4: Three-year kernel bandwidth, median  $k$ -factor and ISE values.

Locations	Bandwidth, $h$	Kernel							
		Gaussian		Triangular		Epanechnikov		Rectangular	
		Median	ISE	Median	ISE	Median	ISE	Median	ISE
Bloemfontein	0.007	1.21	0.0332	1.21	0.0334	1.21	0.0331	1.22	0.0334
	0.008	1.21	0.0330	1.21	0.0332	1.21	0.0332	1.22	0.0343
	0.009	1.21	0.0329	1.21	0.0333	1.21	0.0333	1.22	0.0349
Cape Town	0.006	1.27	0.0149	1.26	0.0147	1.26	0.0146	1.25	0.0147
	0.007	1.27	0.0147	1.26	0.0148	1.26	0.0148	1.25	0.0158
	0.008	1.27	0.0148	1.26	0.0150	1.26	0.0153	1.25	0.0160
Durban	0.006	1.26	0.0153	1.25	0.0153	1.26	0.0152	1.25	0.0149
	0.007	1.26	0.0151	1.25	0.0152	1.26	0.0153	1.25	0.0159
	0.008	1.26	0.0152	1.25	0.0154	1.26	0.0155	1.25	0.0163
Polokwane	0.006	1.26	0.0211	1.25	0.0205	1.25	0.0197	1.25	0.0193
	0.007	1.26	0.0203	1.25	0.0201	1.25	0.0198	1.25	0.0195
	0.008	1.26	0.0200	1.25	0.0200	1.25	0.0199	1.25	0.0208
Pretoria	0.006	1.20	0.0107	1.20	0.0107	1.21	0.0104	1.21	0.0099
	0.007	1.20	0.0105	1.20	0.0106	1.21	0.0105	1.21	0.0111
	0.008	1.20	0.0104	1.20	0.0107	1.21	0.0107	1.21	0.0112
Upington	0.005	1.20	0.0131	1.21	0.0129	1.20	0.0121	1.20	0.0113
	0.006	1.20	0.0126	1.21	0.0130	1.20	0.0127	1.20	0.0128
	0.007	1.20	0.0127	1.21	0.0130	1.20	0.0132	1.20	0.0149
Bethlehem	0.006	1.17	0.0567	1.18	0.0562	1.18	0.0555	1.17	0.0546
	0.007	1.17	0.0556	1.18	0.0560	1.18	0.0556	1.17	0.0576
	0.008	1.17	0.0552	1.18	0.0559	1.18	0.0563	1.17	0.0569

Table 5: Median ( $k_{50\%}$ ) values compared, 200 m a.g.l. Table 6:  $k_{eff}$  ( $k_{99.9\%}$ ) values compared, 200 m a.g.l.

Location	Measured	Curve-fitting	Kernel	Location	Measured	Curve-fitting	Kernel
Bloemfontein	1.22	1.24	1.21–1.22	Bloemfontein	0.51	0.53	0.52–0.53
Cape Town	1.29	1.29	1.26–1.27	Cape Town	0.49	0.51	0.50–0.51
Durban	1.27	1.27	1.25–1.26	Durban	0.53	0.55	0.55–0.56
Polokwane	1.26	1.23	1.25–1.26	Polokwane	0.63	0.64	0.63–0.64
Pretoria	1.2	1.19	1.20–1.21	Pretoria	0.66	0.68	0.67–0.68
Upington	1.18	1.17	1.19–1.20	Upington	0.49	0.50	0.52–0.53
Bethlehem	1.16	1.20	1.17–1.18	Bethlehem	0.73	0.75	0.76–0.77

1.19 to 1.20 for Upington and finally 1.17 to 1.18 for Bethlehem. It is observed that the Rectangular kernel produces the best error performance in five of the seven locations, i.e., Durban, Polokwane, Pretoria, Upington and Bethlehem. The Gaussian kernel produces the best error performance for Bloemfontein while the Epanechnikov kernel is the best for Cape Town. It observed that, in the neighbourhood of the optimum  $h$  for each kernel, the values of the  $k$ -factor obtained are the same. The resulting plots are so close that discerning the difference between them is difficult. For each kernel, the optimum value of  $h$  is the one where the minimum error is obtained. Median  $k$ -factor results obtained from measurements, curve-fitting and kernel methods are tabulated in Table 5 for ease of comparison. Modelling  $k$ -factor values exceeded 99.9% of the time are compared against the measured ones in Table 6. From the curve-fitting models, the values are; 0.53 for Bloemfontein, 0.51 for Cape Town, 0.55 for Durban, 0.64 for Polokwane, 0.68 for Pretoria, 0.5 for Upington and 0.75 for Bethlehem. For the kernel models, the values vary between 0.52 to 0.53 for Bloemfontein, 0.5 to 0.51 for Cape Town, 0.55 to 0.56 for Durban, 0.63 to 0.64 for Polokwane, 0.67 to 0.68 for Pretoria, 0.52 to 0.53 for Upington and 0.76 to 0.77 for Bethlehem.

## 6. CONCLUSION

Both kernel and normal distribution models of the effective earth radius factor for South Africa have been determined. From these models, median and effective values of the  $k$ -factor have been

obtained. These modelling results have also been compared with those obtained using measurements. It is observed that the curve-fitting, kernel and measured values obtained are quite close to each other. Also, the kernel models are found to follow the measured probability density function estimate as much as possible and as such their error performance is far much superior compared to the curve-fitting ones. The rectangular kernel is seen to produce progressively lower errors and is proposed as the best kernel for modelling the  $k$ -factor in South Africa. The results obtained in this presentation will go a long way in making sure that diffraction ( $k$ -type) fading is adequately addressed during link budgeting to counter any interference associated with  $k$ -factor variations for both UHF/VHF and terrestrial microwave links. In particular, both median and effective  $k$ -factor values obtained will be used by radio link planners to determine optimum antenna heights required to attain adequate path clearance in South Africa. The results will also serve as a benchmark for extension to cover the rest of the country by way of making predictions (interpolation) or more direct measurements to cover more areas for a longer period.

## REFERENCES

1. Palmer, A. J. and D. C. Baker, "Predicting the long-term average of the effective earth radius factor for South Africa using ground based observations," *SAIEE Journal*, Vol. 97, No. 2, 182–185, June 2006.
2. Palmer, A. J. and D. C. Baker, "Predicting the monthly average cumulative distribution of the effective earth radius factor for South Africa," *SAIEE Journal*, Vol. 99, No. 2, 186–190, June 2006.
3. Palmer, A. J. and D. C. Baker, "A novel semi-empirical model of the effective earth radius factor," *IEEE Transactions on Broadcasting*, Vol. 52, No. 4, 557–565, December 2006.
4. Palmer, A. J. and D. C. Baker, "A proposed empirical model of the effective earth radius factor for telecommunications use in South Africa," *IEEE AFRICON*, 511–516, 2002.
5. Afullo, T. J., M. O. Adongo, and T. Motsoela, "Seasonal variation of radio refractivity in Botswana," *Proceedings of URSI Climpara'98 Conference on Climatic Parameters in Radio Wave Propagation Prediction*, 195–198, Ottawa, Canada, April 1998.
6. Afullo, T. J. and P. K. Odedina, "Effective earth radius factor measurement and modelling for radio link design in Botswana," *South Africa Institute of Electrical Engineers Research Journal*, Vol. 99, No. 3, 77–86, September 2008.
7. Afullo, T. J., T. Motsoela, and D. F. Molotsi, "Refractivity gradient and  $k$ -factor in Botswana," *Proceedings of the Third Regional Workshop on Radio Africa'99*, 107–110, Gaborone, Botswana, October 25–29, 1999.
8. Afullo, T. J. and P. K. Odedina, "On the  $k$ -factor distribution and diffraction fading for Southern Africa," *SAIEE Journal*, Vol. 97, No. 2, 172–181, 2006.
9. Afullo, T. J., T. Motsoela, and D. F. Molotsi, "Estimates of refractivity gradient and  $k$ -factor ranges for Botswana," *SAIEE Journal*, Vol. 92, 1–6, 2001.
10. Afullo, T. J. and P. K. Odedina, "Effective earth radius factor characterization for line-of-sight paths in Botswana," *IEEE AFRICON*, 227–232, 2004.
11. Fulgence, D., "Effective earth radius distribution for Central Africa: Rwanda and north-western Tanzania," MSc. Thesis, National University of Rwanda, August 2012.
12. Adediji, A. T. and M. O. Ajewole, "Vertical profile of the radio refractivity gradient in Akure, south-west Nigeria," *Progress In Electromagnetics Research C*, Vol. 4, 157–168, 2008.
13. Oyedum, O. D., "Radio refraction and atmospheric ray bending in Nigeria," *Nigerian Journal of Space Research*, No. 3, 99–110, November 2007.
14. Silverman, B. W., *Density Estimation for Statistics and Data Analysis*, Chapter 2–4, Chapman & Hall, 1990, ISBN 0-412-24620-1.
15. Sheather, S. J., "Density estimation," *Statistical Science*, Vol. 19, No. 4, 588–597, 2004.
16. Zucchini, W., *Applied Smoothing Techniques, Part 1: Kernel Density Estimation*, October 2003.
17. Ouyang, Z., "Univariate kernel density estimation," August 2005.

# A 60 GHz Marchand Balun with Floating Ground Centre-tap in CMOS Technology

Leijun Xu<sup>1</sup>, Henrik Sjöland<sup>2</sup>, Markus Törmänen<sup>2</sup>,  
Tianhong Pan<sup>1</sup>, and Xue Bai<sup>1</sup>

<sup>1</sup>Jiangsu University, Zhenjiang 212013, China

<sup>2</sup>Lund University, Lund 22100, Sweden

**Abstract**— A novel Marchand Balun with floating ground centre-tap is proposed for silicon-based millimeter-wave applications. Implemented in 65 nm CMOS technology, the Marchand Balun is designed with broadside coupling lines by using two top metals. To reduce the size, the balun was folded and both ends of the two secondary lines are connected together to floating ground, two by-pass capacitances are connected between the real ground and floating ground. The balun is simulated by ADS Momentum, different width of the lines are compared to find the optimal value. The proposed balun has small size and floating ground centre-tap for feeding DC bias conveniently. Compared with transformer balun, the layout of this Marchand balun is more symmetric due to the open-end of its primary side, which also improves the bandwidth and imbalances of the balun.

## 1. INTRODUCTION

With the increase of the circuit frequency, more balanced structures are used in millimeter-wave designs for reducing noise and high order harmonics, such as Mixers and Amplifiers. As a passive component, on-chip baluns play an important role in the design of balanced circuits. To reduce size and provide a simple DC bias for active devices, transformer baluns are commonly used in millimeter-wave applications [1, 2] for their easy connected centre-tap to bias and compact structure. However, one of the problems for millimeter-wave transformer is that its primary turn connection to ground will lead asymmetrical layout, which will degrade the performance of the balun at such high frequency. Compared with transformer balun, the Marchand balun doesn't have this problem due to its open-ended primary side, as shown in Fig. 1, it is also widely used in millimeter-wave circuits [3–5]. But Marchand baluns with centre-tap for DC bias are seldom reported due to the inherent structure.

In this paper, a novel Marchand balun with floating ground centre-tap is proposed for silicon-based millimeter-wave applications. The balun uses a stacked structure and bended lines to reduce the size and provide a centre-tap for DC bias. It overcomes the drawback of the planar Marchand balun where it is difficult to make a grounded centre-tap, meanwhile, it has symmetric layout for both primary and secondary sides. In the following sections, the design of this balun is discussed in detail.

## 2. BALUN DESIGN

The conventional Marchand balun (Fig. 1) consists of two symmetrical quarter-wave coupled lines, where the primary line is open-ended and the two secondary lines are connected to ground separately. Implemented in a 65 nm CMOS process, this balun uses the top two metal layers as broadside coupled lines. Unlike edge coupled lines, broadside coupling has large coupled area and

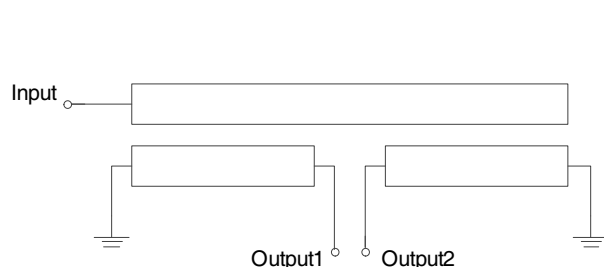


Figure 1: The structure of Marchand balun.

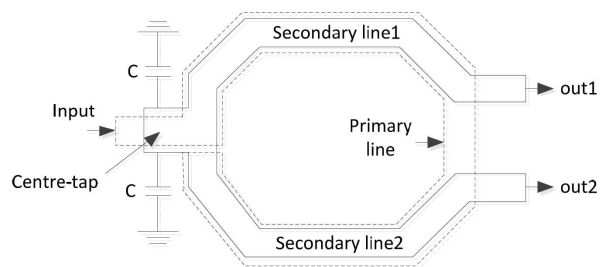


Figure 2: The proposed Marchand balun with centre-tap.

confines the electric field between the two lines. The coupled lines of the balun are bent so that the two separated grounds can be connected together as a centre-tap with the additional benefit of reduced size. To allow DC bias, two symmetric capacitances are connected between the centre-tap and ground, the structure is shown in Fig. 2.

The centre frequency of the balun is 60 GHz, and the value of each capacitance is 5 pF. The balun was implemented in a ST 65 nm standard CMOS process with 7 metal layers, where the coupled lines use the two top metal layers of copper, M7 and M6. The thickness of each metal layer is 0.9  $\mu\text{m}$  and the isolation between them is 0.6  $\mu\text{m}$ . The layout of the balun is shown in Fig. 3, occupying an area of 150  $\mu\text{m}$   $\times$  100  $\mu\text{m}$  excluding centre-tap capacitances.

### 3. LAYOUT OPTIMIZATION

To get good insertion loss and balance of the balun, the width and length of the coupled lines were optimized using the EM simulation tool ADS Momentum. The insertion loss, amplitude and phase imbalance are three main figures of merit for the balun, and to find suitable line dimensions, they were simulated for different length and width of the primary line at the frequency of 60 GHz, see Fig. 4 to Fig. 6.

When the line length increases, the amplitude imbalance decreases and phase imbalance increases monotonically. For a given line width ( $w$ ), on the other hand, the insertion loss has a minimum value for a certain line length. Meanwhile, the minimum insertion loss and amplitude imbalance decrease, whereas the phase imbalance increases with increased line width. Considering the above results, the figures of merit are traded off and we chose a line length of 320  $\mu\text{m}$  and a width of 6  $\mu\text{m}$

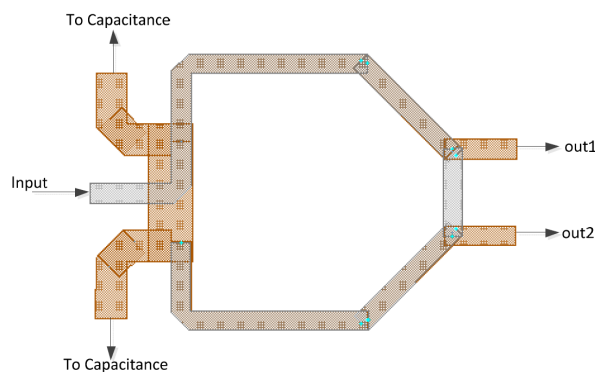


Figure 3: The layout of the balun.

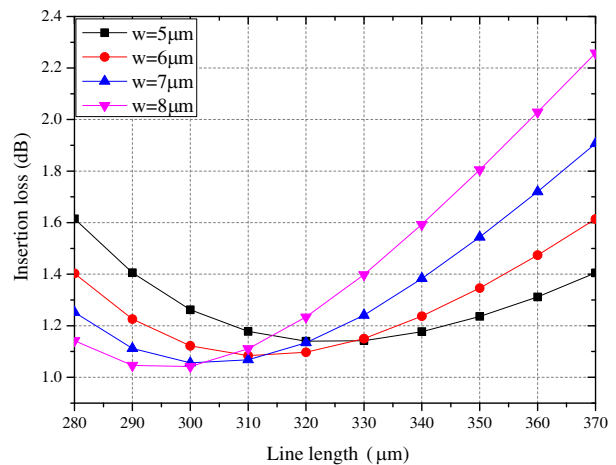


Figure 4: Insertion loss with different line length and width.

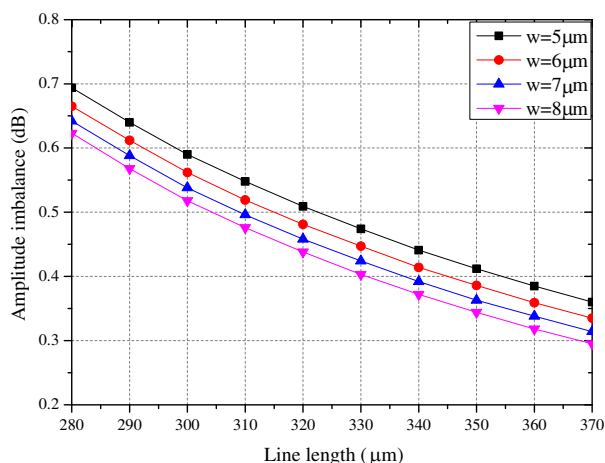


Figure 5: Amplitude imbalance with different line length and width.

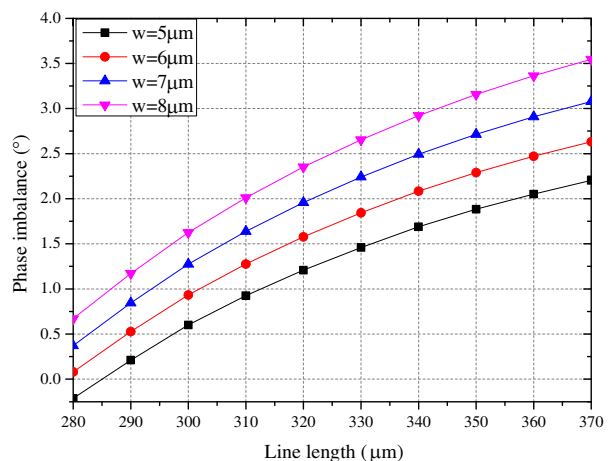


Figure 6: Phase imbalance with different line length and width.

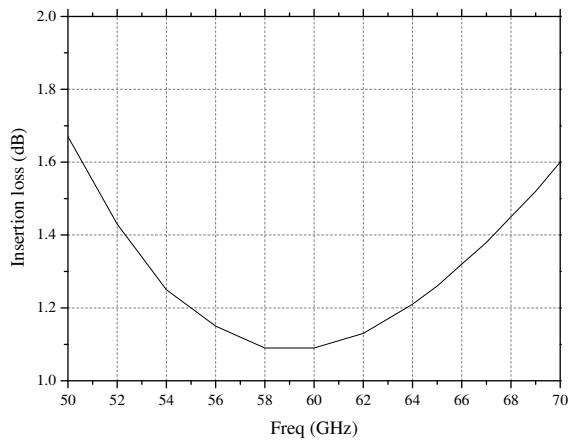


Figure 7: Insertion loss of the proposed balun.

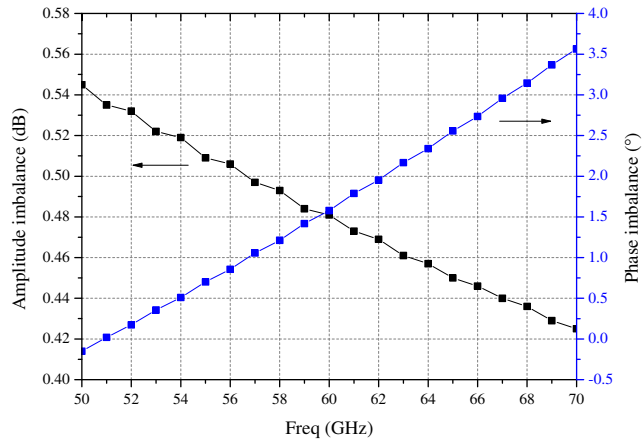


Figure 8: Amplitude and phase imbalance of the proposed balun.

for the balun. The results for the optimized balun are shown in Fig. 7 and Fig. 8.

The insertion loss of the designed balun is 1.1 dB at 60 GHz and less than 1.2 dB in the band from 57 GHz to 64 GHz. In this frequency band, the amplitude imbalance is less than 0.5 dB and the phase imbalance is less than  $2.5^\circ$ .

#### 4. CONCLUSIONS

A millimeter wave Marchand balun with floating ground centre-tap for DC bias was proposed. Implemented in a 65 nm CMOS process, the balun was optimized for low insertion loss and imbalances at 60 GHz. The balun has wide bandwidth and compact size, and it can be applied in millimeter wave circuits such as amplifiers and mixers which need DC bias, resulting in area efficient implementations.

#### ACKNOWLEDGMENT

The authors would like to thank the department of Electrical and Information Technology, Lund University, Lund, Sweden, for supporting this research. The authors would also like to thank ST Microelectronics for their support. This work is also supported by Jiangsu Provincial Natural Science Foundation of China (Grant No. BK2011466), National Natural Science Foundation of China (Grant No. 61273142), Natural Science Fund for Colleges and Universities in Jiangsu Province (10KJB510002), and the Priority Academic Program Development of Jiangsu Higher Education Institutions (PAPD).

#### REFERENCES

1. Liu, J. Y., R. Berenguer, and M. F. Chang, "Millimeter-wave self-healing power amplifier with adaptive amplitude and phase linearization in 65-nm CMOS," *IEEE Transactions on Microwave Theory and Techniques*, Vol. 60, No. 5, 1342–1352, 2012.
2. Yi, Z. and J. R. Long, "A wideband, dual-path, millimeter-wave power amplifier with 20 dBm output power and PAE above 15% in 130 nm SiGe-BiCMOS," *IEEE Journal of Solid-State Circuits*, Vol. 47, No. 9, 1981–1997, 2012.
3. Uemichi, Y., H. Hatakeyama, T. Aizawa, K. Okada, H. Kiumarsi, S. Tanoi, N. Ishihara, and K. Masu, "Low-loss and compact millimeter-wave balun on Si," *2011 IEEE MTT-S International Microwave Symposium Digest (MTT)*, 1–4, Baltimore, USA, Jun. 2011.
4. Xu, L. and J. Wei, "Characterization and analysis of patterned shields for millimeter-wave broadside-coupled balun in CMOS technology," *2012 International Conference on Microwave and Millimeter Wave Technology (ICMMT)*, 1–4, Shenzhen, China, May 2012.
5. Howard, D. C., C. Choon Sik, and J. D. Cressler, "A broadband, millimeter wave, asymmetrical Marchand balun in 180 nm SiGe BiCMOS technology," *2012 IEEE Radio Frequency Integrated Circuits Symposium (RFIC)*, 425–428, Montreal, Canada, Jun. 2012.

# Compact UWB Monopole Antenna with Tapered Ground Plane

A. Subbarao and S. Raghavan

National Institute of Technology, Tiruchirappalli 620015, India

**Abstract**— A compact CPW-fed UWB antenna with band-notched characteristic is presented in this paper. It has compact size of  $30 \times 31 \text{ mm}^2$ . A ‘C’ shaped slot is introduced to achieve notched band from 5 GHz to 6 GHz to avoid interference from WLAN. The proposed antenna has ultra-wideband frequency range from 3 GHz to 10 GHz for return loss below  $-10 \text{ dB}$ , except for the rejected WLAN band. Details of antenna are presented with parametric study. The antenna is omni directional in operating bandwidth and it has good radiation efficiency. The fundamental parameters such as return loss, radiation patterns are obtained, which meet standard specifications. Method of moments based IE3D electromagnetic simulator is used to analyze this antenna.

## 1. INTRODUCTION

Ultra wideband (UWB) communication systems have received great attraction in wireless world. It is popularly used technology in radar and remote sensing. UWB technology provides promising solutions for future communication systems due to excellent immunity to multi path interference, large bandwidth and high speed data rate. A bandwidth from 3.1 GHz to 10.6 GHz is allocated for UWB systems by Federal Communication Commission (FCC) in 2002. From then, the design of UWB antenna has become challenging task for engineers in UWB systems. One major issue in UWB is the design of compact size and wide band antenna [1]. Several UWB antennas have been studied for UWB applications [2, 3]. Recently slot antennas have become popular for UWB applications [4]. Bow-tie antenna is one technique for UWB antenna systems [5]. The planar monopole antennas [6, 7] are better for UWB applications due to small size and stable radiation patterns. The CPW-fed antennas are useful for microwave and millimeter applications because they offer low profile, wide bandwidth and ease of integration with circuits when compared to microstrip fed antennas. The CPW feed has low radiation leakage and less dispersion than conventional microstrip line. A UWB antenna is also susceptible to interference by narrow band signal of neighboring RF system such as IEEE 802.11a WLAN having operating frequency range 5.125–5.825 GHz. Hence, it is desirable to design UWB antenna with band-notched characteristic to avoid interference from the band. The conventional methods to achieve the notched band are cutting a slot (U-shaped, V-shaped and arc shaped slots) on the patch [8, 9] or embedding a quarter wavelength stub with in a large slot on the patch [10].

A compact CPW-fed UWB antenna is proposed with notched band from 5 GHz to 6 GHz, which avoids entire WLAN. The antenna provides stable radiation patterns and high radiation efficiency. The antenna geometry is specified. The antenna parameters such as return loss, radiation characteristics are discussed in this paper.

## 2. ANTENNA STRUCTURE

The antenna is fabricated with low cost FR4 substrate with relative permittivity  $\epsilon_r = 4.4$  and thickness  $h = 1.6 \text{ mm}$ . It has compact area of  $30 \times 31 \text{ mm}^2$  as shown in Figure 1. The antenna is fed by  $50 \Omega$  CPW feed line. The gap ‘ $g$ ’ between centre conductor and ground plane is 0.4 mm. The various optimized parameters of antenna are  $W = 30 \text{ mm}$ ,  $W_1 = 13.1 \text{ mm}$ ,  $W_2 = 5 \text{ mm}$ ,  $W_3 = 3 \text{ mm}$ ,  $W_4 = 15 \text{ mm}$ ,  $W_5 = 5.75 \text{ mm}$ ,  $W_6 = 3.5 \text{ mm}$ ,  $W_7 = 2.8 \text{ mm}$ ,  $W_8 = 6 \text{ mm}$ ,  $L = 31 \text{ mm}$ ,  $L_1 = 4.75 \text{ mm}$ ,  $L_2 = 9 \text{ mm}$ ,  $L_3 = 14 \text{ mm}$ ,  $L_4 = 8.825 \text{ mm}$ ,  $L_5 = 1.175 \text{ mm}$ ,  $L_6 = 1 \text{ mm}$ ,  $L_7 = 0.5 \text{ mm}$ ,  $L_8 = 3.6 \text{ mm}$ ,  $L_9 = 6 \text{ mm}$ . The antenna has two resonating frequencies 3.63 GHz and 7.51 GHz. The obtained resonant frequencies vary depending on the location of inner tuning stub and the gap between CPW-feed line and ground. The antenna has only one layer of substrate with single sided metallization part. This allows easy manufacturing of antenna with low cost.

## 3. RESULTS AND DISCUSSION

The proposed antenna was simulated and optimized using Zeland IE3D simulator. The photograph of fabricated antenna is shown in Figure 2. The comparison of return loss of fabricated antenna with that of simulated antenna is shown in Figure 3. The return loss curve shows that the antenna

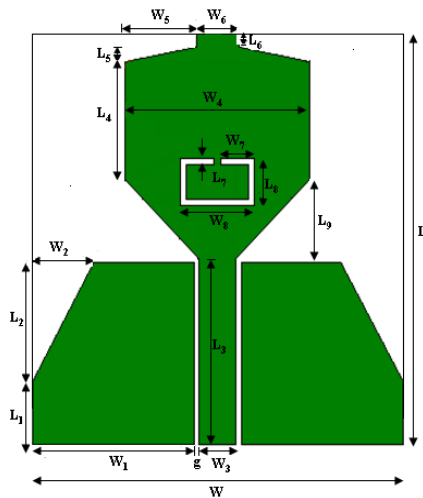


Figure 1: Structure of proposed antenna.



Figure 2: Photo of fabricated antenna.

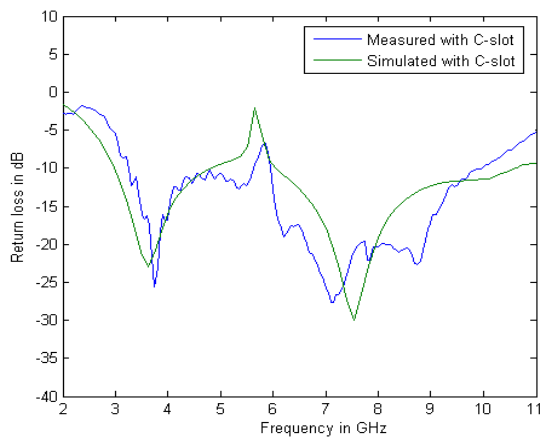
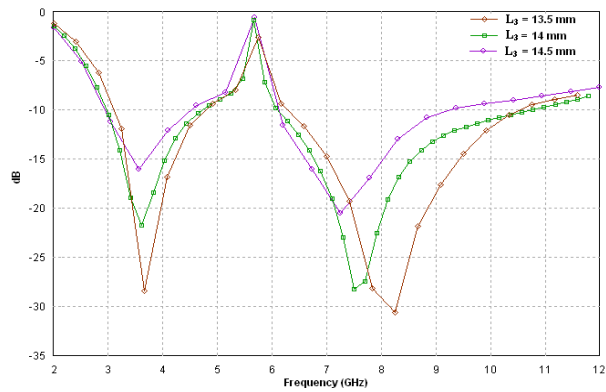


Figure 3: Simulated and measured returned losses for proposed antenna.

Figure 4: Return loss of proposed antenna for different values of  $L_3$ .

achieves an impedance bandwidth of 7 GHz ranging from 3 GHz to 10 GHz for return loss below  $-10$  dB except for notched bandwidth from 5 GHz to 6 GHz. This band is avoided by inserting 'C' shaped slot in conductive layer to reduce interference from WLAN. The proposed antenna has good performance to reject unwanted WLAN band. By controlling the size and location of 'C' slot, desired notched band can be obtained. The important feature of proposed antenna is the capability of impedance matching at both resonating frequencies 3.62 GHz and 7.54 GHz using CPW feed line.

The performance of the antenna has been analyzed by using Method of moments based IE3D simulator. The effect of  $L_3$  on the antenna return loss and bandwidth are studied. As  $L_3$  increases from 13.5 mm to 14.5 mm, the band width increases to 7.6 GHz from 7 GHz and then decreases to 7.03 GHz due to change in impedance matching. The higher resonant frequency decreases. The effect of  $L_3$  on resonant frequencies and bandwidth are shown in Figure 4.

Far field radiation characteristics were also studied. The Figures 5 and 6 plot radiation patterns in  $E$ -plane and  $H$ -plane at 3.62 GHz and 7.54 GHz. The radiation patterns are omni directional in  $H$ -plane and monopole like in  $E$ -plane. The different frequencies across the operating bandwidth exhibit similar radiation patterns. Hence, stable radiation patterns have been obtained for proposed antenna.  $H$ -plane patterns show large cross polarization due to strong horizontal surface current components and electric field. The peak antenna gain varies from 1.5 dBi to 2.8 dBi as shown in Figure 7 and it has maximum value of 2.8 dBi at 4.3 GHz. The antenna has high radiation efficiency of 80% in operating region.

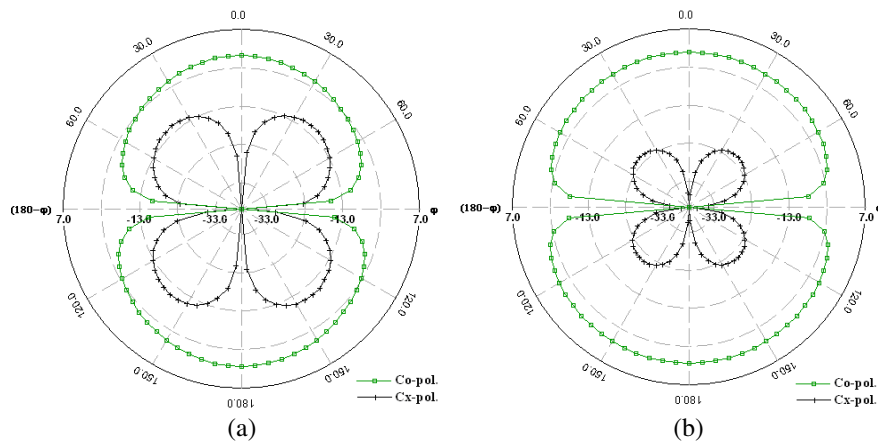


Figure 5: Radiation patterns in  $E$ -plane at (a) 3.62 GHz, (b) 7.54 GHz.

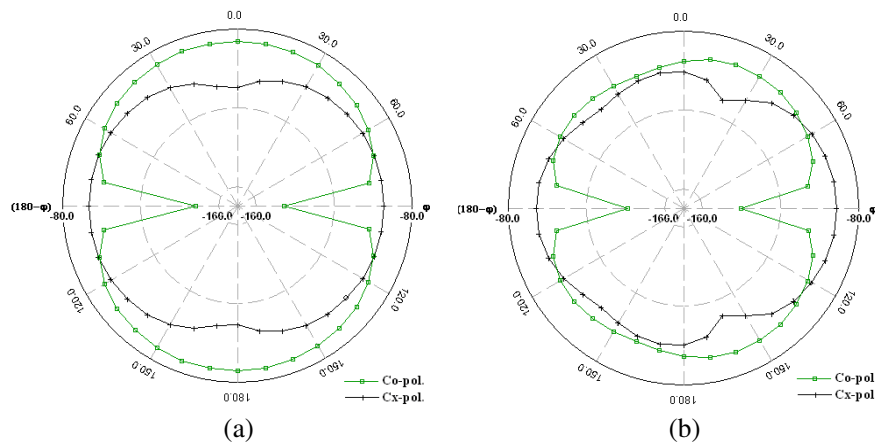


Figure 6: Radiation patterns in  $H$ -plane at (a) 3.62 GHz, (b) 7.54 GHz.

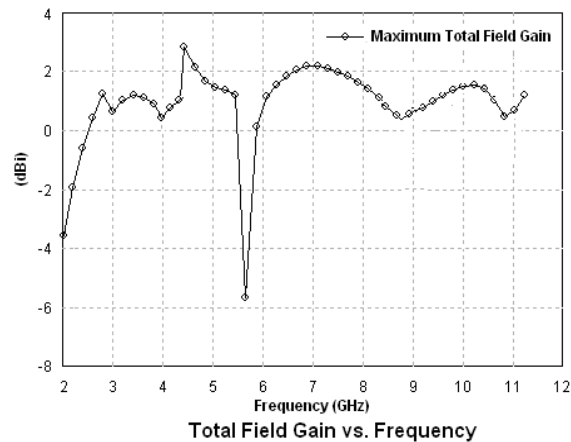


Figure 7: Gain of proposed antenna against frequency.

#### 4. CONCLUSIONS

A compact CPW fed antenna with band notched characteristic is presented to avoid interference from WLAN. Notch band is achieved by inserting ‘C’ shaped slot in conductive layer. It has good impedance matching. It has total impedance bandwidth of 7.6 GHz. Parametric study is performed by varying  $L_3$  of inner tuning. The antenna exhibits omni directional radiation patterns in  $H$ -plane with compact size. It has simple structure. The gain and radiation pattern of antenna have been

investigated and found to be stable. The antenna has high gain of 2.5 dBi in the operating band width. The antenna has highest radiation efficiency of 80% in the operating region. The antenna is also useful for radio communications.

#### REFERENCES

1. Li, P., J. Liang, and X. Chen, "Study of printed elliptical/circular slot antennas for ultrawide-band applications," *IEEE Trans. Antennas Propag.*, Vol. 54, No. 6, 1670–1675, 2006.
2. Zhang, G. M., J. S. Hong, B.-Z. Wang, Q. Y. Qin, J. B. Mo, and D. M. Wan, "A novel multi-folded UWB antenna fed by CPW," *Journal of Electromagnetic Waves and Applications*, Vol. 21, No. 14, 2109–2119, 2007.
3. Qu, S. W., J. L. Li, and Q. Xue, "A band notched ultra wide band printed monopole antenna," *IEEE Antennas Wireless Propa. Lett.*, Vol. 5, 495–498, 2006.
4. Ma, T. G. and S. K. Jeng, "Planar miniaturized-slot-fed annular slot antennas for ultra-wideband radios," *IEEE Trans. Antennas Propag.*, Vol. 53, 1194–1202, 2005.
5. Huang, C. Y. and D. Y. Lin, "CPW-fed bow-tie slot antenna for ultra-wideband communications," *Electron. Lett.*, Vol. 42, No. 19, 1073–1074, 2006.
6. Jacob, K. F., M. N. Suma, R. K. Raj, M. Joseph, and P. Mohanan, "Planar branched monopole antenna for UWB applications," *Microw. Opt. Technol. Lett.*, Vol. 49, No. 1, 45–57, 2007.
7. Cho, Y. J., K. H. Kim, D. H. Choi, S. S. Lee, and S. O. Park, "A miniature UWB planar monopole antenna with 5-GHz band rejection filter and time domain characteristics," *IEEE Trans. Antennas Propag.*, Vol. 54, 1453–1460, 2006.
8. Lee, W. S., D. Z. Kim, K. J. Kim, and J. W. Yu, "Wideband planar monopole antennas with dual band-notched characteristics," *IEEE Trans. Microw. Theory Tech.*, Vol. 54, No. 6, 2800–2806, 2006.
9. Qu, X., S.-S. Zhong, and W. Wang, "Study of band-notched function for a UWB circular disc monopole antenna," *Microw. Opt. Technol. Lett.*, Vol. 48, No. 8, 1667–1670, 2006.
10. Gao, Y., B. L. Ooi, and A. P. Popov, "Band notched ultra wide band ring monopole antenna," *Microw. Opt. Technol. Lett.*, Vol. 48, No. 1, 125–126, 2006.

# The Effects of Low Power Microwaves at 500 MHz and 900 MHz on Yeast Cells Growth

Hamad S. Alsuheim<sup>1</sup>, Vuk Vojisavljevic<sup>1</sup>, and Elena Pirogova<sup>1,2</sup>

<sup>1</sup>School of Electrical and Computer Engineering  
Royal Melbourne Institute of Technology (RMIT) University  
Melbourne, Victoria 3001, Australia

<sup>2</sup>Health Innovation Research Institute, RMIT University, Victoria, Australia

**Abstract**— In the last few decades, the use of microwave radiation has greatly increased in radar and communication systems, food-processing technology and medical field. Development of consumer and medical microwave devices for clinical diagnosis and therapy has also prompted widespread interest and stimulated much research into the mechanisms of interaction between microwave radiation and living matter. Two types of effects can be ascribed to microwaves, i.e., thermal and non-thermal. Non-thermal biological effects are measurable changes in biological systems that may or may not be associated with adverse health effects. It was shown that low power microwaves can affect enzymes activities. Little is known about the molecular mechanisms involved in putative non-thermal effects. One hypothesis is that low power microwave radiation can induce dipole oscillations in a protein's active site and thus, can alter its function. This study evaluates the effect of low power microwave radiation on the proliferation rate of yeast *Saccharomyces cerevisiae* strains type II, which were exposed to the microwaves at the frequencies of 500 MHz and 900 MHz and the selected powers of 0 dBm, 10 dBm, –10 dBm, 13 dBm, –13 dBm, 17 dBm and –17 dBm using the Transverse Electro-Magnetic (TEM) cell. The average specific absorption rate (SAR) for a single cell was 0.12 W/kg. SAR was calculated by averaging the individual parameters of the cell components in accordance with their volume fraction in live cells. A comparative analysis of changes in the proliferation rate of the irradiated vs. non-irradiated yeast cells was performed for the selected frequencies and powers, with the results being presented and discussed.

## 1. INTRODUCTION

In recent years microwave radiation, which is a type of non-ionizing electromagnetic radiation, has been widely used for different applications in medicine, food technology and mobile communication. Use of mobile phones is growing exponentially and consequently, the exposure to weak radiofrequency microwave radiation generated by these devices is markedly increasing. Accordingly, public concern about the potential hazards on human health has grown [1]. In this study, we investigated non-thermal effects of low power microwaves which, as reported, can induce changes at the molecular and cellular levels.

It is well-documented that yeast cells are representatives of eukaryotes, including human cells, in many aspects of fundamental cellular processes [2]. Yeast *Saccharomyces cerevisiae* was recommended as a model organism to study effects of electromagnetic radiation (EMR) and conduct experiments under well-controlled conditions [3]. Two types of yeast cells are commonly employed as models for biomedical research, i.e., the budding or brewer's yeast *Saccharomyces cerevisiae* and fission yeast *Schizosaccharomyces pombe* [4, 5]. In culture, yeast cells follow a very predictable pattern of growth that can easily be divided into four phases: (i) lag — no growth occurs as newly pitched yeast mature and acclimate to the environment; (ii) log — cells are rapidly growing and dividing, the growth rate in this phase will follow first order kinetics, as cell-number increases, cell growth begins to slow; (iii) deceleration — no growth occurs due to high waste concentration or complete substrate consumption; and (iv) stationary phases [6]. Likewise, in most growing eukaryotic cells, the cell cycle is divided into two basic parts: mitosis and inter-phase (three phases). The phases proceed successively, taking for 10–20 hrs depending on cell type and developmental state [8]. Although yeast cells are single cells, they are true eukaryotes, and share fundamental cell features with metazoan systems [9, 10]. Both yeast cells, *Saccharomyces cerevisiae* and *Schizosaccharomyces pombe*, are typically maintained as haploid cells; they also have a diploid sexual cycle, e.g., haploid cells of opposite mating types can mate, resulting in cell and nuclear fusion. Thus, the entire life cycle of yeast cells provides a simple model for events occurring in human cells [3].

A number of studies investigated the growth pattern of yeast cells exposed to microwaves. In a research by Grundler [11], a diploid wild strain of *S. cerevisiae* cells were exposed to microwaves

at 40–60 GHz and powers of up to 50 mW, which were transmitted by a waveguide. The findings showed that these exposures induced alterations in the yeast growth rate. Grundler and colleagues also reported that yeast cell growth was affected by low intensity microwave radiation at the frequencies of 41.64–41.835 GHz. These effects were shown to be strongly frequency-dependent and not correlated with the microwave powers used [12]. In other studies, yeast cells were exposed to both static and alternative Magnetic Fields (MFs) of varying strengths and durations [13]. As reported, *Saccharomyces cerevisiae* yeast cells were exposed to homogeneous and inhomogeneous magnetic fields to study the effects of MFs on yeast cell growth and development. Yeast cells were dispersed in a reagent and then exposed to a strong magnetic field using a magnetic circuit with the strength of 2.93 T. Researchers observed the differences in the budding angles of the yeast cells between the homogeneous and the inhomogeneous MFs, which were caused by alteration of the budding mechanism [13].

In [14], *Saccharomyces cerevisiae* yeast cells were preserved on malt extract agar slopes at room temperature and then exposed to microwaves (quasi-optical setup for more accurate result) ranging from 192 to 341 GHz with the selected powers in mW range. The tests were performed in 3 different groups according to the microcolonies' size and different time exposures (30 to 150 min). A statistically significant difference was observed between the control and exposed groups. That was apparent for all of the exposure times except for that at 150 min. The results suggest that exposure duration has the greatest impact on cells at an early growth stage [14]. In [15], TEM cell was used to expose b-tubulin mutant *Saccharomyces cerevisiae* yeast cells. The possibility of using a device to detect electromagnetic emission of yeast cell at 42 GHz was studied. The device was composed of the wave resonator, wave low noise amplifier, temperature control, and the spectrum analyser. The yeast cells were kept inside the waveguide resonator and then exposed to microwaves at 42 GHz. The main outcome of the study was that the system could provide threshold conditions for electromagnetic waves emitted by the yeast cell [15]. Noteworthy, the effect of microwave radiation on the mammalian cells are controversial and no conclusion has been reached [16–18]. The results of various studies on mammalian cells could not demonstrate microwave-induced DNA damage and cell proliferation. In contrast, other studies have reported that modulated microwave radiation is capable of causing DNA lesions and inhibition of cell proliferation [19, 20].

In this study, the experimental testing was conducted on yeast cells of *Saccharomyces cerevisiae* strain, which were exposed to microwave radiation at the frequencies of 500 MHz and 900 MHz and a power of 1 W. The commercial TEM cell was used to irradiate yeast cells. The parameters considered were test volume, microwave frequencies, and electric field distribution. A 3D model based on the finite element method (FEM) using COMSOL Multi-physics software was created. The modelling results were then validated by a simulation using Finite-Difference Time-Domain (FDTD), as well as experimental testing of the scattering parameters and voltage standing wave ratio.

## 2. MATERIALS AND METHODS

As a source of microwave radiation, we used a TC-5062AUHF TEM cell (100 kHz–3 GHz) from TESCOM Ltd (Unitechvill, Goyang, Korea). Through the input port, an external signal was applied to generate a predictable field inside the Gigahertz Transverse Electro-Magnetic (GTEM) cell. The GTEM was used to irradiate the yeast samples; the TC-5062A is an accurate, broad band RF coupler with a high quality shielding wall. The use and calibration of GTEM was described in details in our previous work [33].

The *S. cerevisiae* yeast powder was purchased from Sigma (Australia). The experimental solution was prepared as follows: 50 g/l of YPD broth (Sigma, Australia); 20 g/l of *S. cerevisiae* yeast, and ionized water. The solution was incubated at 24°C for 72 hrs. Then the solution was kept at 40°C. The yeast samples were prepared by diluting the experimental solution as 1 ml in 100 ml of the ionized water (1 : 100). The yeast samples were placed in the 2 ml cuvettes (GMBH + coKG post fach 1155). The cuvettes (dimensions are: 12.5 × 12.5 × 45 mm) were filled with the aliquot. In these experiments, three yeast samples were irradiated continuously for 6 hrs and other three control yeast samples were sham-exposed for the same time duration. The intensity characteristics of each (3 exposed and 3 non-exposed) samples were measured every 1 hr. Changes in yeast culture growth were monitored using the spectrophotometry method. Spectrophotometric analysis is based on turbidity and allows for indirect measurement of a number of yeast cells. The intensity of the yeast samples absorbance was measured using an Ocean Optics USB2000 spectrometer.

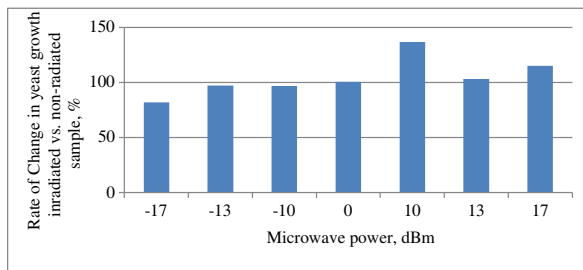


Figure 1: Changes in yeast growth upon microwave exposures at 500 MHz and different powers.

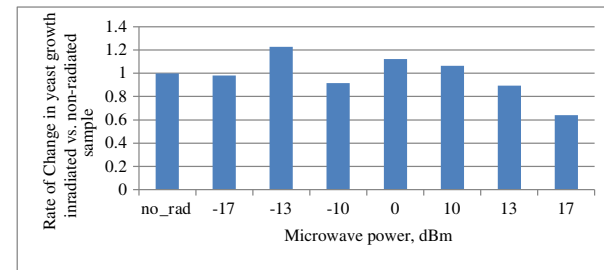


Figure 2: Changes in yeast growth upon microwave exposures at 900 MHz and different powers.

### 3. RESULTS AND DISCUSSION

The control group (non-exposed yeast cells at the same experimental conditions) and yeast cells were exposed to microwaves at 500 MHz and 900 MHz and powers of  $-17$  dBm,  $-13$  dBm,  $-10$  dBm,  $0$  dBm,  $10$  dBm,  $13$  dBm and  $17$  dBm. The results are presented in Figures 1 and 2 respectively. Figure 1 and Figure 2 clearly show that, in comparison with the control group of non-irradiated yeast cells (100%), the microwave exposures of 500 MHz and 900 MHz can induce changes in yeast cell growth/proliferation. Interestingly, these observed effects are power dependent for both studied frequencies. From Figure 1, it can be seen that at the frequency of 500 MHz and power of  $-17$  dBm the decrease of 20% in yeast cell growth is achieved. At the powers of  $-13$  dBm and  $-10$  dBm we can see only a slight decrease in cells growth. We also can observe no effect on cells at the power of  $0$  dBm. In contrast, slight increase is seen at the power of  $13$  dBm, more significant increase of 18% is achieved at  $17$  dBm. The maximum increase (38%) in yeast cell proliferation is at the power of  $10$  dBm.

Figure 2 shows that at the frequency of 900 MHz and powers of  $-13$  dBm,  $0$  dBm and  $10$  dBm the yeast cell proliferation rate is increased (21%, 12% and 6% respectively). In contrast, at the same frequency of 500 MHz and the powers of  $-17$  dBm,  $-10$  dBm,  $13$  dBm and  $17$  dBm the opposite effect is observed. The exposures at these particular parameters decrease the growth and proliferation of yeast cells with the different degree. The maximum decrease in yeast cells growth (38%) is seen at the power of  $17$  dBm. Hence, the findings reveal that applied microwaves of 500 MHz and 900 MHz can modulate yeast cells growth and these effects are power dependent.

### 4. CONCLUSIONS

This experimental evaluation was aimed to test the hypothesis that the external low power MW radiation can affect the biological activity (proliferation rate) of the yeast cells. In this study, we applied the MW exposures at 500 MHz and 900 MHz and the selected powers of  $0$  dBm,  $10$  dBm,  $-10$  dBm,  $13$  dBm,  $-13$  dBm,  $17$  dBm and  $-17$  dBm to the experimental yeast solutions. The yeast samples were exposed and sham-exposed for 6 hours. The results obtained show that the MW radiation at 500 MHz and 900 MHz produce modulating effects on the growth of yeast samples. However, the observed effects vary significantly. The results obtained show that the MW exposures at both frequencies 500 MHz and 900 MHz and different powers can increase or inhibit the proliferation of yeast cells. These findings imply that the external non-thermal MW radiation at the selected frequency and powers can modulate the proliferation of the exposed yeast cells.

### REFERENCES

1. World Health Organization (WHO), "Electromagnetic fields and public health: Mobile telephones and their base stations," Feb. 22, 2010.
2. Leszczynski, D., S. Joenvr, J. Reivinen, and R. Kuokka, "Non-thermal activation of the hsp27/p38MAPK stress pathway by mobile phone radiation in human endothelial cells: Molecular mechanism for cancer- and blood-brain barrier-related effect," *Differentiation*, Vol. 70, Nos. 2–3, 120–129, 2002.
3. Susan, L. F., "The yeasts *Saccharomyces cerevisiae* and *Schizosaccharomyces pombe*: Models for cell biology research," *Gravitational and Space Biology*, Vol. 18, No. 2, 3–10, 2005.
4. Gos, P., B. Eicher, J. Kohli, and W. D. Heyer, "Extremely high frequency electromagnetic fields at low power density do not affect the division of exponential phase. *Saccharomyces cerevisiae* cells," *Bioelectromagnetics*, Vol. 18, 142–155, 1997.

5. Heckman, D. S., D. M. Geiser, B. R. Eidell, R. L. Stauffer, N. L. Kardos, and S. B. Hedges, “Molecular evidence for the early colonization of land by fungi and plants,” *Science*, Vol. 293, 1129–1133, 2001.
6. “Monitoring growth of beer brewing strains of *Saccharomyces cerevisiae*. The utility of synergy H1 for providing high quality kinetic data for yeast growth applications,” BioTek Instruments, Inc., 2010.
7. Lodish, H., A. Berk, S. L. Zipursky, et al., “The life cycle of cells,” *Molecular Cell Biology*, 4th Edition, Section 1.4, W. H. Freeman, New York, 2000.
8. Forsburg, S. L., “The best yeast,” *Trends Genet*, Vol. 15, 340–344, 1999.
9. Forsburg, S. L. and P. Nurse, “Cell cycle regulation in the yeasts *Saccharomyces cerevisiae* and *Schizosaccharomyces pombe*,” *Annu. Rev. Cell. Dev. Biol.*, Vol. 7, 227–256, 1991.
10. Lew, D. J., T. Weinert, and J. R. Pringle, “Cell cycle control in *S. cerevisiae*,” *The Molecular and Cellular Biology of the Yeast Saccharomyces. Cell Cycle and Cell Biology*, J. Pringle, J. Broach, and E. W. Jones, Eds., Vol. 3, 607–695, Cold Spring Harbor Laboratory, New York, 1997.
11. Grundler, W., F. Keilmann, and H. Fröhlich, “Resonant growth rate response of yeast cells irradiated by weak microwaves,” *Physics Letters A*, Vol. 62, 463–466, 1977.
12. Grundler, W., F. Keilmann, V. Putterlik, and D. Strube, “Resonant-like dependence of yeast growth rate on microwave frequencies,” *British Journal of Cancer*, Vol. 45, 206–208, 1982.
13. Egami, S., Y. Naruse, and H. Watarai, “Effect of static magnetic fields on the budding of yeast cells,” *Bioelectromagnetics*, Vol. 31, 622–629, 2010.
14. Hadjiloucas, S., M. S. Chahal, and J. W. Bowen, “Preliminary results on the non-thermal effects of 200–350 GHz radiation on the growth rate of *S. cerevisiae* cells in micocolonies,” *Physics in Medicine and Biology*, Vol. 47, 3831–3839, 2002.
15. Jelinek, F., J. Saroch, O. Kucera, J. Hasek, J. Pokorny, N. Jaffrezic-Renault, and L. Ponsonnet, “Measurement of electromagnetic activity of yeast cells at 42 GHz,” *Radioengineering*, Vol. 16, 36–39, 2007.
16. Grundler, W., F. Keiser, F. Keilmann, and J. Walleczek, “Mechanisms of electromagnetic interaction with cellular systems,” *Naturwissenschaften*, Vol. 79, 551–559, 1992.
17. Pacini, S., M. Ruggiero, I. Sardi, S. Aterini, F. Gulisano, and M. Gulisano, “Exposure to global system for mobile communication (GSM) cellular phone radiofrequency alters gene expression, proliferation, and morphology of human skin fibroblasts,” *Oncol. Res.*, Vol. 13, 19–24, 2002.
18. Zeni, O., M. Romano, A. Perrotta, M. B. Lioi, R. Barbieri, G. d’Ambrosio, et al., “Evaluation of genotoxic effects in human peripheral blood leukocytes following an acute in vitro exposure to 900 MHz radiofrequency fields,” *Bioelectromagnetics*, Vol. 26, 258–265, 2005.
19. Phillips, J. L., O. Ivaschuk, T. Ishida-Jones, R. A. Jones, M. Campbell-Beachler, and W. Haggren, “DNA damage in Molt-4 T-lymphoblastoid cells exposed to cellular radiofrequency field in vitro,” *Bioelectrochem Bioenerg*, Vol. 45, 103–110, 1998.
20. Diem, E., C. Schwarz, F. Adlkofer, O. Jahn, and H. Rüdiger, “Non-thermal DNA breakage by mobile-phone radiation (1800 MHz) in human fibroblasts and in transformed GFSH-R17 rat granulosa cells in vitro,” *Mutat. Res.*, Vol. 583, 178–183, 2005.
21. Vojisavljevic, V., E. Pirogova, and I. Cosic, “Low intensity microwave radiation as modulator of the L-lactate dehydrogenase activity,” *Medical Biology Engineering Computing*, Vol. 49, No. 2, 2011.

# Design of 4 GHz Multiplier Based on Sigma-Delta Modulation in a 0.18- $\mu\text{m}$ CMOS Technology

Xiao-Dan Guo<sup>1,2</sup>, Qiao Meng<sup>1,2</sup>, and Yiong Liang<sup>1,2</sup>

<sup>1</sup>Institute of RF- & OE-ICs, Southeast University, China

<sup>2</sup>Engineering Research Center of RF-ICs & RF-Systems, Ministry of Education, China

**Abstract**— This paper presents an implementation of a high speed multiplier for direct sigma-delta modulated digital signals. Compared with some other conventional structures, this multiplier can reduce the circuit-loop delay and work efficiently at a high speed. The multiplier's circuit has also been improved with a pipe-line structure and the source coupled logic (SCL) technology. It is fabricated in a TSMC's 0.18- $\mu\text{m}$  CMOS process. Simulation results show that the chip meets the function and performance demand of the design and have zero bit error ratio (BER) at a frequency higher than 4 GHz. Analysis of the multiplier's noise performance is also presented.

## 1. INTRODUCTION

Sigma delta modulation (SDM), as a high precision signal modulation technique, is widely used in the field of digital-to-analog converters or phase-locked loops. It is one of the methods adopted for being able to accurately convert analog or multi-bit inputs into binary signals. Recently, the direct digital signal processing (DSP) based on the binary output of this type of modulator has become a favorite topic for research [1–3], especially in the areas of artificial neural networks etc. where single-bit is more preferable [4]. But most of these studies are carried out only on field programmable gate arrays (FPGAs), and as a result the input signal frequency from SDM is limited by the clock of FPGA which is very low.

However, the output signal frequency of the modulator which equals to its sample rate is in fact ever becoming higher. The reason behind it is undoubtedly the close relationship between precision and clock frequency. The higher the sample rate within a certain band, the higher the over-sampling ratio (OSR) will be. And this increase of OSR could in turn improve the signal-to noise ratio (SNR) of the modulated bit stream. Hence high-speed sigma-delta modulator has become one of the research directions [5, 6]. Of course, the subsequent DSP units also have to work at a high frequency, so obviously FPGA will not be able to meet the requirements and thus these units should be implemented on chips [7].

This paper presents a high speed multiplier based on SDM which is implemented by integrated circuit and able to complete multiplication of two single-bit streams. Through the optimization of traditional structures and key elements, the logic gate delay of the multiplier is reduced while the speed increased. In addition, the pipe line and the source-coupled logic technology are also used during the IC design for the purpose that the whole circuit could work at a higher frequency. The chip is fabricated in a TSMC's 0.18- $\mu\text{m}$  CMOS process, and the total area occupied is  $575\ \mu\text{m} \times 700\ \mu\text{m}$ . The simulation results show that the multiplier can work at 4 GHz while the bit error ratio (BER) is almost zero.

## 2. STRUCTURAL IMPROVEMENT

There are several kinds of traditional sigma-delta multipliers mentioned in the references [8–10], but most of them can not accomplish the multiplication of bit-streams in its real sense. Among them there is an analog asynchronous multiplier [8], with which the problem consists in that one of the inputs is not bit stream but analog signal. And there is another multiplier [9] built in the structure that could be described as algorithm  $(x + y)^2 - (x - y)^2$ , only that its output has an unwanted factor of 4 and its real accuracy is not so high.

### 2.1. L-level Multiplier

A multiplier which can really execute high precision bit-stream multiplication is mentioned in reference [10] and shown in Fig. 1. Both the input signals  $x(n)$  and  $y(n)$  pass through  $(L - 1)D$  flip-flops (three in all in Fig. 1) respectively. And the multiplication could be accomplished by using the mean of these L-level bits to represent the instantaneous value of the input signals as shown in formula (1). The sub-multiple module is implemented by an XOR gate and the structure

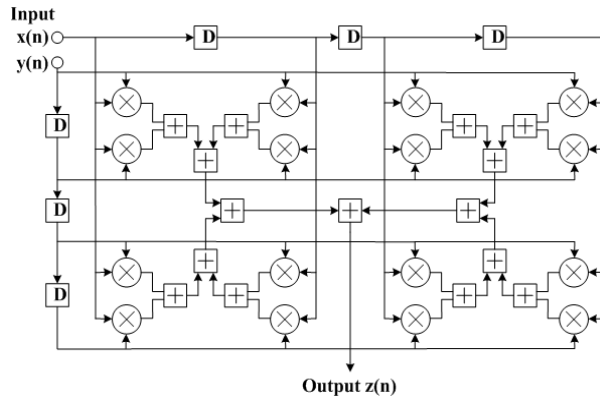


Figure 1: Structure of the 4-level multiplier.

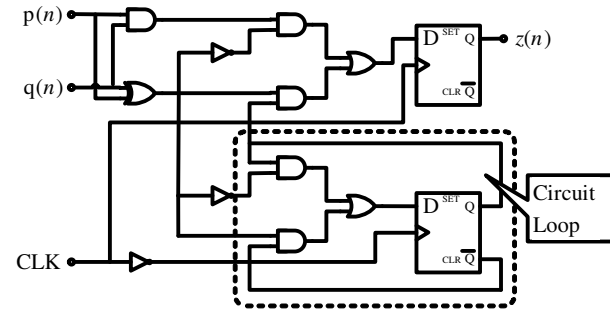


Figure 2: Structure of the traditional Adder.

of adder module is shown in Fig. 2. As can be seen from the figure, the circuit in the presence has a complex loop, resulting in a great delay, in which the pipe line structure could not be inserted. Therefore, the operating frequency of the entire circuit is difficult to get a big promotion.

$$z(n) = \left[ \frac{1}{L} \sum_{i=n-L+1}^n x(i) \right] \left[ \frac{1}{L} \sum_{j=n-L+1}^n y(j) \right] = \frac{1}{L^2} \sum_{i,j=n-L+1}^n x(i)y(j) \quad (1)$$

## 2.2. Novel Structure

To solve the problems mentioned above and to increase the sample frequency, two main improvements on the structure are proposed and designed.

Firstly, on structural analysis, it can be seen that the adder carries out the operation as defined in formula (2)

$$\begin{cases} z(n) = p(n) & p(n) = q(n) \\ z(n) = 0 & p(n) \neq q(n) \end{cases} \quad (2)$$

Therefore, a new adder is designed following the structure shown in Fig. 3.

As can be seen from the figure, the XOR of  $x(n)$  and  $y(n)$  is '1' when they are different. At this time, the voltage level in node  $X$  stays high and the output of  $D$  flip-flop reverses once being triggered. So the novel structure can complete the logical operation in formula (2) with only one  $D$  flip-flop in the circuit loop, thus greatly reducing the delay caused by adders. As a result the speed of the multiplier is increased and the hardware consumption decreased.

Secondly, if the first stage adder and the sub-multiple module are taken into consideration as a whole (Fig. 3), we can find the inputs of it are  $x(k) \oplus y(k)$  and  $x(n) \oplus y(k+1)$ . So the signal in node  $X$  can be given by formula (3).

$$X(n) = p(n) \oplus q(n) = (x(k) \oplus y(k)) \oplus (x(k) \oplus y(k+1)) = y(k) \oplus y(k+1) \quad (3)$$

So the two sub-multiple module and the bit-stream adder in Fig. 4 can be merged and simplified as a XOR-Adder unit which is also shown in the same figure. With this improvement the logic gate delay is reduced, resulting in a higher speed.

## 3. CIRCUIT AND LAYOUT DESIGN

The source-coupled logic (SCL) structure has been adopted to realize the logic gates in the circuit design [11]. Consequently the logic delay of every gate is reduced and the whole circuit is capable of working at a very high frequency. Furthermore, all the NAND gates can be omitted in the circuit due to the application of the SCL.

As the delay of the XOR-Adder is in such complete consistency with that of an ordinary adder, that the entire multiplier can also be designed in the pipe line structure. First, multiple  $D$  flip-flops are added in between the adder and the XOR-Adder or in between the adders themselves. Then a pipe line structure is inserted inside the adder unit as well as the XOR-Adder unit respectively to ensure that the signal only needs to go through two logic gates at most in one clock interval.

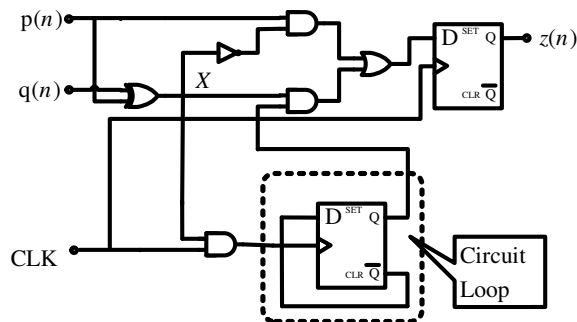


Figure 3: Structure of the novel Adder.

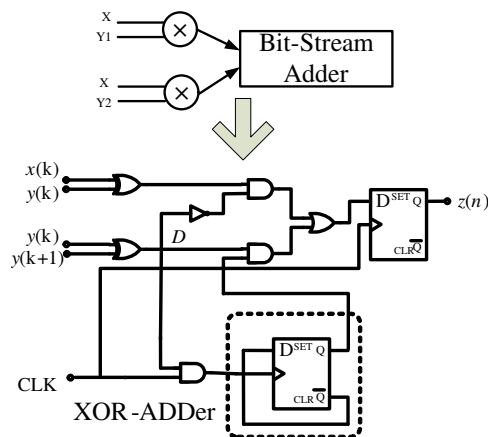


Figure 4: Structure of the XOR-Adder

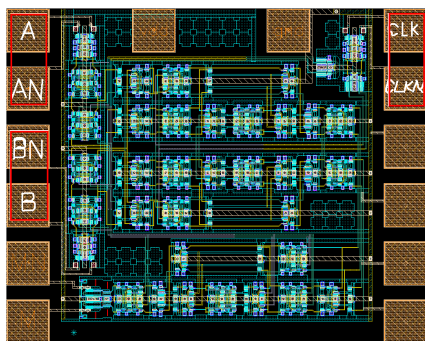


Figure 5: Layout of the multiplier.

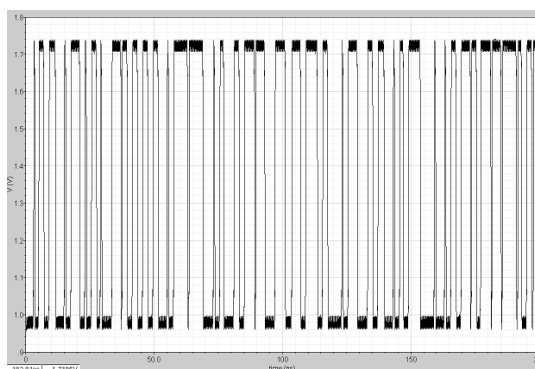


Figure 6: Output of multiplier in candance.

The entire chip, the layout of which is as shown in Fig. 4, is fabricated in a TSMC’s 0.18- $\mu\text{m}$  CMOS process and occupies an area of  $575 \mu\text{m} \times 700 \mu\text{m}$ . As can be seen from the layout the input and output signals of all the modules in the circuit are differential signals in SCL.

#### 4. NOISE ANALYZE

The output noise in the band can be calculated according to the structure of the multiplier. In fact, this noise mainly consists of two parts. The first part is the quantization noise of the input signal which is actually brought in by the  $\Sigma\Delta$  modulator, and Equation (4) gives the expression.

$$E(w) = 2e_{rms} \sqrt{\frac{2}{f_s}} \sin\left(\frac{w}{2f_s}\right), \quad e_{rms} = \delta/\sqrt{12} \quad (4)$$

where  $\delta$  is the sampling interval, and  $f_s$  is the sampling frequency. Multiplication in the time-domain corresponds to the convolution in the frequency domain. So during the process a large quantity of quantization noise which has been shaped is involved in the signal band again. This part of the noise can be given as:

$$S_1(w) = |H(w)|^2 (S_x(w) * E_y(w) + S_y(w) * E_x(w) + E_x(w) * E_y(w)) \quad (5)$$

where  $H(w)$  is the transfer function, which due to the fact that  $L = 4$  in this multiplier can be expressed as

$$H(w) = \frac{1}{4} \sum_0^3 \exp(-jwm/f_s) \quad (6)$$

The second part of the noise which has no relationship with the input is brought about by the

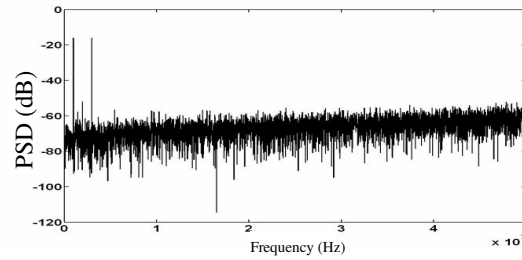


Figure 7: Spectrum of the output signal.

logical algorithm itself which is expressed by formula (7).

$$P_2(w) = \left( r(0) + 2 \sum_{m=1}^{\infty} r(m) \cos(wm/f_s) \right) \sum_{k=0}^{2M-1} \frac{1}{2^k} \quad (7)$$

where  $r(m)$  is the autocorrelation coefficient of the Bernoulli sequence.

## 5. SIMULATION RESULT

In practice, the input of this chip should be the binary bit-stream based on SDM. But how to obtain the bit-stream in simulation becomes a hard nut. Here, a method is devised to imitate the real output of a sigma-delta modulator by using the **vwplf** module in Candance. Firstly we get the numerical output of SDM in Matlab simulation, where two sinusoidal input signals with a frequency of 20 MHz and 30 MHz are modulated at 4 GHz clock frequency. Secondly all the output data in Matlab are loaded into the input end of the multiplier at a designated interval through **vwplf** module file in Candance, thus accomplishing the multiplication of the two sinusoidal signals. Here, the signal rising and falling edge is set to 2 ps. The final post-simulation output waveform is shown in Fig. 6. By comparing the output with the theoretical values no error code can be found when the sampling frequency is 4 GHz. The spectrum of the multiplier output signal is shown in Fig. 7, where the SNR calculated in Matlab is 38.53 dB.

## 6. CONCLUSION

A multiplier unit which is capable of handling high-speed sigma-delta modulated bit streams is presented in this paper. Several improvements have been made upon conventional multiplier: first, the XOR-Adder applied to the first level and a short loop delay adder are designed to shorten the delay of the gates and improve the speed. At the same time SCL technology and pipeline structure are used in IC design to raise the clock frequency of the chip. The simulation results indicate that the chip with its BER at the 4 G frequency being almost 0, can definitely be applied to high speed DSPs for sigma-delta modulated bit-streams.

## REFERENCES

1. Fujisaka, H., T. Kamio, C. J. Ahn, M. Sakamoto, and K. Haeiwa, "Sorter-based arithmetic circuits for sigma-delta domain signal processing; Part I: Addition, approximate transcendental functions, and log-domain operations," *IEEE Transactions on Circuits and Systems I: Regular Papers*, Vol. 59, 1952–1965, 2012.
2. Fujisaka, H., M. Sakamoto, C. J. Ahn, T. Kamio, and K. Haeiwa, "Sorter-based arithmetic circuits for sigma-delta domain signal processing; Part II: Multiplication and algebraic functions," *IEEE Transactions on Circuits and Systems I: Regular Papers*, Vol. 59, 1966–1979, 2012.
3. Ng, C. W., N. Wong, and T. S. Ng, "Efficient FPGA implementation of bit-stream multipliers," *Electronics Letters*, Vol. 43, 496–497, 2007.
4. Liang, Y., Q. Meng, Z. G. Wang, and X. D. Guo, "Design of bit-stream neuron based on direct Sigma-Delta signal process," *International Conference on Wireless Communications & Signal Processing, WCSP 2009*, 1–3, 2009.
5. Hart, A. and S. P. Voinigescu, "A 1 GHz bandwidth low-pass delta sigma ADC with 20–50 GHz adjustable sampling rate," *IEEE Journal of Solid-state Circuits*, Vol. 44, 1401–1414, 2009.

6. Dagher, E. H., P. A. Stubberud, W. K. Masenten, M. Conta, and T. V. Dinh, “A 2-GHz analog-to-digital delta-sigma modulator for CDMA receivers with 79-dB signal-to-noise ratio in 1.23-MHz bandwidth,” *IEEE Journal of Solid-state Circuits*, Vol. 39, 1819–1828, 2004.
7. Liang, Y., Z. G. Wang, Q. Meng, and X. D. Guo, “Design of high speed high SNR bit-stream adder based on Sigma-Delta modulation,” *Electronics Letters*, Vol. 46, 752–753, 2010.
8. Matic, T., T. Svedek, and M. Herceg, “An analog multiplier based on asynchronous sigma-delta pulse amplitude modulation,” *2011 10th International Conference on Telecommunication in Modern Satellite Cable and Broadcasting Services (TELSIKS)*, 707–710, 2011.
9. Zrilic, D. G., “Circuit for multiplication of two sigma-delta modulated pulse streams,” *World Automation Congress (WAC)*, 1–5, 2010.
10. Fujisaka, H., R. Kurata, M. Sakamoto, and M. Morisue, “Bit-stream signal processing and its application to communication systems,” *IEE Proceedings — Circuits, Devices and Systems*, Vol. 149, 159–166, 2002.
11. Alioto, M. and G. Palumbo, “Design strategies for source coupled logic gates,” *IEEE Transactions on Circuits and Systems I: Fundamental Theory and Applications*, Vol. 50, 640–654, 2003.

# Effect of Low-power Microwave Radiation on Seed Growth Rate

M. Fuangfoong, K. Eaipresertsak, T. Chim-Oye, and K. Dungkanya

Department of Physics, Faculty of Science and Technology  
Thammasat University, Rangsit Center, Klongluang, Pathum Thani 12120, Thailand

**Abstract**— In this paper, the influence of power density and exposure time of low power microwave radiation on seeds growth rate is reported. A 9.44 GHz X-band Gunn diode based microwave test bench was used as a source of microwaves for the experiment. Seed samples were mung bean. Two experiments were carried out. First, the effect of microwave radiation power and exposure time on seed germination and stem length was studied under irradiation for 5 days. Second, the effect of watering seeds with treated water was measured in terms of germination rate and length of stems at 5th days after sowing. The treatment water was irradiated at varied exposure time from 10, 20, 30, 40, 50 to 60 minutes.

## 1. INTRODUCTION

The influence of electromagnetic wave on biological objects was studied by Devyatkov and Golant in the early 1960s [1]. Banik et al. reviewed the effects of microwaves, on animal and human health. In their paper, the most popular opinion outlined was that the effect of microwaves can be attributed mainly to heating. Some authors have investigated the influence of microwaves treatment on different properties of seeds. Yoshida et al. treated soybean seeds with microwave radiation (2.45 GHz) for 6 to 12 min with the aim of improving the distribution of triglycerides in the seed coat [2]. L. Oprică has studied microwave treatment with power density of 1 mW/cm on rape seed (*Brassica napus*) and concluded that the microwaves variation of catalase and peroxidase activities depended on the age of the plants, time of exposure and state of seeds (germinated and non-germinated) [3] However, the treatment with microwave radiation as a stimulation agent in agriculture is not yet sufficiently investigated.

This research explored the effects of microwave exposure in two ways. First, mung bean (*Vigna radiate*) seeds were exposed to low power radiation at 9.44 GHz, at varying power densities and for varying periods of time. Secondly, water was exposed to microwave radiation for varying time periods. The treated water was then used to water seeds.

## 2. MATERIALS AND METHODS

The first experiment investigated the effect of microwave power density and exposure time on seed germination and stem length. The experimental set up as shown in Figure 1 consisted of a 9.44 GHz X-band generated by a Gunn diode with horn antenna, power supply, reflector plate, seed sample and sample container. The other instruments used comprised an  $E$ -field detector, beakers, cylinders and a ruler. The radiation power was varied by varying the distance between the horn antenna and the sample. Gaps of 5.4 cm, 7.0 cm and 8.6 cm were used. The sample seeds were divided into three groups — a control and two treatment groups. The number of seeds in each group was fifty seeds. Table 1 and Table 2 give the microwave parameters used. The seeds were cultured on wet paper in a small Petri dish ( $\varnothing = 15$  cm and  $h = 2$  cm) and 30 ml of water was added every day. The first treatment group was placed under the horn antenna and the seed sample was exposed to microwave radiation for 5 days in a laboratory with exposure to natural light. Seeds sample in the second treatment group were exposed to microwave radiation for 20, 30, 40, 50 and 60 seconds daily at a distance of 5.4 cm. Seed germination was observed daily and root length at 5th day was measured. The second experiment was designed to test the effect of water treatment on the growth rate of seed germination. The samples were watered using treated water every day for 5 days and the stem length was measured at the 5th day. The treated water was irradiated with 9.44 GHz microwave radiation and the exposure times were varied from 20, 30, 40, 50 to 60 minutes. The beaker of 30 mL water was placed under the horn antenna instead of seed samples in Figure 1. The microwave parameters for this experiment are shown in Table 3.

## 3. RESULTS AND DISCUSSION

The results for power density on seed germination are shown in Table 4. The rate of seed germination under microwave irradiation was slightly higher compared to that of the control sample

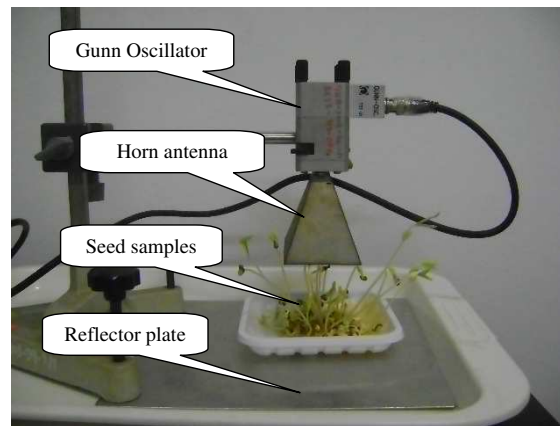


Figure 1: Experimental set up for microwave exposure.

Table 1: Variation of power density.

Gap between sample and Antenna (cm)	Frequency (GHz)	Power to Gunn diode (mW)
5.4	9.44	20
7.0	9.44	20
8.6	9.44	20

Table 2: Variation of exposure time on seeds.

Gap between samples and Antenna (cm)	Frequency (GHz)	Power to Gunn diode (mW)	Exposure time (min.)
7.0	9.44	20	10
7.0	9.44	20	20
7.0	9.44	20	30
7.0	9.44	20	40
7.0	9.44	20	50
7.0	9.44	20	60

Table 3: Variation of exposure time to water.

Gap between water and Antenna (cm)	Frequency (GHz)	Power to Gunn diode (mW)	Water volume (mL)	Exposure time (min.)
7.0	9.44	20	30	10
7.0	9.44	20	30	20
7.0	9.44	20	30	30
7.0	9.44	20	30	40
7.0	9.44	20	30	50
7.0	9.44	20	30	60

in the first two days, but these differences disappeared after 4 days. The results for the effect of microwave power density on stem length after 5 days are shown in Figure 2. It can be seen that the length of the stem changes with microwave power density. The higher the power density, the longer the stem length. For the fixed microwave power density but varied exposure time, the stem of the samples with exposure time of 30 seconds daily increased faster than that of the control group as shown in Figure 3. This result was similar to that of Contrary [6]. The explanation may be that there is certain microwave power density that is suitable for plant growth.

Figure 4 shows the results for the stem length of mung bean seeds after being watered with irradiated water. The results for the stem length on the 5th day indicate that the stem length ranged from 10.3 cm to 11.1 cm depending on water exposure time. Stem length of the seed watered by water with an exposure time of 40 minutes increased faster than of the control group but there

Table 4: Effect of power density on numbers of seed germination.

Day	Controlled	Gap 5.4 cm	Gap 7.0 cm	Gap 8.6 cm
1	2	7	5	1
2	31	42	37	36
3	48	50	49	47
4	49	50	50	50

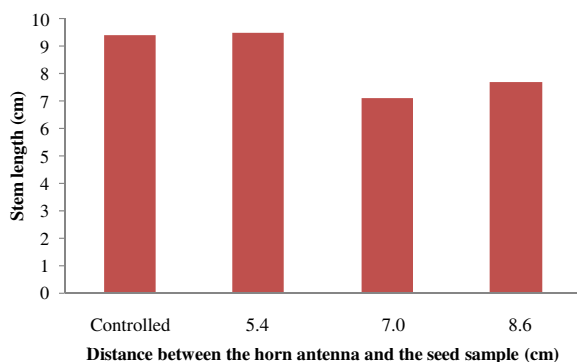


Figure 2: Effect of power density on stem length (in cm) at 5th day.

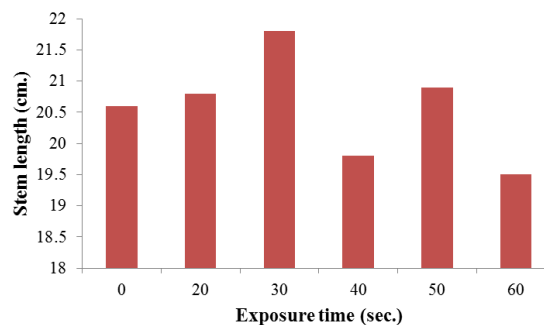


Figure 3: Effect of microwave radiation exposure time on stem length at the distance 5.4 cm.

was little difference with the control group for test groups with other exposure time. The reason may be the ease of transportation of water molecules in the osmosis system of water treated by microwave irradiation. The experiment on effect of water treatment to the growth rate should be further investigated.

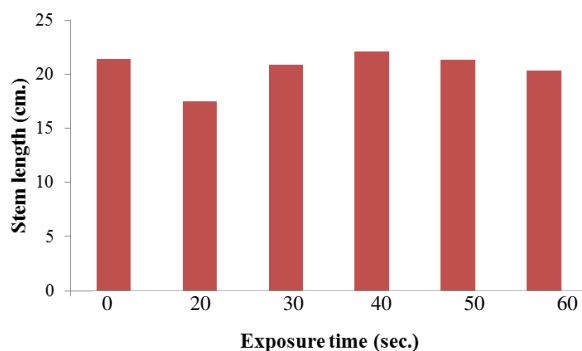


Figure 4: Effect of water treatment on stem length in cm at 5th day.

#### 4. CONCLUSIONS

The influence of power density of continuous microwave radiation at the frequency 9.44 GHz on the germination of mung bean seeds did not show any positive impact on the rate of seed germination or on the length of the stem after 5 days. The influence of microwave power density on seed growth rate may occur only at some certain density. Moreover, after sowing, the seeds watered by water exposed to microwave radiation for 40 minutes grow faster than that of the control sample.

#### ACKNOWLEDGMENT

The authors would like to thank Thammasat University for providing necessary facilities to carry out this research study.

#### REFERENCES

1. Karpovich, V. A., V. N. Rodionova, and G. Ya. Lepyanyan, "Application of microwave energy in modern biotechnologies," *MSMw'2001 Symposium Proceedings*, 909–910, Kharkov, Jun. 4–9, 2001.

2. Yoshida, H., S. Takagi, and Y. Hirakawa, “Molecular species of triacylglycerols in the seed coats of soybeans following microwave treatment,” *Food Chemistry*, Vol. 70, 63–69, 2000.
3. Oprică, L., “Effect of microwave on the dynamics of some oxidoreductase enzymes in *Brassica napus* germination seeds,” *Analele Științifice ale Universității, “Alexandru Ioan Cuza”, Secțiunea Genetică și Biologie Moleculară*, Vol. 9, No. 4, 11–16, 2008.
4. Aladjajiyan, A., “Effect of microwave irradiation on seeds of *Lenitils* (*Lens Culinais*, Med.)”, *Romanian J. Biophys.*, Vol. 20, No. 3, 213–221, Bucharest, 2010.
5. Kala, B. K. and V. R. Mohan, “Effect of microwave treatment on the antinutritional factors of two accessions of velvet bean, *Mucuna Pruriens*, (L.) DC. *Var. utilis* (Wall.ex Wigth) Bak. Ex Burek,” *International Food Research Journal*, Vol. 19, No. 3, 961–969, 2012.
6. Contrary, M., “Does microwaving bean seeds have an effect on their germination?,” new 1-doc-d308426029, posted, Feb. 12, 2012, <http://ebookbrowse.com>.

# Additional Efficiency Enhanced for DL-ARC Triple-junction GaAs/Ge Solar Cells Based on Indium Nanoparticles Surface Plasmon Light Scattering

Chi-He Lin, Wen-Jeng Ho, Yi-Yu Lee, Jheng-Jie Liu,  
Po-Hung Tsai, and Yu-Peng Chang  
Department of Electro-Optical Engineering  
National Taipei University of Technology, Taipei 106, Taiwan

**Abstract**— In this paper, we experimentally demonstrated the photovoltaic performance enhancement of a double layer (DL) anti-reflective coating (ARC) triple-junction GaAs/Ge solar cells by using indium nanoparticles surface plasmonics light scattering. The epitaxial structure of triple-junction GaAs/Ge solar cell was grown by metal-organic chemical vapor deposition (MOCVD) and the cell was deposited with TiO<sub>2</sub> and Al<sub>2</sub>O<sub>3</sub> anti-reflective layers by e-beam evaporator on the top surface. A 3-nm thick indium film was then deposited on ARC-layer surface by e-beam evaporation system and subsequently annealed by RTA at 200°C for 20 min in H<sub>2</sub> ambient to obtain nano-size indium nanoparticles. The performances of the fabricated DL-ARC triple-junction GaAs/Ge solar cell without indium nanoparticles show that the short circuit current ( $I_{SC}$ ) of 12.46 mA, open circuit voltage ( $V_{OC}$ ) of 2.53 V, fill factor (FF) of 0.87, and conversion efficiency ( $\eta$ ) of 32.59% are obtained under 1 sun AM1.5G solar simulation. As the cell coated with indium nanoparticles, however,  $I_{SC}$  increase to 12.59 mA and  $\eta$  increase to 33.18% are presented. The increase in  $I_{SC}$  and  $\eta$  are attributed to the contribution from the indium nanoparticles surface plasmonics light scattering. Additional efficiency of 1.79% enhanced for a DL-ARC triple-junction GaAs/Ge solar cell was obtained in this study.

## 1. INTRODUCTION

High conversion efficiency of GaAs-based solar cells under one-sun and/or multi-sun concentrated condition has been demonstrated for used in space applications and in the terrestrial solar power plants. However, GaAs-based multiple-junction (MJ) solar cells can be further absorbed a wide range of solar energy spectrum to obtain higher conversion efficiency. To optimize the epitaxial layer quality and device processing as well as using broadband double-layer anti-reflective coating (DL-ARC) for further high efficiency MJ solar cells have been proposed in recent years [1]. Because the bare-type MJ solar cells and the MJ solar cell coated with ARC always have a current mismatched between the top-cell and middle-cell. Improving the current-limited cell's photocurrent to approach the other one sub-cell can be enhanced the total photocurrent generated and conversion efficiency. Schaadt et al. shown that the resonant excitation of plasmon in metallic nanoparticles can be caused a strong absorption in the Si-based photodiode [2]. In addition, as deposited metallic nanoparticles such as gold (Au) and silver (Ag) nanoparticles on the surface of solar cells to enhance the photovoltaic performance have been successfully demonstrated by some researchers [3–5]. However, there is rarely research on using Indium material for nanoparticles to enhance the conversion efficiency of solar cells, especially, for GaAs-based multiple-junction solar cells.

In this paper, we demonstrate experimentally the performance enhancement of a middlecell current-limited DL-ARC triple-junction GaAs/Ge solar cell using a nano-sized indium-nanoparticles surface plasmonics light scattering. The reflectance spectra are used to examine and compare before and after applied indium-nanoparticles on the surface of the DL-ARC triple-junction GaAs/Ge cell. The dark current-voltage (I-V) and light I-V under AM1.5G illumination are also measured and analyzed. Moreover, the enhanced photovoltaic performance be confirmed by reflectance spectrum, short-circuit current ( $I_{sc}$ ), and conversion efficiency ( $\eta$ ) parameters, before and after the DL-ARC triple-junction GaAs/Ge solar cells coated with the indium nanoparticles.

## 2. EXPERIMENT

The schematic of triple-junction GaAs/Ge solar cell consisted of a GaInP top cell with an absorbed range from 300 nm to 650 nm, a GaAs middle cell with an absorbed range of 650–900 nm and a Ge bottom cell with absorbed range of 990–1850 nm, as shown in Fig. 1. The epitaxial layers of the top-cell and middle-cell were grown by metal-organic chemical vapor deposition (MOCVD). The Ge bottom cell junction was created during MOCVD growth of the middlecell and topcell

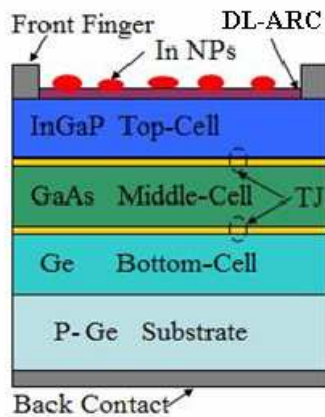


Figure 1: Schematic of DL-ARC triple-junction GaAs/Ge solar cell with indium nanoparticles.

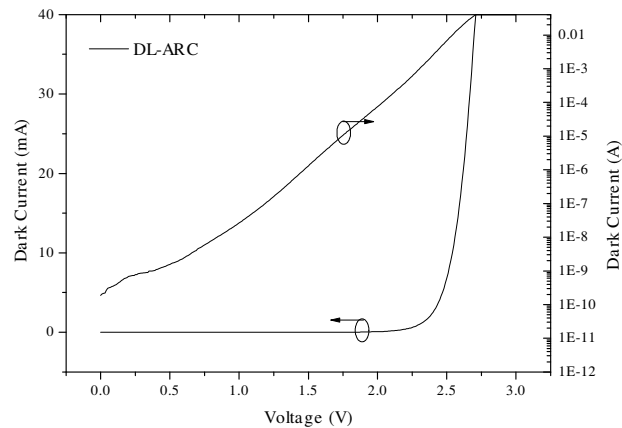


Figure 2: Typical dark forward current-voltage (I-V) characteristics of the DL-ARC triple-junction GaAs/Ge solar cell.

by diffused n-type dopant (As) into a p-type Ge substrate. The subcells are connected in series by means of the tunnel diodes. After MOCVD growth, the Ni/Ge/Au/Ag/Au and Au/Ag/Au for ohmic-contacts were deposited on front-side and back-side by e-beam evaporation, respectively. Next,  $\text{TiO}_2$  and  $\text{Al}_2\text{O}_3$  double layer (DL) with quarter wavelength thickness were deposited on the top surface by e-beam evaporator. The solar cell with a chip size of  $1 \times 1 \text{ cm}^2$  was obtained after isolated etching and sawed dicing. Finally, the 3-nm thick indium ( $I_n$ ) film was then deposited on ARC-layer surface by e-beam evaporation system and subsequently annealed by RTA at  $200^\circ\text{C}$  for 20 min in  $\text{H}_2$  ambient to obtain nano-size indium nanoparticles.

To characterize device performance, dark forward current-voltage (I-V) characteristics was first measured by a semiconductor component analyzer to examine the turn-on voltage, ideality factor ( $n$ ) and saturation current ( $I_0$ ) of triple-junction GaAs/Ge solar cell. Light I-V was then measured under 1 sun AM1.5G solar simulation to obtain the photovoltaic performance parameters. In addition, we also measured the reflectance response of the fabricated cell with double layers coating. For further understanding the nanoparticles plasmonic light scattering effects, the DL-ARC triple-junction GaAs/Ge solar cell deposited with indium nanoparticles was also characterized again by reflectance and light I-V measurements, compared to the cell without coated with indium nanoparticles. The enhanced photovoltaic performance of DL-ARC triple-junction GaAs/Ge solar cells can be confirmed by reflectance spectrum, short-circuit current ( $I_{sc}$ ), and conversion efficiency ( $\eta$ ) parameters, before and after coated the indium nanoparticles on the cell.

### 3. RESULTS AND DISCUSSION

Figure 2 shows the typical dark forward current-voltage (L-I) characteristics of the DL-ARC triple-junction GaAs/Ge solar cell at temperature of  $25^\circ\text{C}$ . The turn-on voltage of 2.25 V, ideality factor ( $n$ ) of 4.62 and saturation current ( $I_0$ ) of  $4.05 \times 10^{-12} \text{ A}$  are obtained. Such low values of  $n$  and  $I$  indicated that the deposited  $\text{TiO}_2$  and  $\text{Al}_2\text{O}_3$  layers serve as a good passivation layer and the epitaxial layers had excellent film quality in the fabricated cell. Fig. 3 plots the reflective spectrum of the DL-ARC triple-junction solar cell coated without and with indium nanoparticles. The oscillated reflectance-curves are presented at wavelength range 650–900 nm and beyond 900 nm, which corresponding to the middle-cell and bottom-cell operation range, due to the cavity oscillation of incident light in the middle-cell and bottom-cell. The reflectance of the cell coated with indium nanoparticles can be also observed smaller than that of the cell without indium nanoparticles as the wavelengths below 750 nm. On the other hand, the wavelength of the incident light beyond 750 nm, the reflectance was higher for the cell coated with indium nanoparticles. Which suggest that the low reflectance between the wavelength of 350 nm and 750 nm was due to the indium nanoparticles plasmonic light scattering and can be enhanced the photocurrent generated in the top-cell and middle-cell.

Figure 4 illustrates the light I-V of the cell without and with indium nanoparticles under 1 sun AM1.5G illumination. The  $I_{sc}$  increase from 12.46 mA to 12.59 mA and the  $\eta$  increase from 32.59% to 33.18% are obtained. The increase in  $I_{sc}$  by 1.08% are mainly contributed from middle

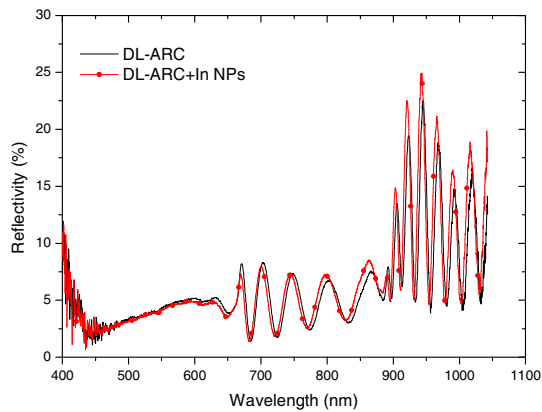


Figure 3: Reflective spectrum of the DL-ARC triple-junction solar cell coated without and with indium nanoparticles.

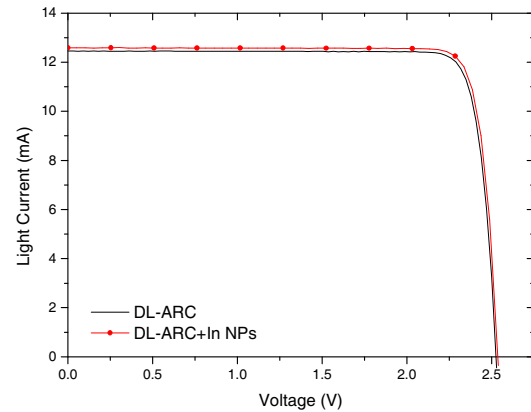


Figure 4: Light I-V of the DL-ARC triple-junction solar cell without and with indium nanoparticles under 1 sun AM1.5G illumination.

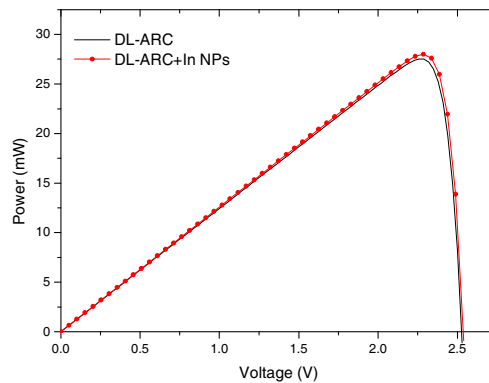


Figure 5: Output power-voltage (P-V) characteristics of the DL-ARC triple-junction solar cell without and with indium nanoparticles.

cell due to a significant light scattering at wavelengths 650–750 nm band which was the middle-cell operation range. Fig. 5 shows the output power-voltage (P-V) characteristics of the cell without and with indium nanoparticles. The maximum output-power ( $P_{\max}$ ) was 28.02 mW and 27.52 mW corresponding to the cell with and without indium nanoparticles, respectively. Similarly,  $P_{\max}$  increase by 1.79% was observed which mainly contributing from the maximum current ( $I_{\max}$ ). In conclusion the increase in  $I_{SC}$ ,  $\eta$  and  $P_{\max}$  are attributed to the contribution from the indium nanoparticles surface plasmonics light scattering.

#### 4. CONCLUSIONS

Additional efficiency of 1.79% enhanced for a DL-ARC triple-junction GaAs/Ge solar cell based on indium nanoparticles surface plasmon light scattering was demonstrated. The short-circuit current increase from 12.46 mA to 12.59 mA, the maximum output-power increase from 27.52 mW to 28.02 mW, and the conversion efficiency increase from 32.59% to 33.18% are obtained as the DL-ARC triple-junction GaAs/Ge solar cell coated with indium nanoparticles, compared to the cell without coated indium nanoparticles.

#### ACKNOWLEDGMENT

The authors would like to thank the National Science Council of the Republic of China for financial support under grant NSC-100-2221-E-027- 053-MY3. The authors also like to thank the Win Semiconductor Corp for providing the triple-junction solar cell wafer.

#### REFERENCES

1. Aiken, D. J., "Antireflection coating design for series interconnected multi-junction solar cells," *Prog. Photovolt: Res. Appl.*, Vol. 8, No. 6, 563–570, 2000.

2. Schaadt, D. M., B. Feng, and E. T. Yu, “Enhance semiconductor optical absorption via surface Plasmon excitation in metal nanoparticles,” *Appl. Phys. Lett.*, Vol. 86, 063106–063108, 2005.
3. Pillai, S., K. R. Catchpole, T. Trupke, and M. A. Green, “Surface plasmon enhanced silicon solar cells,” *Journal of Appl. Phys.*, Vol. 101, 093105–093112, 2007.
4. Kalfagiannis, N., P. G. Karagiannidis, C. Pitsalidis, N. T. Panagiotopoulos, C. Gravalidis, S. Kassavetis, P. Patsalas, and S. Logothetidis, “Plasmonics for organic solar cells,” *Solar Energy Materials and Solar Cells*, Vol. 104, 165–174, 2012.
5. Nakayama, K., K. Tanabe, and H. A. Atwater, “Plasmonic nanoparticles enhanced light absorption in GaAs solar cells,” *Appl. Phys. Lett.*, Vol. 93, 121904-1–121904-3, 2008.

# Analysis and Construction of Output Capacitance Filter for High Power LLC Resonant Converter

J. Lettl and O. Plhak

Department of Electric Drives and Traction, Faculty of Electrical Engineering  
Czech Technical University in Prague, Technicka 2, 166 27 Prague 6, Czech Republic

**Abstract**— The authors propose capacitive output filter for resonant inverter type DC/DC converter designed for trolley vehicles. There is designed solution based on real sample, which is further discussed, particularly in terms of their volume. Optimal solution of the printed circuit board (PCB) design requires compliance with certain rules. Their non-compliance leads to local overload, etc.. Here are summarized the results obtained by measurements on the sample.

## 1. INTRODUCTION

Series-parallel resonant converter, often called LLC, is the most famous topology with soft commutated switches (Figure 1). This is the type DC/DC converter. It consists of half-bridge with MOSFETs. Next, there is resonant part, which is in most cases integrated into the high-frequency transformer. The last part is followed by a rectifier, filter, and load. Switches Q1 and Q2 switch softly thank to a resonance. The goal is that the soft switching frequency may be higher than for hard switching. To understand the principle of gain characteristic is important (Figure 1).

Resonant cell have two peaks ( $f_0$ ,  $f_P$ ). On the  $x$ -axis there is the normalized frequency  $f_N$  equal to the ratio of the switching frequency and  $f_0$ . On the  $y$ -axis there is the ratio of the output voltage divided by the transformer ratio times the output voltage. Each curve corresponds to a different load ( $Q =$  quality factor). The drive is controlled by complementary pulses with duration  $T/2$  (for simplicity we do not discuss dead time). This frequency control is used above  $f_0$  for obtaining zero voltage switching (ZVS), which is suitable for the MOSFET. As it can be seen from Figure 1, reducing the switching frequency leads to increase gain, the converter is opening. On the other side, when the load is decreasing the driver have to increase the switching frequency. The principle of this inverter is very well described, in an example [1, 2].

For practical use in trolley applications, it is necessary a wide input voltage range, where the converter is still working. For this we need a large slope of the gain curve. It is tuned by ratio of inductances ( $L_r/L_m$ ) [1]. The implementation of this topology is very well described, e.g., [3]. Due to the high switching frequency we can realize inductances small and often integrate with transformers and resonant capacitor into one (e.g., by using planar cores). Another condition provides electrical isolation between the primary and secondary of step-down transformer. Therefore, this type of converter could be ideal for replacing existing converters supplied from trolley with hard switching. Upon deeper analysis, it can be proven that on the filter  $C_f$  appears large peak current.

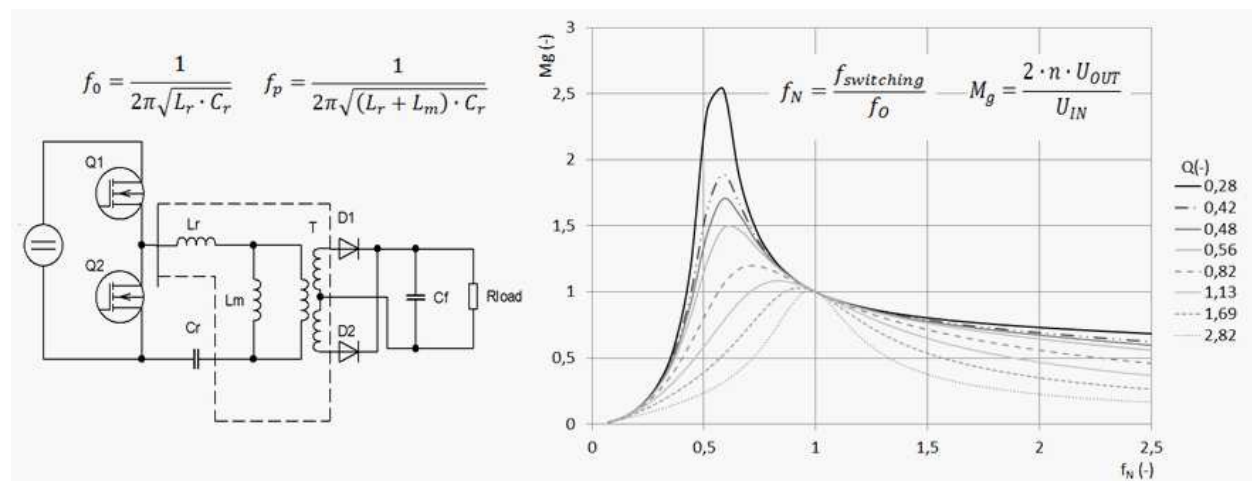


Figure 1: Converter topology and gain curve.

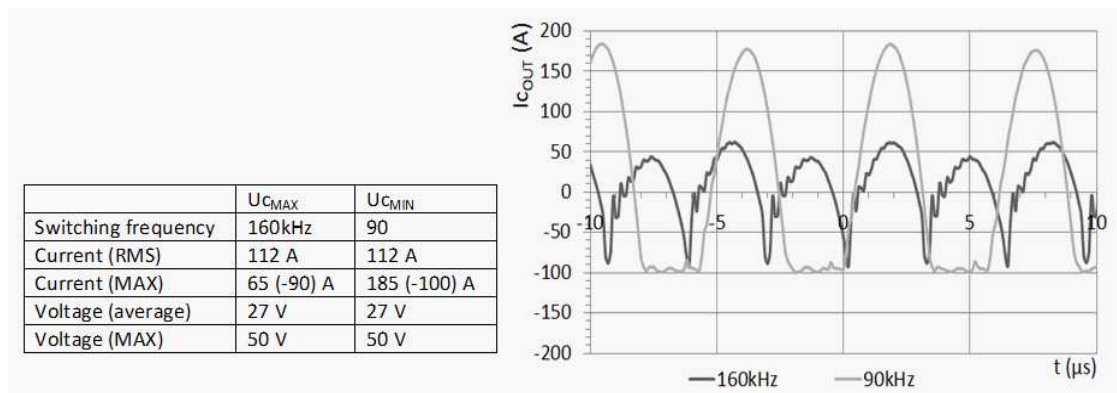


Figure 2: Modelling current waveform of the output filter capacitor (conditions is maximum output power and minimum/maximum input power).

Table 1: Proposed solutions of capacitor filter.

Solution	Volume	Company
DC link capacitor (bottle electrolytic)	2.3 dm <sup>3</sup>	WIMA DCH3G07200
Snubbed capacitor (high current)	28.0 dm <sup>3</sup>	ZEZ SILKO DVPJ
High Current capacitor, Ultra Ripple	2 dm <sup>3</sup>	CDE Cornell Dubilier Electronics
Electrolytic capacitor (extended)	1 dm <sup>3</sup>	Keindeil K02
Electrolytic capacitor (standard, leaded) +DPS	0.3–0.5 dm <sup>3</sup>	Jamicon TM

For small power converter, there are not so noticeable extremes. For medium power these can not be ignored and must be analysed in greater depth. There will be an analysis based on real data.

## 2. STEADY STATE OF OUTPUT FILTER OF THE PROPOSED CONVERTER

The converter has the following parameters, the power is 3kW, output current  $I_{OUT} = 110$  A, output voltage 27V. The resonant frequency is controlled from 90 kHz to 160 kHz. To achieve soft switching during no load condition there has to be implemented drive skipping pulses (so-called burst mode) [5]. The theory [1] says that the critical parameters of the filter capacitor are obtained with maximum load and minimum power inverter input voltage. The second critical case is the maximum load and maximum input voltage. The values are plotted, see Figure 2. Model was analysed using Matlab (toolbox SimPowerSystems).

From the output values it is clear that the selection or design of the output filter is very critical due to high current values (Figure 2). Choosing capacitor further aggravates the requirement for output voltage ripple 5%. Then the required minimum capacity  $C_{MIN} = 1.12$  mF. Furthermore, the solution can only include capacitors that meet railway standard condition of working temperature  $-40$  to  $105^{\circ}\text{C}$ . Table 1 summarizes possible capacitors. Each row contains selected capacitor, which represents one specific type and then calculates final volume of the filter.

Among the various types of filter design are considerable differences in the final volume. Use of extended electrolytic capacitors is very simple, but it turns out that they take up much space. Similarly, the use of snubbed capacitors, designed for high impulse current, is not appropriate, because they have little capacity and the resulting volume is again enormous. Using large capacitors is not optimal; because LLC topology was chosen for high density transferred power to 28 W/in<sup>3</sup> (reduced volume). Hence, from analysis (Table 1) appears the optimal solution: filter designed using conventional standard lead electrolytic capacitor, connected on the PCB, to achieve a simple structure repeatability.

## 3. CONSTRUCTION OF OUTPUT CONVERTER WITH DPS TECHNOLOGY

The basic issue is how to choose capacitors from a wide variety of different manufacturers and how to organize it in PCB together with pins in order to prevent unwanted partial secondary effects. To achieve small losses of capacitors there is needed to select capacitor with a low equivalent resistance (losses are given by) and package size (an important parameter for cooling). Then heating is given

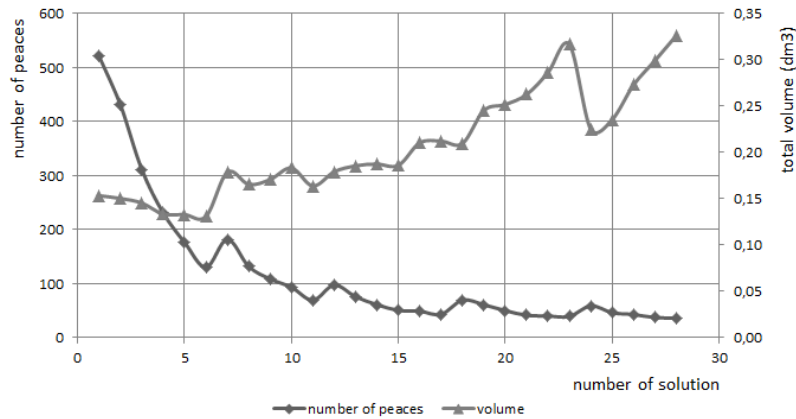


Figure 3: Comparison of total volume with used various cases. Reference is  $I_{\text{RIPPLE}} = 112 \text{ A}$ . (Size of cases and  $I_{\text{RIPPLE}}$  is from Table 2).

Table 2: Sizes of cases (used from [6]).

Number of solution	1	2	3	4	5	6	7	8	9	10	11	12	13	14	15
Diameter	5.0	6.3	6.3	8.0	8.0	8.0	10.0	10.0	10.0	10.0	10.0	12.5	12.5	12.5	12.5
High	15.0	11.2	15.0	11.5	15.0	20.0	12.5	16.0	20.0	25.0	30.0	15.0	20.0	25.0	30.0
Number of solution	16	17	18	19	20	21	22	23	24	25	26	27	28	29	
Diameter	12.5	12.5	16.0	16.0	16.0	16.0	16.0	16.0	18.0	18.0	18.0	18.0	18.0	18.0	
High	35.0	40.0	15.0	20.0	25.0	31.5	35.5	40.0	15.0	20.0	25.0	31.5	35.5	40.0	

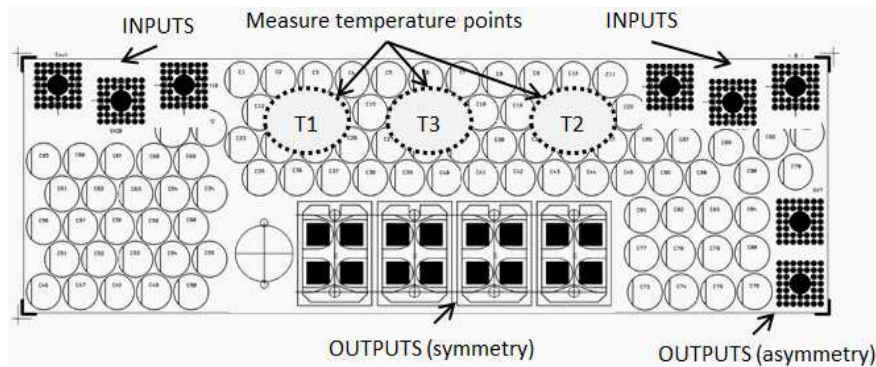


Figure 4: Proposed testing DPS.

by the product of power dissipation and thermal resistance  $\Delta T = P \cdot R_{th(\text{capacitor-core-ambient})}$ . The size of the case is also related to the size of the maximum ripple current in one case. The bigger case has worse cooling and decrease the allowable current ripple. Conversely using small case increases design complexity. To compare the use of different cases with different sizes a graph is created (Figure 3, Table 1). Reference wave has 112 A, effective. On the  $y$ -axis (left side) required number of capacitors is plotted and on the right side the total volume of the filter is calculated. The total volume for the individual solution increases with larger selection of cases. From this point of view it is advantageous to use the smallest cases to obtain a small volume solutions at the cost of a higher number of parallel connection in order to reach the required capacity and the ripple current ( $I_{\text{RIPPLE}}$ ). Data of function  $I_{\text{RIPPLE}} = f(\text{size of case})$  is from Panasonic [6].

For practical verification of knowledge listed below is PCB circuit that can be connected via four inner layers or two inner layers of PCB. There are more of used positions for capacitors. Hence, position can be variable for induce symmetry or asymmetry. Outputs and inputs are placed in two sets, symmetrically and asymmetrically (Figure 4).

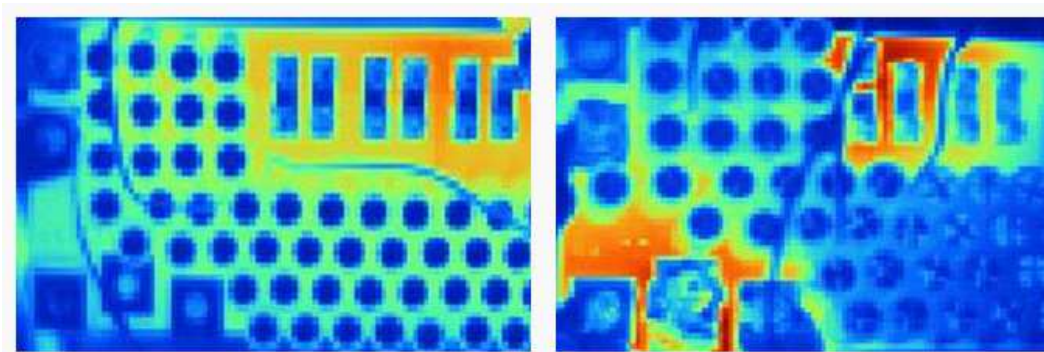


Figure 5: DPS, configurations of two layers and four layers.

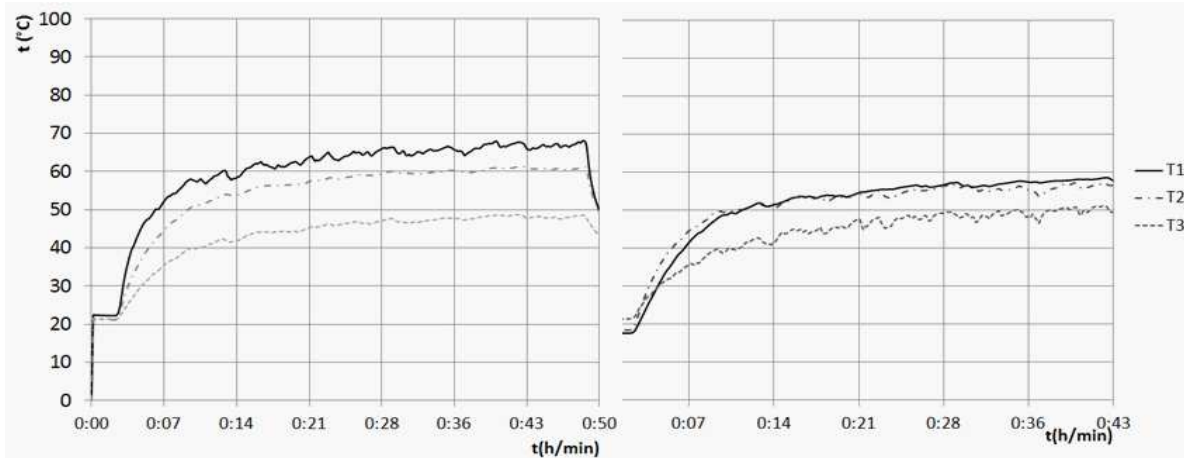


Figure 6: DPS connected via asymmetry outputs and via symmetry outputs.

For a small volume and occupied area DPS is suitable four-layer PCB, which consider integrated rectifier diodes, capacitors, pins from transformer, and connectors for deliver power out of the converter. This solution is not good for the violation of current paths at the positive and negative pole. In Figure 5 the first part shows the temperature distribution on double-layer design, the second part shows the four-layer PCB with incurred exposed places (due to crossing layers). Therefore acceptable solution is to use a two-layer PCB, where the exposed areas can be eliminated. Provide solution covers a larger area, but does not contain critical points and also provide better cooling properties due to a larger area.

Another point that affects the temperature distribution is the location of pins. If position of pins is asymmetrically on the side of PCB there is a significant temperature gradient across the area of the capacitors due to uneven current distribution. As a result is overheating of some capacitors, thereby reducing their overall lifetime. If the terminals are located symmetrically, this effect is eliminated (Figure 6).

Losses caused in the DPS are a matter of good design (e.g., cross-section of DPS). Good choice of current density make  $J_{MAX} = 33 \text{ A/mm}^2$ . The warming is made by apparent pulsating current (Figure 2) at the junction between the transformer and diode, diode and capacitor, which naturally brings additional losses. These paths must be short to reduce the resistivity of the tracks. Plus and minus pole must be directly above each other to reduce the mutual inductance. The current behind the filter has a DC value and produce minimal losses. It was further verified that the warming is radical when there is asymmetry than the warming of separated capacitors.

The next step should be optimization leading to further reduce losses in the output filter. The only way is to edit a topology in the form of confusion converter output filter for robust filter consisting of a number of passive elements. In this case, the final converter considered several converters interwork in the same capacitor. It ensures lower peaks of current, i.e., the reduction of the resulting ripple current.

#### 4. CONCLUSIONS

In the previous paragraphs are summarized recommendations for design of the filter capacitor on PCB. It is formed on the realized sample. On its construction is placed requirement of a small volume, the highest possible load current and long life. It seems the best to use only two-layer PCB using small cases of capacitors for better dissipation of generated heat. It can enhance their current capability. The design also needed to comply with design principles such as mutual symmetry of outputs and inputs and symmetry components to prevent local overloading and subsequent shortening life.

#### REFERENCES

1. Yang, B., F. C. Lee, and A. J. Zhang, “LLC resonant converter for front end DC/DC converter,” *IEEE Applied Power Electronics Conference and Exposition (APEC'02)*, 2002.
2. Fang, Y., D. Xu, Y. Zhang, F. Gao, and L. Zhu, “Design of high power density LLC resonant converter with extra wide input range,” *Graduate Problem Papers*, Ben-Gurion University of the Negev Papers, 2007.
3. Andreycaak, B., “Zero voltage switching resonant power conversion,” *Aplication Note U-138*, Texas Instruments, 1999.
4. Dranga, O., B. Buti, and I. Nagy, “Stability analysis of a feedback-controlled resonant DC-DC converter,” *IEEE Transactions on Industrial Electronics*, Vol. 50, No. 1, February 2003.
5. “8-pin high-performance resonant mode controller,” *Technical Documents*, Texas Instruments, September 2008–revised July 2011.
6. “Aluminum electrolytic capacitors, radial lead type FC/A,” *Technical Documents*, Panasonic Ltd., EE81-90.00, September 2010.

# Stable Adaptive Signal Generation in Current Based MRAS Induction Motor Sensorless Speed Control

M. Bednar, J. Lettl, and M. Vlcek

Department of Electric Drives and Traction, Faculty of Electrical Engineering  
Czech Technical University in Prague, Technicka 2, 166 27 Prague 6, Czech Republic

**Abstract**— The paper deals with generation of adaptive signal in current based MRAS speed estimation scheme. Transformation of machine equivalent impedance in steady state is used. The gained signal fulfils criterion of stability in the whole speed range (excluding situation, when  $\dot{\Psi}_r = 0$ ) and in both operating modes (motor and generator).

## 1. INTRODUCTION

Realization of the induction machine sensorless drive control is quite difficult technical problem. Many solutions with different quality degree have been found, but many of them have stability problems in some operating mode. The current based MRAS (Model Reference Adaptive Signal) method was chosen as one of the best from the view of accuracy and dynamic of speed estimation according to literature [1–8]. The only values needed for estimation algorithm are parameters of substitute scheme of the controlled machine, actual values of phase currents and voltage. The most important value for the speed estimation in MRAS system is adaptive signal, which has to enable stable speed estimation in the whole speed range (excluding situation, when  $\dot{\Psi}_r = 0$ ). Finding of proper adaptive signal is the aim of this contribution.

## 2. CURRENT BASED MRAS ALGORITHM DESCRIPTION

Induction machine speed estimation should be independent on control algorithm. It should be able to determine speed of machine working with constant supply voltage and frequency as well as speed of machine controlled by any sophisticated method. The only values needed for estimation algorithm are actual values of phase currents and voltage (easy measured in converter). The scheme of current based MRAS is depicted at the Figure 1.

The reference model, representing real machine can be seen in upper part of the scheme. The machine state is determined by supply voltage  $U_1$  and its rotational speed  $n$ . Machine state is characterised by the stator current vector. The same value of stator voltage  $U_1$  inputs into machine model in lower part of the scheme. Estimated speed obtained as a feedback signal is the second parameter of the model. Stator current is an output of the model. The adaptive signal should be obtained by comparison of reference and adaptive stator currents. The canonical  $\Gamma$  induction machine scheme is used as adaptive model, because it consists of the less possible amount of components. It makes next deduction easier.

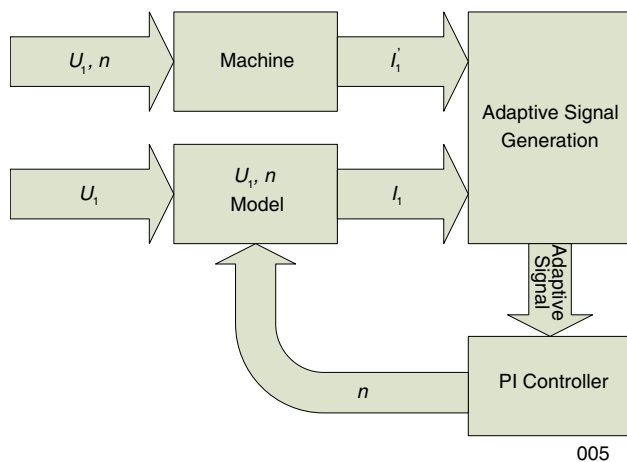


Figure 1: Current based MRAS scheme.



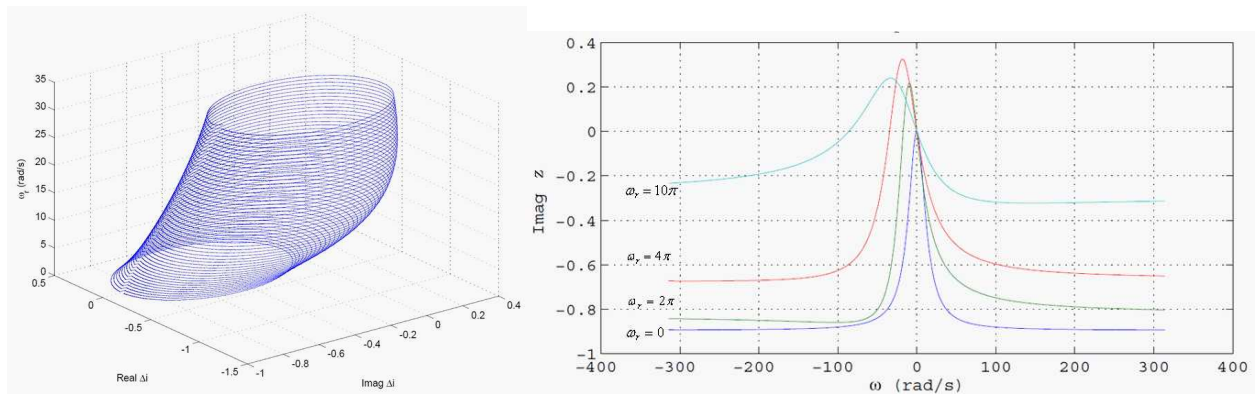


Figure 3: Transfer function shape.

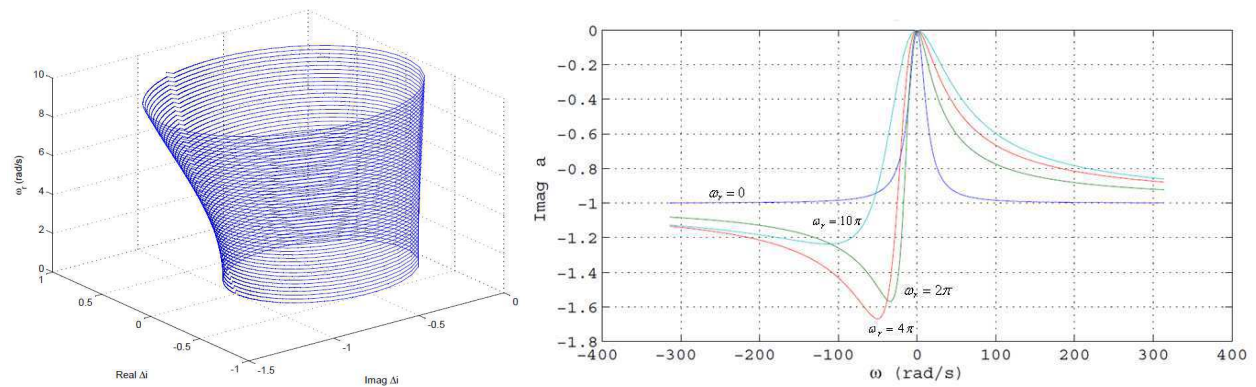


Figure 4: Transformed transfer function shape.

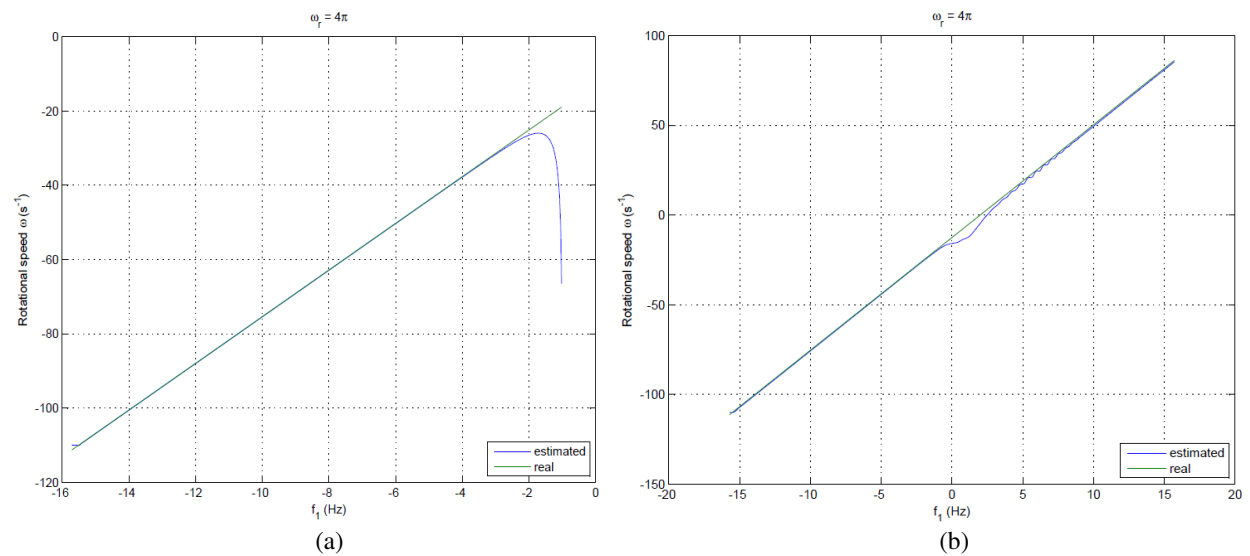


Figure 5: Difference in speed estimation (a) without using  $c$  formula and (b) with using  $c$  formula.

#### 4. ADAPTIVE SIGNAL TRANSFORMATION

The main merit of this contribution is to find the formula  $c$  which is able to transform function  $z$  into a form suitable for using as an adaptive signal. The transformation should be generally described by the following equation

$$a = \Delta\omega \cdot c \cdot z(\omega_r, \omega_s) \tag{6}$$

where  $a$  is transformed adaptive signal,  $c = f(\omega_r)$  is coefficient of transformation. It can be found by moving of function  $z$  in complex area according to criterion of having negative imaginary part for each  $\omega_r$  and each  $\omega_s$ .

The transformation formula  $c$  than has the form

$$c = \frac{(R_s + j\rho L_\mu \omega_r)(R_r^2 + L_\sigma^2 \omega_r^2)}{\rho L_\mu L_\sigma \omega_r^2 + R_r R_s} \quad (7)$$

The most important fact is that  $c$  has the constant form for the whole operating area. The shape of the adaptive transfer function is given as a proof on the next figure.

## 5. CONCLUSION

According to previous chapters,  $a$  can be used as a proper adaptive signal, because it fulfils stability requirements and enables speed identification in the whole range of drive operation area (except of the state with  $\dot{\Psi}_r = 0$ ). The main advantage of this solution is that the expression of coefficient  $c$  depends at one variable ( $\omega_r$ ) only and its realization should be easy in drive control system.

If the proper adaptive signal is available, classical PI controller can be used for feedback speed signal generation. The last figure shows the simulation of slow speed changing ( $0.5\pi/s$ ) across the zero speed area with constant  $\omega_r$ . The left side of the figure shows the situation, when the coefficient  $c$  is not used in the estimation structure. The estimation collapses in low speed brake state. The right side of the figure shows the same situation when using the coefficient  $c$ . The estimation is stable, only by very low stator frequency (when  $\dot{\Psi}_r$  is closed to zero) it has an accuracy problem, which must be solved by control of the machine, outside of the estimation algorithm.

## REFERENCES

1. Brandstetter, P., M. Kuchar, and D. Vinklerek, "Estimation techniques for sensorless speed control of induction motor drive," *IEEE Int. Symposium on Industrial Electronics*, Vol. 1–7, 154–159, Montreal, Canada, 2006.
2. Depenbrock, M. and Ch. Evers, "Model-based speed identification for induction machines in the whole operating range," *IEEE Trans. on Industrial Electronics*, Vol. 53, No. 1, 31–40, 2006.
3. Depenbrock, M., F. Hofmann, and S. Koch, "Speed sensorless high performance control for traction drives," *Proceedings of 7th Eur. Power Electronic Conference (EPE)*, Vol. 1, 1.418–1.423, Trondheim, Norway, 1997.
4. Tarchala, G., T. Orłowska-Kowalska, and M. Dybkowski, "MRAS-type speed and flux estimator with additional adaptation mechanism for induction motor drive," *IEEE Trans. on Electrical Engineering*, Vol. 1, No. 1, 7–12, 2012.
5. Kubota, H., K. Matsuse, and T. Nakano, "DSP-based speed adaptive flux observer of induction motor," *IEEE Trans. on Ind. Appl.*, Vol. 29, No. 2, 344–348, 1993.
6. Holtz, J., "Sensorless control of induction motor drives," *IEEE ETATS-UNIS*, Vol. 90, 1359–1394, New York, USA, 2002.
7. Yan, Z. and V. Utkin, "Sliding mode observer for electric machines — An overview," *IEEE Annual Conference of the Industrial Electronics Society, IECON'2002*, Vol. 3, 1842–1847, 2002.
8. Orłowska-Kowalska, T. and M. Dybkowski, "Stator current-based MRAS estimator for wide range speed-sensorless induction motor drive," *IEEE Trans. on Industrial Electronics*, Vol. 57, No. 4, 1296–1308, 2010.

# Comparison of DTC and Sliding Mode Control of IM Drive

J. Lettl, S. Fligl, and J. Bauer

Department of Electric Drives and Traction, Faculty of Electrical Engineering  
 Czech Technical University in Prague, Czech Republic

**Abstract**— This contribution strives to compare behaviors of the IM drive controlled by classical DTC and modified direct torque control strategy based on state space variable description of the IM and first order sliding mode controller. Simulations on SW Matlab/Simulink were carried out to test proposed control strategy and compare them with model of ST-DTC.

## 1. INTRODUCTION

Recently induction machines (IM) are often used in controlled electric drives. They are robust, durable and they do not need much maintenance. However their control is more difficult compared to DC machines or permanent magnet synchronous machines due to absence of separate source of electromagnetic flux. Therefore the output of the regulation algorithm for the IM must be desired current resp. voltage vector which application on terminals of the IM will produce desired flux and torque of the IM. This requirement can be reached by splitting IM control into two separate branches [1]. One component is responsible for flux production and second one is responsible for torque production. The demanded vector is then vector combination of both components.

Several control algorithms are known that offer possibility of separate control of torque and flux current component. To them belongs Field oriented control (FOC) [1] or Direct Torque Control (DTC) [2, 3]. The DTC offers high dynamics and utilization of the drive, however requires greater computational power from the controller. The control of switching frequency and thus current harmonics is problem too. The DTC controller does not include modulator, output voltage is switched more or less based on the switching table. Therefore also modified DTC strategies were developed. However most of them needs for their operation information about hardly measurable inner motor values like electromagnetic flux and torque. To estimate these values models of the machines are used. Models based on the machine’s equations are commonly used, but it seems to be useful to use model of the IM base on the state space variables, because apart from information about flux and torque it also enables to analyze analytically behavior of the IM. Fig. 1 shows the equivalent circuit of induction machine (IM).

The direct torque control algorithm is based on control of stator variables, therefore stator and rotor flux and voltage equations in stator coordinate system have to be used to describe machine. For the sliding mode control seems to be better to use flux connected coordinate system. Machine

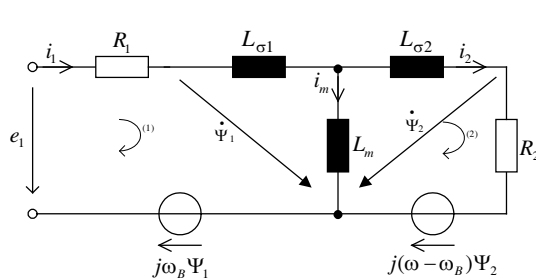


Figure 1: Induction machine equivalent circuit.

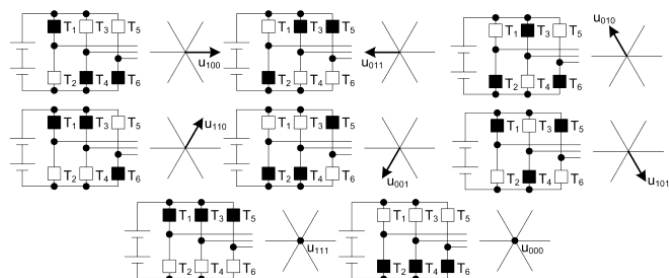


Figure 2: Visualization of the inverter output vectors.

Equation (1) both coordinate systems are:

$$\begin{aligned}
 u_{s\alpha} &= R_s i_{s\alpha} + \frac{d}{dt} \Psi_{s\alpha} & u_{sd} &= R_s i_{sd} + \frac{d}{dt} \Psi_{sd} - \omega_s \Psi_{sq} \\
 u_{s\beta} &= R_s i_{s\beta} + \frac{d}{dt} \Psi_{s\beta} & u_{sq} &= R_s i_{sq} + \frac{d}{dt} \Psi_{sq} + \omega_s \Psi_{sd} \\
 0 &= R_r i_{r\alpha} + \frac{d}{dt} \Psi_{r\alpha} + \omega_r \Psi_{r\beta} & 0 &= R_r i_{rd} + \frac{d}{dt} \Psi_{rd} - (\omega_s - \omega_r) \Psi_{rq} \\
 0 &= R_r i_{r\beta} + \frac{d}{dt} \Psi_{r\beta} - \omega_r \Psi_{r\alpha} & 0 &= R_r i_{rq} + \frac{d}{dt} \Psi_{rq} + (\omega_s - \omega_r) \Psi_{rd} \\
 \Psi_{s\alpha} &= L_s i_{s\alpha} + L_h i_{r\alpha} & \Psi_{sd} &= L_s i_{sd} + L_h i_{rd} \\
 \Psi_{s\beta} &= L_s i_{s\beta} + L_h i_{r\beta} & \Psi_{sq} &= L_s i_{sq} + L_h i_{rq} \\
 \Psi_{r\alpha} &= L_r i_{r\alpha} + L_h i_{s\alpha} & \Psi_{rd} &= L_r i_{rd} + L_h i_{sd} \\
 \Psi_{r\beta} &= L_r i_{r\beta} + L_h i_{s\beta} & \Psi_{rq} &= L_r i_{rq} + L_h i_{sq}
 \end{aligned} \tag{1}$$

Torque of IM can be calculated as:

$$M_E = \frac{3}{2} p (\Psi \times i) = \frac{3}{2} p (\Psi_d i_q - \Psi_q i_d) \tag{2}$$

The inverter will be used to supply the machine there will be only 8 voltage vectors with the value of DC-link voltage. Situation is depicted in Fig. 2.

### 2. DIRECT TORQUE CONTROL PRINCIPLE

Since the first publishing of the DTC principles by Depenbrock in 1985 [2] (Direct Self Control — DSC) and Takahashi and Noguchi in 1986 [3] (Switching Table Based DTC, ST-DTC for short), many DTC schemes have been developed by various researches. A DTC method selected for the implementation in this paper is the ST-DTC, being the most widely adopted DTC method.

The estimated torque and flux are compared with their reference values, and if they are out of their tolerance bands, an adequate voltage vector is applied to the motor stator windings. The flux is controlled by a two-level hysteresis controller and the torque is controlled by a three-level hysteresis controller. The outputs of these controllers ( $c_\Psi$  and  $c_T$ ), together with the current flux vector sector are used in the Voltage vector selection table block to select the appropriate voltage vector according to Table 1.

Controller structure is depicted in Fig. 3. Simulation results are then shown in Fig. 4. It shows reaction of the drive onto different torque steps. In order to compare results with proposed sliding mode control structure, results are transformed to the coordinate system rotating with the flux vector. Therefore the stator flux is constant and torque control is done by the current component  $i_q$ .

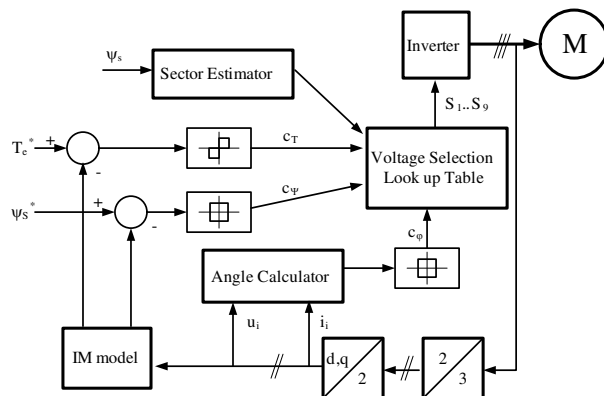


Figure 3: ST-DTC controller structure.

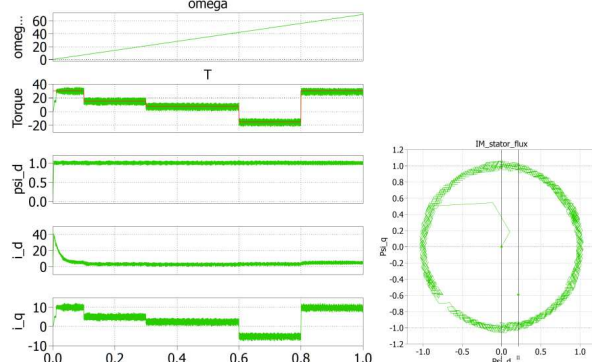


Figure 4: Simulation results ST-DTC (Torque steps, stator flux vector movement).

Table 1: Voltage selection look up table.

		1	2	3	4	5	6			1	2	3	4	5	6
$c_\Psi = 0$	$c_T = 1$	$\underline{u}_2$	$\underline{u}_3$	$\underline{u}_4$	$\underline{u}_5$	$\underline{u}_6$	$\underline{u}_1$	$c_\Psi = 1$	$c_T = 1$	$\underline{u}_3$	$\underline{u}_4$	$\underline{u}_5$	$\underline{u}_6$	$\underline{u}_1$	$\underline{u}_2$
	$c_T = 0$	$\underline{u}_7$	$\underline{u}_0$	$\underline{u}_7$	$\underline{u}_0$	$\underline{u}_7$	$\underline{u}_0$		$c_T = 0$	$\underline{u}_0$	$\underline{u}_7$	$\underline{u}_0$	$\underline{u}_7$	$\underline{u}_0$	$\underline{u}_7$
	$c_T = -1$	$\underline{u}_6$	$\underline{u}_1$	$\underline{u}_2$	$\underline{u}_3$	$\underline{u}_4$	$\underline{u}_5$		$c_T = -1$	$\underline{u}_5$	$\underline{u}_6$	$\underline{u}_1$	$\underline{u}_2$	$\underline{u}_3$	$\underline{u}_4$

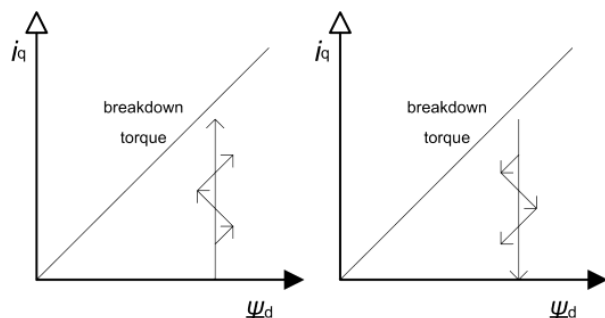


Figure 5: Sliding mode controller example.

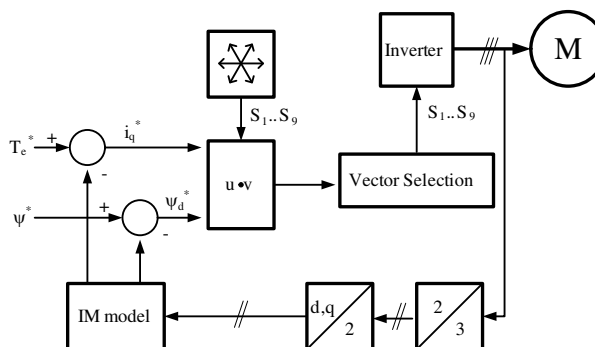


Figure 6: Proposed SM controller structure.

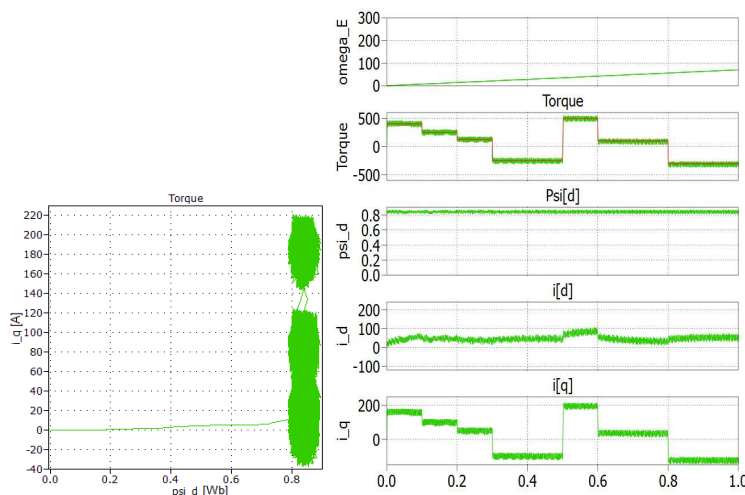


Figure 7: SM controlled IM ( $i_q$  control on sliding plane, torque steps).

### 3. SLIDING MODE CONTROLLER DESIGN

Generally sliding mode controllers were developed to control systems with relays [4]. To apply traditional control theory on such system will not bring sufficient output. The power electronics is can be classified as system which is ideal to apply sliding mode, due to switching of transistors and nonlinearity of the semiconductors. The sliding mode control is based on an exact guiding of the system state space vector via suitable switching following the prepared switching surface. However, the state vector has to first of all reach the switching plane and then the state space vector will move more or less directly to the destination position. This can cause time delay before the space vector reaches its desired position, but controller can be realized very simply with the help of comparator.

The aim is to design torque controller of IM [5]. As a first step have to be defined sliding plane. When we use coordinate system connected with flux space vector only one flux space vector component  $\Psi_d = \Psi$  will remain and thus (2) will be reduced to multiplication of  $\Psi_d$  and  $i_q$ . This means the sliding plane have been find, on  $x$  axis is machine's flux and on  $y$  axis is current component  $i_q$  and any point on this plane defines torque of the machine. Usually the flux of IM is kept constant and electrical torque of the machine is regulated by the means of regulation of current

components. So the sliding line is defined too. In this way designed sliding mode controller selects output voltage vectors that should be applied to the terminals of the machine to produce demanded torque. The sliding mode existence condition can be defined so that this control works until there is a voltage vector that can be applied to produce desired movement of the torque (Fig. 3).

When the controller reaches the destination point it starts to oscillate around this point. Analysis of the IM behaviors based on its state description was done in [6]. The block diagram of the IM drive with the sliding mode controller is in Fig. 4. Selection of the suitable voltage vector is based on the fact that fastest movement from one point to another in a space is line. Therefore the most suitable vector is selected to be nearest to the direct connecting line between actual torque and desired torque (Fig. 6). This can be seen in Fig. 7 that shows the movement of the machine state (torque). The chattering around the desired point can be clearly seen.

#### 4. CONCLUSIONS

The main goal of this paper was to compare two different torque control strategies for induction machines. The ST-DTC is well known method and is often used. IM with proposed sliding mode controller shows similar results concerning dynamics and shape of flux vector movement. However switching frequency is controlled via calculation steps of the controller. The simulation results look very promising and show that the sliding mode control outputs similar results as DTC. However the real impact of the modulation can be evaluated first after the realization of the algorithm on the real converter prototype.

#### ACKNOWLEDGMENT

This research was supported by the Grant Agency of the Czech Technical University, Prague, grant No. SGS12/067/OHK3/1T/13 and Technology Agency of the Czech Republic, grant No. TA010114-08.

#### REFERENCES

1. Vas, P., *Sensorless Vector and Direct Torque Control*, Oxford, Oxford University Press, 1998.
2. Depenbrock, M., "Direkte selbstregelung (DSR) für hochdynamische drehfeldantriebe mit stromrichterspeisung," *ETZ Archive*, No. 7, 211–218, 1985.
3. Takahashi, I. and T. Noguchi, "A new quick-response and high-efficiency control strategy of an induction motor," *IEEE Trans. Ind. Appl.*, Vol. 22, 1820–1827, Sep.–Oct. 1986.
4. Utkin, V. I., J. Gldner, and J. Shi, *Sliding Mode Control in Electromechanical System*, Taylor & Francis, London, Philadelphia, 1999.
5. Chen, F. and M. W. Dunnigan, "Sliding-mode torque and flux control of an induction machine," *IEE Proceedings — Electric Power Applications*, Vol. 150, No. 2, 227–236, 2003.
6. Flígl, S., J. Bauer, and S. Ryvkin, "Matrix converter sliding mode based control for induction motor drive," *Book of Abstracts of the 13th Conference on Optimatization of Electrical and Electronic Equipment*, Transilvania University of Brasov, Brasov, 2012.

# Design and Implementation of a Variable-frequency Multiphase VRM with Optimized Phase-reduction Control

Sheng-Yuan Ou, Yi-Peng Lin, and Jui-Chien Wang

Department of Electrical Engineering, National Taipei University of Technology, Taiwan

**Abstract**— This paper proposes a control method to improve the efficiency in voltage regulator module (VRM) at light loads which is an important application on motherboard in personal computer (PC). The proposed control strategy is a combination of variable-frequency control method and phase-reduction control method. The proposed variable-frequency control method is used to modulate the switching frequency high as the load becomes low or light to achieve zero voltage switching (ZVS) on both high-side and low-side switches and to improve the light load efficiency significantly. The phase-reduction control method associates with the proposed variable-frequency control to enhance the efficiency improvement further as the load becomes light gradually. In addition, compared to conventional control methods, one advantage of the proposed variable-frequency control method can keep the ripple low to meet the desired design specification even at light load. To verify the proposed control strategy, an eight-phase VRM is implemented and the design specifications are output current 81 A, output voltage 1.3 V, the maximum power about 10 W and the ripple below 1% for full-range load, in which the switching is modulated from 240 kHz to 550 kHz as the load varies. The experimental results shows comparisons the proposed control method and other conventional constant frequency techniques and efficiency can be increased up to 30%.

## 1. INTRODUCTION

In industrial applications such as motherboards in personal computers, the most favorite voltage regulator module (VRM) [1–10] topology is shown in Fig. 1, the multiphase interleaved VRM [11, 12] and a conventional method is used to control the VRM with constant-frequency control. Generally, VRM must has low-voltage and high-current features so that [7–10] provide many multiphase architectures well as the related interleaved control [11, 12] to satisfy larger loads and to suppress the output voltage ripple, such as the eight-phase VRM shown in Fig. 1.

With the conventional constant-frequency control method, Fig. 2 shows the efficiency traces measured from an eight-phase VRM under various loads at the two constant switching frequencies respectively. In Fig. 2, the lighter the load is and the larger the switching frequency is, the higher the efficiency is, and vice versa. To improve the efficiency over all loads, this paper therefore proposes a variable-frequency control scheme associated with phase-reduction control in which the output voltage can be regulated by continuously changing the switching frequency and the proposed variable-frequency scheme can be carried out from slightly modifying the existing controller. It should be a preferred solution to improve efficiency.

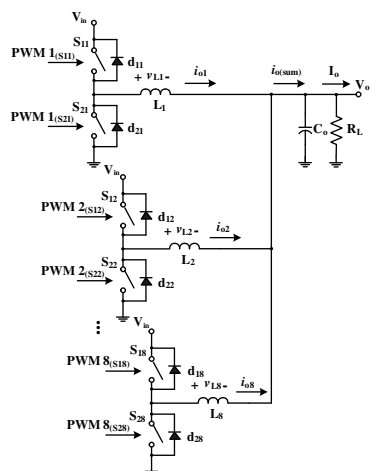


Figure 1: An eight-phase VRM used in motherboard.

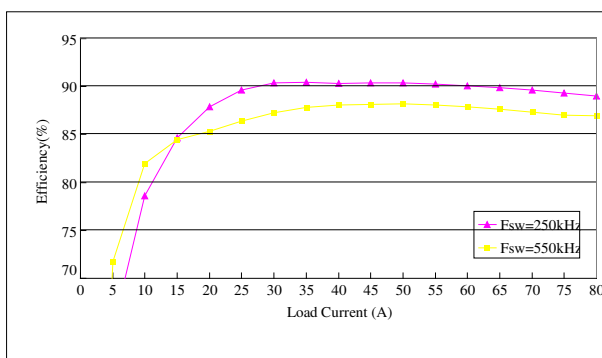


Figure 2: The efficiency traces actually measured from an eight-phase VRM.

## 2. PROPOSED CONTROL TECHNIQUE AND THEORY

### 2.1. Variable-frequency Control Rule

From the VRM operations and to implement ZVSs on both switches  $S_1$  and  $S_2$  [13], one half of current variance  $1/2(\Delta i_L)$  should be slightly larger than output current  $I_O$  to ensure the enough energy to turn on the body diode, as shown in Fig. 3

$$F_{SW} < \frac{V_{in} - V_O}{2L} \times (D_1 + d) \times \frac{n}{I_O} \quad (1)$$

wherein  $F_{SW}$  is the switching frequency,  $I_O$  is output load current and is the phase number.

By (1), the switching frequency  $F_{SW}$  is inversely proportional to load current  $I_O$  which illustrates the higher the load current is, the lower the switching frequency must be modulated as. In practical systems, for the reasons of circuit design and output ripple and so forth, the switching frequency can not be reduced infinitely while the loading increases, thereby the switching frequency  $F_{SW}$  must be fixed constant after one predetermined threshold is reached. Noted that the preset minimum switching frequency corresponding to the mode threshold is independent of whether ZVS on the high-side switch  $S_1$  can be achieved or not. It depends on the element values of the designed circuit parameter, output ripple specifications and so forth.

### 2.2. Optimized Efficiency Curve

The multiphase VRM with interleaved control can be applied to the large load situations and can restrain the output voltage ripple effectively, but while operating at light-load situations, the efficiency of VRM will be quite low. Therefore this paper provides a control method and circuit with both variable-frequency modulation and phase-reduction to improve the light-load efficiency significantly. Depending on the load situations, the proposed circuit turns on or off the operating phases. Fig. 4 shows example efficiency curves for four-phase VRM. To obtain the optimum operating efficiency curve, VRM only operates with one phase during  $I_o/I_{o,max} < A$ , operates with two phases during  $A < I_o/I_{o,max} < B$  because the efficiency for VRM operating with two phases is higher than that with one phase. For the same reasons, VRM operates with three phase during  $B < I_o/I_{o,max} < C$  and operates with four phase during  $I_o/I_{o,max} > C$ , thereby the optimum efficiency noted with a dotted line can be acquired.

### 2.3. The Proposed Control Scheme

Figure 5 shows the proposed variable-frequency control composed of a variablefrequency enable/disable circuit, a switching frequency modulation circuit, a current/voltage converter and a switch. Similarly, Fig. 6 shows the proposed phase-reduction control system including a VRM power stage, the drive IC, a phase-reduction enable/disable circuit, a current/voltage converter and a switch. The phase-reduction enable/disable circuit is shown in Fig. 7 and includes a comparator and an amplifier. The output voltage of the non-inverting amplifier is  $V_{Iot}$  which is inputted from the converted voltage  $V_{Io}$ . The switch  $S_w$  is turned on to connect the drive IC to the power supply VCC and pass the gate driving signal to the power stage for one phase operation when  $V_{Iot} > V_{ref}$ . Conversely, the switch  $S_w$  is turned off to disable the phase when  $V_{Iot} < V_{ref}$ .

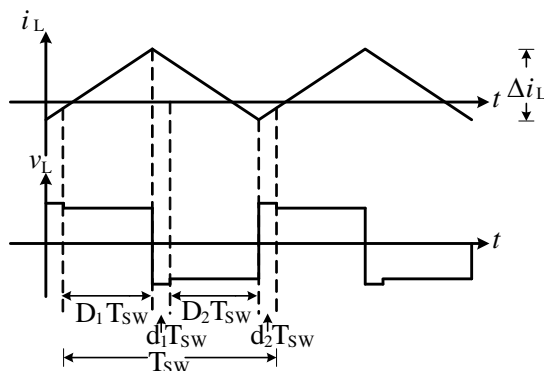


Figure 3: The inductor current and voltage with ZVS function.

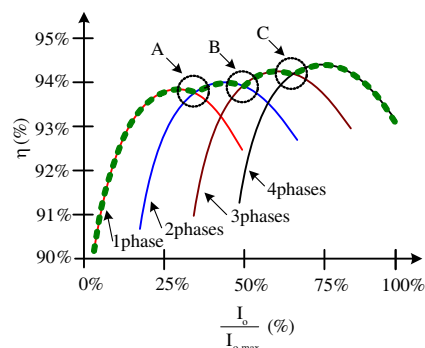


Figure 4: The optimum efficiency curve.

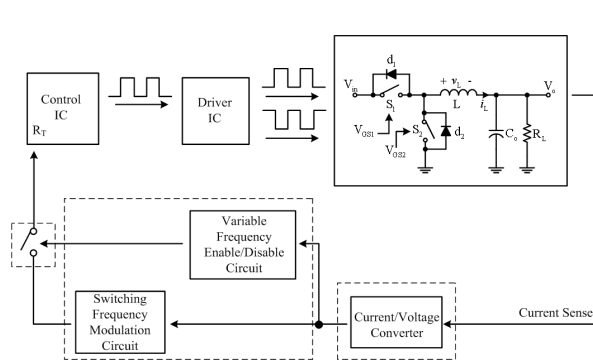


Figure 5: The proposed variable-frequency control system.

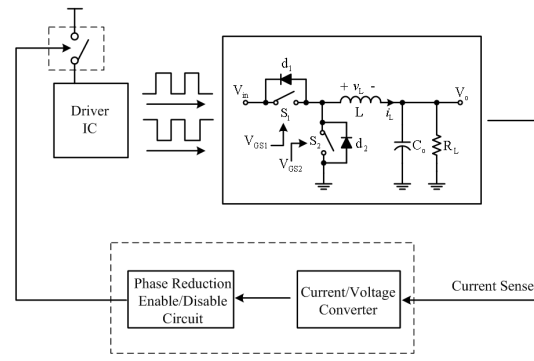


Figure 6: The proposed phase-reduction control system.

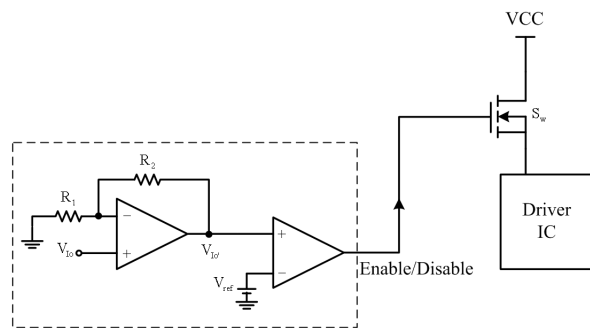


Figure 7: The phase-reduction enable/disable circuit.

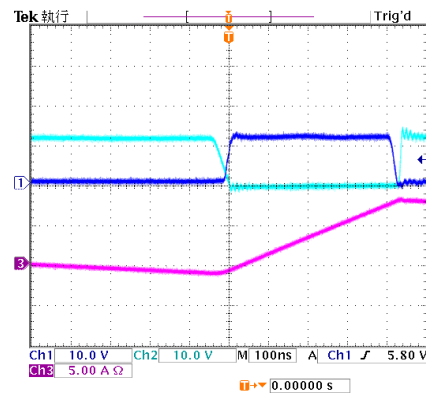


Figure 8: Waveforms of switch and inductor current at  $I_O = 20$  A.

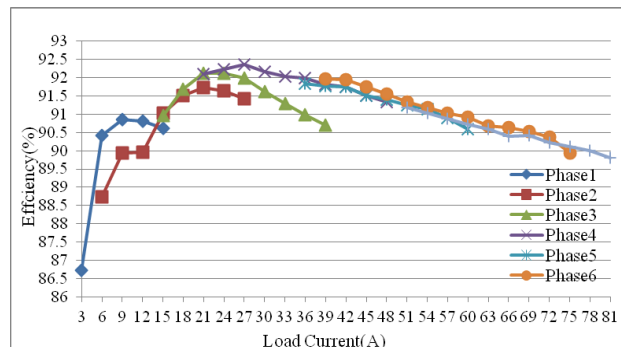


Figure 9: Respective efficiency curves for operating in some phases.

### 3. EXPERIMENTAL RESULTS

The experiments to verify the proposed control method and performance are made by implementation of an eight-phase VRM with the specifications are input voltage 12 V, output voltage 1.3 V, output current range 0 A ~ 81 A, variable-frequency load range 0 A ~ 24 A, and switching frequency range 240 kHz ~ 550 kHz. Fig. 8 shows the measured drain-source voltage  $v_{DS}$  and gate-source voltage  $v_{GS}$  of upper switch and the also inductor current as the proposed VRM is switching at 240 kHz respectively corresponding to 20 A to verify the ZVS property.

Figure 9 shows respective efficiency curves for some individual operating phases in which all curves are actually measured from the implemented eight-phase VRM. With efficiency curves in Fig. 9 to acquire the optimal entire efficiency under all load conditions, VRM should be operated in three-phase from one-phase while the load current reaches 15 A, operated in four-phase from

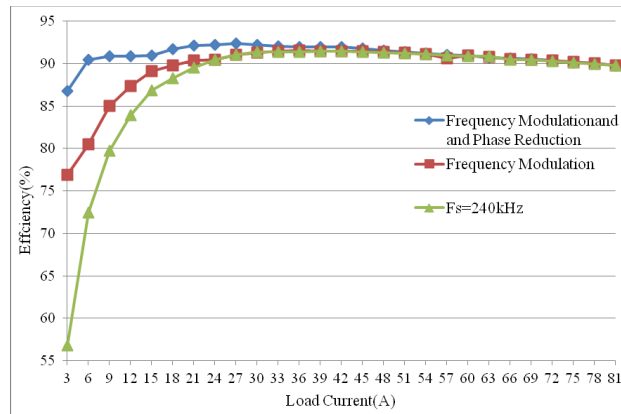


Figure 10: The VRM efficiency traces for various loads with different control methods.

three-phase while the load current reaches 24 A, operated in six-phase from four-phase while the load current reaches 39 A and operated in eight-phase from six-phase while the load current reaches 75 A.

Compared with two conventional control methods under various loads, including constant-frequency control for switching frequency 240 kHz and variable-frequency control from 240 kHz to 550 kHz, Fig. 1 shows the measured efficiency traces of the completed eight-phase VRM using the proposed control method. As can be seen significantly, the efficiency of VRM with the proposed control method under any loads is more excellent than those with the conventional controls, especially at the light-load, the improvement is quite high and up to 30%.

#### 4. CONCLUSIONS

This paper proposes a control method to improve the efficiency in VRM at light loads and implemented with predetermined specifications including output voltage 1.3 V from 12 V and output current 81 A. The combination of variable-frequency control method and phase-reduction control method is used to modulate the switching frequency and achieve ZVSs both on high-side and low-side switches. Furthermore, the phase-reduction control method associates with the proposed variable-frequency control to enhance the efficiency improvement further as the load becomes light gradually. In addition to be carried out with slightly modifying the PWM controller easily available from market, compared with conventional control methods, one advantage of the proposed variable-frequency control method can keep the ripple low to meet the desired design specification even at light load. The experimental results shows comparisons the proposed control method and other conventional constant frequency techniques and efficiency can be increased up to 30%.

#### ACKNOWLEDGMENT

Authors would like to thank National Science Council of Taiwan under NSC 101-2221-E-027-119 for this paper achievement.

#### REFERENCES

1. Zhang, Z., W. Eberle, Y.-F. Liu, and P. C. Sen, "A nonisolated ZVS asymmetrical buck voltage regulator module with direct energy transfer," *IEEE Trans. Ind. Electron.*, Vol. 56, No. 8, 3096–3105, Aug. 2009.
2. Castilla, M., L. G. de Vicuna, J. M. Guerrero, J. Matas, and J. Miret, "Designing VRM hysteretic controllers for optimal transient response," *IEEE Trans. Ind. Electron.*, Vol. 54, No. 3, 1726–1738, Jun. 2007.
3. Simon-Muela, A., S. Petibon, C. Alonso, and J. L. Chaptal, "Practical implementation of a high-frequency current-sense technique for VRM," *IEEE Trans. Ind. Electron.*, Vol. 55, No. 9, 3221–3230, Sep. 2008.
4. Chen, R. T., "Single-stage autotransformer-based VRM with input current shaper," *IEEE Trans. Power Electron.*, Vol. 22, 2375–2385, Nov. 2007.
5. Abedinpour, S., B. Bakkaloglu, and S. Kiaei, "A multistage interleaved synchronous buck converter with integrated output filter in 0.18  $\mu\text{m}$  SiGe process," *IEEE Trans. Power Electron.*, Vol. 22, 2164–2175, Nov. 2007.

6. Qian, T. and B. Lehman, “Dual interleaved active-clamp forward with automatic charge balance regulation for high input voltage application,” *IEEE Trans. Power Electron.*, Vol. 23, 38–44, Jan. 2008.
7. Simon-Muela, A., S. Petibon, C. Alonso, and J. L. Chaptal, “Practical implementation of a high-frequency current-sense technique for VRM,” *IEEE Trans. Ind. Electron.*, Vol. 55, 3221–3230, Sep. 2008.
8. Saggini, S., D. Zambotti, E. Bertelli, and M. Ghioni, “Digital autotuning system for inductor current sensing in voltage regulation module applications,” *IEEE Trans. Power Electron.*, Vol. 23, 2500–2506, Sep. 2008.
9. Mao, H., L. Yao, C. Wang, and I. Batarseh, “Analysis of inductor current sharing in nonisolated and isolated multiphase dc-dc converters,” *IEEE Trans. Ind. Electron.*, Vol. 54, No. 6, 3379–3388, Dec. 2007.
10. Peng, X., J. Wei, and F. C. Lee, “Multiphase coupled-buck converter—a novel high efficient 12 V voltage regulator module,” *IEEE Trans. Power Electron.*, Vol. 18, 74–82, Jan. 2003.
11. Wang, J. B. and C. Y. Chuang, “Design considerations of microprocessor-controlled multiphase battery charger with fast-charging strategy,” *IEEE Trans. Electric Power Appl.*, Vol. 1, 143–152, Mar. 2007.
12. De Jodar, E., J. A. Villarejo, F. Soto, and J. S Muro, “Effect of the output impedance in multiphase active clamp buck converters,” *IEEE Trans. Ind. Electron.*, Vol. 55, No. 9, 3231–3238, Sep. 2008.

# An Adaptive Current-sharing Control Technology for Multi Power Module with Hot Swapping

Sheng-Yuan Ou and Fu-Sung Chen

Department of Electrical Engineering, National Taipei University of Technology, Taiwan

**Abstract**— This paper achieves an adaptive current-sharing control strategy for multi power modules to solve the output current imbalance problem even caused by hot swapping while some power modules are paralleled or removed to provide higher or lower power the load requires. The conventional hot swapping techniques used in multi power module are easy to perform flexibility and precision, but generally easy to result in both the output voltage and current imbalances of operating modules so that some paralleled modules will be overloaded to mistake the operation even damage. Therefore, one of the solutions to balance the each module voltage and current while hot swapping uses the current control IC in each modules, but it increases complexity, cost and volume of each power circuit as well as degrades the efficiency under tiny-load and no-load situations. This paper provides a simple and low-cost adaptive current-sharing control method using off-the-shelf PWM control IC which only needs to be simply and easily modified. This paper discusses and illustrates the issues caused by hot swapping, the current-sharing control theory, and the proposed control scheme to easily implement the required control function. A multi power supply comprised of two power modules is implemented for verification of the proposed control in which one module has the design specification including 20 V output voltage, 5 A maximum output current, and 100 W maximum output power, the other has 20 V output voltage, 2.5 A maximum output current, and 50 W maximum power. The total multi power module has 7.5 A maximum output current and 150 W maximum output power. The experimental results verify the theoretic analysis and feasibility of the proposed control method, and show the required proportional current-sharing function with actually-measured waveforms.

## 1. INTRODUCTION

In portable industrial applications such as notebooks and tablet personal computers, the portable property becomes an important issue and enhances the design difficulty of the power supply. To provide a stable and reliable power for portable devices, there is a need of small sized portable power supply with high power while working outside or traveling. Directly shunting several power modules is the simplest and easiest control method as shown in Fig. 1, but the output current imbalance may easily destroy or fail one power module because of overloading. For improvements of the above-illustrated issues, this paper introduces the concept of distributed power supply [1] and combines two power supply module in experiments, one low-power module and one high-power module, with parallel into a detachable power supply system rather than a single power supply system. Compared to the conventional single power supply, one advantage of the detachable power supply system is flexible in applications; someone can use the combined power supply to charge the portable device while the needing to be fast charged and may take one of the two power supplies outside while working or traveling to enhance the convenience.

There are several current-sharing control methods in the distributed power supply system to balance each output current and distribute the power and heat dissipation [2, 3]. The voltage droop method [4, 5] is the popular one, but this method has some drawbacks, including degraded current-sharing outcome at light-load situation and worse load characteristics because of changing the internal resistance to achieve the required proportional current-sharing. Another popular method is average current method [6–9] of which the primary disadvantage is very difficult to solve the issue between system stability and load current-sharing dynamic response. The dedicated master method [10, 11] has a fatal shortcoming, that is, the entire system will fail once the master unit fault appears; in addition, the communication among units complicates the entire system and cost more. To improve the above-mentioned issues, this paper utilizes the automatic master method [12] that equips high accuracy of proportional current-sharing, superior load regulation, improved dynamic response, and easy to redundant the redundant power system. This paper applies the automatic master method to the two power modules combined with parallel to get the related benefits.

## 2. PROPOSED CONTROL TECHNIQUE AND THEORY

For each unit with parallel in detachable power supply system, the proportional current-sharing control is based on the highest output current with the automatic master method to adjust output

currents of other modules, therefore the output current in each module should be detected and pass the sensed current signal to a current-sharing bus which only feed the highest current signal into the controller to be the control base signal. The control of output current in each other unit should follow the base signal to balance each current. The control scheme is shown in Fig. 2.

The hardware used in this paper is constructed with off-the-shelf PWM control IC with slight modification, the controller associates with the automatic master method and outer loop control method in which the current control loop is built up with a high accuracy current detection amplifier to make sure the highest one among all output currents from each power module to be the control base signal and the corresponding power module will become the primary one. Then, a current-sharing adjustable signal is generated by the primary power module to effect the required current balance function.

### 3. EXPERIMENTAL RESULTS

The experiments to verify the proposed control method and performance are made by implementation of a detachable power supply constructed with two paralleled power modules, one has the rating output power 50 W for output current 2.5 A and output voltage 20 V and the other has 100 W for 5 A and 20 V respectively. Under different load situations, Fig. 3 shows the output voltage and output current of each module when the two power modules have shunted for 60% load, 90 W. The low-power module for 50 W rated power outputs about 1.15 A and the high module outputs for 100 W rated power 3.37 A in Fig. 3 to verify the proportional current-sharing scheme works well

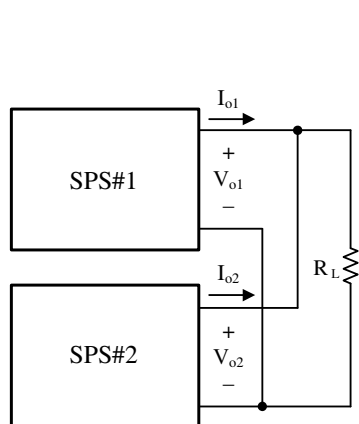


Figure 1: A conventional parallel method with directly shunting several power modules.

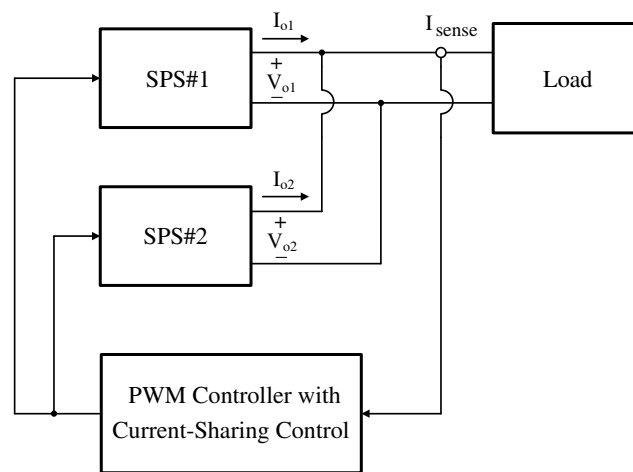


Figure 2: Implemented power supply system in this paper.

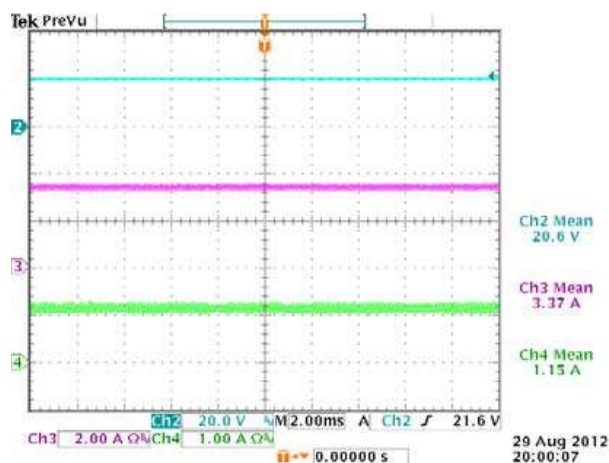


Figure 3: Output voltage and currents under 60% rated load.

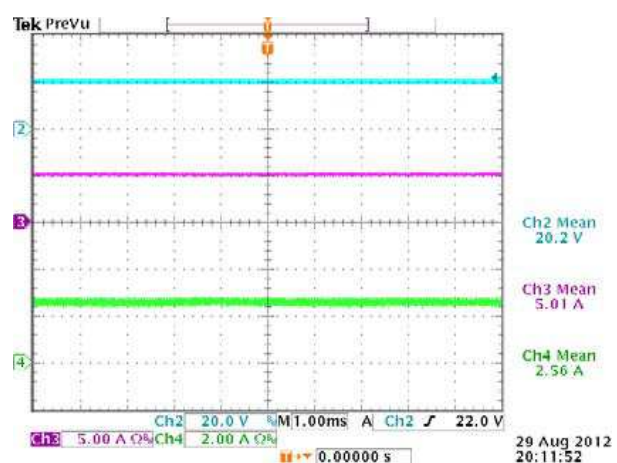


Figure 4: Output voltage and currents under 100% full-load.

and the output voltage won't be degraded. Fig. 4 shows the output voltage and the output currents of two power modules under 100% full-load, 100 W, in which the output currents are 2.56 A and 5.01 A respectively and also verifies the appropriate control of the used proportional current-sharing control.

#### 4. CONCLUSIONS

This paper implements an adaptive and proportional current-sharing control scheme for multi power modules to overcome the current imbalance issue for each power module in a detachable power supply system. The used proportional current-sharing strategy and the associated control system are also illustrated in this paper. The experimental results are connected with the design specification of total output power 150 W supplied by two power modules of which rated power are 50 W for 2.5 A load current and 100 W for 5 A load current respectively. In the experiments, the designed 50 W low-power module and 100 W high-power module proportionally share 1.15 A and 2.37 A respectively under 60% load. Furthermore, the experiments show these two shunted power modules also proportionally provide 2.56 A and 5.01 A even under 100% full-load. The actually measured waveforms and data in this paper verify the implemented proportional current-sharing control scheme and the associated design.

#### ACKNOWLEDGMENT

Authors would like to thank National Science Council of Taiwan under NSC 101-2221-E-027-119 for this paper achievement.

#### REFERENCES

1. Mammano, B., "Distributed power systems," *Unitrode Power Supply Design Seminar*, SEM 900, 1993.
2. Balogh, L., "Paralleling power-choosing and applying the best technique," *Unitrode-Seminar*, 2003.
3. Luo, S., Z. Ye, R. Lin, and F. C. Lee, "A classification and evaluation of parallel methods for power supply modules," *CPES Seminar*, 221–231, 1998.
4. Kim, J. W., H. S. Choi, and B. H. Cho, "A novel droop method for converter parallel operation," *IEEE Transactions on Power Electronics*, Vol. 17, No. 1, 25–32, 2002.
5. Luo, S., Z. Ye, R. Lin, and F. C. Lee, "A classification and evaluation of parallel methods for power supply modules," *Proceedings of IEEE Power Electronics Specialists Conference*, 901–908, 1999.
6. Zafrany, I. and S. Ben-Yaakov, "Average modeling, analysis and simulation of current shared DC-DC converters," *Proceedings of IEEE Power Electronics Specialists Conference*, Vol. 1, 640–646, 1998.
7. Wu, R., T. Kohama, Y. Kodera, T. Ninomiya, and F. Ihara, "Load-current-sharing control for parallel operation of DC-DC converters," *Proceedings of IEEE Power Electronics Specialists Conference*, 101–107, 1993.
8. Jovanovic, M. M., "A novel low-cost implementation of democratic load current sharing of parallel converter modules," *IEEE Transactions on Power Electronics*, 604–611, 1996.
9. Small, K. T., "Single wire current share paralleling of power supply," US Patent, Patent No. 4,717,833, Jan. 5, 1998.
10. Siri, K., C. Q. Lee, and T. F. Wu, "Current distribution control for parallel connected converters," *IEEE Trans. on Aerospace and Electronic Systems*, Part 2, 841–850, 1992.
11. Wu, T. F., K. Siri, and C. Q. Lee, "Reliability improvement in parallel connected converter systems," *Proc. of IEEE IECON*, 429–434, 1991.
12. Texas Instruments, "UCC39002 advanced 8-pin load-share controller," Datasheet, 2007.

# Implementation and Study of Super-capacitor Cell Power Management System

Shao-Wei Chieh<sup>1</sup>, Wen-Hsien Ho<sup>2</sup>, Chung-Bo Tsai<sup>2</sup>, Po-Chou Chen<sup>2</sup>, and Sheng-Yuan Ou<sup>1</sup>

<sup>1</sup>Department of Electrical Engineering, National Taipei University of Technology, Taiwan

<sup>2</sup>Taiwan Textile Research Institute, Taiwan

**Abstract**— This paper proposes a novel super-capacitor cell power management system to monitor current and balance state of charge for each cell while charging and discharging a multi-cell super-capacitor stack. Generally, the super-capacitor cells are in series connection to form a multi-cell stack for practical applications due to the much lower operating voltage of super-capacitor. The cells should suffer from the imbalance charging issue caused by intrinsic property differentials among separate cells even labeled the same specification. The imbalance charging phenomenon can cause some super-capacitor cells in stack overcharging to be destroyed and decrease their lifetime. The imbalance charging also results in other super-capacitor cells in the same stack undercharging and makes the cells as well as the cell stack utilization and performance very low. One popular conventional balance charging control method uses some passive networks comprised of resistors so that there are some fatal disadvantages, including the poor efficiency resulting from the resistor dissipation and the difficulty for resistor selection and setting as well as the accuracy degrading. Therefore, this paper provides an active balancing circuit which can maintain equal voltages across each super-capacitor cell and clamp the peak voltage across each cell to a selectable maximum value by monitoring cell state of charge in the stack. The proposed adaptive and active charging balance control method utilizes off-the-shelf control IC which only needs to be simply and easily modified in which charging strategy is the pulse charging method which is implemented easily and simply in view of super-capacitor lifetime and fast charging. The experimental results verify the theoretic analysis and feasibility of the proposed control method.

## 1. INTRODUCTION

Based on the requirements for modern industry development, there is a need of utilizing a variety of power sources for applications in widespread use of which super-capacitor is one. Super-capacitor is also called electrical double-layer capacitor and has an invertible reaction for storage process so that super-capacitor can be charged and discharged repeatedly for hundred thousands of times and still keeps the useful characteristics which property is one of super-capacitor advantages in applications. In addition, super-capacitor has speedy response and fast charging and discharging capability compared to secondary battery to shorten the charging time and rapidly supply high energy for load requirement. Applications of super-capacitors include camera flashlight, smart meter, toys, LED display, UPS, electric vehicle and so on.

But currently, super-capacitor faces an important issue, the smaller operating voltage, and can't be used in the high voltage applications such that should be series with many other super-capacitors generally. This situation makes the super-capacitor string unfavorable because of simultaneously charging to easy downgrade the super-capacitor property even lifetime. Therefore, we need a balance charging and discharging control scheme to uniform the charging state and to avoid overcharging phenomenon on some super-capacitors of the series string.

Conventionally, a simple, favorite and widely-adopted solution to uniform the charging state is so called passive even charging and discharging method that uses some matched resistors to balance the voltages across each super-capacitor. Nevertheless, this traditional method has some drawbacks of which one is the overcharged super-capacitors will be discharged through the matched resistors and there are significant energy wasted in the resistors while stopping charging in addition to the redundant resistor bank. For the reasons, this paper uses the active balance method to charge and discharge the super-capacitor string and combines a DC-DC converter to regulate the required output voltage.

## 2. PROPOSED CONTROL TECHNIQUE AND THEORY

Figure 1 illustrates the proposed system in this paper, including a super-capacitor stack with series, a secondary battery stack, a charger/discharger circuit with balance control, a load regulator comprises of a DC-DC power converter, and a micro-controller to response for entire system control.

In the proposed system as shown in Fig. 1, the design load regulator is used to provide power from super-capacitor or secondary battery to load with high efficiency, and the micro-controller acts as the control core to detect and monitor the states of charge (SOC) for both super-capacitor and secondary battery and thereby handle operations of other devices to achieve the predetermined functions. In addition, the micro-controller can perform the control strategy for retrieve energy from super-capacitor or secondary battery to load depending on the load variations. The charging/discharger circuit for super-capacitor and secondary battery and the load regulator circuit are shown in Figs. 2 and 3 in which the pulse charging method is used to get the fast charging and the high charging efficiency.

### 3. EXPERIMENT RESULTS

The experimental specifications for super-capacitor charging circuit under normal charging mode are listed in Table 1 wherein the input voltage is predetermined as 4 V, the output voltage is 3.998 V, and the charging current are about 20 mA–200 mA and 200 mA–2 A respectively corresponding to different external program resistances. With two super-capacitors both having 2 V to be charged, the used PWM control IC is programmed to output 4 V to charge the super-capacitor stack. Based on the inherently distinct characteristics such as the internal resistances between the two super-capacitors, the required charging time for the rated voltage 2 V is different while charging therefore the control IC should control the charging state of super-capacitors and maintain equal voltages across each super-capacitor, reducing the higher voltage across one super-capacitor and increasing the lower voltage across the other to achieve the charging balance.

Figure 4 illustrates the actually measured data from voltage meters and shows that the completely discharged voltages across these two super-capacitors are 0.449 V and 0.393 V respectively where one super-capacitor is 10.7 F/2 V and the other is 13.8 F/2 V. The different capacitances are selected to verify and confirm the proposed balance scheme in this paper. Fig. 5 shows the voltage

Table 1: Specifications for charging circuit.

Input voltage	4 V	Output voltage	3.9980 V
External program resistance (1)	5 k $\Omega$	External program resistance (2)	500 $\Omega$
External program voltage (1)	0.1 V–1 V	External program voltage (2)	0.1 V–1 V
Charging current $I_{CHAR(1)}$	20 mA–200 mA	Charging current $I_{CHAR(2)}$	200 mA–2 A

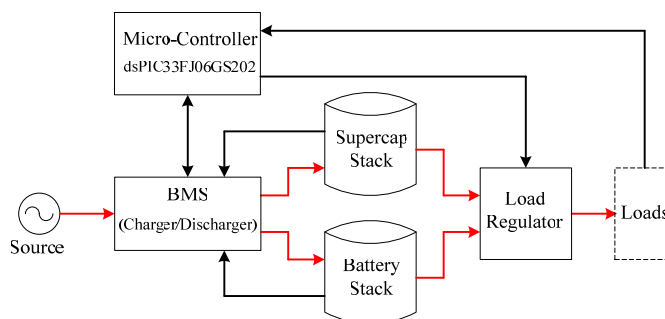


Figure 1: The proposed system in this paper.

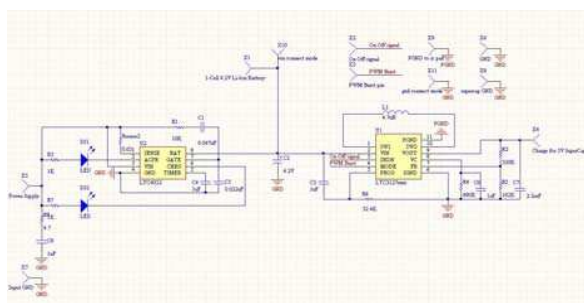


Figure 2: Charger/discharger circuit for secondary battery and load regulator circuit.

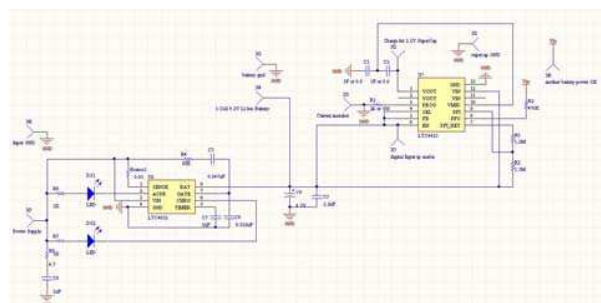


Figure 3: Charger/discharger circuit for super-capacitor.



Figure 4: Voltages across completely discharged super-capacitors.

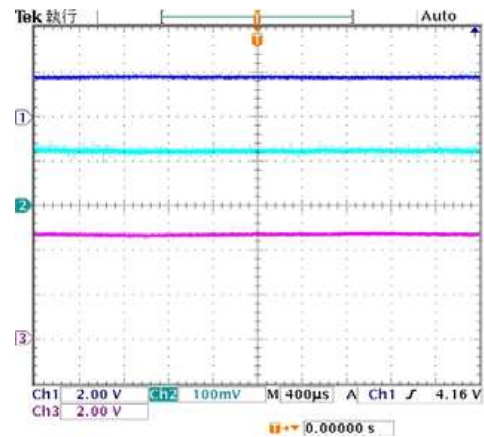


Figure 5: Waveforms for voltage difference larger than 750 mV.

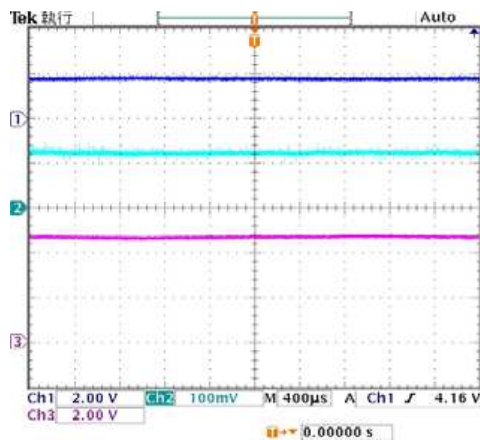


Figure 6: Waveforms for voltage difference about 750 mV.

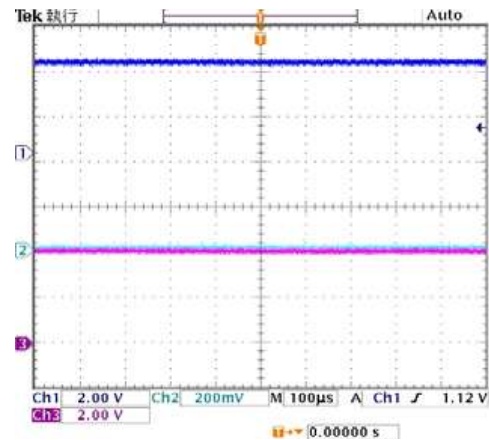


Figure 7: Waveforms for voltage difference about 250 mV.



Figure 8: Imbalance voltages across completely charged super-capacitors.



Figure 9: balance voltages across completely charged super-capacitors.

across one super-capacitor is about 1.7 V and the program voltage  $V_{\text{PROG}}$  is about 0.1 V in CH3 when the voltage difference between input and output voltages is larger than 750 mV wherein CH1 represents the input voltage 4 V. Fig. 6 shows the waveforms for early charging state and Fig. 7 shows the program voltage decreases to be about zero because the voltage difference lowers to be about 0.25 V while completely charged.

Figure 8 shows the imbalance voltages across completely charged super-capacitors measured from voltage meters where one is 1.888 V and the other is 2.07 V. The voltage difference is up to 182 mV due to the distinct characteristics between two super-capacitors. Fig. 9 shows the actually-measured balance voltages across the two split super-capacitors under the balance control to verify the design and control, in which the voltage difference is down to 12 mV.

#### 4. CONCLUSIONS

This paper proposes a super-capacitor cell power management system including a super-capacitor stack, a secondary battery stack, a charging/discharging circuit, a load regulator, and micro-

controller. Both super-capacitor stack and secondary battery stack supplies the required energy to load corresponding to the control of micro-controller with detecting and monitoring SOCs of the two power sources. The charger/discharger performs the uniform charging strategy for super-capacitors in series to maintain the important operation characteristics and enlarge the lifetime. The implemented system verifies the used uniform balance charging method with experiments in which the voltage difference can be suppressed as 12 mV from 180 mV.

#### REFERENCES

1. Camara, M., H. Gualous, F. Gustin, A. Berthon, and B. Dakyo, "DC/DC converter design for supercapacitor and battery power management in hybrid vehicle applications — Polynomial control strategy," *IEEE Transactions on Industrial Electronics*, Vol. 57, No. 2, 587–597, 2010, DOI:10.1109/TIE.2009.2025283.
2. Camara, M., B. Dakyo, and H. Gualous, "Polynomial control method of DC/DC converters for DC-bus voltage and currents management — Battery and supercapacitors," *IEEE Transactions on Power Electronics*, Vol. 27, No. 3, 1455–1467, 2012, DOI:10.1109/TPEL.2011.2164581.
3. Choi, M. E., S. W. Kim, and S. W. Seo, "Energy management optimization in a battery/supercapacitor hybrid energy storage system," *IEEE Transactions on Smart Grid*, Vol. 3, No. 1, 463–472, 2012, DOI:10.1109/TSG.2011.2164816.
4. Jayasinghe, S. S., D. D. Vilathgamuwa, and U. K. Madawala, "Diode-clamped three-level inverter-based battery/supercapacitor direct integration scheme for renewable energy systems," *IEEE Transactions on Power Electronics*, Vol. 26, No. 12, 3720–3729, 2011, DOI:10.1109/TPEL.2011.2148178.
5. Zandi, M., A. Payman, J. P. Martin, S. Pierfederici, B. Davat, and F. Meibody-Tabar, "Energy management of a fuel cell/supercapacitor/battery power source for electric vehicular applications," *IEEE Transactions on Vehicular Technology*, Vol. 60, No. 12, 433–443, 2011, DOI:10.1109/TVT.2010.2091433.
6. Uno, M. and K. Tanaka, "Single-switch cell voltage equalizer using multistacked buck-boost converters operating in discontinuous conduction mode for series-connected energy storage cells," *IEEE Transactions on Vehicular Technology*, Vol. 60, No. 8, 3635–3645, 2011, DOI:10.1109/TVT.2011.2165229.
7. Cheng, Y. H., "Assessments of energy capacity and energy losses of supercapacitors in fast charging-discharging cycles," *Transactions on Energy Conversion*, Vol. 25, No. 1, 253–261, 2010, DOI:10.1109/TEC.2009.2032619.
8. Leuchter, J., P. Bauer, and V. Stekly, "Battery-supercapacitors mixed as electrical power buffers," *5th IET International Conference on Power Electronics, Machines and Drives, PEMD*, 1–6, 2010, DOI:10.1049/cp.2010.0124.
9. Jarushi, A. M. and N. Schofield, "Battery and supercapacitor combination for a series hybrid electric vehicle," *5th IET International Conference on Power Electronics, Machines and Drives, PEMD*, 1–6, 2010, DOI:10.1049/cp.2010.0100.
10. Lambert, S. M., V. Pickert, J. Holden, X. He, and W. Li, "Comparison of supercapacitor and lithium-ion capacitor technologies for power electronics applications," *5th IET International Conference on Power Electronics, Machines and Drives, PEMD*, 1–5, 2010, DOI:10.1049/cp.2010.0115.

# Design and Implementation of an LED Switching Regulator Using Inverse Buck Topology

Sheng-Yuan Ou and Hong-Hsiang Chang

Department of Electrical Engineering, National Taipei University of Technology, Taiwan

**Abstract**— This paper proposes an LED switching regulator using inverse buck topology to achieve dimming improvement, eliminating spike from diode reverse recovery time and LED string short and dimming short operation and protection. The used pulse width modulation technique is fixed off time adjustment by easily setting the additional elements comprised of a resistor and a capacitor to achieve variable-frequency control under continuous current mode (CCM) or discontinuous current conduction mode (DCM). Recently, LED is largely used in lighting system to save energy and space in human life instead of cold-cathode fluorescent lamps. In order to solve the problem of voltage deviation in each LED string, this paper provides an LED switching regulator to achieve the acceptable current-equalization function, and also solve the problem of voltage deviation in the multi-string panel construction. In this paper, the inverse buck topology is used with constant off time control IC to implement a LED string panel control to verify the proposed analysis. Finally, the experimental results show good confirm and meet the required specification.

## 1. INTRODUCTION

In order to solve energy problem in TV system, LED has come instead of cold-cathode fluorescent lamps (CCFL) [1] in modern backlight modules, because the power consumption of CCFL modules is 2~3 times than LED in the same backlight size. The common topology of LED module is the so-called linear control scheme [2–5] as shown in Figure 1. Up to date, the larger panel size is more popular in which the different voltage  $V_f$  between each LED strings in backlight module becomes larger. This problem may cause larger power loss and reduce efficiency by using the linear control scheme to drive LED backlight module. The inverse buck topology [6–11] as shown in Figure 2 to drive LED backlight module can overcome the problem and achieve good current balance in each string. With the inverse buck backlight module, LED output current is linearly proportional to duty cycle in PWM dimming function [11, 12] so that the dimming can be easily performed.

## 2. PROPOSED CONTROL TECHNIQUE AND THEORY

Figure 3 shows the used inverse buck system including two LED strings, two inverse buck topologies and the associated PWM controller. Once the PWM controller receives the sensed signal from LED

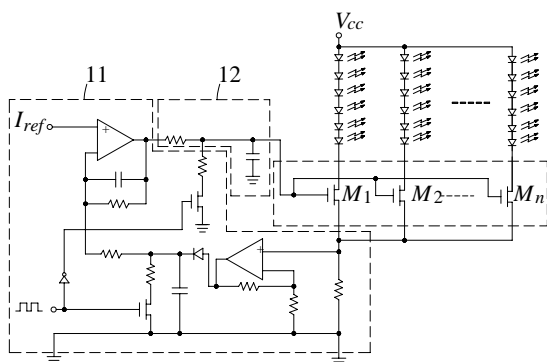


Figure 1: Conventional linear control LED driver topology.

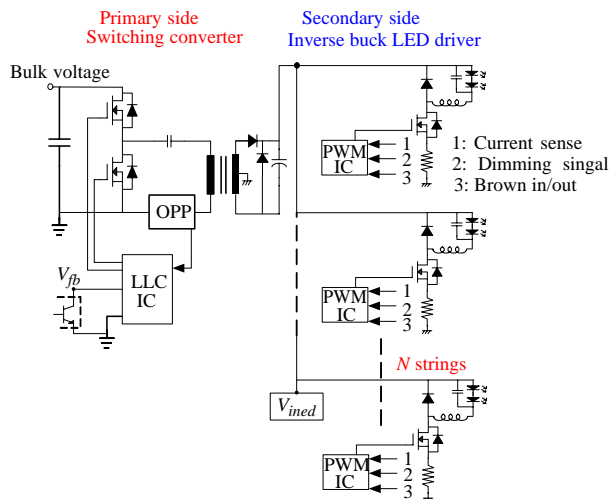


Figure 2: Inverse buck LED driver topology.

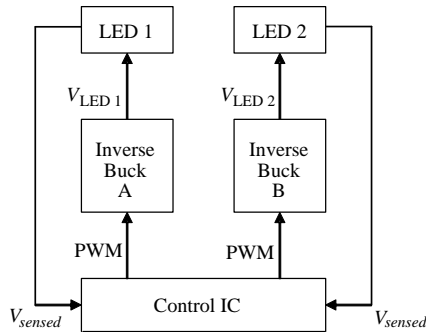


Figure 3: Inverse buck LED driver topology.

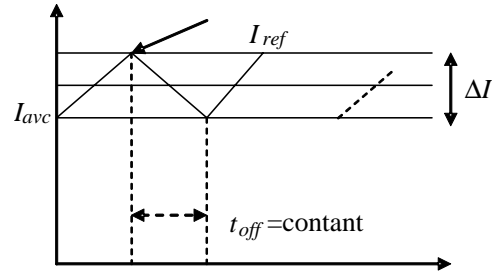
Figure 4: Relationship between the reference current  $I_{ref}$  and the.

Table 1: Specifications for implemented LED switching regulator with inverse buck topology.

Input voltage ( $V_{in}$ )	155 V
LED output voltage ( $V_{LED}$ )	100 V~122 V
LED output current ( $I_{LED}$ )	280 mA
Inductor ripple current	290 mA
Switch off time	2 $\mu$ s

strings to generate an error signal and adjust the pulse width to control the inverse buck topology and regulate the required output.

Figure 4 illustrates the relationship between the reference current  $I_{ref}$  and the average inductor current  $I_{ave}$  under the constant off time control for constant current output control. Under the control method, there is a reference current command  $I_{ref}$  is set in the used PWM controller, the switch is turned off while the inductor current reaches the reference current  $I_{ref}$  and turned on again while experiencing for a constant off time as shown in Figure 4. The variation in inductor current  $\Delta I$  is constant because switch off time and the constant voltages across LED strings are constant. It can be seen that the ripple current  $\Delta I$  almost comes into the LED strings if the voltage across LED strings are fixed and the required inductance can be determined as

$$L = \frac{V_{LED}}{I_{max} - I_{min}} t_{off} \quad (1)$$

Based on (1), the corresponding switch of time and the required switching frequency can be designed as

$$t_{off} = \frac{L}{V_{in} - V_{LED}} (I_{max} - I_{min}) \quad (2)$$

$$f_s = \frac{1}{t_{on} + t_{off}} \quad (3)$$

### 3. EXPERIMENTAL RESULTS

The experiments to verify the proposed control method and performance are made with the specifications listed in Table 1 wherein the input voltage is 155 V, LED output voltages are from 100 V to 122 V and the current for each LED string is 280 mA. The operating switching frequency varies from 150 kHz to 200 kHz because the constant off time operation.

Figure 5 show the actually measured waveforms of one LED string current and voltage, the ripple inductor current, and the switch control signal to verify the analysis and design as above mentioned. Figure 6 illustrates the actually measured current and voltage waveforms of the two LED string. The results in Figure 6 shows the LED string voltages are about 122 V and 100 V respectively and the two LED string currents can be regulated as the same power effectively and appropriately even the voltage difference between two LED strings is up than 20 V.

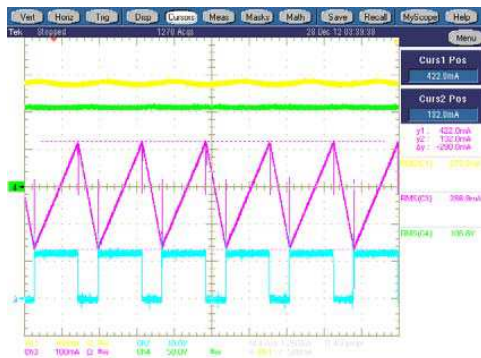


Figure 5: Corresponding waveforms for each LED string.



Figure 6: Current and voltage waveforms for two LED strings.

#### 4. CONCLUSIONS

This paper first illustrates the prior arts in drivers for multi LED strings and designs an LED switching regulator using inverse buck topology to verify the operation and analysis. The inverse buck topology is used with constant off time control IC to implement a LED string panel control to verify the proposed analysis. The LED current can be regulated with varying the duty cycle of control signal which depends on the voltage difference between the two LED strings even the difference is up to 20 V. Finally, the experimental results show good confirm and meet the required specification.

#### ACKNOWLEDGMENT

Authors would like to thank National Science Council of Taiwan under NSC 101-2221-E-027-119 for this paper achievement.

#### REFERENCES

1. Guo, R., "A high efficiency transformerless step-up DC-DC converter with high voltage gain for LED backlight applications," *2011 Twenty-sixth Annual IEEE Applied Power Electronics Conference and Exposition (APEC)*, 1350–1356, Mar. 6–11, 2011.
2. Chen, Y., Y. Nan, and Q. Kong, "A loss-adaptive self-oscillating buck converter for led driving," *IEEE Transactions on Power Electronics*, Vol. 27, No. 10, 4321–4328, Oct. 2012.
3. Zhang, Z., E. Wu, Z. Yang, Y. F. Liu, and P. C. Sen, "Optimal design of current source gate driver for a buck voltage regulator based on a new analytical loss model," *IEEE Power Electronics Specialists Conference, PESC2007*, 1556–1562, Jun. 17–21, 2007.
4. Chiu, H. J., Y. K. Lo, J. T. Chen, S. J. Cheng, C. Y. Lin, and S. C. Mou, "A high-efficiency dimmable LED driver for low-power lighting applications," *IEEE Transactions on Industrial Electronics*, Vol. 57, No. 2, 735–743, Feb. 2010.
5. Leung, W. Y., T. Y. Man, and M. Chan, "A high-power-LED driver with power-efficient LED-current sensing circuit," *34th European Solid-State Circuits Conference, ESSCIRC 2008*, 354–357, Feb. 2010.
6. Oh, I. H., "An analysis of current accuracies in peak and hysteretic current controlled power LED drivers," *Twenty-third Annual IEEE Applied Power Electronics Conference and Exposition, APEC2008*, 572–577, Feb. 24–28, 2008.
7. Chen, C. C., C. Y. Wu, and T. F. Wu, "LED back-light driving system for LCD panels," *Twenty-first Annual IEEE Applied Power Electronics Conference and Exposition, APEC2006*, Mar. 19–23, 2006.
8. Hu, Y. and M. M. Jovanovic, "LED driver with self-adaptive drive voltage," *IEEE Transactions on Power Electronics*, Vol. 23, No. 6, 3116–3125, Nov. 2008.
9. Choi, S. and T. Kim, "Symmetric current-balancing circuit for LED backlight with dimming," *IEEE Transactions on Industrial Electronics*, Vol. 59, No. 4, Apr. 2012.
10. Zhang, T., Y. Yang, Z. Song, and Y. Fan, "A dual mode dimming white LED driver based on buck DC-DC converter," *International Conference on Computer Science and Information Processing (CSIP)*, 24–26, Aug. 2012.

11. Xu, X. and X. Wu, “High dimming ratio LED driver with fast transient boost converter,” *IEEE Power Electronics Specialists Conference, PESC2008*, 15–19, Jun. 2008.
12. Nam, H., K. Y. Oh, and S. W. Lee, “CCFL backlight solution for low-cost liquid crystal televisions without image artifacts,” *IEEE Transactions on Consumer Electronics*, Vol. 55, No. 3, 1021–1027, Aug. 2009.

# Efficient Solutions of Volume Integral Equations with Inhomogeneous Materials

K. Yang, Y. Q. Zhang, M. H. Wei, and M. S. Tong

Department of Electronic Science and Technology, Tongji University  
4800 Cao'an Road, Shanghai 201804, China

**Abstract**— Volume integral equations (VIEs) are essential and indispensable for solving inhomogeneous electromagnetic problems by integral equation approach. Traditionally, the VIEs are solved by the method of moments (MoM) with the Schaubert-Wilton-Glisson (SWG) basis function. The SWG basis function requires conformal meshes in geometric discretization and may be inconvenient for inhomogeneous problems. In this work, we propose a Nyström-like scheme for solving the VIEs. The scheme chooses some representative discrete nodes in each tetrahedral element and uses a point-matching procedure to transform the VIEs into matrix equations. The scheme can allow an inhomogeneity of materials in each tetrahedron and may simplify the geometric discretization. A numerical example for electromagnetic scattering by a multilayered dielectric object illustrates the effectiveness of the scheme.

## 1. INTRODUCTION

Volume integral equations (VIEs) are indispensable for solving electromagnetic (EM) problems with inhomogeneous or anisotropic materials by integral equation approach [1]. Traditionally, the VIEs are solved by the method of moments (MoM) in which the unknown volumetric electric and magnetic currents are represented with the divergence-conforming Schaubert-Wilton-Glisson (SWG) basis function [2]. The SWG basis function is defined over a pair of tetrahedrons with a common face and requires conformal tetrahedral meshes in geometric discretization. The conformal meshes will result in a high cost in discretization, especially for multiscale structures in which the meshes with different sizes need to perfectly merge near material interfaces [3, 4].

The conformal meshes imply that the tetrahedral elements cannot stride across material interfaces or each tetrahedron cannot include inhomogeneous materials in the geometric discretization. This is because the SWG basis function cannot be defined over a discontinuous material boundary [2]. Therefore, we have to locate the material boundaries for a given arbitrarily inhomogeneous structure and discretize each material individually without striding across its boundary. However, if we need to discretize the geometries along their material boundaries, why do we need to bother the VIEs? The surface integral equations (SIEs) can also be used and are more convenient to implement if we must locate the boundaries because they only require the discretization of material interfaces [1]. Hence, it seems that solving the VIEs is unnecessary in the case when the material boundaries are impenetrable in geometric discretization.

In this work, we propose a Nyström-like point-matching scheme to solve the VIEs. The scheme does not use any basis function and only works with individual tetrahedrons instead of tetrahedron pairs. Therefore, the scheme allows an inhomogeneity of materials in each tetrahedron or permits to stride across material boundaries without enforcing a conformity in geometric discretization. The scheme chooses some representative discrete nodes in each tetrahedral element and uses a point-matching procedure to transform the VIEs into matrix equations. Due to its distinctive feature, the scheme can more conveniently handle arbitrarily inhomogeneous or anisotropic structures though requiring an efficient treatment of hypersingularity in the integral kernel [5]. A numerical example for electromagnetic scattering by a multilayered dielectric sphere is presented to demonstrate the scheme and its robustness can be observed.

## 2. VOLUME INTEGRAL EQUATIONS (VIES)

Consider the EM scattering by a three-dimensional (3D) inhomogeneous object embedded in the free space with a permittivity  $\epsilon_0$  and a permeability  $\mu_0$ , the VIEs can be written as [1]

$$\mathbf{E}(\mathbf{r}) = \mathbf{E}^{inc}(\mathbf{r}) + i\omega\mu_0 \int_V \bar{\mathbf{G}}(\mathbf{r}, \mathbf{r}') \cdot \mathbf{J}_V(\mathbf{r}') d\mathbf{r}' - \nabla \times \int_V \bar{\mathbf{G}}(\mathbf{r}, \mathbf{r}') \cdot \mathbf{M}_V(\mathbf{r}') d\mathbf{r}', \quad \mathbf{r} \in V \quad (1)$$

$$\mathbf{H}(\mathbf{r}) = \mathbf{H}^{inc}(\mathbf{r}) + i\omega\epsilon_0 \int_V \bar{\mathbf{G}}(\mathbf{r}, \mathbf{r}') \cdot \mathbf{M}_V(\mathbf{r}') d\mathbf{r}' + \nabla \times \int_V \bar{\mathbf{G}}(\mathbf{r}, \mathbf{r}') \cdot \mathbf{J}_V(\mathbf{r}') d\mathbf{r}', \quad \mathbf{r} \in V \quad (2)$$

where  $\mathbf{E}^{inc}(\mathbf{r})$  and  $\mathbf{H}^{inc}(\mathbf{r})$  are the incident electric and magnetic field, respectively, while  $\mathbf{E}(\mathbf{r})$  and  $\mathbf{H}(\mathbf{r})$  are the total electric and magnetic field inside the object, respectively. Also, the integral kernel

$$\bar{\mathbf{G}}(\mathbf{r}, \mathbf{r}') = \left( \bar{\mathbf{I}} + \frac{\nabla \nabla}{k_0^2} \right) g(\mathbf{r}, \mathbf{r}') \quad (3)$$

is the 3D dyadic Green's function in which  $\bar{\mathbf{I}}$  is the identity dyad,  $k_0 = \omega \sqrt{\mu_0 \epsilon_0}$  is the free-space wavenumber, and  $g(\mathbf{r}, \mathbf{r}') = e^{ik_0 R} / (4\pi R)$  is the 3D scalar Green's function. In addition,  $R = |\mathbf{r} - \mathbf{r}'|$  is the distance between an observation point  $\mathbf{r}$  and a source point  $\mathbf{r}'$  in the scalar Green's function and

$$\mathbf{J}_V(\mathbf{r}') = i\omega[\epsilon_0 - \epsilon(\mathbf{r}')] \mathbf{E}(\mathbf{r}') \quad (4)$$

$$\mathbf{M}_V(\mathbf{r}') = i\omega[\mu_0 - \mu(\mathbf{r}')] \mathbf{H}(\mathbf{r}') \quad (5)$$

are the induced volumetric electric and magnetic current densities inside the object with a permittivity  $\epsilon(\mathbf{r}')$  and a permeability  $\mu(\mathbf{r}')$ , respectively. Usually, the object is nonmagnetic or  $\mu(\mathbf{r}') = \mu_0$ , so the magnetic current density vanishes and the above two equations can be reduced to

$$\mathbf{E}(\mathbf{r}) = \mathbf{E}^{inc}(\mathbf{r}) + i\omega\mu_0 \int_V \bar{\mathbf{G}}(\mathbf{r}, \mathbf{r}') \cdot \mathbf{J}_V(\mathbf{r}') d\mathbf{r}', \quad \mathbf{r} \in V \quad (6)$$

$$\mathbf{H}(\mathbf{r}) = \mathbf{H}^{inc}(\mathbf{r}) + \nabla \times \int_V \bar{\mathbf{G}}(\mathbf{r}, \mathbf{r}') \cdot \mathbf{J}_V(\mathbf{r}') d\mathbf{r}', \quad \mathbf{r} \in V. \quad (7)$$

We only need to solve the first equation to obtain the unknown electric current density  $\mathbf{J}_V(\mathbf{r}')$ , or equivalently, the total electric field  $\mathbf{E}(\mathbf{r}')$ . However, the electric flux density  $\mathbf{D}(\mathbf{r}') = \epsilon(\mathbf{r}') \mathbf{E}(\mathbf{r}')$  is usually chosen as the unknown function in the MoM since it is normally continuous across the common faces of paired tetrahedrons.

### 3. NYSTRÖM-LIKE SCHEME FOR SOLVING THE VIES

We propose a Nyström-Like Scheme to solve the VIEs. In the scheme, we first select some representative discrete nodes in each tetrahedron and then transform the VIEs into matrix equations by performing a point-matching procedure over those nodes. These nodes are chosen as equally as possible in each tetrahedron without the constraint of a quadrature rule, so the scheme is different from the Nyström method in which the distribution of nodes obeys a quadrature rule. The current densities instead of the total fields or flux densities are chosen as unknown functions to be solved in the scheme. For a nonmagnetic object, Eq. (6) can be written as

$$\frac{1}{i\omega[\epsilon_0 - \epsilon(\mathbf{r})]} \mathbf{J}_V(\mathbf{r}) = \mathbf{E}^{inc}(\mathbf{r}) + i\omega\mu_0 \int_V \bar{\mathbf{G}}(\mathbf{r}, \mathbf{r}') \cdot \mathbf{J}_V(\mathbf{r}') d\mathbf{r}', \quad \mathbf{r} \in V \quad (8)$$

if Eq. (4) is applied to. We can see that there are not explicit material parameters in the integral of the above equation and this characteristic allows the discretization to stride across material boundaries or each tetrahedron to include different materials. To evaluate the integral of the above equation, we have to represent the unknown current density at an arbitrary point within a tetrahedron. We can use an interpolation scheme to represent the current density at an arbitrary point based on its values at those chosen nodes. For example, if we want to represent an unknown function  $f$  within a local region, we can approximate it with a first-order polynomial function (linear approximation) in a local coordinate system  $(u, v, w)$ , i.e.,

$$f = a_1 + a_2 u + a_3 v + a_4 w = f(u, v, w) \quad (9)$$

where  $a_1, a_2, a_3,$  and  $a_4$  are the unknown coefficients to be determined. We can then obtain a set of equations by matching the unknown function on those chosen nodes within the same region, i.e.,

$$f_l = a_1 + a_2 u_l + a_3 v_l + a_4 w_l, \quad l = 1, 2, \dots, L \quad (10)$$

where  $f_l$  ( $l = 1, 2, \dots, L$ ) are the values of unknown function on those chosen nodes and  $L$  is the total number of chosen nodes in the region. The set of equations can only be solved with the least square method (LSM) by defining a functional

$$F = \sum_{l=1}^L \{ \xi_l [f_l - (a_1 + a_2 u_l + a_3 v_l + a_4 w_l)]^2 \} \quad (11)$$

which is the sum of weighted residue errors for the equations ( $\xi_l$  is the  $l$ th weight). Minimizing the functional or enforcing the derivative of the functional with respect to the coefficients to vanish, i.e.,

$$\frac{\partial F}{\partial \mathbf{a}} = 0 \quad (12)$$

we can determine the unknown coefficients  $\mathbf{a} = [a_1, a_2, a_3, a_4]^T$  and the relevant details can found in [7]. When the unknown coefficients are solved, the unknown function within the region can be expressed as

$$f(u, v, w) = a_1 + a_2u + a_3v + a_4w = \boldsymbol{\phi}^T \cdot \mathbf{f} \quad (13)$$

where  $\boldsymbol{\phi} = [\phi_1, \dots, \phi_L]^T$  is called shape function and  $\mathbf{f} = [f_1, \dots, f_L]^T$  is the vector of unknown function values at those chosen nodes. With the shape function, we can represent the unknown current density within the same region of a tetrahedron as

$$\mathbf{J}(\mathbf{r}') = \sum_{l=1}^L \phi_l(\mathbf{r}') \mathbf{J}_l \quad (14)$$

where  $\mathbf{J}_l = J_l^u \hat{u} + J_l^v \hat{v} + J_l^w \hat{w}$  is the value of unknown current density at the  $l$ th chosen node in the region.

After the unknown current density is represented, the matrix elements can be evaluated numerically when the observation node is outside a source tetrahedron. If the observation node is inside a source tetrahedron, we have to evaluate the hypersingular integrals resulting from the dyadic Green's function. The scheme may not be feasible when one cannot handle the hypersingularity in the integrals, but it has become feasible when we developed the robust technique of treating the hypersingularity in recent years [5, 6]. We have built some special subroutines for evaluating the hypersingular integrals in our code library and they can be used here.

#### 4. NUMERICAL EXAMPLE

To illustrate the effectiveness of the new scheme for solving the VIEs, we present one numerical example for EM scattering by a multilayered concentric dielectric sphere as shown in Figure 1. The sphere is chosen because it has exact solutions or Mie-series solutions [8] that can be used to verify the numerical solutions of the scheme. It is assumed that the incident wave is a plane wave with a frequency  $f = 300$  MHz and is propagating along the  $-z$  direction in free space. We calculate the bistatic radar cross section (RCS) observed along the principal cut ( $\phi = 0^\circ$  and  $\theta = 0^\circ - 180^\circ$ ) for the scatterer with both vertical polarization ( $VV$ ) and horizontal polarization ( $HH$ ). We consider a three-layer concentric dielectric sphere which is piecewise-homogeneous but treated as an inhomogeneous object. The radii of three interfaces are  $a_1 = 0.2\lambda$ ,  $a_2 = 0.25\lambda$ , and  $a_3 = 0.3\lambda$ , respectively, where  $\lambda$  is the wavelength in free space. The relative permittivity of the dielectric material in each layer is  $\epsilon_{r1} = 4.0$ ,  $\epsilon_{r2} = 3.0$ , and  $\epsilon_{r3} = 5.0$ , respectively (the relative permeability  $\mu_r = 1.0$  is assumed for dielectric materials). The object is discretized into 2352 tetrahedral elements and some elements could stride across the material interfaces. Figure 2 plots the bistatic RCS solutions of the object obtained from the scheme and we can see that they are close to the corresponding exact solutions.

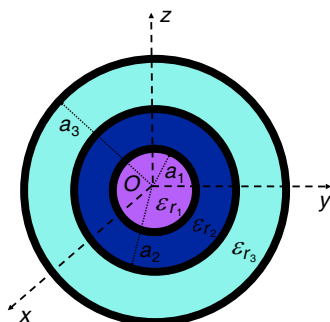


Figure 1: Geometry of a multilayered concentric dielectric sphere.

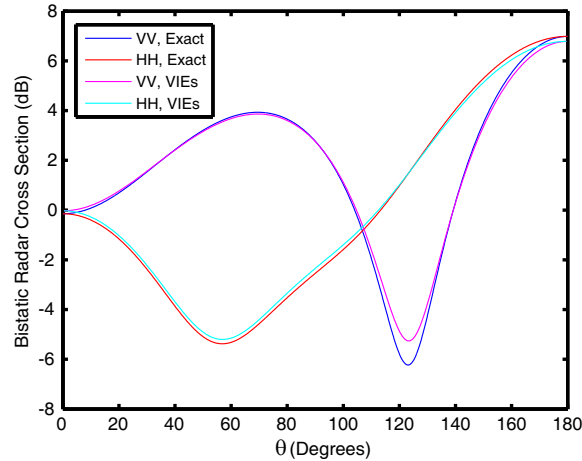


Figure 2: Bistatic RCS solutions for a three-layer concentric dielectric sphere. The radii of three material interfaces are  $a_1 = 0.2\lambda$ ,  $a_2 = 0.25\lambda$ , and  $a_3 = 0.3\lambda$ , respectively. The relative permittivities of dielectric materials in the three layers are  $\epsilon_{r1} = 4.0$ ,  $\epsilon_{r2} = 3.0$ , and  $\epsilon_{r3} = 5.0$ , respectively, and the relative permeability  $\mu_r = 1.0$  is assumed in each layer.

## 5. CONCLUSION

The MoM with the SWG basis function is the primary numerical method for solving the VIEs in electromagnetics but the SWG basis function requires conformal meshes in geometric discretization. In this work, we present a Nyström-like scheme for solving the VIEs. The scheme does not rely on any basis and testing functions and uses a point-matching procedure to change the VIEs into matrix equations based on some chosen nodes in each tetrahedron. The main advantage of the scheme is the permission of inhomogeneous materials in each tetrahedron, resulting in much convenience in geometric discretization. We present a numerical example for EM scattering by a multilayered dielectric sphere to demonstrate the scheme and good results have been observed.

## ACKNOWLEDGMENT

This work was supported by the National Natural Science Foundation of China with the Project No. 61271097.

## REFERENCES

1. Chew, W. C., M. S. Tong, and B. Hu, *Integral Equation Methods for Electromagnetic and Elastic Waves*, Morgan & Claypool, San Rafael, CA, 2008.
2. Schaubert, D. H., D. R. Wilton, and A. W. Glisson, "A tetrahedral modeling method for electromagnetic scattering by arbitrary shaped inhomogeneous dielectric bodies," *IEEE Trans. Antennas Propagat.*, Vol. 32, No. 1, 77–85, 1984.
3. Li, M. K. and W. C. Chew, "Multiscale simulation of complex structures using equivalence principle algorithm with high-order field point sampling scheme," *IEEE Trans. Antennas Propagat.*, Vol. 56, No. 8, 2389–2397, 2008.
4. Qian, Z.-G. and W. C. Chew, "Fast full-wave surface integral equation solver for multiscale structure modeling," *IEEE Trans. Antennas Propagat.*, Vol. 57, No. 11, 3594–3601, 2009.
5. Tong, M. S. and W. C. Chew, "Super-hyper singularity treatment for solving 3D electric field integral equations," *Microw. Opt. Technol. Lett.*, Vol. 49, No. 6, 1383–1388, 2007.
6. Tong, M. S., Z. G. Qian, and W. C. Chew, "Nyström method solution of volume integral equations for electromagnetic scattering by 3D penetrable objects," *IEEE Trans. Antennas Propagat.*, Vol. 58, No. 5, 1645–1652, 2010.
7. Tong, M. S., "Meshfree solutions of volume integral equations for electromagnetic scattering by anisotropic objects," *IEEE Trans. Antennas Propagat.*, Vol. 60, No. 9, 4249–4258, 2012.
8. Ruck, G. T., D. E. Barrick, W. D. Stuart, and C. K. Krichbaum, *Radar Cross Section Handbook*, Plenum Press, New York, 1970.

# Electromagnetic Scattering from Aggregates Embedded in Absorbing Media

R. Ceolato<sup>1</sup>, N. Riviere<sup>1</sup>, M. J. Berg<sup>2</sup>, and B. Biscans<sup>3</sup>

<sup>1</sup>Onera, The French Aerospace Lab, FR 31000, France

<sup>2</sup>Department of Physics and Astronomy, Mississippi State University  
Mississippi State, MS 39762, USA

<sup>3</sup>LGC, UMR CNRS 5503, Universite de Toulouse, FR 31432, France

**Abstract**— Electromagnetic scattering occurs by the presence of discontinuities or scatterers. Ensemble of particles often form clusters or aggregates of particles. Most scattering models assume that such complex ensemble are placed in non-absorbing media. However, for many applications, absorption of the host media cannot be neglected for particular frequency or spectral ranges. In this paper, we study theoretically and numerically the electromagnetic scattering properties of fractal-like aggregates of silicon dioxide particles embedded in water at 193.4 THz or 1550 nm. The volume-integral equation is solved using the Discrete Dipole Approximation. These properties depend upon primary particle parameters as their size, shape or complex refractive index in addition to aggregate structure as its fractal dimension or gyration radius. Such properties are of interest in a range of scientific and industrial applications. The scattered Stokes vectors are calculated for an aggregate and applications in the fields of remote-sensing as RADAR or LiDAR but also materials characterization are discussed.

## 1. INTRODUCTION

The scattering of electromagnetic (EM) waves by objects is of crucial interest for research and engineering problems in remote-sensing, telecommunication, microwave and optics [1, 2]. Scattering may occur by the presence of scatterers or any kind of discontinuity of the complex refractive index. It results, for instance, in a change of the direction of propagation and the state of polarization of the EM wave. Particles such as silicon dioxide, titanium dioxide or carbon soot frequently form three-dimensional systems by aggregation in various situations as combustion, turbulent jets or dense particulate media. These aggregates have a fractal-like structure [3] and their electromagnetic scattering properties are of interest in a range of scientific and industrial applications [4]. These properties depend upon primary particle parameters as their size, shape or complex refractive index in addition to the internal aggregate structure described by its fractal dimension and gyration radius.

In this paper, we define the electromagnetic scattering problem for aggregate of particles embedded in an absorbing host medium [5]. Analytic solutions of this problem are known only for regular-shaped particles [6]. Dedicated numerical methods are required for complex systems of particles such as aggregates. A numerical method derived from the discrete-dipole approximation (DDA) [7] solves the Maxwell equations using the volume-integral equation (VIE) [8]. Results for fractal-like aggregate of silicon dioxide particles in an averaged orientation in water at absorbing wavelength or frequency are reported and compared with equivalent-sphere scattering. The utility of accurate electromagnetic scattering models is discussed for a wide range of applications such as remote-sensing, RADAR or LiDAR but also materials characterization.

## 2. ELECTROMAGNETIC PROBLEM

The electromagnetic scattering problem refers to the perturbation of the propagation of an EM wave by the presence of an object, i.e., a scatterer, with a refractive index different from the surrounding medium, i.e., host medium. We assume here that the EM plane wave is described by its time-dependent and frequency-dependent electric field vector as:

$$\mathbf{E}(\mathbf{r}, \omega, t) = \mathbf{E}(\mathbf{r}, \omega)e^{-i\omega t} \quad (1)$$

where  $\mathbf{r}$  is the position vector,  $\omega = 2\pi f = 2\pi c\lambda^{-1}$  is the angular frequency,  $f$  is the frequency,  $\lambda$  is the wavelength,  $c$  is the speed of light in vacuum and  $i = (-1)^{1/2}$ . The time-dependant term  $e^{-i\omega t}$  is omitted for simplicity in the rest of this paper.

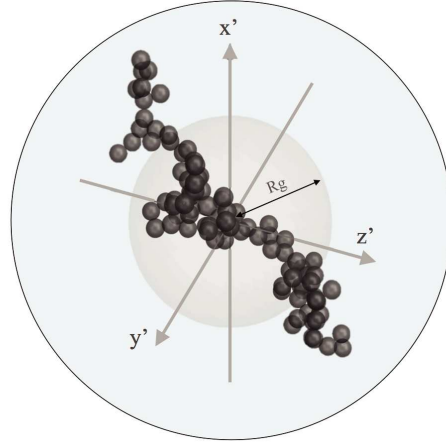


Figure 1: Schematic of electromagnetic scattering from an aggregate composed of spherical particles embedded in absorbing host medium.

Let's consider an arbitrary aggregate of  $N_p$  homogeneous spherical particles embedded in a homogeneous, linear, isotropic and absorbing host medium as depicted in Fig. 1. The unitary volume of the particles is  $V_p$ . The total volume of the aggregate is  $V_a = \sum_i v_i$  where  $i$  ranges from 1 to  $N_p$  and  $v_i$  is the  $i$ -th particle volume. The absorbing host medium of volume  $V_h = V - V_a$ . Both the particles and the host medium have a frequency-dependent or spectral-dependent complex refractive indexes, respectively  $m_p(\omega)$  and  $m_m(\omega)$ , which are defined from the complex permeability  $\varepsilon$  and the permittivity  $\mu$ :

$$m_p(\omega) = m'_p(\omega) + im''_p(\omega) = (\varepsilon_p(\omega)\mu_p(\omega))^{1/2} \quad (2)$$

$$m_m(\omega) = m'_m(\omega) + im''_m(\omega) = (\varepsilon_m(\omega)\mu_m(\omega))^{1/2} \quad (3)$$

For reference, the electromagnetic scattering problem is derived from the Helmholtz equations in the frequency-domain [8] and can be written as a single differential equation, i.e.:

$$\nabla^2 \mathbf{E}(\mathbf{r}, \omega) - k_m^2(\mathbf{r}, \omega) \mathbf{E}(\mathbf{r}, \omega) = k_m^2(\mathbf{r}, \omega) [m^2(\mathbf{r}, \omega) - 1] \mathbf{E}(\mathbf{r}, \omega) \quad (4)$$

where  $k_m(\omega) = k'_m(\omega) + ik''_m(\omega) = \omega m_m(\omega) c^{-1}$  is the complex wave vector in the host medium. The *relative* refractive index  $m(\mathbf{r}, \omega)$  between inside and outside the aggregate is introduced. It is equal to unity and to  $m_p(\omega)/m_m(\omega)$  respectively outside and inside the aggregate [5].

The commonly volume-integral equation (VIE) related to the electromagnetic scattering problem is determined from Eq. (4), i.e.:

$$E(\mathbf{r}, \omega) = E_i(\mathbf{r}, \omega) + \int_{V_a} \mathcal{G}(\mathbf{r}, \mathbf{r}') [m^2(\mathbf{r}, \omega) - 1] \mathbf{E}(\mathbf{r}', \omega) d^3 \mathbf{r}' \quad (5)$$

where  $E_i(\mathbf{r}, \omega)$  is the incident field,  $\mathcal{G}(\mathbf{r}, \mathbf{r}')$  is the free-space dyadic Green's function defined using the identity dyadic  $\mathcal{I}$  as:

$$\mathcal{G}(\mathbf{r}, \mathbf{r}') = (\nabla^2 + k_m^2) \frac{e^{ik_m |\mathbf{r} - \mathbf{r}'|}}{4\pi |\mathbf{r} - \mathbf{r}'|} \quad (6)$$

The scattered electric field vector  $E_{sca}(\mathbf{r}, r, \omega)$  is expressed, in the far-field where  $r \gg r'$  where  $r' \in V_a$ , in term of the angular scattering amplitude  $E_{1,sca}(\mathbf{r}, \omega)$ . This amplitude depends on the direction  $\mathbf{r}$  but not on the distance  $r$  [5].

$$E_{sca}(\mathbf{r}, r, \omega) = e^{-k''_m r} \frac{e^{ik'_m r}}{r} E_{1,sca}(\mathbf{r}, \omega) \quad (7)$$

For practical and experimental purpose, one can compute the scattered Stokes vector elements from the scattered electric field vector at a fixed distance  $r$  in the far-field but still in the host

medium as:

$$I_{sca}(\mathbf{r}, r, \omega) = \frac{e^{-2k''_m r}}{r^2} [E_{1\theta, sca} E_{1\theta, sca}^* + E_{1\phi, sca} E_{1\phi, sca}^*] \quad (8)$$

$$Q_{sca}(\mathbf{r}, r, \omega) = \frac{e^{-2k''_m r}}{r^2} [E_{1\theta, sca} E_{1\theta, sca}^* - E_{1\phi, sca} E_{1\phi, sca}^*] \quad (9)$$

$$U_{sca}(\mathbf{r}, r, \omega) = \frac{e^{-2k''_m r}}{r^2} [-E_{1\theta, sca} E_{1\phi, sca}^* - E_{1\phi, sca} E_{1\theta, sca}^*] \quad (10)$$

$$V_{sca}(\mathbf{r}, r, \omega) = \frac{e^{-2k''_m r}}{r^2} i [E_{1\phi, sca} E_{1\theta, sca}^* - E_{1\theta, sca} E_{1\phi, sca}^*] \quad (11)$$

In the following section, an accurate numerical method is briefly introduced to solve the VIE and to calculate the scattered Stokes vector for arbitrary aggregate.

### 3. NUMERICAL METHOD

Different techniques are available to solve the VIE for aggregate such as the  $T$ -Matrix method [9], Rayleigh-Debye-Gans approximation [10] or the Method of Moments [11]. Our versatile method is based on the DDA [7, 12] to compute accurately the scattering properties of arbitrary aggregates. First, the aggregate is discretized on a cubic lattice. The discretization by the DDA requires modifications of the VIE as shown by [12] because the shape of aggregate cannot be exactly described by a cubic lattice. The DDA requires the integration of two dyadic terms:  $\mathcal{M}$  related to the finiteness of the excluded volume and  $\mathcal{L}$  is the self-term dyadic related to the interaction of the excluded volume with itself. The VIE can be rewritten where  $\delta V$  is the unitary cubic volume and  $N_{dda}$  the total number of cubes included in  $V_a$ :

$$E(\mathbf{r}, \omega) = E_i(\mathbf{r}, \omega) + \sum_{j=0}^{N_{dda}} \mathcal{G}(\mathbf{r}, \mathbf{r}_j) [m^2(\mathbf{r}, \omega) - 1] \mathbf{E}(\mathbf{r}_j, \omega) \delta V - (\mathcal{M}_j - \mathcal{L}_j) \mathbf{E}(\mathbf{r}_j, \omega) \quad (12)$$

After discretization, an electric dipole is assigned to each cube element of the lattice. The electric dipole moment is related to the polarization of each cubic volume as:  $\mathbf{p}_j = \alpha \mathbf{E}(\mathbf{r}_j, \omega)$  where  $\alpha$  is the polarizability and depends on  $m(\mathbf{r}, \omega)$ . It responds to the incident wave and couples to the other dipoles in the aggregate. The Lattice Dispersion Relation (LDR) is used in this paper for fast computation [12]. At last, the discretized VIE is written as a system of coupled linear equations to be easily solved numerically.

### 4. RESULTS AND DISCUSSION

Fractal aggregates satisfy a scaling law [3] between the number of particles  $N_p$ , the particles radius  $R_p$ , the gyration radius  $R_g$ , the fractal dimension  $D_f$  that relates the structure of the aggregate and the fractal prefactor  $k_0$ :

$$N_p = k_0 \left( \frac{R_g}{R_p} \right)^{D_f} \quad (13)$$

The standard aggregate studied here was generated by a DLCA model [13]. It has a linear or chain-like structure as represented in Fig. 1 and has  $N_p = 90$ ,  $R_p = 100$  nm,  $R_g = 1097$  nm,  $k_0 = 1.3$  and  $D_f = 1.8$ . The parameters  $D_f$  and  $R_g$  relate respectively the internal structure of the aggregate and the overall size. The incident EM wave is considered  $p$ -polarized with a frequency  $f = 193.4$  THz or wavelength  $\lambda = 1550$  nm. In this frequency range, water is absorbing and silicon oxide is considered non-absorbing. We applied our DDA method by discretizing the aggregate on the DDA lattice. The typical size of the lattice is  $100 \times 100 \times 100$  sites for a single aggregate containing approximately 4000 dipoles.

Figure 2 is a representation of the normalized scattered Stokes vector elements  $I$ ,  $Q$ ,  $U$  and  $V$  for an aggregate of silicon dioxide embedded in water. The internal structure of the aggregate is described above. Numerical simulations are carried out for an aggregate in a random orientation in order to be directly compared to electromagnetic scattering measurements. Our results shows strong angular depolarization of the incident EM wave. We report an inversion of the polarization state, from  $p$ -state to  $s$ -state. It occurs once in the forward scattering region and twice at in the backscattering region. These simulated scattered Stokes vector elements may serve as angular and

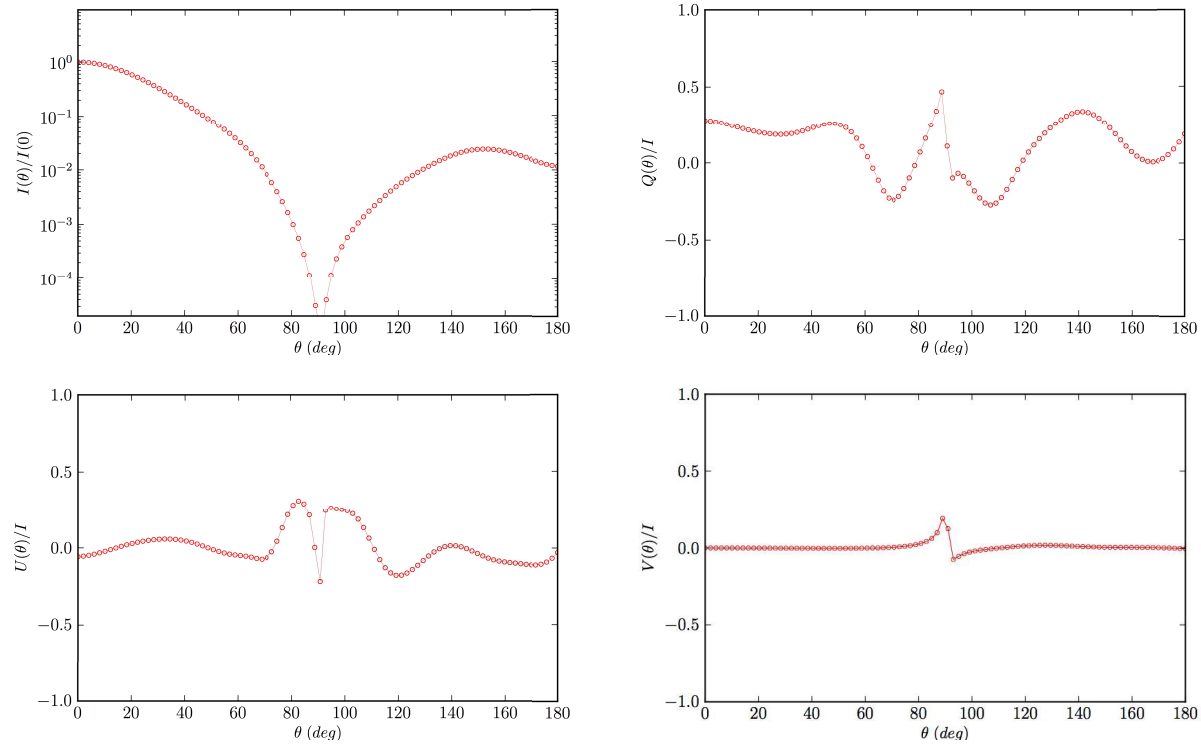


Figure 2: Normalized scattered Stokes vector elements  $I$ ,  $Q$ ,  $U$  and  $V$  at 193.4 THz ( $= 1550$  nm) for an aggregate of silicon dioxide particles embedded in water with  $R_g = 1097$  nm. Complex refractive indexes are  $m_m = 1.31 + i5 \cdot 10^{-5}$  and  $m_p = 1.44 + i0.0$ .

polarimetric scattering fingerprint, of sorts, independent of the orientation of the aggregate. They may also be useful in the simulation of the propagation of EM wave in scattering and absorbing media for remote-sensing applications.

## 5. CONCLUSION

This work applies a theoretical and numerical model to solve the VIE using the DDA. We apply our model to compute the electromagnetic scattering properties of a DLCA-simulated fractal-like aggregate of particles embedded in absorbing media. Simulations of angular and polarimetric scattering properties are done for silicon dioxide particles embedded in water at 193.4 THz or  $= 1550$  nm. We report the simulated scattered Stokes elements for the aggregate placed in a random orientation. It may be that such scattering properties contain useful information about the aggregate structure and morphology that would survive orientational averaging, and as such could find application in experimental characterization of aggregating particle-systems.

## ACKNOWLEDGMENT

The authors are thankful to Flint Pierce for providing the DLCA-simulated aggregates. This work was supported by Mississippi State University and Onera, the French Aerospace Lab. It was funded by the contract BQR-NANOPTIC and by Institut Supérieur de l'Aéronautique et de l'Espace (ISAE), the Institut National Polytechnique (INP) and Region Midi-Pyrenees.

## REFERENCES

1. Berg, M. J., S. C. Hill, G. Videen, and K. P. Gurton, "Spatial-filtering technique to image and measure two-dimensional near-forward scattering from single particles," *Opt. Express*, Vol. 18, No. 9, 9486–9495, 2010.
2. Ceolato, R., N. Riviere, and L. Hespel, "Reflectances from a supercontinuum laser-based instrument: Hyperspectral, polarimetric and angular measurements," *Opt. Express*, Vol. 20, No. 28, 29413–29425, 2012.
3. Sorensen, C. M., "Light scattering by fractal aggregates. A review," *Aerosol. Sci. Technol.*, Vol. 35, 648–687, 2001.

4. Dlugach, J. M., M. I. Mishchenko, and D. W. Mackowski, “Numerical simulations of single and multiple scattering by fractal ice clusters,” *J. Quant. Spectrosc. Radiat. Transfer.*, Vol. 112, 1864–1870, 2011.
5. Mishchenko, M. I., “Electromagnetic scattering by a fixed finite object embedded in an absorbing medium,” *Opt. Express*, Vol. 15, No. 13, 13188–13202, 2007.
6. Qiang, F. and S. Wenbo, “Mie theory for light scattering by a spherical particle in an absorbing medium,” *Appl. Opt.*, Vol. 40, 1354–1361, 2001.
7. Purcell, E. M. and C. R. Pennypacker, “Scattering and absorption of light by nonspherical dielectric grains,” *Astrophys. J.*, Vol. 186, 705–714, 1973.
8. Mishchenko, M. I., *Scattering, Absorption, and Emission of Light by Small Particles*, Cambridge University Press, Cambridge, 2002.
9. Liu, L., M. I. Mishchenko, and W. P. Arnott, “A study of radiative properties of fractal soot aggregates using the superposition  $T$ -matrix method,” *J. Quant. Spectrosc. Radiat. Transfer.*, Vol. 109, 2656–2663, 2008.
10. Farias, T., U. Koylu, and M. Carvalho, “Range of validity of the Rayleigh-Debye-Gans theory for optics of fractal aggregates,” *J. Appl. Opt.*, Vol. 35, No. 33, 6560–6567, 1996.
11. Kazakov, A. and M. Frenklach, “Dynamic Modeling of soot particle coagulation and aggregation: Implementation with the method of moments and application to high-pressure laminar premixed flames,” *Combust. Flame*, Vol. 114, No. 3, 484–501, 1998.
12. Yurkin, M. A. and A. G. Hoekstra, “The discrete dipole approximation: An overview and recent developments,” *J. Quant. Spectrosc. Radiat. Transfer.*, Vol. 106, 558–589, 2007.
13. Tang, S., J. M. Preece, C. M. McFarlane, and Z. Zhang, “Fractal morphology and breakage of DLCA and RLCA aggregates,” *J. Colloid. Interf. Sci.*, Vol. 221, No. 1, 114–123, 2000.

# A New Parallel Version of the DDSCAT Code for Electromagnetic Scattering from Big Targets

R. W. Numrich<sup>1</sup>, T. L. Clune<sup>2</sup>, and K.-S. Kuo<sup>2,3</sup>

<sup>1</sup>The Graduate Center, City University of New York, New York, New York, USA

<sup>2</sup>NASA Goddard Space Flight Center, Greenbelt, Maryland, USA

<sup>3</sup>Earth System Science Interdisciplinary Center, University of Maryland  
College Park, Maryland, USA

**Abstract**— We have modified the publicly available electromagnetic scattering code called DDSCAT to handle bigger targets with shorter execution times than the original code. A big target is one whose sphere equivalent radius is large compared to the incident wavelength. DDSCAT uses the discrete-dipole approximation and an accurate result requires the spacing between dipoles to be small relative to the wavelength. This requirement, along with the big target size, implies that the number of discrete grid cells defining the computational grid box surrounding the target must be large. The memory requirement is thus significant and the execution time long. The original version of the code cannot handle large enough targets that we would like to consider because they require memory exceeding what is available on a single node of our cluster and execution time extending to days.

We have removed two limitations of the original version of the code. First, to speed up the execution involving multiple target orientations, the original code assigned one, but only one, MPI process to each independent orientation. We surmount this limitation by assigning each orientation a team of processes. Second, the original code allocated all the memory for the full problem for each MPI process. We surmount this limitation by decomposing the data structures across the members of a team. With these changes, the new version can handle much bigger targets. Moreover, it exhibits strong scaling for fixed problem size. The execution time decreases very nearly  $1/p$  as the processor count  $p$  increases. Execution time measured in days with the original code can now be reduced to fractions of an hour.

## 1. INTRODUCTION

The discrete-dipole approximation (DDA), based on the original work of Purcell and Pennypacker [7], is a standard method for calculating electromagnetic scattering cross sections of irregularly shaped targets [6]. One of the more effective codes for this kind of calculation is the DDSCAT code from Draine and Flatau [1]. A comparable one is the ADDA code from Yurkin and Hoekstra [9]. Kahnert provides a review of other solution methods in a recent review paper [3].

DDA reduces the scattering problem to the solution of a large, dense, complex symmetric system of linear equations,

$$\mathbf{Ax} = \mathbf{b} \tag{1}$$

Design of a code to solve these equations and the resulting performance of the code depend on the data structures chosen to represent the matrix and the solution technique selected to solve the system of equations. Since the matrix is a symmetric Toeplitz matrix, only the elements of a single row need be stored, and these elements can be decomposed and distributed across processors in a straightforward way. To solve the system of equations, the community has, after many years of experimentation and analysis, settled on using one or another variation of Krylovbased solvers [8, Chs. 6–7]. These iterative solvers require several matrix-vector multiplications at each iteration. Since the matrix is Toeplitz, representing a convolution, this operation can be performed using Fast Fourier Transforms. The matrix-vector multiplication, then, becomes a forward FFT of two vectors followed by multiplication in Fourier space followed by inverse FFT back to physical space.

The parallel strategy adopted in the original version of the code assigns a separate MPI process to each independent target orientation. Each MPI process allocates all the memory for the full problem, which may exceed the memory available on a node for big targets, and the number of processes that could be used is limited by the number of orientations. The new code assigns a team of MPI processes to each independent orientation and partitions the data structures by the size of the team. The problem now fits in memory and more processes can be used to reduce the execution time.

## 2. THE DISCRETE-DIPOLE APPROXIMATION

DDA surrounds the target with a three-dimensional computational grid box discretized into cubical cells of volume  $d^3$  with a dipole located at the center of each of the cells occupied by the target [7]. If there are  $n$  dipoles in the target, the volume occupied by these dipoles is  $nd^3$ , resulting in an sphere-equivalent radius of  $a$ , defined by the relationship,  $nd^3 = (4\pi/3)a^3$ . Scattering cross sections are often measured in units equal to the cross sectional area,  $\pi a^2$  [2, Ch. 16, 4, Ch. 2].

The accuracy of the method requires [1, 10, 11] that the grid spacing between cells,  $d$ , be small relative to the wavelength,

$$2|m|kd < 1 \quad (2)$$

where  $m$  is the complex refractive index of the target and  $k = 2\pi/\lambda$  is the wavenumber.

A target is considered “big” if its *size parameter*,  $ka$ , is much bigger than one, i.e.,  $ka \gg 1$ . Coupled with requirement (2), it implies a large number of dipoles,  $n > (2|m|ka)^3$ , and almost always an even larger number of grid cells. The memory requirement for a large target may thus exceed what is available on a single computer or a node in a cluster. Furthermore, the computational work that must be done to solve the system of equations increases with the size of the grid box and the execution time for large targets may easily expand to days if only a single node can be used. To address these two problems, we decompose the computational box such that each partition of the box fits into the memory of a single node, and we assign a team of processors to work in parallel on each partition to reduce the execution time.

## 3. THE PARTITIONED COMPUTATIONAL PROBLEM

The parallel implementation strategy for any application code involves two issues: how to partition data structures and how to assign work. The original code takes into consideration one of these issues, the assignment of work, but does not consider the partition of data structures. The new version addresses both issues.

The details of the partition depend on the details of how the system of Equation (1) is represented on the grid points of the discretized computational grid box. The vector on the right side is proportional to the incoming plane wave,  $\exp(i\mathbf{k} \cdot \mathbf{r})$ , with wavelength  $\lambda$ , wavenumber  $k = |\mathbf{k}|$ , and the direction of the wave vector relative to the target by three Euler angles  $(\alpha, \beta, \gamma)$ . At each grid point of the computational grid box, the vector on the right side of the system of equations,  $b_{ijk} = \exp[i\mathbf{k} \cdot (r_i, r_j, r_k)]$ , has values proportional to the value of the plane wave at each grid point  $\mathbf{r} = (r_i, r_j, r_k)$ . In the same way, the values of the elements of the matrix  $\mathbf{A}$  are evaluated relative to the grid points, and the solution vector  $\mathbf{x}$  is found at each grid point. In practice, indices for the points on the three-dimensional grid are serialized so that the quantities  $\mathbf{b}$  and  $\mathbf{x}$  can be thought of as vectors of length  $n^3$  and the matrix  $\mathbf{A}$  can be thought of as a matrix of size  $n^3 \times n^3$ .

The decomposition strategy is straightforward. The vectors involved are partitioned along one of the directions of the computational grid box. If the grid points have been serialized in lexical order, the  $x$ -direction first, followed by the  $y$ -direction and then by the  $z$ -direction, the vectors can be partitioned in the  $z$ -direction by the team size (i.e., number of processes per team) assigned to the partition. Correspondingly, the rows of the matrix are partitioned along the  $z$ -direction. This partitioning introduces overhead into the code due to the requirement for moving distributed data structure among team members, but for big targets, this overhead is small as our results show in later sections.

## 4. PARALLEL CONVOLUTION

Special properties of the matrix  $\mathbf{A}$  make the problem tractable. The matrix is a function of the magnitude of the plane wave vector,  $k = |\mathbf{k}|$ , not its direction, i.e.,  $\mathbf{A} = \mathbf{A}(k)$ . The matrix can thus be calculated once for each wavelength and used for all orientations of the incoming wave. It is also a Toeplitz matrix. The values of its elements depend on the distance between grid points such that, in the serialization representation, the matrix elements have the property,  $a_{ij} = a_{i-j}$ . It can then be represented by one of its rows, a vector of length  $n^3$ , rather than a matrix of size  $n^3 \times n^3$ .

The vector  $\mathbf{b}(\mathbf{k})$  and the solution vector  $\mathbf{x}(\mathbf{k})$ , on the other hand, are necessarily functions of both the magnitude and the orientation of the incoming wave. Thus, for each orientation, the matrix remains the same but the right-hand-side vector changes so the system of equations,

$$\mathbf{A}(k) \mathbf{x}(\mathbf{k}) = \mathbf{b}(\mathbf{k}), \quad (3)$$

must be solved for the solution vector for each orientation.

When iterative Krylov solvers are used to solve this system, several matrix-vector multiplications of the kind:  $\mathbf{y} = \mathbf{A}\mathbf{x}$ , must be performed for each iteration. Since the matrix is Toeplitz, its elements depend only on the difference of the indices, and the matrix-vector multiplication becomes a convolution,  $y_i = \sum_j a_{i-j}x_j$ . The operation count for this multiplication is on the order of the square of the rank of the matrix if done in the usual way. But since the Fourier transform of a convolution is the product of the Fourier transforms of the two factors,  $\mathcal{F}(\mathbf{y}) = \mathcal{F}(\mathbf{A}) \cdot \mathcal{F}(\mathbf{x})$ , the operation count can be reduced to the order of the matrix size times the logarithm of the matrix size. This difference results in a significant saving of computation time. The result vector is retrieved with the inverse transform,  $\mathbf{y} = \mathcal{F}^{-1}[\mathcal{F}(\mathbf{A}) \cdot \mathcal{F}(\mathbf{x})]$ .

The Fourier transform is a three-dimensional transform over the grid points of the computational box. Since the box has been decomposed along the  $z$ -direction, data communication among processors is required, which is not required on a single processor. Each processor can perform the transform independently for the grid points it owns in the  $xy$ -plane, but the data structure must be transposed to do the transform in the  $z$ -direction. The matrix can be transformed once for each wavelength and left in the transposed data structure in Fourier space. It does not need to be transformed back to the original decomposed data structure. The vectors at each iteration of the Krylov solver are also left in transformed Fourier space and multiplied by the matrix. Only then is the product of the two vectors transformed back to the original partitioned data structure.

An important optimization of the convolution step results from treating the zeros that must be padded onto the vectors before performing the Fourier transform [5]. Total time for the transform, using a Fast Fourier Transform (FFT) library, is the sum of the time in each of the three dimensions,  $t_1 = t_x + t_y + t_z$ . If the dimensions are about the same in each dimension, the time for the transform is the same in each direction,  $t_x = t_y = t_z = t_0$ , and  $t_1 = 3t_0$ . During the FFT in the  $x$ -direction, the time reduces by half by not computing over the zeros in the  $y$ -direction and again by half by not computing over the zeros in the  $z$ -direction. Likewise, in the  $y$ -direction, the time reduces by half by not computing over the zeros in the  $z$ -direction. The time in the  $z$ -direction remains the same so the reduced time becomes,  $t_2 = t_0/4 + t_0/2 + t_0 = (7/4)t_0$ , and the speedup in performance becomes  $t_1/t_2 = 3t_0/(7t_0/4) = 12/7 \simeq 1.71$ .

For large targets, where the FFT dominates the execution time, this modification of the code may lead to significant performance speedup. For smaller targets, where the FFT is only a fraction of the total execution time, the benefit will be lower. If the transpose represents 50% of the execution time, the benefit may only be about 20%. We have measured a 12% benefit per grid point on a single processor for a test case.

## 5. PARALLEL MATRIX TRANSPOSE

For multiple processors, the analysis of the time saved due to the treatment of the padding is somewhat different from that of a single processor due to the nontrivial cost for the matrix transpose. The amount of data transferred between the  $xy$ -direction to the  $z$ -direction, during the matrix transpose reduces by a factor of 2. For large problem sizes, we have observed that the time required for the transpose was comparable to the total time for the FFT. If the transpose is bandwidth limited, the net speedup for FFT with transpose can be estimated as  $t_1/t_2 = (3t_0 + 3t_0)(3t_0/2 + 7t_0/4) = 24/13 \simeq 1.85$ . We have, in fact, measured an overall speedup equal to  $1.7 \times$  with the new treatment of the padding.

## 6. SCALING ANALYSIS

To compare performance of the old version of the code with the new version, we examine two different targets referred to here as *medium* and *large*. The medium target fits within the memory of a single node on our machine, and allows direct performance comparisons between the two code versions. The large target, does not fit in the memory of a single node, and can only be run with the new version. The large target illustrates that the new version of the code can handle larger targets and that, for these big targets, it exhibits strong scaling.

An important advantage of the new implementation, is that it allows the code to utilize far more processors. Whereas the original code limited the number of MPI processes to the number of target orientations, typically  $O(10^2)$  the new version uses a team of processes for each orientation. The number of MPI processes in a team is only limited by the size of the computational grid.

Parallel strategy for the new version of the code is good for the large case which does not fit in the memory of a single node. With the new version of the code, we use teams of size 20 and distribute the MPI processes across nodes with each process requiring one-twentieth of the memory.

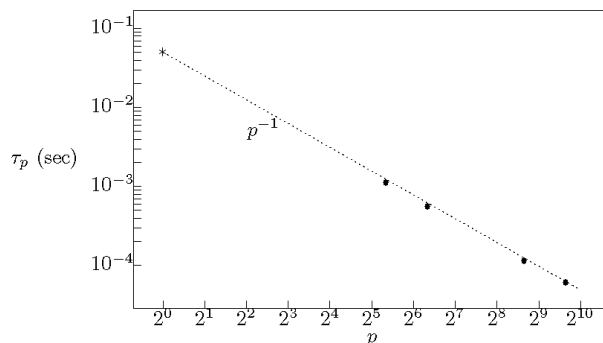


Figure 1: Execution time per grid point,  $\tau_p = t(p)/n_x n_y n_z$ , as a function of processor count. Large target with  $|m|kd = 0.3563$  contained in a box of size  $(n_x, n_y, n_z) = (256, 360, 360)$  marked with bullets ( $\cdot$ ) measured in seconds. The dotted line represents perfect scaling of  $p^{-1}$ . The intercept at  $\log(\tau_1) = -1.3$ , marked with an asterisk (\*), suggests that the problem on a single processor would require at least 19 days to complete compared with about half an hour on 800 processors.

For this problem, the FFT dominates the execution time taking almost 99% of the total. This part of the code is fully parallelized and the execution time, for the fixed problem size, exhibits strong scaling — decreasing inversely with the processor count as illustrated in Figure 1.

## 7. ACCURACY OF THE METHOD

The accuracy, as well as the performance, of codes that implement the discrete-dipole approximation depends on a number of empirically determined parameters [10, 11]. The distance between cells, for example, must be small relative to the wavelength of the incident wave as displayed in inequality (2). The rate of convergence of the iterative solver also depends on the value of this parameter, smaller values generating larger matrices requiring more iterations to converge.

Now that the execution time has been reduced to a few minutes of time for very big targets, we can perform parameter studies to test the accuracy of the results. In particular, we can follow the technique suggested by Yurkin and coworkers [11] to extrapolate the results to zero cell size.

## 8. SUMMARY

The major changes to the code, after decomposing the data structures, required a 3D transpose for the FFT and a global reduction for the scalar products and norms in the iterative solver. Data decomposition was by far the hardest change to make to the original code. Performance of the code improved when we removed unnecessary calls to the FFT routine for padded zeros required for the convolution. For big targets, the new code exhibits almost perfect strong scaling as the processor count increases.

## ACKNOWLEDGMENT

The authors are grateful to the NASA High-End Computing program for making this improvement possible.

## REFERENCES

1. Draine, B. T. and P. J. Flatau, “Discrete-dipole approximation for scattering calculations,” *J. Opt. Soc. Am. A*, Vol. 11, No. 4, 1491–1499, 1994.
2. Jackson, J. D., *Classical Electrodynamics*, 1st Edition, John Wiley & Sons, 1962.
3. Kahnert, F. M., “Numerical methods in electromagnetic scattering theory,” *J. Quant. Spectrosc. Radiat. Transfer*, Vols. 79–80, 775–824, 2003.
4. Newton, R. G., *Scattering Theory of Waves and Particles*, 1st Edition, McGraw-Hill Book Company, New York, 1966.
5. Nukada, A., Y. Hourai, A. Hishida, and Y. Akiyama, “High performance 3D convolution for protein docking on IBM blue gene,” *Parallel and Distributed Processing and Applications: 5th International Symposium, ISPA 2007*, Vol. 4742 of *Lecture Notes in Computer Science*, 958–969, Springer, 2007.

6. Penttilä, A., E. Zubko, K. Lumme, K. Muinonen, M. A. Yurkin, B. Draine, J. Rahola, A. G. Hoekstra, and Y. Shkuratov, “Comparison between discrete dipole implementations and exact techniques,” *J. Quant. Spectrosc. Radiat. Transfer*, Vol. 106, 417–436, 2007.
7. Purcell, E. M. and C. R. Pennypacker, “Scattering and absorption of light by nonspherical dielectric grains,” *Astrophys. J.*, Vol. 186, 705–714, 1973.
8. Saad, Y., *Iterative Methods for Sparse Linear Systems*, 2nd Edition, SIAM, 2003.
9. Yurkin, M. A. and A. G. Hoekstra, “The discrete-dipole-approximation code ADDA: Capabilities and known limitations,” *J. Quant. Spectrosc. Radiat. Transfer*, Vol. 112, 2234–2247, 2011.
10. Yurkin, M. A., V. P. Maltsev, and A. G. Hoekstra, “Convergence of the discrete dipole approximation. I. Theoretical analysis,” *J. Opt. Soc. Am. A*, Vol. 23, No. 10, 2578–2591, 2006.
11. Yurkin, M. A., V. P. Maltsev, and A. G. Hoekstra, “Convergence of the discrete dipole approximation. II. An extrapolation technique to increase the accuracy,” *J. Opt. Soc. Am. A*, Vol. 23, No. 10, 2592–2601, 2006.

# Analysis of Electromagnetic Scattering from Absorptive Dielectric Rough Surfaces with Underneath Target

Yinhui Wang and Yang Du

Department of Information Science and Electronics Engineering  
Zhejiang University, Hangzhou 310027, China

**Abstract**— In the current work, we consider the problem of electromagnetic scattering from absorptive dielectric rough surfaces with underneath target. Previously we have extended the spectral acceleration method, which is restricted to nonabsorptive medium, to the more general cases of absorptive media. Here we combine the extended spectral acceleration method with the right preconditioned GMRES method, to analyze the scattering problem. Numerical results validate its efficiency and robustness. The proposed method is useful in a number of important applications such as target detection.

## 1. INTRODUCTION

Electromagnetic scattering from absorptive dielectric rough surfaces with underneath target carries rich information of the target and medium, which can be used for many important ends. The main concerns of conducting the analysis lie in the capability of the proposed numerical approach to be computationally efficient, robust, and able to handle large scale problems. Also since the popular spectral acceleration (SA) technique can deal with both time and storage complexity, it is desirable to extend its applicability to absorptive media as well.

In the application of the Method of Moment (MoM) [1], there have been several algorithms proposed in the literature, including the Generalized Forward-Backward Method (GFBM) [2], Generalized Forward-Backward Method Spectrum Acceleration algorithm, (GFBM-SA) [3], Canonical Grid Method (CAG) [4], Physics-based Two Grid CAG method (PBTG-CAG) [5]. The spectral acceleration (SA) method [6, 7] is very effective to improve the efficiency of computation and storage, yet is restricted to non-absorptive medium [8]. Given the ubiquitous presence of absorptive medium and the interest in the electromagnetic coupling between a surface and targets, in particular those below the surface, in the current work we propose a method, which takes advantage of the Extended SA (ESA) method which extends the SA method to absorptive media, a method that we have just developed, in combination with the very effective and robust right preconditioned GMRES (GMRES-RP) method [9], to deal with the problem of electromagnetic scattering from a target beneath an absorptive rough surface.

## 2. THE SCATTERING PROBLEM

Consider a tapered plane wave  $\psi_{inc}(x, z)$  incident upon a one-dimensional (1D) dielectric rough surface with a PEC target beneath it. The random height profile is  $z = f(x)$ . The upper medium has relative permittivity  $\epsilon$  and permeability  $\mu$ . The lower medium has relative permittivity  $\epsilon_1$  and permeability  $\mu_1$ . The field  $\psi$  in the upper medium satisfies the following surface integral equation

$$\frac{1}{2}\psi_0(\bar{r}') = \psi^{in}(\bar{r}) + \int_{s_r} \left[ \psi_0(\bar{r}') \frac{\partial g_0(\bar{r}, \bar{r}')}{\partial n'} - g_0(\bar{r}, \bar{r}') \frac{\partial \psi_0(\bar{r}')}{\partial n'} \right] ds' \quad (1)$$

$$\frac{1}{2}\psi(\mathbf{r}') - \int_s \left[ \psi(\mathbf{r}) \frac{\partial G(\mathbf{r}, \mathbf{r}')}{\partial n} - G(\mathbf{r}, \mathbf{r}') \frac{\partial \psi(\mathbf{r})}{\partial n} \right] ds = \psi_{inc}(\mathbf{r}') \quad (2)$$

The field  $\psi_1$  in the lower medium satisfies the following surface integral equation for *TE* polarization

$$\frac{1}{2}\psi_1(\bar{r}') = - \int_{s_r} \left[ \psi_1(\bar{r}') \frac{\partial g_1(\bar{r}, \bar{r}')}{\partial n'} - g_1(\bar{r}, \bar{r}') \frac{\partial \psi_1(\bar{r}')}{\partial n'} \right] ds' + \int_{s_o} g_1(\bar{r}, \bar{r}') \frac{\partial \psi_1(\bar{r}')}{\partial n'} ds' \quad (3)$$

while for *TM* polarization it is

$$\frac{1}{2}\psi_1(\bar{r}') = - \int_{s_r} \left[ \psi_1(\bar{r}') \frac{\partial g_1(\bar{r}, \bar{r}')}{\partial n'} - g_1(\bar{r}, \bar{r}') \frac{\partial \psi_1(\bar{r}')}{\partial n'} \right] ds' - \int_{s_o} \psi_1(\bar{r}') \frac{\partial g_1(\bar{r}, \bar{r}')}{\partial n'} ds' \quad (4)$$

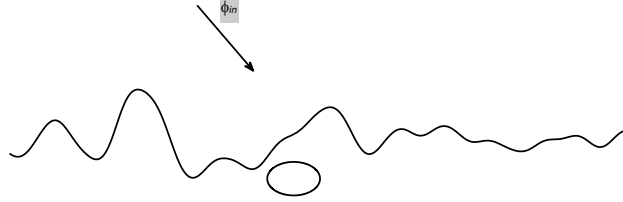


Figure 1: Electromagnetic scattering from an absorptive rough surface with a target underneath.

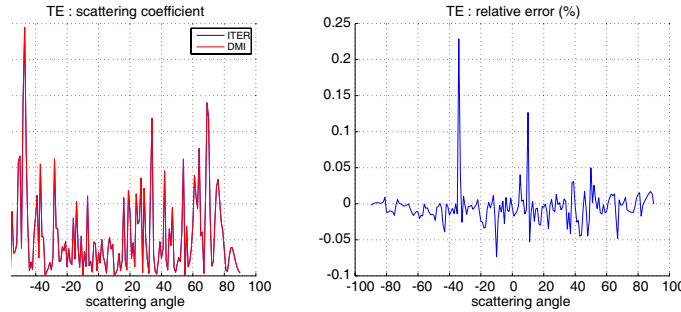


Figure 2: Comparison between the proposed method and DMI. *TE* polarization.

where the point  $\mathbf{r} = \hat{x}x + \hat{z}f(x)$  is on the surface with the unit surface normal  $\hat{n}$  pointing upward,  $g$  is the two-dimensional Green's function in the upper medium and  $g_1$  in the lower medium,  $s_o$  and  $s_r$  refer to the target surface and rough surface respectively. It should be emphasized here that in the above the integral involving the rough surface is the Cauchy principle value integral.

The boundary conditions on the rough surface are  $\psi(\mathbf{r}) = \psi_1(\mathbf{r})$  and  $\partial\psi_1(\mathbf{r})/\partial n = \mu_1/\mu\partial\psi(\mathbf{r})/\partial n$  for the transverse electric (TE) case, and are  $\psi(\mathbf{r}) = \psi_1(\mathbf{r})$  and  $\partial\psi_1(\mathbf{r})/\partial n = \varepsilon_1/\varepsilon\partial\psi(\mathbf{r})/\partial n$  for the transverse magnetic (TM) case. The second condition can be put in a more compact form as  $\partial\psi_1(\mathbf{r})/\partial n = \rho\partial\psi(\mathbf{r})/\partial n$  where  $\rho = \mu_1/\mu$  for the TE case and  $\rho = \varepsilon_1/\varepsilon$  for the TM case.

The discretized system in the MoM can be expressed compactly in matrix and vector form as

$$\mathbf{Z}\mathbf{x} = \mathbf{b} \quad (5)$$

where  $\mathbf{Z}$  is the impedance matrix,  $\mathbf{b}$  is related to the incidence wave, and  $\mathbf{x}$  is the surface unknown vector. For the cases under consideration, the matrix  $\mathbf{Z}$  is often of near singular nature, which will lead to the slowdown of a Krylov method such as GMRES; moreover, there is uncertainty about whether GMRES iterates converge safely to a least-squares solution or to the pseudoinverse solution. A preconditioning process is thus called for. The right preconditioned system is  $\mathbf{Z}\mathbf{M}^{-1}\mathbf{v} = \mathbf{b}$  with  $\mathbf{x} = \mathbf{M}^{-1}\mathbf{v}$ . The design of a good preconditioner  $\mathbf{M}$  is of great importance here. It is required to approximate  $\mathbf{Z}$  and in the meanwhile ensure an inexpensive solution to the linear systems  $\mathbf{M}\mathbf{x} = \mathbf{v}$ .

Here we extend the design principle of GMRES-RP [9] to the case where a target below the rough surface is at concern. In computing the matrix-vector product, the ESA is utilized for the absorptive medium, with the relative error of the value of the approximated spectral representation to the exact value of Green's function under one ten thousandth, so as to ensure that the impact on accuracy in the application of ESA is negligible.

### 3. NUMERICAL RESULTS

In this section, we present some numerical results. The rough surface is Gaussian correlated unless explicitly stated otherwise. The relative dielectric constant of the lower medium is  $4 + i0.1$ , and the target is a PEC circular cylinder. The sampling rate is 16 samples per wavelength. The tapering parameter for the incident wave is  $g = L/4$ . The incidence angle is  $60^\circ$ .

We start by confirming the accuracy of the proposed method, where we compare its normalized bistatic scattering coefficient (NBSC) with that obtained by direct matrix inversion (DMI). The *rms* height is  $1\lambda$ , and *rms* height to correlation length ratio is  $s = 0.2$ . The surface length is  $128\lambda$ , with a total number of unknowns being 4159. The target has a radius of  $3\lambda$ , with its center to the mean surface being  $h = 6\lambda$ . The relative error threshold for the GMRES-RP is set to be  $10^{-5}$ . From Fig. 2, it is seen that the maximum absolute relative error is below 0.25% for TE. The accuracy is even higher for TM, with a maximum absolute relative error around 0.01%.

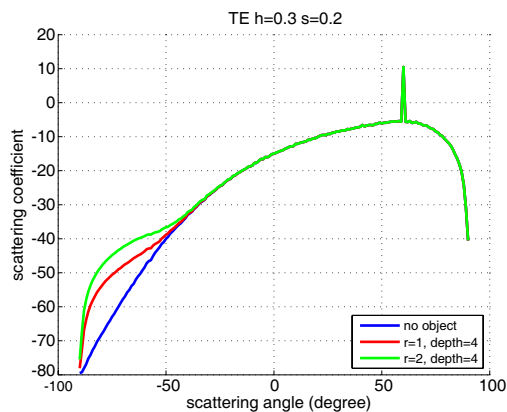


Figure 3: Impact of the presence and size of target on the NBSC.

Now we examine the impact of the target size on the NBSC. The length of rough surface is  $1024\lambda$ , the relative error threshold for the GMRES-RP is set to be  $10^{-4}$ , and the results shown in Fig. 3 are the average of 1000 realizations. The polarization is TE. The distance between the target center to the mean surface is  $h = 4\lambda$ . We consider two radii for the target:  $1\lambda$  and  $2\lambda$ , respectively.

From Fig. 3, it is seen that the size or even the presence of the target has negligible effect on NBSC in the forward scattering directions. However, in the backward directions, the presence and size of the target has profound impact on the NBSC, with larger NBSC for larger target size, as intuition would suggest. The case of TM shows similar pattern.

#### 4. CONCLUSION

We have proposed a highly efficient and robust numerical approach for the analysis of scattering from a rough surface with a target beneath it. The medium under the rough surface is allowed to be absorptive. The proposed method is useful in a number of important applications such as target detection.

#### REFERENCES

1. Harrington, R. F., *Field Computation by Moment Methods*, Macmillan, 1968.
2. Pino, M. R., L. Landesa, J. Rodriguez, F. Obelleiro, and R. J. Burkholder, "The generalized forward-backward method for analyzing the scattering from targets on ocean-like rough surfaces," *IEEE Trans. Antennas Propagat.*, Vol. 47, No. 6, 961–969, 1999.
3. Li, Z. and Y. Q. Jin, "Bistatic scattering from a fractal dynamic rough sea surface with a ship presence at low grazing-angle incidence using the GFBM/SAA," *Microw. Opt. Technol. Lett.*, Vol. 31, No. 2, 146–151, 2001.
4. Tsang, L., C. H. Chan, K. Pak, and H. Sangani, "Monte Carlo simulations of large scale problems of random rough surface scattering and applications to grazing incidence with the BMIA/canonical grid method," *IEEE Trans. Antennas Propagat.*, Vol. 43, No. 8, 851–859, 1995.
5. Li, Q., C. H. Chan, and L. Tsang, "Monte-Carlo simulations of wave scattering for lossy dielectric random rough surfaces using the physics-based two-grid method and canonical grid method," *IEEE Trans. Antennas Propagat.*, Vol. 47, No. 4, 752–763, 1999.
6. Chou, H.-T. and J. T. Johnson, "A novel acceleration algorithm for the computation of scattering from rough surfaces with the forward-backward method," *Radio Sci.*, Vol. 33, No. 5, 1277–1287, 1998.
7. Torrungrueng, D. and J. T. Johnson, "Some issues related to the novel spectral acceleration method for the fast computation of radiation/scattering from one-dimensional extremely large scale quasi-planar structures," *Radio Sci.*, Vol. 37, No. 2, 2002.
8. Kubick, G., C. Bourlier, and J. Saillard, "Scattering by an object above a randomly rough surface from a fast numerical method: Extended PILE method combined to FB-SA," *Waves in Random and Complex Media*, Vol. 18, No. 3, 495–519, 2008.
9. Yang, G. and Y. Du, "A robust preconditioned GMRES method for electromagnetic scattering from dielectric rough surfaces," *IEEE Trans. Geosci. Remote Sens.*, Vol. 50, No. 9, 3396–3408, Sep. 2012.

# Investigating the Radar Returns of a Wind Turbine

M. B. Raza and T. H. Fickenscher

Helmut Schmidt University, Hamburg, Germany

**Abstract**— In this paper, a comparison of different numerical methods for the calculation of the radar returns of a wind turbine is presented. Electromagnetic (EM) Simulation Software FEKO is used to obtain the Radar Cross Section (RCS) of a wind turbine for a wide range of frequencies using the different solution methods supported by the software. A comparison of simulation results, resource requirements and CPU run times for the implemented numerical methods is presented along with a brief discussion about the application and features of each method.

## 1. INTRODUCTION

The rapid growth in the deployment of wind turbines across the globe in recent years has raised concerns about their effects on existing radio communication links and radar systems. The increase in the number of wind farms, as well as their larger sizes, leads to an increase in the possibility of electromagnetic interference (EMI) with nearby radar systems, fixed radio links and broadcasting services [1–3]. Reflection, scattering and diffraction of electromagnetic signals can seriously deteriorate the performance of different communication services operating at a wide range of frequencies from fixed radio links at the higher end of the VHF band to radar systems and point to point links operating at 30 GHz and above [4].

Before the installation of a wind farm, it is vital to investigate the possible interference that may be caused to the existing radars and other communication link systems. This can be done by either carrying out a field measurement to determine the fields scattered by a wind turbine, or by predicting the interference by employing computational electromagnetic (CEM) techniques on computer software platforms. In this work, different CEM techniques offered by FEKO have been used to predict the radar cross section (RCS) of a wind turbine at 200 MHz, 300 MHz, 500 MHz and 1 GHz. A comparison of results and memory requirements has been presented to highlight the suitability of the available numerical methods for different frequencies.

## 2. CEM METHODS

FEKO is based on full wave analysis technique Method of Moments (MoM) that can be applied at any frequency range, but with the disadvantage that the computational costs scale up quickly as the electrical size of the object increases. One approach to overcome this shortcoming is the use of Multilevel Fast Multipole Method (MLFMM). This method is based on MoM, but it computes the interaction between groups of basis functions, rather than between individual basis functions as in the case of MoM. Another solution can be found in hybrid methods combining MoM with asymptotic techniques [5, 6]. In principle, a distinction is made between current-based techniques and ray-based methods. FEKO supports hybridization of MoM with Physical Optics (PO), Geometrical Optics (GO) and Uniform Theory of Diffraction (UTD). PO is a current based asymptotic method that only determines the currents on the directly illuminated parts of a structure, reducing the memory requirement and run-time. However, it has the disadvantage that fields in the shadowed regions are inaccurately calculated. GO is a ray tracing method which is generally applied to structures with dimensions larger than  $20\lambda$ . The mesh can be very coarse, thus no major mesh storage problems are faced. It is good for scattering analysis with multiple reflections. Its major disadvantage is that diffraction effects are not accounted for. UTD is another ray tracing technique used for the scattering analysis of very large structures where diffraction effects are important. However, UTD has the disadvantage that in its current FEKO implementation, it is only applicable for flat PEC surfaces and does not account for dielectrics and curved surfaces.

## 3. 3D MODELING OF THE WIND TURBINE

A wind turbine structure typically consists of a metallic supporting tower, a metallic nacelle containing the fundamental machinery and a rotor with three blades usually made up of fiber-glass materials. The wind turbine tower has traditionally been cylindrical in shape. Recently however, conical and tapered towers have become more popular owing to their lower RCS values [7]. The

turbine blades are usually composed of an outer fiberglass composite shell and an internal metallic lightning conductor. The effect of the blades on electromagnetic propagation has not been well characterized. It has been noted that at lower frequencies (VHF) the fiberglass in the blades will be transparent with only the metallic lightning conductor contributing to the reflected fields. At higher frequencies, the blades are no longer transparent and become more reflective. However, some researchers believe that the blades are highly reflective at all frequencies [8].

The computer aided design (CAD) model of a wind turbine used in this analysis was obtained from the online CAD library GrabCad. After importing the geometry into FEKO, the size of the turbine components was scaled to obtain a tower height of 60 m and blade length of 38 m. The modeled turbine geometry is shown in Figure 1. The material is assumed to be perfect conductor.

#### 4. RESULTS

Due to the memory constraints on the local system, first only the blades and the nacelle of the geometry are considered. Bistatic RCS calculations are performed by illuminating the turbine blades with a horizontally polarized plane wave parallel to the blades rotation axis (front incidence). For this simulated scenario,  $0^\circ$  represents a side view of the blade geometry,  $90^\circ$  is the direction of the approaching plane wave and also applies to the monostatic backscatter. Frequencies of 200 MHz, 300 MHz, 500 MHz and 1 GHz have been considered in the analysis in order to gain an insight into the application and usability of the different solution techniques. The simulations were run on a 3.40 GHz Intel (R) Core (TM) i7-2600K CPU (multi-core CPU with max. 4 cores per physical CPU).

Figures 2, 3, 4 and 5 show the RCS values calculated at 200 MHz, 300 MHz, 500 MHz and 1 GHz respectively. At 200 MHz, some differences can be observed between the solutions obtained by using hybrid methods of MoM with PO and GO and the full wave analysis (MLFMM) solution. Moreover MoM-PO and MoM-GO solutions do not completely agree with each other. At the frequency of 300 MHz, MoM-PO and MoM-GO show a higher degree of agreement with MLFMM. At 500 MHz, an MLFMM solution could not be obtained due to memory constraints of the local system. However, it can be noted, that at this frequency, the MoM-PO and MoM-GO solutions

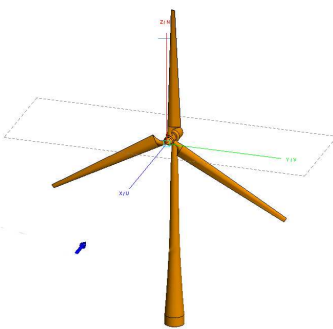


Figure 1: Wind turbine geometry.

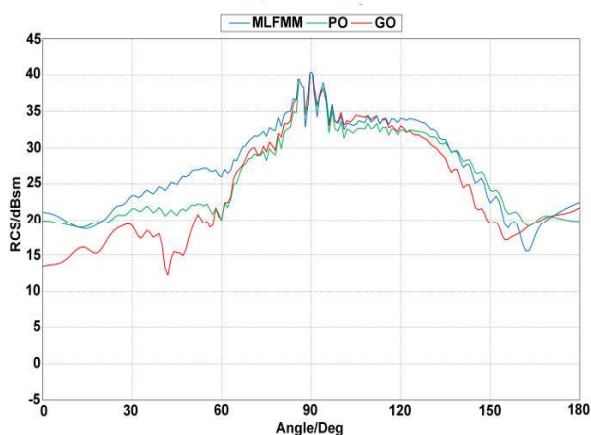


Figure 2: Bistatic RCS at 200 MHz.

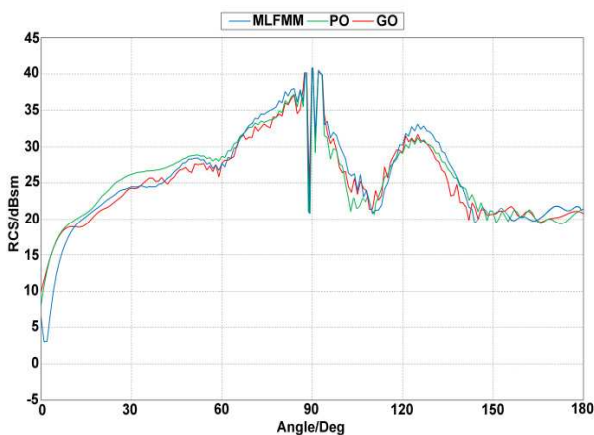


Figure 3: Bistatic RCS 300 MHz.

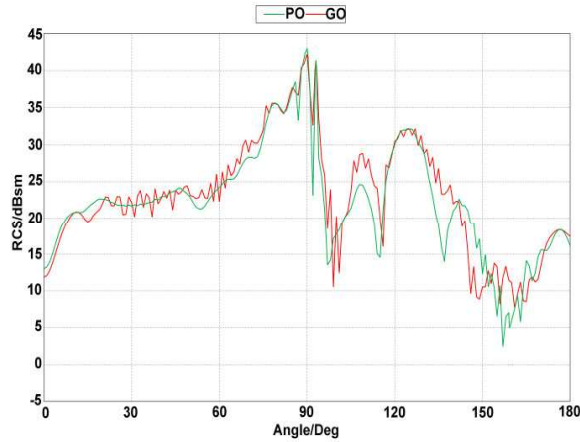


Figure 4: Bistatic RCS at 500 MHz.

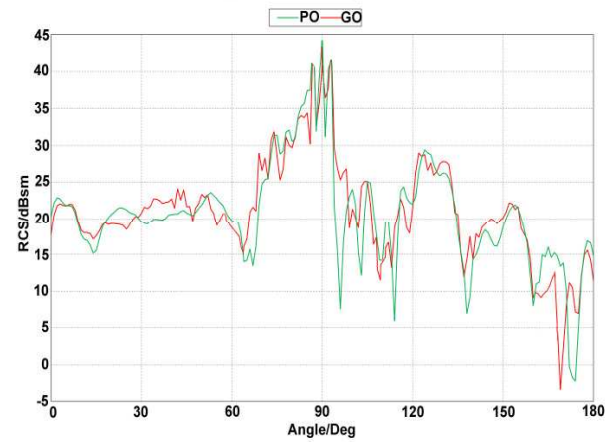


Figure 5: Bistatic RCS at 1 GHz.

Table 1: Performance comparison of different Solution methods.

Frequency	Solution Method	Memory Requirement	Run-Time (Hours)
200 MHz	MLFMM	1.557 GByte	0.447
	MoM-PO	24.904 MByte	0.002
	MoM-GO	3.510 MByte	0.005
300 MHz	MLFMM	14.700 GByte	2.680
	MoM-PO	50.384 MByte	0.005
	MoM-GO	5.600 MByte	0.012
500 MHz	MLFMM	33.70 GByte	-
	MoM-PO	134.110 MByte	0.014
	MoM-GO	12.400 MByte	0.034
1 GHz	MLFMM	56.140 GByte	-
	MoM-PO	522.460 MByte	0.060
	MoM-GO	12.260 MByte	0.035

start to converge (Fig. 4). At 1 GHz, these solutions become even more similar. This is due to the fact that all the components of the geometry at lower frequencies are not electrically large enough for the requirements of the high frequency techniques to be satisfied. As the frequency increases, the electrical size of the structure increases and the results of MoM-PO and MoM-GO start to converge.

It was observed that the MoM-UTD solutions for the wind turbine geometry used in this work, over predict the RCS (upto about 30 dBsm) in all of the above cases. A potential reason for this can be the problem of caustics and the presence of curved surfaces in the blade geometry. These results have not been included in this paper.

Table 1 lists the required memory and simulation run-times for the bistatic RCS calculation of the wind turbine blades and nacelle for each of the above mentioned methods at the mentioned frequencies. It can be seen that as the frequency increases, the memory requirement for performing a full wave analysis also increases. The higher frequency techniques require less memory resources and run the same job much faster than the full wave analysis methods. At 1 GHz, MLFMM solution requires slightly over 56 Gigabytes of memory, whereas the high frequency techniques require tens of Megabyte for the execution of the same job. By using PO, the size of the matrices to be solved is significantly reduced, since current is assumed to be zero in the shadowed region, resulting in a sparse matrix. GO does not involve the solution of any matrix further reducing the memory requirements.

Next, the entire wind turbine geometry, including the tower, the nacelle and the blades is considered. From Table 1, it can be seen that MoM-GO has the lowest memory requirements

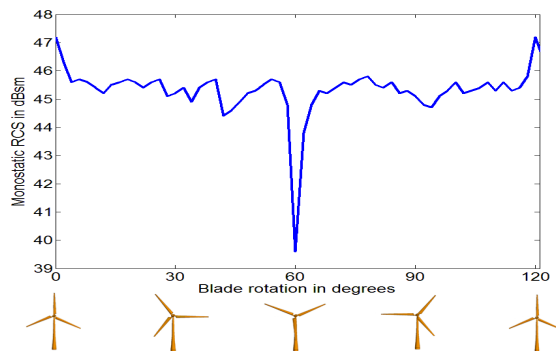


Figure 6: RCS of the wind turbine at 5 GHz for different blade orientations.

and the shortest run-time among the solution methods discussed in this paper. Therefore, this method is used to obtain the RCS of the entire wind turbine structure at 5 GHz for varying blades positions. The blade rotation angle of  $0^\circ$  represents the case where one of the blades is aligned with the tower. Assuming anti-clockwise rotation, The blade positions are changed upto an angle of  $120^\circ$  with a step size of  $2^\circ$ . The angle between the vertically polarized incident plane wave and the axis of rotation of the blades is  $0^\circ$ . Figure 6 shows the obtained monostatic RCS values. It can be observed that the RCS is almost constant, except for the instances where one of the blades is aligned with the electric field vector. The peak occurs at  $0^\circ$  when one blade is vertically positioned above the tower. Around  $60^\circ$ , the blade shadows the tower which seems to reduce the RCS value.

## 5. CONCLUSIONS

An investigation of the radar returns of a wind turbine using different numerical solution techniques supported in the software FEKO has been presented. At any given frequency, full wave analysis techniques based on MoM require more memory resources and have longer execution times, compared to hybrid methods combining MoM with high frequency asymptotic techniques. For scattering analysis of an electrically large structure at higher frequencies, the best option seems to be the use of asymptotic methods. However, the decision has to be made depending on the problem at hand. MoM hybrids with GO and PO do not account for diffraction effects. If multiple interactions involving reflections and diffractions are important, then UTD solutions can be sought by using flat plate approximations for the curved surfaces.

## REFERENCES

1. Poupart, J. M., "Wind farms impact on radar aviation interests — Final report," DTI PUB URN 03/1294, 2003.
2. Brenner, M., "Wind farms and radar," JSR-08-126, The Mitre Corporation, Jan. 2008.
3. Lemmon, J. J., J. E. Carroll, F. H. Sanders, and D. Turner, "Assessment of the effects of wind turbines on air traffic control radars," NTIA Technical Report TR-08-454, Jul. 2008.
4. De La Vega, D., C. Fernandez, O. Grande, I. Angulo, D. Guerra, Y. Wu, P. Angueira, and J. L. Ordiales, "Software tool for the analysis of potential impact of wind farms on radiocommunication services," *IEEE International Symposium on Broadband Multimedia Systems and Broadcasting*, 1–5, Jun. 2011.
5. Bouche, D. P., F. A. Molinet, and R. Mittra, "Asymptotic and hybrid techniques for electromagnetic scattering," *Proc. IEEE*, Vol. 81, No. 12, 1658–1684, Dec. 1993.
6. Knott, E. F., "A progression of high-frequency RCS prediction techniques," *Proc. IEEE*, Vol. 73, Feb. 1985.
7. Matthews, J. C. G., J. Pinto, and C. Sarno, "Stealth solutions to solve the radar-wind farm interaction problem," *Antennas and Propagation Conference, LAPC 2007*, Loughborough, Apr. 2007.
8. Sellner, T. and A. Zalay, "TV/radio interference measurements for large commercially available MW class wind turbines," *IEEE/PES Transmission and Distribution Conference and Exposition, T & D*, Apr. 2008.

# Tapered Fiber Mach-Zehnder Interferometer for Liquid Level Sensing

Hun-Pin Chang, Chai-Ming Li, Cheng-Ling Lee, and Jui-Ming Hsu

Department of Electro-Optical Engineering, National United University  
Miaoli 360, Taiwan, R.O.C.

**Abstract**— A low cost, simple, and in-line liquid level sensor based on a dual-tapered fiber Mach-Zehnder interferometer (DTFMZI) is proposed. In the study, the configuration, operation principle, experiment results and discussion for the proposed fiber-optic liquid level sensor are investigated. Experimental results show that the proposed TFMZI sensor is extremely sensitive and linear in response; the sensitivity of about 0.28 nm/mm is achieved.

## 1. INTRODUCTION

Fiber-optic liquid level sensors (FOLLSs) with many smart and hybrid structures have been proposed in recent years. These FOLLSs especially based on the in-line fiber interferometer have attracted much attention due to their compact highly sensitive and especially long distance sensing properties. Furthermore, FOLLSs are particularly suitable for using in a storage tank of chemical or industry liquor due to its anti-corrosiveness.

In general, there are two types of FOLLSs: point sensors [1,2] and continuous level sensors [3–9]. For the continuous level sensors, the interference scheme based on long period gratings (LPGs) [3], fiber Bragg gratings (FBGs) [4–7], Fabry-Pérots (FPs) [7], and Michelson interferometers [8,9] had been proposed. The sensitivities represented in the previous works are 0.15 nm/cm (0.015 nm/mm) [5], 0.06 nm/cm (0.006 nm/mm) [6], and 0.1491 nm/cm (0.00149 nm/mm) [7], respectively.

In this study, we present a low cost, simple, and in-line liquid level sensor by using a dual-tapered fiber Mach-Zehnder interferometer (DTFMZI) which can be effectively fabricated by tapering a single-mode fiber (SMF) twice with an interval of certain length. The new configuration of DTFMZI was subsequently pasted onto a slice of uniform elastic-plastic to form a sensing element of bending cantilever; a stick of polyamide adheres to the cantilever and droops into the liquid tank. The bending curvature of the sensing element varies with the liquid level rising and makes the interference spectra shifts during the liquid level rises or drops.

Experimental results show that the proposed DTFMZI-FOLLS is extremely sensitive and linear in response; a sensitivity of about 0.28 nm/mm was achieved. Comparing with the previous works, the proposed DTFMZI-FOLLS has extremely high sensitivity, easy to fabricate and has all-fiber configuration characteristics which can be further developed into a favorable fiber-optic liquid level sensor for a wide range of applications.

## 2. CONFIGURATION AND PRINCIPLES

Figure 1 indicates the experimental setup of the proposed DTFMZI-FOLLS. The sensor was pasted onto a slice of uniform elastic-plastic to form a sensing element of bending cantilever; a stick of polyamide adhered to the cantilever and drooped into the liquid tank. Light from a broadband light source (BBS) launched into the DTFMZI, and transmission spectra were directly obtained by an optical spectrum analyzer (OSA). The abrupt tapers in the DTFMZI shown as Fig. 2(a) were simply fabricated by a commercial fusion splicer. For the first and second tapers, the lengths of the tapered regions were measured as 776  $\mu\text{m}$  and 783  $\mu\text{m}$ , while the waist diameters were about 42.3  $\mu\text{m}$  and 41.5  $\mu\text{m}$ , respectively. Fig. 2(b) indicates the configuration of the DTFMZI, the interval  $L$  between two tapers was 1.0 cm. The SMF with dual-taper was embedded in a capillary tube with an internal diameter of 150  $\mu\text{m}$  and a length of 2 cm. The two ends of the tube were fixed with epoxy resin. The abrupt taper with a suddenly changed profile breaks the adiabaticity of light power to generate higher-order cladding modes. Therefore, a light beam from the first taper split into two parts, the core and cladding modes and propagated through the fiber. By the second taper the core and cladding modes are collected. A phase difference is thus introduced to bring about a periodic oscillation spectrum in the OSA due to optical path difference (OPD).

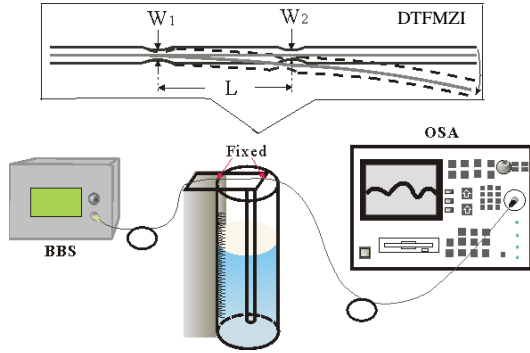


Figure 1: Experimental setup of the proposed DTFMZI-FOLLS. BBS: Broadband light source, OSA: Optical spectrum analyzer, DTFMZI: Dual-tapered fiber Mach-Zehnder interferometer.

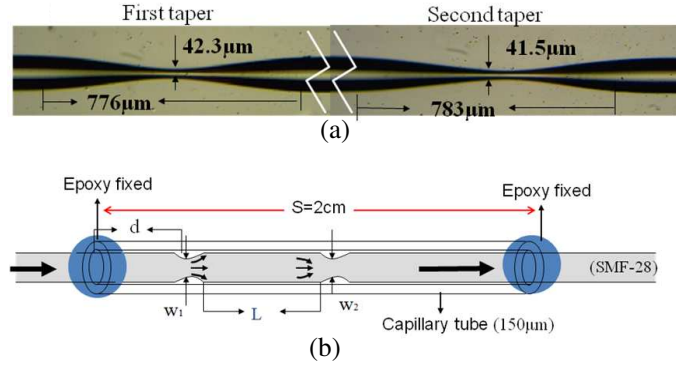


Figure 2: (a) Micrographs of the abrupt tapers made by a fusion splicer. (b) Configuration of the dual-tapered fiber Mach-Zehnder interferometer (DTFMZI)  $W_1 = 42.3 \mu\text{m}$ ,  $W_2 = 41.5 \mu\text{m}$ , and  $L = 1.0 \text{ cm}$ .

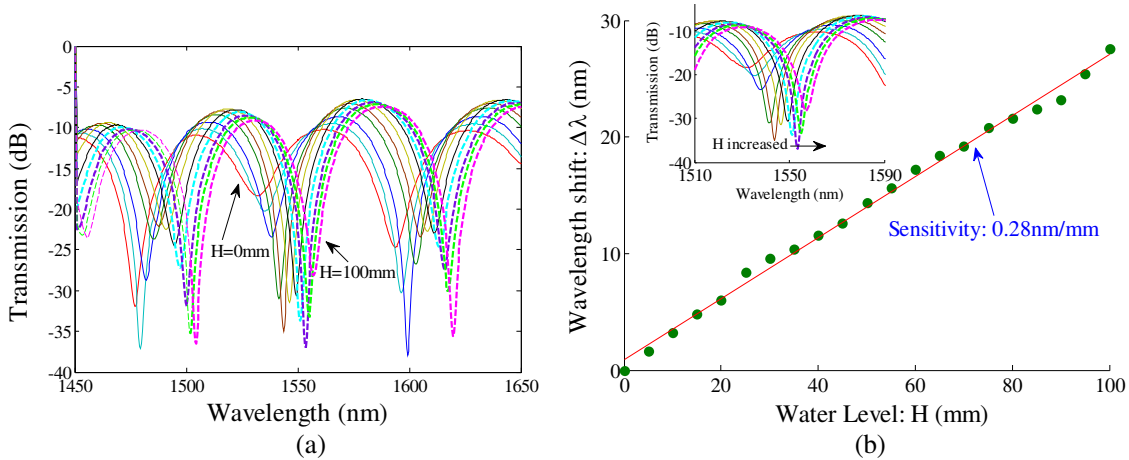


Figure 3: (a) Experimental transmission spectra of the proposed DTFMZI-FOLLS for various liquid levels ( $H$ ). (b) Sensitivity of spectral shifts in wavelengths of the DTFMZI-FOLLS which is depicted from a group of the spectral data near a wavelength of 1550 nm as indicated in the inset.

The phase difference between the core and the  $m$ th-order cladding modes after propagating through the length  $L$  of the taper interval can be easily written as:

$$\phi_m = \frac{2\pi}{\lambda} \left( n_{eff}^{co} - n_{eff}^{cl,m} \right) L = \frac{2\pi}{\lambda} \Delta n_{eff}^m L \quad (1)$$

where  $\Delta n_{eff}^m$  is the effective index difference between the core mode and the  $m$ th cladding modes.  $\lambda$  is the wavelength in vacuum. The wavelength of spectral minima  $\lambda_{min}^m$  can be deduced by substituting the condition of interference minima  $\phi_m = (2n + 1)\pi$  where  $n$  is an integer, into Equation (1):

$$\lambda_{min}^m = \frac{2}{2n + 1} \Delta n_{eff}^m L \quad (2)$$

The cantilever is most curved initially; it is driven by the buoyancy of the liquid and reduces its bending curvature during the liquid level rises. The coupling cladding modes, which dominate the interference in the DTFMZI, are determined upon the evanescent mechanism resulted from the bending taper regions. Therefore, the interference spectra will shift during the liquid level rises or drops. The quantitative data of the liquid level is then obtained from the wavelength shifts based on the above-mentioned bending interference.

### 3. EXPERIMENTAL RESULTS AND DISCUSSIONS

Figure 3(a) displays the experimental transmission spectra of the proposed DTFMZI-FOLLS for various liquid levels ( $H$ ). As shown in the figure, the interference minima shift to longer wavelengths

as the liquid level  $H$  increases. This phenomenon can be explained as follows: for lower liquid level, the DTFMZI is more curved as mentioned previously. The higher order cladding modes are prone to evanesce from the bending taper regions. The remaining lower order cladding modes couple with the core mode and dominate the interference in the proposed DTFMZI-FOLLS. Because the effective index of the lower order cladding modes is close to the core mode, thus results in a smaller  $\Delta n_{eff}^m$ . Therefore, according to Equation (2), the spectral minima locate at a shorter wavelength for a lower liquid level.

A group of the spectral data near a wavelength of 1550 nm is used to depict the sensitivity of the proposed DTFMZI-FOLLS. Fig. 3(b) indicates the fitted linear response of the sensitivity, a linear sensitivity of about 0.28 nm/mm was estimated, it is considerably larger than that of the other previous published studies mentioned in the introduction. The  $H$ -increment for the experimental measurement is 5 mm which is appeared in Fig. 3(b). For the sake of clearly exhibiting the interference spectra, the  $H$ -increment of 10 mm for each spectral line is used in Fig. 3(a).

#### 4. CONCLUSIONS

This study proposes an in-line fiber-optic liquid level sensor (FOLLS) based on a dual-tapered fiber Mach-Zehnder interferometer (DTFMZI). The sensing element with two abrupt tapers, which were easily fabricated by a fusion splicer, was setup with a bending cantilever to accomplish an all-fiber liquid level sensor. Experimental results reveal that an extremely high sensitivity of about 0.28 nm/mm and a good linear response of the sensor have been achieved. Comparing with the previous works, the advantages of the proposed fiber-optic sensor are low cost, simple and easy to fabricate, in-line, long distance sensing and extremely sensitive. The sensor has considerable potential applications, and can be further improved to enhance the sensing capabilities of multi-sensing parameters, such as refractive index and specific gravity of liquids.

#### REFERENCES

1. Ilev, I. K. and R. W. Waynant, "All-fiber-optic sensor for liquid level measurement," *Rev. Sci. Instrum.*, Vol. 70, No. 5, 2551–2554, 1999.
2. Nath, P., P. Datta, and K. C. Sarma, "All fiber-optic sensor for liquid level measurement," *Microw. Opt. Technol. Lett.*, Vol. 50, No. 7, 1982–1984, Jul. 2008.
3. Khaliq, S., S. W. James, and R. P. Tatam, "Fiber-optic liquid-level sensor using a long-period grating," *Opt. Lett.*, Vol. 26, No. 16, 1224–1226, 2001.
4. Yun, B., N. Chen, and Y. Cui, "Highly sensitive liquid-level sensor based on etched fiber Bragg grating," *IEEE Photonics Technol. Lett.*, Vol. 19, No. 21, 1747–1749, 2007.
5. Sohn, K. R. and J. H. Shim, "Liquid-level monitoring sensor systems using fiber Bragg grating embedded in cantilever," *Sensors and Actuators A: Physical*, Vol. 152, 248–251, 2009.
6. Guo, T., Q. Zhao, Q. Dou, H. Zhang, L. Xue, G. Huang, and X. Dong, "Temperature-insensitive fiber Bragg grating liquid-level sensor based on bending cantilever beam," *IEEE Photonics Technol. Lett.*, Vol. 17, No. 11, 2400–2402, 2005.
7. Lai, C. W., Y. L. Lo, J. P. Yur, and C. H. Chuang, "Application of fiber Bragg grating level sensor and Fabry-Pérot pressure sensor to simultaneous measurement of liquid level and specific gravity," *IEEE Sens. Jour.*, Vol. 12, No. 4, 827–831, 2012.
8. Yuan, L., J. Yang, Z. Liu, and J. Sun, "In-fiber integrated Michelson interferometer," *Opt. Lett.*, Vol. 31, No. 18, 2692–2394, 2006.
9. Tian, Z., S. S.-H. Yam, and H. P. Loock, "Refractive index sensor based on an abrupt taper Michelson interferometer in a single-mode fiber," *Opt. Lett.*, Vol. 33, No. 10, 1105–1107, 2008.

# Reflection and Transmission Characteristics of Lattice Grid with Lossy Clad for Optical CT

Yasumitsu Miyazaki<sup>1</sup>, Koichi Takahashi<sup>1</sup>, and Nobuo Goto<sup>2</sup>

<sup>1</sup>Department of Media Informatics, Aichi University of Technology  
50-2 Manori, Nishihasama-cho, Gamagori 443-0047, Japan

<sup>2</sup>Institute of Technology and Science, The University of Tokushima  
2-1 Minamijosanjima-cho, Tokushima 770-8506, Japan

**Abstract**— Medical image diagnosis and computer aided diagnosis are modern important medical techniques developed with computer technology. Particularly, medical image diagnosis using optical waves of lasers is very important technical tools for physiological examination of human body. Image responses of optical transmitted projection include optical scattering characteristics that disturb transmission properties through biological structures depending on optical absorption effects due to biological characteristics consisting of atomic and molecular structure. We have studied spatial filtering for optical scattering superposed on transmitted and attenuated waves to improve image diagnosis. Spatial filtering characteristics of grid structure are shown for exact image optical projection excluding scattering effects through physiological media by FDTD method. In waveguide-type grid filters with lossy clads, scattered fields from biological structures with large scattering angles have large attenuations. Transmitted and scattered fields of small scattering angles have small attenuations and can pass through the waveguide grids. We studied statistical scattering characteristics of biological objects surrounded by inhomogeneous biological media using FDTD method and showed that spatial filtering by waveguide-type grid filter with lossy clads is very effective to suppress scattered waves with large scattering angles and to obtain accurate target object image.

In this paper, reflection and transmission characteristics of waveguide-type spatial filter consisting of clad and core with relatively long length and complex refractive index of lossy clad for incident angles of the incident beam are studied by FDTD method, comparing with approximate analytical method, such as physical and geometrical optics, for optimum design of structure of spatial filter to accomplish accurate image diagnosis by optical CT. For large incident angles of the incident beam, attenuation of the amplitudes of transmitted waves become large due to the absorption by lossy clads and realization of effective spatial filter is expected. In this study, electric field distributions in waveguide-type grids are shown precisely using FDTD method. Also, field distributions are studied by approximate analytical method which gives physical interpretation for numerical results obtained by FDTD. The numerical and analytical methods can provide optimum design of lattice grid spatial filter with desired performance for accurate image diagnosis by optical CT.

## 1. INTRODUCTION

Medical image diagnosis using optical waves of lasers is very important technical tools for physiological examination of human body. Image responses of optical transmitted projection include optical scattering characteristics that disturb transmission properties through biological structures depending on optical absorption effects due to biological characteristics consisting of atomic and molecular structure [1–5]. We have studied spatial filtering by lossy grid array for optical scattering superposed on transmitted and attenuated waves to improve image diagnosis [6–9]. Spatial filtering characteristics of lossy grid structure are shown for exact image optical projection excluding scattering effects through physiological media by FDTD method. In waveguide-type grid filters with lossy clads, scattered fields from biological structures with large scattering angles have large attenuations. Transmitted and scattered fields of small scattering angles have small attenuations and can pass through the waveguide grids. We studied statistical scattering characteristics of biological objects surrounded by inhomogeneous biological media using FDTD method and showed that spatial filtering by waveguide-type grid filter with lossy clads is very effective to suppress scattered waves with large scattering angles and to obtain accurate target object image.

In this paper, reflection, transmission and filtering characteristics of waveguide-type spatial filter consisting of clad and core with relatively long length and complex refractive index of lossy clad for incident angles of the incident beam are studied by FDTD method, comparing with approximate analytical method, such as physical and geometrical optics, for optimum design of structure of

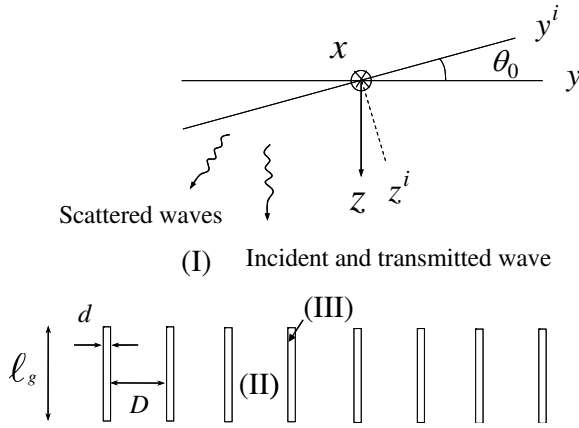
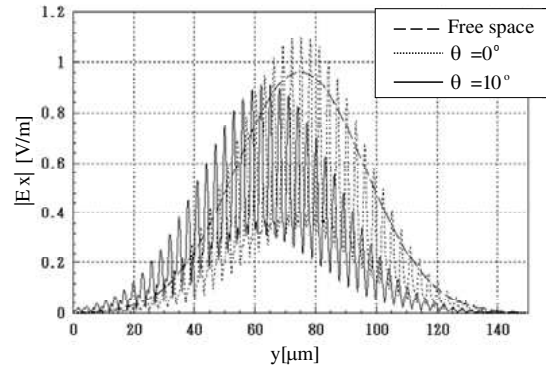


Figure 1: Lattice grid for optical CT.

Figure 2: Electric field amplitude at  $z = 100 \mu\text{m}$ ,  $\theta = 0, 10^\circ$ .

spatial filter to accomplish accurate image diagnosis by optical CT. Fig. 1 shows the FDTD analysis model for lattice grid with width of lossy clad  $d$ , width of transparent core  $D$ , length of grid  $\ell_g$  and complex refractive index  $n_g^*$ . The amplitudes of transmitted and attenuated waves in core and clad regions are evaluated. For large incident angles of the incident beam, attenuation of the amplitudes of transmitted waves become large due to the absorption by lossy clads and realization of effective spatial filter is expected. In this study, electric field distributions in waveguide-type grids are shown precisely using FDTD method. Also, field distributions are studied by approximate analytical method which gives physical interpretation for numerical results obtained by FDTD. The numerical and analytical methods can provide optimum design of lossy lattice grid spatial filter with desired performance for accurate image diagnosis by optical CT.

Figure 2 shows the amplitudes of transmitted electric field at  $z = 100 \mu\text{m}$ , when Gaussian beam with beam spot size  $30 \mu\text{m}$  is incident to lossy grid with  $d = 0.5 \mu\text{m}$ ,  $D = 2.5 \mu\text{m}$ ,  $\ell_g = 10 \mu\text{m}$  and  $n_g^* = 2 - j0.5$ . When the incident angle  $\theta$  corresponding to scattering angle in optical CT is larger than  $\theta = 10^\circ$ , the amplitude of transmitted wave is attenuated due to the absorption of lossy clads of lattice grid.

## 2. REFLECTION AND TRANSMISSION CHARACTERISTICS OF GRID WALL

For fundamental study on reflection and transmission of optical wave by lossy grid, reflection and transmission coefficients of the incident plane wave on the interfaces of core and clad are evaluated. In Fig. 1, we define region I of free space, region II of core of grid with refractive index  $n_1$  and region III of lossy clad with complex refractive index  $n_2 = n_{r2} - jn_{i2}$ . Wave numbers are  $k_1 = k_0 n_1$  in regions I and II, and  $k_2 = k_0 n_2$  in region III, where  $k_0 = 2\pi/\lambda$  is wave number and  $\lambda$  is wavelength in free space.

Fresnel reflection and transmission coefficients  $R$  and  $T$  of TE waves are, when the plane wave incident from region II to region III

$$R = \frac{\cos \theta_i - \sqrt{n^2 - \sin^2 \theta_i}}{\cos \theta_i + \sqrt{n^2 - \sin^2 \theta_i}}, \quad T = \frac{2 \cos \theta_i}{\cos \theta_i + \sqrt{n^2 - \sin^2 \theta_i}} \quad (1)$$

where  $n = \frac{n_t}{n_i}$ ,  $n_i = n_1$ ,  $n_t = n_2$ . In case the plane wave incident from region III to region II,  $n = \frac{n_t}{n_i}$ ,  $n_i = n_2$ ,  $n_t = n_1$ ,  $|n_2| > |n_1|$  and for incident angles  $\theta_i > \theta_c$ , incident waves are reflected as total reflection, where critical angle  $\theta_c$  is

$$|n| = \left| \frac{n_1}{n_2} \right| = \sin \theta_c < 1 \quad (2)$$

Figs. 4, 5 and Fig. 6 show reflection and transmission coefficients for incident angle  $\theta'_i = \frac{\pi}{2} - \theta_i$  when  $n_1 = 1$  and  $n_2 = 2 - j0.05, 1.5 - j0.05$ .

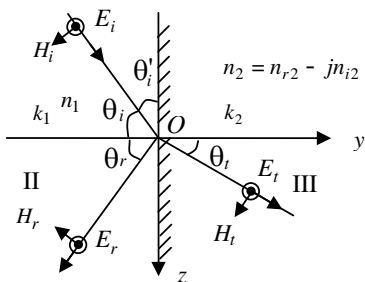


Figure 3: Reflection and transmission of plane wave in case of TE incidence.

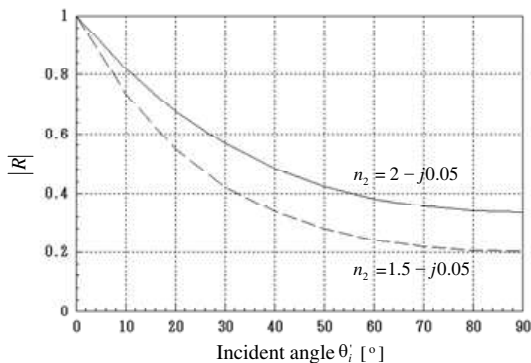


Figure 4: Reflection coefficient when the wave incident from region II to region III.

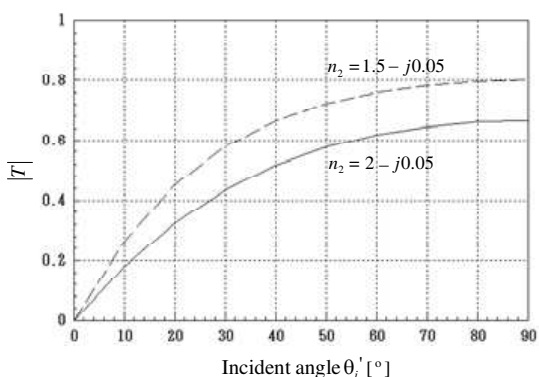


Figure 5: Transmission coefficient when the wave incident from region II to region III.

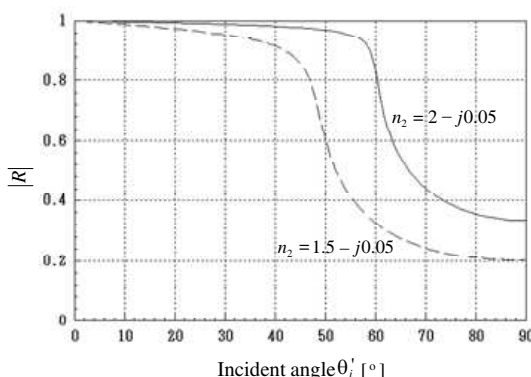


Figure 6: Reflection coefficient when the wave incident from region III to region II.

### 3. REFLECTION AND TRANSMISSION CHARACTERISTICS OF LATTICE GRID BY KIRCHHOFF-HUYGENS EQUATION

Far electromagnetic field can be approximately studied by Kirchhoff-Huygens equation. We consider two-dimensional problem of incident  $x$ -polarized plane wave in  $yz$  plane. We define A and B for the boundary between regions I and II, III.

Using Green's function in two-dimensional free space

$$G(\mathbf{r}, \mathbf{r}') = -\frac{j}{4} H_0^{(2)}(k|\mathbf{r} - \mathbf{r}'|) = -\frac{j}{4} H_0^{(2)}(k\rho) \tag{3}$$

where,  $\rho = |\mathbf{r} - \mathbf{r}'| = \sqrt{(y - y')^2 + (z - z')^2}$  for the incident plane wave with propagation angle  $\theta_0$ , far field is

$$E_x(y, z) = \sqrt{\frac{k}{8\pi}} e^{j\frac{\pi}{4}} \int_S (\cos\theta_0 + \cos\theta_\rho) \frac{e^{-jk\rho}}{\sqrt{\rho}} E_x^{(0)}(y') dy' \tag{4}$$

where,  $\cos\theta_\rho = \frac{z-z'}{\rho}$  and  $E_x^{(0)}(y')$  is the electric field on the surface A and B given by incident wave. In case of  $\cos\theta_0 \approx 1$  and  $\cos\theta_\rho \approx 1$ , Eq. (4) is

$$E_x(y, z) = \sqrt{\frac{k}{2\pi}} e^{j\frac{\pi}{4}} \int_S \frac{e^{-jk\rho}}{\sqrt{\rho}} E_x^{(0)}(y') dy' \tag{5}$$

Reflected and scattered fields in region I are obtained by  $E_x^{(0)} = RE_x^{(inc)}$  on surface B using  $k = k_0n_1$  and reflection coefficient of grid wall  $R$ . Electric field in region II is obtained by  $E_x^{(0)} = E_x^{(inc)}$  using  $k = k_0n_1$  as radiated field from source field on A. Electric field in region III is obtained by  $E_x^{(0)} = TE_x^{(inc)}$  on B using  $k = k_0n_2$  and transmission coefficient of grid wall  $T$ .

Using reflection and transmission coefficients  $R_1, T_1$  and  $R_2, T_2$  on interfaces at media 1 and 2 for incident waves from media 1 and 2, multiple reflections and transmissions by geometrical optics for plane waves  $e^{-jk_{wz}z \mp jk_{wy}y}$ ,  $w = 1, 2$ , with finite width amplitude  $u(D')$  and  $u(d')$ , where  $D' = \frac{D}{\cos \theta'_i}$ ,  $d' = \frac{d}{\cos \theta'_t}$  are shown as

$$E_x^{(w)} = u(D') \sum_{\substack{n_1, n_2 \\ u_1, u_2}} \dots \sum_{\substack{m_1, m_2 \\ v_1, v_2}} R_1^{n_1} T_1^{n_2} R_2^{m_1} T_2^{m_2} P_{(1)}^{(+u_1)} P_{(1)}^{(-u_2)} P_{(2)}^{(+v_1)} P_{(2)}^{(-v_2)} \quad (6)$$

Here, propagation factors for forward and backward plane waves in media 1 and 2 are for media  $w = 1, 2$

$$P_{(w)}^{(\pm)} = e^{-jk_{wz}z \mp jk_{wy}y}, \quad k_1 \cos \theta'_i = k_2 \cos \theta'_t, \quad k_{1z} = k_1 \cos \theta'_i, \quad k_{1y} = k_1 \sin \theta'_i$$

$$y_{\ell 1} = D - y_s, \quad z_{\ell 1} = \frac{D}{\tan \theta'_i} - z_s, \quad y_{\ell 2} = d - y_s, \quad z_{\ell 2} = \frac{d}{\tan \theta'_t} - z_s$$

$y_s$  and  $z_s$  are zero and finite section values determined by output characteristics, as  $0 \leq y_s \leq D$  or  $d$  and  $0 \leq z_s \leq \frac{D}{\tan \theta'_i}$  or  $\frac{d}{\tan \theta'_t}$ . Reflection and transmission coefficients  $R_1, T_1$  are for interfaces from  $II_{(w)}^{(+)}$  to  $II_{(w)}^{(-)}$  and  $III_{(w)}^{(+)}$ , and from  $II_{(w)}^{(-)}$  to  $II_{(w)}^{(+)}$  and  $III_{(w-1)}^{(-)}$  in regions  $(w)$  and  $(w-1)$ .  $R_2$  and  $T_2$  are for interfaces from  $III_{(w)}^{(+)}$  to  $III_{(w)}^{(-)}$  and  $II_{(w+1)}^{(+)}$ , and from  $III_{(w)}^{(-)}$  to  $III_{(w)}^{(+)}$  and  $II_{(w)}^{(-)}$  in region  $(w)$  and  $(w+1)$ . Propagation factors are concerned with transit connections between  $II_{(w)}^{(\pm)}$  and  $III_{(w)}^{(\pm)}$ .

#### 4. FDTD ANALYSIS OF LATTICE GRID CHARACTERISTICS

Filtering characteristics of optical wave by lattice grid are analysed by FDTD method. Fig. 7 shows the analysis model for lattice grid. Incident wave is assumed to be generated by equivalent current at  $z = z_0$  ( $j = 1$ ),

$$J_x^n(i, 1) = J_0 \left\{ \frac{1}{1 + e^{-u(i\Delta s \cos \theta_0 - y_1)}} + \frac{1}{1 + e^{u(i\Delta s \cos \theta_0 - y_2)}} - 1 \right\}$$

$$\left\{ \frac{1}{1 + e^{-w(n\Delta t - t_1)}} + \frac{1}{1 + e^{w(n\Delta t - t_2)}} - 1 \right\} \sin \{2\pi (fn\Delta t - (i\Delta s - y_0) \sin \theta_0 / \lambda_0)\} \quad (7)$$

where  $\theta_0$  is the incident angle. For grid structure, width of lossy clad  $d = 1 \mu\text{m}$  with complex refractive index  $n_g^* = 2 - j0.05$ , core width  $D = 20 \mu\text{m}$ , length  $\ell_g = 40 \mu\text{m}$  are considered. Using the model shown in Fig. 7, reflected and transmitted electric field amplitude in and out of grid space for  $\theta_0 = 0, 10^\circ$  at  $z = 0-50 \mu\text{m}$  are shown in Figs. 8–10. Comparison of results by FDTD

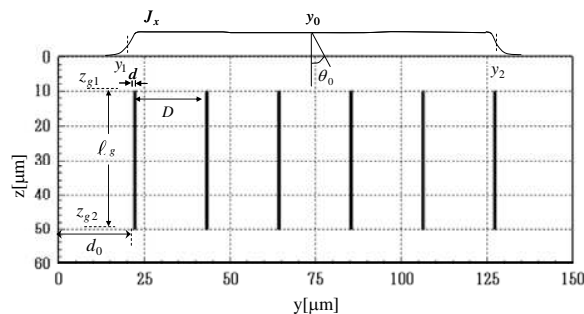


Figure 7: FDTD analysis model for lattice grid  $n_g^* = 2.0 - j0.05$ ,  $d = 1 \mu\text{m}$ ,  $D = 20 \mu\text{m}$ ,  $\ell_g = 40 \mu\text{m}$ ,  $d_0 = 22 \mu\text{m}$ ,  $z_{g1} = 10 \mu\text{m}$ ,  $z_{g2} = 50 \mu\text{m}$ .

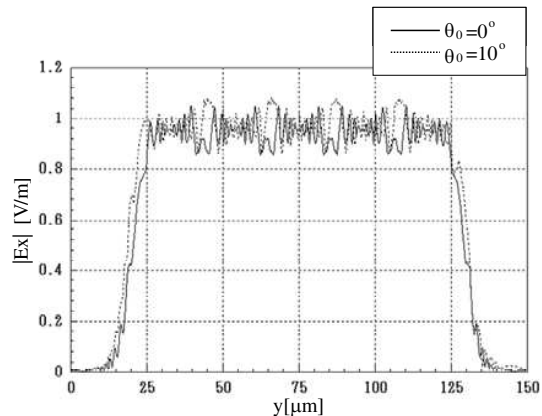


Figure 8: Transmitted electric field amplitude in region I at  $z = 0 \mu\text{m}$  by FDTD analysis.

and approximate analytical theory is shown in Figs. 11–13. As shown in Fig. 8, the electric field amplitude in region I is complicated distribution when  $\theta_0 = 0, 10^\circ$ , due to the interference in the incident, reflected and diffracted waves. Fig. 9 shows attenuated amplitude fluctuation after long propagation distance  $z$ . As shown in Fig. 10, electric field in region III is strongly attenuated due to the absorption of lossy clad. Figs. 11 and 12 of transmitted field show relatively good agreement among FDTD results and approximate analytical results using Kirchhoff — Huygens equation, in

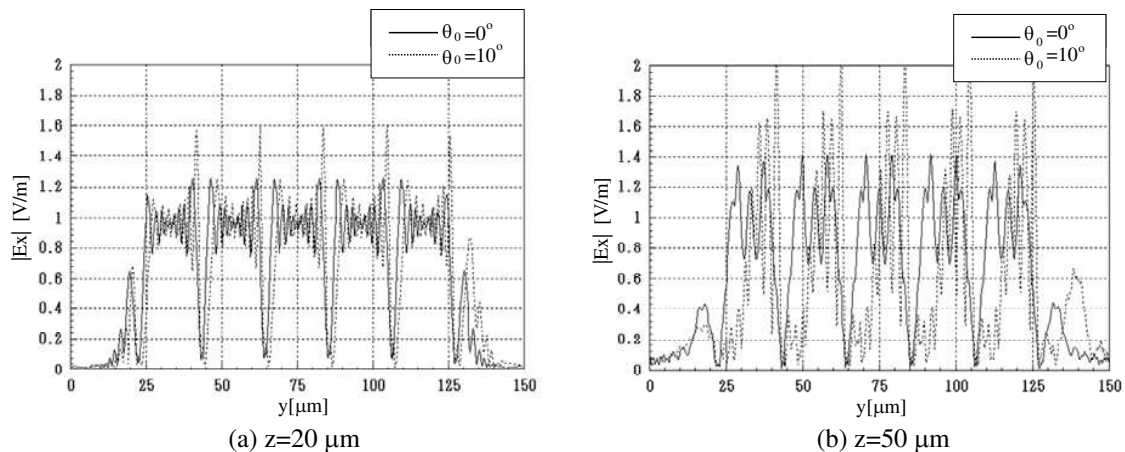


Figure 9: Transmitted electric field amplitude by FDTD analysis.

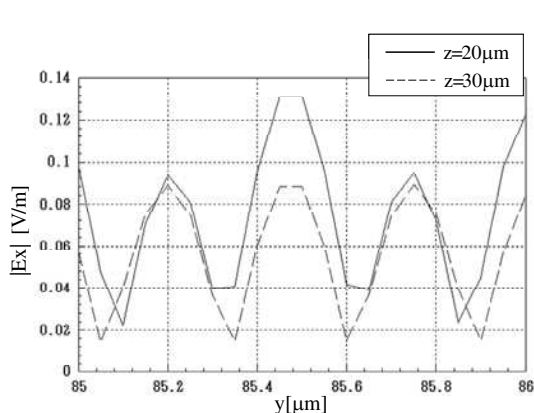


Figure 10: Attenuated electric field amplitude in region III by FDTD analysis.

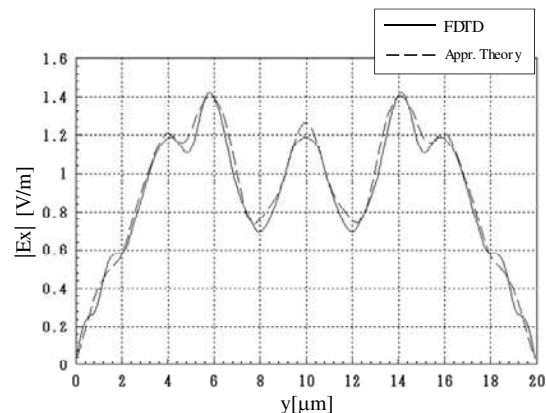


Figure 11: Comparison of transmitted electric field at  $z = 50 \mu\text{m}$  in region II,  $\theta_0 = 0^\circ$ .

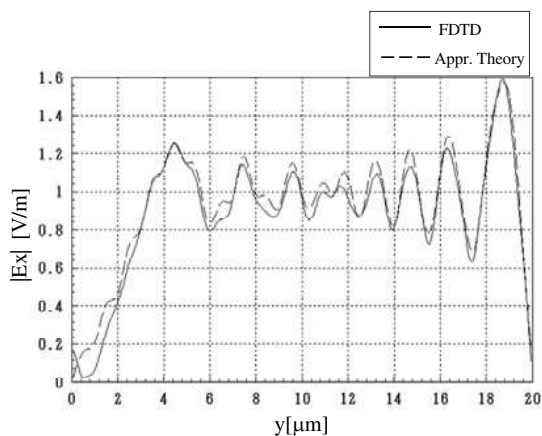


Figure 12: Comparison of transmitted electric field at  $z = 20 \mu\text{m}$  in region II,  $\theta_0 = 10^\circ$ .

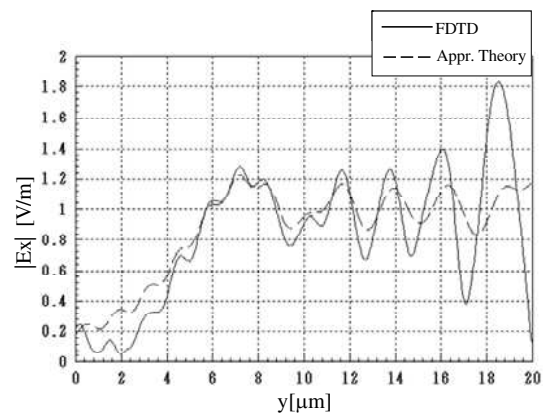


Figure 13: Comparison of transmitted electric field at  $z = 30 \mu\text{m}$  in region II,  $\theta_0 = 10^\circ$ .

case reflection from grid wall is very weak. When there are scattering objects and  $\theta_0 = 0^\circ$ , scattered waves with scattering angle more than  $30^\circ$  are filtered by lossy grid with grid distance  $20\ \mu\text{m}$  and length  $40\ \mu\text{m}$ .

## 5. CONCLUSION

In this paper, reflection and transmission characteristics of waveguide-type spatial filter consisting of clad and core with relatively long length are studied by FDTD method, comparing with approximate analytical method based on Kirchhoff-Huygens equation. For large incident angles of the incident beam, attenuation of the amplitudes of transmitted waves become large due to the absorption by lossy clads and realization of effective spatial filter is expected.

## REFERENCES

1. Miyazaki, Y., "Light scattering of laser beams by random micro-inhomogeneities in glasses and polymers," *Jpn. Jour. Appl. Phys.*, Vol. 13, 1238–1248, 1974.
2. Miyazaki, Y., "Spatial filtering of optical scattered waves in bio-medical media by inhomogeneous waveguide grids for optical CT," *Proc. of APMC 2007*, 527–530, Bangkok, 2007.
3. Miyazaki, Y. and K. Kouno, "FDTD analysis of spatial filtering of scattered waves for optical CT of medical diagnosis," *IEE J. Trans. FM*, Vol. 129, No. 10, 693–698, 2009.
4. Schmitt, J. M., "Optical coherence tomography (OCT): A review," *IEEE Selected Topics in QE*, Vol. 5, No. 4, 1205–1215, 1999.
5. Cheong, W. F., S. A. Prahl, and A. J. Welch, "A review of the optical properties of biological tissues," *IEEE Jour. QE*, Vol. 26, No. 12, 2166–2185, 1990.
6. Miyazaki, Y., "Partially coherent optical waves in random gradient fibers," *Optical and Quantum Electronics*, Vol. 9, 153–165, 1977.
7. Miyazaki, Y., "Electromagnetic characteristics of grid structures for scattering fields of nanometer electromagnetic waves and X-rays," *PIERS Proceedings*, 543–547, Tokyo, Japan, Aug. 2–5, 2006.
8. Miyazaki, Y. and K. Takahashi, "Computer simulation of X-ray scattering characteristics for medical image diagnosis," *Trans. IEE Japan*, Vol. 126-C, No. 12, 1431–1440, 2006.
9. Takahashi, K., Y. Miyazaki, and N. Goto, "FDTD parallel computational analysis of grid-type scattering filter characteristics for medical X-ray image diagnosis," *IEE J. Trans. EIS*, Vol. 127, No. 12, 1973–1981, 2007.

# Reconstruction of Dielectric Objects by Solving Volume Integral Equations with Tetrahedral Discretization

G. C. Wan<sup>1,2</sup>, Q. F. Li<sup>1,2</sup>, K. Yang<sup>1,2</sup>, and M. S. Tong<sup>1,2</sup>

<sup>1</sup>Department of Electronic Science and Technology, Tongji University  
4800 Cao'an Road, Shanghai 201804, China

<sup>2</sup>State Key Laboratory of Millimeter Waves, Nanjing 210096, China

**Abstract**— In the integral equation approach for reconstructing unknown dielectric objects, the volume integral equations (VIEs) should be solved because the imaging domain with both true unknown objects and part of background is inhomogeneous. When solving the forward scattering integral equation (FSIE), the Nyström method with tetrahedral discretization is used since the traditional method of moments (MoM) with the Schaubert-Wilton-Glisson (SWG) basis function may not be convenient due to the inhomogeneity of the imaging domain. The benefits of the Nyström method include the simple implementation without using any basis and testing functions and lower requirement on geometrical discretization, so it could be more suitable for inhomogeneous problems. When solving the inverse scattering integral equation (ISIE), the Gauss-Newton minimization approach (GNMA) with a multiplicative regularization method (MRM) is employed. The numerical example for reconstructing two contacting identical dielectric spheres is presented to illustrate the inversion approach.

## 1. INTRODUCTION

In the integral equation approach for reconstructing dielectric objects through the Born iterative method (BIM) or distorted Born iterative method (DBIM) [1], the volume integral equations (VIEs) are solved because the imaging domain including both real unknown objects and part of background is inhomogeneous. There are forward scattering integral equation (FSIE) and inverse scattering integral equation (ISIE) in the reconstruction and we need to alternatively solve them in the context of BIM or DBIM. The FSIE is used to calculate the total electric field in the imaging domain by assuming that the material property of the imaging domain is known, while the ISIE is used to solve the material property of the imaging domain by assuming that the total electric field is known.

The FSIE is mainly solved by the conventional method of moments (MoM) though other schemes can also be used [2]. However, the MoM may not be convenient for solving inverse scattering problems because the imaging domain is inhomogeneous and the Schaubert-Wilton-Glisson (SWG) basis function [3] requires conforming meshes. In this work, we employ the Nyström method with tetrahedral discretization to replace the MoM for solving the FSIE. The advantages of this method include the fast preprocessing, lower requirement on mesh quality, and removal of basis and testing functions [4]. On the other hand, the ISIE is insolvable by direct inversion because the matrix equation is inherently ill-posed due to the limited data diversity of measurement in general. One usually transforms the inversion of model parameters from measured data into an optimization problem and it can be solved by the Gauss-Newton minimization approach (GNMA) with a regularization scheme [5]. The determination of regularization parameter is a key in the regularization and we use the multiplicative regularization method (MRM) in this work [6]. The MRM was proposed for gradient-type algorithms and was adapted by Habashy and Abubakar for Newton-type algorithms in the inversion by the finite difference time domain (FDTD) approach [5], but we use it for integral equation approach by modification here. The method can adaptively vary the regularization parameter as the iteration proceeds and a large number of numerical experiments are unnecessary in the inversion. A numerical example for reconstructing two contacting identical dielectric objects is presented to illustrate the approach and good result can be observed.

## 2. INTEGRAL EQUATIONS

In the integral equation approach, reconstructing an unknown dielectric object is to determine its profile and material property within an imaging domain which is chosen in advance by guessing. The imaging domain is usually a cubic box or block and should be as large as possible at the beginning so that the unknown object can be fully enclosed. The reconstruction begins from solving the ISIE,

which is a VIE given by [4]

$$\mathbf{E}^{sca}(\mathbf{r}) = \int_V \bar{\mathbf{G}}(\mathbf{r}, \mathbf{r}'; k_b) \cdot \Delta k(\mathbf{r}') \mathbf{E}(\mathbf{r}') dV', \quad \mathbf{r} \in S \quad (1)$$

where  $\mathbf{E}^{sca}(\mathbf{r})$  represents the scattered electric field at an observation point  $\mathbf{r}$  on an observation surface  $S$ , which is obtained by measurement, and  $\mathbf{E}(\mathbf{r}')$  is the total electric field on a source point  $\mathbf{r}'$  inside the imaging domain  $V$ . Also,

$$\bar{\mathbf{G}}(\mathbf{r}, \mathbf{r}'; k_b) = \left( \bar{\mathbf{I}} + \frac{\nabla \nabla}{k_b^2} \right) g(\mathbf{r}, \mathbf{r}'; k_b) \quad (2)$$

is the dyadic Green's function in which  $g(\mathbf{r}, \mathbf{r}'; k_b) = e^{ik_b R}/(4\pi R)$  with  $R = |\mathbf{r} - \mathbf{r}'|$  is the 3D scalar Green's function. In addition,  $\Delta k(\mathbf{r}') = [k^2(\mathbf{r}') - k_b^2] = k_b^2[\varepsilon_r(\mathbf{r}') - 1]$  where  $\varepsilon_r(\mathbf{r}')$  is the relative permittivity inside the imaging domain, and  $k(\mathbf{r}')$  and  $k_b$  are the wavenumbers related to the materials of the imaging domain and background, respectively. Here  $S$  is the chosen surface at which the point sources (transmitters) and observation or measurement points (receivers) are located and it should enclose the imaging domain. In numerical simulations, the measured scattered field is replaced with the numerical solution of scattering by a known object which is assumed to be unknown in the reconstruction. The material property in the imaging domain is characterized by the wavenumber  $k(\mathbf{r}')$  which is only related to its permittivity distribution if the unknown object is assumed to be dielectric or nonmagnetic. In the ISIE, the total electric field is unknown and is replaced with the incident field in the first iteration, and this is known as the Born approximation [1]. When the material property  $k(\mathbf{r}')$  of the imaging domain is obtained after the first iteration, a new total electric field is obtained by solving the FSIE, i.e.,

$$\mathbf{E}(\mathbf{r}) = \mathbf{E}^{inc}(\mathbf{r}) + \int_V \bar{\mathbf{G}}(\mathbf{r}, \mathbf{r}'; k_b) \cdot \Delta k(\mathbf{r}') \mathbf{E}(\mathbf{r}') dV', \quad \mathbf{r} \in V \quad (3)$$

where  $\mathbf{E}^{inc}(\mathbf{r})$  is the incident electric field from a transmitter. The above ISIE and FSIE are alternatively solved in the context of the BIM or its variations until the solution of  $k(\mathbf{r}')$  converges. Specifically, the iteration scheme of reconstruction is as follows: (a) Solving the ISIE for  $k(\mathbf{r}')$  by assuming that the total electric field is the incident field; (b) Substituting the obtained  $k(\mathbf{r}')$  to the FSIE and solving the FSIE for the total electric field; (c) Using the obtained total electric field to update the ISIE and solving the ISIE for a new  $k(\mathbf{r}')$ ; (d) Using the new  $k(\mathbf{r}')$  to update the FSIE and solving the FSIE for a new total electric field. This process continues until  $k(\mathbf{r}')$  converges. The final solution of  $k(\mathbf{r}')$  in the imaging domain, if convergent, should reflect the real distribution of permittivity in the domain and the profile of unknown object can be distinguished from the background in the imaging domain. If the imaging domain does not fully enclose the unknown object, then the above iteration process cannot be convergent and reguessing the imaging domain is necessary.

### 3. NYSTRÖM METHOD SOLUTION FOR FSIE

Traditionally, the FSIE in Eq. (3) is solved with the MoM, but the solution strongly relies on the well-designed basis and testing functions. For example, the divergence-conforming SWG basis function is used in most applications while the curl-conforming basis function as shown in [2] is employed sometimes. These basis functions are usually defined in tetrahedral element pairs and they have a higher requirement on geometrical discretization. Also, in the MoM with the SWG basis function, there exist surface charges on the common faces of tetrahedral element pairs when the object is inhomogeneous and it is very inconvenient to account for their contribution. In the contrast, there is not a surface charge problem in the Nyström Method because it works on a single element instead of an element pair. The Nyström Method is mainly used for solving surface integral equations (SIEs) and has never been employed to solve VIEs in inverse problems. Consider a volume integration in VIEs under a quadrature rule

$$\int_{\Delta V} f(\mathbf{r}') dV' = \sum_{j=1}^P w_j f(\mathbf{r}'_j) \quad (4)$$

where  $f(\mathbf{r}')$  is a general smooth function,  $P$  is the number of quadrature points and  $w_j$  is the  $j$ th weight over a volume element  $\Delta V$ . The quadrature rule can be directly applied in the discretized VIEs when the integral kernels are regular. For a typical 3D VIE

$$\int_V F(\mathbf{r}, \mathbf{r}') u(\mathbf{r}') dV' = -\phi(\mathbf{r}), \quad \mathbf{r} \in V \quad (5)$$

where  $F(\mathbf{r}, \mathbf{r}')$  is the integral kernel related to the scalar Green's function in wave problems,  $u(\mathbf{r}')$  is the unknown function to be solved, and  $\phi(\mathbf{r})$  represents an excitation or incident wave in wave scattering problems, we can discretize the integral domain into tetrahedral elements and apply a collocation procedure by choosing quadrature points as observation points to yield the following matrix equation

$$\sum_{i=1}^N \sum_{j=1}^{P_i} w_{ij} F(\mathbf{r}_{mn}, \mathbf{r}'_{ij}) u(\mathbf{r}'_{ij}) = -\phi(\mathbf{r}_{mn}) \quad (6)$$

where  $P_i$  is the number of quadrature points in the  $i$ th element,  $w_{ij}$  represents the weight of the quadrature rule on the  $j$ th point of the  $i$ th element,  $m = 1, 2, \dots, N$ ,  $n = 1, 2, \dots, P_m$ , and  $N$  is the total number of elements. However, the above transformation cannot be implemented when the integral kernels are singular and a local correction scheme is needed. We have developed an efficient local correction scheme for tetrahedral elements in our previous work [7] and it can be used here.

#### 4. GNMA FOR SOLVING ISIE

When the ISIE is transformed into a matrix equation by expanding the unknown wavenumber or permittivity distribution and matching the scattered field with the measured data, the matrix equation in the form  $\bar{\mathbf{Z}} \cdot \mathbf{x} = \mathbf{b}$  is insolvable directly because it is very ill-posed and a regularization procedure is usually needed. In the conventional regularization scheme of BIM or DBIM, one minimizes the following cost functional

$$C(\mathbf{x}) = \|\bar{\mathbf{Z}} \cdot \mathbf{x} - \mathbf{b}\|^2 + \gamma \|\bar{\mathbf{W}} \cdot \mathbf{x}\|^2 \quad (7)$$

where  $\gamma$  is the regularization factor and  $\bar{\mathbf{W}}$  is the regularization matrix. The minimization of the function leads to

$$[\bar{\mathbf{Z}}^* \cdot \bar{\mathbf{Z}} + \gamma \bar{\mathbf{W}}^* \cdot \bar{\mathbf{W}}] \cdot \mathbf{x} = \bar{\mathbf{Z}}^* \cdot \mathbf{b} \quad (8)$$

or

$$\mathbf{x} = [\bar{\mathbf{Z}}^* \cdot \bar{\mathbf{Z}} + \gamma \bar{\mathbf{W}}^* \cdot \bar{\mathbf{W}}]^{-1} \cdot \bar{\mathbf{Z}}^* \cdot \mathbf{b} \quad (9)$$

where the asterisk represents the conjugate transpose. However, the regularization scheme strongly relies on the selection of regularization factor and there is no universal method to surely choose the factor except performing a large number of numerical experiments. In this work, we use the MRM in the GNMA which was employed by Habashy and Abubakar for FDTD-based inversion [5] and it is more robust than the conventional regularization scheme.

In the GNMA, the regularization parameter is defined as the inverse of Lagrange multiplier, and is used to adjust the relative importance of the two terms in the cost functional. One effective way to choose the regularization parameter or equivalently, choose the Lagrange multiplier is to adaptively vary it as the iteration proceeds. This automatic scheme treats the regularization as a multiplicative factor in the cost functional and therefore the regularization parameter is set to be proportional to the original or non-regularized cost functional. The MRM has been shown very effective for both gradient-type and Newton-type algorithms in FDTD-based approaches [5] and we adapt it for the integral equation approach. It is found that the above adaptive choice for the regularization parameter is also very effective for the GNMA in the integral equation approach.

#### 5. NUMERICAL EXAMPLE

To demonstrate the proposed inversion approach, we consider the reconstruction of typical 3D dielectric objects. The measured data for scattered fields are calculated based on the experimental setup of Institute Fresnel [8]. Specifically, the spherical measured surface has a radius  $r = 1.796$  m for both transmitting and receiving antennas and the imaging domain is chosen as a  $100 \text{ mm} \times 100 \text{ mm} \times 100 \text{ mm}$  cubic box. On the measured surface, the source locations are characterized by

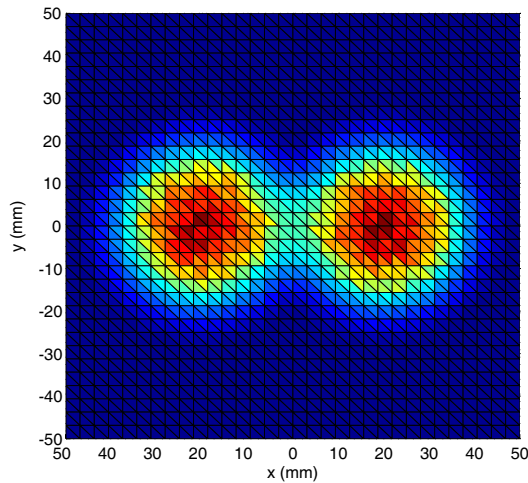


Figure 1: Image of two contacting identical dielectric spheres with a radius  $a = 20$  mm and a relative permittivity  $\epsilon_r = 3.0$  (2D view at the central cut on the  $xy$  plane). A cubic image domain  $100 \text{ mm} \times 100 \text{ mm} \times 100 \text{ mm}$  is chosen and the two spheres are located at  $(-20 \text{ mm}, 0, 0)$  and  $(20 \text{ mm}, 0, 0)$ , respectively.

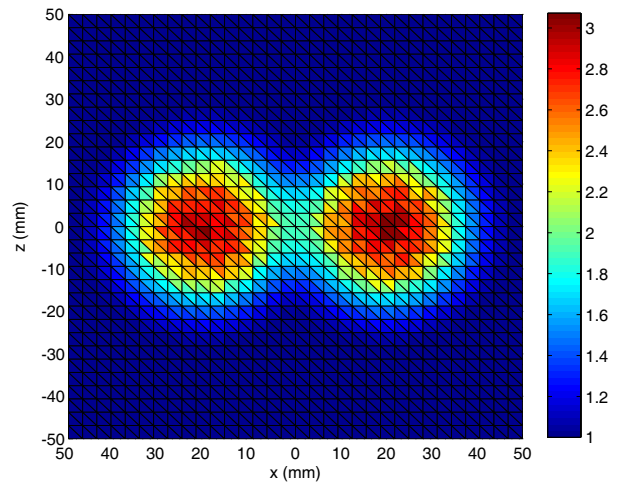


Figure 2: Image of two contacting identical dielectric spheres with a radius  $a = 20$  mm and a relative permittivity  $\epsilon_r = 3.0$  (2D view at the central cut on the  $xz$  plane). A cubic image domain  $100 \text{ mm} \times 100 \text{ mm} \times 100 \text{ mm}$  is chosen and the two spheres are located at  $(-20 \text{ mm}, 0, 0)$  and  $(20 \text{ mm}, 0, 0)$ , respectively.

$\phi^s$  ranging from  $30^\circ$  to  $150^\circ$  with a step  $15^\circ$  and  $\theta^s$  ranging from  $20^\circ$  to  $340^\circ$  with a step  $40^\circ$ , while the receiver locations are defined by  $\theta^s$  ranging from  $0^\circ$  to  $350^\circ$  with a step  $10^\circ$  and  $\phi^s = 90^\circ$ . We discretize the imaging domain into 25362 tetrahedral elements in the reconstruction. Figure 1 and Figure 2 show the reconstructed images, which are observed at the central cut on the  $xy$  and  $xz$  plane, respectively, for two contacting identical dielectric spheres with a radius  $a = 20$  mm and a relative permittivity  $\epsilon_r = 3.0$  for each. This object corresponds to Target I of Institut Fresnel experiments [8]. Note that the 2D images in the figures are sketched by projecting the permittivity values at the centroids of tetrahedrons to the nearest triangles on the cutting planes. This is because the tetrahedrons are automatically generated by commercial software without regularity and 3D sliced images cannot be plotted for such discretizations.

## 6. CONCLUSION

In this work, we employ the Nyström method with a tetrahedral discretization to solve the FSIE of inverse problems which is usually solved with the MoM. Although solving the FSIE is not difficult, the MoM implementation could be inconvenient due to the involvement of inhomogeneity in the imaging domain and unknown profile of object. It is found that the Nyström method is more versatile because it is flexible in geometrical discretization and simple in implementation without resorting to basis and testing functions. For solving the ISIE, we employ the GNMA with the MRM to adaptively vary the regularization parameter as the iteration proceeds. The MRM allows a faster convergence for the inversion of model parameters and easy selection of the regularization parameter. A numerical example for reconstructing two contacting identical dielectric spheres has been presented to demonstrate the robustness of the inversion approach.

## ACKNOWLEDGMENT

This work was supported by the opening projects of the State Key Laboratory of Millimeter Waves, Nanjing, China, under the contract K201310.

## REFERENCES

1. Chew, W. C., *Waves and Fields in Inhomogeneous Media*, IEEE Press, New York, 1995.
2. Sun, L. E. and W. C. Chew, "A novel formulation of the volume integral equation for electromagnetic scattering," *Waves in Random and Complex Media*, Vol. 19, No. 1, 162–180, 2009.
3. Schaubert, D. H., D. R. Wilton, and A. W. Glisson, "A tetrahedral modeling method for electromagnetic scattering by arbitrary shaped inhomogeneous dielectric bodies," *IEEE Trans. Antennas Propagat.*, Vol. 32, No. 1, 77–85, 1984.

4. Chew, W. C., M. S. Tong, and B. Hu, *Integral Equation Methods for Electromagnetic and Elastic Waves*, Morgan & Claypool, San Rafael, CA, 2008.
5. Habashy, T. M. and A. Abubakar, “A general framework for constraint minimization for the inversion of electromagnetic measurements,” *Progress In Electromagnetics Research*, Vol. 46, 265–312, 2004.
6. Van den Berg, P. M., A. Abubakar, and J. T. Fokkema, “Multiplicative regularization for contrast profile inversion,” *Radio Science*, Vol. 38, No. 2, 23.1–23.10, 2003.
7. Tong, M., S. Tong, and W. C. Chew, “Super-hyper singularity treatment for solving 3D electric field integral equations,” *Microw. Opt. Technol. Lett.*, Vol. 49, No. 6, 1383–1388, 2007.
8. Geffrin, J. M. and P. Sabouroux, “Continuing with the Fresnel database: Experimental setup and improvements in 3D scattering measurements,” *Inverse Problems*, Vol. 25, No. 2, 1–18, 2009.

## Low SAR, Compact and Multiband Antenna

Kamel S. Sultan<sup>1</sup>, Haythem H. Abdullah<sup>1</sup>,  
Esmat A. Abdallah<sup>1</sup>, and Essam A. Hashish<sup>2</sup>

<sup>1</sup>Electronics Research Institute, Dokki, Giza, Egypt

<sup>2</sup>Faculty of Engineering, Cairo University, Giza, Egypt

**Abstract**— This paper proposes a new mobile handset antenna structure to reduce the value of the specific absorption rate (SAR) and to cover most of the mobile operating bands and other wireless applications. The covered bands are the GSM 900, DCS 1800, PCS 1900, UMTS 2100, and most of the LTE bands. Furthermore, it covers the ISM, WiMAX and the WLAN bands. The electromagnetic radiation in the direction of the human head is reduced via the use of electromagnetic band gap structure (EBG). The antenna is constructed from a monopole and a meander line. The operating bands ranges from (850–1030 MHz) and (1.71–7.8 GHz). Moreover, the first band of the antenna can be tuned by using various meander line lengths or by adjusting the spacing between the monopole and the meander line, while the second band can be tuned by adjusting the monopole length or the meander line area. The antenna volume is  $20 \times 20 \times 1.5 \text{ mm}^3$  ( $0.6 \text{ cm}^3$ ), so the proposed antenna is suitable for many wireless handheld devices. The simulation results are compared to the experimental measurements and a good agreement is observed.

### 1. INTRODUCTION

Recently, the communication technologies have a rapid growth in such a way that it allows mobile phone to be operated in various communication services. This has led to a great competition for designing antennas with some desirable features such as multiband operation, light weight, low SAR and low profile. Nowadays, the fourth generation of mobile communications, the Long Term Evolution (LTE), is expected to deliver multimedia services anywhere, anytime. The LTE standard is scheduled to operate in different frequency bands that range from 400 MHz to 4 GHz with bandwidths of 1.4 and 20 MHz [1]. As the usage of the mobile phone is increased, the research on the health risk due to the electromagnetic (EM) fields generated from wireless terminals is widely in progress. Many factors may affect the EM interaction while using cellular handset in close proximity to head and hand. The specific absorption rate (SAR) is defined as a figure of merit to evaluate the power absorbed by biological tissues. The SAR quantifies the power absorbed per unit mass of tissue. This quantity is defined as:

$$SAR = \frac{\sigma}{2\rho} |E_i|^2 \quad (1)$$

where  $E_i$  is the maximum value of the electric field strength in the tissue in V/m,  $\sigma$  is the conductivity of body tissue in S/m, and  $\rho$  is the density of body tissue in  $\text{kg/m}^3$ . The SAR limit specified in IEEE C95.1: 2005 has been updated to 2 W/kg over any 10-g of tissue [2]. This new SAR limit specified in IEEE C95.1: 2005 is comparable to the limit specified in the International Commission on Non-Ionizing Radiation Protection (ICNIRP) guidelines [3]. In designing antennas for mobile communications, it is important to investigate the SAR value produced by the radiation from the mobile handsets.

Through the last years, different methods to reduce the SAR produced by handset antenna were used, specifically, auxiliary antenna elements, ferrite loading, EBG/Artificial magnetic conductors (AMC) surfaces and metamaterials [4–8]. The SAR value is influenced by various parameters such as antenna positions relative to the human body, radiation patterns of the antenna, radiation power, and antenna types [9]. The EBG structures reduce the surface waves and prevent the undesired radiation from the ground plane. Thus, the EBG structure which is designed for mobile terminal enables to comply with the exposure guideline. This technique reduces the radiation pattern toward the direction of human head and reduces the SAR value. On other hand, extensive research efforts are exerted in minimizing mobile handset antennas in size and cost in conjunction with increasing the services provided by the antenna [10, 11].

In this paper, a novel internal antenna consisting of a monopole with a meander line to cover the multibands including the LTE bands is proposed. The proposed antenna support the following operating bands; GSM 900, DCS 1800, PCS 1900, UMTS 2100, ISM 2450, most LTE bands (LTE

850, LTE 900, LTE 2100, LTE 2300, LTE 2500, LTE 3500, LTE 3600), WiMAX (2.3–2.4 GHz, 2.5–2.69 GHz, 3.3–3.8 GHz, 3.4–3.6 GHz, and 5.1–5.8 GHz), and WLAN (2.4–2.5 GHz, 4.8–5 GHz, 4.825–5.515 GHz, 5.425–5.875 GHz, 5.125–5.875 GHz). Uniplanar EBG structure is added to the antenna to reduce the SAR values.

## 2. ANTENNA DESIGN

The proposed antenna is a planar microstrip antenna with compact dimensions of  $(20 \times 20 \times 1.5) \text{ mm}^3$ . One of the disadvantages of this antenna is the low front to back ratio and its large SAR value. The EBG structure is applied to the antenna reduce the surface waves and prevent the undesired radiation from the ground plane. This technique reduces the radiation pattern toward the direction of human head and hence reduces the SAR value. The advantages of the EBG technique are its low cost and its ease of implementation. However, more development is required to produce a practical wideband and small size EBG surface for multiband handsets. The EBG surface is positioned between the user and the handset antenna.

These periodic structures have high electromagnetic surface impedance, which is capable of suppressing the propagation of surface currents and acting as a perfect magnetic conductor in a certain frequency range so the antenna dimensions are reduced to  $(20 \times 20 \times 1.5) \text{ mm}^3$  compared to the  $(20 \times 20 \times 1.5) \text{ mm}^3$  without the use of the EBG. The antenna can be easily integrated in small and sleek mobile device. Fig. 1 depicts the geometry of a typical mobile with a size of  $45 \times 110 \times 1.5 \text{ mm}^3$ . A planar EBG structure is positioned between the user and the handset antenna. All the labeled dimensions are tabulated in Table 1. A prototype of the antenna was fabricated using FR4 substrate ( $\epsilon_r = 4.5$ ) with 1.5 mm thickness and loss tangent of 0.025. The planar EBG structure is periodic square patches with dimensions of  $(9 \times 9) \text{ mm}^2$  and gaps of 1 mm. The EBG is fabricated over FR4 substrate ( $\epsilon_r = 4.5$ ) with 0.8 mm thickness and loss tangent of 0.025. Fig. 2 shows the prototype of the proposed antenna.

The proposed antenna is composed of a planar monopole and meander line sections. The monopole antenna is an inverted-L shape. The electrical length of the monopole is a quarter-wavelength at 2350 MHz. The monopole operating bands are (1700–3000) MHz and (4600–5500) MHz. The dimensions of the monopole area is  $18 \times 7 \text{ mm}^2$ . Furthermore, the meander line increases the path over which the surface current flows and that eventually results in lowering the resonant frequency. The electrical length of the meander line is optimized to resonant at 900 MHz. The optimized length of the meander line is 111 mm. The combination of the monopole and the meander line contributes to open the higher bands to operate from 1710 MHz up to 7.8 GHz. One of the advantages of the proposed antenna is that its performance does not depend on the position of the ground plane. The ground plane may be coplanar with the antenna or on opposite side of the substrate. This adds more flexibility for the electronics designer to arrange the components in its

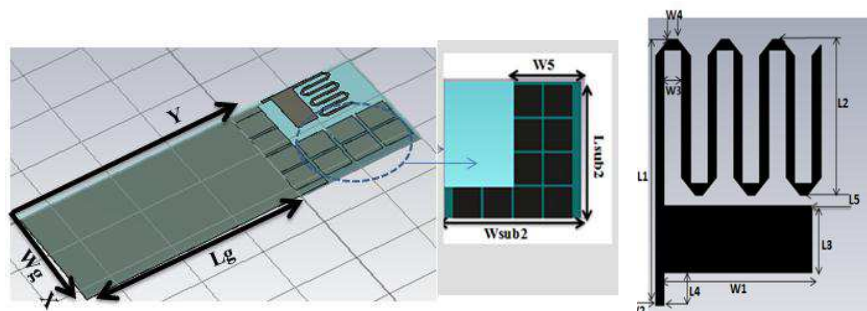


Figure 1: Geometry of the proposed antenna in mobile phone.



Figure 2: Photo of the fabricated antenna.

Table 1: Parameters of the proposed antenna (all dimensions in mm).

Parameter	Value	Parameter	Value	Parameter	Value	Parameter	Value
L1	20	L5	1	W3	2	W5	22
L2	9.5	Lg	79	W4	1	W6	9
L3	7	W1	17	Wg	45	Wsub2	45
L4	3	W2	1	Lsub2	40		

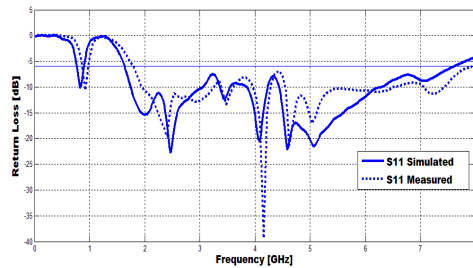


Figure 3: Simulated and measured return loss of the proposed antenna.

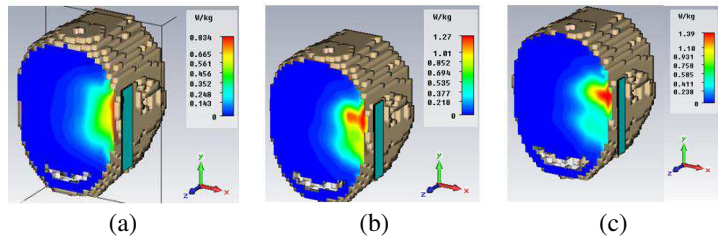


Figure 4: SAR distribution on human head. (a) 0.9 GHz, (b) 1.8 GHz, and (c) 2.1 GHz.

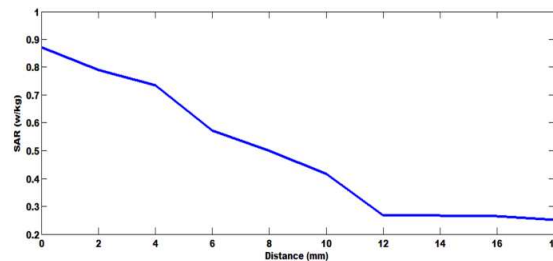


Figure 5: The SAR value at 0.9 GHz with separation distance between head and antenna.

suitable position.

### 3. SIMULATION AND MEASURED RESULTS

The EBG structure is investigated by simulating its behaviour within the required band by some iterations. The dimensions of the EBG is selected to be  $(9 \times 9)$  mm<sup>2</sup> with a separation distance of 1 mm to achieve a band gap in the range from 1.54 to 2.48 GHz. The proposed antenna is simulated using the CST Microwave Studio Ver. 2011. Fig. 3 shows a comparison between the simulated and the experimental results of the return loss. The simulated and the experimental results ensure that the antenna covers all the aforementioned mobile and wireless applications bands. Taking the 6 dB return loss reference, the antenna operates in the two bands (850–1030 MHz) and (1.71–7.8 GHz).

### 4. SAR CALCULATION

In this paper, the output power of the cellular phone is set to 500 mW at the operating frequency of 0.9, 1.8, and 2.1 GHz. Fig. 4 shows the SAR calculations on human head model in the presence of the antenna in the ZY plane with the EBG structure. The SAR is tested at 0.9, 1.8 and 2.1 GHz when the antenna is close to the human head. The SAR values are calculated according to the 10 gram standard of the human tissue mass. The SAR calculations are done using the CST Ver. 2011 commercial package. As expected, the SAR values depend on the operating frequency, the antenna type and the distance between the antenna and the human body. Table 2 shows the averaged 10 g SAR at the aforementioned operating frequencies when the antenna is close to the body. As the results are scalable when the power level changes, the SAR values could be controlled by adjusting the separation between the antenna and the head as shown in Fig. 5 which illustrates that the SAR values decrease with the increase of the separation distance between the antenna and the head.

Table 2: Simulated SAR value.

<b>F (GHz)</b>	<b>Without EBG</b>	<b>With EBG</b>
0.9	2.63 W/kg	0.872 W/kg
1.8	2.05 W/kg	1.27 W/kg
2.1	1.78 W/kg	1.39 W/kg

## 5. CONCLUSION

A challenging antenna that operates in most of the mobile applications is introduced. The antenna is based on the use of a simple monopole and meander line in conjunction with an artificial magnetic conductor made of an EBG structure. The introduction of the EBG structure increases the front to back radiation ratio which indeed reduces the SAR with the human head. The SAR calculations are done using the CST 2011 commercial package. An averaged 10 gram SAR values are calculated at different operating bands and distances.

## ACKNOWLEDGMENT

This work is funded by the National Telecom. Regulatory Authority (NTRA), Ministry of Communication and Information Technology, Egypt.

## REFERENCES

1. Bhatti, R. A., S. Yi, and S. Park, "Compact antenna array with port decoupling for LTE-standardized mobile phones," *IEEE Antennas and Wireless Propagation Letters*, Vol. 8, 1430–1433, 2009.
2. IEEE C95.1-2005, "IEEE standards for safety levels with respect to human exposure to radio frequency electromagnetic fields, 3 kHz to 300 GHz," Institute of Electrical and Electronics Engineers, New York, NY, 2005.
3. International Non-Ionizing Radiation Committee of the International Radiation Protection Association, "Guidelines on limits on exposure to radio frequency electromagnetic fields in the frequency range from 100 kHz to 300 GHz," *Health Physics*, Vol. 54, No. 1, 115–123, 1988.
4. Kwak, S. I., D. U. Sim, J. H. Kwon, and J. H. Yun, "Design of multilayer PIFA based on an EBG structure for SAR reduction in mobile applications," *APMC*, 645–648, 2009.
5. Ilvonen, J., O. Kivekas, J. Holopainen, R. Valkonen, K. Rasilainen, and P. Vainikainen, "Mobile terminal antenna performance with the user's hand: Effect of antenna dimensioning and location," *IEEE Antennas and Wireless Propagation Letters*, Vol. 10, 772–775, 2011.
6. Kwak, S. I., D. Sim, and J. H. Kwon, "Design of optimized multilayer PIFA with the EBG structure for SAR reduction in mobile applications," *IEEE Transactions on Electromagnetic Compatibility*, Vol. 53, No. 2, 325–333, May 2011.
7. Kwak, S. I., D. Sim, and J. H. Kwon, "SAR reduction on a mobile phone antenna using the EBG structures," *The 38th European Microwave Conference*, 1308–1311, Oct. 2008.
8. Villanueva, R. G., H. J. Aguilar, and R. L. Miranda, "State of the art methods for low SAR antenna implementation," *2010 Proceedings of the Fourth European Conference on Antennas and Propagation (EuCAP)*, 1–4, 2010.
9. Jung, M. and B. Lee, "SAR reduction for mobile phones based on analysis of EM absorbing material characteristics," *Proc. Antennas and Propagation Society International Symposium*, Vol. 2, 1017–1020, Jun. 2003.
10. Tang, C. L., J. Y. Sze, and Y. F. Wu, "A compact coupled-fed penta-band antenna for mobile phone application," *APMC*, 2260–2263, 2010.
11. Young, C. W., Y. B. Jung, and C. W. Jung, "Octaband internal antenna for 4G mobile handset," *IEEE Antennas and Wireless Propagation Letters*, Vol. 10, 817–819, 2011.

# Creeping Wave Antenna Design and Application for On-body Surface Communication

Shih-Chung Tuan<sup>1</sup>, Hsi-Tseng Chou<sup>2</sup>, and Ching-Hui Chen<sup>2</sup>

<sup>1</sup>Department of Communication Engineering, Oriental Institute of Technology, Pan-Chiao, Taiwan

<sup>2</sup>Department of Communication Engineering, Yuan Ze University, Chung-Li, Taiwan

**Abstract**— This paper presented a design of patch array antenna for human body surface communication. This antenna design is also known as creeping wave antenna (CWA). The fundamental characteristic of CWA is that the antenna radiation direction can be tuned to allow the wave propagation to get close to the body surface for maximized coupling performance of CWA on human body surface communication. This study introduces an antenna array possessing high gain and high directivity. It is designed with the concept of slotted micro-strip patch antenna which is light weight, small size and thin, suitable for mounting over the surface of human body or over clothing materials for communication. In this paper we designed the slotted micro-strip patch antenna array with  $1 \times 6$  slots, having a center frequency of 5.8 GHz.

## 1. INTRODUCTION

This paper aims to design a patch antenna for human body surface communication. This antenna design is also known as creeping wave antenna (CWA) [1–4]. The fundamental characteristic of CWA is that the antenna radiation direction can be tuned to allow the wave propagation to get close to the body surface for maximized coupling performance of CWA on human body surface communication. This study introduces an antenna array possessing high gain and high directivity. It is designed with the concept of slotted micro-strip patch antenna which is light weight, small size and thin, suitable for mounting over the surface of human body or over clothing materials for communication. In this paper, we designed the slotted micro-strip patch antenna array with  $1 \times 6$  slots, having a center frequency of 5.8 GHz. Each radiating element of the patch antenna can create unique phase differences using different path length and traveling path selected from the micro-strip lines, so that the adjusted direction of antenna radiation can produce maximized coupling performance on CWA, fulfilling the main objective of our design. On the application side, our invention has several sensors to detect many physiological signals in the human body, and the signals are collected by this antenna through wireless communication over the body surface. To fulfill our requirements, the direction of power radiation shall be tuned with appropriate phase shift to get close to the body surface to maximize the coupling performance of CWA mounted over the body surface. After completely collecting physiological signals from the human body, this antenna then sends out the signals to outside medical units for on-line real time monitoring and home care applications.

## 2. MOTIVATION OF OUR RESEARCH

In recent years, with the development of biomedical technologies, the size of medical instruments and devices is gradually reduced, and wireless transmission has become the dominant mode of data transfer as shown in Fig. 1, even achieving real-time physiological monitoring [5]. There has been significant growth in wireless communication devices for tele-medical applications in recent years. However, the design of this type of antenna must take into account many factors, such as permittivity of human body, depth of electromagnetic wave penetration, free frequency bandwidth (ISM Band), return loss in electromagnetic wave transmission, and safety requirements in the electromagnetic wave transmission over the human body, among others. Further, it is required to conform with the theory of antenna radiation and antenna design and structure in practical applications. On the application side, many physiological signals from the human body may be detected by the sensors (as shown in Fig. 2), which are then converted to weak voltage current signals, such as electrocardiogram (ECG), Electromyography (EMG), Electroencephalography (EEG), blood pressure, body temperature, etc.. This study designs a slotted micro-strip patch antenna array at 5.8 GHz frequency. This device acts very much like a control center collecting physiological signals from the human body through wireless signal transmission, and after processing, send them to outside medical units, so that the physiological data of patients can be used by doctors in real time monitoring and diagnosis of patient conditions.

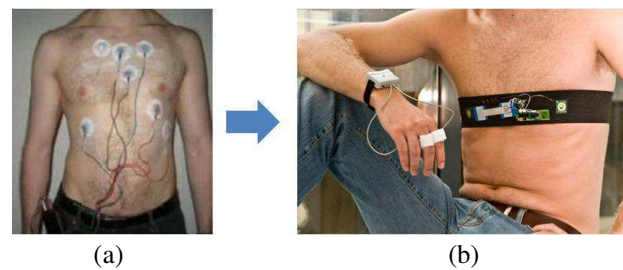


Figure 1: (a) Data transfer of physiological signals by wires. (b) Data transfer of physiological signal through wireless transmission. [Source]: Imec-body Area Network Monitors Arousal Level.

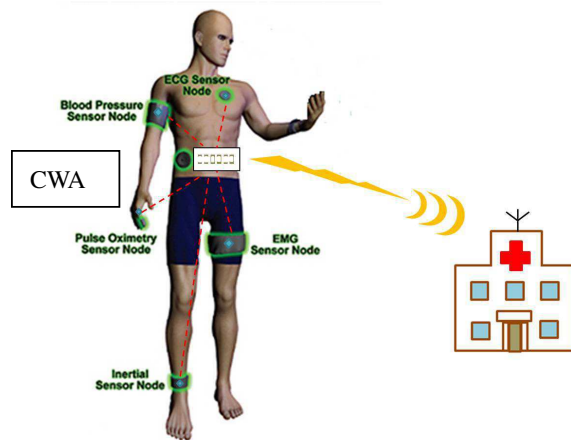


Figure 2: Applications for CWA (Creeping Wave Antennas). [Source]: Design World-Sensors Advance Medical and Healthcare Applications.

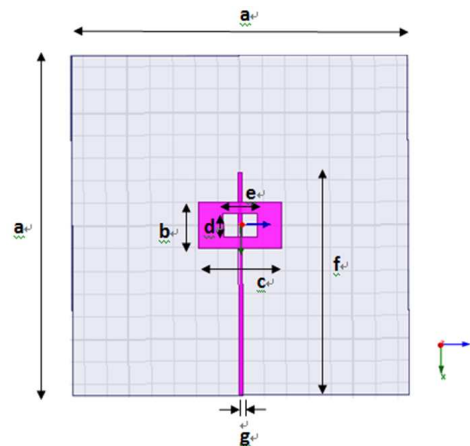


Figure 3: Geometrical structure of one unit of slotted micro-strip patch antenna.

Under the design concept of this study [6–9], physiological signals are first measured by the sensors, and then sent to this antenna through wireless transmission. The design of this antenna is different from traditional antennas in that the antenna radiation for maximized coupling performance of CWA is not signal wave propagation in a straight forward direction, but CWA is designed for creeping wave propagation over the surface of human body, in such a way that the power radiation from the antenna can maximize the coupling performance of CWA, which is the key factor in our antenna design.

### 3. ANTENNAS DESIGN AND IMPLEMENTATION

#### 3.1. Design and Simulation of the Slotted Micro-strip Antenna

Figure 3 shows the geometrical structure of one unit of slotted micro-strip patch antenna, the antenna plate is made with two layers of Rogers 4003 with thickness ( $h$ ) of 0.508 mm, and dielectric constant ( $\epsilon_r$ ) 3.38, and center frequency of 5.8 GHz. The slotted micro-strip antenna has a ground plane with the size of 75 mm  $\times$  75 mm. From Fig. 4, the simulation results shows that return loss can reach nearly  $-30$  dB, and directivity can be up to 6.3 dB.

#### 3.2. Design and Simulation of Antenna Array

The purpose of our antenna array design is to improve the power gain, and to be able to adjust the direction of power radiation from the antenna for maximizing the efficiency of antennas. On the one hand, the power gain will influence the strength of received signals in the communication system, and on the other hand, through adjustment of the distance between antenna units and input phase difference, the direction of power radiation from the antenna can be tuned with appropriate phase shift to get close to the mounting plane for maximizing the coupling performance of CWA on the human body surface communication. It's presents the simulated radiation pattern using the antenna structures shown in Fig. 5. When using micro-strip lines to simulate the coupling feed, the

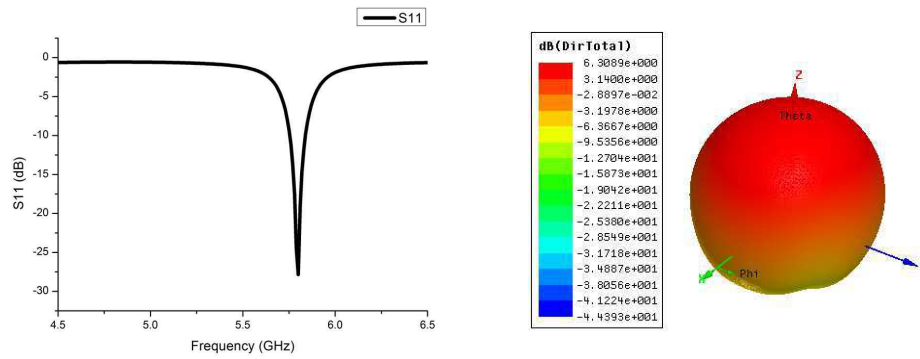


Figure 4: Return loss and 3-D radiation pattern of one unit of slotted micro-strip patch antenna.

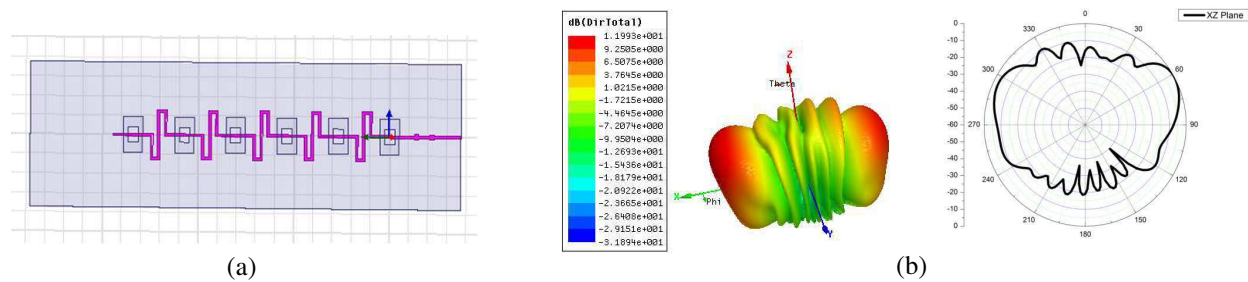


Figure 5: Using micro-strip lines to simulate the coupling feed. (a) With different phase excited for micro-strip patch array antenna. (b) 3-D and  $\phi = 0^\circ$  plane radiation pattern.

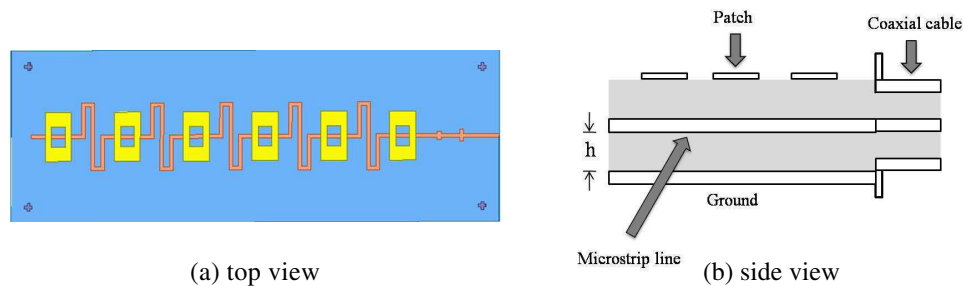


Figure 6: Actual implementation for antenna.

starting phase of excitation for all radiating elements are different due to different traveling paths and path length created between the micro-strip lines.

### 3.3. Design and Implementation of the Antenna Structure

As shown in Fig. 6, the antenna is designed as a three-layered structure. The uppermost layer is the slotted micro-strip patch antenna array, which mainly houses the radiating elements; the middle layer is the microstrip line; and the bottom layer is a plate of metal to be used as a ground plane. For antenna materials, we used two layers of Rogers 4003 with thickness ( $h$ ) of 0.508 mm, dielectric constant ( $\epsilon_r$ ) of 3.38, and center frequency of 5.8 GHz to make the slotted micro-strip patch antenna array, and the size of the ground plane is 190 mm  $\times$  65 mm.

## 4. MEASUREMENT DATA

As shown in Fig. 7 presents the radiation patterns produced from this antenna in actual implementation and simulation, for the purpose of comparison. It can be seen that the difference on co-pole and cross-pole is more than 20 dB in both simulation and implementation. We can tune the direction of power radiation from the antenna with an included angle of 60 plus degrees from the  $z$ -axis for maximizing the coupling performance of CWA, achieving the main objective of our study — to be able to adjust the antenna radiation with appropriate phase shift and get close to the mounting plane surface for maximizing the coupling performance of CWA on the human body

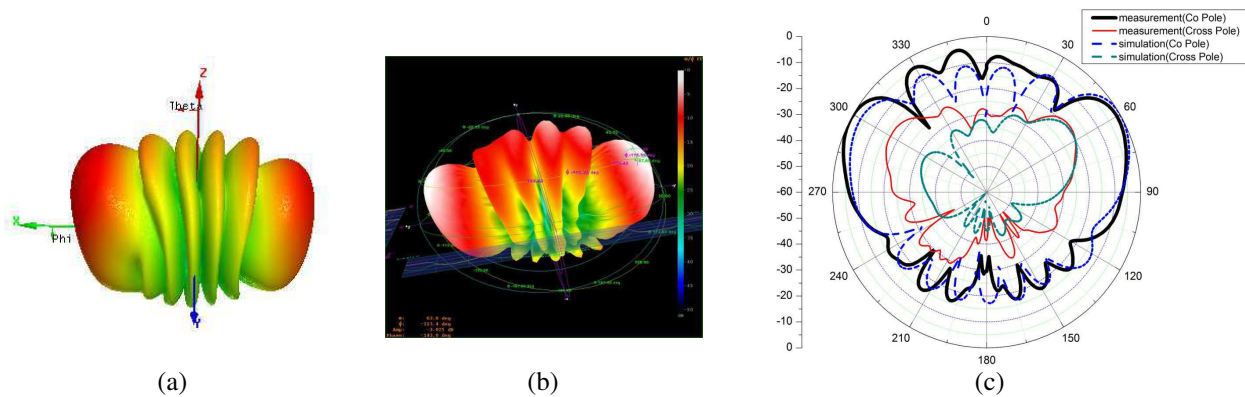


Figure 7: Radiation pattern of slotted patch antenna array at 5.8 GHz. (a) Simulation. (b) Measurement. (c) Compared for measurement and simulation data.

surface communication.

## 5. CONCLUSIONS

This paper presented a  $1 \times 6$  slotted micro-strip patch antenna array with a frequency of 5.8 GHz. From the above discussions concerning the characteristics and performance measurements of CWA, it is obvious that this antenna array has met the design goals. In simulation, this slotted micro-strip antenna at 5.8 GHz produces directivity of more than 6 dB, and return loss ( $S_{11}$ ) at operating frequency amounts to under  $-25$  dB. To improve power gain and create the necessary offset in antenna radiation, this paper implemented the micro-strip patch antenna employing the coupling feed. The antenna radiation can be tuned by adjusting the distance between various elements and input phase difference, so that an offset angle of 60 plus degrees to the  $z$  axis is realized in maximizing the coupling performance of CWA.

## REFERENCES

1. Ali, M. and K. Masood, "Robust on-body communications using creeping wave," *Methodology and Analysis World Academy of Science, Engineering and Technology*, Vol. 58, 2011.
2. Akhoondzadeh-Asl, L., Y. Nechayev, and P. S. Hall, "Surface and creeping waves excitation by body-worn antennas," *Antennas and Propagation Conference (LAPC)*, 2010.
3. Yazdandoost, K. Y., "Antenna for over body surface communication," *2011 Asia-Pacific Microwave Conference Proceedings (APMC)*, 578–581, 2011.
4. Herrmann, G. F., "A direct look at creeping waves," *Antennas and Propagation Society International Symposium*, 1988.
5. Fensli, R., E. Gunnarson, and O. Hejlesen, "A wireless ECG system for continuous event recording and communication to a clinical alarm station," *Proceedings of the 26th Annual International Conference of the IEEE EMBS San Francisco*, 2208–2211, Sep. 1–5, 2004.
6. Lee, C. M., T. C. Yo, C. H. Luo, C. H. Tu, and Y. Z. Juang, "Compact broadband stacked implantable antenna for biotelemetry with medical devices," *Electron. Lett.*, Vol. 43, No. 12, 660–662, Jun. 2007.
7. Karacolak, T., A. Z. Hood, and E. Topsakal, "Design of a dual-band implantable antenna and development of skin mimicking gels for continuous glucose monitoring," *IEEE Trans. Microw. Theory Tech.*, Vol. 56, No. 4, 1001–1008, Apr. 2008.
8. Yoshimura, Y., "A microstripline slot antenna," *IEEE Trans. Microwave Theory Tech.*, Vol. 20, 760–762, 1972.
9. Constantine, A. and P. Balanis, *Antenna Theory: Analysis and Design*, 3rd Edition, Wiley-Interscience, 2005.

# Compact Folded Meander PIFA Antennas in MedRadio Bands

Chiu-Yueh Huang, Chi-Lin Tsai, and Chin-Lung Yang

National Cheng Kung University, Tainan 701, Taiwan

**Abstract**— This study proposes a novel compact antenna design for MedRadio Band (401–406 MHz). The basic structure is based on the PIFA antenna. The ground plane is bent to the other side of the substrate to reduce the size. The point of C is connected to the C'. The proposed miniaturized antenna is printed on the PCB board (FR4 substrate with thickness of 0.8 mm, dielectric constant of 4.4), with a total size of  $320 \text{ mm}^3$  ( $0.0269\lambda_0 \times 0.0269\lambda_0 \times 0.00108\lambda_0 \text{ mm}^3$ ). The proposed antenna is the single layer design, which total size is compact. Its return loss is more than 15 dB at 404 MHz. The antenna simulated gain and efficiency are  $-24 \text{ dBi}$  and 0.26%. Moreover, its bandwidth covers the whole MedRadio band (401–406 MHz). This compact antenna is suitable for implantable applications.

## 1. INTRODUCTION

As biomedical microwave systems grow and develop fast and widely. Implantable antenna is one of the crucial points, and its quality influences the efficiency and transmission of the entire system. Accordingly, there are many requirements of the implantable antennas such as compact size, high gain, low specific absorption rate (SAR), and biocompatibility performance in various parts of the human body. In order to overcome the size limitation, many studies on the implantable antenna miniaturization have been proposed, aiming at reducing the physical size of the antenna, while increasing its electrical size. Two different shapes (spiral and serpentine) implantable antenna designs built on MACOR substrate ( $\epsilon_r = 6.1$ ), which size is  $1340.64 \text{ mm}^3$  [1]. A  $1265.625\text{-mm}^3$  rectangular implantable antenna for continuous glucose-monitoring applications has been reported [2], which is fabricated on the high-permittivity ( $\epsilon_r = 10.2$ ) Rogers 3210 dielectric and applies a serpentine radiator to reduce the total size. It can be considered as a meandered monopole antenna to reduce the size. Besides, the electrical path is increased by the grounding pin design, which likes a ground plane on a monopole antenna (planar inverted-F antenna, PIFA). Therefore, the design of grounding pin (PIFA antennas), has been proven to be very effective ways of reducing the dimensions of the antenna [3]. Consisting of the  $\pi$ -shape with two meandered strips, the PIFA structure of a  $843.6\text{-mm}^3$  size can achieve dual-modes resonance over a large bandwidth [4, 5]. Other implantable antennas applying similar miniaturization techniques include multilayer structures PIFA, which occupies a miniaturized volume of  $335.76 \text{ mm}^3$  [6].

In this paper, a compact PIFA structure is designed for MedRadio Band (401–406 MHz). Utilising the PIFA structure can excite a resonant frequencies at 404 MHz, and its return loss is more than 15 dB. The ground plane is bent to the other side of the substrate to reduce the size to  $320 \text{ mm}^3$  ( $0.0269\lambda_0 \times 0.0269\lambda_0 \times 0.00108\lambda_0 \text{ mm}^3$ ). Thus, this compact antenna is suitable for implantable applications.

## 2. ANTENNA DESIGN

The proposed structure is based on the meandering PIFA antenna. The geometry is shown in Fig. 1, the ground plane is bent to the other side of the substrate to reduce the size. In addition, we bent the radiator to the backside of the substrate By varying those parameters ( $W_1$ ,  $W_2$  and  $W_3$ ), we can achieve the input impedance matching. The point C is connected to the C'. Point A is the feeding point, and point B is the shorting point. The proposed antenna is printed on the PCB board (FR4 substrate with thickness of 0.8 mm, dielectric constant of 4.4), with a total size of  $320 \text{ mm}^3$  ( $0.0269\lambda_0 \times 0.0269\lambda_0 \times 0.00108\lambda_0 \text{ mm}^3$ ).

The operating principle is studied in Fig. 2(a) in which results of the simulated return loss of the proposed antenna in Fig. 2(b), including in the case of the design1 (the overall size of the antenna, which is about a quarter-wavelength radiator at 404 MHz, and the width of  $50 \Omega$  impedance matching), in the case of the design2 (adjust the linewidth  $W_1 = 2.2 \text{ mm}$ ), in the case of the design3 (adjust the linewidth  $W_2 = 0.6 \text{ mm}$ ) and in the case of the whole proposed antenna (adjust the linewidth  $W_3 = 3.5 \text{ mm}$ ). The corresponding dimensions of the antennas in above cases are the same as those of the proposed antenna. In the case of the design1, a resonant mode is seen to occur at about 450 MHz, although the impedance matching of this resonant mode still needs to

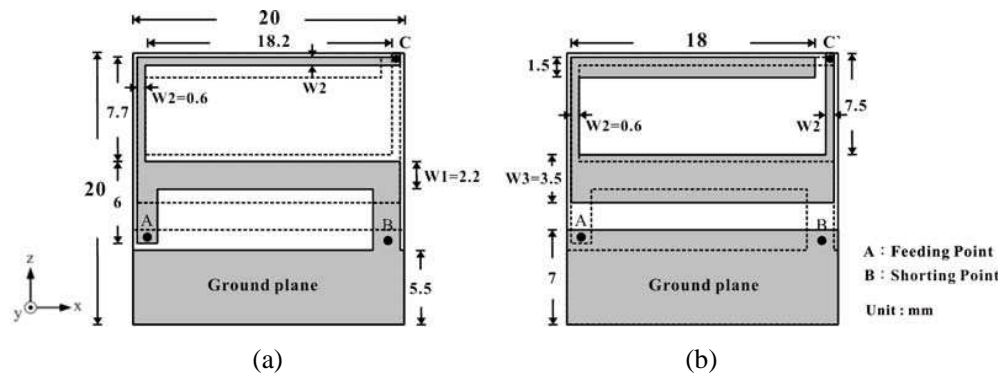


Figure 1: (a) Top view of the proposed antenna. (b) Bottom view of the proposed antenna.

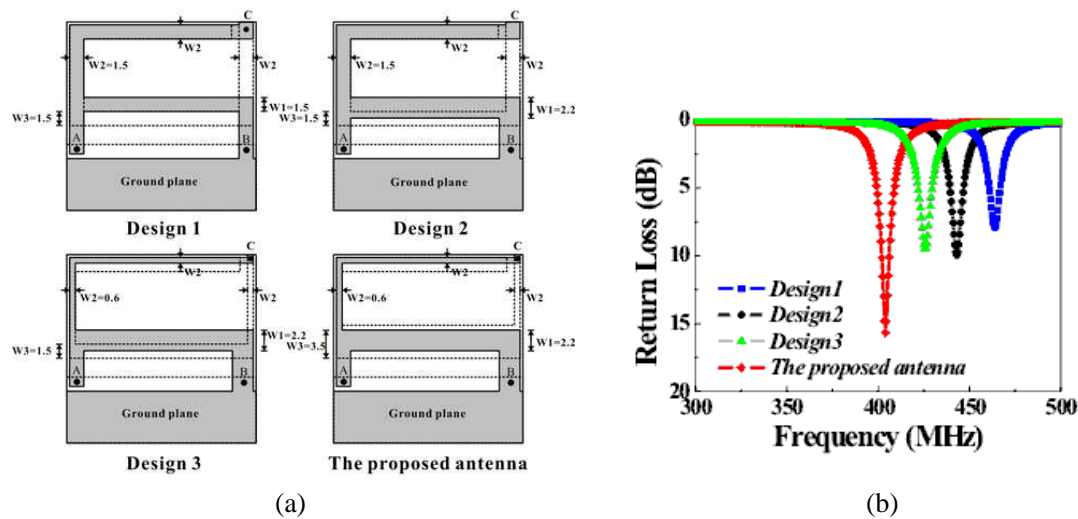


Figure 2: Simulated return loss of the proposed antenna, in the case of the design1, in the case of the design2, in the case of the design3 and in the case of the whole proposed antenna.

be improved. In the case of the design2 and design3, the resonant mode drops to approximately 430 MHz and the impedance matching is better than design1. In the case of the proposed antenna, it is operating in MedRadio Band (401–406 MHz) and its return loss is more than 15 dB at 404 MHz.

### 3. RESULTS

The optimal performance of proposed antenna is obtained by using the Ansoft simulation software high-frequency structure simulator (HFSS). Fig. 3 shows the simulated and measured return loss of the proposed antenna. Clearly, the resonant frequency is dominated by the PIFA structure. Therefore the input impedance can be adjusted by changing the parameters of the width and the length ( $W_1$ ,  $W_2$  and  $W_3$ ). The simulated and measured return loss results are 15.68 dB and 29 dB, respectively. It is operated in MedRadio Band (401–406 MHz). The simulated gain and efficiency is shown in Fig. 4, the antenna simulated gain and efficiency are  $-24$  dBi and 0.26% at 404 MHz. Moreover, since in electrically small antennas the efficiency can be very low.

As shown in Fig. 5, the two-dimensional simulated far-field radiation patterns (404 MHz) of the proposed antennas. It can be observed that the  $H$ -plane ( $xy$ -plane) radiation patterns are nearly omnidirectionally, and the cross polarizations of the radiation patterns are quite low. Fig. 6 shows the three-dimensional simulated far-field radiation patterns (404 MHz) of the proposed antennas, and the maximum gain value is  $-24$  dB. This gain is similar to other implantable antennas presented in the [4, 5], although our design presents the advantage of a smaller size.

### 4. MEASURED SETUP

The proposed antenna was fabricated on a FR4 substrate (the thickness of 0.8 mm, dielectric constant of 4.4). The total size is  $320 \text{ mm}^3$  ( $0.0269\lambda_0 \times 0.0269\lambda_0 \times 0.00108\lambda_0 \text{ mm}^3$ ). A  $50 \Omega$  coaxial

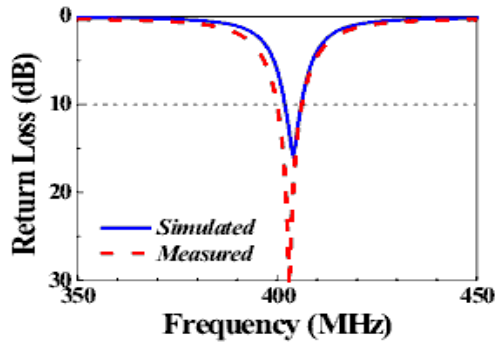


Figure 3: The simulated and measured return loss of the proposed antenna.

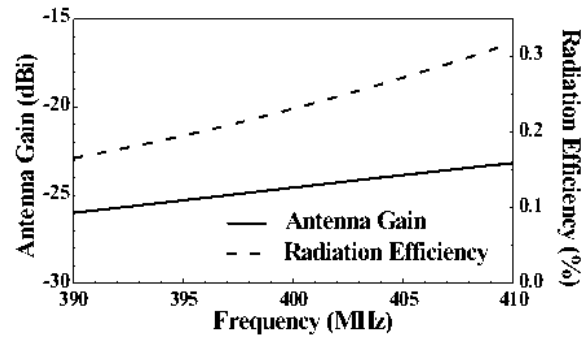


Figure 4: The simulated gain and efficiency plot for 404 MHz.

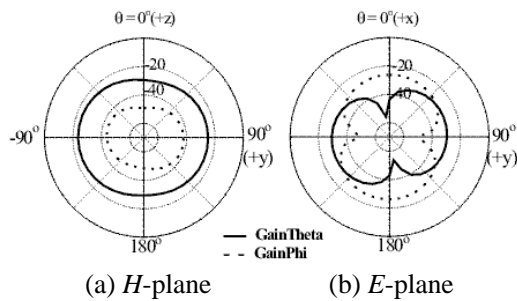


Figure 5: Simulated 2-D radiation pattern for 404 MHz. (a) *H*-plane. (b) *E*-plane.

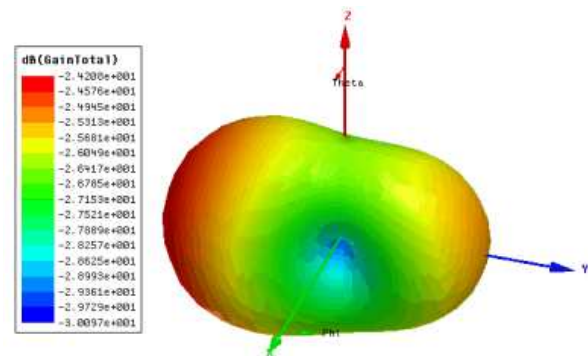


Figure 6: Simulated 3-D radiation pattern for 404 MHz.



Figure 7: The designed antenna of fabricated prototype.

cable was used to feed the proposed antenna. In order to verify the simulation results, antenna prototypes were built and were tested with an Agilent E5071C network analyzer. Fig. 7 shows the designed antenna of fabricated prototype.

## 5. CONCLUSIONS

The compact PIFA implantable antenna for MedRadio Band (401–406 MHz) has been proposed. The ground plane is bent to the other side of the substrate to reduce the size. The PIFA antenna radiation main branches bent to the back substrate surface extending into a spiral shape by varying linewidth ( $W_1$ ,  $W_2$  and  $W_3$ ) to achieve impedance matching. The proposed antenna's measured return loss is 29 dB at 404 MHz. The simulated gain and efficiency are  $-24$  dBi and 0.26% at 404 MHz, respectively. This compact antenna is suitable for implantable applications.

**REFERENCES**

1. Soontornpipit, P., C. M. Furse, and C. C. You, “Design of implantable microstrip antenna for communication with medical implants,” *IEEE Transactions on Microwave Theory and Techniques*, Vol. 52, No. 8, 1944–1951, Aug. 2004.
2. Karacolak, T., A. Z. Hood, and E. Topsakal, “Design of a dual-band implantable antenna and development of skin mimicking gels for continuous glucose monitoring,” *IEEE Transactions on Microwave Theory and Techniques*, Vol. 56, No. 4, 1001–1008, Apr. 2008.
3. Yahya, R. S. and J. Kim, *Implanted Antennas in Medical Wireless Communications*, 1st Edition, Morgan and Claypool, USA, 2006.
4. Lee, C. M., T. C. Yo, F. J. Huang, and C. H. Luo, “Dual-resonant  $\pi$ -shape with double L-strips PIFA for implantable biotelemetry,” *Electronics Letters*, Vol. 44, No. 14, 837–838, Jul. 3, 2008.
5. Huang, F. J., C. M. Lee, L. K. Chen, B. M. Jeng, C. L. Chang, T. F. Chien, and C. H. Luo, “Compact PIFA with three-resonators for dual-band implantable biotelemetry,” *2011 Asia-Pacific Microwave Conference Proceedings (APMC)*, 618–621, Dec. 5–8, 2011.
6. Lee, V. M., T. C. Yo, and C. H. Luo, “Compact broadband stacked implantable antenna for biotelemetry with medical devices,” *Proc. IEEE Annu. Wireless Microw. Tech. Conf.*, 1–4, Clearwater Beach, FL, Dec. 2006.

# Metamaterial Loaded Wideband Patch Antenna

S. Raghavan<sup>1</sup> and Anoop Jayaram<sup>2</sup>

<sup>1</sup>Electronics and Communication Department, National Institute of Technology, Trichy, India

<sup>2</sup>National Institute of Technology, Trichy, India

**Abstract**— A new design technique for producing wideband patch antenna is introduced in this paper. The methodology involves complementary square split ring resonators and an inset fed rectangular patch antenna both designed to resonate at the same frequency. The dimensions of the complementary square split ring resonator are same as that of the split ring resonator's physical dimensions, which are optimized using Artificial Neural Network. A Cascade Forward Backpropagation neural network using Levenberg Marquardt learning algorithm is utilized for optimization. The proposed neural network for optimization contains four hidden layers with variable number of neurons in each layer, which is created and trained using neural network toolbox 5.1 of MATLAB. The proposed antenna is constructed by cutting out the split ring resonator from the two corners of the patch where the feed is given to antenna. HFSS simulation of the proposed antenna shows improved bandwidth and return loss at the centre frequency of 2.4 GHz. The simulation result shows remarkable improvement in antenna parameters when compared to a normal inset fed rectangular patch antenna, the only loss being a negligible decrement in the antenna gain.

## 1. INTRODUCTION

Patch antennas play a very significant role in today's world of wireless communication systems as these cover a broad range of frequencies. These patch antennas are simple and are used for the most demanding applications. Low weight, low fabrication cost, circular polarizations, dual band operation, frequency agility, feed line flexibility, beam scanning are a few notable advantages of microstrip patch antenna. Even though there are many advantages a few critical drawbacks which limit the applicability of microstrip patch antennas are low efficiency, low gain, narrow bandwidth, low power handling capability [11].

There are a lot of techniques to improve on the antenna parameters like defected ground structures, parasitic elements or slots, thick substrate with low permittivity, stacked patches [11]. Metamaterials can also be used to enhance the antenna parameters. These structures can be applied to various radiating structures to reduce the size, improve the bandwidth, and achieve dual band operations [1, 2, 10]. The core idea of this work is to improve the bandwidth of the inset fed rectangular patch antenna by incorporating the metamaterial structure into the patch. As explained in [10] CSRR structures can be used to attain dual band operation in a patch. Here instead of designing the antenna and CSRR structure for two different frequencies they are designed to resonate at the same frequency. CSRR requires axial electric field for excitation and hence the CSRR structure in the patch is placed close to the radiating edges where electric field lines have a higher density.

Artificial neural networks are made use of to optimize the CSRR dimensions. Neural network toolbox (nntool) of MATLAB is used for this purpose. The network uses Backpropagation network and uses Levenberg-Marquardt learning algorithm. The metamaterial media is loaded on the patch and Ansoft HFSS software is used to analyze the various parameters of the resulting wideband antenna.

## 2. INSET FED RECTANGULAR MICROSTRIP PATCH ANTENNA

Microstrip antennas consist of a metallic strip (usually copper) placed a small fraction of wavelength above the ground plane. The patch width affects the input resistance and bandwidth, the patch length determines the resonant frequency of the antenna. The design equations for the patch can be obtained from [3, 8, 9]. At the edge of the strip the  $H$ -field drops to zero and is maximum in the centre. The  $E$ -field intensity is at maximum magnitude at the edges and zero at the centre. The ratio of  $E$  to  $H$  field is proportional to the impedance that you see when you feed the patch. So by adjusting the position of feed, the impedance of the patch can be adjusted to any desired value [3].

$$Z_{in}(d) = \cos^2\left(\frac{\pi d}{L}\right) Z_{in}(0) \quad (1)$$

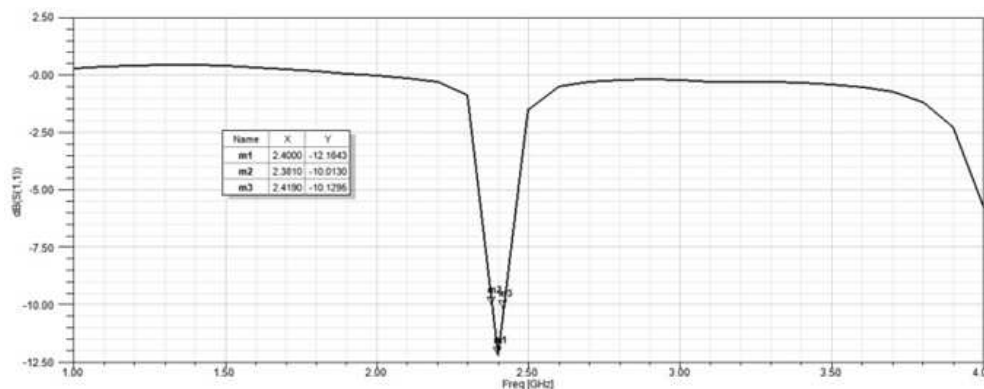


Figure 1: Return loss characteristics of the designed antenna.

where  $Z_{in}(d)$  represents the impedance at a distance  $d$  from the edge of the patch,  $L$  represents the length of patch and  $Z_{in}(0)$  represents the impedance at the edge of the patch. The antenna used is designed for a resonant frequency of 2.48 GHz. The inset feed is given at a distance of 12.6 mm from the edge. The return loss at resonance is found to be  $-12.1643$  dB and the absolute bandwidth are measured to be 1.58%.

### 3. SPLIT RING RESONATOR DESIGN

A single cell SRR is a pair of enclosed loops with splits in them at opposite ends. The loops are made of metal and have a small gap between them. A magnetic flux incident on the metal rings will induce rotating currents in the rings, which in turn produce their own flux to enhance or oppose the incident field. Due to splits in the rings the structure can support resonant wavelengths much larger than the diameter of the rings. The SRR can be mainly considered as a resonant magnetic dipole that can be excited by an axial magnetic field [4, 5], whereas the CSRR (Figure 2(a)) essentially behaves as an electric dipole (with the same frequency of resonance) that can be excited by an axial electric field. The equivalent circuit of the complementary square split ring resonator will be a parallel LC tank circuit as shown in Figure 2(b). The design equations of SRR (CSRR) is given in [6]. The equivalent inductance and capacitance relations are given as

$$L_0 = \frac{4.86\mu_0}{2}(a - w - d) \left[ \ln \left( \frac{0.98}{\rho} + 1.84\rho \right) \right] \quad (2)$$

$$\rho = \frac{w + d}{a - w - d} \quad (3)$$

$$C_0 = (a - 1.5(2 + d))C_{pul} \quad (4)$$

where  $C_{pul}$  is capacitance per unit length between the rings.

The resonant frequency of the CSRR structure is given as

$$f_0 = \frac{1}{2\pi\sqrt{L_0C_0}} \quad (5)$$

### 4. ARTIFICIAL NEURAL NETWORK

ANN is formed from interconnected layers of interconnected processing elements. The number of input and output neurons depends on those of the corresponding system that is being implemented. Artificial Neural Network (ANN) represents a promising modeling technique, especially for data sets having non-linear relationships [7]. In the course of developing an ANN model, the architecture of ANN and the learning algorithm are the two most important factors. In this paper, Multi Layered Perceptron (MLP) neural network architecture is used in optimizing the physical dimensions of the square split ring resonator. The model used in this paper (Figure 3) is a cascade forward Backpropagation network with Levenberg Marquardt training algorithm for minimizing the error of the non linear function. The equation for finding the resonant frequency of the metamaterial structure depends on three variables  $a$ ,  $d$  and  $w$  (Equations (2)–(5)). So by giving the frequency ' $f$ ', size of resonant structure ' $a$ ' and dielectric constant ' $\epsilon_r$ ' as inputs to the neural network the

Table 1: Typical values obtained from the proposed neural network.

Input to Network			Output from Network		Calculated Value of Frequency
$\epsilon_r$	$f$ GHz	$a$ mm	$w$ mm	$d$ mm	$f_{\text{calculated}}$ GHz
2.2	2.52	5.2	0.6995	0.1204	2.5151
<b>2.2</b>	<b>2.45</b>	<b>5.1</b>	<b>0.6511</b>	<b>0.1003</b>	<b>2.4584</b>
3.78	2.47	4.5	0.6749	0.1076	2.4650

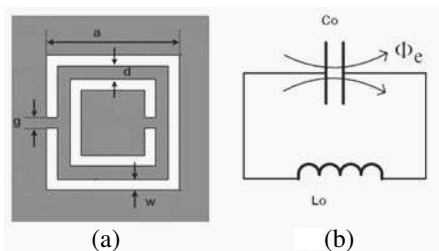


Figure 2: (a) Geometrical dimensions of the complementary square split ring resonator and (b) its equivalent LC circuit [6].

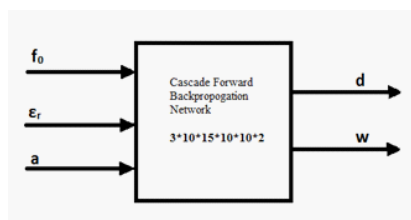


Figure 3: The black box model of the proposed neural network.

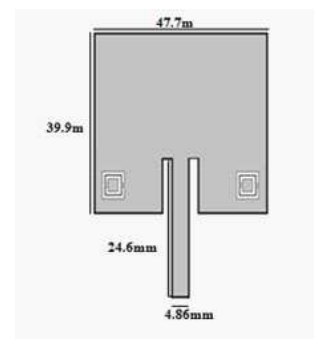


Figure 4: Metamaterial loaded patch antenna.

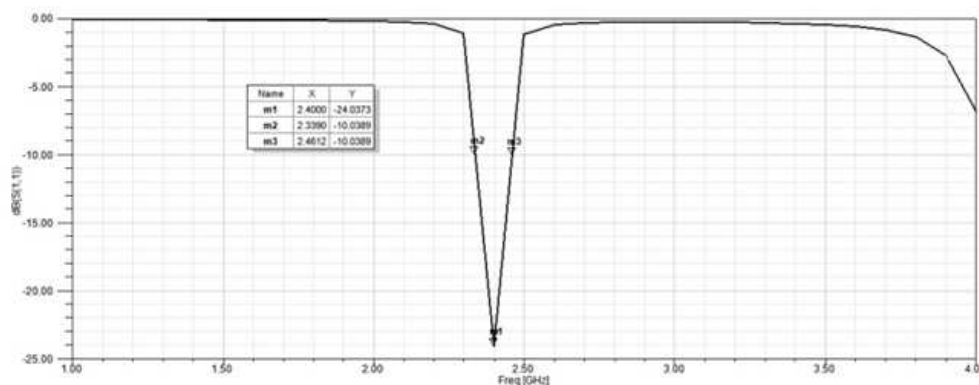


Figure 5: Return loss characteristics of the metamaterial loaded patch antenna.

optimized values of ' $w$ ' and ' $d$ ' can be obtained. The range of values for ' $f$ ' is  $3 \text{ GHz} < f < 16 \text{ GHz}$ , and ' $a$ ' is  $1 \text{ mm} < a < 10 \text{ mm}$  and  $\epsilon_r$  takes standard discrete values. The network has therefore 3 input neurons and 2 output neurons. Table 1 gives a few typical values of ' $w$ ' & ' $d$ ' obtained from the proposed network. The calculated value of frequency using the dimensions obtained from neural network is also included in the table.

## 5. CSRR LOADED PATCH ANTENNA

The CSRR structure behaves as an electric dipole. This high  $Q$  structure may not radiate well but is capable of transferring the energy to the patch and make the patch radiate at that particular resonant frequency [10]. This idea is utilized in dual band patch antenna to obtain smaller patch dimensions but in our work both patch and CSRR structure are designed for the same resonant frequency, the designed patch is shown in Figure 4. This particular design results in a wider bandwidth centered on resonant frequency of 2.4 GHz as compared to the regular inset fed rectangular patch antenna. The structure is analyzed using Ansoft HFSS software.

From the Figures 1 and 5, we could infer that the return loss at resonance is higher for the CSRR loaded antenna ( $-24.037 \text{ dB}$ ) as well as there is significant improvement in bandwidth. The

absolute bandwidth is calculated to be 5.07%. The gain of the antenna is measured to be 7.467 dB and the antenna is having radiation efficiency of 94.03 %.

## 6. CONCLUSION

The metamaterial loaded patch antenna is designed using ANN and simulated using HFSS software. The output of the multilayer perceptron network is shown in Table 1. Using the network the CSRR dimensions for any frequency, within the prescribed range, can be obtained. The return loss curve obtained from HFSS for both the antennas are shown in Figures 1 and 5. When compared with the parameters of inset fed rectangular patch antenna described in Section 2, we could observe a remarkable improvement in the absolute bandwidth as well as the return loss. There is a  $-12.63$  dB improvement in the antenna return loss and the bandwidth has improved approximately 3 times. The simulated value of radiation efficiency also shows slight improvement. The proposed design achieved the desired result without any change in rest of the parameters except gain, which is reduced by 0.2 dB as compared to the rectangular patch antenna. As a future work the design could incorporate methods to improve gain while providing a wider bandwidth.

## REFERENCES

1. Mahdy, M. R. C., Md. R. A. Zuboraj, A. Al Noman Ovi, and Md. A. Matin, "An idea of additional modified modes in rectangular patch antennas loaded with metamaterial," *IEEE Antennas and Wireless Propagation Letters*, Vol. 10, 2011.
2. Ha, J., K. Kwon, Y. Lee, and J. Choi, "Hybrid mode wideband patch antenna loaded with a planar metamaterial unit cell," *IEEE Transactions on Antennas and Propagation*, Vol. 60, No. 2, Feb. 2012.
3. Matin, M. A. and A. I. Sayeed, "A design rule for inset-fed rectangular microstrip patch antenna," *WSEAS Transactions on Communications*, Vol. 9, No. 1, Jan. 2010.
4. Marques, R., F. Mesa, J. Martel, and F. Medina, "Comparative analysis of edge and broad-side coupled split ring resonator for metamaterial design-theory and experimentation," *IEEE Transactions on Antennas and Propagation*, Vol. 51, No. 10, 2572–2581, Oct. 2003.
5. Baena, J. D., J. Bonche, F. Martin, R. M. Sirello, F. Falcone, T. Lopetegi, M. A. G. Laso, J. Garcia Garcia, and I. Gill, "Equivalent circuit models for split ring resonators and complementary split ring resonators coupled to planar transmission lines," *IEEE Microwave Theory and Techniques*, Vol. 53, No. 4, Apr. 2005.
6. Vidyalakshmi, M. R. and S. Raghavan, "Comparison of optimization techniques for square split ring resonator," *International Journal of Microwave and Optical Technology*, Vol. 5, No. 5, Sep. 2010.
7. Sri Rama Krishna, K., J. Lakshmi Narayana, and L. Pratap Reddy, "ANN models for microstrip line synthesis and analysis," *International Journal of Electrical and Computer Engineering*, Vol. 3, No. 15, 2008.
8. Balanis, C. A., *Antenna Theory Analysis and Design*, 3rd Edition, A John Wiley & Sons, Inc., Publication, 2005.
9. Garg, R., P. Bhartia, I. Bhal, and A. Ittiboon, *Microstrip Antenna Design Handbook*, Artech House, London, 2001.
10. Dong, Y. and T. Itoh, "Metamaterial-based antennas," *Proceedings of the IEEE*, Feb. 2012.
11. Lee, K.-F. and K.-F. Tong, "Microstrip patch antenna-basic characteristics and some recent advances," *Proceedings of the IEEE*, Vol. 100, No. 7, Jul. 2012.

# Wideband Small Loop-monopole HF Transmitting Antenna with Implications for Maxwell's Equations and the Chu Criterion

Michael J. Underhill

Underhill Research Ltd, Lingfield, UK

**Abstract**— A small un-tuned wideband loop-monopole transmitting antenna has been discovered and developed. A typical example can be fully contained in a sphere of radius  $a = 0.75$  m and has been measured to be efficient ( $> \sim 90\%$ ), in terms of power lost as heat, between 1.7 MHz and  $> 200$  MHz. This antenna can be considered to be small below 64 MHz. The antenna SWR typically varies from 11 : 1 at the lowest frequency to  $\sim 6 : 1$  at twice this (3.4 MHz) and  $< 6 : 1$  at higher frequencies. After matching at a given frequency, the operating bandwidth is thus  $> 16\%$ . An equivalent antenna  $Q$  can be estimated as  $< 6.6$ . This practically measured performance contradicts the Chu small antenna  $Q$  criterion by four orders of magnitude ( $\sim 11,000$ ) at the lowest frequency of operation.

To explain this discrepancy we introduce a simple explanation of radiation, reception and antenna  $Q$  in terms of currents, charges, and potentials as derived from the Coupled Transmission Line model of Electromagnetics [1]. This 'theory of radiation and reception' has been compared with, and calibrated by, available single mode small antenna  $Q$  value measurements. Thereafter good agreement between theory and practice is then (obviously) to be found. Part of the 'radiation and reception' theory includes a value of  $\kappa = 1/2\pi$  for the asymptotic electromagnetic coupling factor [2]. This value is confirmed by the measured small (loop) antenna  $Q$  values. Maxwell's equations should therefore be modified accordingly [2].

The Chu small antenna  $Q$  theory and criterion [3] is thus not validated either in theory or in practice, and should now, on the basis of the latest practical and theoretical evidence, be discarded and never used in the future for small antenna performance prediction.

A new fundamental discovery arising from this new antenna is the strong coupling that can take place between magnetic and electric modes in a small antenna. With the correct phase relationship enforced between the modes the radiation resistance is considerably enhanced and the effective antenna  $Q$  is considerably reduced. This process also accounts for the typical measured bandwidths of half-wave dipoles.

The conclusion is that such an effective small antenna could never have been predicted, or believed to be credible, without modification of Maxwell's Equations [2] to include electromagnetic coupling, and the creation of the new 'theory of radiation and reception'.

## 1. INTRODUCTION

A small antenna was required to meet the need for a highly portable wideband transmitting antenna for 'anomalous' wave-tilt measurements in the HF band [4]. Over fresh water or wet ground the wave-tilt direction was found to be reversed, hence 'anomalous', below about 5.3 MHz. The measurements were made for 40 to 70 m paths over wet ground and a freshwater lake for frequencies from 1.8 to 52 MHz. Over forty measurements, each taking about 20 minutes, were made. The transmitting antenna was a 80 cm diameter two turn multi-mode tuned loop with operating  $Q$  typically 170 at the lower frequencies, shown in Figure 4 of [4]. Such a loop has a  $Q$  reduced by about  $1/\sqrt{2}$  over a single turn single mode tuned loop of the same diameter. Re-tuning the transmitting antenna for a new frequency accounted for a large proportion of the measurement time. A portable wideband small transmitting antenna covering 1.8 to 52 MHz was required.

The  $\sqrt{2}$  increased bandwidth found for a pair of coupled magnetic loop modes gave an indication of how to proceed. The postulate was that if small antenna electric and magnetic modes could be tightly coupled together a further increase in bandwidth could be obtained. The results exceeded all expectations. And fundamental revision of antenna theory was now required.

## 2. DESCRIPTION OF NEW LOOP-MONOPOLE

Figure 1 is a picture and Figure 2 is a schematic of a 90 cm loop version of the new antenna. This loop-monopole consists of a vertical copper loop of 1 cm diameter tubing that is top fed directly by a sufficiently long 50 ohm coaxial cable. Two turns of the coaxial cable are loosely twisted around the copper loop. The lowest usable frequency is obtained with the copper loop connected to the

coaxial cable as shown giving favourable between the copper loop and the two turns of cable. In Figure 1, the lower coil of coaxial cable is about 43 m in length. The total cable length is 50 m. With the feeder cable coiled below the loop the total vertical extent of this antenna is 1.45 m. It appears that the coupled coaxial cable turns launch a travelling wave on the outside of the feeder cable even when it is coiled under the loop part of the antenna as shown in Figure 1. The lowest frequency of operation depends mainly on the total length of the cable. The two turns of cable and the copper loop act as the upper part of the monopole with the rest of the feeder cable, whether coiled or not, acting as the ground or counterpoise for the upper monopole. The loop is a vertically polarised magnetic mode antenna and the monopole is a vertically polarised electric mode antenna as a vertical dipole.

For two turns of the 50 ohm line and cable wound around the 90 cm loop of 10 mm copper tube, the antenna SWR varies from 11 : 1 at 1.7 MHz to  $\sim 6 : 1$  at twice this frequency (3.4 MHz) and  $< 6 : 1$  at higher frequencies, measured up to 200 MHz. Such SWR values are easy to match at any frequency with a standard Antenna Tuning Unit (ATU) to give at least a 16% operating bandwidth. An equivalent antenna  $Q$  can be estimated from the stored energy on a mismatched transmission line for a given SWR and Return Loss  $\rho$ . In this case we have  $Q < 6.6$  from the following equations.

$$SWR = (1 + \rho)/(1 - \rho) \quad \text{with} \quad Q = 2/(1 - \rho^2) \quad (1)$$

A useful reduction of the SWR at the lower frequencies was subsequently found by winding one more turn of the feeder cable onto the copper loop to give three wound turns without altering the total cable length of 50 m. The 11 : 1 SWR frequency is lowered by about 10% and the 6 : 1 SWR by 25%, as seen in Figure 3. This is now the recommended design for any size or diameter of loop.

Both Figure 2 and Figure 3 are results obtained from a ‘miniVNA pro’ Vector Network Analyser, made by mRS mini Radio Solutions, seen at the bottom of Figure 1. Two particular features are its small size and its Bluetooth connection to the control and display computer. Any explanation that small antennas can only radiate efficiently from the feeders outside the small antenna volume can thereby be discounted.

The total length of the feeder cable was found to be the main parameter determining the lowest frequency of operation of the antenna. In Figure 4, the SWR steps down to  $\sim 10 : 1$  when the total coaxial cable length is a quarter wave  $\lambda/4$ , and steps down to  $\sim 6 : 1$  when the cable length is  $\lambda/2$ .

A surprising discovery was that coiling the feeder cable as shown in Figures 1 and 2 makes practically no difference to the lowest frequency of antenna operation. The change in measured antenna SWR and impedance were found to be insignificant. This was also confirmed by the ‘Bluetooth-isolated’ Vector Network Analyser, miniVNA pro. When the cable is coiled the loop-dipole is a true small antenna. This discovery implies that the main part of the energy of the surface wave on a cable or wire is confined to no more than about two or three wire conductor diameters in total distance outside the conductor, confirming  $n = 3$  in Equation (1) of [1].

### 3. IMPACT ON THE CHU SMALL ANTENNA $Q$ CRITERION

The original Chu-Wheeler small antenna  $Q$  criterion [3] states that for antennas completely contained inside a sphere of radius  $a$ , and where  $k$  is the propagation constant  $2\pi/\lambda$ , the  $Q$  cannot



Figure 1: Picture of 90 cm loop-monopole with MiniVNApro (Bluetooth connected) vector network analyser at bottom.



Figure 2: Schematic of loop-monopole seen in Figure 1.

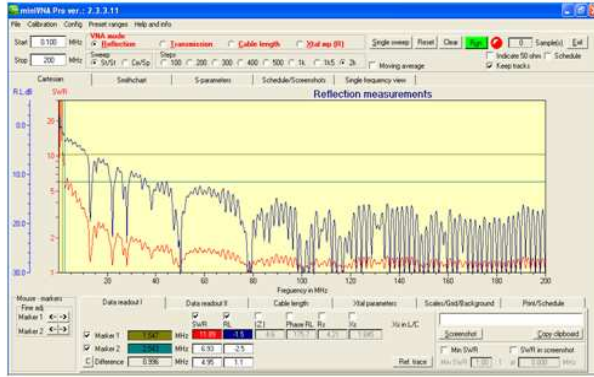


Figure 3: For frequency range 0.1 to 200 MHz the SWR (lower red plot) and Return Loss (upper blue plot) for loop-monopole of 3 turns on loop of a total feeder length of 50 m.

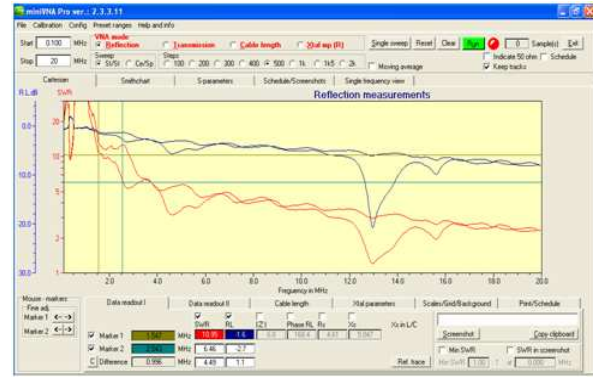


Figure 4: As in Figure 2 but for frequency range 0.1 to 20 MHz.

be less than  $1/(ka)^3$  unless the antenna is inefficient and has a significant loss resistance. The new loop-monopole design can for example be contained in a sphere of radius  $a = 0.75$  m and it can be considered to be small below 64 MHz. It has been measured to be efficient ( $> \sim 90\%$ ), in terms of power lost as heat and discounting internal cable losses, between 1.8 MHz and 200 MHz. The antenna can radiate 700 watts continuous power at 3.7 MHz without appreciable heat being generated. This was tested first by hand and then confirmed by a Protek IR camera.

Taking an antenna  $Q$  value of 6.6 as calculated from Equation (2), the practically measured performance contradicts the Chu-Wheeler small antenna  $Q$  criterion by four orders of magnitude ( $\sim 11,000$ ) at the lowest frequency of operation. At the heat test frequency of 3.7 MHz the loop dipole  $Q$  is about 4.5 and then the discrepancy with respect to the Chu Wheeler  $Q$  is about 1,100.

The above  $Q$  and antenna efficiency results firmly contradict the Chu Small Antenna  $Q$  Criterion. References [5] and [6] are now confirmed as valid and not to be challenged. Thus the Chu criterion has no credibility and should no longer be used. The claim is that the Chu criterion is derived directly from Maxwell's Equations. It follows that Maxwell's Equations should now be modified and improved [2] to agree with the measured facts.

#### 4. THE GENERALISED POYNTING VECTOR

The Poynting Vector (PV) can be modified to become a Generalised Poynting Vector (GPV),  $S$ , where its in-phase or 'real' ( $\Re$ ) component represents travelling wave energy per unit volume and its quadrature or 'imaginary' ( $\Im$ ) component the stored energy density per unit volume. For convenience the components may be expressed as power and standing wave power per unit surface [2]. In either representation the  $Q$  is the ratio of the quadrature component to the in-phase component. We can also represent the Poynting Vector in terms of like pairs of potentials  $\Phi$  and currents  $I$  [7, 8]. We thus have

$$S = E \times H = \Phi \times I \quad \text{with} \quad Q = \frac{\Im[E \times H]}{\Re[E \times H]} = \frac{\Im[Q \times I]}{\Re[Q \times I]} \quad (2)$$

Because the antenna is small it is contained within a region in which the EM coupling is strong so the potentials and induced energy densities are essentially uniform in the 'coupled' region of space. Also by observing that along a transmission line the peak energy densities of charge and current per unit length are the same, we can define charge per unit length  $q$  as quadrature current  $-ji$ . We can also define the respective potentials  $\Phi_i$  and  $\Phi_q$  as being in quadrature. In this way, we find that radiation from charges and currents are separate processes that can take place in different parts of an antenna, as seen in Figures 5(a) and 5(d). Thus we have

$$\Phi_q = j\Phi_i, \quad i = jq, \quad \Phi = \Phi_i - j\Phi_q, \quad I = i + jq \quad (3)$$

#### 5. THEORY OF RADIATION AND RECEPTION

A simple physical theory of (small) antenna operation is: "it is the *coupling* in the antenna that radiates or receives". This concept is in agreement with the 'Ether Lens' model [7]. Figure 5 shows two types of coupling. Self-coupling causes radiation in electric or magnetic single mode small

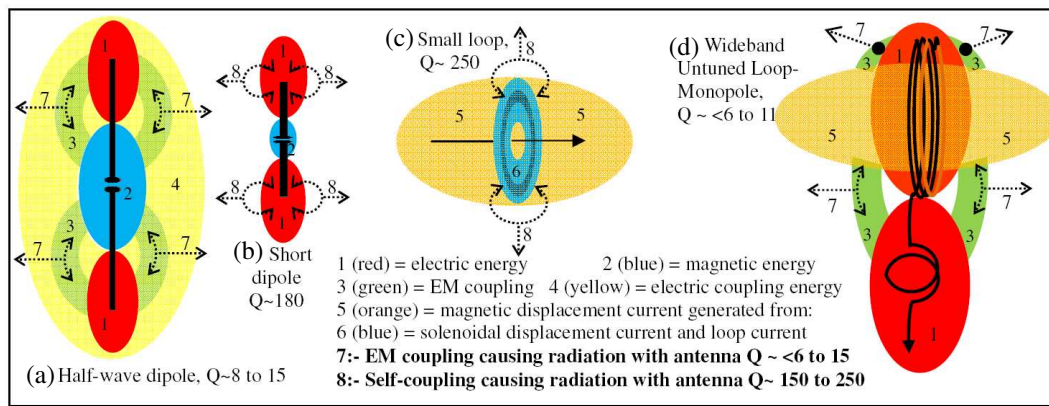


Figure 5: Electric and magnetic antenna radiation mechanisms in (a) half-wave dipole, (b) short dipole, (c) small loop, and (d) wideband untuned loop-monopole. **“It is the coupling that radiates”**.

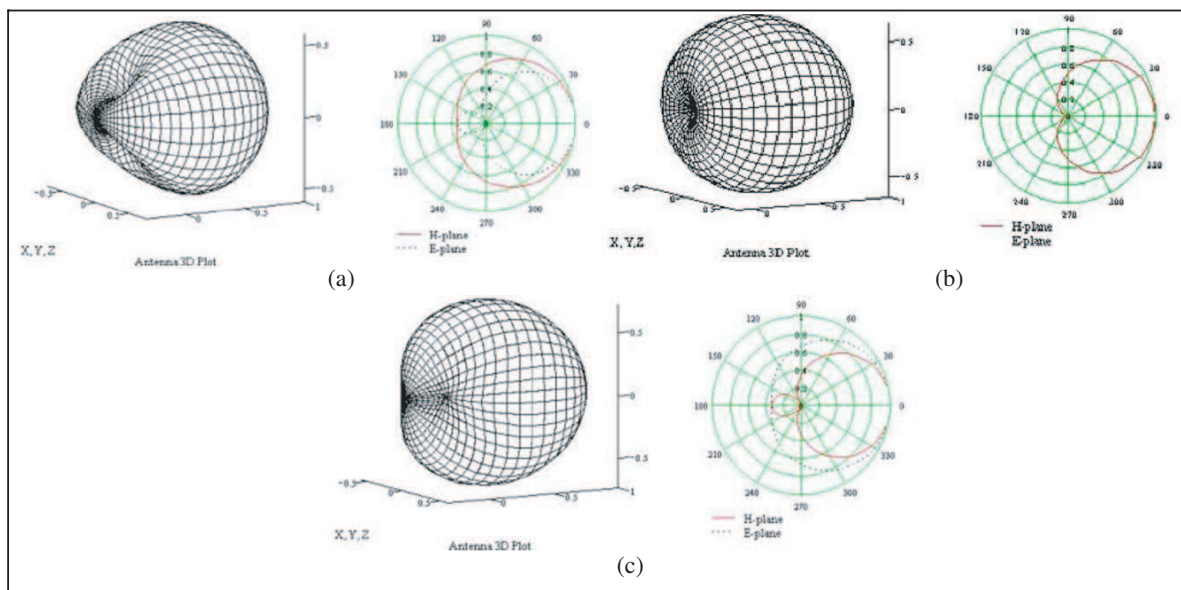


Figure 6: Loop-monopole antenna patterns for ratios of electric  $E$  mode to magnetic  $M$  mode: (a)  $E/M = 2$ , (b)  $E/M = 1$ , and (c)  $E/M = 1/2$ .

antennas and it typically gives antenna  $Q$ s between 180 and 250. EM or mixed mode coupling between two modes of different types, electric and magnetic, gives  $Q$ s between  $\sim 6$  and  $\sim 15$ .

An equivalent explanation of the new ‘radiation and reception’ theory is: “an antenna conductor surface is transmitting when the external potential has a component that is in-phase with the current, and the antenna surface is receiving when the external potential has a component that is out of phase with the current induced in the antenna surface”. This can be deduced from the properties of the Generalised Poynting Vector.

The half wave dipole (a) in Figure 5 can be seen to be a mixed mode antenna, because the ends of the antenna can radiate from the oscillating charges and the centre of the antenna radiates from the oscillating current. In fact most of the radiation comes from the EM coupling of the two mode types. In this respect the loop-monopole (d) is similar. Both antennas are found to have low  $Q$ s,  $\sim 2\pi$  to  $5\pi$ , or  $\sim 6$  to  $15$ . The two small antennas (b) and (c) radiate by ‘self-coupling’, which is weaker, and are found to have  $Q$ s of  $\sim (1/\sqrt{2})(2\pi)^3 \approx 175$  and  $(2\pi)^3 \approx 250$  respectively. The  $(1/\sqrt{2})$  reduction of  $Q$  is found when two modes of the same type are strongly coupled as for the ends of a short dipole (b). A thin half-wave dipole has less coupling from the ends to the centre and thus a higher  $Q$ , up to about  $5\pi$ .

For convenience we temporarily define currents and potentials in units that give them equal energy. We have  $\kappa_0 = 1/(2\pi)$  as the limiting or asymptotic EM coupling factor at a point. Also for

antennas we find that  $Q$  is the reciprocal of the total coupling factor. We can then observe that self-coupling is 3 step coupling process with induced displacement current around the conductor as an intermediary. Its basic  $Q$  is thus expected to be  $(1/\kappa_0)^3 = (2\pi)^3 \approx 250$ . The coupling between different mode types that are simultaneously excited with the correct phase is single step and a  $Q$  of about  $1/\kappa_0 = 2\pi \approx 6$  is to be expected.

Note that potentials combine according to the classical rules of vector addition, whereas displacement currents combine according to the RSS (Root-Sum-of-the-Squares) vector addition rule [2]. We also find that radiation and loss resistances of a ‘multi-mode’ antenna all combine according to the RSS rule [5, 6]. Thus ‘process capture’ occurs where the strongest antenna mode with highest radiation resistance dominates and suppresses all other modes and any loss resistances.

## 6. ANTENNA PATTERN OF LOOP-MONOPOLE

The loop-monopole has been found to be usefully uni-directional (3 to 12 dB) over significant parts of the operating frequency range. The antenna pattern depends on the proportion of the electric monopole mode to the magnetic loop mode as shown in the Mathcad simulations in Figure 6. The simulation methodology is that of ‘Analytic Region Modelling, ARM’ [10].

## 7. CONCLUSIONS

A novel small high power wideband loop-monopole emphatically contradicts the Chu small antenna  $Q$  criterion, and this criterion can no longer safely be used as a small antenna design rule. The classical Maxwell equations need to be revised and extended to include ‘electromagnetic coupling’ and ‘energy conservation’. The unexpectedly low value of effective antenna  $Q$  has been shown to be the result of strongly (electromagnetically) coupled and approximately equally excited electric and magnetic modes occupying the same near-field volume. The importance of ‘electromagnetic coupling’ has once again been demonstrated [1, 2]. The polar diagram of the loop-monopole antenna has been found to be usefully uni-directional at some frequencies (3 to 12 dB). Improved variants of the loop-monopole design appear to be feasible.

## REFERENCES

1. Underhill, M. J., “A physical model of electro-magnetism for a theory of everything,” *PIERS Online*, Vol. 7, No. 2, 196–200, 2011.
2. Underhill, M. J., “Maxwell’s transfer functions,” *PIERS Proceedings*, 1766–1770, Kuala Lumpur, Malaysia, Mar. 27–30, 2012.
3. Chu, L. J., “Physical limitations of omni-directional antennas,” *J. Appl. Phys.*, Vol. 19, 1163–1175, Dec. 1948.
4. Underhill, M. J., “Anomalous ground wave tilt measured over wet ground,” *IET Conf. on Ionospheric Radio Systems and Techniques*, Royal York Hotel, York, UK, May 15–17, 2012.
5. Underhill, M. J. and M. Harper, “Simple circuit model of small tuned loop antenna including observable environmental effects,” *IEE Electronics Letters*, Vol. 38, No. 18, 1006–1008, 2002.
6. Underhill, M. J. and M. Harper, “Small antenna input impedances that contradict the Chu-Wheeler  $Q$  criterion,” *Electronics Letters*, Vol. 39, No. 11, May 23, 2003.
7. Underhill, M. J., “A local ether lens path integral model of electromagnetic wave reception by wires,” *PIERS Proceedings*, 1005–1008, Moscow, Russia, Aug. 19–23, 2012.
8. Underhill, M. J., “Antenna pattern formation in the near field local ether,” *PIERS Proceedings*, 1009–1012, Moscow, Russia, Aug. 19–23, 2012.
9. Underhill, M. J. and M. J. Blewett, “Unidirectional tuned loop antennas using combined loop and dipole modes,” *8th Int. Conf. on HF Radio Systems and Techniques*, (*IEE Conf. Publ. No. 474*), 37–41, 2000.
10. Underhill, M. J., “Novel analytic EM modelling of antennas and fields,” *PIERS Proceedings*, 1771–1775, Kuala Lumpur, Malaysia, Mar. 27–30, 2012.

# Performance Characteristics of Loop Antennas above a Ground Plane of Finite Extent

A. A. Ayorinde<sup>1</sup>, S. A. Adekola<sup>1,2</sup>, and A. Ike Mowete<sup>1</sup>

<sup>1</sup>Department of Electrical and Electronics Engineering, Faculty of Engineering  
University of Lagos, Lagos, Nigeria

<sup>2</sup>Department of Electrical and Electronics Engineering, Niger Delta University  
Wilberforce Island, Yenegoa, Nigeria

**Abstract**— This paper examines the characteristic behaviors of the feed-point input impedance and radiation fields of two thin-wire loop antenna types (one a circular-loop and the other, a square-loop antenna) both, one wavelength ( $1\lambda$ ) long at the operating frequency, and located over a ground plane which is of the wire-grid variety [1], and whose extent is finite.

Using the moment-method approach, computational results are obtained in the presentation, for the antennas' performance parameters alluded to in the foregoing, to suggest that the square loop antenna resonates when located at a distance of  $0.054\lambda$  above the ground plane; whereas the corresponding distance for the circular-loop emerges as  $0.132\lambda$ . The results also indicate that the antennas' directive gains and input impedance profiles are such as to suggest that they may be suitable for practical applications over a wide range of frequencies.

A comparison carried out in the paper, between computed values of input impedance and corresponding measurement results reported elsewhere [2], very clearly indicate that the approach described in this presentation is valid.

## 1. INTRODUCTION

Whereas the first analysis of the single element circular-loop antenna was that reported by Pockington [7], in which the antenna configuration did not include a backing structure, in practical applications, a number of advantages are offered when the loop antenna is mounted over a ground plane: for example, the inclusion of the ground plane permits the use of a coaxial feed without significantly affecting the wire antenna's input impedance characteristics [8]. Most of the subsequent analytical efforts [2, 3], addressed the problem of the loop antenna located over a ground plane, and it is then the norm to regard the ground plane as being a perfect conductor of infinite extent; so that the image theory applies, to simplify analysis. One important consequence, of the infinite ground plane, for the loop antenna's performance features, is that the antenna's characteristic bidirectional radiation pattern is transformed to a unidirectional pattern in the vertical plane [8], so that its directivity in that plane also increases. Crowell [10], described analytical results, which indicate that the infinite ground plane significantly influences the impedance of any antenna that it serves as a backing structure. It would appear though, that these influences of the ground plane are not reproduced, when the plane is of finite extent. Meier [9] in 1949, investigated the influences of a finite ground on the radiation patterns and input impedances of wire antennas located over it, and reported measurement results to suggest that although input impedance is very sensitive to the shape and size of the ground plane, it is relatively independent of the plane's thickness. On the other hand, Crowell [10], reports that the radiation pattern of wire antennas backed by finite ground planes is a strong function of the size of the ground plane. And as noted by him, this antenna type finds common use as an array element in array antennas deployed for use in aircraft landing aids installed close to all airports.

Quite a few research efforts have focused on the nature of the radiation pattern of loop antennas located over a finite ground plane. These include the paper by Hassan and his associates [11], which, using the Fourier series and a FFT algorithm, investigated the effects of finite ground plane size on antenna maximum gain; as well as established the bounds on size, below which the 'infinite plane approximation' may not apply. The computational results obtained in that presentation indicate, among other things, that when the circular loop antenna is located over a rectangular-shaped ground plane of finite dimensions, the antenna's radiation pattern varies significantly with both plane size and height of antenna above the ground plane. Crowell [10] also described similar results, observing that the directions of both pattern null and maximum depend of ground plane dimensions and height of antenna above the plane.

In this presentation, we investigate the electromagnetic response (in terms of radiation pattern and feed point impedance) of the loop antenna located over a finite ground plane, in a moment method approach that utilizes the circular loop and the square loop as source candidates. A rectangular-shaped wire grid is selected as ground plane, as it has been reported elsewhere that the wire grid tends to improve the stability of the input impedance of wire antennas located over them [1], and also improves bandwidth performance [6]. Computational results described in the paper suggest that for a given size of the finite-dimensioned wire-mesh ground plane, input impedance depends significantly on height above the ground plane; and that the nature of the dependence is different for the square and circular loops. Results obtained for the directive gain are consistent with those reported earlier in the literature [2, 10].

## 2. THEORY

Figure 1 describes the problem geometry for a loop antenna mounted above a finite wire-grid ground plane in which both the grid elements and the loop are regarded as satisfying the thin-wire approximation of interest to a moment-method [5] analysis. Accordingly, it is taken that the antenna structure is illuminated by a plane wave here denoted by  $E_{inc}$  such that the field scattered by the antenna assumes the form

$$E_{\theta} = E_{c\theta} + \sum_{n=1}^N E_{n\theta}^x + \sum_{n=1}^N E_{n\theta}^y \quad (1a)$$

and

$$E_{\phi} = E_{c\phi} + \sum_{n=1}^N E_{n\phi}^x + \sum_{n=1}^N E_{n\phi}^y \quad (1b)$$

provided that  $E_{c\theta}$ ,  $E_{n\theta}^x$  and  $E_{n\theta}^y$  represent the  $\hat{\mathbf{a}}_{\theta}$ -components of the electric fields due, respectively, to the distributions of current along the axes of the circular loop,  $n$ th  $x$ -directed, and  $n$ th  $y$ -directed thin-wires; whilst  $E_{c\phi}$ ,  $E_{n\phi}^x$  and  $E_{n\phi}^y$  are the corresponding  $\hat{\mathbf{a}}_{\phi}$ -components. It is readily established that these far-zone field components are, for the  $\hat{\mathbf{a}}_{\theta}$ -components given by

$$E_{c\theta} = \frac{-j\omega\mu_0 e^{-jk_0 r} \cos\theta}{4\pi r} \int_0^{2\pi} \sin(\phi - \phi') I(\phi') e^{jk_0 [a \cos(\phi - \phi') \sin\theta + h \cos\theta]} d\phi' \quad (2a)$$

$$E_{n\theta}^x = \frac{-j\omega\mu_0 e^{-jk_0 r} \cos\theta \cos\phi}{4\pi r} \int_{-L/2}^{L/2} I(x') e^{jk_0 [x' \cos\phi \sin\theta + (n-5)\frac{\lambda}{8} \sin\phi \sin\theta]} dx' \quad (2b)$$

and

$$E_{n\theta}^y = \frac{-j\omega\mu_0 e^{-jk_0 r} \cos\theta \sin\phi}{4\pi r} \int_{-L/2}^{L/2} I(y') e^{jk_0 [y' \sin\phi \sin\theta + (n-5)\frac{\lambda}{8} \cos\phi \sin\theta]} dy' \quad (2c)$$

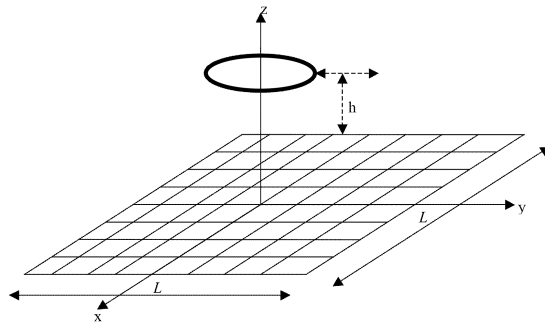


Figure 1: Problem geometry: loop antenna mounted over a finite wire-grid ground plane.

$$E_{c\phi} = \frac{-j\omega\mu_0 e^{-jk_0 r}}{4\pi r} \int_0^{2\pi} \cos(\phi - \phi') I(\phi') e^{jk_0 [a \cos(\phi - \phi') \sin \theta + h \cos \theta]} d\phi' \quad (3a)$$

$$E_{n\phi}^x = \frac{j\omega\mu_0 e^{-jk_0 r} \sin \phi}{4\pi r} \int_{-L/2}^{L/2} I(x') e^{jk_0 [x' \cos \phi \sin \theta + (n-5) \frac{\lambda}{8} \sin \phi \sin \theta]} dx' \quad (3b)$$

$$E_{n\phi}^y = \frac{-j\omega\mu_0 e^{-jk_0 r} \cos \phi}{4\pi r} \int_{-L/2}^{L/2} I(y') e^{jk_0 [y' \sin \phi \sin \theta + (n-5) \frac{\lambda}{8} \cos \phi \sin \theta]} dy', \quad (3c)$$

for the  $\hat{\mathbf{a}}_\varphi$ -components.

The moment-method solution to the unknown distributions of current emerges from the well-known [5] matrix expression given as

$$\begin{bmatrix} [I_k^l] \\ [I_k^g] \end{bmatrix} = \begin{bmatrix} [Z_{ik}^{ll}] & [Z_{ik}^{lg}] \\ [Z_{ik}^{gl}] & [Z_{ik}^{gg}] \end{bmatrix}^{-1} \begin{bmatrix} [V_i^l] \\ [0] \end{bmatrix} \quad (4a)$$

where, for this problem,

$$\begin{bmatrix} [Z_{ik}^{ll}] & [Z_{ik}^{lg}] \\ [Z_{ik}^{gl}] & [Z_{ik}^{gg}] \end{bmatrix} = \begin{bmatrix} [\langle W_i^l, L [T_k^l] \rangle] & [\langle W_i^l, L [T_k^g] \rangle] \\ [\langle W_i^g, L [T_k^l] \rangle] & [\langle W_i^g, L [T_k^g] \rangle] \end{bmatrix} \quad (4b)$$

The superscripts 'l' and 'g' appearing in (4) identify contributions to the generalized impedance matrix by loop and grid elements, respectively, of the antenna structure; whilst  $W_i$  and  $T_k$  respectively represent the piece-wise linear weighting and expansion functions utilized.

Having, in this manner, determined the distribution of currents and associated radiated fields by virtue of Equations (3) and (4), the feed-point input impedance and the directive gain of the antenna system can now be computed using the standard formulas. The input impedance symbolized by  $Z_{in}$  is given by

$$Z_{in} = R_{in} + jX_{in} = \frac{V_{in}}{I_{in}} \quad (5)$$

where  $V_{in}$  is the excitation voltage of a delta-gap generator connected to the loop antenna,  $I_{in}$  the current at the feed-point,  $R_{in}$  the resistive component of the input impedance and  $X_{in}$  the reactive component of the input impedance. On the other hand, the directive gain of the antenna system is calculated using the standard formula [4]:

$$G_d(\theta, \phi) = \frac{[|E_\theta(\theta, \phi)|^2 + |E_\phi(\theta, \phi)|^2] r^2}{60P_{in}} \quad (6)$$

where  $r$  is the distance from the origin to the far-field observation point.

### 3. RESULTS

For the numerical computations of antenna parameters of interest to the presentation, use is made of the following values: wire radius =  $0.001\lambda$ ; centre frequency  $f_o = 1.25$  GHz; loop perimeter =  $1\lambda$ ; square ground plane size:  $1\lambda \times 1\lambda$  which is divided into 64 grids; loop height above the gridded ground plane ranges as  $0.025\lambda \leq h \leq 0.3\lambda$ ; excitation voltage =  $1.0$  V; in the computer program developed for the problem. It should be pointed out that the circular loop is fed at  $\varphi = 0^\circ$  while the feed-point of the corner-fed square loop is identified by the coordinates  $x = 0.125\lambda$  and  $y = -0.125\lambda$ . The numerical results obtained are presented in graphical formats and discussed in the ensuing sections.

### 3.1. Far-zone Fields

One of the main outcomes of backing an antenna with a large ground plane is the occasioning of a unidirectional radiation pattern in the forward direction. In this regard, we focus mainly on the radiated fields in the two vertical planes viz.  $\varphi = 0^\circ$  and  $\varphi = 90^\circ$ , as a means of evaluating the effectiveness of the wire-grid plane as a good reflector when compared with the conventional metallic ground plane. Of course, the resultant radiated fields as expressed by Eqs. (2) and (3) are the superposition of fields due to the current excited on the loop and the fields due to induced currents on the grid wires.

The  $E_\varphi$  patterns on the  $\varphi = 0^\circ$  plane for the square and circular loops at different antenna heights are shown in Figures 2(a)–(d). The radiation patterns, when  $h$  is fixed at  $0.05\lambda$  and  $0.1\lambda$ , which are depicted in Figures 2(a) and (b), respectively, show a significant radiation in the backward direction, although the main lobe is in the forward direction. However, at  $h = 0.25\lambda$  and  $0.3\lambda$ , the back-lobe has diminished remarkably as evident in Figures 2(c) and 2(d), but the beam directivity has reduced when compared with those patterns at  $h = 0.05\lambda$  and  $0.1\lambda$ . It is noteworthy that at antenna height  $0.25\lambda$  which is the typical antenna height above a flat ground plane, the wire-grid ground plane deployed in this paper yields desirable radiation patterns from both the one-wavelength circular and square loops as can be seen from Figure 2(c). This observation is also true for the patterns at  $h = 0.3\lambda$ .

Although not shown here, at antenna height above  $0.3\lambda$ , the main lobe of the radiation pattern is somewhat distorted, and later degenerated into multiple lobes as the height increases. The difference between the  $E_\varphi$  patterns of the circular loop and square loop is negligible as observed from Figures 2(a)–(d).

The  $E_\theta$  patterns in the  $\varphi = 90^\circ$  plane when  $h$  varies between  $0.05\lambda$  and  $0.3\lambda$  for both the circular and square loops are displayed in Figures 3(a)–(d). As observed for the  $E_\varphi$  patterns when  $h = 0.05\lambda$  and  $0.1\lambda$ , that is, when the loop is close to the wire-grid ground plane, there is significant radiation in the backward direction based on Figures 3(a) and (b). On the other hand, at  $h = 0.25\lambda$  and  $0.3\lambda$ , there is a marked reduction in the back-lobe with an associated decrease in the main-beam directivity. Furthermore, it is noted that the patterns when  $h = 0.05\lambda$  and  $0.1\lambda$  are more directive than those ones at  $h = 0.25\lambda$  and  $0.3\lambda$ . As earlier noticed for the  $E_\varphi$  patterns in the  $\varphi = 0^\circ$  plane,

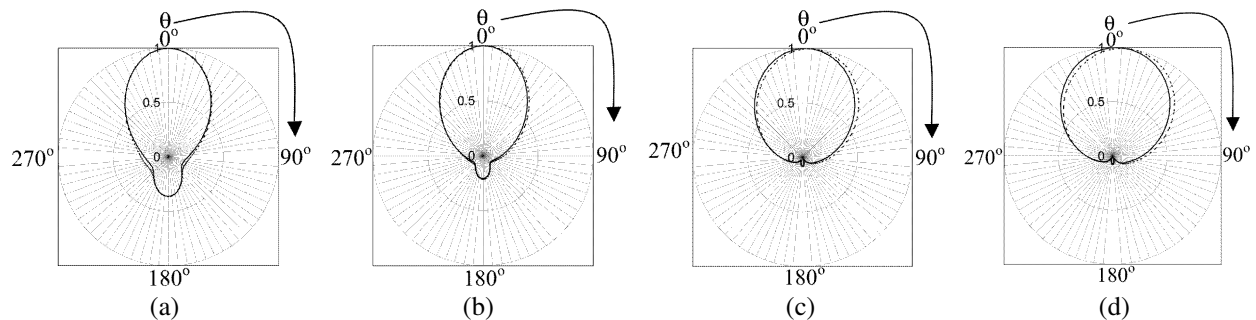


Figure 2: Radiated  $E_\varphi$  component on the  $\varphi = 0^\circ$  plane by the circular and square loop antennas: — circular loop; - - - square loop.

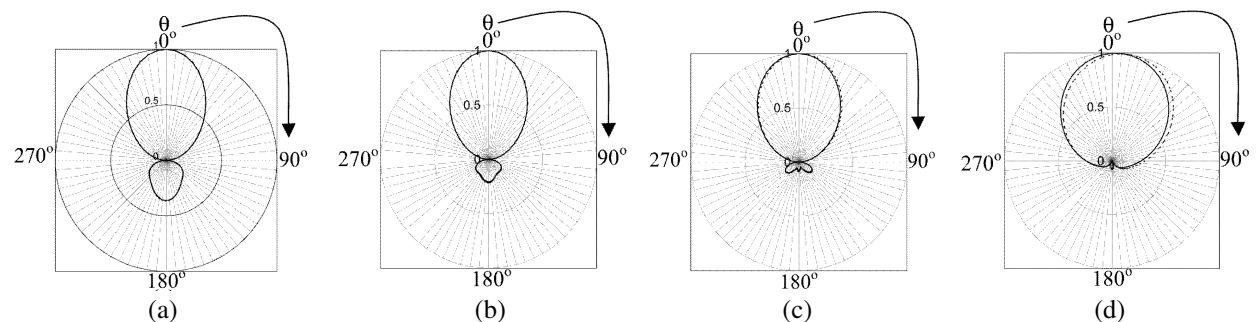


Figure 3: Radiated  $E_\theta$  component on the  $\varphi = 90^\circ$  plane by the circular and square loop antennas: — circular loop; - - - square loop.

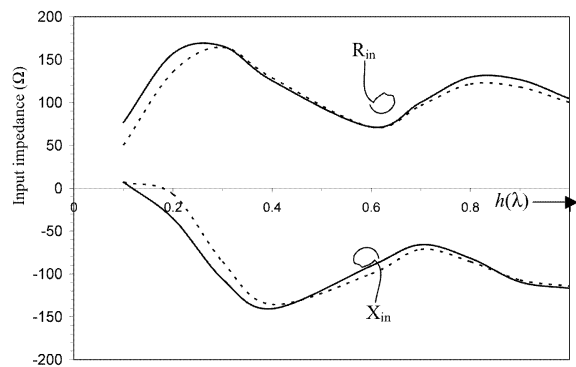


Figure 4: Comparison between the computed input resistance ( $R_{in}$ ) and reactance ( $X_{in}$ ) of the circular loop antenna against the antenna height and the corresponding measured results of Rajarayamonet and Sekiguchi (1976): — computed; - - - measured.

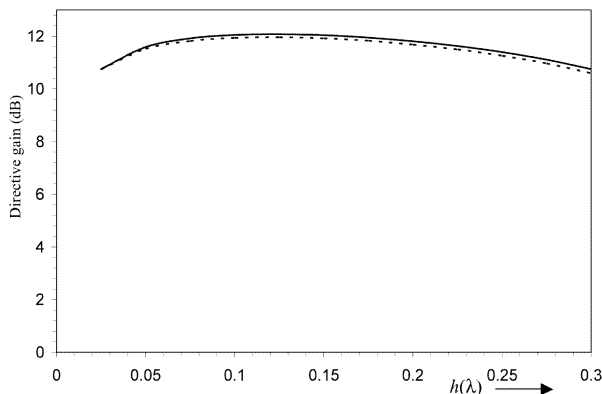


Figure 5: The directive gain of the circular and square loop antennas against the antenna height: — circular loop; - - - square loop.

the  $E_\theta$  patterns in the  $\varphi = 90^\circ$  plane for both circular and square loops are almost identical. It is worthy of mention that the patterns obtained at  $h = 0.25\lambda$  are essentially the same as that reported by Rojarayamont and Sekiguchi [2], who utilized a solid reflector as the backing structure for a one-wavelength circular loop antenna.

### 3.2. Input Impedance

Computational results (not displayed here) reveal that the input resistance increases somewhat linearly for values of  $h$  less than  $0.2\lambda$ , and remains fairly constant for those values of  $h$  greater than  $0.2\lambda$ , in both cases of square and circular loops. It is also observed that for all the antenna heights specified, the input resistance of the square loop is lower in magnitude than that of the circular loop. At lower values of  $h$ , the input reactance is inductive while at higher values of  $h$ , it is capacitive. We find also, that the circular loop resonates when  $h = 0.132\lambda$  while the square loop resonates at  $h = 0.054\lambda$ , suggesting that a desirable input impedance at the terminals of a one-wavelength loop antenna may be achieved through a choice of the antenna height above the wire-mesh ground plane. To check the validity of the foregoing observations, the computed input impedance results for values of  $h$  between  $0.1\lambda$  and  $1.0\lambda$  are compared, as shown in Figure 4, with the measured impedance data reported by Rajarayamont and Sekiguchi [2], who employed the conventional ground plane.

Clearly, the agreement between the calculated and measured values is satisfactory and indicative of a valid formulation..

### 3.3. Directive Gain

Figure 5 describes the computational results obtained for the antennas' directive gains, in the forward direction ( $\theta = 0^\circ$ ,  $\varphi = 0^\circ$ ) as a function antenna height.

It is interesting to observe that the directive gain profiles are almost flat for both loops with an average value of 11.5 dB. But the directive gain of an isolated circular loop is calculated, on the average, to be 3.42 dB while that of an isolated square loop is 3.08 dB. This distinct increase in the directive gain may be attributed to the presence of the wire-mesh ground plane, which, as noted by Wait and Spies [1], leads to a marked improvement of the radiation in the forward direction.

## 4. CONCLUDING REMARKS

The dependence of feed-point input impedance and radiation properties of one-wavelength circular and square loop antennas on the antenna height above a wire-grid ground plane have been presented here. Numerical results obtained indicate that the circular loop resonates at the loop height of  $0.132\lambda$  while the square loop resonates at  $0.054\lambda$ , where  $\lambda$  stands for the operating wavelength. However, both loops have an average directive gain of 11.5 dB in the forward direction when the loop height varies from  $0.025\lambda$  to  $0.3\lambda$ . The calculated feed-point input impedance is compared with the measured data of Rajarayamont and Sekiguchi [2], which shows good agreement.

**REFERENCES**

1. Wait, J. R. and K. P. Spies, "On the radiation from a vertical dipole with an inductive wire-grid system," *IEEE Trans. Ant. & Prop.*, Vol. 18, No. 4, 558–560, 1970.
2. Rajarayamont, B. and T. Sekiguchi, "One-element loop antenna with finite reflector," *Elect. & Comm.*, Vol. 59B, No. 5, 68–75, 1976 (in Japanese).
3. Nakano, H., N. Suzuki, T. Ishii, and J. Yamauchi, "Mesh antennas for dual polarization," *IEEE Trans. Ant. & Prop.*, Vol. 49, No. 5, 715–723, 2001.
4. Stutzman, W. L. and G. A. Thiele, *Antenna Theory and Design*, 306–374, John Wiley & Sons, New York, 1997.
5. Harrington, R. F. and M. S. Mautz, "Electromagnetic behaviour of circular wire loops with arbitrary excitation and loading," *Proc. IEE*, Vol. 115, No. 1, 68–77, 1968.
6. Nakano, H. and K. Nakayana, "A curved spiral antenna above a conducting cylinder," *IEEE Trans. Ant. & Prop.*, Vol. 47, No. 1, 3–8, 1999.
7. Pocklington, H. C., "Electrical oscillations in wire," *Camb. Philos. Soc. Proc.*, Vol. 9, 324–332, 1897.
8. Smith, G. S., "Loop antennas," *Antenna Engineering Handbook*, Richard C. Johnson, Ed., 3rd Edition, Chapter 5, McGraw-Hill, 1984.
9. Meier, A. S., "Measured impedance of vertical antennas over finite ground plane," *Proc. IRE*, Vol. 37, No. 6, 609–616, 1949.
10. Croswell, W. F., "Types of antennas," *Standard Handbook of Electronic Engineering*, Chapter 5, McGraw-Hill Book Company, 2004.
11. Hassan, H. A. N., S. D. Gedney, and K. W. Whites, "Effect of a finite ground plane on radiated emissions from a circular loop antenna," *Trans. IEEE EMC*, Vol. 36, No. 4, 364–370, 1994.

# Design and Analysis of a Stripline Archimedean Snail Antenna

T.-K. Chen and G. H. Huff

Department of Electrical and Computer Engineering  
Texas A&M University, College Station, TX 77843, USA

**Abstract**— This paper presents an analysis of a stripline Archimedean snail antenna on its impedance properties and radiation mechanism. The Archimedean snail antenna has similar structure to the spiral one but with asymmetric spiral turns on arm structures. Power can be transmitted from stripline mode to spiral radiating mode because of impedance matching between the two transmission line structures, i.e., stripline and parallel elevated slot-lines. The radiation occurs when the two elevated slot-line modes are in-phase, namely, common mode radiation. A design process can then be developed by impedance matching for the stripline Archimedean snail antenna. A compact ( $45\text{ mm} \times 40\text{ mm} \times 1.016\text{ mm}$ ) stripline-fed snail antenna is fabricated for demonstration. The measurement shows a good agreement with the simulated result from 2 GHz to 20 GHz. The snail type antenna has better performance than the spiral antenna due to its radiation mechanism. Compared to the traditional spiral antenna, this antenna design is a completely planar antenna, which provides a platform for integration of impedance matching circuits or other circuit elements easily inside the antenna structure without additional need of wideband balun and matching circuit designs.

## 1. INTRODUCTION

The highly demand for broadband wireless communications has been increasing by reason of higher communication data rate with data transmission on several separate spectrum [1, 2] or integration of assorted wireless services [3, 4]. As a result, a lot of researches and development have been focused on the study of modeling, design, optimization, and measurement methodology of broadband antennas [5, 6]. The spiral antennas, which easily cover the bandwidth over 20 : 1 with excellent circular polarization, have long been a popular choice for broadband radiating systems and continue to be relevant in high-performance communication systems based on multifunctional or hybrid concepts. From a design point of view, the Archimedean and equiangular spiral antennas have received wide attention and can be classified in frequency independent antennas [7]. However, the most difficult part in designing these spiral antennas is the way to feed at the spiral center. It turns out that the three dimensional central feeding makes the whole antenna systems very bulky [8, 9], and it is also hard to design a wideband balun and a matching circuit to match the frequency response of spiral antenna [10, 11]; the feeding method limits the performance of spiral antennas. On the other hand, printed antennas have been reported and widely used because of their simple planar design with low-cost fabrication technology [12, 13]. Researches on the broadband microstrip antennas have been intensively investigated recently [14, 15], but their bandwidth are limited by their resonant mechanism. Therefore, it is desirable to design a broadband, low-cost, and totally planar antenna for circular polarization applications.

This paper proposes a stripline Archimedean snail antenna and its analysis on impedance properties and radiation mechanism. The analysis shows that the radiation occurs when the two elevated slotline modes are propagating in-phase. The snail antenna uses asymmetric arm structures to complete the radiating mode and provides better VSWR, bandwidth, and axial ratio compared to traditional Archimedean spiral in symmetric structures. The presented antenna has a planar PCB design which is suitable for inexpensive fabrication and outer-fed by striplines which can be integrated with RF circuitry or other feeding networks easily without additional wideband balun designs. The antenna structure and operating principle are described in Section 2. The experimental verification is provided in Section 3, followed by a brief conclusion in Section 4.

## 2. ANTENNA DESIGN AND OPERATING MECHANISM

Figure 1 shows the configuration and coordinate system of a stripline Archimedean snail antenna. One of the antenna arms is configured in stripline structure as a feeding network (Arm1), composed of inner conductor layer at  $z = 0$  and top and bottom ground layers at height of  $h$  and  $-h$ , respectively. The dielectric substrate has thickness of  $2h$  and relative permittivity  $\epsilon_r$ . The expressions describing the Archimedean curves are  $r = a\theta + r_{in}$ , where  $r$  is the radius of curve,  $\theta$  is the winding angle in radian,  $a = RC/2\pi$  is the radius growth rate, and  $r_{in}$  is the inner radius. The

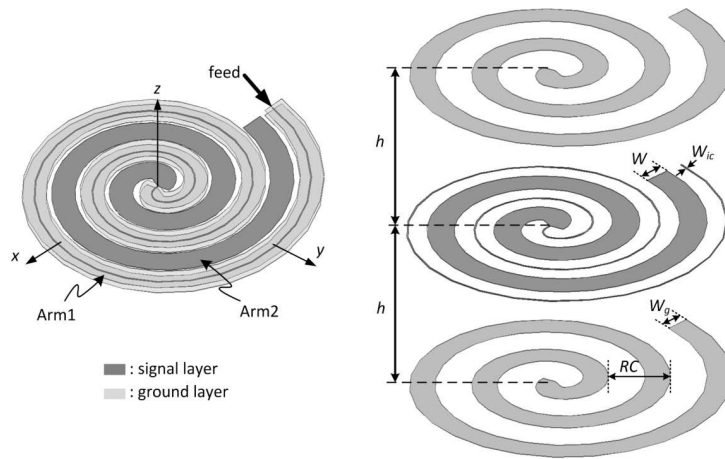


Figure 1: Designs of a stripline-fed Archimedean snail antenna.

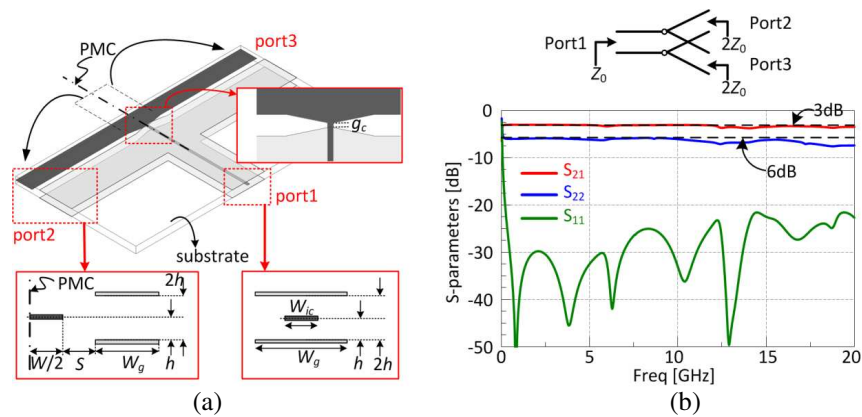


Figure 2: (a) A three-port network of unwound snail antenna around center, and (b) its simulated  $S$ -parameters (geometry parameters:  $W = W_g = 4.0$  mm,  $S = 0.96$  mm,  $W_{ic} = 0.36$  mm,  $g_c = 0.2$  mm, and  $h = 0.508$  mm).

snail antenna has asymmetric arm structure compared to the spiral one, where Arm1 and Arm2 has the number of Archimedean turns of  $(N + 0.5)$  and  $N$ , respectively. The antenna is supported by Rogers RT/duroid 5880 substrate ( $\epsilon_r = 2.2$ ).

For any antenna design, the impedance matching is a key factor to radiate power effectively. To investigate the impedance properties, the antenna design in Figure 1 is unwrapped into a straight transmission line structure. Assuming the traveling wave on the Arm2 is symmetric, a perfect magnetic conductor (PMC) wall is placed in the middle perpendicular plane of Arm2. The three-port network is then obtained as shown in Figure 2(a) with the port1 of stripline structure and the ports 2 & 3 given names as elevated slot line structures. It is noted that the field distribution of stripline mode is assumed to be confined between two ground plates with little effect on the elevated slot line modes and therefore the inner conductors of stripline are removed at ports 2 & 3.

The commercial numerical software based on the finite element method (FEM) [16] is employed to analyze the antenna structure in this paper. Figure 2(b) shows the simulated  $S$ -parameters of unwrapped snail antenna, where the  $S_{11}$  indicates that the reflection at the stripline port is low and the  $S_{21}$  shows the power transmission from port 1 to port 2 is about 3 dB, implying that the power is split equally from stripline mode into two elevated slot line modes. Specifically, the central design of snail antenna performs as a power splitter and a mode converter. The 6 dB line shown in Figure 2(b) represents the reflection at port 2 (or port 3) due to the mismatch between the impedance of port 2 (port 3) and the parallel impedance of port 1 and port 3 (port 2).

Knowing the impedance properties between the stripline and the elevated slot lines, a modified design shown in Figure 3(a) is used to explore the power transmission through the center of snail

antenna design. The port 3 in Figure 2(b) is paralleled to port 2 with the two cylindrical vias connecting the top and bottom ground. Figure 3(b) shows that the  $S_{11}$  still has low reflection at stripline port due to the impedance matching between two transmission lines, namely, the parallel elevated slot line and the stripline. However, the  $S_{21}$  indicates that the power cannot be transmitted at 15.5 GHz. The volumetric electric field distributions shown in Figure 4 illustrate the power loss at 15.5 GHz, where the two elevated slot line modes are in-phase at 15.5 GHz while they are not in-phase at other frequency points. The phase difference between two elevated slot lines is due to the path difference from the outer and inner curves around the center of snail antenna. When the two elevated slot line modes are in-phase, the radiation incurs the power loss into free space. Therefore, if the straight transmission line structures shown in Figure 3(a) are wound in Archimedean curves, it is easy to conjecture that the two elevated slot line modes at different frequencies may meet somewhere in-phase on the antenna structure rendering radiation.

However, when the two slotline modes propagate to the end of symmetric Archimedean spiral arms, as shown in Figure 5(a) (left), one slotline mode stops and another slotline mode keep propagating. The purpose of snail antenna with asymmetric Archimedean turns as shown in Figure 5(a) (right) is to extend the common mode radiation and to remove the effect of incomplete single slotline

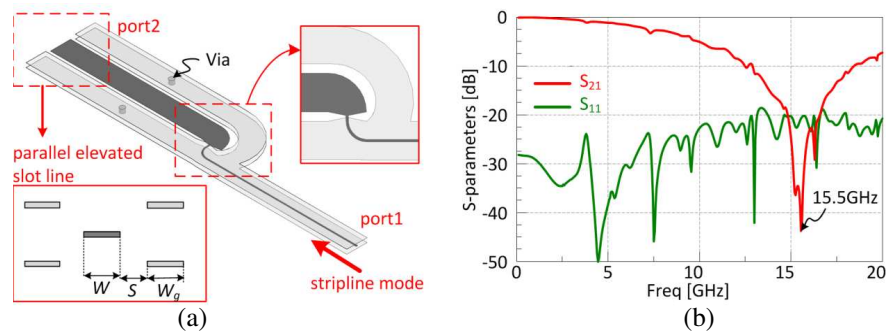


Figure 3: (a) A modified design from the three-port network to parallel the two elevated slot lines and to recover the center of snail antenna, and (b) its simulated  $S$ -parameters (geometry parameters:  $W = W_g = 4.0$  mm,  $S = 0.96$  mm,  $W_{ic} = 0.36$  mm,  $g_c = 0.2$  mm, and  $h = 0.508$  mm).

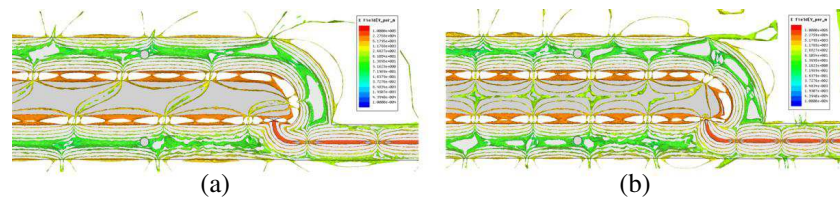


Figure 4: Magnitude of electric field distribution in the substrate at (a) 10 GHz and (b) 15.5 GHz.

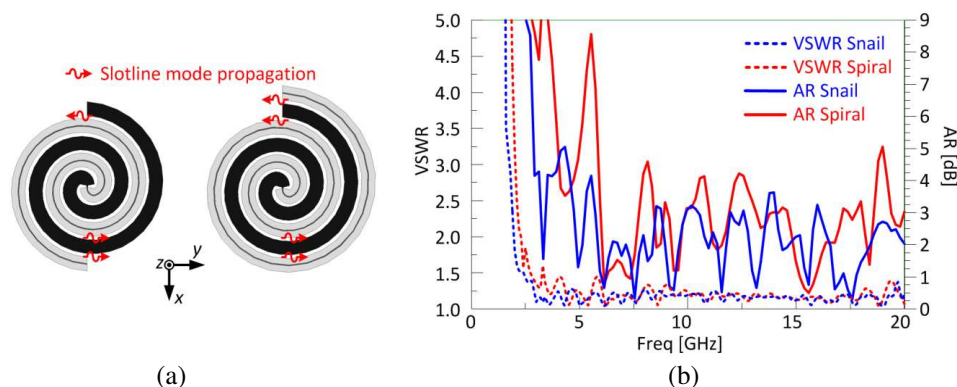


Figure 5: (a) Overlay of stripline Archimedean spiral antenna (left) and stripline Archimedean snail antenna (right); (b) simulated VSWR and axial ratio (AR) with geometry parameters of  $W = W_g = 4.0$  mm,  $S = 0.96$  mm,  $W_{ic} = 0.36$  mm,  $g_c = 0.2$  mm, and  $h = 0.508$  mm.

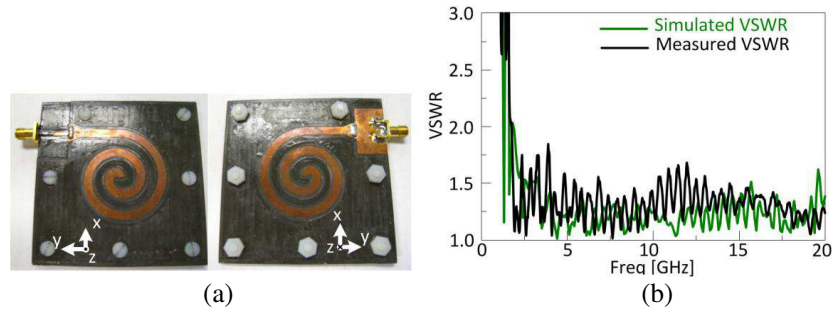


Figure 6: (a) The photo of fabricated antenna with SMA connector, and (b) measured and simulated VSWR.

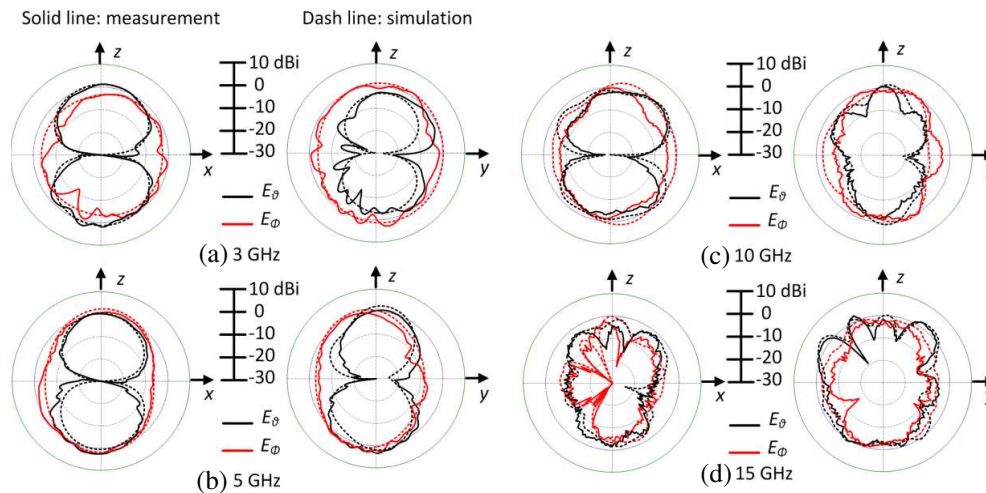


Figure 7: Measured and simulated elevation ( $xz$  and  $yz$ ) radiation patterns at (a) 3 GHz, (b) 5 GHz, (c) 10 GHz, and (d) 15 GHz.

mode. Figure 5(b) shows the simulated VSWR and axial ratio (AR) of stripline Archimedean spiral and snail antenna, respectively. The AR spike at 5.5 GHz of stripline Archimedean spiral antenna is removed by the snail antenna structure due to complete common mode radiation. In general, the snail-type antenna has similar size as spiral antenna but with better VSWR, bandwidth, and AR. The AR can be simply improved by increasing the Archimedean turns.

### 3. FABRICATION AND MEASUREMENTS

In order to measure the antenna performance, several extra dimensions are added to enable accurate and repeatable impedance and radiation pattern measurements. Figure 6(a) shows the photo of fabricated antenna of which dimensions of design parameters are  $W = W_g = 4.0$  mm,  $S = 0.96$  mm,  $W_{ic} = 0.36$  mm, and  $g_c = 0.2$  mm. For measurement purpose, a tapered impedance transformer to match antenna impedance of  $75\ \Omega$  to a standard impedance and a stripline-to-microstrip transition are employed to solder with SMA connector. This transition design is not optimized but provides a low reflection over the antenna bandwidth. The stripline structure is implemented by using two Rogers RT/duroid 5880 substrates of thickness 0.508 mm with a PDMS layer of  $\epsilon_r = 2.55$  as a glue between two substrates.

The measured VSWR is shown in Figure 6(b) compared with the simulated results. They are in good agreements basically and below 2 over wide frequency range, while a little discrepancy is due to the non-ideal fabrication of stripline structure. Figure 7 shows the measured and simulated radiation patterns of the fabricated antenna at 3 GHz, 5 GHz, 10 GHz, and 15 GHz each in the  $xz$  and  $yz$  elevation cut-planes. The little discrepancies can be explained by the non-ideal fabrication, spurious radiations caused by the feed cable, and the supporting material presented around the antenna during the measurement process. Figure 7 shows the simulated and measured radiation patterns at several frequency points.

#### 4. CONCLUSIONS

This paper presents a stripline Archimedean snail antenna with asymmetric arm structures and very broadband circular polarization. The radiation mechanism and impedance properties of this antenna structure are also examined. The power can be radiated because of two elevated slotline modes propagating in-phase and impedance match between the stripline mode and parallel elevated slotline mode. The snail antenna has better performance on VSWR, bandwidth, and AR compared to the spiral one, due to the completeness of two propagating slotline modes. The antenna design may be achieved easily by impedance matching between the stripline mode and the parallel elevated slotline mode. This snail design is a planar antenna without three-dimensional feeding structure, providing a platform for integration of impedance matching circuits or other circuit elements easily.

#### REFERENCES

1. Waldschmidt, C. and W. Wiesbeck, "Compact wide-band multimode antennas for MIMO and diversity," *IEEE Trans. Antennas Propag.*, Vol. 52, No. 8, 1963–1969, 2004.
2. Murch, R. D. and K. B. Letaief, "Antenna systems for broadband wireless access," *IEEE Commun. Mag.*, Vol. 40, No. 4, 76–83, 2002.
3. Li, R., B. Pan, J. Laskar, and M. M. Tentzeris, "A novel low-profile broadband dual-frequency planar antenna for wireless handsets," *IEEE Trans. Antennas Propag.*, Vol. 56, No. 4, 1155–1162, 2008.
4. Li, R., B. Pan, J. Laskar, and M. M. Tentzeris, "A compact broadband planar antenna for GPS, DCS-1800, IMT-2000, and WLAN applications," *IEEE Antennas Wireless Propag. Lett.*, Vol. 6, 25–27, 2007.
5. Kim, Y., S. Keely, J. Ghosh, and H. Ling, "Application of artificial neural networks to broadband antenna design based on a parametric frequency model," *IEEE Trans. Antennas Propag.*, Vol. 55, No. 3, 669–674, 2007.
6. Yi, H., K. Chan, and B. Cheeseman, "Review of broadband antenna measurements," *Europ. Conf. Antennas Propag., EuCAP*, 1–4, 2006.
7. Rumsey, V., "Frequency independent antennas," *IRE Int. Conv. Rec.*, 114–118, 1957.
8. Rao, P. H., M. Sreenivasan, and L. Naragani, "Dual band planar spiral feed backed by a stepped ground plane cavity for satellite boresight reference antenna applications," *IEEE Trans. Antennas Propag.*, Vol. 57, No. 12, 3752–3756, 2009.
9. Liu, C., Y. Lu, C. Du, J. Cui, and X. Shen, "The broadband spiral antenna design based on hybrid backed-cavity," *IEEE Trans. Antennas Propag.*, Vol. 58, No. 6, 1876–1882, 2010.
10. Tu, W.-H., M.-Y. Li, and K. Chang, "Broadband microstrip-coplanar stripline-fed circularly polarized spiral antenna," *Proc. IEEE AP-S Int. Symp.*, 3669–3672, 2006.
11. Thaysen, J., K. B. Jakobsen, and J. Appel-Hansen, "A wideband balun — How does it work?," *Applied Microwave & Wireless*, Vol. 12, No. 10, 40–50, 2000.
12. Pozar, D., "Considerations for millimeter wave printed antennas," *IEEE Trans. Antennas Propag.*, Vol. 31, No. 5, 740–747, 1983.
13. Herscovici, N. I. and D. M. Pozar, "Analysis and design of multilayer printed antennas: A modular approach," *IEEE Trans. Antennas Propag.*, Vol. 41, No. 10, 1371–1378, 1993.
14. Bao, X. L., M. J. Ammann, and P. McEvoy, "Microstrip-fed wideband circularly polarized printed antenna," *IEEE Trans. Antennas Propag.*, Vol. 58, No. 10, 3150–3156, 2010.
15. Thomas, K. G. and G. Praveen, "A novel wideband circularly polarized printed antenna," *IEEE Trans. Antennas Propag.*, Vol. 60, No. 12, 5564–5570, 2012.
16. *HFSS*, v12.0 Ed., Ansoft Corporation, Pittsburgh, PA, 2010.

# Experimental Verification of the Suppression of Crosstalk between Bended Parallel Microstrips via Designer Surface Plasmon Polaritons

Hung Erh Lin<sup>1</sup>, Tzong-Jer Yang<sup>1</sup>, Yao-Huang Kao<sup>2</sup>, Jin-Jei Wu<sup>3</sup>, Clark Li<sup>3</sup>,  
Chien-Jang Wu<sup>4</sup>, and Xianmin Zhang<sup>5</sup>

<sup>1</sup>College of Engineering, Chung Hua University, Hsinchu 30012, Taiwan, R.O.C.

<sup>2</sup>Department of Communication Engineering, Chung Hua University, Hsinchu 30012, Taiwan, R.O.C.

<sup>3</sup>Department of Electrical Engineering, Chung Hua University, Hsinchu 30012, Taiwan, R.O.C.

<sup>4</sup>Institute of Electro-Optical Science and Technology, National Taiwan Normal University  
Taipei 11677, Taiwan, R.O.C.

<sup>5</sup>Department of Information Science and Electronic Engineering, Zhejiang University  
Zhejiang 310027, China

**Abstract**— In this paper, we propose a novel microstrip using the concept of designer surface plasmon polaritons (designer SPPs) to construct the bended parallel microstrips to suppress the crosstalk in between, which is realized by introducing subwavelength periodic corrugations onto the edges of one conventional microstrip. The transmission properties of this microstrip are numerically analyzed. The suppression effect of the coupling between the bended corrugated microstrip and conventional microstrip is also experimentally investigated, especially in the time domain signal measurement. A good agreement between the numerical and experimental results in this microstrip structure is found. Thus, such a structure can effectively suppress the cross talk in the high speed digital signal transmission.

## 1. INTRODUCTION

Surface plasmon polaritons (SPPs), which is electromagnetic (EM) excitations of surface wave along the interface of metal-dielectric, has highly confined field localizing around the interface and attenuating along both directions into the metal and dielectric medium [1, 2]. As a result, it can be expected that the crosstalk between adjacent circuitry could be effectively suppressed if such SPPs could be realized in practical circuitry. However, as the plasma frequencies of metals mostly locate in the ultra-violet (UV) regime, metals behave as perfect electric conductor (PEC) and can't support SPPs at low frequency such as in terahertz (THz) or microwave regime. In 2004, Pendry proposed a new mechanism of subwavelength periodic corrugation to mimic the SPPs at low frequency, called designer SPPs, which can be controlled by the geometric parameters [3]. In this paper, we realize a new kind of microstrip with subwavelength periodic corrugation on the edges to designer spoof SPPs in microwave regime, and investigate its transmission properties by using numerical method. For this kind of microstrip, it is verified to possess the ability of suppressing crosstalk with conventional microstrip in our experimental measurement, especially in the case of bended parallel microstrips which is not investigated up to the present in our knowledge.

## 2. NUMERICAL ANALYSIS

The proposed microstrip structure is shown in Figure 1(a), which consists of a bended parallel corrugated microstrip and conventional microstrip. The geometric parameters of the proposed structure in Figure 1(a) are: the period  $d$  ( $d \ll \lambda$ ,  $\lambda$  is the working wavelength), the substrate thickness  $h$ , the substrate dielectric constant  $\epsilon_r$ , the metallic microstrip width  $w$ , the periodic slot depth  $b = 0.3w$ , the slot width  $a = 0.5d$  and the metal (copper) thickness  $t$ . The ability of the structured microstrip line for confining the EM fields can be revealed via the electric field distribution in the periodically corrugated metal strip line. Figure 1(b) depicts the electric field distribution of bended parallel conventional coupling microstrips at 12 GHz. Figure 1(c) shows the electric field distribution of the coupling microstrips composed of corrugated and conventional microstrip lines at 12 GHz, with the interval spacing  $w_2 = 1.2$  mm, the corrugation period  $d = 1.0$  mm, the substrate dielectric constant  $\epsilon_r = 3.37$ ,  $h = 0.508$  mm, and strip width  $w_1 = w_3 = 1.2$  mm. The other geometric parameters are:  $L_1 = L_2 = 4.494$  cm,  $c_1 = 4.15$  mm,  $c_2 = 3.16$  mm,  $c_3 = 2.16$  mm, and  $c_4 = 1.17$  mm.

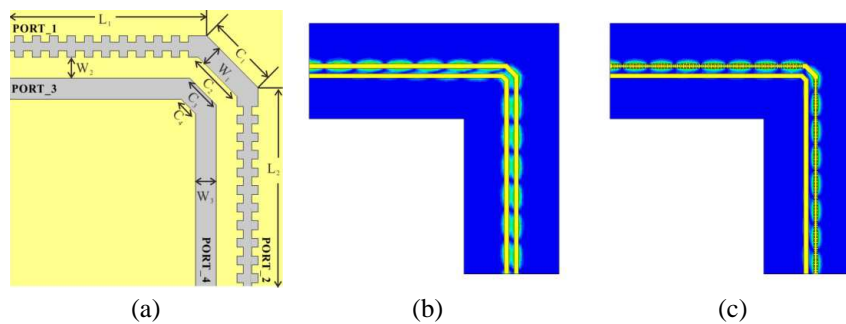


Figure 1: (a) Schematic of coupling between the bended parallel groove corrugated microstrip line and the conventional microstrip line. (b) Field distributions for two coupled conventional microstrip lines. (c) Field distributions for the coupled conventional and corrugated microstrip lines.

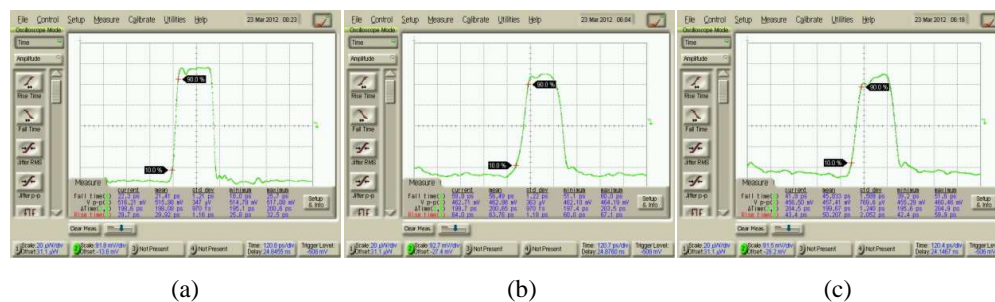


Figure 2: (a) 5 GHz input signal at port-1, the peak value is 515.98 mv, the rising and falling time are 29.92 ps and 21.41 ps. (b) Output signal at port-2 of conventional microstrip, the peak value is 462.98 mv, the rising and falling time are 63.76 ps and 56.49 ps. (c) Output signal at port-2 of groove corrugated microstrip line, the peak value is 457.41 mv, the rising and falling time are 50.2 ps and 45.833 ps.

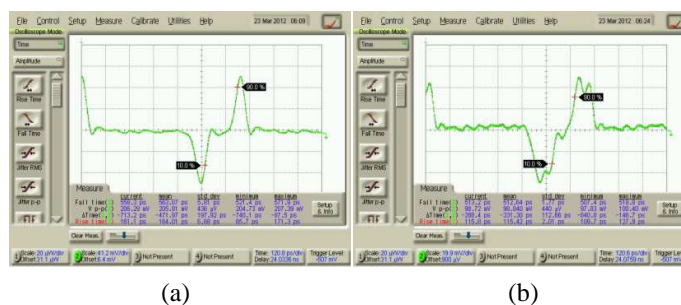


Figure 3: Measured results of far end crosstalk for (a) coupled conventional microstrips, (b) coupled groove corrugated microstrip line with  $d = 1.0$  mm and conventional microstrip.

We can see that the electric field is squeezed substantially inside the slits when the microstrip line is corrugated with subwavelength periodic slits. Hence, such effect of EM field localization dramatically decreases the crosstalk between neighboring microstrip lines. Clearly, the periodically structured microstrip line with subwavelength hairpin slits exhibits the ability of efficiently confining the EM fields.

### 3. EXPERIMENTAL RESULTS

To verify that the proposed structure can be utilized to suppress the crosstalk in bended parallel microstrips, we experimentally measure the time domain transmission properties of this periodic structure. Figure 2(a) is the input signal into port-1 with 5 GHz square wave with the peak value of 515.98 mV, and the rising time and falling time of 29.92 ps and 21.41 ps, respectively. Figure 2(b) is the measured output waveform at port-2 of a conventional couple strip lines. It can be seen that the peak value of the output signal at port-2 drops to 462.98 mV, and the rising time and falling time become 63.76 ps and 56.49 ps, respectively. The increase of rising and falling time is due to the connection between substrate and connector [4]. Figure 3(a) is the measured far end

crossstalk for conventional microstrip, whose peak-to-peak value is 205.81 mv. Figure 2(c) is the measured waveform at port-2 for the subwavelength periodic groove corrugated microstrip with period  $d = 1.0$  mm, the peak value is 457.41 mv, rising and falling time are 50.2 ps and 45.833 ps, respectively. The far end crossstalk is shown in Figure 3(b), with the peak-to-peak value of 98.84 mv. As a result, the proposed subwavelength corrugated microstrip is superior to be applied in high speed digital circuit with better signal integrity.

#### 4. CONCLUSIONS

It is verified in experiment and in numerical simulation that a microstrip with subwavelength periodic corrugation is able to suppress the crossstalk with conventional microstrip. Measured time domain signal indicates that the suppression effect of crossstalk between corrugated and conventional microstrips is greater than that between conventional microstrips.

#### ACKNOWLEDGMENT

The authors acknowledge the financial supports from the National Science Council of ROC (NSC 100-2112-M-216-002, NSC 100-2221-E-216-015) and the National Natural Science Foundation of China (No. 61071059).

#### REFERENCES

1. Raether, H., *Surface Plasmons*, Springer-Verlag, Berlin, 1988.
2. Stepanov, A. L., J. R. Krenn, H. Ditlbacher, A. Hohenau, A. Drezet, B. Steinberger, A. Leitner, and F. R. Aussenegg, "Quantitative analysis of surface plasmon interaction with silver nanoparticles," *Optics Lett.*, Vol. 30, 1524–1526, 2005.
3. Pendry, J. B., L. Martin-Moreno, and F. J. Garcia-Vidal, "Mimicking surface plasmons with structured surfaces," *Science*, Vol. 305, 847–848, 2004.
4. Koo, S. K. and H. S. Lee, "Crosstalk reduction effect of asymmetry stub loaded lines," *Journal of Electromagnetic Waves and Applications*, Vol. 25, Nos. 8–9, 1156–1167, 2011.

# A New Proof on Boundary Conditions in Electromagnetic Theory

Cavour Yeh and Fred Shimabukuro

California Advanced Studies, 2432 Nalin Dr., Los Angeles, CA 90077, USA

**Abstract**— Although electromagnetic waves have been the subject of intense study by many researchers for many years, there still exist elementary yet fundamental aspects of the theory that have not been carried out. It is well known that, for time varying fields with a source free boundary, satisfying the continuity of the tangential electric and magnetic fields across the boundary surface of two different material media automatically implies the continuity of the normal magnetic induction vector and electric displacement vector across that boundary surface. However, the converse is not true. A proof on this statement has not been found in the literature. Here, we shall provide this proof. In addition, it will be shown that unlike the case for the time-varying fields, for the static field case, satisfying the boundary conditions on the tangential electric and/or magnetic fields does not imply the satisfaction of the boundary conditions on the normal electric displacement and/or magnetic induction fields.

Boundary conditions are the cornerstones in electromagnetics [1–6]. Although it is well known that for time-varying electromagnetic fields on a source free boundary, satisfying the continuity of electric ( $\mathbf{E}$ ) and magnetic ( $\mathbf{H}$ ) fields at the interface implies that the continuity conditions of the normal components of the magnetic induction vector ( $\mathbf{B}$ ) and the electric displacement vector ( $\mathbf{D}$ ) are satisfied, the converse is not true. In other words, for time varying electromagnetic fields, the satisfaction of the continuity conditions for the tangential  $\mathbf{E}$  and  $\mathbf{H}$  fields at a dielectric interface is a necessary and sufficient requirement, while the satisfaction of the continuity conditions for the normal  $\mathbf{B}$  and  $\mathbf{D}$  at that interface is only a necessary but not sufficient requirement. On the other hand, for time-independent (static) electric or magnetic fields, satisfying the continuity conditions on tangential  $\mathbf{E}$  does not imply the satisfaction of the continuity of the normal component of  $\mathbf{B}$  at the dielectric interface, and satisfying the continuity on tangential  $\mathbf{H}$  does not imply the satisfaction of the continuity of the normal component of  $\mathbf{D}$  at the interface. It is surprising to learn that the proof is not commonly known. The first proof, given by Yeh appeared in 1993 [7, 8] A different version is given here.

## 1. TIME HARMONIC CASE

Let  $P$  be a smooth surface separating two media, 1 and 2 (See Fig. 1). Let the unit vector normal to the boundary be  $\mathbf{n}$ , pointing from medium 1 into medium 2. Media 1 and 2 are dielectrics having constitutive parameters  $(\epsilon_1, \mu_1, \sigma_1)$  and  $(\epsilon_2, \mu_2, \sigma_2)$ , respectively. To thoroughly understand the boundary conditions for the field quantities  $\mathbf{E}$ ,  $\mathbf{D}$ ,  $\mathbf{H}$ , and  $\mathbf{B}$ , let us consider the following scenario.

Across the boundary, as shown in Fig. 1, let us introduce two small parallel surface areas of rectangular shape that are mirror images of each other. The top rectangle with area  $\Delta S_1$ , parallel to the interface, is located in medium 1, while the bottom rectangle with area  $\Delta S_2$ , also parallel to the interface, is located in medium 2. The unit vectors  $\mathbf{n}_1$  and  $\mathbf{n}_2$  are normal to the rectangular surfaces. The unit vectors  $\mathbf{e}_x$ ,  $\mathbf{e}_y$ , and  $\mathbf{e}_z$ , are the three unit vectors in the  $x$ ,  $y$ , and  $z$  directions, respectively.  $P$  is the plane that separates medium 1 and medium 2. The source free Maxwell equation are

$$\nabla \times \mathbf{E}(\mathbf{r}, t) = -\frac{\partial \mathbf{B}(\mathbf{r}, t)}{\partial t} \quad (1)$$

$$\nabla \times \mathbf{H}(\mathbf{r}, t) = \frac{\partial \mathbf{D}(\mathbf{r}, t)}{\partial t} \quad (2)$$

Integrating (1) over the rectangular area  $\Delta S_1$  in region 1 yields

$$\int_{\Delta S_1} (\nabla \times \mathbf{E}_1) \cdot \mathbf{n}_1 dS = -\frac{\partial}{\partial t} \left( \int_{\Delta S_1} \mathbf{B}_1 \cdot \mathbf{n}_1 dS \right) \quad (3)$$

and integrating (1) over the rectangular area  $\Delta S_2$  in region 2 yields

$$\int_{\Delta S_2} (\nabla \times \mathbf{E}_2) \cdot \mathbf{n}_2 dS = -\frac{\partial}{\partial t} \left( \int_{\Delta S_2} \mathbf{B}_2 \cdot \mathbf{n}_2 dS \right) \quad (4)$$

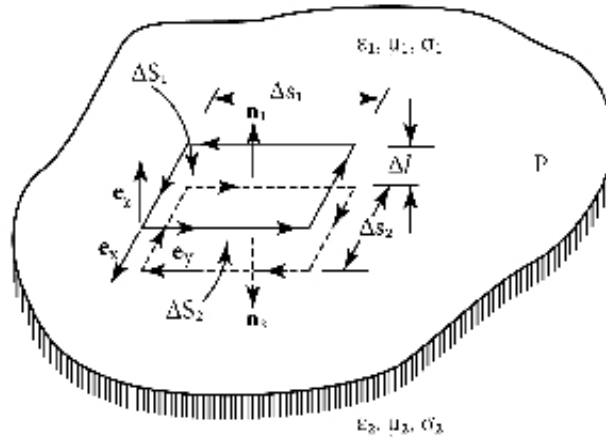


Figure 1: Geometry for scenario 1, showing the relationship between the tangential electric fields and the normal magnetic magnetic fluxes across the dielectric boundary, as well as the tangential magnetic fields and the normal displacement vectors. The rectangular area  $\Delta S_1$  is parallel to the rectangular area  $\Delta S_2$ . The sides of the rectangle are  $\Delta s_1$  and  $\Delta s_2$  and the separation between the two rectangles is  $\Delta l$ .  $P$  is the plane that separates medium 1 and medium 2.

Application of Stokes theorem to (3) and (4) and adding the resultant equations yield

$$\int_{c_1} \mathbf{E}_1 \cdot d\mathbf{s}_1 + \int_{c_2} \mathbf{E}_2 \cdot d\mathbf{s}_2 = -\frac{\partial}{\partial t} \left( \int_{\Delta S_1} \mathbf{B}_1 \cdot \mathbf{n}_1 dS \right) + \frac{\partial}{\partial t} \left( \int_{\Delta S_2} \mathbf{B}_2 \cdot \mathbf{n}_2 dS \right) \quad (5)$$

where  $c_1$  and  $c_2$  are, respectively, the circumferences of the rectangular areas  $\Delta S_1$  and  $\Delta S_2$ . In rectangular coordinates, with  $\Delta s_1 \rightarrow 0$  and  $\Delta s_2 \rightarrow 0$ ,  $\mathbf{E}$  has a constant value along each side. Allowing the separation  $\Delta l$  between the two parallel rectangular areas in medium 1 and in medium 2 to approach zero, one has,

$$(E_{1x} - E_{2x})2\Delta x + (E_{1y} - E_{2y})2\Delta y = -\frac{\partial}{\partial t}(B_{1z} - B_{2z})\Delta x\Delta y \quad (6)$$

where  $\Delta s_1 = \Delta x$ ,  $\Delta s_2 = \Delta y$ ,  $\mathbf{s}_1 = \mathbf{e}_x$ ,  $\mathbf{s}_2 = \mathbf{e}_y$ ,  $\mathbf{n}_1 = -\mathbf{n}_2 = \mathbf{n} = \mathbf{e}_z$ ,  $E_{1x}$  and  $E_{2x}$  are, respectively, the  $x$ -directed electric field tangential to the boundary in region 1 and in region 2,  $E_{1y}$  and  $E_{2y}$  are, respectively, the  $y$ -directed electric field tangential to the boundary in region 1 and in region 2,  $B_{1z}$  and  $B_{2z}$  are, respectively, the  $z$ -directed  $\mathbf{B}$  field normal to the boundary surface in region 1 and in region 2.

In a similar manner, one may derive the following relation from (2) for the tangential components of  $\mathbf{H}$  and the normal component of  $\mathbf{D}$  on the boundary surface:

$$(H_{1x} - H_{2x})2\Delta x + (H_{1y} - H_{2y})2\Delta y = \frac{\partial}{\partial t}(D_{1z} - D_{2z})\Delta x\Delta y \quad (7)$$

The boundary conditions derived in the traditional way is given in many textbooks [1–6]. They are:

$$\mathbf{n} \times (\mathbf{E}_1 - \mathbf{E}_2) = 0 \quad (8)$$

$$\mathbf{n} \times (\mathbf{H}_1 - \mathbf{H}_2) = 0 \quad (9)$$

$$(\mathbf{B}_1 - \mathbf{B}_2) \cdot \mathbf{n} = 0 \quad (10)$$

$$(\mathbf{D}_1 - \mathbf{D}_2) \cdot \mathbf{n} = 0 \quad (11)$$

The discussion on the necessary and sufficient boundary conditions at the boundary of two dielectrics was first given by Yeh in 1993 [7]. Referring to (6) and (7), for time-harmonic fields, we may replace  $\partial/\partial t$  by  $j\omega$  resulting in

$$(E_{1x} - E_{2x})2\Delta x + (E_{1y} - E_{2y})2\Delta y = -j\omega(B_{1z} - B_{2z})\Delta x\Delta y \quad (12)$$

and

$$(H_{1x} - H_{2x})2\Delta x + (H_{1y} - H_{2y})2\Delta y = j\omega(D_{1z} - D_{2z})\Delta x\Delta y \quad (13)$$

Here,  $\omega$  is the frequency of the time-harmonic fields. All field symbols are now time-independent phasors. These equations are valid at the interface boundary. Equation (12) shows that if the boundary conditions on the tangential electric field are satisfied, i.e.,  $E_{1x} = E_{2x}$  and  $E_{1y} = E_{2y}$ , then the left hand side of the equation is identically zero. Since, for time-varying fields,  $\omega$  is non-zero, and  $\Delta x \Delta y \neq 0$ , then  $B_{1z} - B_{2z} = 0$ ; or  $B_{1z} = B_{2z}$ , which is the boundary condition on the normal component of  $\mathbf{B}$ . This is proof that satisfying the boundary conditions on the tangential components of electric field means that the boundary condition on the normal component of  $\mathbf{B}$  is satisfied. On the other hand, if the boundary condition on the normal component of  $\mathbf{B}$  is satisfied, i.e., if the right hand side of Eq. (12) is zero, it only means that

$$(E_{1x} - E_{2x})2\Delta x + (E_{1y} - E_{2y})2\Delta y = 0 \quad (14)$$

It is not possible to conclude that the boundary conditions on the tangential components of  $\mathbf{E}$  are satisfied. Equation (14) only indicates that the combined terms of  $(E_{1x} - E_{2x})2\Delta x$  and  $(E_{1y} - E_{2y})2\Delta y$  must be zero and not necessarily each term must be zero. A similar conclusion can be reached from Eq. (13), i.e., satisfying the boundary conditions on the tangential components of magnetic field  $\mathbf{H}$ , Eq. (21) means that the boundary condition on the normal component of  $\mathbf{D}$ , Eq. (11) is satisfied, while the converse is not true.

*To summarize, the necessary and sufficient boundary conditions on the time-varying electromagnetic fields across two distinct dielectric media in a source free region are that the tangential electric fields must be continuous across the boundary and the tangential magnetic fields must be continuous across the boundary. Satisfying the boundary conditions for the normal components of  $\mathbf{D}$  and  $\mathbf{B}$ , i.e., Eq. (10) and Eq. (11) does not guarantee that all the necessary boundary conditions are satisfied.*

Since the constitutive relations were never used to arrive at the above proof, the proof is equally applicable to isotropic or anisotropic, dispersive or non-dispersive, moving or stationary, linear or nonlinear, and left-handed (metamaterial), or right-handed media.

## 2. STATIC FIELD CASE

Let us now investigate the special case of static fields. Here,  $\omega$  is identically zero. In that case, (2.0) and (21) can be read as follows:

$$(E_{1x} - E_{2x})2\Delta x + (E_{1y} - E_{2y})2\Delta y = 0 \quad (15)$$

$$(H_{1x} - H_{2x})2\Delta x + (H_{1y} - H_{2y})2\Delta y = 0 \quad (16)$$

There is no connection between electric and magnetic fields. Hence, unlike the time-dependent case, satisfying the boundary conditions on the tangential electric or magnetic fields says nothing about the satisfaction of the boundary conditions on the normal component of  $\mathbf{D}$  and  $\mathbf{B}$ . Furthermore, Eq. (15) only shows that, on the boundary, the conditions  $E_{1x} = E_{2x}$  and  $E_{1y} = E_{2y}$  must be satisfied simultaneously. Indeed, for electrostatic problems, the complete boundary conditions require the satisfaction of the continuity of the tangential components of  $\mathbf{E}$  across the boundary as well as the condition that the normal  $\mathbf{D}$  must also be continuous across the boundary. Using the same argument on Eq. (16) for the magnetostatic case, one may reach similar conclusion, i.e., the complete magnetostatic boundary conditions require the condition that the tangential components of  $\mathbf{H}$  be continuous across the boundary as well as the continuity of normal  $\mathbf{B}$  across the boundary.

*The necessary and sufficient boundary condition on the static electric and magnetic fields across two distinct dielectric media in a source free region are that (a) for the electrostatic fields, the tangential component of  $\mathbf{E}$  must be continuous and the normal component of  $\mathbf{D}$  must also be continuous across the boundary, and, (b) for the magnetostatic fields, the tangential component of  $\mathbf{H}$  must be continuous and the normal component of  $\mathbf{B}$  must be continuous across the boundary.*

## REFERENCES

1. Maxwell, J. C., *A Treatise on Electricity and Magnetism*, Dover, New York, 1954.
2. Stratton, J. A., *Electromagnetic Theory*, McGraw-Hill, New York, 1941.
3. Sommerfeld, A., *Electromagnetics*, Academic, New York, 1949.
4. Feynman, R. P., R. B. Leighton, and M. Sands, *Feynman Lectures on Physics*, The Definitive and Extended Edition, 2/E, Addison-Wesley, Reading, MA, 2006.
5. Kong, J. A., *Electromagnetic Wave Theory*, Wiley, New York, 1986.
6. Schelkunoff, S. A., *Electromagnetic Waves*, Van Nostrand, New York, 1943.

7. Yeh, C., “Boundary conditions in electromagnetics,” *Phys. Rev.*, Vol. E48, 1993.
8. Yeh, C. and F. I. Shimabukuro, *The Essence of Dielectric Waveguides*, Springer, New York, 2008.

# Design of Ultra Low-power Voltage Controlled Oscillator in 0.18- $\mu\text{m}$ CMOS Technology

Shao-Ping Yu and Chin-Lung Yang

National Cheng Kung University, Tainan 701, Taiwan

**Abstract**— A design of ultra low-power voltage controlled oscillator (VCO) is presented and fabricated in TSMC 1P6M CMOS 0.18  $\mu\text{m}$  technology. The power consumption is reduced by current-reused topology combined with PMOS and NMOS cross pair. Moreover, using differential Colpitts topology achieves low power consumption and also improves phase noise. The simulation results show that when the supply voltage is 1.8 V, the frequency tuning range is from 22.74 to 24.63 GHz, phase noise is  $-102.4$  dBc/Hz @ 1 MHz, power consumption is merely 2.4 mW and FOM is  $-186.1$  dBc/Hz.

## 1. INTRODUCTION

The voltage controlled oscillator (VCO) is an important component in frequency-modulated continuous-wave (FMCW) radar system. In general, the VCO is difficult to achieve the requirements of both wide tuning range and low phase noise simultaneously at high frequency. Both of them affect minimal detectable range resolution and noise level of FMCW radar system.

There were many papers in literature that propose some improvement for VCO. For example, VCO is designed to oscillate in low frequency and the following multiplier up-converts to the frequency we wanted. The advantage of [1] is wider tuning range and easy to design VCO, but its output power becomes smaller resulting poor effects on next stage circuit integration. High supply voltage causes large power consumption. In order to lower power consumption, the tail current of VCO can control a specific low level of current and reduce power consumption. However, tail current introduces extra noise leading to the increase of phase noise. The solution is applying a bias filter technique [2]; larger  $C_{filter}$  is added to short the noise to ground and  $L_1$  &  $C_p$  resonates achieve high impedance at 48 GHz. Transformer topology-based VCO makes the width of the inductor asymmetry, so the quality factor ( $Q$  value) can be upgraded by change inductor ratio [3]. In [3], when the supply voltage is 0.65 V, both phase noise and output amplitude are excellent, but it takes larger area and tuning range is narrow. [4] combines Colpitts-topology with a current-reused topology that easily oscillates by increasing transconductance of VCO. And current-reused topology consumes only a half of power compared with a traditional VCO, so power consumption reduces significantly. Therefore, the proposed design combines both the advantages of these two architectures, and achieve ultra-low power consumption and phase noise

## 2. CIRCUIT DESIGN

This paper presents a 24 GHz VCO that combines Colpitts with a current-reused topology. The schematic of 24 GHz VCO is shown in Figure 1. This circuit fabricated in TSMC 1P6M CMOS 0.18  $\mu\text{m}$  technology. We obtain simulation results by Advanced Design System (ADS) software, and do electromagnetic simulation by High Frequency Structure Simulator (HFSS) software.

The green area is to combine the “Gm-Boosted Colpitts” and “current-reused” topologies. Therefore, we can achieve a very low power consumption and improve phase noise. The red area is a LC tank. We chose a PMOS as varactor and let the body of PMOS connected to supply voltage. So the PMOS operates in its inversion region to increase the tuning range. The orange area is the output buffer. Buffer can isolated the next stage circuit which may affect VCO performance.

### 2.1. Gm-boosted Colpitts VCO

The principle of gm-boosted Colpitts VCO is enhanced by the differential characteristics. By the small-signal analysis of single-ended Colpitts VCO, we can obtain the oscillating frequency in (1). And the frequency can be determined by variables  $C_1$  and  $C_2$ . In general,  $C_2$  is much larger than  $C_1$ . The value of capacitor is typically at femto-level. The ratio  $C_2$  to  $C_1$  can be appropriately designed to obtain lower phase noise [5].

$$\omega_0 = \frac{1}{\sqrt{L \left( C + \frac{C_1 C_2}{C_1 + C_2} \right)}} \quad (1)$$

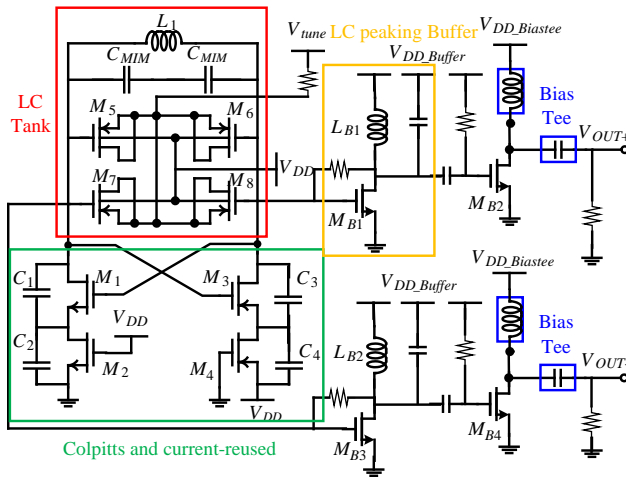


Figure 1: Schematic of 24 GHz VCO.

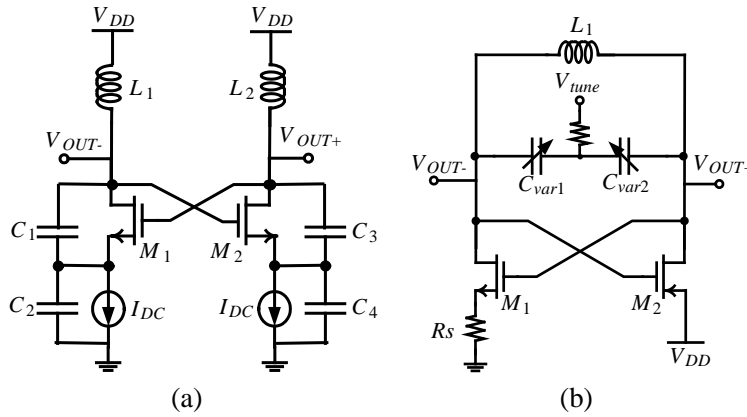


Figure 2: (a) Gm-boosted Colpitts VCO. (b) Current-reused topology VCO.

Figure 2(a) is gm-boosted Colpitts VCO. The negative conductance of gm-boosted Colpitts VCO is shown as (2), and it is amplified by  $(2 + C_2/C_1)$  compared with that of a traditional Colpitts VCO. It means that the Start-up condition is much easier. So the power consumption can be saved by  $(2 + C_2/C_1)$ . Therefore, the initial oscillating condition is improved by gm-boosted Colpitts VCO, and low phase noise and low power consumption can be achieved at the same time. Finally, the gate of  $M_2$  is connected to the supply voltage and  $M_4$  is connected to the ground. This can further increase the negative conductance of VCO, to relax the startup oscillation conditions.

$$\text{Re}[Y_{in}] = -\frac{g_m \omega^2 C_2 [2C_1 + C_2]}{g_m^2 + \omega^2 (C_1 + C_2)^2} \quad (2)$$

## 2.2. Current-reused Topology

The principle of a current-reused VCO is oscillating by PMOS and NMOS pair which produces a negative impedance to compensate leakage impedance of LC-Tank. From the drain of PMOS and NMOS, the negative conductance of a current-reused VCO and traditional differential LC-Tank VCO look the same. The negative conductance of current-reused VCO is shown as (3). However, the required biasing current is not the same. Both PMOS and NMOS are opened and closed at same time. During the first-half period, PMOS and NMOS are on-status, and the current flows from  $V_{DD}$  to the ground. During the second-half period, PMOS and NOS are off-status, and the current flows in the opposite direction through the capacitors. Therefore, the current is only half of a traditional VCO and achieves low power consumption.

$$\text{Re}[Y_{in}] = -\frac{g_m}{2} \quad (3)$$

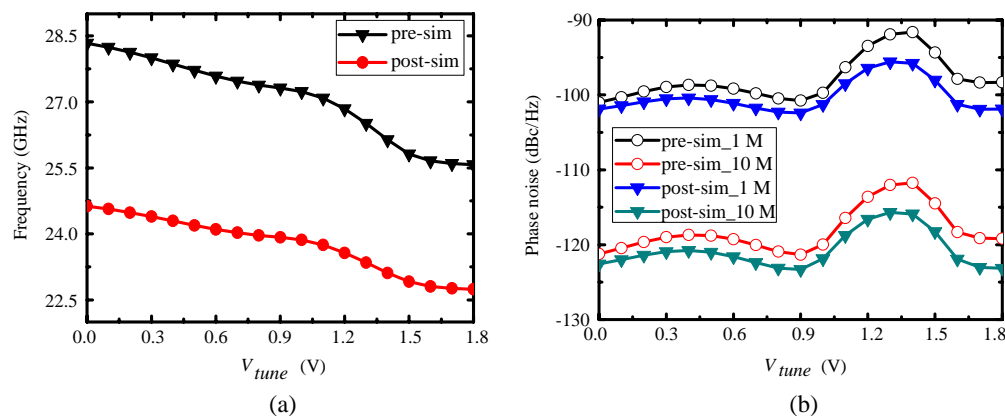


Figure 3: (a) The tuning behavior of the VCO. (b) Phase noise (dBc/Hz) @ 1 MHz & 10 MHz.

Table 1: Performance comparisons with the reported works.

Reference	Fabrication Process	Topology	Tuning Range (GHz)	Core $P_{DC}$ (mW)	Phase Noise (dBc/Hz)	FOM (dBc/Hz)
[1]	CMOS 0.18 $\mu\text{m}$	VCO+ Double Mixer	22~25.1	11	-99.4	-177.5
[2]	CMOS 90 nm	NMOS Cross-coupled	24.2~29.1	2.8	-101.0	-184.0
[3]	CMOS 0.18 $\mu\text{m}$	Transformer-feedback	24~24.54	7.8	-100.3	-179.0
[6]	CMOS 90 nm	NMOS Cross-coupled	24.7~28.8	5.5	-104.7	-186.1
[7]	CMOS 0.18 $\mu\text{m}$	Current-reused+ Tripler	21.18~24.98	9.0	-105.1	-187.2
<b>This work*</b>	<b>CMOS 0.18 <math>\mu\text{m}</math></b>	<b>Current-reused+ Colpitts</b>	<b>22.74~24.63</b>	<b>2.4</b>	<b>-102.4</b>	<b>-186.1</b>

\*post simulation

### 2.3. Varactors

There are all kinds of varactors in different modes such as diode varactors, inversion-MOS varactors and accumulation-MOS varactors. From [8], we can find the inversion-MOS varactors have the wider tuning range than others. So we let the body of PMOS connect to supply voltage and enforce to operate on inversion region increase tuning range.

### 3. SIMULATION RESULTS

Figure 3(a) shows the tuning behavior of the VCO. The frequency of pre-simulation is higher than post-simulation, because the parasitics effect causes the frequency to drop down. Previous experiments implied that frequency shifts down about 4 GHz. Tuning range of the VCO is from 22.74 GHz to 24.66 GHz. Figure 3(b) shows the phase noise of the VCO at 1 MHz and 10 MHz offset. When control voltage is 0.9 V, the phase noise is -102.387 dBc/Hz at 1 MHz offset.

Table 1 summaries the performance comparisons among the reported works. The power consumption of this work is superior to the other papers. The power consumption is reduced by 14%~78%. FOM is -186.1 dBc/Hz. In [1, 7], VCOs are oscillating in low frequency and followed by the frequency multiplier to up-convert to the desired frequency. The advantage is its wider tuning range at a cost of the increase of power consumption. Transformer topology VCO in [3] applies asymmetry width of the inductor to enhance the quality factor by varying inductor ratio. However, it requires larger area and suffers a narrow tuning range. The proposed VCO can achieve lowest power consumption while remaining other performances outstanding.

#### 4. CONCLUSIONS

A design of ultra low-power voltage controlled oscillator (VCO) is presented Utilizing Colpitts and current-reused topology achieves extremely low power consumption. And both phase noise and tuning range are also very good. Tuning range are improved by shunting two pairs of PMOS that operate on inversion region. This work reveals potential ultra low-power local oscillators for future automotive radar applications.

#### ACKNOWLEDGMENT

Thanks for the fabrication support from National Chip Implementation Center.

#### REFERENCES

1. Ozis, D., N. M. Neihart, and D. J. Allstot, "Differential VCO and passive frequency doubler in 0.18  $\mu\text{m}$  CMOS for 24 GHz applications," *2006 IEEE Radio Frequency Integrated Circuits (RFIC) Symposium*, 4, Jun. 11–13, 2006.
2. Yang, D., H. Wang, D. Zeng, H. Zheng, L. Zhang, and Z. Yu, "Design of a 24 GHz low phase-noise, wide tuning-range VCO with optimized switches in capacitor array and bias filtering technique," *2010 10th IEEE International Conference on Solid-State and Integrated Circuit Technology (ICSICT)*, 696–698, Nov. 1–4, 2010,
3. Yang, J., C.-Y. Kim, D.-W. Kim, and S. Hong, "Design of a 24-GHz CMOS VCO with an asymmetric-width transformer," *IEEE Transactions on Circuits and Systems II: Express Briefs*, Vol. 57, No. 3, 173–177, Mar. 2010.
4. Su, Y. P., W. Y. Hu, J. W. Lin, Y. C. Chen, S. Sezer, and S. J. Chen, "Low power gm-boosted differential Colpitts VCO," *2011 IEEE International SOC Conference (SOCC)*, 247–250, Sep. 26–28, 2011.
5. Aparicio, R. and A. Hajimiri, "A noise-shifting differential Colpitts VCO," *IEEE Journal of Solid-State Circuits*, Vol. 37, No. 12, 1728–1736, Dec. 2002.
6. Yang, D., L. Zhang, H. Wang, D. Zeng, C. Zhou, D. Yang, and H. Qian, "A 24 GHz low phase noise feedback CMOS LC-VCO," *2011 International Conference of Electron Devices and Solid-State Circuits (EDSSC)*, 1–2, Nov. 17–18, 2011.
7. Tsai, P. K. and T. H. Huang, "Integration of current-reused VCO and frequency tripler for 24-GHz low-power phase-locked loop applications," *IEEE Transactions on Circuits and Systems II: Express Briefs*, Vol. 59, No. 4, 199–203, Apr. 2012.
8. Andreani, P. and S. Mattisson, "On the use of MOS varactors in RF VCO's," *IEEE Journal of Solid-State Circuits*, Vol. 35, No. 6, 905–910, Jun. 2000.

# Road-vehicle Cooperation for Lateral Guidance

N. Houdali, T. Ditchi, E. Géron, J. Lucas, and S. Holé

Laboratoire de Physique et d'Étude des Matériaux, LPEM

ESPCI-ParisTech, CNRS, UPMC Univ Paris 06,

UMR8213, 10 rue Vauquelin, Paris 75005, France

**Abstract**— The aim of this paper is to describe an Advanced Driver Assistance System (ADAS) based on the cooperation between a vehicle and the road. It includes passive transponders integrated in the side white strips of the road and on-board devices allowing the communication with the transponders and the signal processing for estimating the vehicle lateral position used by the Driving Assistance System. The vehicle lateral position estimated by the developed system is provided in real-time with an accuracy of the order of  $\pm 2$  cm.

## 1. INTRODUCTION

A great number of traffic accidents results from a loss of control. Consequently, Various Advanced Driver Assistance Systems are studied in order to laterally locate the vehicle on the road in-real time and then to compensate the vehicle trajectory in case of danger. Some Advanced Driver Assistance Systems use image processing to detect the side white strips on the road [1]. However, optical techniques are not effective under heavy rain, in presence of snow or fog for instance, situations for which assistance systems are of particular interest. Radar and Global Positioning Systems (GPS) are also impaired by weather or environmental conditions.

Therefore cooperative systems have been developed in which on-board sensors are used to detect markers embedded in the road [2]. Magnetic field is particularly well suited for that application because it is almost not perturbed by weather conditions and can be generated without any supply. However the magnetic field generated by magnets weakens relatively rapidly with the distance making it necessary to bury strong magnets or to deposit a magnetic line just under the vehicle path. That results in expensive installation, or possible visual artifacts. Active magnetic guidance has also been proposed in the form of a wire buried in the road and powered by an alternative current [3]. The alternative magnetic field is then measured by on-board sensors with a very good accuracy by a lock-in technique. However, the installation is very expensive, it requires a power supply, and the whole system fails if the wire is cut.

In this paper, we introduce a low cost active cooperative system based on passive flat electromagnetic transponders included in the side white strips and interrogated by an on-board system in order to deduce its distance to the vehicle. The transponders operate in the UHF band, providing a large penetration depth in water and snow, the most problematic environmental conditions when using electromagnetic waves. In the first section the cooperative system and each of its elements are described. The second section shows the signals obtained from the transponders as a function of distance and how these signals can be processed to retrieve the distance in ideal and complex environment.

## 2. COOPERATIVE SYSTEM DESCRIPTION

The passive transponders included in the side white strips consist of an antenna and a resonator. When an electromagnetic wave is emitted by an on-board antenna toward a transponder, the electromagnetic wave is partially reflected and one part reaches the on-board receiving antennae. In a perfect world, the phase between the emitted and the received waves would directly depend on the distance between the transponders and the antennae. Nevertheless, other electromagnetic waves superimpose on the wave reflected by the transponders modifying in turn the received signal. The resonator inside the transponder is used as a signature and make it possible to separate the noise from the useful signal.

### 2.1. Transponder Description

The transponders should respond to various constraints. First, their frequency should be sufficiently low to ensure a good penetration in still water or snow on the road. Second, they should be sufficiently small to be easily integrated in the side white strips. Third, the directivity of their antenna should be sufficiently large to ensure a good detection at various angles. Fourth, their

production and installation should be as cheap as possible. Fifth, the frequency band must be free. For all these reasons, a working frequency of  $f_0 = 868.3$  MHz has been chosen. The transponder is composed of an half-wave antenna and a Surface Acoustic Wave (SAW) resonator with a quality factor of the order of 4000. The structure of the SAW resonator is illustrated in Figure 1. It is composed of two inter-digital transducers (IDT), one for the input and the other for the output, and two grating reflectors [4]. The measurement of  $S_{11}$  and  $S_{21}$  of the SAW resonator by a network analyzer when a  $50\text{-}\Omega$  resistor is connected at the output port is presented in Figure 2. As expected, the central frequency is 868.3 MHz and the bandwidth at  $-3$  dB is 200 kHz, thus the measured quality factor is approximately 4350. Around the resonance frequency, the SAW resonator can be assimilated to a high quality pass-band filter which will be used as the transponder signature.

## 2.2. On-board Antennas

For integration and cost reasons, patches are used for the on-board antennae. Their directivity and polarization have been adjusted to well excite and detect the transponders. All patches are printed on a 1.6-mm-thick FR-4 dielectric substrate. Their dimension is  $7.5\text{ cm} \times 8.3\text{ cm}$  and they are fed by a  $50\text{ }\Omega$  line. Matching between the  $50\text{ }\Omega$  impedance feed line and the patch is achieved by properly connecting the feed line to the center of one of the small patch edges.

Concerning the emitting antenna, four patches separated by  $\lambda/2$  are array arranged as shown in Figure 3 in order to obtain identical  $E$ -plane and  $H$ -plane array factor patterns. All patches are supplied in phase, therefore the maximum of emission is perpendicular to the antenna surface [5]. The  $S_{11}$  parameter simulated with Ansoft HFSS software and measured with a network analyzer presents a resonance frequency at 868 MHz, and a 20 MHz bandwidth at 10 dB loss. The radiating diagram measured in an anechoic chamber as shown in Figure 3 is also in agreement with simulated one with Ansoft HFSS software. The  $-3$ -dB aperture is similar in both  $E$ -plane and  $H$ -plane and reaches  $55^\circ$ . The gain is about 11 dBi and the backward radiations are about 25 dB under the main beam.

Concerning the receiving antenna, a single patch is connected from underneath via a probe. The  $S_{11}$  parameter simulated with Ansoft HFSS software and measured with a network analyzer presents again a resonance frequency at 867 MHz, and a 20 MHz bandwidth at 10 dB loss. The radiating diagram simulated with Ansoft HFSS software and measured in an anechoic chamber is in good agreement. The  $-3$ -dB aperture is  $90^\circ$  in  $E$ -plane and is  $110^\circ$  in  $H$ -plane. The gain is about 2.5 dB.

## 3. ANALYSIS AND RESULTS

### 3.1. Experimental Set-up and Protocol

In order to evaluate the influence of each parameter, all experiments were carried out in an anechoic chamber. Figure 4 presents the experimental setup. It is composed of the emitting and receiving antennas positioned in the same plane at the same height and a transponder positioned at a variable distance from the antennas and at the same height. The emitting antenna is fed by a 10 dBm RF signal at frequency  $f_0$  in the  $[867.5\text{ MHz}, 869.5\text{ MHz}]$  frequency range. The signal received by the receiving antenna is mixed with a local oscillator at a frequency  $f_0 + 10\text{ kHz}$ . A low-pass filter selects the low frequency part of the spectrum that is digitized by an oscilloscope. The amplitude and phase of the digitized signal are used for the numerical treatments.

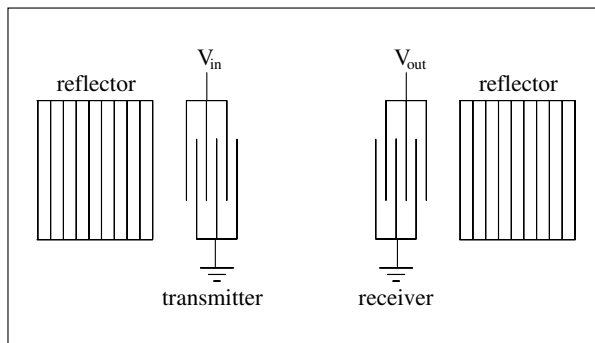


Figure 1: Design of SAW resonator.

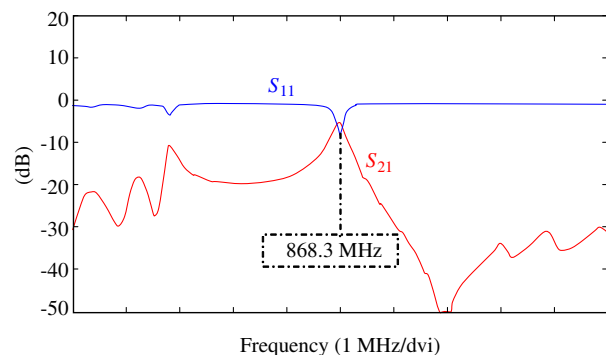


Figure 2: Measured  $S_{11}$  and  $S_{21}$  parameters.

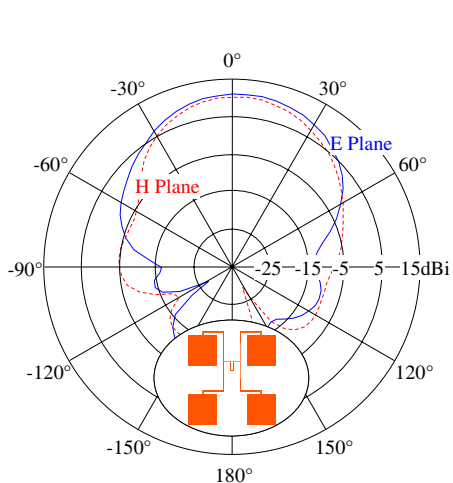


Figure 3: Measured radiation patterns in  $E$  (azimuthal) plane and  $H$  (vertical) planes..

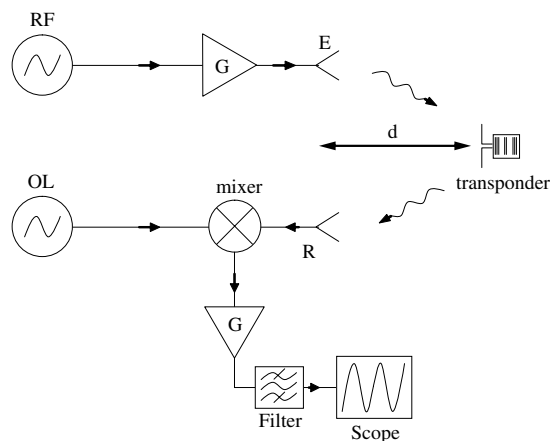


Figure 4: Experimental setup.

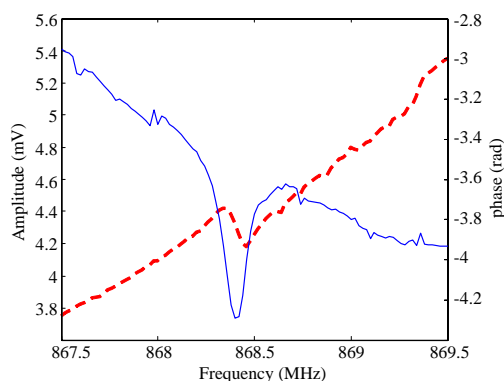


Figure 5: Amplitude and phase (dotted line) of the signal when the transponder is at 1 m from the emitting antenna.

The measurement protocol consists of (1) the initialization of the transponder distance, (2) the initialization of the first frequency in the range, (3) the measurement of the signal, (4) the transmission of the signal to a computer, (5) the increment of the frequency and repeating the steps from (3) until the frequency exceed the last frequency in the range. Because the bandwidth of the transponder is very small owing to the SAW resonator, the frequency increment is 20 kHz.

### 3.2. Transponder Response

The digitized signal depends on the emitted frequency, on the transponder bandwidth, on the transponder distance and on additional noises. The amplitude and phase of the received signal when the transponder is at 1 m from the emitting antenna is shown in Figure 5.

It can be noticed that the signal experiences rapid amplitude and phase variations at the frequency of the resonator. These variations act as a signature of the transponder. In a polar representation, the transponder signature appears as a loop as those shown in Figure 6(a).

When the transponder distance varies, the phase of the transponder signature varies accordingly, since the speed of light  $c$ , the phase  $\varphi$  and the distance  $d$  are connected together by the Equation (1).

$$\varphi = 2\pi f_0 d/c, \quad (1)$$

### 3.3. Numerical Processing

The signal phase can not directly be used to evaluate the transponder distance because the reflected waves from the transponder add with the ambient electromagnetic noise, hence the phase is modified. It is therefore necessary to separate the transponder signal from the noise. Because the noise varies relatively slowly with frequency compared to the transponder signal thanks to the resonator high-Q factor, it is possible to fit the signal with the known transponder response to which

a low unknown signal variation representing the noise is added. The transponder is assimilated as a band-pass filter whose response is

$$G \times \frac{\iota f f_0}{Q(f_0^2 - f^2) + \iota f f_0} \tag{2}$$

where  $G$  is the complex gain whose phase is related to the distance  $d$ ,  $Q$  is the resonator quality factor and  $\iota = \sqrt{-1}$ . Since noise is completely unknown, it is assumed it can be represented by a polynomial function of max order 3 with complex coefficients. Because  $Q$  and  $f_0$  may vary from one transponder to another, the fitting algorithm searches for the best  $Q$ ,  $f_0$ ,  $G$  and polynomial coefficients that reconstruct the measure signal. The fitting algorithm is a plain least mean square algorithm where the criterion is the sum of square real error and of the square imaginary error. Figure 6(a) shows both the signals and the fitted signals for a transducer distance from 0.7 m to 1 m by step of 5 cm. It can be noticed that loops are well estimated. These signals have been obtained in a relatively ideal environment, that is to say, in an anechoic chamber where reflecting elements have been reduced as much as possible. For each signal, the fitting algorithm yields  $Q$ ,  $f_0$ ,  $G$  and the polynomial coefficients of the noise. Only the phase  $\varphi$  of the gain  $G$  is used since it directly gives the distance  $d$  from (1). Figure 7 shows in solid line the estimated distance from the calculated phase  $\varphi$  in an ideal environment. The error between the estimated distance and the real distance is about  $\pm 2$  cm.

In order to evaluate the robustness of the fitting algorithm, some large metallic reflectors have been introduced at various positions in the anechoic chamber around the transponder and the antennas. The metallic reflectors are 30 cm squares except one which is a 20 cm  $\times$  50 cm rectangle in order to cover both emitting and receiving antennas.

The measurements carried out in such an environment are presented in Figure 6(b). It can be rapidly noticed when comparing Figures 6(a) and 6(b) that reflectors have a great influence on the noise. The loops are indeed deformed. That is due to the amplitude and phase of the signal

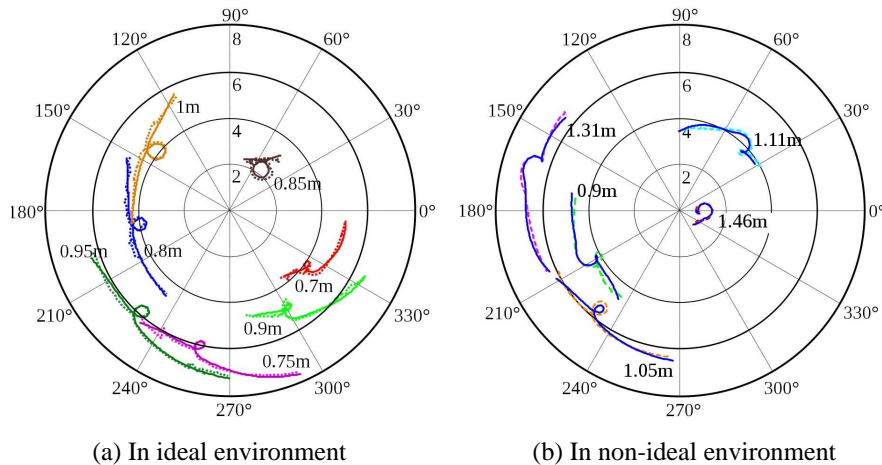


Figure 6: Measured signals in dotted line and fitted signals in solid line.

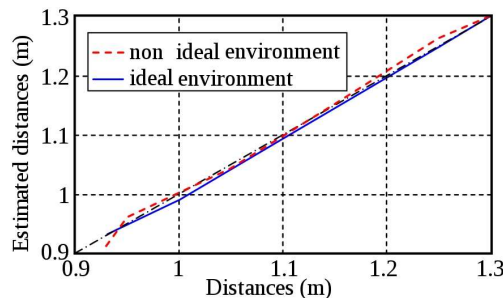


Figure 7: Estimated distance as a function of the real distance in an ideal (solid line) and a non ideal (dotted line) environment.

produced by the reflectors that superimpose on the transponder signal. The measured signals are however obtained with good accuracy by the implementation of the fitting algorithm.

The distance  $d$  estimated from the phase of the gain  $G$  obtained by the fitting algorithm is presented in dotted line in Figure 7. Despite the large influence of the noise introduced by the reflectors, the fitting algorithm still allows the distance to be estimated with a good accuracy, of the order of  $\pm 2$  cm which is the same as in the ideal case.

It can be concluded that the procedure used to estimate the distance  $d$  is almost insensitive to spurious reflections thanks to the detection of the transponder signature. The system efficiency will be maintained in any environment.

#### 4. CONCLUSION

To deal with the inefficiency of current Advanced Driver Assistance Systems in estimating the vehicle road position in some atmospheric or geographic conditions, the present paper describes a solution based on a radio-frequency system. The system presented is composed of electromagnetic reflectors inserted in the side white strip of the road and embedded sensors in the vehicle. The resonant signature of reflectors is used to separate useful signal to environment noises, and to estimate the distance between the vehicle and the side white strip. The choice of patch antennas for emitter and receiver is compatible with an easy implementation in the vehicle, and it optimizes the signal to noise ratio used by the numerical process of the sensors. The system exhibits a precision of  $\pm 2$  cm in the evaluation of the distance from the reflectors in the range  $[0.2, 2]$  m in laboratory experimental conditions, even in presence of artificial parasitic reflectors.

Because firsts results are encouraging. This system will be implemented in a vehicle to be tested in real conditions.

#### REFERENCES

1. Chen, M., T. Jochem, and D. Pomerleau, "Aurora: A vision-based roadway departure warning system," *IEEE/RSJ International Conference on Intelligent Robots and Systems 95' Human Robot Interaction and Cooperative Robots', Proceedings*, Vol. 1, 243–248, 1997.
2. Santos, P., S. Holé, C. Filloy, and D. Fournier, "Magnetic vehicle guidance," *Sensor Review*, Vol. 28, No. 2, 132–135, 2008.
3. Weliman, T. A., "Wire guidance control system," 1991.
4. Shreve, W. R., "Surface-wave two-port resonator equivalent circuit," *1975 Ultrasonics Symposium*, 1975.
5. Chang, D.-C., B.-H. Zeng, and J.-C. Liu, "High performance antenna array with patch antenna elements," *PIERS Proceedings*, 710–713, Xi'an, China, March 22–26, 2010.

# A Compact Wilkinson Power Divider Utilizing Coupled Lines for Unequal Power Division and Equal Port Impedance

Yi-Fan Chen and Yi-Hsin Pang

Department of Electrical Engineering, National University of Kaohsiung, Taiwan, R.O.C.

**Abstract**— A compact Wilkinson power divider is presented for unequal power distribution. The proposed circuit is designed with only a pair of quarter-wavelength ( $\lambda/4$ ) coupled lines and exhibits the characteristic of equal port impedance. No additional  $\lambda/4$  transformer is hence required at each output terminal. The proposed power divider has been designed at 2 GHz and fabricated on an FR4 substrate for verification. The implemented power divider exhibits 15 dB return loss, 21 dB isolation, and 1.73 dB power ratio at the designed frequency.

## 1. INTRODUCTION

A Wilkinson power divider plays an important role in the feeding network of an antenna array. For the synthesis of radiation pattern, an unequal-split power divider is required. The conventional unequal Wilkinson power divider, as shown in Fig. 1(a), consists of two  $\lambda/4$  transformers [1]. Two-section transmission lines with/without shunt stubs have been used to replace the  $\lambda/4$  transformer for dual-band unequal power operation [2, 3]. Unequal power dividers with dual-harmonic suppression or filter response have also been presented [4, 5]. In these designs, however, the port impedances are different and additional impedance transformers are required at the output ports. Based on the optimization scheme of least squares, an unequal-split Wilkinson power divider of identical port impedance has been designed [6]. Due to its multisection structure, the power divider is broadband but occupies a large area. Besides, an additional impedance transformer at each port is presented. Shunt-stub unequal Wilkinson power dividers with identical port impedance have been proposed [7]. Additional power loss in the isolation resistor is however presented. Dual-band and unequal split Wilkinson power dividers have also been realized [8]. Although impedance transformers are absent, additional isolation stubs are required and still occupy large area.

In this paper, an unequal Wilkinson power divider with identical port impedance is proposed. The proposed power divider requires only a pair of  $\lambda/4$  coupled lines along with an isolation resistor. No additional impedance transformer is presented and the power divider is therefore compact in size.

## 2. PROPOSED DESIGN

Figure 1(b) shows the proposed Wilkinson power divider. It consists of two coupled lines and a resistor for isolation. The impedances shown in Fig. 1 are normalized to the port impedance  $Z_0$  of which default value is  $50\ \Omega$ . The normalized even- and odd-mode characteristic impedances of the coupled line between Ports 1 and 2 are, respectively,  $z_{eA}$  and  $z_{oA}$ . For the coupled line between Ports 1 and 3, they are respectively  $z_{eB}$  and  $z_{oB}$ . The electrical length of each coupled line is  $\theta = 90^\circ$  at the center frequency. A resistor of normalized resistance  $r$  is utilized for good isolation between Ports 2 and 3. Using the equal-phase and anti-phase excitation analysis, explicit design formulae can be obtained [4]. In the following analysis,  $k^2$  ( $k > 1$ ) represents the power ratio between Ports 2 and 3; that is, the power delivered to Port 3 is  $k^2$  times the power delivered to Port 2.

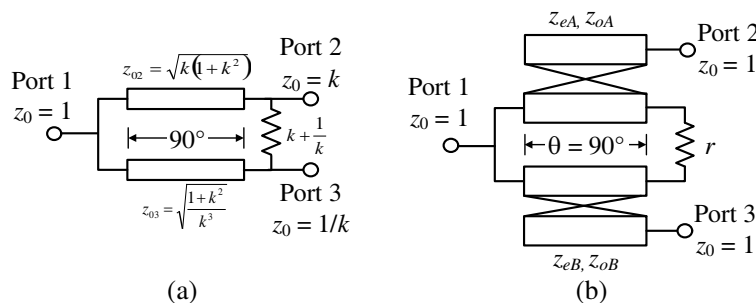


Figure 1: Unequal-split Wilkinson power divider: (a) conventional structure; (b) proposed structure.

### 2.1. Equal-phase Excitation

When the voltage ratio of Port 3 to Port 2 is  $k$ , no current flows through the isolation resistor  $r$  so that the resistor can be ignored in the equal-phase analysis. Since the impedance is matched and the power ratio is  $k^2$ , the input admittances at Port 1 looking into the signal paths to Port 2 and Port 3 are, respectively,  $1/(1+k^2)$  and  $k^2/(1+k^2)$ . The equivalent half circuit for Port 2 is therefore depicted in Fig. 2(a) in which Port 1 is equivalently represented by a load of resistance  $r_{1A} = 1+k^2$ . According to the impedance matrix of the four-port parallel coupled-line section [1], the input impedance looking into the equivalent circuit at Port 2 can be obtained as

$$z_{in,A}^e = \frac{1}{1+k^2} \left( \frac{z_{eA} - z_{oA}}{2} \right)^2 \quad (1a)$$

The equivalent half circuit for Port 3 is similar to Fig. 2(a) where Port 1 is instead represented by a load of resistance  $r_{1B} = (1+k^2)/k^2$ . The input impedance at Port 3 looking into the equivalent half circuit which is not shown for simplicity is

$$z_{in,B}^e = \frac{k^2}{1+k^2} \left( \frac{z_{eB} - z_{oB}}{2} \right)^2 \quad (1b)$$

### 2.2. Anti-phase Excitation

When the voltage ratio of Port 3 to Port 2 is  $-1/k$ , by the principles of superposition and reciprocity, no current flows into Port 1 and Port 1 is equivalently short-circuited [4]. The isolation resistor can be represented by the series combination of two resistors, of which resistances are  $k^2r/(1+k^2)$  and  $r/(1+k^2)$ , and the common node of the two series connected resistors is a virtual ground. The equivalent half circuit for Port 2 with anti-phase excitation is therefore shown in Fig. 2(b). The input impedance looking into the equivalent circuit at Port 2 is

$$z_{in,A}^o = \frac{k^2r}{1+k^2} \left( \frac{z_{eA} - z_{oA}}{z_{eA} + z_{oA}} \right)^2 \quad (2a)$$

The equivalent half circuit for Port 3 is similar to Fig. 2(b) where the resistance of the isolation resistor is replaced by  $r/(1+k^2)$ . The input impedance looking into the equivalent circuit at Port 3 is then derived as

$$z_{in,B}^o = \frac{r}{1+k^2} \left( \frac{z_{eB} - z_{oB}}{z_{eB} + z_{oB}} \right)^2 \quad (2b)$$

### 2.3. Proposed Design Methodology

For impedance matching,  $z_{in,j}^e = z_{in,j}^o = 1$  are enforced, where  $j = A$  and  $B$ . Let

$$z_j = \sqrt{z_{ej}z_{oj}}, \quad (j = A, B) \quad (3)$$

$$C_j = \frac{z_{ej} - z_{oj}}{z_{ej} + z_{oj}} \quad (j = A, B) \quad (4)$$

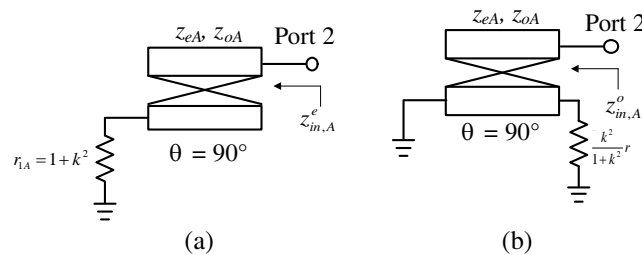


Figure 2: Equivalent half circuit: (a) with equal-phase excitation; (b) with anti-phase excitation.

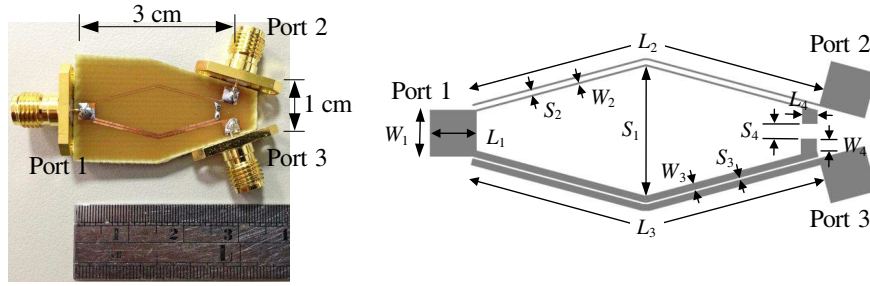


Figure 3: Photograph and layout of the fabricated power divider.  $L_1 = 3.1$  mm,  $W_1 = 3.0$  mm,  $S_1 = 8.4$  mm,  $L_2 = 23.2$  mm,  $W_2 = 0.12$  mm,  $S_2 = 0.29$  mm,  $L_3 = 23.4$  mm,  $W_3 = 0.44$  mm,  $S_3 = 0.12$  mm,  $L_4 = 1.0$  mm,  $W_4 = 0.75$  mm, and  $S_4 = 0.96$  mm.

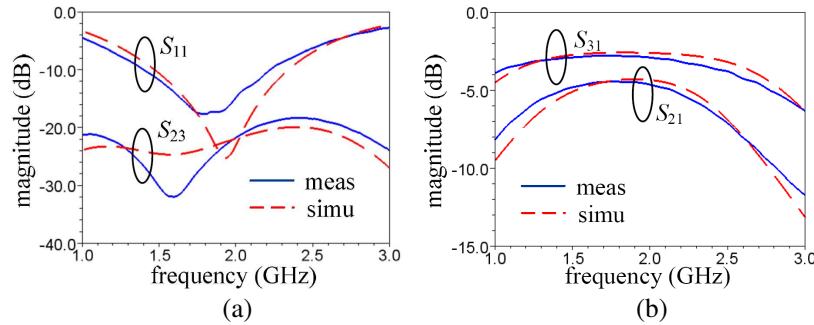


Figure 4: Simulated and measured data: (a)  $S_{11}$  and  $S_{23}$ ; (b)  $S_{21}$  and  $S_{31}$ .

The impedance matching condition  $z_{in,A}^e = z_{in,B}^e = 1$  requires

$$\frac{z_A C_A}{\sqrt{1 - C_A^2}} = \sqrt{1 + k^2} \quad (5a)$$

$$\frac{z_B C_B}{\sqrt{1 - C_B^2}} = \frac{\sqrt{1 + k^2}}{k} \quad (5b)$$

For  $z_{in,A}^o = z_{in,B}^o = 1$ , the resistance  $r$  can be determined by

$$r = \frac{1 + k^2}{k^2} \frac{1}{C_A^2} = \frac{1 + k^2}{C_B^2} \quad (6)$$

A design procedure is proposed as follows. Given the power ratio  $k^2$ , choose  $z_A$  and solve (5a) to find  $C_A$ . By substituting  $C_A$  into (6),  $r$  and  $C_B$  can be obtained. Finally, find  $z_B$  by substituting  $C_B$  into (5b).

### 3. SIMULATION AND MEASUREMENT RESULTS

For verification, an unequal power divider of power ratio  $k^2 = 1.44$  (1.58 dB) at  $f = 2$  GHz has been designed and fabricated on an FR4 substrate of thickness  $h = 1.6$  mm, dielectric constant  $\epsilon_r = 4.33$ , and loss tangent  $\tan \delta = 0.022$ . In this design,  $z_A = 2.59$  are chosen. The other design parameters are found to be  $C_A = 0.516$ ,  $C_B = 0.619$ ,  $z_B = 1.65$ , and  $r = 6.36$ . Fig. 3 shows the layout and photograph of the fabricated power divider of which size is approximately 3 cm  $\times$  1 cm. A 330- $\Omega$  surface mount resistor is used for good isolation. Fig. 4(a) shows the magnitude of  $S_{11}$  and  $S_{23}$ , where the simulated data are obtained by the full-wave solver Agilent Momentum. Frequency shift is measured and may be caused by the fabrication tolerance and the variation of dielectric constant. Return loss of Port 1 larger than 15 dB is observed from 1.64 GHz to 1.99 GHz. In this frequency range, measured isolation is better than 21 dB. The measured magnitude of  $S_{31}$  and  $S_{21}$  at 2.0 GHz are, respectively,  $-2.89$  and  $-4.62$  dB as shown in Fig. 4(b). The power ratio is 1.73 dB and the 0.15-dB deviation is probably caused by the substrate loss and reflection at Port 1.

#### 4. CONCLUSIONS

A Wilkinson power divider for unequal power split has been presented. Compared with the typical unequal Wilkinson power divider, the proposed circuit utilizes a pair of  $\lambda/4$  coupled lines and does not require any additional impedance transformer. Explicit design formulae have been derived and validated by full-wave simulation and measured data.

#### ACKNOWLEDGMENT

This work was supported in part by the National Science Council of Taiwan, R.O.C., under Grant NSC 101-2221-E-390-016-. The authors are also grateful to the National Center for High-performance Computing for computer time and facilities.

#### REFERENCES

1. Pozar, D. M., *Microwave Engineering*, 3rd Edition, Chaps. 7 and 8, John Wiley & Sons, Inc., 2005.
2. Wu, Y., Y. Liu, Y. Zhang, J. Gao, and H. Zhou, "A dual band unequal Wilkinson power divider without reactive components," *IEEE Trans. Microw. Theory Tech.*, Vol. 57, No. 1, 216–222, 2009.
3. Ahn, S.-H., J. W. Lee, C. S. Cho, and T. K. Lee, "A dual-band unequal Wilkinson power divider with arbitrary frequency ratios," *IEEE Microw. Wireless Compon. Lett.*, Vol. 19, No. 12, 783–785, 2009.
4. Ip, W.-C. and K.-K. M. Cheng, "A novel unequal power divider design with dual-harmonic rejection and simple structure," *IEEE Microw. Wireless Compon. Lett.*, Vol. 21, No. 4, 182–184, 2011.
5. Deng, P.-H. and L.-C. Dai, "Unequal Wilkinson power dividers with favorable selectivity and high-isolation using coupled-line filter transformers," *IEEE Trans. Microw. Theory Tech.*, Vol. 60, No. 6, 1520–1529, 2012.
6. Oraizi, H. and A.-R. Sharifi, "Design and optimization of broadband asymmetrical multisection Wilkinson power divider," *IEEE Trans. Microw. Theory Tech.*, Vol. 54, No. 5, 2220–2231, 2006.
7. Zhu, Y.-Z., W.-H. Zhu, X.-J. Zhang, M. Jiang, and G.-Y. Fang, "Shunt-stub Wilkinson power divider for unequal distribution ratio," *IET Microw. Antennas Propagat.*, Vol. 4, No. 3, 334–341, 2010.
8. Xi, L., Y. Lin, and C. Xi, "Novel design of dual-band unequal Wilkinson power divider with isolation stubs," *Int. Conf. Microw. Millimeter Wave Tech.*, Vol. 2, 1–3, Shenzhen, China, May 2012.

# A New Lowpass-to-broadband Synthesis Method which Preserves DC Connection

Tao-Yi Lee, Li-Han Chang, and Yu-Jiu Wang

Institute of Electronics, National Chiao-Tung University, 1001 Ta-Hsueh Road Hsinchu, 30010, Taiwan

**Abstract**— A theory and design procedures for realizing a broadband ( $\omega_L$  to  $\omega_H$ ) impedance transformation network utilizing a LC-ladder with no transmission zero at DC are proposed. For even-order networks, using the new  $\omega^2$ -shifting method on a typical low-pass Chebyshev filter transfer functions directly derives their broadband optimum. In the odd-order cases, numerical optimizations will be required, but the networks are capable of absorbing parasitic capacitance at both RF I/O ports. To experimentally verify the proposed methods, a 10th-order 0.9–4.5 GHz 50-to-250  $\Omega$  impedance transformation network and a three-port 0.45–4 GHz Wilkinson power divider have been designed and fabricated using 1.6-mm two-layer FR4 laminates.

## 1. INTRODUCTION

Impedance matching is fundamental in RF circuit designs. To achieve maximum power transfer over desired bandwidths ( $\omega_L$  to  $\omega_H$ ), passive networks, preferably lossless, are designed to match the load impedance and the source impedance. Fundamental limits on the broadband impedance matching are generally studied by Bode [1] and Fano [2] and many authors have contributed to this topic over the last seven decades since S. Darlington's 1939 seminal paper on insertion loss method [3].

When insertion loss method is utilized in matching broadband multichip module (MCM), a probable scenario is shown in Fig. 1, where MMIC 1 and MMIC 2 are a CMOS transmitter and a Gallium-Arsenide (GaAs) power amplifier respectively. To ensure maximum power transfer between the chips over wide bandwidth (e.g., 5.8 GHz~24 GHz), an impedance matching network is necessary. In addition, it will be convenient if the bias voltages of the Ga/As PA can be controlled directly from the CMOS chip, instead of using an external bias-tee.

Standard filter approximation with the aid of frequency transformation is a proven way to synthesize passive frequency-selective matching networks. In this design case, an  $s \rightarrow s + s^{-1}$  [4] mapping can be adopted to transform to a lowpass prototype network to its broadband matching counterpart. However, there are four disadvantages of this approach:

- 1) The order of the filter and the total number of passive components are doubled.
- 2) An inductor is transformed to a serial LC resonator which blocks Direct Current (DC) path.
- 3) Critical metal etching may be required to realize the serial LC on a planar process.
- 4) Undesired board substrate mode can be easily excited by strong electric fields around the resonant gaps.

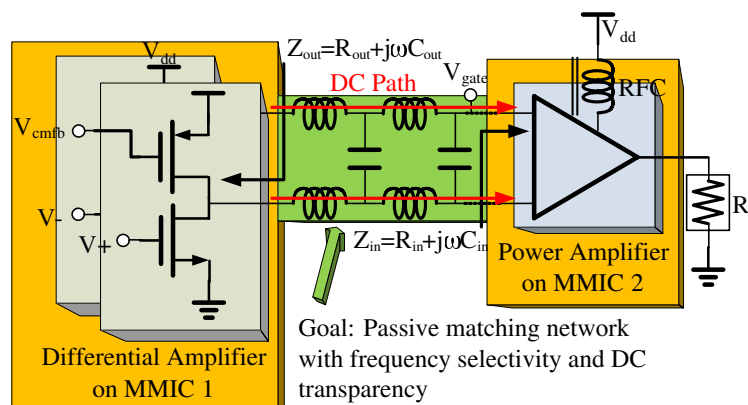


Figure 1: Passive output network is critical in power amplifier design.

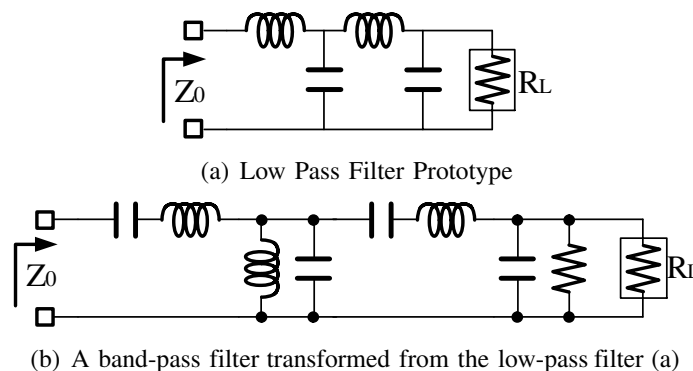


Figure 2: Illustration of low-pass to band-pass transform using  $s \rightarrow s + s^{-1}$  mapping. Number of passive components is doubled typically.

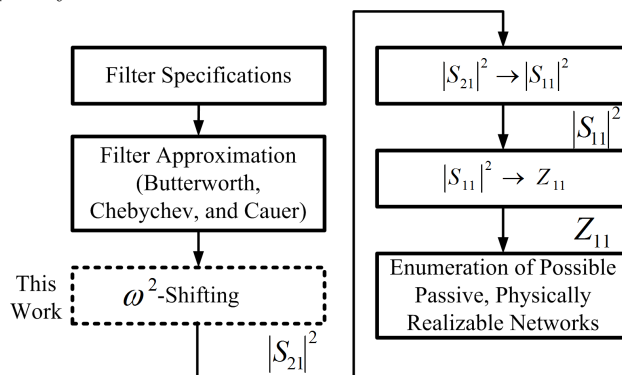


Figure 3: The systematic way to synthesize impedance matched filters. (Refer to chapter 9 of [4] for details).

Numeric approaches, like the method of least-square (MLS), are powerful of choosing component values against specifications. The quality of MLS is subject to its initialization, which is a specified topology. It is a non-trivial task to choose a suitable topology, and this leaves MLS to experienced designers.

In this paper, a systematic way (Fig. 3) to search for suitable candidates that preserves DC connection is proposed. In the following sections, we first formulate the problem and identify key network properties in Part II. In Part III, even-order and odd-order are dealt with the  $\omega^2$ -shifting method and numerical optimizations respectively. Part III also describes how the proposed method provides advantages in broadband MMIC design, which usually relies on technologies without high-quality passive components. Part IV and V will be on the experimental results with a conclusion.

## 2. PROBLEM FORMULATION

Matching a source resistor  $R_s$  to a load resistor  $R_L$  using non-uniform transmission line can be approximated to an LC-ladder with sufficiently high order (as shown in Fig. 4). In this ladder model, serial inductors ( $L_2, L_4, \dots$ ) are connected between adjacent nodes, each with shunt capacitors ( $C_1, C_3, \dots$ ) connected to ground. Since serial branch in ladder generates transmission zero when its impedance approaches infinity, each inductor generates a transmission zero at  $\omega = \infty$ . Similarly, each shunt capacitor also generates a transmission zero at  $\omega = \infty$ . Considering a transfer function  $H(j\omega)$  with all the zeros located at either DC or infinity only, squared magnitude of insertion loss (i.e., transducer gain),  $|S_{21}|^2 = 4R_s/R_L |H(j\omega)|^2$  as in (9.2) from [4], may be simplified to a function of  $\omega^2$ :

$$|S_{21}|^2 = \frac{1}{1 + X(\omega^2)} \quad (1)$$

Classic insertion loss method starts from finding a suitable  $|S_{21}|^2$ , deriving  $|S_{11}|^2$  with  $1 - |S_{21}|^2$ , permutating  $S_{11}$  as a rational function of  $s \equiv j\omega$  from  $|S_{11}|^2$ , and deriving the corresponding input impedance  $Z_{in}$  seen by  $R_s$  using  $R_s \frac{1+S_{11}}{1-S_{11}}$ . The ladder networks are synthesized through

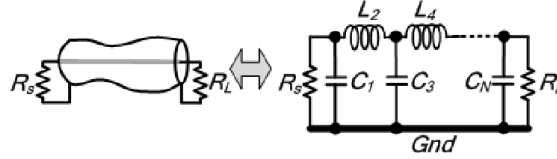


Figure 4: A non-uniform transmission line is approximated to a finite-order LC-ladder.

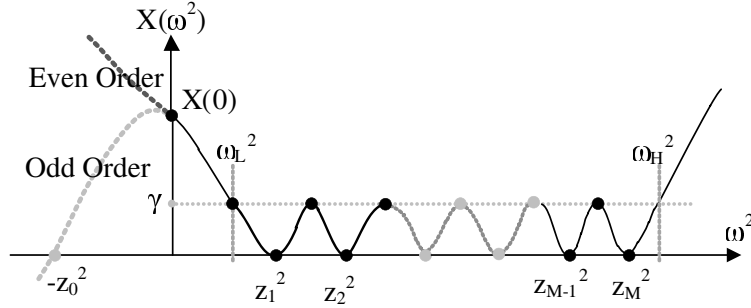


Figure 5:  $X(\omega^2)$  is evaluated over real  $\omega^2$ . Positive and negative  $\omega^2$  correspond to imaginary and real axis in the  $s$ -plane respectively.

iterative zero removals based on the permuted  $Z_{in}$ . Since  $R_s$  is connected to  $R_L$  only through inductors, the  $|S_{21}|^2$  at DC can be directly calculated as if  $R_s$  is shorted to  $R_L$ . This corresponds to  $|S_{21}|^2 = \frac{4R_L R_s}{(R_L + R_s)^2}$  at DC, or equivalently  $X(0) = \frac{(R_L - R_s)^2}{4R_L R_s}$ , which essentially means  $X(0)$  is only determined by impedance transformation ratio  $R_L/R_s$ . Furthermore, to achieve in-band high power transmission,  $|S_{21}|^2$  should be very close to unity. This corresponds to a small positive real  $X(\omega^2)$  from  $\omega_L$  to  $\omega_H$ , and varies between 0 and  $\gamma$ , which is related to in-band ripples (Fig. 5). The relation between impedance conversion ratio,

$$\zeta = Z_L/Z_S, \quad (2)$$

$|S_{21}|^2$  in-band ripple,

$$\delta = \frac{1}{1 + \gamma^2} \quad (3)$$

and relative bandwidth,

$$\beta = \omega_H/\omega_L, \quad (4)$$

based on a given network order,  $N$  is:

$$\zeta_b = 1 + 2 \left( \frac{1}{\delta} - 1 \right) \cos^2 \left( N \cos^{-1} \sqrt{\frac{-1}{\beta^2 - 1}} \right) \quad (5)$$

$$\zeta(\delta, \beta, N) = \zeta_b + \sqrt{\zeta_b^2 - 1}, \quad (6)$$

as shown in Fig. 6(b).

On the other hand, in Fig. 6(a), the relation between  $|S_{21}|^2$  in-band ripple and relative bandwidth based on a given network order is:

$$\delta(\zeta, \beta, N) = \frac{1}{1 + \left( \frac{1}{\zeta} - 1 \right) \cos^2 \left( N \cos^{-1} \sqrt{\frac{-1}{\beta^2 - 1}} \right)} \quad (7)$$

It can be shown that to achieve minimum in-band ripples, there are only two possible choices for  $X(\omega^2)$  as (8) for even-order networks, and (9) for odd-order networks.

$$\text{Even} : X(\omega^2) = C \times \prod_1^M (\omega^2 - z_m^2)^2 \quad (8)$$

$$\text{Odd} : X(\omega^2) = C \times (\omega^2 + z_0^2) \times \prod_1^M (\omega^2 - z_m^2)^2 \quad (9)$$

Impedance transformation ladder network design problem is now reduced to finding the corresponding zeros for  $X(\omega^2)$ , i.e.,  $z_0, z_1, \dots, z_M$ , and constant factor  $C$  that allows the ladder to achieve the required impedance transformation ratio  $\zeta$ , bandwidth ratio  $\beta$  and ripples  $\delta$  impedance transformation at a specified network order. Normalized values in the following text are based on  $z_s = 1$  and  $\sqrt{\omega_H \omega_L} = 1$ .

### 3. OPTIMAL SOLUTIONS

#### 3.1. $\omega^2$ -shifting Technique in Optimal Even-ordered $X(\omega^2)$

Even-ordered broadband impedance transformation networks can be solved directly by substitution of variables with low-pass Chebyshev polynomials. Let  $T_N(\omega)$  be the  $N$ -th order type-I Chebyshev polynomial. If  $N$  is an even number, then  $T_N(\omega)$  is also a function of  $\omega^2$ , denoted as  $T_N(\omega^2)$ . In a typical even-order Chebyshev low-pass filter, we choose

$$X(\omega^2) = C/2^{2N-2} \times T_N^2(\omega^2) \quad (10)$$

The proposed new  $\omega^2$ -shifting method maps low-pass transfer function to band-pass by the following transformation:

$$X'(\omega^2) = C/2^{2N-2} \times T_N^2(\omega'^2) \Big|_{\omega'^2 \rightarrow \frac{\omega^2 - \omega_L^2}{\omega_H^2 - \omega_L^2}}, \quad (11)$$

where  $\omega_L^2$  and  $\omega_H^2$  are transformed from  $\omega'^2 = 0$  and 1, respectively.  $C/2^{2N-2}$  is a constant coefficient.  $\omega^2$ -shifting technique does not work for odd-order Chebyshev polynomials due to unrealizable negative  $X(\omega^2)$  for some positive  $\omega^2$ . Nonetheless, numerical methods may be adopted to solve odd-ordered transfer functions, which is described in the following section. Transfer functions derived from  $\omega^2$ -shifting are optimal, and can be easily proved by contradiction. With  $R_S < R_L, C_0$  in Fig. 6 will be zero.

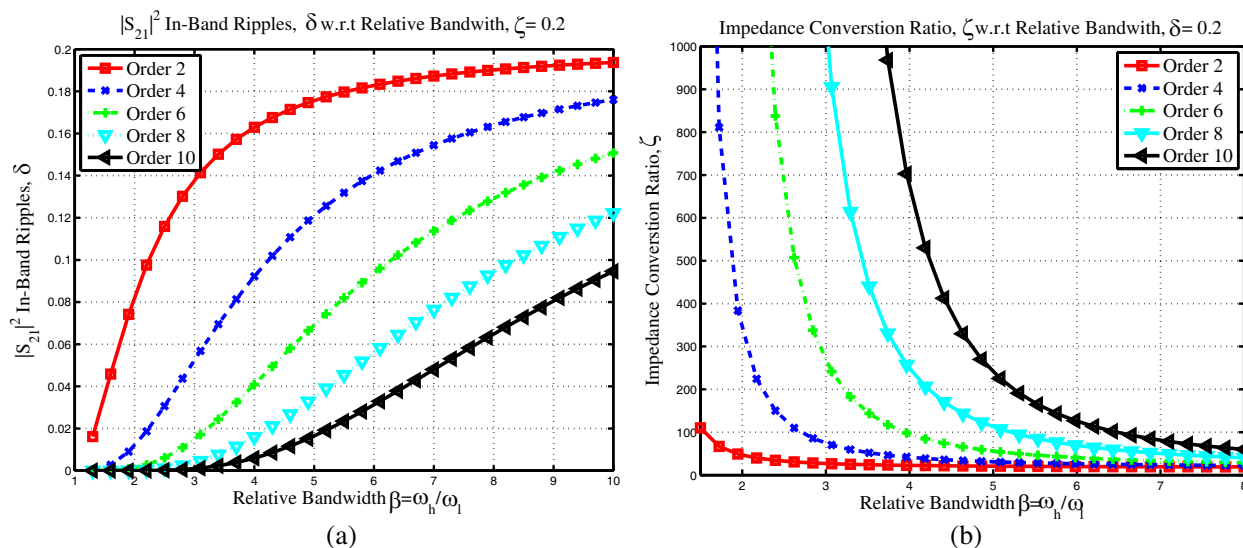


Figure 6: Relations between network order, relative bandwidth  $\beta = \omega_H/\omega_L$ , in-band ripple  $\delta$  and impedance transformation ratio  $\zeta = R_L/R_S$ . (a) Normalized in-band ripple as a function (7) of network order and relative bandwidth with impedance transformation ratio  $\zeta$  set to 0.2. (b) Impedance transformation ratio as a function (6) of network order and relative bandwidth with ripple  $\delta$  set to 0.2.

### 3.2. Numerical Approaches for Odd-ordered $X(\omega^2)$

Odd-ordered ladders based on (9) require more order to achieve the same ripple, impedance transformation ratio and bandwidth in theory. Mini-max optimization is adopted to find the real zeros ( $z_1^2, z_2^2, \dots$ ) with prescribed  $z_0, \omega_L$  and  $\omega_H$ . Once the optimization is converged, a symbolic ladder permutator/synthesizer implemented in MATLAB will carry out transfer function synthesis to find all possible component values.

Because of the presence of designable shunt capacitances on both terminals, odd-ordered network is particularly useful in practical designs. By increasing design parameter  $z_0$  in (9), an improving impedance transformation ratio is traded-off for a reducing source parasitic capacitance  $C_0$ . Hence, if a source parasitic capacitance is given a priori, an optimal  $z_0$  can be determined to realize maxi-

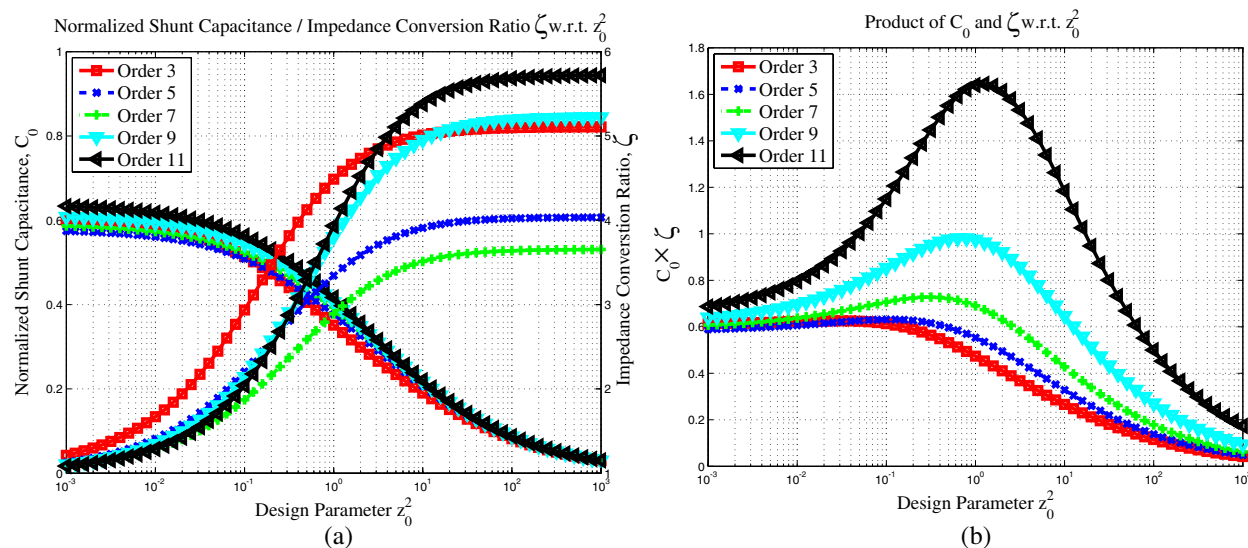


Figure 7: Normalized shunt capacitance versus impedance transformation ratio. (a) Normalized shunt capacitance versus impedance transformation ratio  $R_L/R_S$  as a function of  $z_0^2$  for a normalized bandwidth  $\omega_H/\omega_L = 4$ , where ripple = 0.1 dB and  $\sqrt{\omega_H\omega_L} = 1$ . (b) Product of  $C_0$  and  $\zeta$ , maximum  $C_0 \times \zeta$  may be achieved when  $z_0$  is approximately 1, especially in high order networks.

Table 1: Equi-ripple odd ordered filter prototypes (number of dc transmission zeros = 0, relative bandwidth = 4,  $z_0^2 = 10^0$ ).

$N$	$pC_1$	$sL_2$	$pC_3$	$sL_4$	$pC_5$	$sL_6$	$pC_7$	$sL_8$	$pC_9$	$sL_{10}$	$pC_{11}$	$ S_{21} $ ripple, $\delta$ (dB)	Impedance transformation $\zeta$ ( $\times 50\Omega$ )
3	0.579	0.492	0.515									0.1285	0.713
5	0.627	0.637	1.099	0.546	0.585							0.1177	0.659
7	0.689	0.639	1.269	0.614	1.428	0.461	0.776					0.1312	0.526
9	0.750	0.611	1.444	0.550	1.825	0.443	2.145	0.314	1.233			0.1489	0.348
11	0.809	0.577	1.641	0.471	2.336	0.341	3.226	0.247	4.078	0.166	2.486	0.1695	0.180

Table 2: Equi-ripple odd ordered filter prototypes (number of DC transmission zeros = 0, relative bandwidth = 4,  $z_0^2 = 10^1$ ).

$N$	$pC_1$	$sL_2$	$pC_3$	$sL_4$	$pC_5$	$sL_6$	$pC_7$	$sL_8$	$pC_9$	$sL_{10}$	$pC_{11}$	$ S_{21} $ ripple, $\delta$ (dB)	Impedance transformation $\zeta$ ( $\times 50\Omega$ )
3	0.331	0.395	0.191									0.02389	0.848
5	0.450	0.634	0.837	0.507	0.237							0.02685	0.788
7	0.515	0.673	1.027	0.696	1.041	0.478	0.289					0.03055	0.678
9	0.559	0.670	1.139	0.677	1.332	0.586	1.367	0.386	0.391			0.03476	0.516
11	0.599	0.655	1.248	0.621	1.594	0.508	1.956	0.402	2.125	0.255	0.636	0.03955	0.325

imum impedance transformation ratio through numeric successive approximations. Considering the product of impedance transformation ratio and available terminal capacitance, optimal odd-ordered networks may be achieved when  $z_0 \approx 1$ . The significance of optimality increases in high-ordered networks, as depicted by the increasing peak values for different curves in Fig. 7(b). Also note the extreme case where  $z_0 \rightarrow \infty$ , an odd network is converged into an optimal even-order network which order is smaller by one.

For odd-ordered networks, design tables are shown in Table 1 and Table 2. For comparison,  $z_0^2$  are set to 1 and 10, respectively; For even-ordered networks, design tables are shown in Table 3. In the tables, “pC” stands for shunt (parallel) capacitances; “sL” stands for serial inductances.

#### 4. DESIGN EXAMPLES AND EXPERIMENTS

##### 4.1. One-port Impedance Transformation Network

A 10th-order broadband impedance transformation network is synthesized based on the procedures proposed in previous sections. The  $X(\omega^2)$  function is optimized to achieve flat in-band ripple

Table 3: Equi-ripple even ordered filter prototypes, relative bandwidth = 4.

$N$	$sL_1$	$pC_2$	$sL_3$	$pC_4$	$sL_5$	$pC_6$	$sL_7$	$pC_8$	$sL_9$	$pC_{10}$	$ S_{21} $	in-band ripple, $\delta$ (dB)	Impedance transformation $\zeta(\times 50 \Omega)$
2	0.609	0.341									0.2844		0.559
4	0.813	0.560	1.306	0.349							0.3236		0.429
6	0.920	0.538	1.697	0.445	2.053	0.241					0.3682		0.262
8	1.009	0.500	2.023	0.373	3.022	0.249	4.056	0.124			0.4190		0.123
10	1.087	0.467	2.325	0.315	3.970	0.186	6.723	0.109	9.985	0.051	0.4767		0.047

Table 4: Comparison of  $n$ th order  $\omega^2$ -shifting and the transcendental frequency transformation.

Specification	$\omega^2$ -shifting [This Work]	Conventional Frequency Transformation
Lumped elements	$n$	$2n$
DC characteristics	DC transfer function is a design parameter	Typically Blocked
Max.terminal capacitance absorption through Norton transform	Similar performance	

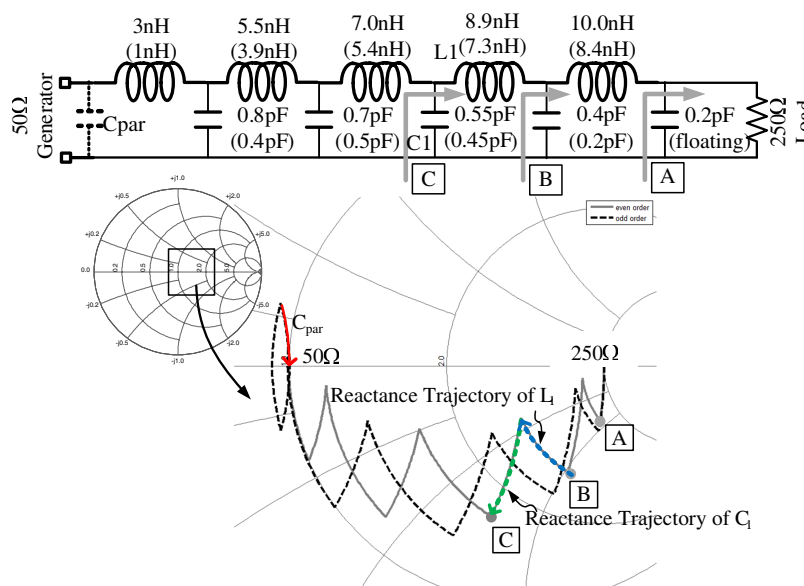


Figure 8: Illustration of impedance transformations per stage of an even-order (10th order, gray line) and an odd-order (11th order, dotted line) network with synthesized design values. Values in parenthesis are components’ nominal values used in our experiments where board parasitics are compensated. Note that the extra trajectory on the Smith chart is introduced by the source capacitance  $C_{par}$ .

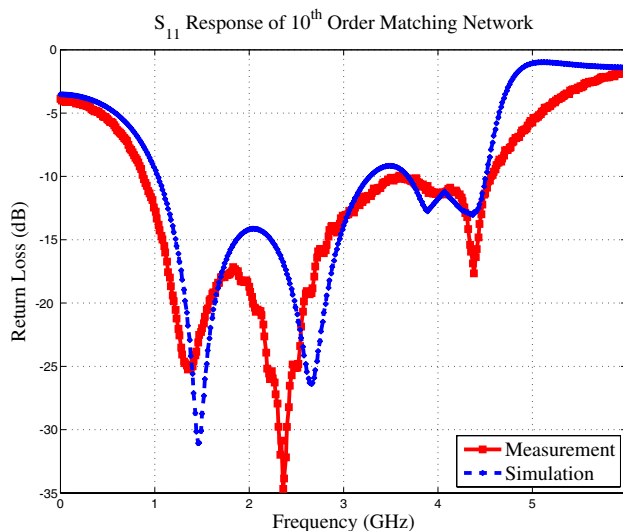


Figure 9:  $S_{11}$  of the 10-order  $50\ \Omega$  to  $250\ \Omega$  transformer. The network demonstrated  $-10$  dB in-band return loss from  $0.9$  GHz to  $4.5$  GHz. Board parasitics and device models are included in simulation setup.

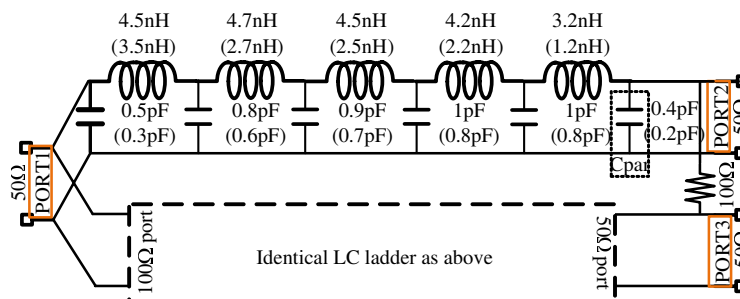


Figure 10: Broadband Wilkinson power divider and synthesized design values (component values in parenthesis). The shunt capacitors at port 2 and port 3 only exist in odd-order cases.

over the prescribed bandwidth, and the normalized transmission zeros are located at  $z_1 = 0.3138$ ,  $z_2 = 1.2422$ ,  $z_3 = 2.7443$ ,  $z_4 = 4.2465$ ,  $z_5 = 5.1749$ . Although the proposed methods can be used to design distributed network, out-of-the-shelf discrete components are used in prototypes, which are mounted on doubled-layered  $1.6$  mm-thickness FR4 laminates. EM simulations are carefully carried out to estimate copper parasitic networks which is later used to compensate the design values when choosing discrete RF components (Fig. 8). From the same figure, it can be seen that a source parasitic capacitor deviates away the trajectory of impedance matching, which makes an odd-order network less optimal than an even-order network in theory. Simulation precisions are mainly limited by the self-resonances of passive components, and component parasitic models are extracted from several other measurements.

#### 4.2. Wideband Wilkinson Power Divider

A Wilkinson power divider [5] typically consists of two parallel section of  $50\ \Omega$  to  $100\ \Omega$  quarter-wave transformers to matches three  $50\ \Omega$  ports simultaneously. These transformers are replaced by two eleventh-order impedance transformation networks as shown in Fig. 10. A  $0.5$ – $5$  GHz decade bandwidth is initially chosen, and designed as well as implemented in the same FR4 process. Similar EM simulations are carried and passive parasitic models are applied in the final simulations. Both simulation and measurement results for Return Loss (RL) are shown in Fig. 11(a), and the Insertion Loss (IL) and Group Delay (GD) are plotted in Fig. 11(b). Based on Fig. 11(a), the designed network achieves  $a < 10$  dB  $S_{11}$  over a decade bandwidth; however, the quality factor of the offchip inductors used in the experiments lie between 10 and 20 for the frequencies of interest. This results in an excessive measured insertion loss. Future revisions can be implemented in a micro-stripline equivalence to reduce this unnecessary loss.

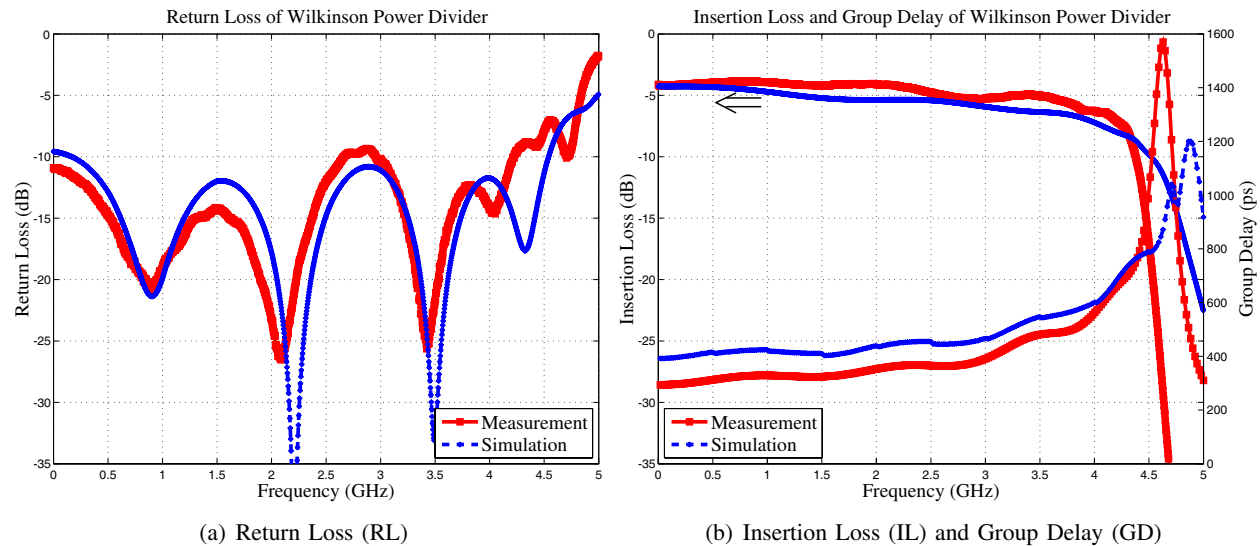


Figure 11: Simulation and measurement results of Wilkinson power divider.

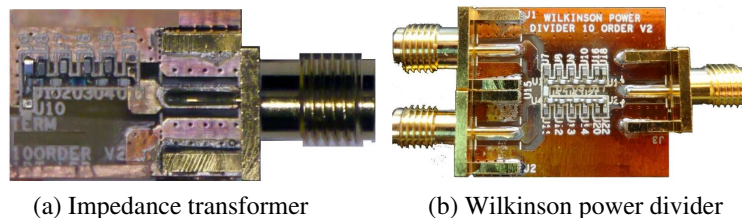


Figure 12: Fabricated PCB prototypes; Board dimension are 15.7 mm × 11.6 mm and 20 mm × 20 mm, respectively

## 5. CONCLUSION

The theory and design procedures proposed in this paper are practical for designs and have been verified through circuit simulations and several experiments. The analytic  $\omega^2$ -shifting technique allows us to explore high-order (distributed) transmission line transformer easier in the future.

## REFERENCES

1. Bode, H., *Network Analysis and Feedback Amplifier Design*, No. 8, Bell Telephone Laboratories Series, Van Nostrand, 1952.
2. Fano, R. M., "Theoretical limitations on the broadband matching of arbitrary impedance," *Journal of the Franklin Institute*, Vol. 249, 57–84 and 139–154, Jan. 1950.
3. Darlington, S., "Synthesis of reactance 4-poles which produce prescribed insertion loss characteristics," *Journal of Mathematics and Physics*, Vol. 18, No. 2, 257–353, Sep. 1939.
4. Wing, O., *Classical Circuit Theory*, Lecture Notes in Mathematics, Springer, 2008.
5. Pozar, D. M., *Microwave Engineering*, 2nd Edition, John Wiley & Sons, Inc., 2004.

# Contactless Power Transmission Track with Core Array Structure Unit for Mobile Apparatuses

Jia-You Lee, Hung-Yu Shen, and Yi-Ying Lee

Department of Electrical Engineering, National Cheng Kung University, Tainan, Taiwan, R.O.C.

**Abstract**— A contactless power transmission track with core array structure unit for mobile apparatuses is proposed. FEA software is adopted to analyze and design the arrangement of core array structure unit and pick up coil. In addition, the connection of each coil of proposed core array structure unit would be discussed to clarify the distribution and density of its magnetic field. High frequency exciting source and control circuit of the proposed contactless power transmission track with core array structure unit are implemented. The feasibility and reliability of the concept which is presented in this research is verified by analyzing the magnetic field distribution of core array structure unit and executing the experiment for test system.

## 1. INTRODUCTION

Traditional power transmission system has two drawbacks. Firstly, it relies on the contact of metals. This can be hazardous and unreliable under certain extreme condition, i.e., environment with dampness, overfilling of explosive gases and so on. Secondly, power cord is needed to transfer power in the traditional power transmission system. This can be inconvenient for powering mobile apparatuses as how and where to place the cord of the mobile apparatuses has to be taken into consideration. In order to overcome the two drawbacks mentioned above, battery is applied. However, some other problems result, like pollution, rise in cost and etc..

In the past two decade, the concept of contactless electromagnetic induction in power transmission has been widely used for the applications of industry [1, 2] and consumer [3, 4]. When contactless power transmission is applied in mobile apparatuses, higher mobility is achieved, i.e., mobile apparatuses are able to move more freely compared to the mobile apparatuses powered by traditional power transmission technique. Several concepts of delivering power to mobile apparatuses by using contactless power transfer are proposed [5–8]. The efficiency of contactless power transmission system is lower than that of traditional power transmission system. However, contactless power transmission system has higher reliability, higher isolation and higher flexibility. Thus, hot to enhance the efficiency effectively is necessary for the contactless power transmission system. Some discussions of improving the efficiency problem of system are presented such as resonant topologies [9], driving circuit of primary winding [10, 11], and inductive coupled structure [12, 13].

The objective of this paper is to investigate the contactless power transmission techniques to implement a contactless power transmission track for mobile apparatuses resulting in the improvement of above inconvenience. Therefore, the core array structure unit is proposed in this paper so as to supply power stably to mobile apparatuses. A uniform magnetic field is established by arranging several cores in a square array with area of  $13 \times 15 \text{ cm}^2$ . The block diagram of proposed contactless power transmission track system with core array structure unit is shown in Fig. 1. The contactless power transmission track system is described, and its resonant topology and reflected impedance are discussed briefly in Section 2. Results from an experimental test system are presented and demonstrated in Section 3 and Section 4 to valid the design concept of this paper.

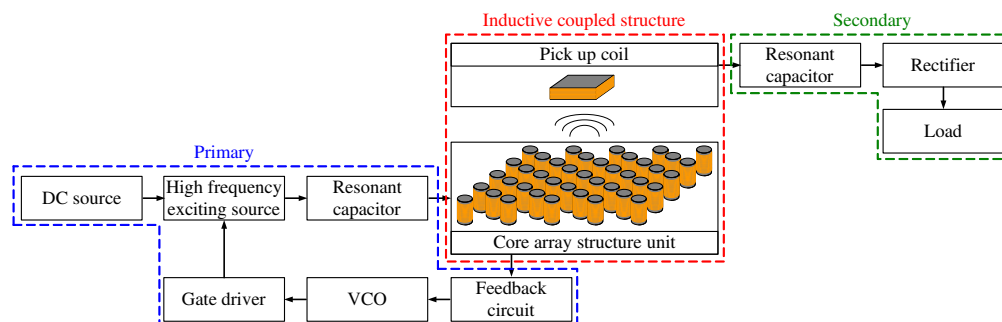


Figure 1: Block diagram of proposed track system.

## 2. ANALYSIS OF RESONANT TOPOLOGIES AND REFLECTED IMPEDANCE

Contactless inductive coupled structure, similar to the loosely coupled transformer, possesses leakage inductance which is especially large to result in the inefficient power transfer. Therefore, the resonant topology is used to reduce the leakage inductance and to improve the power transfer efficiency of system. In [7], the analysis of reflected impedance and the criteria of bifurcation phenomenon are discussed to assure the power transfer capability and controllability. In addition, four equivalent impedances corresponding to these difference connections of primary and secondary resonant tank can be determined through the following equations:

$$Z_P = \begin{cases} r_P + j\omega L_P + \frac{1}{j\omega C_P} & \text{series primary resonant tank} \\ \frac{1}{\frac{1}{r_P + j\omega L_P} + j\omega C_P} & \text{parallel primary resonant tank} \end{cases} \quad (1)$$

$$Z_S = \begin{cases} R_L + r_S + j\omega L_S + \frac{1}{j\omega C_S} & \text{series secondary resonant tank} \\ j\omega L_S + \frac{1}{\frac{1}{R_L + r_S} + j\omega C_S} & \text{parallel secondary resonant tank} \end{cases} \quad (2)$$

where  $\omega$  is the angular frequency of system;  $R_L$  is the load resistance on the secondary;  $Z_P$  and  $Z_S$  are the impedance of primary and secondary resonant tank, respectively;  $L_P$  and  $L_S$ , respectively are the inductance of primary and secondary winding;  $r_P$  and  $r_S$  are the resistance of primary and secondary winding, respectively;  $C_P$  and  $C_S$  are the primary and secondary resonant capacitor, respectively.

Hence the impedance which is reflected from secondary to primary depends on the connection of secondary resonant tank as given by

$$Z_{rS} = \frac{\omega^4 C_S^2 M^2 R_L}{(\omega^2 C_S L_S - 1)^2 + \omega^2 C_S^2 R_L^2} - j \frac{\omega^3 C_S M^2 (\omega^2 C_S L_S - 1)}{(\omega^2 C_S L_S - 1)^2 + \omega^2 C_S^2 R_L^2} \quad (3)$$

and

$$Z_{rP} = \frac{\omega^2 M^2 R_L}{R_L^2 (\omega^2 C_S L_S - 1)^2 + \omega^2 L_S^2} - j \frac{\omega^3 M^2 [C_S R_L^2 (\omega^2 C_S L_S - 1) + L_S]}{R_L^2 (\omega^2 C_S L_S - 1)^2 + \omega^2 L_S^2} \quad (4)$$

where  $M$  is the mutual inductance between primary and secondary winding

The curve depicted in Fig. 2 and Fig. 3 show the frequency response of reflected impedance based on the calculation results according (3) and (4). Figs. 2(a) and (b) display the real part of reflected impedance,  $\text{Re}(Z_{rS})$  and  $\text{Re}(Z_{rP})$  referring to series and parallel connections of secondary resonant tank. Moreover, the imaginary part of reflected impedance,  $\text{Im}(Z_{rS})$  and  $\text{Im}(Z_{rP})$ , respectively are shown in Figs. 3(a) and (b). It can be seen that the best way to decrease the loading effect of system and to enhance the transfer efficiency of system especially the lower  $R_L$  on the secondary must equalize the operating frequency as much as possible to resonant frequency. According to the calculation results, the parallel secondary resonant tank is selected to minimize the loading effect of system in high power operation. Besides the series primary resonant tank should be chosen to

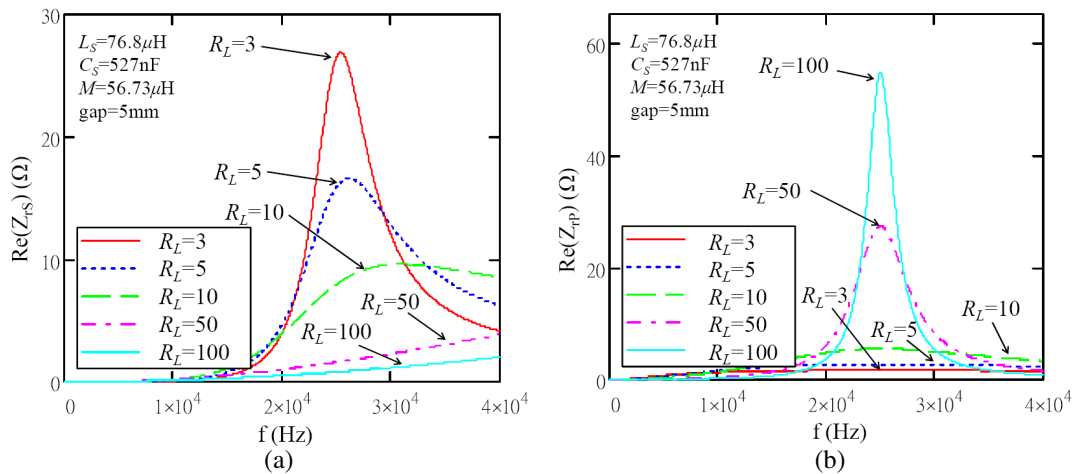


Figure 2: Real part of reflected impedance refers to (a) series and (b) parallel connections on secondary.

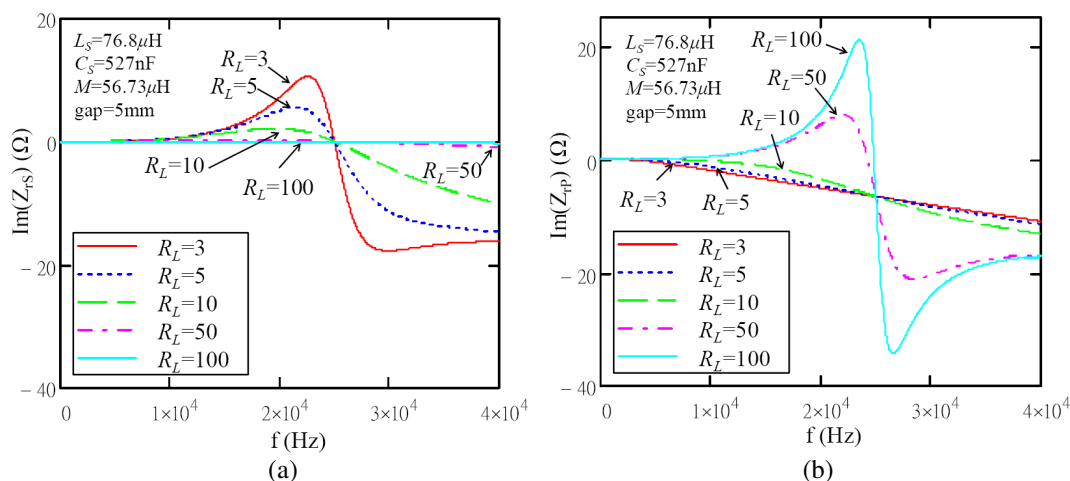


Figure 3: Imaginary part of reflected impedance refers to (a) series and (b) parallel connections on secondary.

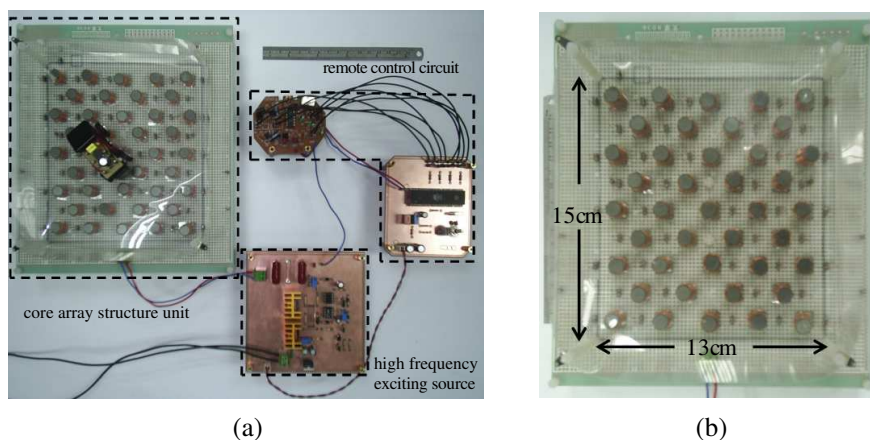


Figure 4: Diagram of (a) proposed test system and (b) core array structure unit.

Table 1: Design specifications and parameters of proposed test system.

DC Input voltage	25 V	Primary coil inductance (@25 kHz)	167.6 $\mu\text{H}$
Operating frequency	25 kHz	Primary resonant capacitance (@25 kHz)	241 nF
Power MOSFET of exciting source	IRF540	Secondary coil inductance (@25 kHz)	76.8 $\mu\text{H}$
Driver IC of exciting source	IR2153	Secondary resonant capacitance (@25 kHz)	527 nF

yield high primary current for core array structure unit as class D inverter is driven by voltage source.

### 3. EXPERIMENTAL RESULTS

To verify the effectiveness of the contactless power transmission track, prototype of the track system with core array structure unit is implemented. The design specifications and parameters of the test system are listed in Table 1. Figs. 4(a) and (b), respectively demonstrate the diagram of test system and core array structure unit.

The experiment is carried out in this paper to test the feasibility of proposed system. The experimental data are presented as follow. Fig. 5(a) shows the signals of gate (i.e.,  $v_{GS1}$  and  $v_{GS2}$ ) with deadtime of 6  $\mu\text{s}$  which are able to avoid short circuit of exciting source. The measured square waveforms in Fig. 5(b) are driving signal and cross voltage of MOSFET. When the cross voltage of MOSFET,  $v_{DS2}$  decreased to zero, driving signal of MOSFET,  $v_{GS2}$  would be triggered, resulting in exciting source possessing the effect of ZVS. Fig. 5(c) represents input voltage and current of core array structure unit. It can be seen the input current of core array structure unit,  $i_{TANK}$

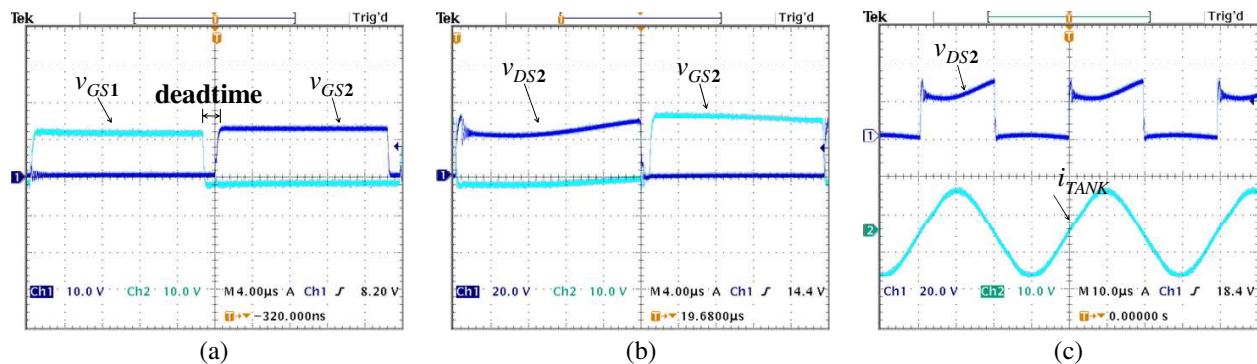


Figure 5: Experimental waveforms of proposed system, (a)  $v_{GS1}$  and  $v_{GS2}$ , (b)  $v_{DS2}$  and  $v_{GS2}$ , and (c)  $v_{DS2}$  and  $i_{TANK}$ .

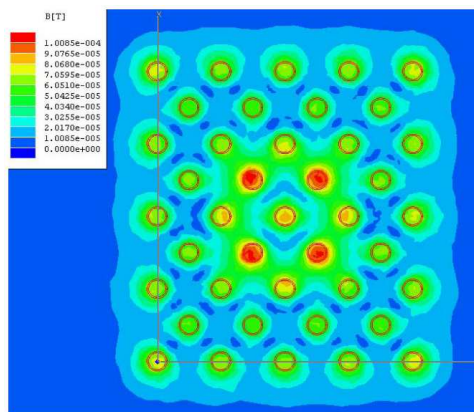


Figure 6: Simulation result of core array structure unit.

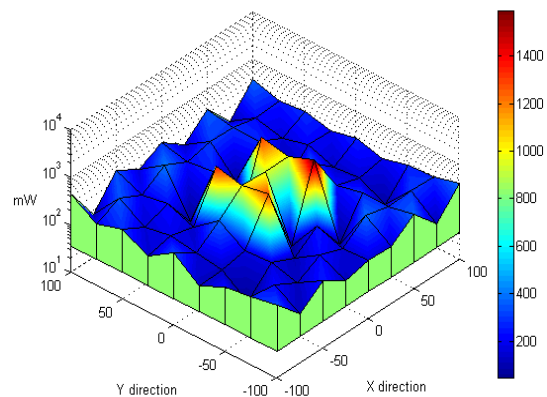


Figure 7: 3D distribution diagram of measured power.

lag the  $v_{DS2}$ , signifying the operating frequency of the system is larger than the frequency of the resonant tank to lead to change the input impedance of tank into inductive. Besides, input current of core array structure unit is indeed a sine wave, thus core array structure unit is capable to establish a continuous alternating magnetic field Fig. 6 illustrates the simulation result of the core array structure unit, using FEA software Maxwell. Fig. 7 represents the 3D distribution diagram of measured transfer power of the contactless power transmission track system with core array structure unit, with highest transfer power, 1.4 W in the central region of the core array structure unit. Consequently, the proposed concept that the mobile apparatuses can pick up enough power to enable it to move around freely by contactless power transmission track is achieved.

#### 4. CONCLUSIONS

In this research, a contactless power transmission track system with core array structure unit for mobile apparatuses was introduced. The core array structure unit was proposed and its arrangement of core are analyzed and simulated to clarify the distribution and density of magnetic field by using FEA software, Maxwell. The SP resonant topology is selected to minimize the loading effect of system in high power operation and to yield high primary current for core array structure unit as class D inverter is driven by voltage source. In addition, high frequency exciting source and feedback control circuit of the contactless power transmission track with core array structure unit are realized. Experimental results show that the proposed system in this research can deliver power 1.4 W stably to mobile apparatus under the condition of air gap 5 mm.

#### ACKNOWLEDGMENT

This work was sponsored in part by the National Science Council, Taiwan, R.O.C. under Grant NSC 99-2221-E-006-232-MY3.

## REFERENCES

1. Sato, F., T. Kojiya, H. Matsuki, and T. Sato, “Automatic power supply system to underwater vehicles utilizing non-contacting technology,” *Proceedings of IEEE Techno-Ocean*, 2341–2345, Kobe, Japan, Nov. 2004.
2. Heeres, B. J., D. W. Novotny, D. M. Divan, and R. D. Lorenz, “Contactless underwater power delivery,” *Proceedings of IEEE Power Electronics Specialists Conference*, 418–423, Taipei, Taiwan, Jun. 1994.
3. Lee, J. Y., H. Y. Shen, and T. W. Chang, “Contactless inductive charging system with hysteresis loop control for small-sized household electrical appliances,” *Proceedings of IEEE Applied Power Electronics Conference and Exposition*, 2172–2178, Orlando, FL, USA, Feb. 2012.
4. Shen, H. Y., J. Y. Lee, and T. W. Chang, “Study of contactless inductive charging platform with core array structure for portable products,” *Proceedings of International Conference on Consumer Electronics, Communications and Networks*, 756–759, Xianning, China, Apr. 2011.
5. Lastowiecki, J. and P. Staszewski, “Sliding transformer with long magnetic circuit for contactless electrical energy delivery to mobile receivers,” *IEEE Transactions on Industrial Electronics*, Vol. 53, No. 6, 1943–1948, 2006.
6. Sato, F., J. Murakami, H. Matsuki, S. Kikuchi, K. Harakawa, and T. Satoh, “Stable energy transmission to moving loads utilizing new CLPS,” *IEEE Transactions on Magnetics*, Vol. 32, No. 5, 5034–5036, 1996.
7. Lorenz, R. D., D. M. Divan, D. W. Novotny, and K. W. Klontz, “Contactless power delivery system for mining applications,” *IEEE Transactions on Industry Applications*, Vol. 31, No. 1, 27–35, 1995.
8. Covic, G. A. and S. Raabe, “Practical design considerations for contactless power transfer quadrature pick-ups,” *IEEE Transactions on Industrial Electronics*, Vol. 60, No. 1, 400–409, 2013.
9. Covic, G. A., C. S. Wang, and O. H. Stielau, “Power transfer capability and bifurcation phenomena of loosely coupled inductive power transfer systems,” *IEEE Transactions on Industrial Electronics*, Vol. 51, No. 1, 148–157, 2004.
10. Valtchev, S., B. Borges, K. Brandisky, and J. B. Klaassens, “Resonant contactless energy transfer with improved efficiency,” *IEEE Transactions on Power Electronics*, Vol. 24, No. 3, 685–699, 2009.
11. Rim, C. T., S. W. Lee, W. Y. Lee, G. H. Cho, and J. Huh, “Narrow-width inductive power transfer system for online electrical vehicles,” *IEEE Transactions on Power Electronics*, Vol. 26, No. 12, 3666–3679, 2011.
12. Sergeant, P. and A. van den Bossche, “Inductive coupler for contactless power transmission,” *IET Electric Power Applications*, Vol. 2, No. 1, 1–7, 2008.
13. Lee, J. Y., H. Y. Shen, and K. W. Lee, “Study on weaving-type contactless inductive charging platform for electric vehicles,” *Applied Mathematics and Information Sciences*, Vol. 7, No. 1S, 115S–123S, 2013.

# Improved Circularly Polarized Bandwidth in Dielectric Resonator Antenna for L-band Satellite Application

A. Heshmati<sup>1</sup>, F. Geran<sup>1</sup>, and R. A. Sadeghzadeh<sup>2</sup>

<sup>1</sup>Faculty of Engineering Research and Science, Islamic Azad University, Iran

<sup>2</sup>Faculty of Electrical and Computer Engineering, Khajeh Nasir Toosi University of Technology, Iran

**Abstract**— Since the introduction of dielectric resonator antennas in 1983, great deal of research has been done to improve the antenna characteristics, including physical dimensions, bandwidth, gain and radiation pattern.

In this paper, a new configuration for circularly polarized Dielectric Resonator Antenna (DRA) is presented. The idea is to use two different dielectric materials and parasitic patches to obtain bandwidth improvement of the axial ratio and reflection coefficient properties ( $S_{11}$ ). In the operating frequency range of this antenna,  $S_{11}$  is less than  $-10$  dB in which the axial ratio is less than 3 dB around the main direction of the antenna.

## 1. INTRODUCTION

Dielectric resonators (DRs) have been widely used in shielded microwave circuits, such as cavity and rectangular resonators, filters and oscillators. In antenna design two major goals considered are the bandwidth enhancement techniques and the miniaturization techniques.

The DRA is an attractive option to achieve the above goals. The DRA is an excellent radiator as it has negligible metallic loss. It offers advantages, such as small size, high radiation efficiency and low weight, low cost and wide bandwidth with the exciting feeding techniques when operating millimeter and microwave frequencies.

The wireless communication applications such as Bluetooth, GPS, direct digital broadcast, satellite communication, etc require wide band operation of antennas to accommodate large data rate. In this paper, a dielectric resonator antenna is used for the GPS and to satellite communications (Inmarsat) with strip-fed line [1]. In design of antenna for satellite communication two important points should be considered; first the frequency bandwidth should be increased and second, transmitters and receivers of these equipments need to have the increase of circular polarization bandwidth, which in this paper has acted to increase the frequency and circular polarization bandwidths simultaneously.

To increase the frequency bandwidth in DRA, its consider to put two different kinds of dielectric on each other above the ground plane with no air gap [2], In this paper we have used a novel method as we put the two different kinds of dielectric with no gap beside each other, so this idea cause the increased frequency bandwidth. For the increase circular polarization bandwidth we can use from parasitic patch in the corner dielectric [3]. That in these proposed antenna we have used from the three parasitic patches in the corner of DR<sub>1</sub>. The proposed DRA can take the advantages of circular polarized, broadband  $S_{11}$  and axial ratio.

## 2. ANTENNA STRUCTURE

As can be seen from Fig. 1, the proposed DRA antenna has a dielectric constant  $\epsilon_{r2}$  beside another dielectric segment of a dielectric constant  $\epsilon_{r1}$ . Below the DRs is a finite conducting ground plane. The DRs have dimensions of  $a_1 \times b_1 \times d$  and  $a_2 \times b_2 \times d$  respectively, and they (DR<sub>1</sub>, DR<sub>2</sub>) are excited by strip-fed line.

Figure 2 shows the three equal parasitic patches in proposed antenna for increasing of circular polarized bandwidth. In these parasitic patches are attached in the corners of DR<sub>1</sub>.

Figure 3 shows the strip-fed line is placed in the middle of the front of the DR<sub>1</sub> that is located in the center of ground plane. The feeding strip was cut from an adhesive conducting tape and soldered to the inner conductor of SMA connector. In this section  $w_1$ ,  $w_2$ ,  $w_3$  are design parameters for strip-fed line.

## 3. ANTENNA CONFIGURATION

The purpose of this section is to investigate the effect of various combinations of dimensions of DR<sub>1</sub>, DR<sub>2</sub> and parasitic patches in order to further enhance the frequency and axial ratio bandwidths of

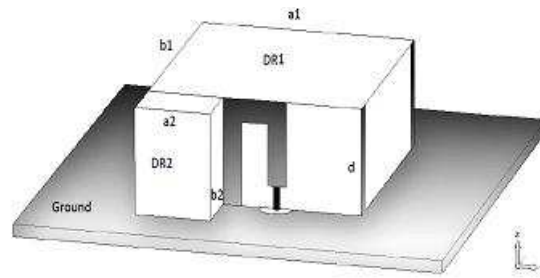


Figure 1: Structure of proposed DRA antenna.

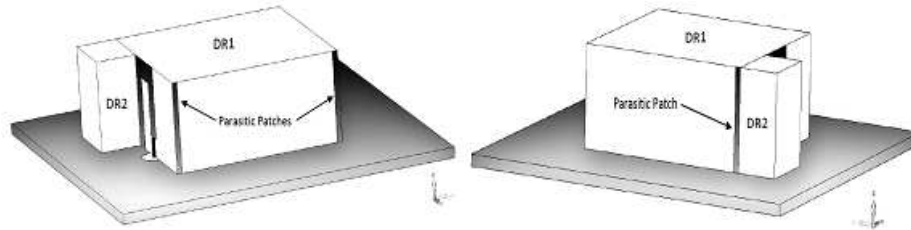


Figure 2: Schematics of parasitic patches in proposed DRA antenna.

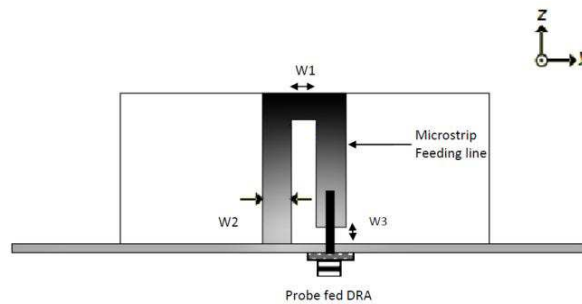
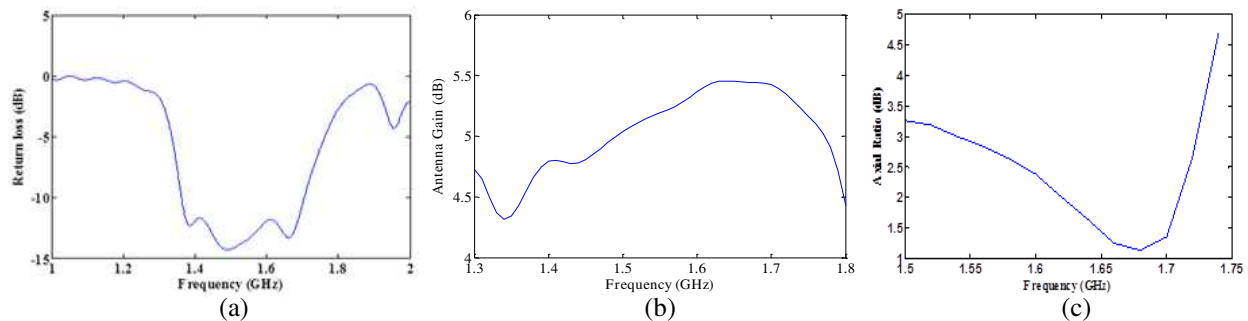


Figure 3: Strip lines feeding in proposed DRA antenna.

Figure 4: (a) Reflection coefficient ( $S_{11}$ ). (b) Gain. (c) Axial ratio in proposed DRA antenna.

operation. Then the optimum dimensions of proposed antenna parameters were determined with experimental optimization.

The dimension of ground plane is  $68 \times 68 \times 1.6 \text{ mm}^3$ . The final dimensions of DR<sub>1</sub> and DR<sub>2</sub> are  $a_1 = 34 \text{ mm}$ ,  $b_1 = 34 \text{ mm}$ ,  $d = 14 \text{ mm}$ ,  $\epsilon_{r1} = 20$  and  $a_2 = 12 \text{ mm}$ ,  $b_2 = 8 \text{ mm}$ ,  $d = 14 \text{ mm}$ ,  $\epsilon_{2r} = 30$ , respectively. The width of strip-fed line are  $w_1 = 3 \text{ mm}$ ,  $w_2 = 4 \text{ mm}$ ,  $w_3 = 3 \text{ mm}$  and the widths of three equal parasitic patches are 1 mm.

#### 4. CONCLUSIONS

The proposed antenna is simulated with CST MWS. In this section we study the strip-fed rectangular DRAs with three parasitic patches for circular polarization and high data rate application.

The computed  $S_{11}$  versus frequency is shown in Fig. 4(a) for the designed antenna structure.

The optimum antenna structure achieves as computed  $S_{11}$  between  $-12$  dB  $\sim -15$  dB at frequencies of  $1.36$  GHz  $\sim 1.71$  GHz and Fig. 4(b) shows the gain of proposed antenna is  $4.5 \sim 5.5$  dB.

The axial ratio of the designed antenna frequency between  $1.54$  GHz  $\sim 1.71$  GHz is less than  $3$  dB reveals and related result is shown in Fig. 4(c), respectively.

The results confirm the capability of our idea to use the proposed configuration in achieving to increase reflection coefficient( $S_{11}$ ) bandwidth and axial ratio bandwidth and obtaining the almost fixed gain (about  $5$  dB) in proposed DRA antenna.

#### ACKNOWLEDGMENT

The authors have special thanks to Faculty of Micro-Electronic (FME), for financial supports.

#### REFERENCES

1. Jeon, S., H. Choi, H. Kim, J. Yeom, and H. Kim, "Design of GPS antenna using dielectric resonator," *The 23rd International Technical Conference Circuit/Systems, Computer and Communication*, 2008.
2. Ge, Y. and K. P. Esselle, "A UWB probe-fed dielectric resonator antenna," Department of Physics and Engineering Macquarie University, Sydney, NSW2109, Australia Elissa, unpublished.
3. Li, B. and K. W. Leung, "Strip-fed rectangular dielectric resonator antenna with/without a parasitic patch," *IEEE Transaction on Antenna and Propagation*, Vol. 53, No. 7, July 2005.

# Real Time Parallel PSO and CFO for Adaptive Beam-forming Applications

Eman Ahmed<sup>1</sup>, K. R. Mahmoud<sup>2</sup>, Safwat Hamad<sup>1</sup>, and Z. T. Fayed<sup>1</sup>

<sup>1</sup>Faculty of Computer and Information Sciences  
Ain Shams University, Abbassia, Cairo 11566, Egypt

<sup>2</sup>Faculty of Engineering, Helwan University, Cairo, Egypt

**Abstract**— The scientific community is still interested in heuristic techniques and optimization algorithms that could be applied in complex problems such as the antenna adaptive beam forming problem. In this paper, we present an empirical study of placing nulls in the antenna patterns to suppress interference and maximizing their gain in the direction of desired signal using Central Force Optimization (CFO) algorithm and compared the results with those obtained using Particle Swarm Optimization (PSO) algorithm. In this work, the complex excitations, amplitudes and phases of the adaptive antenna array elements are calculated for a given 24-antenna elements in a uniform circular array (UCA). The algorithms were implemented using Compute Unified Device Architecture (CUDA) then applied on a graphics processing unit (GPU). Extensive experimentations were applied to compare their performance through a number of case studies. PSO showed to have a good performance, low computational complexity, and gives good results. On the other hand, CFO has a higher computational complexity but it gives better results. The experimentations showed that the resulting beam-pattern optimized by the PSO and CFO required a large processing time which is not acceptable for an on line applications. Hence, the demand for a parallel solution that accelerates these computations is considered. Therefore, a parallel version of PSO and CFO is proposed and implemented using (CUDA) then applied on a (GPU). The comparison is presented to show how the parallel version of the PSO and CFO outperforms the sequential one, thus an online procedure is available for time-critical applications of the antenna adaptive beam-forming.

## 1. INTRODUCTION

Modern optimization techniques are able to solve problems with a non-linear and non-convex dependence of design parameters. So, it has provoked great interest among the scientific and technical community in a wide variety of fields recently. Some of these algorithms have been used successfully in many electromagnetism and antenna problems. Recently, the PSO technique has been successfully applied to the design of antennas and microwave components and its results proved that PSO is powerful and effective in solving such optimization problems. However PSO is similar to other evolutionary algorithms, it requires less computational bookkeeping and generally fewer lines of code [1]. In [2], the parallel implementation of PSO for beamforming application and results are presented. A new nature inspired algorithm such as Central Force Optimization (CFO) is considered in [3]. These algorithms take much time which lead us to use parallel computing techniques to make it take less time. In the work presented here, the problem of antenna adaptive beam forming is introduced to be solved using sequential and parallel implementations of the PSO and CFO algorithms.

This paper presents an approach for the implementation of the CFO algorithm on GPUs, which using the NVIDIA CUDA environment in the adaptive beam-forming applications. Furthermore, a comparative result is included to evaluate the performance of the CFO algorithm against PSO algorithm using a set of case studies. The rest of the paper is structured as follows: Section 2 presents the problem formulation. In Section 3, we present CFO algorithm and our proposed modification in CFO is presented with its parallel implementation. In Section 4, the experimental results are presented. Finally, Section 5 outlines the conclusions.

## 2. PROBLEM FORMULATION

Adaptive antennas refer to a group of antenna technologies that increase the system capacity by reducing the co-channel interference and increase the quality by reducing the fading effects. A smart antenna array containing  $M$  identical elements can steer a directional beam to maximize the signal from desired users, signals of interest (SOI), while nullifying the signals from other directions, signals not of interest.

Different techniques of placing nulls in the antenna patterns to suppress interference and maximizing their gain in the direction of desired signal have received considerable attention in the past and still have great interests recently such as Genetic Algorithm (GA). In addition, various versions of both PSO and CFO algorithms have been successfully used in linear and circular antenna array synthesis problems [1].

In this work, the complex excitations, amplitudes and phases of the adaptive antenna array elements are calculated for a given 24-antenna elements in a uniform circular array (UCA). The antenna elements consist of vertical ( $z$ -directed) half-wave dipole elements equally spaced in the  $x$ - $y$  plane along a circular ring, where the distance between adjacent elements is  $dc = 0.5\lambda$  where  $\lambda$  is the wavelength.

### 3. CENTRAL FORCE OPTIMIZATION (CFO)

Central Force Optimization (CFO) is a nature-inspired gravity-based meta-heuristic for a multi-dimensional search [3]. CFO is an evolutionary algorithm (EA) that locates the extreme of an objective function. The detailed steps of the CFO algorithm and the modifications done on it are explained in [3]. There are some modifications done on CFO; now we will present what was taken from these modifications and the contributions done on it. One of the best modifications done was shrinking the Decision Space (DS) which means to limit the space you search in. The presented modification in [3] was to shrink DS every 20 iterations by half of the distance between the best particle's position and the boundary of DS. To improve the results of this modification we need to make it based on performance measures such as convergence speed and fitness saturation. The results showed that as iterations increasing, CFO converge more to the optimum so we can shrink DS every dynamic number of iterations and by dynamic ratio of the distance between the best particle's position and the boundary of the DS.

So first we introduce shrinking the DS every dynamic number of iterations. This can be done by shrinking DS every 50 iterations and then every 45 iterations and so on until every 5 iterations. This means that after 50 iterations we will make first Shrinking to the Decision Space. Then as CFO converge more to the optimum, the second shrink will be made after 45 iterations and then after 40 iterations and so on; minus 5 each time until reach to shrink after 5 iterations and continue shrinking after 5 iterations till the end. So the DS size is adaptively reduced every 50 to 5 steps around the particle's location that have the best fitness.

Second we introduce shrinking the DS by dynamic ratio of the distance between the best particle's position and the boundary of the DS. This can be done as following: first shrink the DS by small value because CFO still not converge enough to the optimum and then increase the shrinking value as iterations increases. Thus Increase the Shrinking DS Ratio (**shDSratio**) as iterations increases. Thus DS's boundary coordinates are reduced by (**shDSratio**) multiplied by the distance from the best particle's position to the boundary of the DS on a coordinate-by-coordinate basis.

Thus,  $x'_i{}^{\min} = x_i^{\min} + \frac{\vec{R}_{best} \cdot \hat{e}_i - x_i^{\min}}{shDSratio}$  and  $x'_i{}^{\max} = x_i^{\max} + \frac{x_i^{\max} - \vec{R}_{best} \cdot \hat{e}_i}{shDSratio}$ , are the equations that used in the shrinking where (**shDSratio**) changed linearly from 0.1 to 0.5. The proposed CFO algorithm is as the classical CFO but adds shrinking DS step as explained above and uses On-Axis particle initialization.

#### 3.1. Parallel CFO

After analyzing sequential CFO, it is found that the update acceleration is the step that takes the most time as shown in Figure 1 as it takes 99.63% from the total time of the CFO algorithm.

The update acceleration step is the main problem in implementing parallel CFO because the equation of update acceleration is dependent on last updated position and fitness for all particles.

The loop on particles (in Figure 2) that update acceleration, position and fitness cannot be parallelized because the update acceleration step for a specific particle is dependent on the calculated position and fitness of the previous particle in the loop, the detailed explanation for the equations of update acceleration and position are presented in [3]. When trying to isolate update of acceleration for all particles then update position and fitness for all particles the results of our Adaptive beam-forming problem was affected badly as seen in experimental result of CUDA results section.

##### 3.1.1. Implementation of Parallel CFO on the GPU

As in PSO and in any EVs; CFO has two parallel variants one global and other local. *Global*: Where all the mathematical calculations are parallelized, so execute computing fitness function,

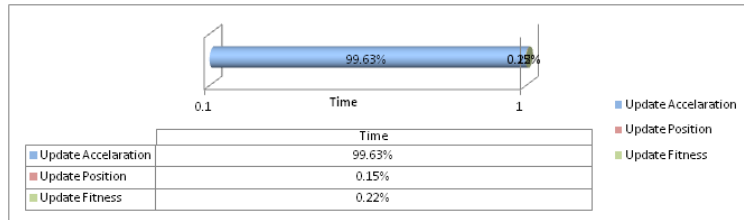


Figure 1: CFO time distribution.

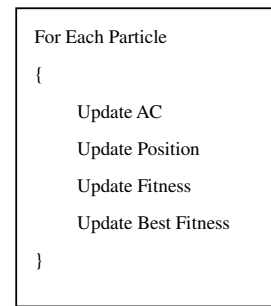


Figure 2: Loop on particles to update acceleration, position and fitness [3].

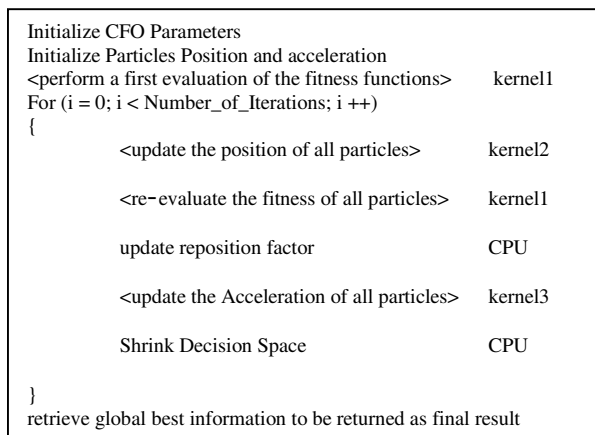


Figure 3: Pseudo Code of the Parallel CFO algorithm using CUDA.

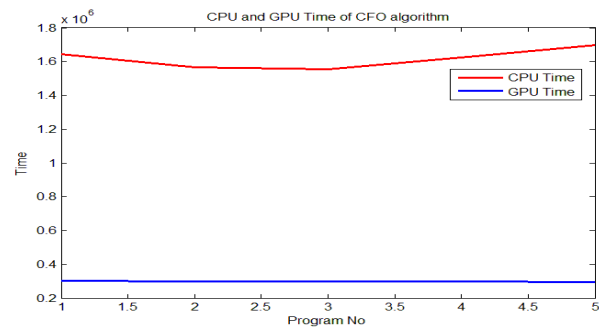


Figure 4: Sample runs and average speed up = 5.5 for CFO.

acceleration, and position for all particles in parallel using two different kernels on GPU. *Local*: Where the Whole entire algorithm executed on the Local Memory of GPU except the initialization of the particles which is executed on the CPU. We implement the global one due to our limited memory of our GPU and to be able to use as many particles as we need without limitation of memory. The sequential CFO algorithm was implemented as reference in order to assess the performance of parallel variants. In any parallel implementations, the programming strategy involved the creation of one thread for each CFO Particle. The rule was to replace all the sequential loops (specifically those where the iterations were in terms of the Particles number) by a single multithreading kernel call.

The structure of the sequential CFO algorithm contain the following functional blocks [3]: *Population initialization* which initializes each particle of the population on axis, *Fitness function evaluation*, and *Update acceleration*, and *Update position*.

The main idea is to create one thread for each CFO particle; Note that in the sequential CFO version all the functional modules are executed in one loop on the host processor. And to be able to execute CFO parallel we split it to 3 independent loops (update fitness, update position, and update acceleration) which affects badly on the results as we will see in the results section in addition that the used GPU is not support the double precision so it lacks for accuracy and if we use GPU that supports double precision this will affects on the time as it will take more time.

In the first parallel variant, the Global one, any arithmetic calculation is distributed to the GPU, replacing both the fitness function evaluation and update position and update acceleration modules by the associated kernel calls (see Figure 3) Use one thread for each particle in each kernel as we use 3 kernels: *Kernel1* for (evaluate the fitness of all particles), *Kernel2* for (update the position of all particles), *Kernel3* for (update the acceleration of all particles).

### 3.1.2. CFO CUDA Results

Here we propose the first version of the adaptive beam forming application with CFO using CUDA and this is sample of the experimental results that show CPU time and GPU time of CFO for a five different test cases of adaptive beam-forming. Experiments were run on a PC equipped with an

Intel Core (TM) 2Duo processor running at 2.80 GHz with a NVIDIA GeForce 9500GT video card from NVIDIA Corporation. All of the simulation runs were performed under the following settings: Number of antenna in antenna array = 24, Number of Particle = 180, Number of Iterations = 250.

The sequential execution of the program took around 1617729 ms while running the CFO algorithm on GPU NVIDIA (GeForce 9500) the execution time was only around 298158 ms. In particular the achieved running speedup was of about 5.5 times as illustrated in Figure 4. Some of selected results is shown in Table 1 where the first column displays images illustrating the optimum normalized radiation pattern resulted from the proposed CFO, the second column shows figures that illustrate the optimum normalized radiation pattern measured in dB, and the last column illustrates the change of fitness value with iterations.

Table 1: Experimental results of CFO using CUDA.

	(a) Radiation Pattern	(b) y-axis is Radiation Pattern in dB and x-axis is angle in radian	(c) y-axis is fitness value and x-axis is iteration number
Desired: 180, 60  Undesired: 240, 30			
Desired: 180  Undesired: 60, 240			

Table 2: Sequential results of beam-forming problem for the two algorithms.

Pattern	PSO	CFO
Desired: 180 Undesired: 60,240		
Desired: 180,60 Undesired: 240,30		

#### 4. EXPERIMENTAL RESULT

In this experiment the algorithms is implemented sequentially using MATLAB tool. For PSO the particles number = 90, iterations number = 1000. It is executed 25 times and obtains the average fitness for five test cases. Two selected test cases are illustrated in the first column of Table 2. The parameter values that used in CFO are: Probs number = 180, Time steps = 500. And its result for two test cases illustrated in the second column of Table 2. The parameter values are defined to use the same evaluation number with both algorithms (PSO and CFO) as PSO algorithm always needs small number of particles to function well while CFO always needs large number of particles. As a conclusion from this experiment it was found that CFO gives better results than PSO in adaptive beam-forming problem.

#### 5. CONCLUSION

In this paper, a parallel version of CFO is proposed, implemented using (CUDA), and applied on a (GPU). Extensive experimentations showed that the parallel version of the CFO outperforms the sequential one, thus a real time adaptive beam-forming algorithm procedure can be used for time-critical applications.

Furthermore, a comparative study showed that; in the sequential mode, CFO algorithm produces more accurate results than the PSO algorithm. However, the PSO algorithm takes less time than CFO algorithm when applied to the problem of adaptive beam-forming in both the sequential and parallel mode. On the other hand; in the parallel mode, the PSO produces more accurate results than the CFO algorithm as illustrated in Parallel CFO section the problems faced in parallel CFO results.

#### REFERENCES

1. Mahmoud, K. R., M. El-Adawy, R. Bansal, S. H. Zainud-Deen, and S. M. M. Ibrahim, "Analysis of uniform circular arrays for adaptive beamforming applications using particle swarm optimization algorithm," *Int. J. of RF and Microwave Computed Aided Eng.*, Vol. 18, 42–52, 2008.
2. Fahmy, E. A., K. R. Mahmoud, S. H. Hamad, and Z. T. Fayed, "Using parallel computing for adaptive beamforming applications," *PIERS Proceedings*, 296–299, Cambridge, USA, Jul. 5–8, 2010.
3. Formato, R. A., "Improved CFO algorithm for antenna optimization," *Progress In Electromagnetics Research B*, Vol. 19, 405–425, 2010.

# Design of a Novel Dual-band Microstrip Patch Antenna for WLAN/WiMAX Applications Using Complementary Split Ring Resonators and Partially Defected Ground Structure

Debdeep Sarkar, Kushmanda Saurav, and Kumar Vaibhav Srivastava  
Department of Electrical Engineering, Indian Institute of Technology, Kanpur, India

**Abstract**— This paper proposes a novel low-profile (single-layer) CSRR-loaded microstrip patch antenna placed on a partially defected ground structure (PDGS). The proposed compact dual-band antenna simultaneously satisfies WLAN (Wireless Local Area Network) and WiMAX (Worldwide Interoperability for Microwave Access) application requirements, providing a significantly wide impedance bandwidth ( $S_{11} < -10$  dB) in the WLAN and upper WiMAX frequency regions. The gain and efficiency of the antenna are also very satisfactory in the two frequency bands of operation.

## 1. INTRODUCTION

Design of compact multi-band antennas for state-of-art wireless communication systems like portable Wi-Fi enabled laptops and smart-phones is one of the challenging problems for microwave engineers. Microstrip patch antennas are attractive candidates for this purpose due to their low-profile and compatibility with planar monolithic microwave integrated circuit (MMIC) components, but they suffer from disadvantages like narrow bandwidth, poor scan performance etc. [1]. To provide desired multi-band performance and specified radiation characteristics, various printed antenna topologies have been proposed by researchers [2–4]. Since the practical realization of artificially engineered metamaterials in the beginning of 21st century [5], researchers have focused on using metamaterial paradigm in performance-enhancement as well as miniaturization of antennas. Use of meta-resonators (like normal and complementary split ring resonators, SRR and CSRR) as well as meta-surfaces like AMC (Artificial Magnetic Surfaces), EBG (Electromagnetic Band-gap) structures have recently caught the attention of metamaterial-inspired antenna designers [6–8].

In this paper, a conventional patch antenna operating at WLAN frequency band (5.15–5.85 GHz) is loaded with two CSRRs of suitable dimensions, which enables the excitation of lower order resonating modes supported by the patch lying in the middle WiMAX band (3.2–3.8 GHz). Also the ground-plane beneath the radiating patch is partially defected to enhance the antenna-bandwidth in the WLAN and upper WiMAX frequency range. The design methodology of the proposed antenna along with description of its radiation performance are provided in the following sections. Finite Element Method (FEM) based electromagnetic solver HFSS is used for the analysis of the antenna and optimization of its geometrical parameters.

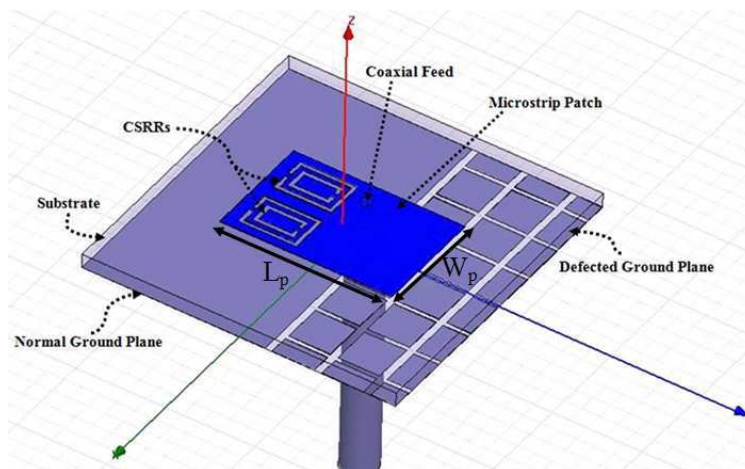


Figure 1: Schematic diagram of coax-fed CSRR-loaded microstrip patch antenna placed over PDGS:  $L_p = 19.2$  mm and  $W_p = 12.4$  mm.

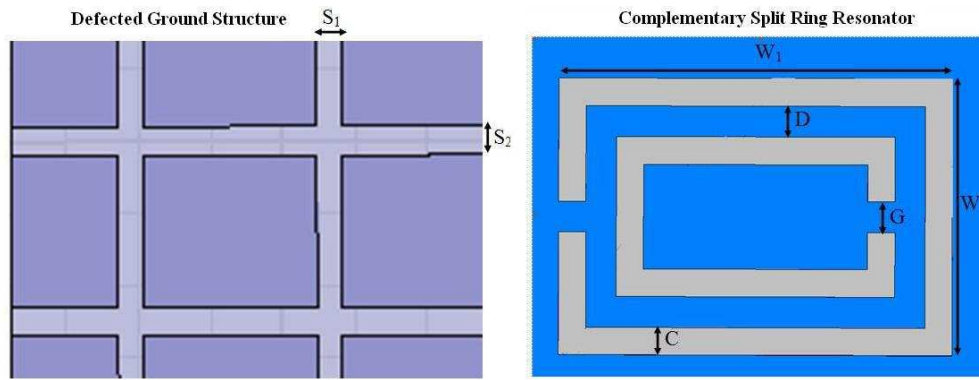


Figure 2: Design parameters of the crossed-slots for partially defected ground structure and the CSRR:  $S_1 = 0.7$  mm,  $S_2 = 0.8$  mm,  $W_1 = 6.5$  mm,  $W_2 = 4.5$  mm,  $C = 0.45$  mm,  $D = 0.5$  mm and  $G = 0.5$  mm.

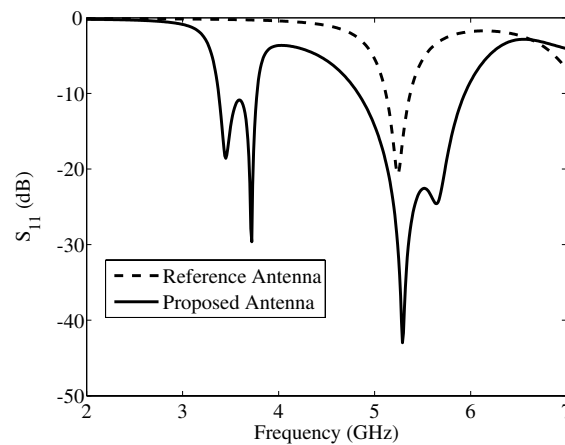


Figure 3: Return loss versus frequency curve of the proposed antenna.

## 2. DESIGN OF THE PROPOSED ANTENNA

One coax-fed microstrip patch antenna operating at its fundamental mode (resonance frequency of 5.24 GHz) is chosen as the reference design. The reference rectangular patch antenna has dimensions  $19.2$  mm  $\times$   $12.4$  mm as shown in Figure 1. FR4-epoxy substrate ( $\epsilon_r = 4.4$ ,  $\tan \delta = 0.02$ ) having thickness  $1.6$  mm is used for the design. In the proposed antenna, two CSRRs are etched near the non-radiating edge of the patch which is over the normal ground-plane. Furthermore, crossed-stripline gaps are also etched on one side of the ground-plane creating a partially defected ground structure (PDGS). The final dimensions of the CSRR and the crossed-strip slots are given in Figure 2. The proposed antenna (Figure 1) is of the same physical size ( $35$  mm  $\times$   $35$  mm) as compared to the reference antenna.

## 3. RESULTS AND DISCUSSION

The proposed antenna along with the reference conventional patch antenna are simulated in HFSS. The return loss versus frequency curves for both the antennas are shown in Figure 3. It is observed that the CSRRs etched on the patch generates resonances at the  $3.33$ – $3.77$  GHz band which encompasses the middle WiMAX frequencies  $3.2$ – $3.8$  GHz. The simulated return loss is minimum at the resonant frequency  $3.72$  GHz ( $|S_{11}| = -29.63$  dB) for this band. Moreover due to the partially defected ground structure, the proposed antenna achieves wide impedance bandwidth ( $4.81$ – $5.90$  GHz) around resonant frequency of  $5.29$  GHz ( $S_{11} = -45.75$  dB) which covers the entire WLAN band ( $5.15$ – $5.85$  GHz) as well as the upper WiMAX band ( $5.2$ – $5.8$  GHz).

The radiation characteristics of the antenna are also studied using HFSS. The simulated peak-gains of the antenna at these two frequencies are  $1.24$  dBi and  $4.43$  dBi respectively. Figure 4 shows the variation of peak-gain with respect to frequency for the proposed dual-band antenna. It is observed that in band-1 the average peak gain ( $1.8$  dBi) is slightly less compared to that in

band-2 (3.75 dBi). Figures 5–7 illustrate the normalized two-dimensional radiation patterns of the proposed antenna along the three principal planes ( $xy$ -plane,  $yz$ -plane and  $xz$ -plane) at frequencies 3.72 GHz and 5.29 GHz respectively. The three-dimensional patterns of the realized far-field gain of the antenna at the two said frequencies are also provided in Figures 8(a) and 8(b).

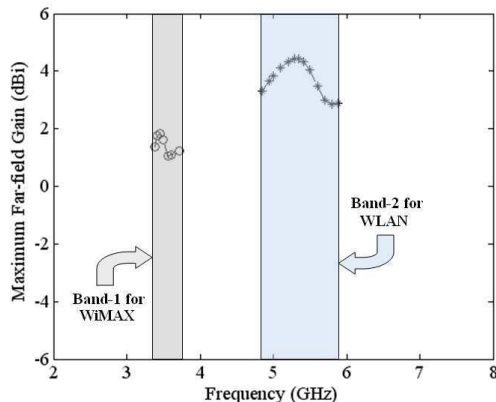


Figure 4: Simulated peak-gain versus frequency curve of the proposed antenna.

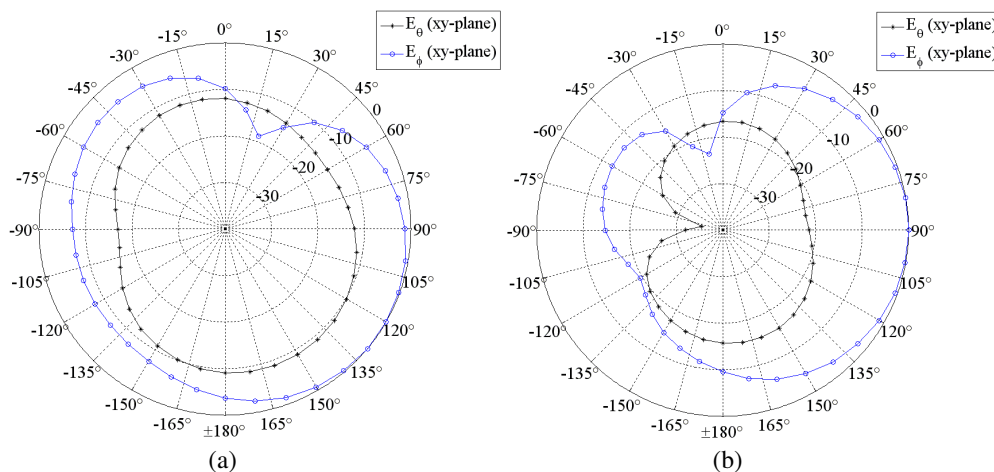


Figure 5: Normalized 2D radiation pattern of the proposed antenna along  $xy$ -plane at: (a) 3.72 GHz and (b) 5.29 GHz.

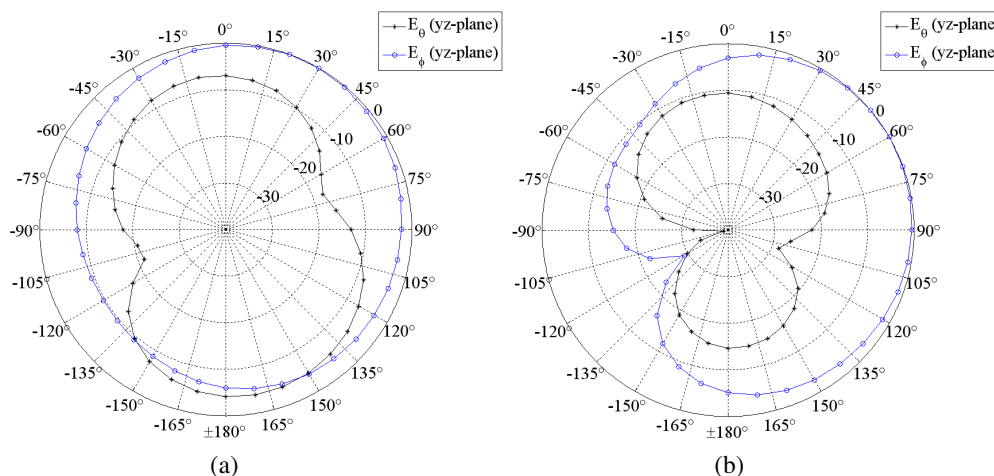


Figure 6: Normalized 2D radiation pattern of the proposed antenna along  $yz$ -plane at: (a) 3.72 GHz and (b) 5.29 GHz.

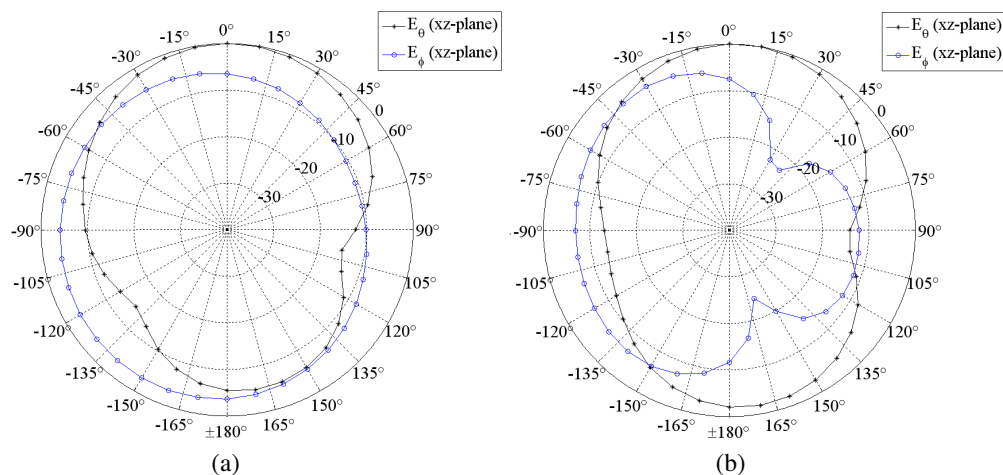


Figure 7: Normalized 2D radiation pattern of the proposed antenna along  $xz$ -plane at: (a) 3.72 GHz and (b) 5.29 GHz.

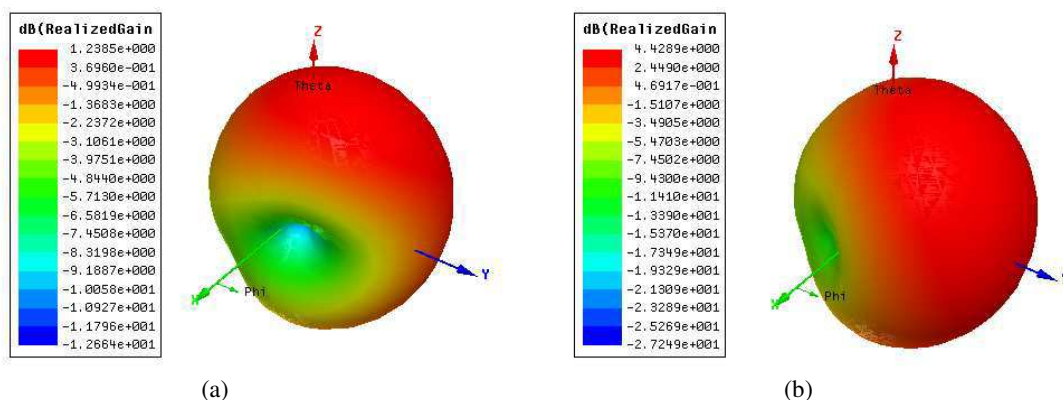


Figure 8: Simulated 3D radiation pattern of the proposed antenna at (a) 3.72 GHz and (b) 5.29 GHz.

#### 4. CONCLUSION

A compact dual-band microstrip patch antenna employing meta-resonators (CSRRs) and partially defected ground structure is proposed. The dual-band characteristics of the antenna is achieved due to the CSRRs, whereas the partially defected ground structure enhances the bandwidth in the WLAN and upper WiMAX band. The return loss characteristics and radiation performance of the antenna are examined by HFSS simulations. The proposed antenna can be used in wireless communication systems where embedded antennas covering both WLAN and WiMAX bands are required.

#### ACKNOWLEDGMENT

The authors would like to acknowledge all the members of the Microwave circuit and Microwave Metamaterials Laboratory (Department of Electrical Engineering, IIT Kanpur) for their inspiration and IIT Kanpur authority for the financial assistance.

#### REFERENCES

1. Balanis, C. A., *Antenna Theory: Analysis and Design*, 2nd Edition, John Wiley and Sons Inc, Wiley Reprint, New Delhi, India, 2007.
2. Lee, Y. C. and J.-S. Sun, "A new printed antenna for multiband wireless applications," *IEEE Antennas and Wireless Propagation Letters*, Vol. 8, 402–404, 2009.
3. Eshtiaghi, R., M. G. Shayesteh, and N. Zad-Shakooian, "Multicircular monopole antenna for multiband applications," *IEEE Antennas and Wireless Propagation Letters*, Vol. 10, 1205–1207, 2011.

4. Naser-Moghadasi, M., R. A. Sadeghzadeh, M. Fakheri, T. Aribi, T. Sedghi, and B. S. Virdee, “Miniature hook-shaped multiband antenna for mobile applications,” *IEEE Antennas and Wireless Propagation Letters*, Vol. 11, 1096–1099, 2012.
5. Smith, D. R., W. J. Padilla, D. C. Vier, S. C. Nemat-Nasser, and S. Schultz, “A composite medium with simultaneously negative permeability and permittivity,” *Physical Review Letters*, Vol. 84, No. 18, 4184–4187, 2000.
6. Mosallaei, H. and K. Sarabandi, “Antenna miniaturization and bandwidth enhancement using a reactive impedance substrate,” *IEEE Transactions on Antennas Propagation*, Vol. 52, No. 9, 2403–2414, 2004.
7. Dong, Y., H. Toyao, and T. Itoh, “Design and characterization of miniaturized patch antennas loaded with complementary split-ring resonators,” *IEEE Transactions on Antennas Propagation*, Vol. 60, No. 2, 772–785, 2012.
8. Malik, J. and M. V. Kartikeyan, “Metamaterial-inspired patch antenna with L-shaped slot loaded ground plane for dual-band (WiMAX/WLAN) applications,” *Progress In Electromagnetics Research Letters*, Vol. 31, 35–43, 2012.

# Mutual Coupling Effects on the Linear Microstrip Array Self-impedance

Cheng-Nan Hu, Kai-Hong Jheng, and Esther Lee  
Oriental Institute of Technology, Taiwan, R.O.C.

**Abstract**— It has been shown that the MIMO performance is strongly affected by the effects of mutual coupling between antenna elements. This study numerically and experimentally investigates the mutual coupling effects on the self-impedance of a five-element microstrip antenna array. Experimental validation shows the effectiveness of the numerical method using *GEMS EM Simulator* for the further analysis on the communication system performance.

## 1. INTRODUCTION

The multi-input multi-output (MIMO) system, employing multi-antenna signal processing at both ends of a wireless link, has shown promising performance in delivering high spectral efficiency with reasonable constellation. IEEE 802.16-2010 and 801.11n\WiMAX\LTE (Long Term Evolution) currently at least support several multiple antenna options including Space-Time Codes (STC), MIMO antenna systems, and Adaptive Antenna Systems (AAS) [1–4]. However, the performance of a MIMO antenna has been shown strongly affected by the electromagnetic characteristics of the antenna array. An important electromagnetic characteristic of an antenna is the mutual coupling between its elements. In most of previous MIMO antenna performance analyses, mutual coupling between the antenna elements was ignored by assuming the antenna elements to be isolated from each other. In practical elements of an antenna array have mutual coupling, which in turn affect the gain, VSWR, and beamwidth, etc., of the array. Mutual coupling becomes particularly significant as the inter-element spacing is decrease. This is especially true for the terminal applications. This paper presents the study of mutual coupling effects on a five-element microstrip closely coupled linear array. Experimental study validates the effectiveness of the numerical analysis for further studying the mutual coupling effects on communication system performance.

## 2. THEORY

Figure 1 shows the basic diagram of an adaptive array in which the signals received by each antenna element is multiplied by the complex weight, and then these signals are summed to come out the array output  $S(t)$ . The output SINR of an adaptive array is the most commonly accepted measure of its steady state performance. With a selected algorithm, the weights are automatically adjusted to optimize the output SINR in accordance. However, the performance of SINR in adaptive array is strongly affected by the mutual coupling between antenna's inter-elements provided that the antennas are placed closely. To tackle the mutual coupling problem, there have been many methods suggested [5–8] employing rigorous full-wave analysis methods. By taking into account of mutual coupling, an  $N + 1$  terminal linear, bilateral network responding to an outside source (Fig. 2) can be used to represent an  $N$ -element array derived by an open circuit voltage  $V_g$  and internal impedance

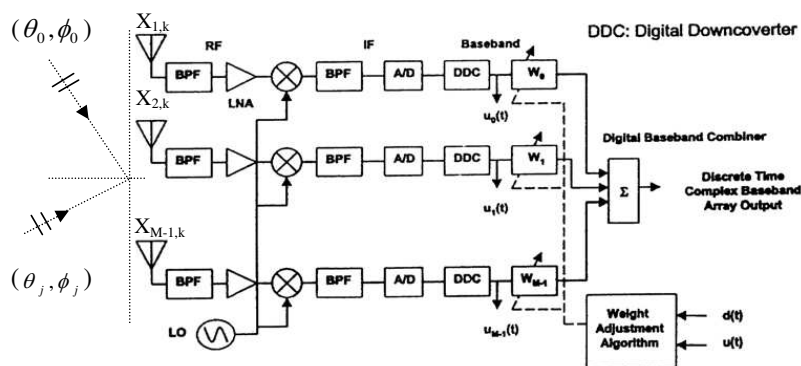


Figure 1: Antenna architecture of an Adaptive Antenna System (AAS) using digital beam-forming.

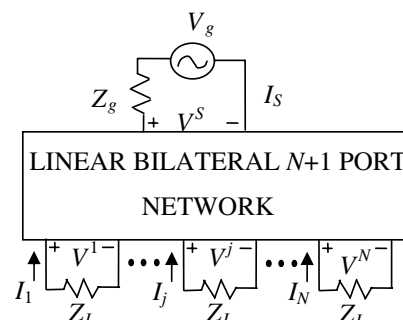


Figure 2: Antenna array as a  $N + 1$  terminal network.

$Z_g$ . Using the standard notation, one can write the Kirchoff relation for the  $N + 1$  terminal network as

$$\begin{aligned} v^1 &= i_1 Z_{11} + \dots + i_j Z_{1j} + \dots + i_N Z_{1N} + i_S Z_{1S} \\ v^j &= i_1 Z_{j1} + \dots + i_j Z_{jj} + \dots + i_N Z_{jN} + i_S Z_{jS} \\ v^N &= i_1 Z_{N1} + \dots + i_j Z_{Nj} + \dots + i_N Z_{NN} + i_S Z_{NS} \end{aligned} \quad (1)$$

where  $Z_{ij}$  represents the mutual impedance between the ports (array elements)  $i$  and  $j$ . Further, making use of the relationship between terminal current and load impedance ( $Z_L$ ) and assuming  $v_{0j} = Z_{jS} i_S$ , one gets

$$\begin{bmatrix} 1 + \frac{Z_{11}}{Z_L} & \frac{Z_{12}}{Z_L} & \dots & \frac{Z_{1N}}{Z_L} \\ \frac{Z_{21}}{Z_L} & 1 + \frac{Z_{22}}{Z_L} & \dots & \frac{Z_{2N}}{Z_L} \\ \vdots & \vdots & \ddots & \vdots \\ \frac{Z_{N1}}{Z_L} & \frac{Z_{N2}}{Z_L} & \dots & 1 + \frac{Z_{NN}}{Z_L} \end{bmatrix} \cdot \begin{bmatrix} v^1 \\ v^2 \\ \vdots \\ v^N \end{bmatrix} = \begin{bmatrix} v_{01} \\ v_{02} \\ \vdots \\ v_{0N} \end{bmatrix} \quad (2)$$

Or, in matrix notation,  $\bar{\bar{Z}}_0 \bar{V} = \bar{V}_0$ , where  $\bar{\bar{Z}}_0$  is the normalized impedance matrix and  $V$ , represents the open circuit voltages at the antenna terminals. Since  $\bar{\bar{Z}}_0$  is not singular, one can find the element output voltages from the open circuit voltages. The element output voltages will be given

$$\bar{V} = \bar{\bar{Z}}_0^{-1} \cdot \bar{V}_0 \quad (3)$$

It should be noted that the matrix  $\bar{\bar{Z}}_0$  is a normalized impedance matrix, normalized to the load impedance. It acts like a transformation matrix, transforming the open circuit element voltages to the terminal voltages. What is normally assumed in analyzing adaptive antenna systems is that the element spacing is large enough so that the mutual coupling between the elements is small and consequently the matrix  $Z_o$  becomes diagonal. If one further assumes that the self-impedances ( $Z_{ii}$ ,  $i = 1, 2; \dots, N$ ) are equal, the input signal vector will be just the open circuit voltage vector multiplied by a trivial scaling factor involving the self and load impedance terms. Thus the array performance will be the same as calculated using the open circuit voltages as the input signals to an adaptive processor.

However, in practical cases, the self-impedance is strongly affected by mutual coupling. In this study, the rigorous full-wave finite-element method using *GEMS EM simulator* is applied to analyze the effect of mutual coupling on self-impedance of the closely coupled microstrip linear array and then an experimental study is done for validation as introduced in following section.

### 3. RESULTS

To validate the effectiveness of using numerical method for further analysis of mutual coupling effects on communication system performance, a linear coupled microstrip antenna array is analyzed

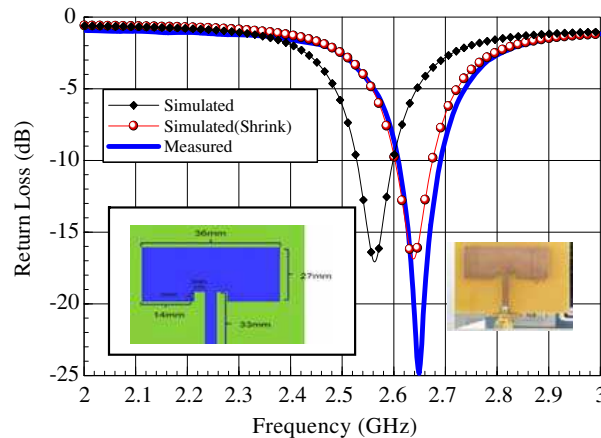


Figure 3: The comparison of the simulated and measured return loss of a single microstrip antenna.

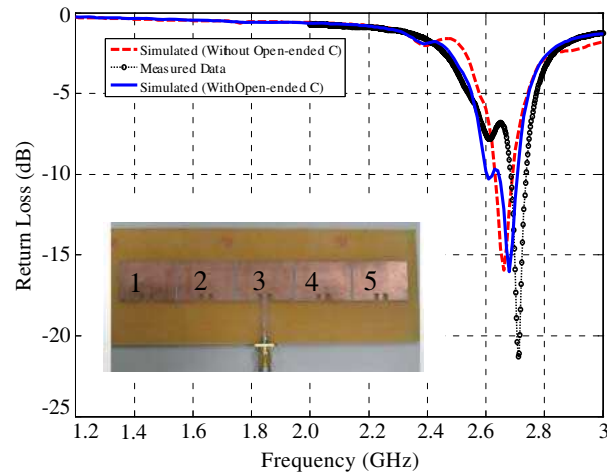


Figure 4: The comparison of the simulated and measured return loss of a 5-element tightly coupled microstrip excited at center element and opened at the rest of antennas. The inset of the figure is the photograph of the experimental antenna array with spacing of 1 mm.

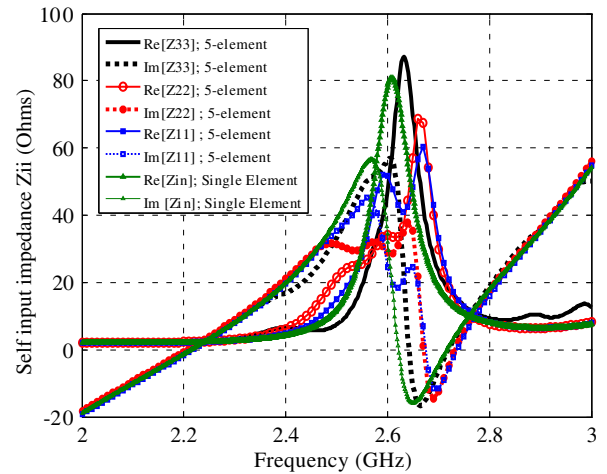


Figure 5: The simulated results of self-input impedance ( $Z_{ii}$ ;  $i = 1, 2, 3$ ), showing not identical but significant deviating from that of a single microstrip antenna.

and built on a FR4 substrate with thickness of 1.6 mm for study. Fig. 3 shows the comparison of the measured and simulated return loss (dashed-line with diamond symbols and solid-line) of a single microstrip antenna, showing the measured resonant frequency about 0.1 GHz resonant frequency shift from the simulated results. This slightly deviation can be attributed by the 0.4 mm shrink error in both width and length dimensions of the manufactured antenna by carefully measuring the prototype antenna. When calibrating the shrink error in both dimensions out, the simulated results (dashed-line with circles in Fig. 3) are found well agreement with the measured results. The  $Z$ -matrix definition is based on all ports opened except for the active-element except for the active element. For example, an experimental five-element array is excited at center-element (element 3 as indicated at inset of Fig. 4), the other ports shall be opened. In practical, the open-circuit is very difficult to be obtained experimentally. In this study, an open-ended capacitance of 0.01 pf, extracted from the EM simulation date, is used to compensate the fringe field effect at the end of the microstrip. Fig. 4 plots the comparison of the measured and simulated results, showing acceptable agreement. Then, the variation of the self-input impedance corresponding to each of individual active element (element 1, 2, 3) is numerically analyzed to compare with that of a single microstrip antenna (Fig. 5). As indicated in Fig. 5, the self-input impedance of each of active elements ( $Z_{ii}$ ;  $i = 1, 2, 3$ ) is not identical but deviation from that of the single microstrip antenna, illustrating that the mutual coupling effects on communication performance of MIMO system shall be considered on the self-calibration algorithm.

#### 4. CONCLUSIONS

A five-element tightly coupled linear microstrip array is analyzed, built, and measured to investigate the mutual coupling effects on the self-input impedance. Well agreement in the comparison between measured and simulated results validates the effectiveness of the numerical approach for the further analysis of the mutual coupling effects on the communication system performance using MIMO technology.

#### REFERENCES

1. Chang, D.-C. and C.-N. Hu, "Smart antennas for advanced communication systems," *Proceedings of IEEE*, Aug. 2012.
2. Parkvall, S., A. Furuskar, and E. Dahlman, "Evolution of LTE toward IMT-advanced," *IEEE Communication Magazine*, Vol. 49, No. 2, 84–91, Feb. 2011.
3. Park, C. S., Y.-P. E. Wang, G. Jongren, and D. Hammarwall, "Evolution of uplink MIMO for LTE-advanced," *IEEE Communication Magazine*, Vol. 49, No. 2, 112–121, Feb. 2011.

4. “UMTS Evolution from 3GPP Release 7 to Release 8 HSPA and SAE/LTE,” <http://www.3gamericas.org>.
5. Wallace, J. W. and M. A. Jansen, “Mutual coupling in MIMO wireless systems: A rigorous network theory analysis,” *IEEE Trans. on Wireless Commu.*, Vol. 3, No. 4, 1317–1325, 2004.
6. Adve, R. S. and T. K. Sarkar, “Compensation for the effects of mutual coupling on direct data domain adaptive algorithms,” *IEEE Trans. on Antennas & Prop.*, Vol. 48, No. 1, 86–94, 2000.
7. Dandekar, K. R., H. Ling, and G. Xu, “Experimental study of mutual coupling compensation in smart antenna applications,” *IEEE Trans. on Wireless Commu.*, Vol. 1, No. 3, 480–486, 2002.
8. Fredrik, J. D., Y. Wang, and T. Itoh, “Smart antennas based on spatial multiplexing of local elements (SMILE) for mutual coupling reduction,” *IEEE Trans. on Antennas & Prop.*, Vol. 52, No. 1, 106–114, 2004.

# A Compact UHF Antenna for Handheld RFID Reader

W. C. Hung<sup>1</sup>, H. L. Su<sup>1</sup>, S. L. Chen<sup>2</sup>, and C. T. Lin<sup>2</sup>

<sup>1</sup>Department of Computer Science and Information Engineering  
National Pingtung Institute of Commerce, Taiwan

<sup>2</sup>China Steel Corporation, Taiwan

**Abstract**— This work presents a compact antenna for a handheld ultra-high-frequency (UHF) radio frequency identification (RFID) reader. This antenna operates at 925 MHz with bandwidth of the return-loss smaller than 10 dB from 917 MHz to 934 MHz. The peak gain is around 3.5 dBi. The antenna is composed of an aluminum stand with 60 mm × 20 mm × 17.5 mm and a radiation metal with 14.5 mm × 56 mm. The effect of the shell of the RFID reader and the human hand are also studied. The shell of the RFID reader is considered as a plastic. Finally, the antenna is fabricated and verified.

## 1. INTRODUCTION

RFID technology has been growing enormously and RFID systems have been widely used in a variety of areas such as supply chain management (SCM), inventory control, and security management. UHF RFID system has been employed widespread for these applications because of long range, and high data rate [1, 2]. While the antenna for fixed RFID reader can be relatively large [3], the antenna for handheld readers should be compact and ergonomically appealing. Because the antenna was assembled on a handheld device, the device shell and the human hand effect should be considered. This work proposes an antenna and discusses the effect of the device shell and the human hand.

## 2. ANTENNA GEOMETRY AND DESIGN CONCEPT

The requirements of the handheld reader antenna must be linearly polarized and compacted and work in UHF RFID band. Fig. 1 shows the configuration and photo of the proposed antenna. This antenna adopts the patch inverted F antenna (PIFA) structure. This antenna consists of an aluminum base (gray part) with dimensions are  $L = 60$  mm,  $W = 20$  mm, and  $h = 17.5$  mm and a radiation metal (yellow part). The parameters of the radiation metal are  $L_1 = 56$  mm,  $W_2 = 14.5$  mm,  $L_3 = 6$  mm and a strip metal with 1.5 mm wide fed from aluminum base to the radiation metal. To enhance the band width, a matching metal, whose dimension were  $L_2 = 12$  mm,  $h_2 = 3$  mm and  $h_1 = 7$  mm, was added between fed-strip-line and radiation metal. The ground of PIFA was folded to reduce size.

## 3. RESULTS AND DISCUSSIONS

Figure 2 shows the comparison of the  $S_{11}$  as a function of frequency with/without matching-metal. The red line is for antenna without matching-metal and the antenna's bandwidth is about 15 MHz (914 MHz–929 MHz). After adding the matching-metal, the antenna's bandwidth is about 17 MHz (918 MHz–935 MHz). Figure 3 shows  $S_{11}$  for various  $h_1$ . Figure 4 to Figure 5 show the measured  $S_{11}$

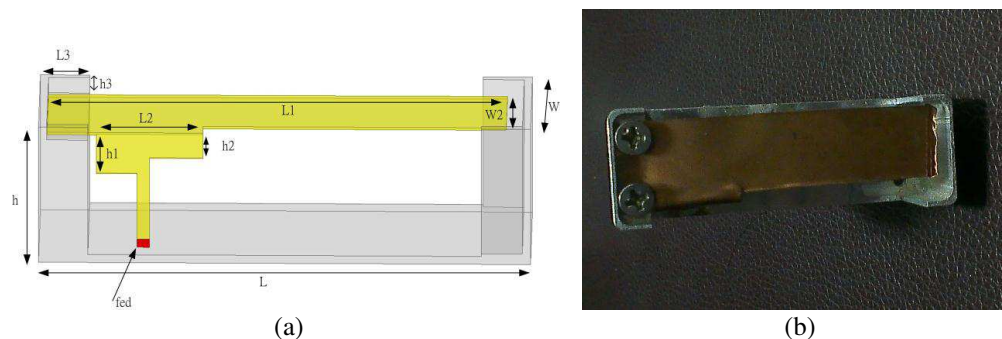


Figure 1: (a) Configuration of the antenna. (b) Photo of the antenna.

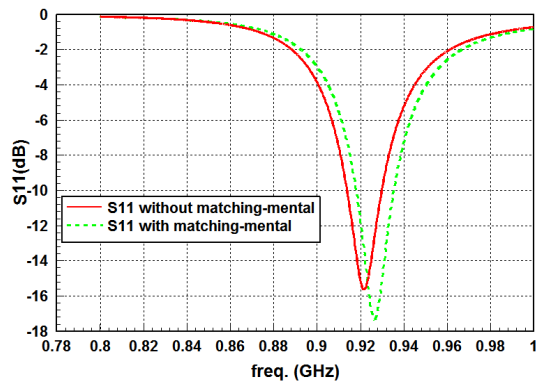


Figure 2: Simulated  $S_{11}$  for with/without matching-mental.

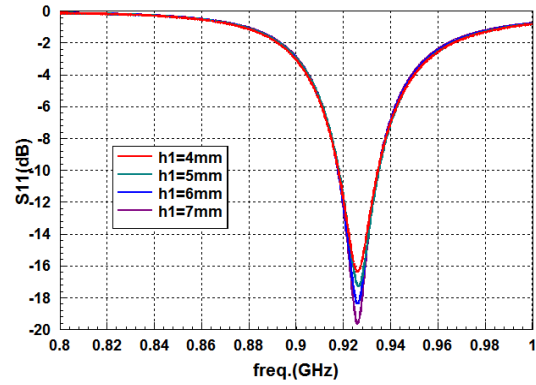


Figure 3: Simulated  $S_{11}$  for various  $h_1$ .

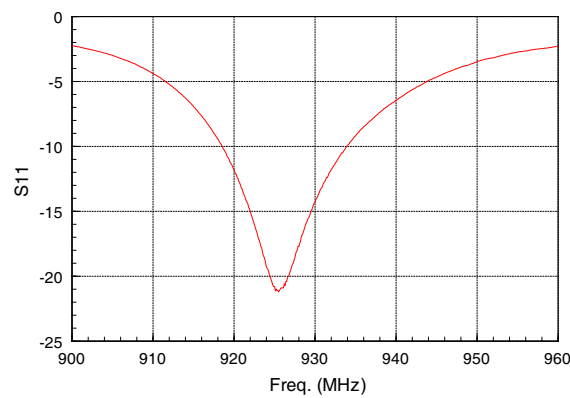


Figure 4: Measured  $S_{11}$ .

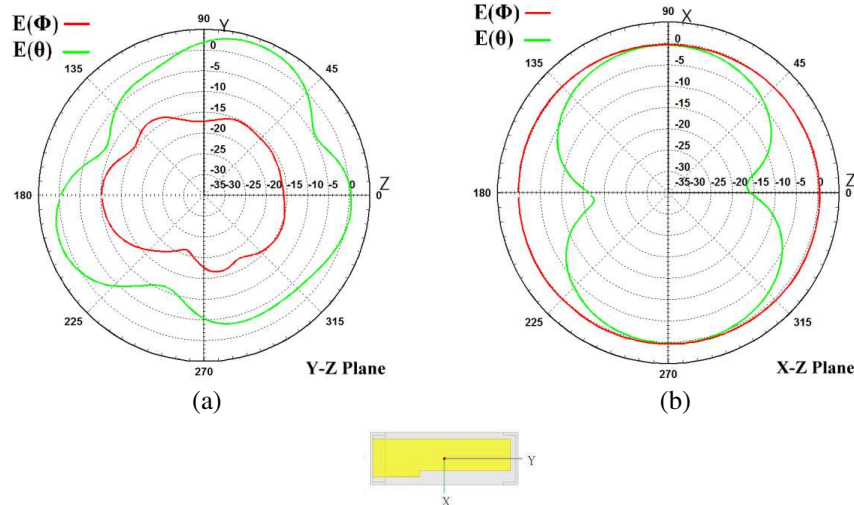


Figure 5: Radiation patterns. (a)  $y$ - $z$  plane. (b)  $x$ - $y$  plane.

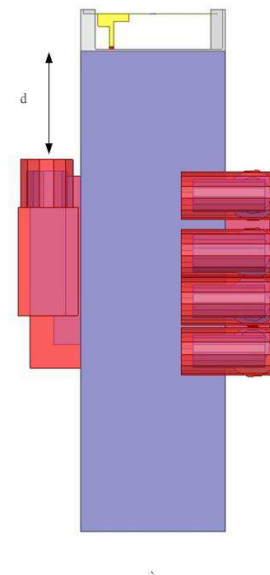
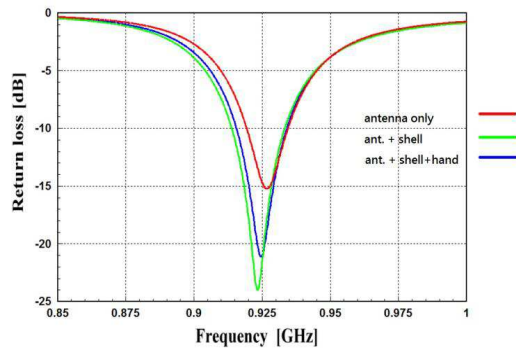
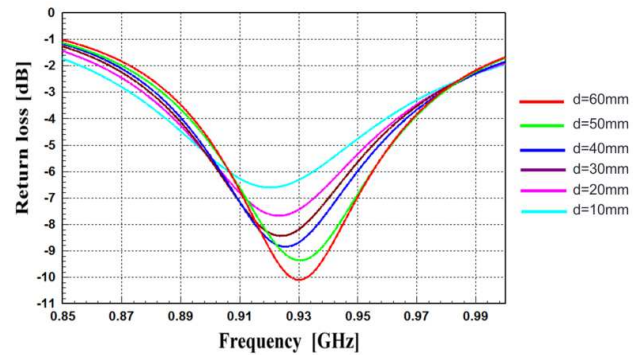


Figure 6: The configuration of the antenna with a shell and a human hand.

and radiation patterns at 925 MHz respectively. The peak gain is 3.5 dBi and radiation efficiency is 75.1%.

This antenna is for handheld RFID device the shell of the device and a human hand will influence the antenna performance. Figure 6 shows the configuration of the antenna with the shell of the

Figure 7: Simulated  $S_{11}$ .Figure 8: Simulated  $S_{11}$  for various  $d$ .

RFID reader and the human hand. The dimension of the shell is  $60 \times 20 \times 200 \text{ mm}^3$ . The material is considered as a plastic ( $\epsilon_r = 3.7$ ). The permittivity and conductivity of the human hand are 41.5 and 0.98 at 900 MHz, respectively. The  $S_{11}$  is shown in Fig. 7. The red line is for antenna only; the green line is for the antenna with a shell and the blue line is for antenna with a shell and a human hand. As we can see, the bandwidth becomes broader and still covers concerned band. The distance ( $d$ ) effect from the antenna to the hand is also discussed and the  $S_{11}$  results are shown in Fig. 8. When the  $d$  is bigger than 10 mm, the  $S_{11}$  still works near at 925 GHz. The impedance matching becomes a little poor but it still is acceptable. However, when the  $d$  is 10 mm, the  $S_{11}$  becomes worse. Fortunately, we won't hold the device so closely.

#### 4. CONCLUSIONS

This work presents a PIFA based antenna for a handheld RFID reader. The size of the antenna is  $60 \text{ mm}$  ( $0.18\lambda_0$ )  $\times$   $20 \text{ mm}$  ( $0.06\lambda_0$ )  $\times$   $17.5 \text{ mm}$  ( $0.05\lambda_0$ ). The impedance matching mechanism is discussed. The effects of the shell of the RFID reader and the human hand are also discussed. This antenna operates at 925 MHz and its bandwidth is from 914 MHz to 929 MHz (17 MHz). The measured peak gain is 3.5 dBi and the efficiency is about 75.1%.

#### ACKNOWLEDGMENT

This work was support by the China Steel Corporation of Taiwan under contract number: 01T1D-RE010.

#### REFERENCES

1. Want. R., "An introduction to RFID technology," *IEEE Pervasive Comput.*, Vol. 5, No. 1, 25–33, 2006.
2. Finkenzeller. K., *RFID Handbook*, 2nd Edition, Wiley, New York, 2004.
3. Wang, Z., S. Fang, S. Fu, and S. Jia, "Single-fed broadband circularly polarized stacked patch antenna with horizontally meandered strip for universal UHF RFID application," *IEEE Trans. on Microwave Theory and Techn.*, Vol. 59, No. 4, 1066–1073, 2011.

# Dual-band Slot Antenna Using CPW Feed Line and Metasurface

Hailiang Zhu, S. W. Cheung, and T. I. Yuk

Department of Electrical and Electronic Engineering  
The University of Hong Kong, Hong Kong, China

**Abstract**— A dual-band antenna designed by combining a coplanar-waveguide-fed (CPW) slot antenna with a metasurface is presented in this paper. The CPW-fed antenna printed on one side the substrate is used as the source antenna. The metasurface consisting of 16 unit cells in a  $4 \times 4$  arrangement is printed on the other side of the substrate. Two operating bands at around 3.4 GHz and 5 GHz are generated, with the radiation patterns pointing at mainly opposite directions.

## 1. INTRODUCTION

Slot antenna with coplanar-waveguide (CPW) fed is increasingly popular because of the simple structure [1–3]. Moreover, more than one slot of different sizes can be easily integrated with the CPW feed line at the same time, so it is widely used for design of multi-band antennas. However, the disadvantages of such antennas are also obvious, one of which is bi-/multi-directional radiation pattern, this could be a problem especially when only one direction is desired. In addition, multi-directional radiation also leads to relatively low gain because of power decentralization.

Metasurface, a two-dimensional equivalent of metamaterial, has been attracting attention for researchers in recent years [4, 5]. Due to its planar structure, metasurface can be easily combined with planar antenna to achieve performance enhancement in terms of bandwidth, gain and radiation pattern. In such application, the original planar antenna is called the source antenna. When the source antenna is combined together with a metasurface, it is called a metasurfaced antenna [4]. Among the reported metasurfaced antennas studied [3–7], the metasurfaces and source antennas were fabricated on different dielectric substrates and placed at a certain distance away from each other. Although the distance between source antenna and metasurface was very close, the thickness of metasurfaced antenna has been increased considerably compared to source antenna. In addition, the complexity of antenna was also increased due to assembly problem. However, this will be different if a CPW feed line is used, if we place the metasurface on the other side, the metasurface and source antenna will be combined perfectly as one single antenna, the thickness of the metasurfaced antenna does not even change at all compared to that of the source antenna.

Previous studies have shown that adding a metasurface to source antenna will produce two main results: 1) creating new resonant frequency bands and 2) changing the radiation patterns [4, 6]. The former result can be used to design antennas with dual-/multi-bands, while the latter result can be used to manipulate the radiation patterns. If we can achieve these two results together, we can have new frequency bands with different radiation patterns.

In this paper, a metasurface consists of a simple CPW-fed slot antenna and a metasurface is proposed to generate two frequency bands. The CPW-fed slot antenna is printed on one side of the substrate, while the metasurface is printed on the other side. This arrangement is different from others where different substrates are used for the antenna and metasurface. Computer simulation shows that our proposed design can generate two operating frequency bands. Moreover, the radiation patterns in these frequency bands are at opposite directions. However, it is yet to find applications for the proposed design.

## 2. ANTENNA DESIGN

The configuration of the proposed dual-band metasurface antenna is shown in Fig. 1, which was designed using planar technology. The source antenna was a CPW-fed antenna consisting of two identical slots etched on one side of the substrate as shown in Fig. 1(a). The two slots were mirror images of each other along the CPW-fed line which was at the center line of substrate. The metasurface consisting of 16 unit cells in a  $4 \times 4$  arrangement was printed on the other side of the substrate as shown in Fig. 1(b). Each unit cell had a square loop implemented using microstrip lines as shown in Fig. 1(c). The metasurfaced antenna was designed on Rogers RO4350B substrate, having the thickness of  $t = 1.524$  mm and area of  $T \times T = 60 \times 60$  mm<sup>2</sup>, with a dielectric constant of  $\epsilon_r = 3.48$  and a lost tangent of  $\delta = 0.0031$ . The performance of the metasurface antenna was optimized using computer simulation with the optimized dimensions listed in Table 1.

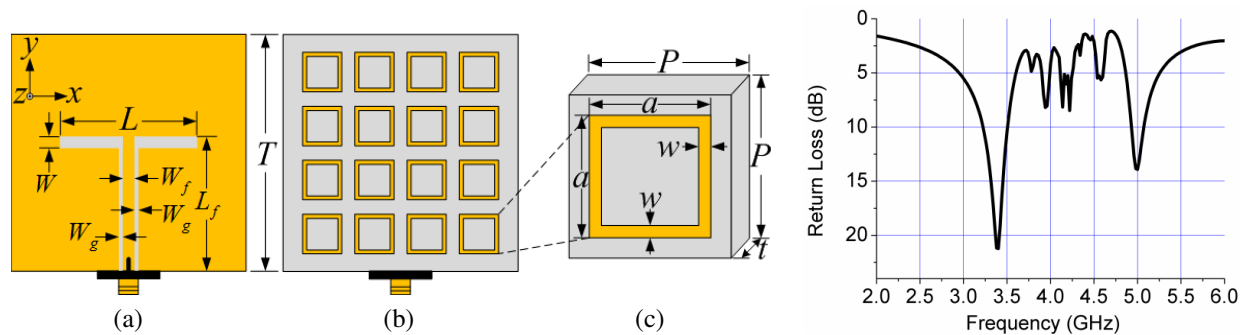


Figure 1: (a) Top view and (b) bottom view of metasurface antenna, (c) unit-cell of metasurface.

Figure 2: Return loss of metasurfaced antenna.

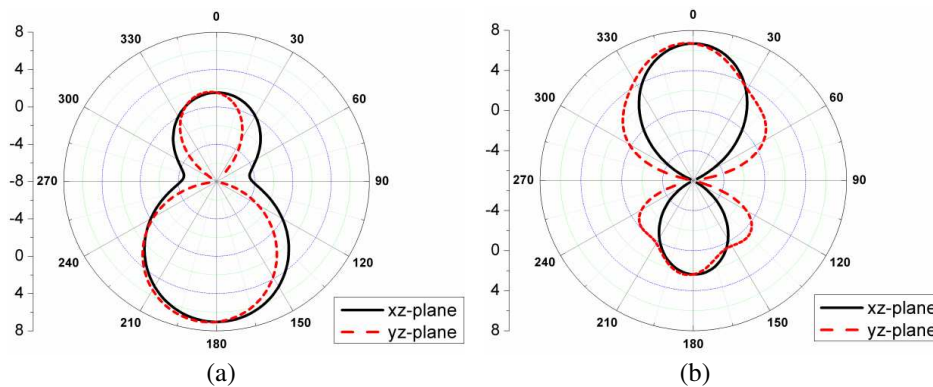


Figure 3: Radiation pattern of metasurface at (a) 3.4 GHz and (b) 5 GHz.

Table 1: Dimensions of dual-band antenna (Unit: mm).

$L$	$W$	$W_f$	$W_g$	$L_f$	$T$	$P$	$a$	$w$	$t$
48.4	3.5	3.6	0.2	31.75	60	14	12.6	0.8	1.524

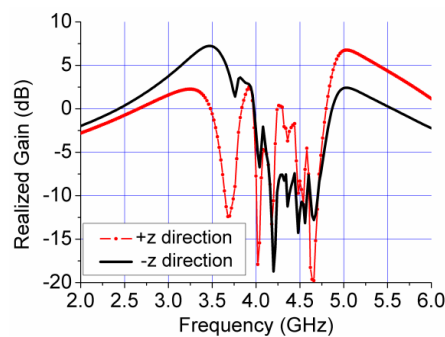


Figure 4: Realized gain of metasurface antenna at  $+ve$  and  $-ve$   $z$ -directions

### 3. SIMULATION AND MEASUREMENT RESULTS

The simulated return loss (RL), realized gain and radiation patterns have been studied using computer simulation. The simulated RL in Fig. 2 indicates that the antenna has the two frequency bands, with a lower band (RL < -10 dB) from 3.2–3.5 GHz and higher band from 4.9–5.1 GHz.

The radiation patterns at 3.4 and 5 GHz are shown in Figs. 3(a) and (b), respectively. It can be seen clearly that, at 3.4 GHz, the radiation pattern was bidirectional with the main lobe pointing at the  $-ve$   $z$ -direction as shown in Fig. 4(a). While at 5 GHz, the radiation pattern was also bidirectional but with the main lobe pointing at the  $+z$  direction as shown in Fig. 3(b).

Since the main lobe of the radiation pattern at the two operating bands were at the  $+z$  or

$-z$  direction, the realized gain of the antenna at the two directions were studied using computer simulation with results shown in Fig. 4. It can be seen that these two curve lines have their own raised part. For the radiation at the  $-z$ -direction, the realized gain was above 5 dB from 3.16 to 3.66 GHz with a maximum value of 7.23 dB at 3.45 GHz. For the higher frequency band, the realized gain was above 5 dB from 4.9 to 5.4 GHz with a maximum value of 6.8 dB at 5.05 GHz.

#### 4. CONCLUSIONS

A dual-band CPW-fed slot antenna using metasurface has been presented in this paper. Two operating frequency bands, located around frequencies of 3.4 GHz and 5 GHz, are created by adding a metasurface onto the plane. The main radiation directions in the two operating bands are opposite to each other.

#### REFERENCES

1. Ho, M. H. and G. L. Chen, "Reconfigured slot-ring antenna for 2.4/5.2 GHz dual-band WLAN operations," *IET Microwaves, Antennas & Propagation*, Vol. 1, No. 3, 712–717, 2007.
2. Gao, X., H. W. Yang, H. W. Lai, K. K. So, H. Wong, and Q. Xue, "CPW-fed slot antenna with dual band-notched characteristic for UWB application," *2012 4th International High Speed Intelligent Communication Forum (HSIC)*, 1–3, May 10–11, 2012.
3. Canhui, C. and E. Yung, "Dual-band dual-sense circularly-polarized CPW-fed slot antenna with two spiral slots loaded," *IEEE Transactions on Antennas and Propagation*, Vol. 57, No. 6, 1829–1833, 2009.
4. Chung, K. L. and S. Chaimool, "Diamagnetic metasurfaces for performance enhancement of microstrip patch antennas," *Proceedings of the 5th European Conference on Antennas and Propagation (EUCAP)*, 48–52, Apr. 11–15, 2011.
5. Holloway, C. L., E. F. Kuester, J. A. Gordon, J. O'Hara, J. Booth, and D. R. Smith, "An overview of the theory and applications of metasurfaces: The two-dimensional equivalents of metamaterials," *IEEE Antennas and Propagation Magazine*, Vol. 54, No. 2, 10–35, 2012.
6. Rakluea, C., S. Chaimool, P. Rakluea, and P. Akkaraekthalin, "Unidirectional CPW-fed slot antenna using metasurface," *2011 8th International Conference on Electrical Engineering/Electronics, Computer, Telecommunications and Information Technology (ECTI-CON)*, 184–187, May 17–19, 2011.
7. Zhu, H., K. L. Chung, X. L. Sun, S. W. Cheung, and T. I. Yuk, "CP metasurfaced antennas excited by LP sources," *2012 IEEE Antennas and Propagation Society International Symposium (APSURSI)*, 1–2, Jul. 8–14, 2012.

# Loaded Circular Patch Rectangular Slit Ultra-wideband (UWB) Microstrip Antenna

Chao Wang, En Li, and Gaofeng Guo

University of Electronic Science and Technology of China, China

**Abstract**— This paper brings forward a small printed rectangular slit ultra-wideband microstrip antenna loaded with a plane of circular patch. Different from the common circular slit microstrip antennae, the circular patch is loaded in the middle of the rectangular slit in order to obtain ultra-wideband characteristics and maintain small physical size at the same time. Experimental results show that the impedance of the antenna bandwidth is 2.7 GHz  $\sim$  6.2 GHz, the width of the lobe level of  $\pm 30$  degrees, and the pitch beamwidth is  $\pm 20$  degrees. And the physical size of the antenna is only 75 mm (length)  $\times$  70 mm (width)  $\times$  7 mm (thickness), which is suitable for ultra-wideband wireless communication system.

## 1. INTRODUCTION

Microstrip antenna, owing to its small size, light weight, low profile, easy carrier conformal and low cost, is widely used in measurement and communication fields. However, there is obvious disadvantage in microstrip antenna: the band is narrow and the bandwidth of the common microstrip antenna is only about 5%. In order to meet the demands of modern communications, people have developed a variety of techniques to overcome this drawback. The commonly-used techniques include using a thick dielectric substrate, the multilayer structure, the L-shaped feed electrical multi-resonance structure of the patch on slotted circuit, using broadband impedance matching of the feed circuit.

This paper introduces a small loaded circular patch of flat-printed rectangular gap ultra-wideband microstrip antenna. The impedance bandwidth of the antenna is from 2.7 GHz to 6.2 GHz (VSWR  $< 2$ ), the gain of the antenna is greater than 6 dB over the whole bandwidth, and the antenna is also resistant to high temperature. The horizontal beamwidth is  $\pm 30$  degrees, and the pitch beamwidth is  $\pm 20$  degrees. Because the antenna can well combine the characteristics of large bandwidth and small size and it is a planar structure, it can be easily integrated. Moreover, its small size makes it easier to form the ultra-wideband antenna array. Therefore, it has a wide application prospect.

The conventional wide slit microstrip antenna engraves the rectangular grooves in the ground plate, and is directly motivated by a short or open circuit of the microstrip line of the groove below. This kind of antenna has a relatively narrow frequency band. Although the bandwidth of the narrow rectangular groove in literature [1] has been broadened to the level of 20%, further increase of the width of the groove will correspondingly lead to the increase of the radiation resistance, which will bring about the mismatch between the radiating slots and feeder wires and the reduction of the impedance bandwidth. This article intends to propose a way to increase the length and width of the rectangular in order to broaden the operating frequency band by changing the shape of the radiating patch on the basis of the conventional microstrip antenna.

## 2. THE STRUCTURE AND PROPERTIES OF THE ANTENNA

The geometrical configuration of the proposed antenna is shown in Figure 1. This antenna is fabricated on one side of the RogersRT/duroid6002 (tm) substrate with a thickness  $T$  of 0.7 mm, relative dielectric constant of 2.94, and loss tangent of 0.0012. The high-frequency electromagnetic simulation software HFSS is used to simulate and optimize the antenna. The reason for selecting this substrate material is that it is light in weight, and resistant to high temperature. The rectangular slots are grooved on the grounding plate in symmetry with the round patch placed on the other side of the dielectric slab. The distance between the edge of feeding round patch and the slot of rectangular waveguide is  $h$  and it is 0.65 mm. The annular slot is etched on a square chassis with size  $75 \times 70 \text{ mm}^2$  and it has an inner radius  $R_p = 0.75 \text{ mm}$ . The antenna is fed with one microstrip line printed on the bottom side of the substrate and disposed as shown in Figure 1. The microstrip line is terminated with one patch to match the antenna with the characteristic impedance of the microstrip line, and this can lead to a broadband impedance bandwidth. The impedance of the feeder is 50 Ohms. The size of rectangular slit is  $54 \times 53 \text{ mm}^2$  and the dimensions of this microstrip

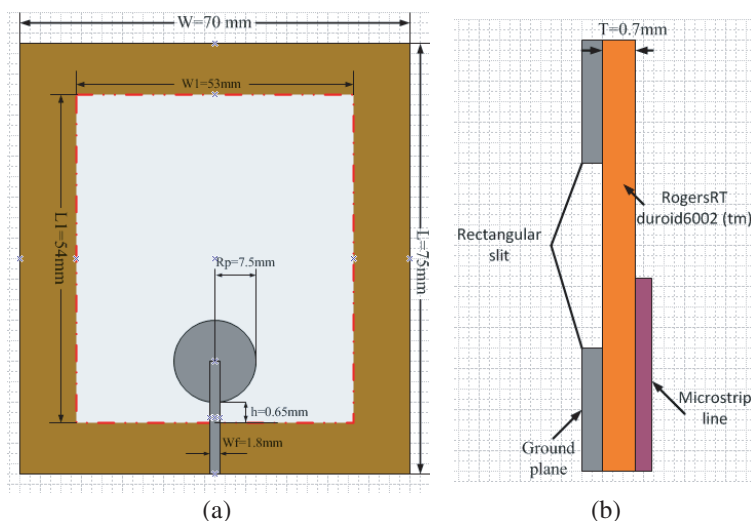


Figure 1: Structure of the antenna.

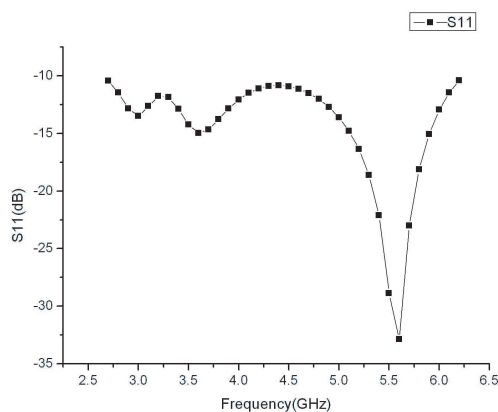


Figure 2: The antenna's reflection coefficient.

line is  $Wf = 1.8$  mm. It can be drawn that the structure of the antenna is easy to be integrated with other microwave circuits.

Figure 1(b) shows a wide-slot antenna with a rectangular ground plate slit. When the aspect ratio of the rectangular wide slit is adjusted to a certain value, a certain impedance bandwidth and center frequency will correspondingly appear. If the aspect ratio is adjusted to the optimum value, we can achieve a rectangular wide slit antenna with ultra-wideband performance.

Wide slit antennae have different gap shapes, such as rectangles, squares, and circles, and different feeding patch shapes, such as T-shaped, cruciform, the tuning fork-shaped, etc.. The antenna studied in this paper selected a circular feeding patch to excite rectangular wide slit because the combination of the two can lead to a wide impedance bandwidth and good radiation properties. Due to the presence of a wide slit in the wide slit antenna ground plate, there is a strong electromagnetic coupling between the wide slit and the feed patch. Therefore, we can adjust the impedance matching of the antenna by changing the shape of the wide slit and feed patch and the edge spacing coupling between them. Thus, there are two factors in the design of this type of ultra wideband antenna that can be taken into consideration. One is the shape of the slit, which can be quite similar to that of the feeding patch. For example, if the feeding patch is rectangular, the shape of the wide slit can be rectangular, square, stepped, etc.. If the feeding patch is circular, the wide slit can be designed as a circular, semicircular, oval, etc.. The other is the distance between the feeding patch edge and the edge of the wide slit which has a significant impact on the impedance matching of the antenna. The impedance bandwidth can be increased by strengthening the coupling between the feeding portion and the wide slit. When the coupling is increased to a certain value, the best impedance matching bandwidth can be obtained. But if the coupling is increased over a certain value, the impedance matching will deteriorate. This phenomenon indicates that excessive coupling

match, just like insufficient coupling, is not conducive to improve the impedance bandwidth of the wide slot antenna. Both of the two factors mentioned above expand the impedance bandwidth of the wide slit by adjusting the electromagnetic coupling between the feeding patch and the wide slit in the ground plate. Therefore, the expansion of the bandwidth of the wide slit antenna can meet the Ultra-wideband system requirements if we can change the shapes of both the wide slit and the feeding microstrip line and change the edge space between them. The reflection coefficient  $S_{11}$  of the antenna designed in this paper is shown in Figure 2.

It can be seen from Figure 2 that the impedance bandwidth of the rectangular wide slit of the circular microstrip feed is 79% (2.7 GHz–6.2 GHz). Literature [2] mentioned that two kinds of antenna are adopted one is the semicircular wide-slit antenna of the rectangular microstrip feeding, and the other is the triangular broadband antenna of the triangle microstrip feeding. Both of the antennae have the properties of ultra wideband. But both of them are fabricated on a substrate material FR4 and the wastage of FR4 is quite large, so the efficiency of the antenna is reduced. Meanwhile, because both areas of the antennae are too large (110 mm × 110 mm), this will limit their integration into a portable communication device. Literature [3] mentioned a ladder-like wide slit antenna of rectangular microstrip feed, a semicircular wide slit antenna of rectangular microstrip feed and a semicircular wide slit antenna of circular microstrip feed. In spite of ultra-wideband performance and good radiation performance, some spikes over  $-10$  dB emerge at some frequency point, and the gain is relatively low, between 2 dBi to 5 dBi over the range. At the high-end of the impedance bandwidth, the radiation performance deteriorates and the cross-polarization becomes more serious. Therefore, the gain correspondingly declines. Figure 3 and Figure 4 give the radiation pattern and gain of the rectangular wide slit antenna of circular microstrip power feeding respectively. Compared with the antennas given in literatures [2] and [3], the antenna designed in this paper has narrower bandwidth, but it achieves a relatively high gain, 6 dB ~ 10 dB in 2.7 GHz ~ 6.2 GHz.

As for the structure designed in literature [2] and [3], if we use HFSS for repeated simulation

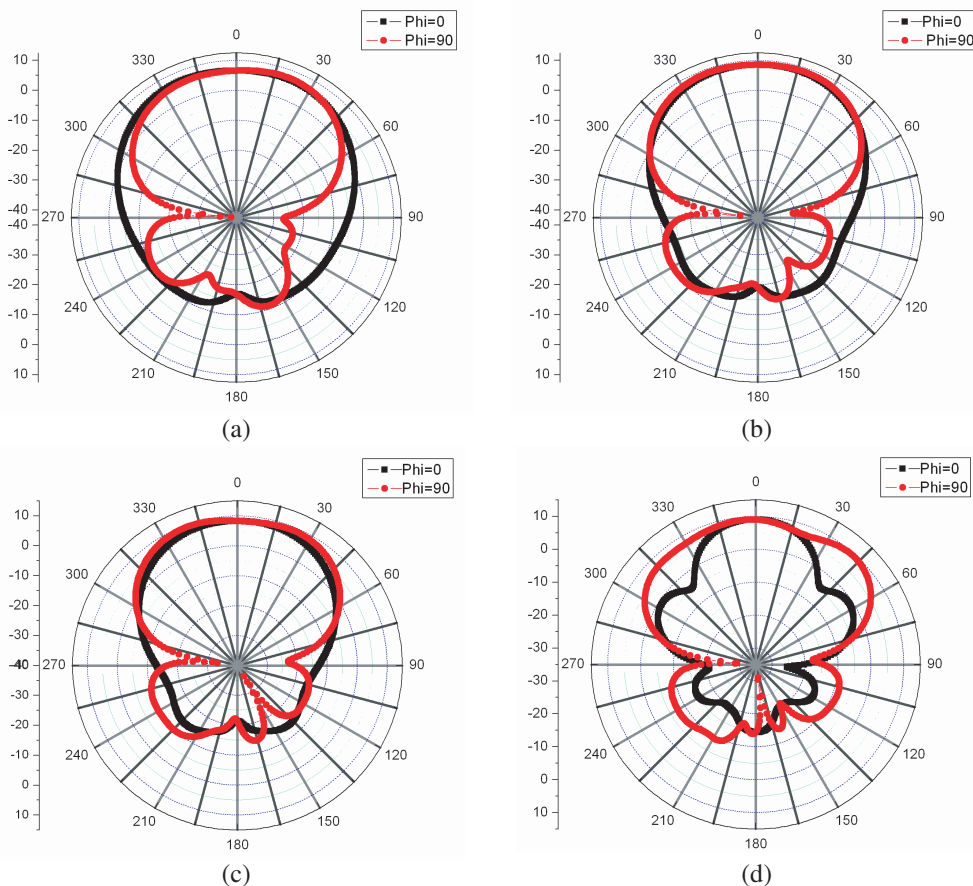


Figure 3: Radiation pattern of the antenna at different frequencies.

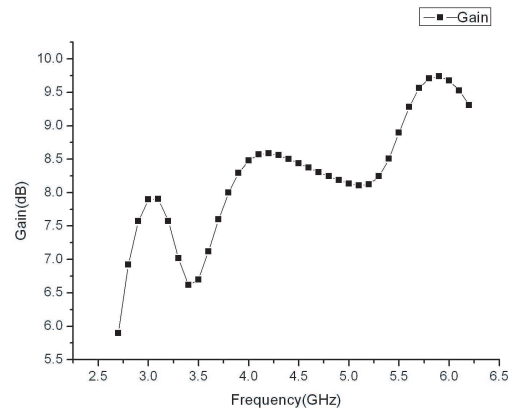


Figure 4: Antenna gain.

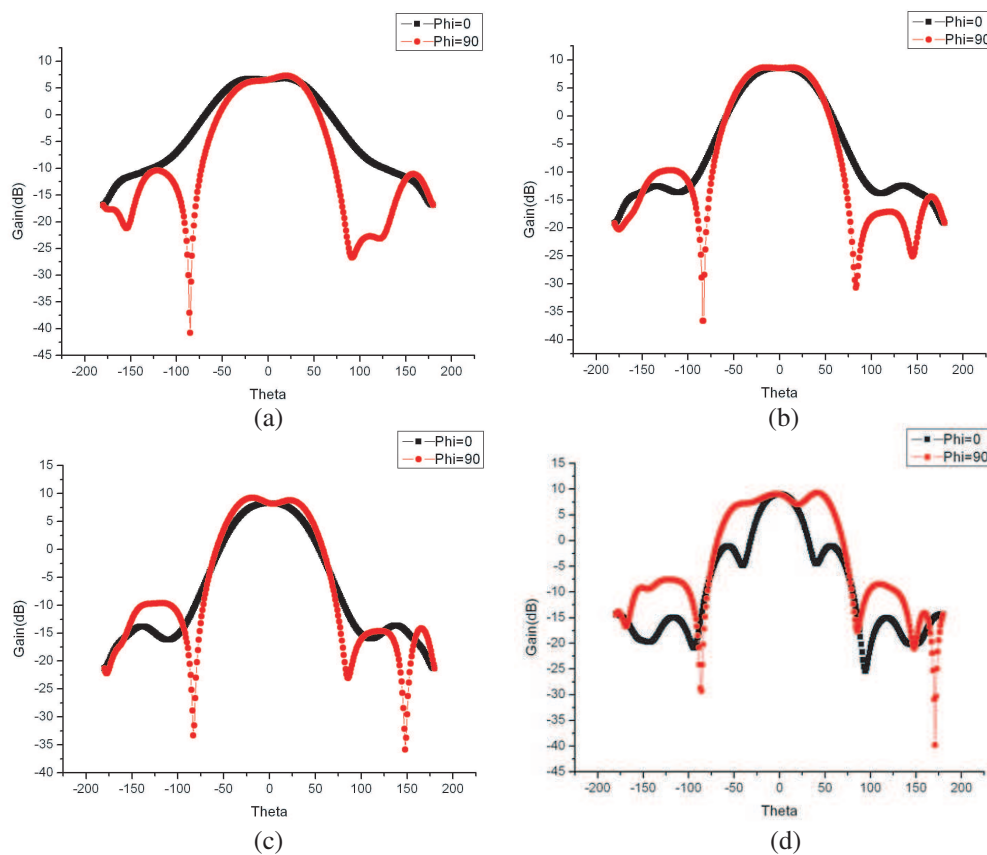


Figure 5: Radiation pattern and beamwidth of the antenna.

trials, we can find that the structure, on condition that it should be resistant to high temperature and be of small size, cannot meet the requirement of horizontal  $\pm 30$  degrees and pitching  $\pm 20$  degrees. However the rectangular wide slot antenna of the circular microstrip feed can achieve this goal, which is shown in Figure 5.

### 3. CONCLUSIONS

By the simulation of the performance of the rectangular wide slit antenna of circular microstrip feeding and the comparisons, we can draw the conclusions that by changing the shape of the wide slit and fed microstrip, making a reasonable combination, and adjusting between the distance of feeding patch edge and the width of the gap, we can significantly increase the bandwidth of the antenna. However from Figure 4 and Figure 5, it can be seen that the maximum gain point of the

frequency point of such antenna is not in the central position and that there is a depression. The reason for this phenomenon is that the ground plate is not infinitely large and that the electric field distribution induced by the notch and the slit width are both uneven. But this does not affect the performance of the antenna. The rectangular wide slot antenna of circular microstrip feeding proposed in this paper has advantages such as simple structure, small material wastage, resistance to high temperature and convenience for processing so that it has a stable gain and radiation performance in the entire frequency band.

#### REFERENCES

1. Gao, X., *Study and Design of Ultra-wideband Antenna*, 27–33, 2008.
2. Axelrod, A., M. Kislud, and J. Maoz, “Broadband microstrip-fed slot antenna,” *Microwave J.*, Vol. 32, 81–94, 1989.
3. Liu, Y. F., K. L. Lau, Q. Xue, and C. H. Chan, “Experimental studies of printed wide slot antenna for wide-band applications,” *IEEE Antennas and Wireless Propagation Letters*, Vol. 3, No. 1, 273–275, 2004.
4. Chen, D. and C. H. Cheng, *Journal of Nanjing University of Posts and Telecommunications*, Vol. 47, 72–75, 2006.
5. Jang, Y. W., “Broadband cross-shaped microstrip-fed slot antenna,” *Electron Lett.*, Vol. 36, 2056–2057, 2000.

# Printed Modified Bow-tie Dipole Antenna with Band-notch Structure

Huai-Yu Lin, I-Fong Chen, Ching-Chih Hung, and Chia-Mei Peng

Institute of Computer and Communication Engineering  
Jinwen University of Science and Technology, Taiwan, R.O.C.

**Abstract**— The ability of a modified bow-tie dipole antenna with band-notch slot, which has an asymmetric-feed structure to operate at UHF-band (470–82 MHz) and dual ISM-band (2.4 GHz and 5.8 GHz) is demonstrated. Experimental results indicate that the VSWR 2.5 : 1 bandwidths achieved were 60.6%, 20.48% and 2% at 660 MHz, 2.45 GHz and 5.5 GHz. The proposed modified bow-tie dipole exhibits a nearly omni-directional radiation pattern with very easy to fabricate structure, and so is suitable for various commercial wideband applications.

## 1. INTRODUCTION

The inter-working wireless technologies such as WLAN with DVB networks, provide the user with a return link for interactive TV, and high bandwidth asymmetric downlink for data transfer to terminals operating in the heterogeneous roaming environment. Therefore the antenna is required to operate at broadband in DVB and WLAN (dual-ISM band) system [1]. Some of the desired features for these antennas include broad bandwidth, simple impedance matching to the feed line and low profile. The bow-tie dipole antenna has become the main candidate for the above application since its bandwidth performances reasonably well compared to other alternatives [2]. But, the bow-tie dipole antenna is difficult to satisfy the multi-band requirement for the respective communication bands, and the terminal resistance is approximately  $300\ \Omega$ . Designing an integrated antenna for wireless product with dual or multi-band operation is straightforward. For this purpose, in this paper, we introduce a printed modified bow-tie dipole antenna with band-notch slot [3], which has an asymmetric-feed structure to yield broad bandwidth, and the terminal resistance is approximately  $50\ \Omega$ . The arms of modified bow-tie dipole are shifted position to yield an asymmetrical structure [4]. The impedance matching of the modified bow-tie dipole structure is obtained by tuning the shifted distance. The band notch of the dipole structure is obtained by inserting some slots on the dipole-arms [5, 6]. Details of the design considerations of the proposed designs and the experimental results of constructed prototype are presented and discussed.

## 2. ANTENNA STRUCTURE AND DESIGN

Figure 1 shows the proposed asymmetric modified bow-tie dipole antenna for DVB and WLAN applications. The presented antenna structure is composed of a modified bow-tie dipole radiating element section of length  $L$ , width  $W$  and flare angle  $\theta$ , and the shifted distance  $D$ , which are both printed on a 1.6 mm-thick FR4 glass epoxy substrate (the relative permittivity is 4.3). The fundamental resonant mode of modified bow-tie dipole is designed to occur at about 660 MHz (the

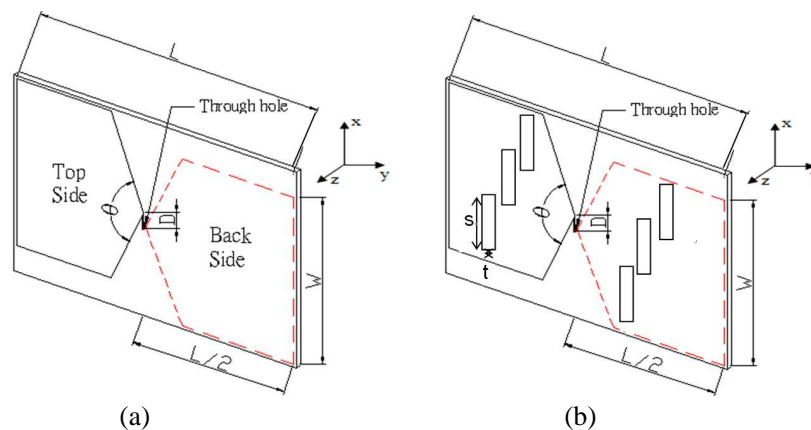


Figure 1: (a) Geometry of the original antenna. (b) Geometry of the proposed antenna.

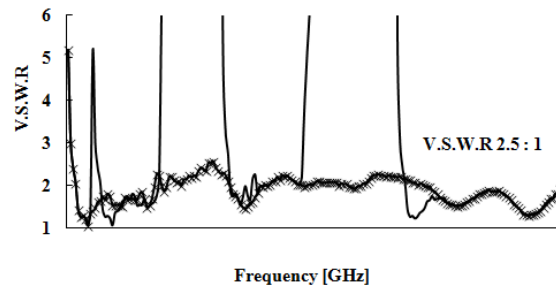


Figure 2: Measured V.S.W.R versus frequency.

center frequency of the lower operating band: 470–862 MHz). The dipole length and width can be determined from the half- and quarter-wave length of the resonant frequencies. For a  $50\ \Omega$  feeding, the shifted distance  $D$  should be  $\lambda/20$ . Note that the flare angle of modified bow-tie dipole is function of operating bandwidth. In general, the bandwidth of the lower operating band increases with an increase in the flare angle. By determining appropriate dimensions ( $L$ ,  $W$ ,  $D$ ,  $\theta$ ) of the antenna structure, good impedance matching of the printed modified bow-tie dipole can be obtained across an extended bandwidth. A feed-strip excites the modified bow-tie dipole arms which were shifted distance  $D$  to be asymmetric structure as shown in Figure 1(a), which was denoted as the original antenna. The shape of the original antenna was designed for wideband operation. The band notch of the dipole structure is obtained by inserting some slots on the dipole-arms. Note that, the sizes of the slots are not identical. The tuning of the notch band was obtained by adjusting the size of slots on the dipole-arms to produce the required frequency response characteristic. The impedance matching at UHF-band (470–862 MHz) and dual ISM-band (2.4 GHz and 5.8 GHz) can be tuned by this structure, which was found to be effective in obtaining a wider impedance bandwidth in the antenna's operating band.

### 3. EXPERIMENTAL RESULTS

In the experiment, the feed point (through hole) of proposed antenna is connected to a  $50\ \Omega$  RG-178 coaxial-cable (the length is 10 cm) with a SMA connector. By using the described design procedure, the original antenna was constructed to operate the  $V.S.W.R \leq 2.5$  in the range of 0.45 GHz to 6 GHz, as shown in the Figure 2. In the case with modified bow-tie dipole-arm's size: length  $L = 22.6$  cm, width  $W = 13.6$  cm and flare angle  $\theta = 120^\circ$ , the shifted distance  $D = 2.1$  cm. To insert some slots on the dipole-arms the optimal length ( $s$ ) and width ( $t$ ) of the slots is 25 mm and 9 mm, a multi-band antenna was constructed to operate in the range of UHF-band (470–862 MHz) and dual ISM-band WLAN system (2.4–2.4835 GHz and 5.15–5.825 GHz). It was found that the  $V.S.W.R \leq 2.5$  bandwidths are 40 MHz (60.6%), 500 MHz (2.48%) and 1100 MHz (20%) at 660 MHz, 2.45 GHz and 5.5 GHz, which meet the required bandwidths of the DVB and dual ISM-band WLAN bands. Figure 2 also shows the V.S.W.R plot of the multiband antenna as a result of this design.

Based on the experimental study by using simulation software package (Ansoft HFSS), the effects of key parameters (e.g., slot sizes, slot numbers, etc.) are discussed and optimized. The simulation results of inserting slots on the bow-tie dipole-arms are shown in Figure 3. In Figure 3, there are four simulation results, the simulation frequencies are 0.66 GHz, 2.45 GHz and 5.5 GHz. The first simulation result is without inserting slots on the bow-tie dipole-arms, and the frequency is 0.66 GHz. To make comparison between these simulation results, the results show the variation in current distribution around the slots. It is also clearly shown those slots will greatly impact the surface current distribution on the bow-tie dipole-arms which affects the impedance characteristic of antenna, to cause band notch response which is illustrated with Figure 2. Figure 4 presents the measured radiation patterns for free space at 0.66 GHz, 2.45 GHz and 5.5 GHz in the  $xy$ -plane ( $H$ -plane) and  $xz$ -plane ( $E$ -plane), respectively. The maximum gains in the  $E$ -plane are 0.24 dBi, 1.12 dBi and 0.97 dBi at 0.66 GHz, 2.45 GHz and 5.5 GHz. The maximum gains in the  $H$ -plane are 0.1 dBi, 0.078 dBi and 0.24 dBi at 0.66 GHz, 2.45 GHz and 5.5 GHz. The operating bandwidth of the proposed antenna with usable broadside radiation patterns is consistent with the specification of DVB and WLAN system. Stable radiation patterns are observed. Acceptable radiation characteristic for the practical applications is obtained for the proposed antenna. The

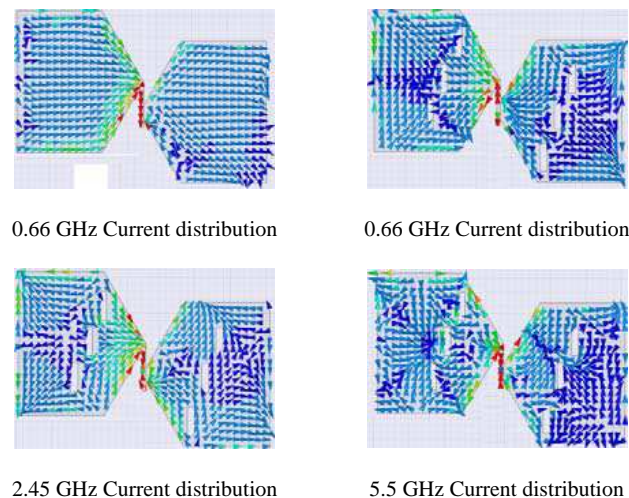


Figure 3: Simulated current distribution versus frequency on the bow-tie dipole-arms.

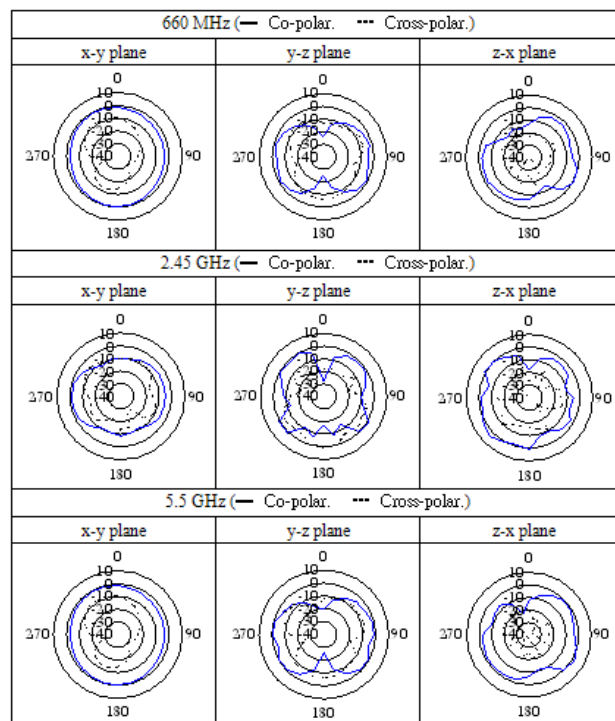


Figure 4: Measured radiation patterns for the proposed antenna.

omni-directional feature of the proposed antenna can also be observed from the Horizontal-plane. The effect of varying the inserting-slot dimensions on the antenna performance has been studied and the results are described below.

The structure of the printed inserting-slot is a rectangle slot, as shown in Figure 1(b). The design parameters and the corresponding characteristics of resonant frequency, input impedance, slot numbers and bandwidth are a function of the geometrical parameters of the inserting-slot structure. Experimental results were obtained for various inserting-slot sizes (there are three same size slots on the bow-tie dipole-arms, respectively). An increase in the inserting-slot length ( $s$ ) leads to an increase impedance bandwidth and an increase resonant frequency in the UHF-band and the dual ISM-band. Conversely, the effects of changing inserting-slot width ( $t$ ) on the antenna operation in the UHF-band and the dual ISM-band are very small.

#### 4. CONCLUSIONS

It has been demonstrated that a printed modified bow-tie dipole provides multi-band operation. By correctly choosing the shifted distance and by modifying the width of the slots, three bandwidths defined for a V.S.W.R lower than 2.5, respectively, 60.6%, 20.48% and 2% at 660 MHz, 2.45 GHz and 5.5 GHz, can be obtained. The contribution of this paper is to implement a simple and easy fabrication antenna for practical DVB and WLAN application. Measurements show that the structure indeed offers very impressive bandwidth characteristics. Although this antenna was designed for DVB and dual ISM-band applications, this design concept can be extended to other frequency bands of interest.

#### ACKNOWLEDGMENT

This work was supported by National Science Council R.O.C., under contract 101-2221-E-228-006, and Wieson Techno. Corp., under contract JW101-F-411-031.

#### REFERENCES

1. Morris, D., P. Pangalos, and A. H. Aghvami, "Mobile terminal location discovery schemes for a 'beyond 3G' inter-worked network," *Proceedings of the Sixth IEEE International Symposium on WoWMoM*, 401–406, 2005.
2. Kraus, J. D. and R. J. Marhefka, *Antennas*, McGraw-Hill, New York, 2002.
3. Jordan, R. and C. T. Abdallah, "Wireless communications and networking: An overview," *IEEE Antennas Propag. Mag.*, Vol. 44, No. 1, 185–193, USA, 2002.
4. Peng, C. M., I. F. Chen, C. C. Hung, and H. C. Chen, "Printed modified bow-tie dipole antenna for multi-band applications," *IEICE Trans. on Common.*, Vol. E92-B, No. 4, 1404–1405, 2009.
5. Chu, Q.-X. and Y.-Y. Yang, "3.5/5.5 GHz dual band-notch ultra-wideband antenna," *Electronics Letters*, Vol. 44, No. 3, 172–174, 2008.
6. Chung, K., S. Hong, and J. Choi, "Ultrawide-band printed monopole antenna with band-notch filter," *IET Microwaves, Antennas and Propag.*, Vol. 1, No. 2, 518–522, 2007.

# Printed Dual-polarization Broadband Directional Antenna

Lu-I Yams, Chia-Mei Peng, I-Fong Chen, and Kang-Ling Li

Institute of Computer and Communication Engineering  
Jinwen University of Science and Technology, Taiwan, R.O.C.

**Abstract**— A four layer odd function symmetric dual-polarization coplanar waveguide (CPW)-fed slot antenna for broadband communications is proposed in this literature. The proposed antenna has a very simple antenna structure and wide impedance bandwidth ( $\sim 400\%$  for  $|S_{11}|$  and  $|S_{22}|$ ,  $VSWR \leq 3$ ) which can cover the 1.5~6 GHz frequency band for Global Positioning System (GPS, 1575 MHz) and dual ISM band (2.4 GHz and 5.8 GHz) applications. Good isolation between the two input ports ( $|S_{21}| \leq -15$  dB) is also achieved at the operating band. The radiation pattern and efficiency of the proposed antenna are also measured, and radiation pattern data are compared with simulation results.

## 1. INTRODUCTION

With rapid progress in wireless communication systems, the demand to enhance the information accessibility and wideband utility has become major importance in wireless technology. An efficient way to increase the capability is the employment of polarization diversity, and thus the dual-polarized antennas have gained more and more popularities. In [1], a tri-polarization antenna was proposed, but isolation between some ports were not sufficient and were hence unacceptable in high-performance applications. Several papers have been published [2,3] to improve isolation in similar antenna applications. However, the antennas of the bandwidth are still not wide enough for modern wireless communication systems. To have wider bandwidth and simple planar antenna configuration, bow-tie dipole and slot antennas are good candidates [4]. To meet the specification of wide bandwidth, simplicity, and high isolation, a dual-polarization CPW-fed bow-tie slot antenna is considered in this paper [5]. Summarize all of the above reference paper, we proposed a new design for high gain and broadband directional antenna, which is brought by the embedded slot with odd function symmetric pair of stubs and stacked of four layer including two antennas and two reflectors, the horizontal and vertical polarization is scattered CPW-fed line on the top and bottom antenna perpendicular. Details of the design considerations of the proposed antenna designs and the experimental results of constructed prototypes are presented and discussed.

## 2. ANTENNA STRUCTURE AND DESIGN

Figure 1 shows the configuration of the proposed odd function symmetric slot antenna. The overall dimensions of the antenna are  $100 \times 100 \text{ mm}^2$ . The antenna is made of FR4 ( $\epsilon_r = 4.4$ ,  $\tan \delta = 0.02$ ),

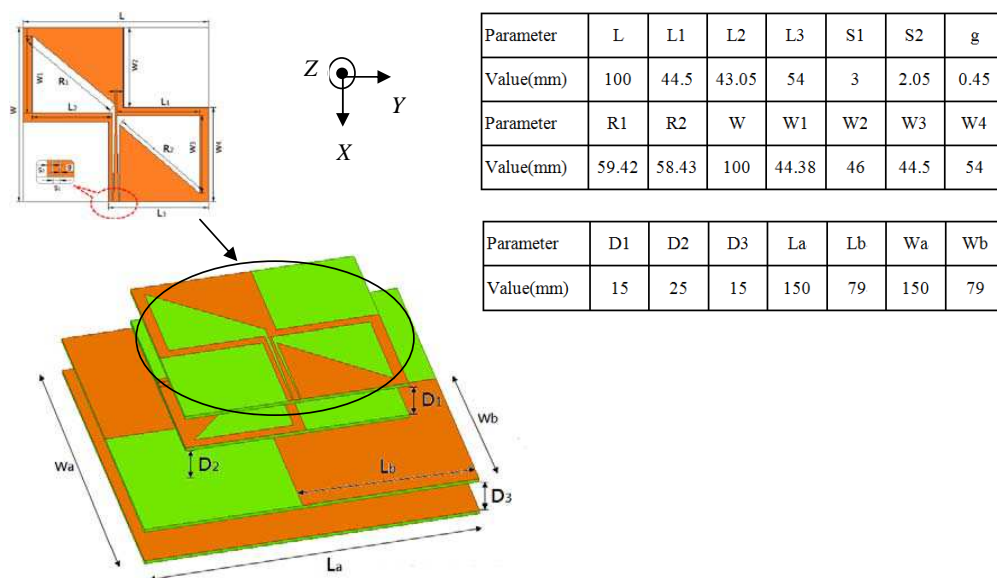


Figure 1: Geometry and dimension of the proposed antenna.

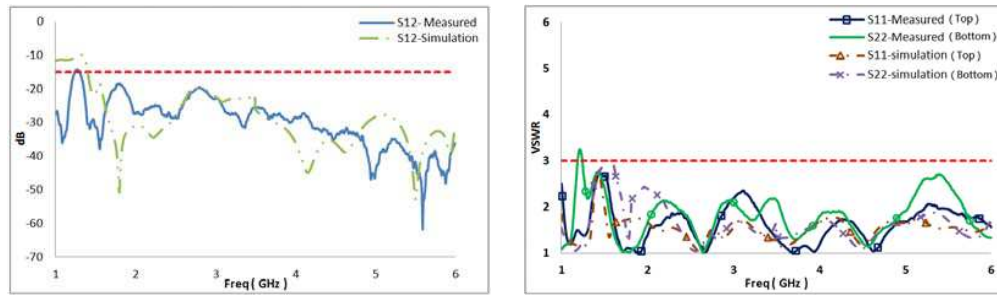


Figure 2: Measured and simulated isolation against frequency.

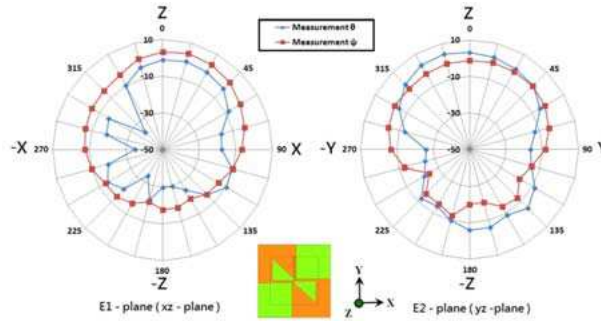


Figure 3: Measured radiation patterns for the proposed antenna at 2.4 GHz in the  $E_1$ -plane and  $E_2$ -plane.

its thickness is 1.6 mm. The CPW-fed line is designed to be  $50\ \Omega$  ( $S_3 = 3\text{ mm}$ ), gap spacing ( $S_2 = 0.45\text{ mm}$ ) and taper to the CPW of signal strip length should be  $0.25\lambda$  ( $W_2 = 46\text{ mm}$ ) that parameter is determined by the required band of the lowest frequency. Antenna dimensions of slot ( $L_1 + R_2 + W_3 = 0.75\lambda$ ) are determined by the lowest frequency of desired band. The proposed high gain and broadband directional antenna, it stacked of four layer including two antennas and two reflectors, and scattered CPW-fed on the top and bottom antenna perpendicular. Etched in the top layer, the antenna serves as the vertical polarization radiation. The CPW is fed in port 1. In the bottom layer, antenna rotates  $90^\circ$  to cover the horizontal polarization radiation. To ensure isolation between two antennas distance,  $D_1 (= 15\text{ mm})$  should be  $0.08\lambda$  at the desired band of the lowest frequency. Reflector stack up odd function between antennas distance,  $D_2 (= 25\text{ mm})$  and  $D_3 (= 15\text{ mm})$  should be  $0.16\lambda$  at the desired band of the lowest frequency.

### 3. EXPERIMENTAL RESULTS

To validate the design, the  $S$ -parameters of the proposed antenna has been fabricated and measured. Figure 2 shows the VSWR and isolation of the two fed ports of the wideband antenna as a result of this geometry. When feeding from ports 1 and 2, the radiation patterns of the propose antenna are shown in Figure 3. From the radiation patterns, we can observe that the  $xz$  plane and  $yz$  plane are almost corresponding to the maximum of each other at frequencies. According to the results, it can be proved that the two odd function is symmetric slot antennas are placed 90 degrees of difference can achieve good isolation and dual polarization.

### 4. CONCLUSIONS

A four layer odd function symmetric dual-polarization CPW-fed slot antenna for broadband communications has been proposed and measured. The antenna structure is brought by the embedded slot with odd function symmetric pair of stubs and stacked of four layer including two antennas and two reflectors, and scattered CPW-fed on the top and bottom perpendicular It can be obtained a much wider impedance bandwidth, dual-polarization and high isolation. The isolation between two ports in the required band is lower than 15 dB. Although this antenna was designed for frequency 1.5 GHz–6 GHz applications, this design concept can be extended to other frequency bands of interest.

**ACKNOWLEDGMENT**

This work was supported by National Science Council R.O.C., under contract 101-2221-E-228-004.

**REFERENCES**

1. Zhong, H., Z. Zhang, W. Chen, Z. Feng, and M. F. Iskander, "A tripolarization antenna fed by proximity coupling and probe," *IEEE Antennas Wireless Propag. Lett.*, Vol. 8, 465–467, 2009.
2. Lee, C.-H., S.-Y. Chen, and P. Hsu, "Isosceles triangular slot antenna for broadband dual polarization applications," *IEEE Trans. Antennas Propag.*, Vol. 57, No. 10, 3347–3351, 2009.
3. Li, Y., Z. Zhang, W. Chen, Z. Feng, and M. F. Iskander, "A dual-polarization slot antenna using a compact CPW feeding structure," *IEEE Antennas Wireless Propag. Lett.*, Vol. 9, 191–194, 2010.
4. Huang, C. Y. and D. Y. Lin, "CPW-fed bow-tie slot antenna for ultrawideband communications," *Electron. Lett.*, Vol. 42, No. 19, 1073–1074, 2006.
5. Wu, C.-J., I.-F. Chen, and C.-M. Peng, "A dual polarization bow-tie slot antenna for broadband communications," *PIERS Proceedings*, 217–221, Marrakesh, Morocco, Mar. 20–23, 2011.

# A Y-shaped Microstrip-line-fed Wide-slot Antenna with Band-controlled for Multiband Applications

S.-J. Wei, Q.-Y. Feng, and D.-H. Jia

School of Information Science and Technology  
Southwest Jiaotong University, Chengdu, Sichuan 610031, China

**Abstract**— In this paper, a printed wide-slot antenna with a Y-shaped microstrip-fed line for multiband applications is proposed and studied. A simple Y-shaped microstrip line is used for exciting the wide slot carved on the ground plane. With the use of equilateral triangle wide-slot reversed along the equilateral triangle ground plane, multi-frequency is obtained. The simulated results demonstrate that the resonant frequency of the proposed antenna is greatly affected by the angle of the Y-Shaped microstrip line. The band is proved to be controllable. One-band, dual-band and tri-band antenna could be obtained by adjusting the angle of the Y-shaped microstrip line. In addition, the current distribution on the radiating patch for the proposed antenna, which corresponds to the frequency band, is presented and discussed. Meanwhile, the radiation patterns of the proposed antenna are simulated with  $E$ -plane and  $H$ -plane. It could be suitable for multiband wireless applications.

## 1. INTRODUCTION

With the rapid development of wireless communication systems, printed slot antennas are widely used in a variety of communication systems [1]. Meanwhile, there has been a growing research activity on many microstrip-line-fed printed slot antennas, especially printed wide-slot antennas [2]. Therefore, a great interest in various microstrip-line-fed slot antennas can be seen in the literature [3–5].

As reported in the published works, various microstrip-line-fed wide-slot antennas are reported. In [6, 7], the performance of bandwidth enhancement is achieved according to the microstrip-line-fed wide-slot antenna. Meanwhile, the wide-slot antennas are used for realizing the patterns improvements and ultra-wideband communications in the literature [8].

In this paper, we present a printed wide-slot antenna with a Y-shaped microstrip-fed line for multiband applications. By adjusting the angle of the Y-shaped microstrip line, one-band, dual-band and tri-band antenna could be obtained. According to the simulated results, the band is proved to be controllable. Details of the proposed antenna are described and discussed.

## 2. ANTENNA STRUCTURE

The geometry of the proposed microstrip-line-fed wide-slot antenna is illustrated in Fig. 1. The proposed antenna is designed on the FR4 dielectric substrate occupied the dimensions of  $125 \times 108 \text{ mm}^2$  ( $L \times W$ ) with the thickness of 1.6 mm, relative permittivity 4.4 and dielectric loss tangent of 0.02. The width of the feed line  $W_f$  is fixed at 3 mm, which corresponds the characteristic impedance of 50 ohm. The detail dimensions of the antenna are listed in Table 1.

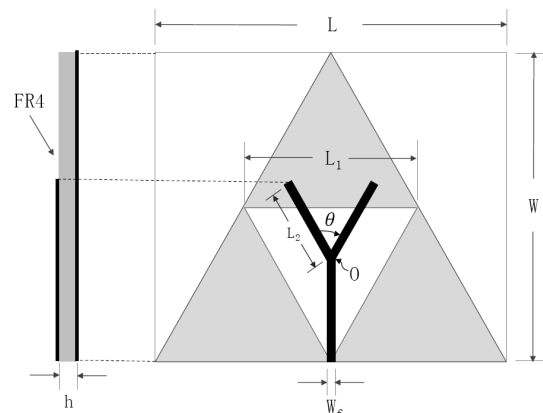


Figure 1: Geometry of the proposed antenna.

As shown in Fig. 1, the proposed antenna consists of a Y-shaped microstrip-fed line used for exciting the wide slot carved on the ground plane. In order to achieve the multi-band, the equilateral triangle wide-slot reversed along the equilateral triangle ground plane is adopted. A Y-shaped microstrip line is used for feeding the structure. With the change of the angle  $\theta$ , different bands could be obtained.

### 3. SIMULATION RESULTS

In this section, the simulation results are carried out to show the performance of the design. Ansoft High Frequency Structure Simulator (HFSS) is employed to analyze the electrical properties and radiation characteristics of the antenna.

Figure 2 shows the simulated return losses of the proposed antenna with different angles  $\theta$ . It could be observed that a single frequency is achieved while the angle  $\theta$  of the Y-shaped microstrip line is 120 degree. The resonant frequency with good matching impedance occurs at 7.96 GHz. The  $-10$  dB band ranges from 7.54 to 8.34 GHz. Meanwhile, dual-band is obtained while the angle  $\theta$  is

Table 1: The parameters of the proposed antenna (Unit: mm).

Parameters	$L$	$W$	$h$	$L_1$	$L_2$	$W_f$
Value (mm)	125	108	1.6	60	30	3

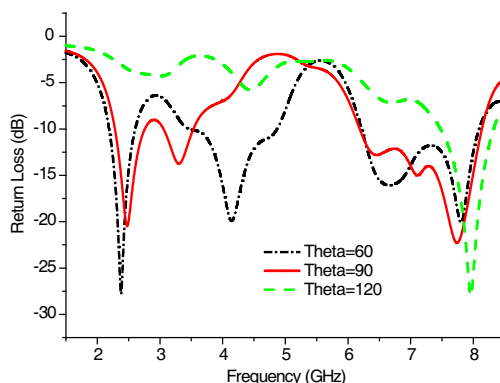


Figure 2: Simulated return losses of the proposed antenna with different angles  $\theta$ .

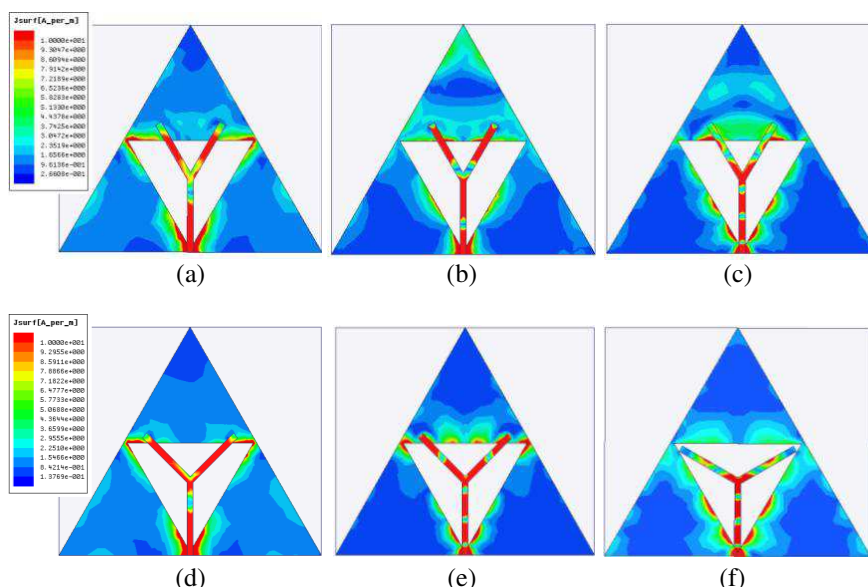


Figure 3: Simulated surface current distributions on radiating patch for the proposed antenna at (a) 2.39 GHz with  $\theta = 60$ . (b) 4.16 GHz with  $\theta = 60$ . (c) 7.75 GHz with  $\theta = 60$ . (d) 2.47 GHz with  $\theta = 90$ . (e) 7.74 GHz with  $\theta = 90$ . (f) 7.96 GHz with  $\theta = 120$ .

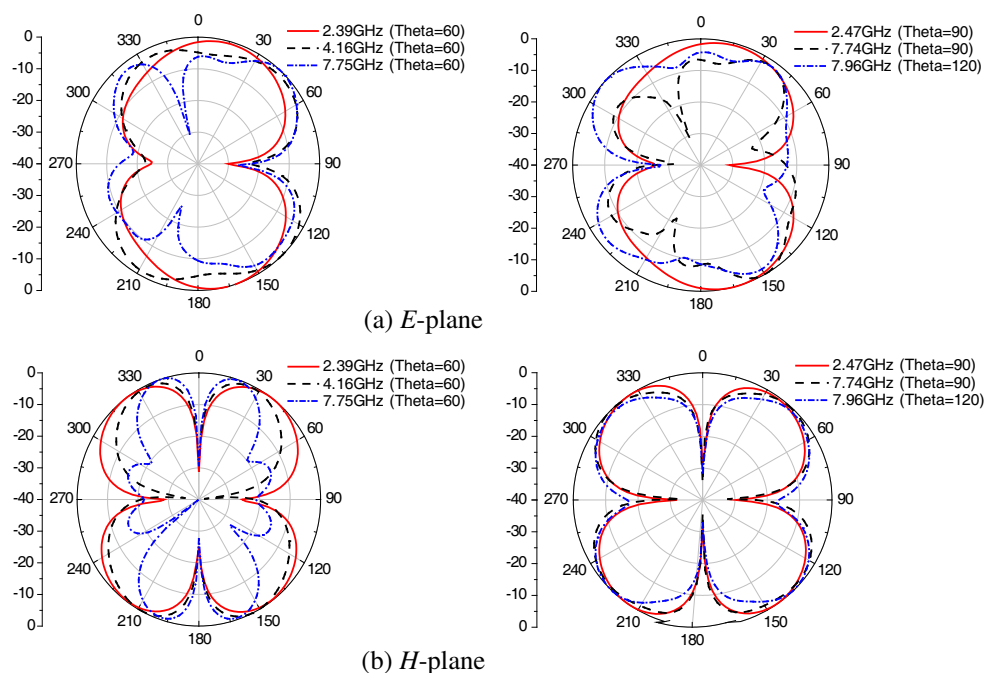


Figure 4: The simulated normalized radiation patterns of the proposed antenna at different frequencies. (a)  $E$ -plane. (b)  $H$ -plane.

90 degree. The frequency band appears at 2.47 GHz and 7.74 GHz. The  $-10$  dB bands are located at the ranges of 2.28–2.63 GHz and 6.19–8.07 GHz. Moreover, tri-band could be acquired while the angle  $\theta$  is set as 60 degree. The center operating frequencies, which are 2.39 GHz, 4.16 GHz and 7.75 GHz, are obtained. The  $-10$  dB bands are located at the ranges of 2.21–2.54 GHz, 3.82–4.84 GHz and 6.16–7.95 GHz. It could be observed that the resonant frequency of the proposed antenna is greatly affected by the angle of the Y-shaped microstrip line. Thus, the band is proved to be controllable. One-band, dual-band and tri-band antenna could be obtained by adjusting the angle of the Y-shaped microstrip line.

The current distribution on the radiating patch for the proposed antenna, which corresponds to the frequency band in Fig. 2, is presented in Fig. 3. It is clear that the current mainly concentrates on the Y-shaped microstrip line and the edge of the equilateral triangle wide slot. Thus, we can believe that the resonant frequency should be mostly influenced by the Y-shaped microstrip line. It accords with the results that the resonant frequency of the proposed antenna is greatly affected by the angle of the Y-shaped microstrip line.

Figure 4 shows the radiation patterns on the  $E$ -plane and  $H$ -plane at the corresponding frequency. However, the omni-directional pattern is not obvious. It is mainly because of the currents focused on the two-arms of the Y-shaped microstrip line disturbing the omni-directional characteristic.

#### 4. CONCLUSIONS

A printed wide-slot antenna with a Y-shaped microstrip-fed line for multiband applications is presented. The equilateral triangle wide-slot reversed along the equilateral triangle ground plane is designed to produce the multiband. By adjusting the angle of the Y-shaped microstrip-fed line, one-band, dual-band and tri-band antenna could be obtained. It could be suitable for multiband wireless applications.

#### ACKNOWLEDGMENT

This work is supported by the National Natural Science Foundation of China (NNSF) under Grant 60990320, 60990323; 61271090, and the National 863 Project of China under Grant 2012AA012305, and Sichuan Provincial Science and technology support Project under Grant 2012GZ0101, and Chengdu Science and technology support Project under Grant 12DXYB347JH-002.

**REFERENCES**

1. Sung, Y., “Bandwidth enhancement of a microstrip line-fed printed wide-slot antenna with a parasitic center patch,” *IEEE Transactions on Antennas and Propagation*, Vol. 60, 1712–1716, Apr. 2012.
2. Jan, J. Y. and J. W. Su, “Bandwidth enhancement of a printed wide-slot antenna with a rotated slot,” *IEEE Transactions on Antennas and Propagation*, Vol. 53, 2111–2114, Jun. 2005.
3. Jan, J. Y. and J. C. Kao, “Novel printed wide-band rhombus-like slot antenna with an offset microstrip-fed line,” *IEEE Antennas and Wireless Propagation Letters*, Vol. 6, 249–251, 2007.
4. Liu, Y. F., et al., “Experimental studies of printed wide-slot antenna for wide-band applications,” *IEEE Antennas and Wireless Propagation Letters*, Vol. 3, 273–275, 2004.
5. Nguyen, N. A., et al., “A T-shaped wide-slot harmonic suppression antenna,” *IEEE Antennas and Wireless Propagation Letters*, Vol. 6, 647–650, 2007.
6. Chen, W. L., et al., “Bandwidth enhancement of a microstrip-line-fed printed wide-slot antenna with a fractal-shaped slot,” *IEEE Transactions on Antennas and Propagation*, Vol. 57, 2176–2179, Jul. 2009.
7. Sze, J. Y. and K. L. Wong, “Bandwidth enhancement of a microstrip-line-fed printed wide-slot antenna,” *IEEE Transactions on Antennas and Propagation*, Vol. 49, 1020–1024, Jul. 2001.
8. Qu, S. W., et al., “Broadband microstrip-line-fed wide slot antenna with improved patterns,” *Electronics Letters*, Vol. 42, 893–894, Aug. 3, 2006.

# Wide Band Frequency Control of Circularly Polarized Patch Antenna with Movable Dielectric

K. Kitatani, M. Wada, and Y. Okamura

Graduate School of Engineering Science, Osaka University  
1-3 Machikaneyama-cho, Toyonaka, Osaka 560-8531, Japan

**Abstract**— This paper presents a circularly polarized microstrip patch antenna for frequency control. The wide band operating frequency of the circular polarization in the proposed antenna can be controlled by using a movable dielectric. Frequency change can be achieved by changing the effective dielectric constant by moving the dielectric plate in the air layer between the ground and the patch. We have been able to achieve a frequency control of 67.7% of the bandwidth from 6.4 GHz to 12.95 GHz, with an axial ratio of less than 3 dB.

## 1. INTRODUCTION

Recently, radio communication systems are being diversified, and their various usages require a reconfigurable antenna operating at different frequencies. The patch antenna discussed in this paper is one of the typical microstrip antennas. The frequency control of the patch antenna was first achieved in 1982 using a semiconductor device [1]. In recent years, the frequency control of the circularly polarized patch antenna has been achieved by using ferrite [2], semiconductor [3], and mechatronics technology [4]. Among these studies, [3] has achieved the frequency control of 13% of the bandwidth, using variable reactance elements. Antennas whose frequency control is achieved using mechatronics (e.g., a motor, a piezo-electric actuator, and MEMS (Micro-Electro-Mechanical-System)) have also been developed [5]. The advantages of these antennas are the low loss, low cost, and low power consumption; on the other hand, they show a response time slower by several milliseconds when compared with antennas incorporated with semiconductor devices. We have previously proposed a circularly polarized patch antenna using a partial dielectric filling whose resonant frequency is controllable using mechatronics technology [6]. We were able to obtain 10% of the control range of the operating frequency in the experiment and of up to 44% in the calculation [7]. Our purpose has been to achieve a continuous change in the resonance frequency of the patch antenna using mechatronics technology.

In this paper, we propose a circularly polarized patch antenna with movable dielectric, whose resonant frequency is controllable over one octave, and describe in detail the operation of the antenna.

## 2. STRUCTURE AND OPERATION OF THE PROPOSED ANTENNA

Figure 1 shows the structure of the proposed antenna. The antenna consists of a square patch, a ground plane, and dielectric substances partially filling the air between the patch and the ground plane. Two dielectric substances are partially inserted on both sides of the patch. Dielectric

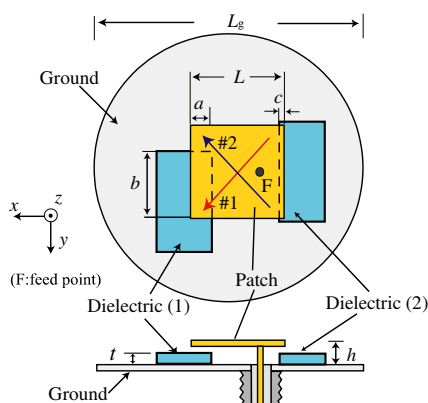


Figure 1: Structure of the proposed antenna.

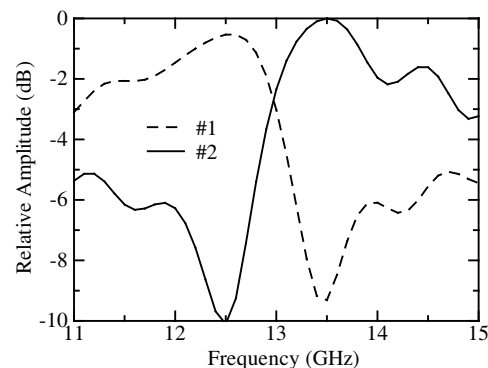


Figure 2: Frequency characteristics of amplitude.

substance (1) is inserted asymmetrically on the patch edge while, the dielectric substance (2) is inserted symmetrically. In the case of  $t < h$ , the dielectric substance inserted into the air layer is mechanically movable. We refer to the amounts of dielectric substance (1) inserted into the patch region on the  $x$ -axis as “ $a$ ”, and on the  $y$ -axis as “ $b$ ”. The insertion of dielectric substance (2) is “ $c$ ” on the  $x$ -axis. The dielectric plate is moved with a linear actuator, controlled with a microcomputer. An SMA connector is placed on the input portion of the antenna. Here, wide frequency operation is possible with high dielectric permittivity. The dielectric material is SV430 ( $Q > 4400$ , dielectric constant = 43 at 10 GHz; made by KYOCERA). The length of the square patch side is  $L = 9$  mm, and the ground side length is  $L_g = 200$  mm; the space between the patch and the ground is  $h = 0.6$  mm, while the thickness of the filling dielectric substance is  $t = 0.58$  mm. The conducting patch is a 0.2 mm thick copper plate and the ground plane is made of aluminium with a thickness of 5 mm. A feed point marked as F is placed 2.3 mm from the center of the patch in the  $x$  direction.

We calculated the parameters of the proposed antenna using the FDTD (Finite Difference Time Domain) method. The patch and the ground were assumed to be complete conductors. A Gaussian pulse was sent through the feeder. The total number of the time steps was 20000. Mur’s second-order absorbing boundary was used as an absorbing boundary. A circularly polarized wave was obtained when the amplitude of the orthogonalized fields is the same, and the phase difference is 90 degrees. Fig. 2, Fig. 3, and Fig. 4 show the antenna operation for the case when the dielectric substance (1) is inserted into one side at the corner. The insertion lengths were  $a = 0$  mm and  $b = 7.6$  mm. Marked as #1 and #2 in Fig. 1 are the current components. Fig. 2 shows the frequency characteristics of amplitude. The induced electricity is higher in the case of the component of #1 mode than in the case of the component of #2 mode. Therefore, we can say that #1 operates with a frequency that is lower than that of #2. The resonant frequency is 12.5 GHz in the #1 mode and 13.5 GHz in the #2 mode. The amplitude of #1 and #2 is the same at 13 GHz. Fig. 3 shows the frequency characteristics of the phase difference. The phase difference was about 90 degrees at a frequency of equal amplitude, and 90.93 degrees at 13 GHz. Fig. 4 illustrates the  $xz$ -plane radiation pattern of the  $E$ -plane and the cross polarization components. The radiation pattern shows a similar pattern to that of the half-wave length dipole antenna, but with an asymmetric pattern. The smallest axial ratio was 0.69 dB for 13 GHz and the return loss was  $-11.84$  dB. The antenna gain was 8.05 dBi. Therefore, we can say that the dielectric substance (1) generates a circularly polarized wave.

We changed the insertion lengths  $a$  and  $b$  to find out the frequency for the minimum axial ratio when the dielectric substance (1) is inserted into one side. The operating frequency of the antenna shifted to the low frequency side when the dielectric material was inserted [6]. This is because the insertion of a dielectric substance makes the dielectric constant increase. When the insertion of the dielectric substance is increased to  $a = 1$  mm or more, the reflection of the antenna is increased. The VSWR (voltage standing wave ratio) was larger than two. The dielectric substance (2) was inserted on the edge of the patch near the feeding point. The impedance matching became possible because the current distribution of the patch became symmetrical. The dielectric substance (2) performs impedance matching [7]. Fig. 5 shows the relationship between the operating frequency and the insertion length when changing the thickness and dielectric constant of the dielectric material.

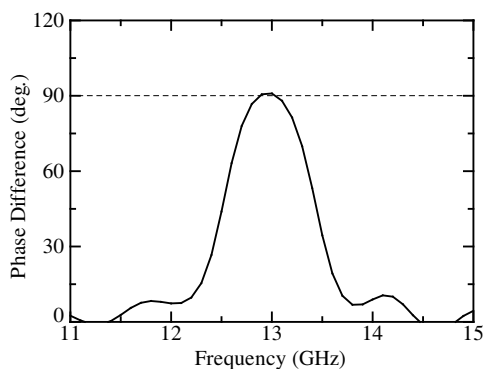


Figure 3: Frequency characteristics of phase difference.

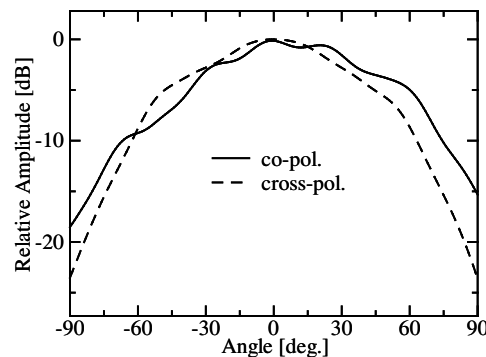


Figure 4: Radiation pattern of  $E$ -plane at 13 GHz.

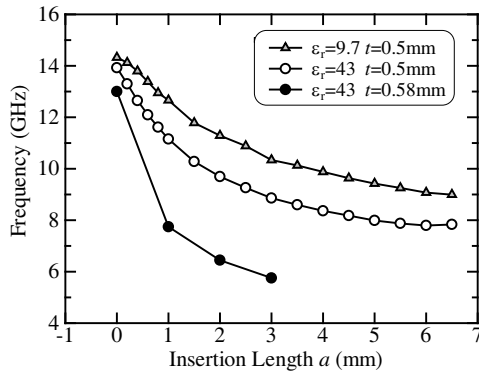


Figure 5: Operation frequency versus insertion length.

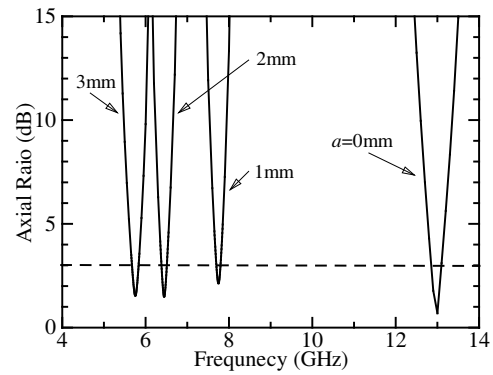


Figure 6: Frequency characteristics of Axial ratio.

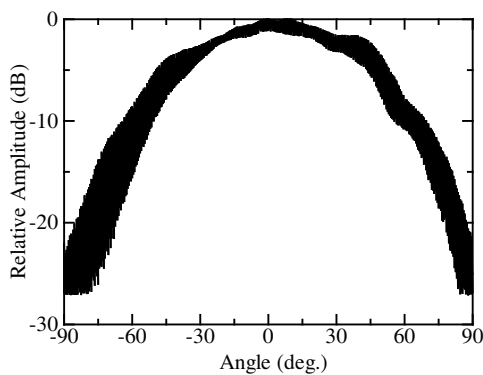


Figure 7: Radiation pattern of  $E$ -plane at 12.95 GHz.

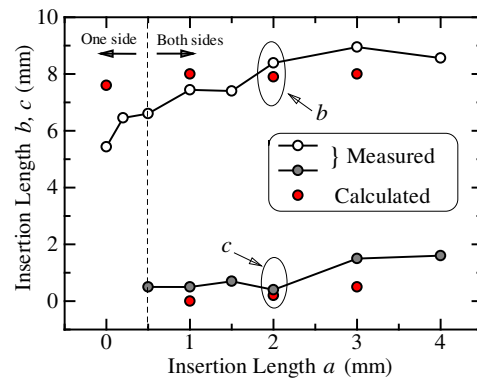


Figure 8: Insertion length for the optimum condition.

When the dielectric constant is high and the thickness of the dielectric substance is increased, the operation frequency is wide. When the dielectric constant is 43 and the thickness is 0.58 mm, the operation frequency changes from 13 GHz to 5.76 GHz. Fig. 6 shows the axial ratio of the frequency characteristics. The axial ratios were 3 dB or less for an insertion length  $a$  of 0 mm to 3 mm. Therefore, it is possible to control the frequency of the antenna over than an octave.

### 3. EXPERIMENT RESULT

We measured the radiation pattern of the fabricated antenna. Fig. 7 shows the spinning linear far-field radiation pattern ( $zx$ -plane) of the proposed antenna at 12.95 GHz. The dielectric substance (1) was inserted into one side at the corner; the insertion length was fixed to  $a = 0$  mm,  $b = 5.436$  mm. The axial ratio of the broadside was good at 1.02 dB. The antenna gain at the broadside was 8.48 dBi and the return loss was  $-14.4$  dB. Next, we investigated the controllability of the frequency. The values of  $a$ ,  $b$  and  $c$  for the optimum operation of circular polarization were calculated by moving the dielectric plate. Fig. 8 shows the insertion lengths of the dielectric plate for the circularly polarized operation. In the case of  $a = 0.5$  mm or more, the both dielectric substances needed to be inserted for impedance matching. Fig. 9 shows the relation between the axial ratio of the antenna measured at the broadside and the insertion length  $a$ . The axial ratios were up to 3 dB for the insertion length  $a$  of 0 mm to 4 mm. The results indicated a tendency similar to that observed through calculations. Fig. 10 shows the frequency response of the return loss when changing the optimum insertion lengths. The white circles in this figure represent the operating frequencies where the axis ratio becomes the smallest. The operating frequency of the antenna shifts to the low frequency side by inserting the dielectric material. The continuous operating frequency changes to about 67.7% of the octave from 6.4 GHz to 12.95 GHz within a VSWR of 2 or less. Thus, bandwidth control of a frequency operating as a circularly polarized patch antenna can be varied by changing the position of the dielectric plate inserted in the air layer. Fig. 11 shows the relation between the insertion length  $a$  and the operating frequency. When increasing the insertion length  $a$  from 0 mm

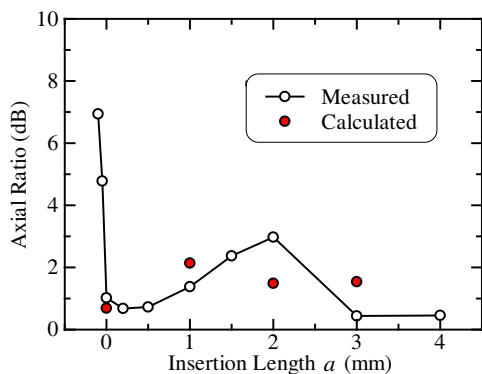


Figure 9: Axial ratio versus insertion length.

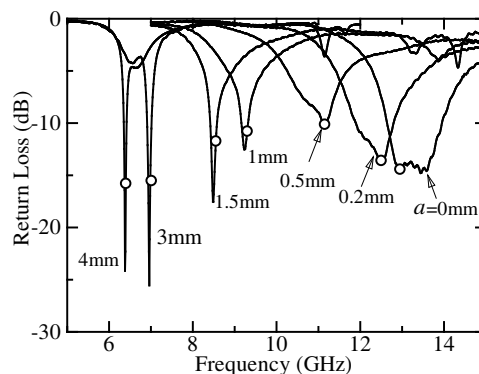


Figure 10: Return loss when changing the optimum insertion lengths.

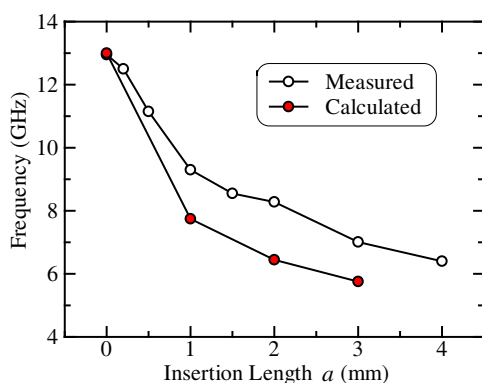


Figure 11: Operation frequency versus insertion length.

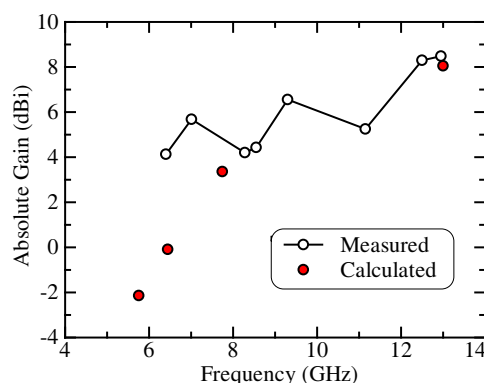


Figure 12: Frequency characteristics of absolute gain.

to 4 mm, the operation frequency changed from 12.95 GHz to 6.4 GHz while the VSWR was 2 or less. Although the measurement results differed from the calculation, the tendency was similar. Fig. 12 shows the frequency characteristics of the antenna gain, which changed from 8.48 dBi to 4.13 dBi.

#### 4. CONCLUSIONS

In this paper, we proposed a circularly polarized wide frequency controllable patch antenna with a movable dielectric plate. The range of frequency variation obtained was 67.7% of one octave or more. This antenna can be used in applications requiring frequency diversity.

#### ACKNOWLEDGMENT

We would like to thank Prof. Hiroshi Murata and Dr. Hidehisa Shiomi for their constant encouragement. Furthermore, we also show our appreciation Mr. Kiyoshi Kawasaki and the technical office of the Graduate School of Engineering Science, Osaka University for their support.

#### REFERENCES

1. Bhartia, P. and I. Bahl, "Frequency agile microstrip antennas," *Microwave Journal*, Vol. 25, No. 10, 67–70, 1982.
2. Hukusako, T., A. Imahase, and N. Mita, "Polarization characteristics of patch antenna using in-plane and weakly biased ferrite substrate," *IEEE Trans. Antennas Propagat.*, Vol. 52, 325–327, 2004.
3. Aoshima, Y., Y. Kimura, and M. Haneishi, "A microstrip antenna with variable reactance elements for polarization control and frequency control of circular polarization," *IEICE Trans. B*, Vol. J93-B, No. 9, 1177–1183, 2010 (in Japanese).

4. Liu, S., M.-J. Lee, C. Jung, G.-P. Li, and F. De Flaviis, “A frequency-reconfigurable circularly polarized patch antenna by integrating MEMS switches,” *IEEE Antenna and Propag. International Symp.*, Vol. 2A, 413–416, 2005.
5. Varadan, V. K., K. J. Vinoy, and K. A. Jose, *RF MEMS and Their Applications*, John Wiley & Sons, New York, 2003.
6. Manno, H., M. Katayama, K. Kitatani, and Y. Okamura, “Circularly polarized frequency controllable microstrip patch antenna using partial dielectric filling,” *2007 International Symposium on Antennas and Propagation*, 1A5-1, Niigata, Japan, Aug. 20–24, 2007.
7. Kitatani, K., M. Wada, and Y. Okamura, “Circularly polarized microstrip patch antenna with wide tunability range,” *2009 International Symposium on Antennas and Propagation*, 755–759, Bangkok, Thailand, Oct. 20–23, 2009.

# Crosstalk Modeling and Analysis of Through-Silicon-Via Connection in 3D Integration

Xiang He, Wensong Wang, and Qunsheng Cao  
Nanjing University of Aeronautics and Astronautics, China

**Abstract**— For the wider bandwidth and the smaller form factor, high-speed I/O channel design in three-dimensional integrated circuit (3D IC) becomes more important. Through-Silicon-Via (TSV) is regarded as a critical component in 3D integration that extends Moore's Law. In TSV based 3D-IC systems, a significant design consideration is the coupling noise between TSVs. This paper focuses on the TSV crosstalk analysis under high speed operations using a 3D electromagnetic field solver and a SPICE simulator. Effects of the TSV radius, insulator thickness, and TSV pitch are investigated in details. In addition, the crosstalk performance of different TSV bus configurations is also evaluated and compared, which is one important consideration in high speed interconnection systems.

## 1. INTRODUCTION

As demands accelerate for increasing density, wider bandwidth, lower power, and increasing demands for on-chip functionality, the conventional two-dimensional (2D) planar integrated circuit (IC) scaling has already hit some limitations. Now, many IC design teams are looking up to the emerging 3D ICs with through-silicon-vias (TSVs). A TSV which provides a vertical interconnection through silicon dies is fast becoming the key enabling technology for achieving 3D integrated systems. With shortened interconnection length from TSV technology, it provides a great reduction of parasitics, improved channel bandwidth, high device integration density, and the potential to combine disparate heterogeneous technologies [1, 2].

With the increasing high integration density of interconnections in 3D ICs, large numbers of TSVs need to be used in the silicon interposer package [3]. Due to fine pitch integration on conductive silicon substrate for smaller form factor in 3D IC, electromagnetic interference that can disturb neighbors becomes highly considerable [4]. Crosstalk in 3D ICs is becoming one of the biggest reliability issues in 3D ICs [3]. In 2D ICs, two adjacent metal wires form a parallel capacitor, and this capacitive coupling is the source of the crosstalk between the two wires. In 3D ICs, however, two adjacent TSVs have a coupling network between them due to the conductance of silicon substrate and thin silicon dioxide insulator which introduces a large capacitance. This TSV-to-TSV coupling could be very problematic in 3D ICs if the TSV channels are not properly designed.

In this paper, we focus on the analysis of crosstalk between TSV connections, which is critical for signal integrity in analog, digital and mixed-signal applications. First, the impacts of TSV physical dimensions on crosstalk between aggressor TSV and victim TSV are investigated. Furthermore, crosstalk performance of different TSV bus configurations is also evaluated and compared. When the signal is transmitted on the aggressor TSV, both the near end crosstalk (NEXT) and far end crosstalk (FEXT) on the victim TSV can be obtained in both frequency domain and time domain using 3D electromagnetic field solver, Ansoft's HFSS and a transient simulator based on SPICE. By comparing the transient coupled waveform, we can directly perceive the coupling effects between TSVs.

## 2. 3D MODEL OF TSV CONNECTION

The via-first approach [5] is used in this TSV fabrication, in which TSVs are fabricated after front-end-of-the-line (FEOL) processing and before back-end-of-the-line (BEOL) processing to enable the interconnection between top trace of the bottom tier and bottom trace of the top tier as shown in the cross section of Fig. 1.

The baseline TSV connection structure in Fig. 1 is used throughout this paper. Cylindrical Cu TSVs (20  $\mu\text{m}$  in diameter and 100  $\mu\text{m}$  in height) are built in a 2-strata configuration. Thin  $\text{SiO}_2$  layers of 0.2  $\mu\text{m}$  serve as the isolation layers between the silicon substrate and TSV conductive material. These TSVs penetrate through the 2  $\mu\text{m}$  interlayer dielectric (ILD), 96  $\mu\text{m}$  thinned silicon substrate, and 2  $\mu\text{m}$  benzocyclobutene (BCB) bonding material from top to bottom. The minimum pitch between TSVs is set to be twice the TSV diameter.

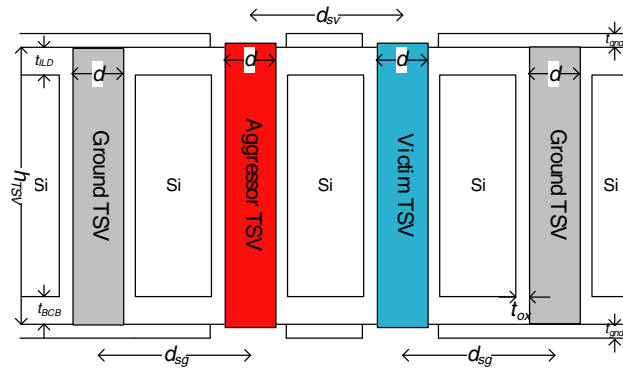


Figure 1: Structure of TSV connection for crosstalk analysis (Configuration 1).

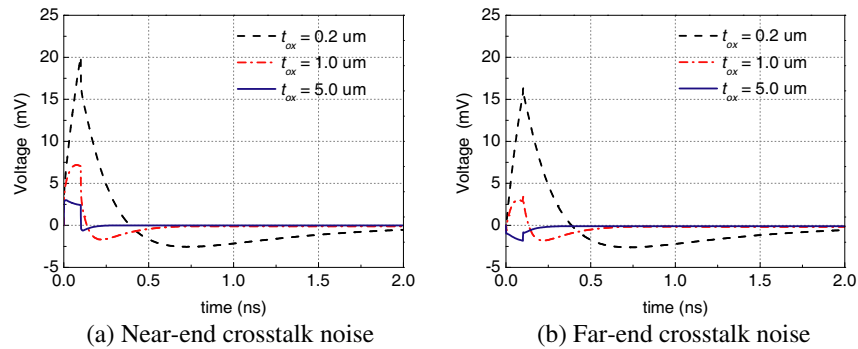


Figure 2: Impacts of insulator thickness on crosstalk.

For the high speed and high performance analysis, 3D electromagnetic field solver (HFSS) is employed. Then, the EM solution is analysed by a SPICE tool to obtain transient waveform of crosstalk noise.

### 3. IMPACTS OF PHYSICAL DIMENSIONS ON CROSSTALK

This section discusses several factors affecting TSV crosstalk, which include TSV radius, insulator thickness, distance between aggressor TSV and victim TSV, distance between signal (either aggressor or victim) TSV and ground TSV. In transient analysis, a pulse of 1 V is injected into the aggressor TSV, with its both ends terminated by  $50\Omega$  to eliminate the reflection. The baseline rise time is set to be 50 picoseconds. The crosstalk noise voltage is measured at the near and far end of the victim TSV, whose two ends are  $50\Omega$  terminated.

#### 3.1. Oxide Insulator Thickness Impact

The copper via, insulating layer and the silicon substrate make up a metal-insulator-silicon (MIS) capacitance which can be analytically calculated by Eq. (1) below,

$$C_{ox} = \frac{2\pi\epsilon_{ox}h_{TSV}}{\ln[(d + 2t_{ox})/d]} \quad (1)$$

where  $\epsilon_{ox}$ ,  $h_{TSV}$ ,  $d$ , and  $t_{ox}$  are the permittivity of the oxide insulator, TSV height and diameter, respectively. Given TSV height and diameter, it is easy to find that thin insulator can introduce a large capacitance which increases the capacitive coupling between aggressor TSV and victim TSV.

Keeping the baseline configurations, we vary the TSV oxide insulator thickness  $t_{ox}$  as 0.2, 1.0, and  $5.0\mu\text{m}$ . The impacts of the oxide insulator thickness on the near-end crosstalk and far-end crosstalk between TSVs are studied, the transient simulation results are shown in Fig. 2. It is noted that the noise voltage of both ends can be reduced by using a thicker sidewall liner.

#### 3.2. TSV Radius Impact

TSV radius is an important parameter in this cylindrical via for the designer or manufacturer when considering the TSVs' density. The copper via, the insulating layer and the silicon substrate make up a metal-insulator-silicon (MIS) capacitance. Given TSV height ( $h_{TSV}$ ) and insulating

layer thickness ( $t_{ox}$ ), the via sidewall area ( $2\pi \times \text{radius} \times h_{\text{TSV}}$ ) increases as the radius increasing, leading to an increasing mutual capacitance and couple noise. We vary the TSV radius as 2  $\mu\text{m}$ , 5  $\mu\text{m}$ , and 10  $\mu\text{m}$ . The crosstalk of TSV is summarized in Fig. 3, which indicated large radius lead to bigger crosstalk.

### 3.3. TSV Pitch Impact

Until now, we have only discussed structures in which the distances between the TSVs are uniform. In other words, the ground TSV is the same distance from the signal TSV as distance from the victim TSV. Reducing the signal-ground distance ( $d_{sg}$ ) and increasing the signal-victim distance ( $d_{sv}$ ) will both have the effect of reducing the mutual inductance as expressed by Eq. (2) and Eq. (3) [6]. Additionally, although less obvious from Eq. (4), they will have the effect of lowering the capacitance. As we know, low capacitive coupling and low inductive coupling lead to low crosstalk.

$$L_S = L_V = \frac{\mu_0}{2\pi} \ln \frac{4d_{sg}^2}{d^2} \tag{2}$$

$$L_m = \frac{\mu_0}{\pi} \ln \frac{d_{sg}^2}{d_{sv}d} \tag{3}$$

$$C_m = \frac{L_m}{v^2 (L_S L_V - L_m^2)} \tag{4}$$

where  $v$  is the velocity of light.

#### 3.3.1. Signal-victim Distance

To more exactly evaluate the impact of  $d_{sv}$ , we keep  $d_{sg}$  equal to 40  $\mu\text{m}$  and vary  $d_{sv}$  from 40, 60 to 80  $\mu\text{m}$  in HFSS and SPICE based tool. The TSV crosstalk performance results are summarized in Fig. 4. As predicted, increasing the signal-victim distance will greatly decrease crosstalk coupling.

#### 3.3.2. Signal-ground Distance Impact

Here, we keep  $d_{sv}$  equal to 40  $\mu\text{m}$  and scan  $d_{sg}$  from 40, 60 to 80  $\mu\text{m}$ . Since transient noise has only a very little different, only frequency domain crosstalk shown here. As the frequency domain

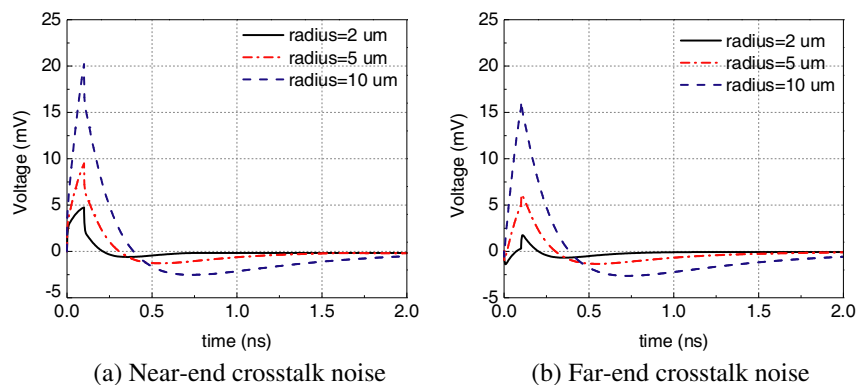


Figure 3: Impacts of aggressor-victim distance on crosstalk.

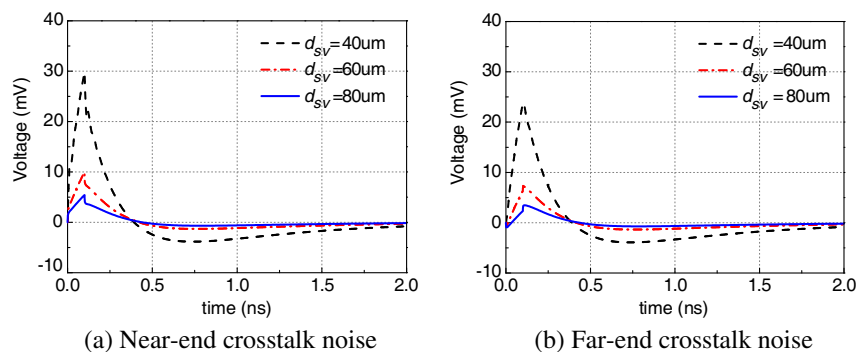


Figure 4: Impacts of aggressor-victim distance on crosstalk.

crossstalk curve shown in Fig. 5, although the effect is less than the effect caused by signal-victim distance, the signal-ground distance of TSV still has a little effect on the crosstalk of the given TSV connection model, suggesting that the signal return TSV should be placed as closely as possible to the corresponding signal TSV.

#### 4. TSV CROSSTALK WITH DIFFERENT CONFIGURATIONS

In high speed circuits and systems, a large number of closely spaced I/O TSVs exist with kinds of mixture of signal and ground TSVs. We have begun with a configuration of two TSV pairs arranged in a straight line with ground TSVs on the left and right side (Fig. 1), named configuration 1. However, there are several other different TSV configurations as shown in Fig. 6.

As shown in Fig. 7, the electric field distribution of these four configurations almost have no difference, which indicate that the mutual capacitances among the four configurations are almost the same; while from the view of magnetic field distribution shown in Fig. 8, we can obviously observe that the magnetic field coupled from aggressor TSV to victim TSV in configuration 1 is the worst case, and configuration 3 is the best one, meanwhile configuration 4 and 5 can reduce the coupling magnetic field but at the sacrifice of area efficiency. Since coupled magnetic field distribution has a strong relationship with mutual inductance, we can easily conclude that it be the small mutual inductance in configuration 3 that reduces the crosstalk from aggressor TSV to victim TSV. To validate this conclusion, transient simulator based on SPICE is used to investigate the crosstalk of these four configurations. As the crosstalk noise presented in Fig. 9, configuration 3 has the lowest crosstalk voltage, which is 5 mV, reduced 75% from configuration 1. Thus, configuration 3 is more favoured in the design of TSV interconnection bus in 3D integration system.

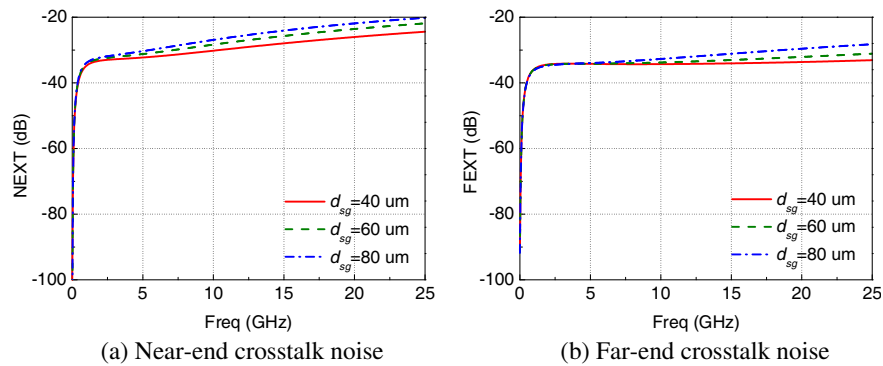


Figure 5: Impacts of signal-ground distance on crosstalk.

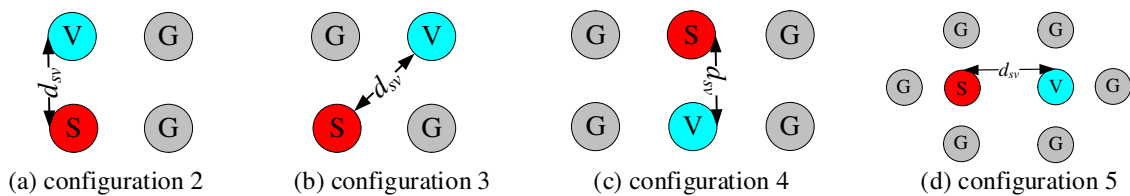


Figure 6: Four different TSV configurations.

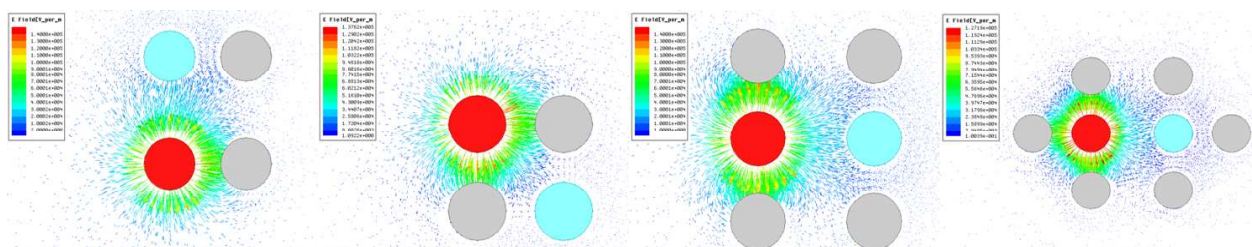


Figure 7: *E*-field distribution of the four different configurations.

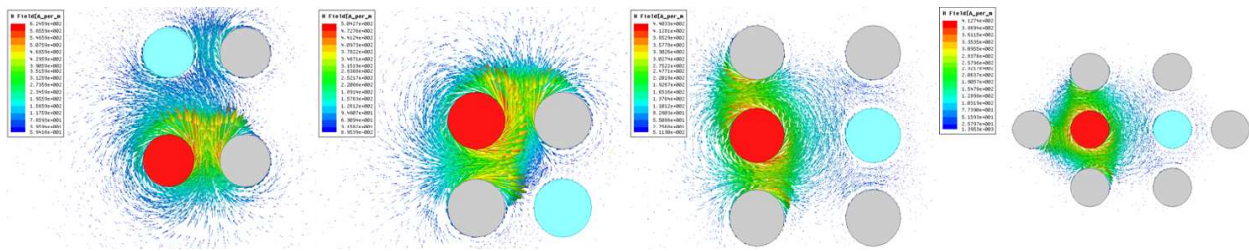
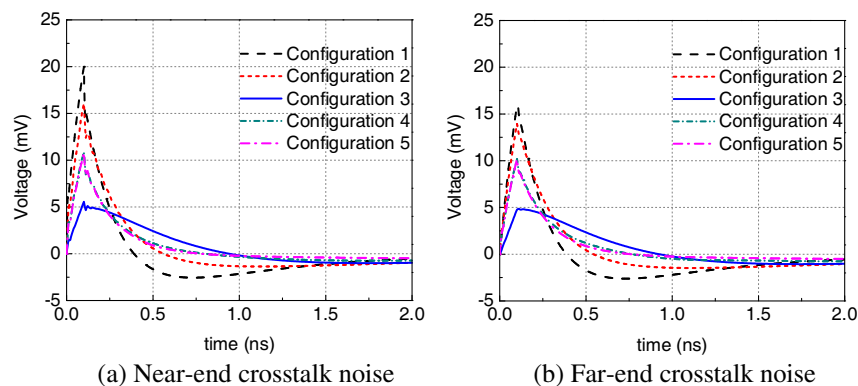
Figure 8:  $H$ -field distribution of the four different configurations.

Figure 9: Crosstalk noise of the four different configurations.

## 5. CONCLUSIONS

This work investigated TSV crosstalk noise under high speed operations using a 3D electromagnetic field solver and a SPICE simulator. Impacts of radius, oxide insulator thickness, and TSV pitch are studied. To decrease the crosstalk, the large TSV diameter should be avoided if there are no problem concerning with the cost and fabrication. Thickening the oxide insulator is favoured unless they exceed the density requirement or fabrication craft in some specific circuit parts. Enlarging the distance between aggressor and victim TSV and decreasing the distance between signal and ground TSV can always reduce the crosstalk noise. In terms of TSV connection bus, appropriately arranging ground between signals should always bear in mind. From these preliminary results, crosstalk in a TSV interconnecting network could be improved, leading to enhanced performance of 3D circuits and systems.

## ACKNOWLEDGMENT

This work is supported by the K201304 Open Research Program from State Key Laboratory of Millimeter Waves, Southeast University.

## REFERENCES

- Knickerbocker, J. U., P. S. Andry, B. Dang, and R. R. Horton, "Three dimensional silicon integration," *IBM Journal of Research and Development*, 2008.
- Takahashi, K. and M. Sekiguchi, "Through silicon via and 3-D wafer/chip stacking technology," *Digest of Technical Papers*, 2006.
- Xie, B., M. Swaminathan, K. J. Han, and J. Xie, "Coupling analysis of through-silicon via (TSV) arrays in silicon interposers for 3D systems," *IEEE International Symposium on Electromagnetic Compatibility*, 16–21, 2011.
- Yoon, K., G. Kim, W. Lee, T. Song, and J. Kim, "Modeling and analysis of near-end crosstalk between TSVs, metal interconnects and RDLs in TSV-based 3D IC and silicon interposer," *Electronic Packaging Technology Conference*, 2009.
- Van Olmen, J., A. Mercha, G. Katti, et al., "3D stacked IC demonstration using a through silicon via first approach," *IEDM Tech. Dig.*, 603–606, 2008.
- Paul, C. R., *Introduction to Electromagnetic Compatibility*, Wiley Interscience, Hoboken New Jersey, 2006.

# Effect of Electromagnetic Interference (EMI) on the DC Shift of NMOSFET Current-mirror

Muhammad Taher Abuelma'atti<sup>1</sup> and Ali M. T. Abuelmaatti<sup>2</sup>

<sup>1</sup>King Fahd University of Petroleum and Minerals, Box 203, Dhahran 31261, Saudi Arabia

<sup>2</sup>18 Lynas Place, Evenwood, Bishop Auckland, County Durham, DL14 9RF, UK

**Abstract**— In this paper, a new approximation is presented for the nonlinear relationship between the input-current and the output-current of an NMOSFET current-mirror. Using this approximation closed-form expressions are obtained for the DC component of the output current resulting from exciting the NMOSFET current-mirror by a DC biasing current plus a superimposed sinusoidal electromagnetic interference. Comparison between calculated and simulated results is included.

## 1. INTRODUCTION

At present, there is a growing interest in designing current-mode circuits; where the input is a current and the output is a current. This is attributed to their simple structures, wider bandwidth and larger dynamic range compared to the voltage-mode circuits; where the input is a voltage and the output is a voltage. Current-mirrors using NMOSFET transistors play a crucial part in the design of current-mode circuits.

The NMOSFET current-mirror is inherently nonlinear. This nonlinearity manifests itself in generating unwanted DC component; which may alter the correct biasing and may therefore prohibit the circuit from functioning correctly. This effect has been extensively studied for MOSFET and bipolar transistors and operational amplifiers [1–6]. However, only very little has been written about these effects in NMOSFET current-mirrors assuming that the amplitude of the electromagnetic interference (EMI) signal is relatively small [7]. This assumption paves the way for using a Taylor series expansion for approximating the nonlinearity of the NMOSFET current-mirror, thus, restricting the validity of the results to relatively small EMI signals only. While attempts to analyze the nonlinear performance of current mirrors due to device mismatch [8–11] and the channel length modulation [12] have been reported, no attempt has been reported for studying the DC shift of the NMOSFET current-mirror under relatively large EMI signal. The major intention of this paper is, therefore, to present such a study.

## 2. ANALYSIS

Figure 1 shows an NMOSFET current-mirror. Assuming that the transistors are matched and working in the saturation region, with  $v_{DS} > v_{GS} - V_{th}$ , the drain current can be expressed as

$$i_D = k(v_{GS} - V_{th})^2(1 + \lambda v_{DS}) \quad (1)$$

In Equation (1),  $i_D$  is the drain current,  $v_{GS}$  is the gate-to-source voltage,  $v_{DS}$  is the drain-to-source voltage,  $V_{th}$  is the threshold voltage,  $\lambda$  is the channel-length modulation parameter,

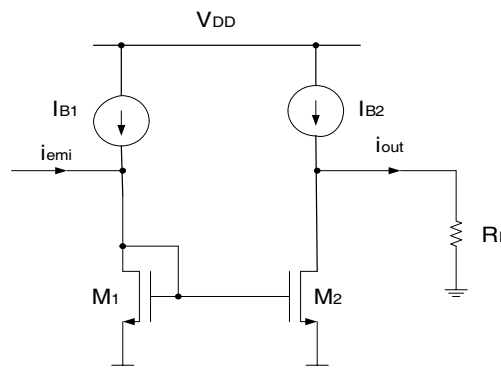


Figure 1: NMOSFET current-mirror.

$k = (W/L)(\mu C_{ox}/2)$  is the transconductance parameter,  $\mu$  is the surface mobility of the channel,  $C_{ox}$  is the gate oxide capacitance density,  $W$  is the effective channel width, and  $L$  is the effective channel length. Assuming that the input current is formed of a DC bias current,  $I_{B1}$ , plus a superimposed EMI multisinusoidal signal,  $i_{emi}$ , of the form

$$i_{IN} = I_{B1} + i_{emi} \quad (2)$$

$$i_{emi} = \sum_{m=1}^M I_m \sin \omega_m t \quad (3)$$

then using Equations (1) and (2), the relationship between the input and output currents can be expressed as

$$\frac{i_{emi} + I_{B1}}{-i_{out} + I_{B2}} = \frac{k_1(v_{GS1} - V_{th1})^2(1 + \lambda_1 v_{DS1})}{k_2(v_{GS2} - V_{th2})^2(1 + \lambda_2 v_{DS2})} \quad (4)$$

In Equation (4),  $I_{B1}$  and  $I_{B2}$  are the DC bias currents of transistors  $M_1$  and  $M_2$  respectively and  $i_{out}$  is the output current. With  $v_{DS2} = i_{out} R_L$  it is obvious that Equation (4) is inherently nonlinear. Thus, with a multisinusoidal EMI, expressed by Equation (3), the current  $i_{out}$  will consist of a DC component plus a large number of fundamental, harmonics and intermodulation components. However, in its present form, it is hard to explore the nonlinearity of Equation (4) and to obtain expressions for the components of the output current  $i_{out}$ . Recourse to some simplifications may, therefore, be inevitable to obtain a first hand appreciation of the effect of EMI on the DC shift of NMOSFET current-mirror. Thus, if the two transistors,  $M_1$  and  $M_2$ , are assumed identical with  $\lambda_1 = \lambda_2 = \lambda$ ,  $k_1 = k_2$  and  $V_{th1} = V_{th2} = V_{th}$ , then Equation (4) reduces to

$$\frac{i_{emi} + I_{B1}}{-i_{out} + I_{B2}} = \frac{(1 + \lambda v_{DS1})}{(1 + \lambda i_{out} R_L)} \quad (5)$$

Using Equation (1), and ignoring the effect of the channel length modulation, the gate-to-source voltage  $v_{GS1}$  can be approximated by

$$v_{GS1} = V_{th} + \sqrt{\frac{i_{emi} + I_{B1}}{k}} \quad (6)$$

Combining Equations (5) and (6), then

$$\frac{i_{emi} + I_{B1}}{-i_{out} + I_{B2}} = \frac{1 + \lambda \left( V_{th} + \sqrt{\frac{i_{emi} + I_{B1}}{k}} \right)}{1 + \lambda i_{out} R_L} \quad (7)$$

Equation (7) represents the nonlinear relationship between the EMI input current,  $i_{emi}$ , and the output current,  $i_{out}$ , of the NMOSFET current-mirror of Fig. 1 assuming identical transistors. However, in its present form Equation (7) cannot yield an expression for the DC shift of the output current resulting from a multisinusoidal EMI. Therefore, recourse to Taylor series approximation, assuming relatively small values of the EMI input current,  $i_{emi}$ , is inevitable [7]. However, by virtue of its derivation the expression obtained for the DC shift is valid only for small values of the amplitudes of the EMI sinusoids. In order to obtain expressions that are valid over a wider range of the amplitudes of the EMI sinusoids, here we perform simple mathematical manipulations to rewrite Equation (7) in the form

$$x + \alpha xy + \alpha y + y/\delta + \beta y/\delta + \gamma\sqrt{x+1}y/\delta = \beta/\delta + \gamma\sqrt{x+1}/\delta + (1-\delta)/\delta \quad (8)$$

In Equation (8),  $x = i_{emi}/I_{B1}$ ,  $y = i_{out}/I_{B2}$ ,  $\delta = I_{B1}/I_{B2}$ ,  $\alpha = \lambda R_L I_{B2}$ ,  $\beta = \lambda V_{th}$  and  $\gamma = \lambda\sqrt{I_{B1}/k}$ . For a typical current mirror using 0.18  $\mu\text{m}$  CMOS technology with  $V_{th} = 0.42\text{V}$ ,  $k = 4.98\ \mu\text{A}/\text{V}^2$ ,  $\lambda = 0.005\text{--}0.03$ ,  $I_{B1} = I_{B2} = 1.0\text{mA}$  and  $R_L = 1\text{k}\Omega$ , then  $\alpha = 0.005\text{--}0.03$ ,  $\beta = 0.0021\text{--}0.0126$  and  $\gamma = 0.0707\text{--}0.424$ . With these values of  $\alpha$ ,  $\beta$  and  $\gamma$ , Equation (8) can be approximated as

$$y = -\frac{x - \beta - \gamma\sqrt{x+1} - (1-\delta)/\delta}{1 + \gamma\sqrt{x+1}} \quad (9)$$

Table 1: Values of the parameters  $a_0$ ,  $a_n = 0$ ,  $n = 2, 4, 6, \dots$ ,  $b_n = 0$ ,  $n = 1, 3, 5, \dots$  for approximating the normalized characteristic of Equation (9) using Equation (10)  $D = 4.0$ ,  $a_n = 0$ ,  $n = 1, 3, 5, \dots$ ,  $b_n = 0$ ,  $n = 2, 4, 6, \dots$

$\lambda = 0.005/V$ , $V_{th} = 0.42 \text{ V}$ , $R_L = 1 \text{ k}\Omega$ , $k = 4.98 \times 10^{-6} \text{ A/V}^2$ $\beta = 0.0021$ , $\gamma = 0.0707$ , $\delta = 1$				$\lambda = 0.03/V$ , $V_{th} = 0.42 \text{ V}$ , $R_L = 1 \text{ k}\Omega$ , $k = 4.98 \times 10^{-6} \text{ A/V}^2$ $\beta = 0.0126$ , $\gamma = 0.424$ , $\delta = 1$			
$a_0$	-0.0078	$b_1$	-0.7345	$a_0$	-0.0235	$b_1$	-0.4965
$a_2$	0.00971	$b_3$	0.08273	$a_2$	0.02956	$b_3$	0.06036
$a_4$	-0.0027	$b_5$	-0.0299	$a_4$	-0.0088	$b_5$	-0.0224
$a_6$	0.00125	$b_7$	0.01529	$a_6$	0.00423	$b_7$	0.01160
$a_8$	-0.0007	$b_9$	-0.0093	$a_8$	-0.0025	$b_9$	-0.0071
$a_{10}$	0.00047	$b_{11}$	0.00620	$a_{10}$	0.00164	$b_{11}$	0.00479
$a_{12}$	-0.0003	$b_{13}$	-0.0044	$a_{12}$	-0.0012	$b_{13}$	-0.0034
$a_{14}$	0.00025	$b_{15}$	0.00334	$a_{14}$	0.00087	$b_{15}$	0.00260
$a_{16}$	-0.0002	$b_{17}$	-0.0026	$a_{16}$	-0.0007	$b_{17}$	-0.0020
$a_{18}$	0.00015	$b_{19}$	0.00208	$a_{18}$	0.00055	$b_{19}$	0.00164
$a_{20}$	-0.0001	$b_{21}$	-0.0017	$a_{20}$	-0.0004	$b_{21}$	-0.0013
$a_{22}$	0.00010	$b_{23}$	0.00142	$a_{22}$	0.00038	$b_{23}$	0.00112
$y_{offset}$		-0.06799		$y_{offset}$		-0.3066	
RRMS error		0.0011%		RRMS error		0.0013%	

Here we propose to approximate Equation (9) using a Fourier-series expansion of the form

$$y = a_0 + \sum_{n=1}^N \left[ a_n \cos\left(\frac{2n\pi}{D}x\right) + b_n \sin\left(\frac{2n\pi}{D}x\right) \right] \quad (10)$$

In Equation (10),  $D$ ,  $a_0$ ,  $a_n$ ,  $b_n$ ,  $n = 1, 2, \dots, N$  are fitting parameters that can be obtained using the procedure described in [13]. This procedure is simple and does not require extensive computing facilities or well-developed software. For convenience, a brief description of this procedure is given here. First, the function of Equation (9) is calculated for certain values of the parameters  $\beta$ ,  $\gamma$  and  $\delta$  for  $-1 \leq x \leq 1$ , then the offset,  $y_{offset}$ , at  $x = 0$  is removed, and the resulting function is mirror-imaged to produce a periodic function with a complete period  $= D$ . Second, the resulting function is approximated by a number of straight-line segments joined end to end. Using the slopes of these segments, it is easy to obtain the parameters  $a_0$ ,  $a_n$ ,  $b_n$ ,  $n = 1, 2, \dots, N$  using simple algebraic calculations. The results obtained are shown in Table 1 for different values of the parameters  $\beta$ ,  $\gamma$  and  $\delta$ . Using Equation (10) and the parameters in Table 1, the function of Equation (10) was calculated and compared with Equation (9). The results show that very small values of the relative root-mean-square errors (RRMSEs) = 0.0011% and 0.0013% can be achieved. This confirms the validity of Equation (10) for approximating Equation (9).

### 3. DC SHIFT

Equation (10) can be used for predicting the DC component of the output current resulting from a multisinusoidal EMI current. Thus, combining Equations (3) and (10), the normalized output current can be expressed as

$$y = a_0 + \sum_{n=1}^N \left[ a_n \cos\left(\frac{2n\pi}{D} \sum_{m=1}^M \frac{I_m}{I_{B1}} \sin \omega_m t\right) + b_n \sin\left(\frac{2n\pi}{D} \sum_{m=1}^M \frac{I_m}{I_{B1}} \sin \omega_m t\right) \right] \quad (11)$$

Using the trigonometric identities of  $\sin(\phi + \theta)$ ,  $\cos(\phi + \theta)$ ,  $\sin(\rho \sin \theta)$  and  $\cos(\rho \sin \theta)$ , and after simple mathematical manipulations, it is easy to show that the magnitude of the normalized DC

component can be expressed as

$$Y_{DC} = y_{offset} + a_0 + \sum_{n=1}^N a_n \prod_{m=1}^M J_0 \left( \frac{2n\pi}{D} \frac{I_m}{I_{B1}} \right) \quad (12)$$

In Equation (12),  $J_l(\rho)$  is the Bessel function of order  $l$ . Assuming that the EMI current is formed of two equal-amplitude sinusoids, Equation (3) reduces to

$$i_{emi} = I(\sin \omega_1 t + \sin \omega_2 t) \quad (13)$$

and Equation (12) yields the following expression for the magnitude of the normalized DC, component of the output current.

$$Y_{DC} = y_{offset} + a_0 + \sum_{n=1}^N a_n J_0 \left( \frac{2n\pi}{D} X \right)^2 \quad (14)$$

In Equation (14),  $X = I/I_{B1}$  is the normalized amplitude of the EMI sinusoid. For sufficiently small values of the amplitudes of the EMI currents, so that  $2n\pi X/D \ll 1$ , the Bessel functions can be approximated by  $J_l(\rho) \cong (\rho/2)^l/l!$  and Equation (14) reduce to

$$Y_{DC} = y_{offset} + a_0 + \sum_{n=1}^N a_n \quad (15)$$

Inspection of Equation (15) shows that for sufficiently small normalized EMI sinusoid amplitudes, the normalized output DC current component will be constant and independent of the normalized input amplitude.

Using Equation (14) the normalized DC output current component of the NMOSFET current-mirror of Fig. 1 were calculated for a two-tone equal-amplitude EMI signal for different values of the normalized input amplitude  $X$  and the results are shown in Fig. 2. Inspection of Fig. 2 clearly shows that the normalized DC component of the output current is strongly dependent on the channel length modulation parameter  $\lambda$ . For example, with  $\lambda = 0.0051/V$  the normalized DC component equals 0.068 and with  $\lambda = 0.03/V$  the normalized DC component equals 0.307 for normalized input current amplitude = 0.05. Moreover, Fig. 2 shows that for  $\lambda = 0.03/V$  the normalized DC component changes with the normalized input amplitude,  $X$ , while for  $\lambda = 0.0051/V$  the normalized DC component is almost constant with relatively slight dependence on the normalized input amplitude. Therefore, it appears that the value of  $\lambda$  will affect the magnitude of the DC output current component as well as its dependence on the normalized input current amplitude.

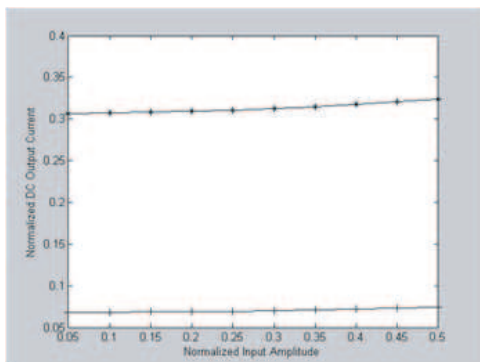


Figure 2: Calculated values of the normalized DC using Equation (14). +:  $\lambda = 0.0051/V$ ,  $V_{th} = 0.42$  V,  $k = 4.98 \times 10^{-6}$  A/V<sup>2</sup>,  $R_L = 1$  k $\Omega$ ,  $\beta = 0.0021$ ,  $\gamma = 0.0707$ ,  $\delta = 1$ ; \*:  $\lambda = 0.0300/V$ ,  $V_{th} = 0.42$  V,  $k = 4.98 \times 10^{-6}$  A/V<sup>2</sup>,  $R_L = 1$  k $\Omega$ ,  $\beta = 0.0126$ ,  $\gamma = 0.4240$ ,  $\delta = 1$ .

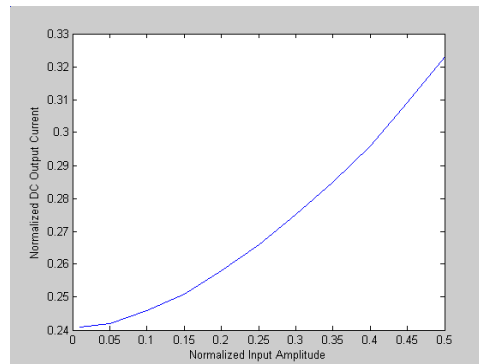


Figure 3: Simulated values of the normalized DC.  $\lambda = 0.03/V$ ,  $V_{th} = 0.42$  V,  $k = 4.98 \times 10^{-6}$  A/V<sup>2</sup>,  $R_L = 1$  k $\Omega$ ,  $\beta = 0.0126$ ,  $\gamma = 0.424$ ,  $I_{B1} = I_{B2} = 1$  mA.

In order to validate the procedure described in this paper, the circuit of Fig. 1 was simulated using 0.18  $\mu\text{m}$  RFCMOS process technology using the harmonic balance simulator controller in the advanced design system (ADS) design automation software. As an illustrative example, the simulated results obtained for a two-tone equal-amplitude EMI signal with DC supply voltage = 1.8 V,  $W = 5\mu\text{m}$ ,  $L = 0.18\mu\text{m}$ ,  $Nf = 5$ ,  $I_{B1} = I_{B2} = 1.0\text{ mA}$  and  $I_m = 0.01 - 0.5\text{ mA}$  with the two EMI frequencies around 10 MHz, are shown in Fig. 3. Comparison of the results reported in Fig. 2 and Fig. 3 show that in all cases the calculated and simulated results are in reasonably good agreement. For example, inspections of Fig. 2 and Fig. 3 show that when the normalized input tone amplitude = 0.3, the calculated normalized output DC current component is 0.305 while the simulated value is 0.276.

#### 4. CONCLUSION

In this paper, a new Fourier-series approximation has been presented for the nonlinear relationship between the normalized input current and the normalized output current of the NMOSFET current mirror. Contrary to previously published approximations, this Fourier-series approximation is valid over a wide range of EMI amplitudes and can be used for evaluating the nonlinear performance of the NMOSFET current mirror under large EMI amplitudes. The parameters of this Fourier-series approximation are dependent on the bias currents of the current mirror, the channel length modulation parameter, the threshold voltage and the transconductance parameter.

Using this approximation a closed-form expression, in terms of the ordinary Bessel functions, has been obtained for the normalized DC component resulting from exciting the NMOSFET current mirror by a DC biasing current plus a superimposed multisinusoidal EMI. This expressions are valid over a wide range of the EMI amplitudes and can provide a better insight into the performance of the NMOSFET current mirror under the effect of EMI. The results obtained show that the DC shift tend to be monotonically increasing with the normalized amplitude of the EMI. Comparison between calculated and simulated results shows a reasonably good agreement both in the trends and the magnitudes. Thus, once the physical and the process parameters of the used technology are available it is easy, using the procedure described in this paper, to predict the performance of the NMOSFET current mirror under the effect of EMI.

#### ACKNOWLEDGMENT

The authors acknowledge with thanks the support of King Fand University of Petroleum and Minerals.

#### REFERENCES

1. Abuelma'atti, M. T. and A. M. T. Abuelmaatti, "Effect of electromagnetic interference (EMI) on the DC shift, harmonic and intermodulation performance of diode-connected NMOSFET," *Analog Integrated Circuits and Signal Processing*, Vol. 67, 109–116, 2011.
2. Richardson, R. E., "Quiescent operating point shift in bipolar transistors with AC excitation," *IEEE Journal of Solid-state Circuits*, Vol. 14, 1087–1094, 1979.
3. Forcier, M. L. and R. E. Rishardson, "Microwave-rectification RFI response in field effect transistors," *IEEE Transactions on Electromagnetic Compatibility*, Vol. 21, 312–315, 1979.
4. Poulton, A. S., "Effect of conducted EMI on the DC performance of operational amplifiers," *Electronics Letters*, Vol. 30, 282–284, 1994.
5. Abuelma'atti, M. T., "Analysis of the effect of radio frequency interference on the DC performance of bipolar operational amplifiers," *IEEE Transactions on Electromagnetic Compatibility*, Vol. 45, 453–458, 2003.
6. Abuelma'atti, M. T., "Analysis of the effect of radio frequency interference on the DC performance of CMOS operational amplifiers," *Analog Integrated Circuits and Signal Processing*, Vol. 45, 123–130, 2005.
7. Redoute, J.-M. and M. Steyaert, *EMC of Analog Integrated Circuits*, Springer Sciences + Business Media, 2010.
8. Bruun, E., "Analytical expressions for harmonic distortion at low frequencies due to device mismatch in CMOS current mirrors," *IEEE Transactions on Circuits and Systems-II: Analog and Digital Signal Processing*, Vol. 46, 937–941, 1999.
9. Bruun, E., "Worst case estimate of mismatch induced distortion in complementary CMOS current mirrors," *Electronics Letters*, Vol. 34, 1625–1627, 1998.

10. Bruun, E., “Harmonic distortion in CMOS current mirrors,” *Proceedings of the IEEE International Symposium on Circuits and Systems*, 567–570, 1998.
11. Abuelma’atti, M. T., “Improved analysis for the nonlinear performance of CMOS current mirrors with device mismatch,” *Frequenz*, Vol. 56, 164–169, 2002.
12. Palmisano, G., G. Plaumbo, and S. Pennisi, “High linearity CMOS current output stage,” *Electronics Letters*, Vol. 31, 789–790, 1995.
13. Abuelma’atti, M. T., “Simple method for calculating Fourier coefficients of experimentally obtained waveforms,” *Proceedings IEE — Science Measurement, Technology*, Vol. 141, 177–178, 1994.

# Effect of Electromagnetic Interference (EMI) on the DC Shift of NMOSFET Current Mirror with Capacitor Between Mirror Node and Ground

Muhammad Taher Abuelma'atti<sup>1</sup> and Ali M. T. Abuelmaatti<sup>2</sup>

<sup>1</sup>King Fahd University of Petroleum and Minerals, Box 203, Dhahran 31261, Saudi Arabia

<sup>2</sup>18 Lynas Place, Evenwood, Bishop Auckland, County Durham, DL14 9RF, UK

**Abstract**— In this paper, a new procedure is presented for predicting the effect of electromagnetic interference (EMI) on the DC shift of an NMOSFET current mirror with a capacitor connected between the mirror node and the ground. Closed-form expressions are obtained for the DC output current component resulting from exciting the mirror by a DC biasing current plus a superimposed multisinusoidal EMI. Simulation results are included.

## 1. INTRODUCTION

At present current mirrors are widely used in the design of analog integrated circuits. A classical NMOS-based current mirror comprises two identical NMOS transistors configured to produce an output DC current which is determined by an input DC current. If an electromagnetic interference (EMI) is coupled to the input DC current then, because of the nonlinearities of the NMOS transistors, the output DC current component will change. Obviously this will affect the subsequent stages which are biased by this current mirror.

In an attempt to reduce the effect of the EMI, a capacitor is usually connected between the gates of the NMOS transistors (mirror node) and the ground as shown in Fig. 1. This capacitor will introduce a low frequency pole at a  $g_{m1}/C$  where  $g_{m1}$  is the transconductance of the transistor  $M_1$ . At signal frequencies lower than the mirror pole frequency, the output current can be expressed as [1]

$$I_{out} = I_{in} - C \frac{dV_{gs}}{dt} \quad (1)$$

Assuming that all the input current flows through transistor  $M_1$ , and the transistors are working in the saturation region with

$$I_{in} = k(V_{gs} - V_{th})^2 \quad (2)$$

where  $k = \frac{W}{L} \frac{\mu C_{ox}}{2}$  is the transconductance parameter,  $\mu C_{ox} = 355 \mu\text{A}/\text{V}^2$  for the  $0.18 \mu\text{m}$  CMOS technology and  $V_{th}$  is the threshold voltage of the transistors, Equation (1) yields [3, 6]

$$I_{out} = I_{in} - \frac{C}{\sqrt{k}} \frac{d}{dt} \left( \sqrt{I_{in}} \right) \quad (3)$$

By virtue of its derivation, Equation (3) is valid only on the assumption that all the input current flows through transistor  $M_1$  which implies that the frequency components of the input current are much lower than the pole frequency introduced by the capacitor  $C$ . Moreover, assuming that the EMI is formed of a small single sinusoid, a Taylor series expansion is used to obtain expressions for the DC component of the output current [3, 5, 6]. By virtue of their derivations, these expressions are valid only for relatively small amplitudes of the EMI. Thus, it appears that no attempt has been reported in the open literature for investigating the performance of the current-mirror circuit of Fig. 1 under large EMI amplitudes and with no restrictions set on the value of the pole frequency introduced by the capacitor  $C$  and/or the input frequencies. The major intention of this paper is, therefore, to investigate the performance of the current mirror of Fig. 1 under large amplitudes of the EMI and without any restrictions on the relationship between the pole frequency introduced by the capacitor  $C$  and the input frequencies.

## 2. ANALYSIS

Using Equations (1) and (2) and without any restrictions on the frequencies of the EMI, the output current of the current mirror of Fig. 1 can be expressed as

$$I_{out} = I_{in} - C \frac{d}{dt} \left( V_{th} + \sqrt{\frac{I_{out}}{k}} \right) \quad (4)$$

With  $V_{th} = \text{constant}$ , Equation (4) can be rewritten as

$$I_{out} + C \frac{d}{dt} \left( \sqrt{\frac{I_{out}}{k}} \right) = I_{in} \quad (5)$$

Equation (5) is a nonlinear differential equation. A possible solution for Equation (5) starts by setting

$$I_{out} = \gamma^2 \exp(2u) \quad (6)$$

Thus, Equation (5) is transformed into

$$\gamma^2 \exp(2u) + \frac{C}{\sqrt{k}} \gamma \exp(u) \frac{du}{dt} = I_{in} \quad (7)$$

Assuming that the input current is formed of a DC biasing current component plus a multisinusoidal EMI of the form

$$I_{in} = I_{DC} + i_{emi} = I_{DC} + \sum_{n=1}^N I_n \cos \omega_n t \quad (8)$$

where  $I_n$  is the amplitude of the  $n$ th EMI current component of frequency  $\omega_n$ , then combining Equations (7) and (8) yields

$$I_{DC} + \sum_{n=1}^N I_n \cos \omega_n t = \gamma^2 \exp(2u) + \frac{C}{\sqrt{k}} \gamma \exp(u) \frac{du}{dt} \quad (9)$$

Equation (9) is a nonlinear differential equation for which a solution of the form

$$u = \sum_{n=1}^N \alpha_n \cos \omega_n t \quad (10)$$

is assumed as a first approximation. Substituting Equation (10) into Equation (9) yields

$$\gamma^2 \exp\left(2 \sum_{n=1}^N \alpha_n \cos \omega_n t\right) - \frac{C}{\sqrt{k}} \gamma \exp\left(\sum_{n=1}^N \alpha_n \cos \omega_n t\right) \left(\sum_{n=1}^N \alpha_n \omega_n \sin \omega_n t\right) = I_{DC} + \sum_{n=1}^N I_n \cos \omega_n t \quad (11)$$

Using Sonine's expansion

$$\exp(z \cos \phi) = I_0(z) + 2 \sum_{m=1}^{\infty} I_m(z) \cos m\phi$$

where  $I_m(z)$  is the modified Bessel function of the first kind of order  $m$ , Equation (11) reduces to

$$\begin{aligned} & \gamma^2 \prod_{n=1}^N \left( I_0(2\alpha_n) + 2 \sum_{m=1}^{\infty} I_m(2\alpha_n) \cos m\omega_n t \right) - \frac{C}{\sqrt{k}} \gamma \prod_{n=1}^N \left( I_0(\alpha_n) + 2 \sum_{m=1}^{\infty} I_m(\alpha_n) \cos m\omega_n t \right) \\ & \left( \sum_{n=1}^N \alpha_n \omega_n \sin \omega_n t \right) = I_{DC} + \sum_{n=1}^N I_n \cos \omega_n t \end{aligned} \quad (12)$$

Using the principle of harmonic balance, then

$$I_{DC} = \gamma^2 \prod_{n=1}^N I_0(2\alpha_n) \quad (13)$$

$$I_n = \left( \left[ 2\gamma^2 \left( \prod_{\substack{r=1 \\ r \neq n}}^N I_0(2\alpha_r) \right) I_1(2\alpha_n) \right]^2 + \left[ \frac{C}{\sqrt{k}} \gamma \left( \prod_{n=1}^N I_0(\alpha_n) \right) \alpha_n \omega_n \right]^2 \right)^{1/2} \quad \text{for } n = 1, 2, \dots, N \quad (14)$$

Equations (13) and (14) are nonlinear algebraic equations and can be solved numerically to yield values of  $\gamma$ ,  $\alpha_n$ ,  $n = 1, 2, \dots, N$ . However, for  $\alpha_n < 1$ , the modified Bessel functions can be approximated by

$$I_m(\alpha_n) = \frac{(\alpha_n/2)^m}{m!} \quad (15)$$

Using the approximations of Equation (15), Equations (13) and (14) reduce to

$$I_{DC} = \gamma^2 \quad (16)$$

and

$$I_n = \left( 4\gamma^4 \alpha_n^2 + \frac{C^2}{k} \gamma^2 \alpha_n^2 \omega_n^2 \right)^{1/2} \quad \text{for } n = 1, 2, \dots, N \quad (17)$$

Combining Equations (16) and (17) yields

$$\alpha_n = \frac{I_n}{\sqrt{4I_{DC}^2 + \frac{C^2}{k} I_{DC} \omega_n^2}} \quad \text{for } n = 1, 2, \dots, N \quad (18)$$

From Equations (6), (10) and (15), the output current can be expressed as

$$I_{out} = I_{DC} \exp \left( \sum_{n=1}^N 2\alpha_n \cos \omega_n t \right) \quad (19)$$

Using Sonine's expansion in Equation (19), the DC output current component can be expressed as

$$I_{out,DC} = I_{DC} \prod_{n=1}^N I_0(2\alpha_n) \quad (20)$$

For  $\alpha_n < 1$ ,  $n = 1, 2, \dots, N$  the modified Bessel function of the first kind and order zero can be approximated by  $I_0(z) = 1 + z^2/4$ , and using Equation (18), Equation (20) reduces to

$$I_{out,DC} = I_{DC} \prod_{n=1}^N \left( 1 + \frac{I_n^2}{(4I_{DC}^2 + \frac{C^2}{k} I_{DC} \omega_n^2)} \right) \quad (21)$$

Equation (21) implies that the DC output current component will be formed of a fixed DC component =  $I_{DC}$  plus a DC shift component. Inspection of Equation (21) clearly shows that the DC shift component decreases with the increase of the both capacitance  $C$  and the frequencies of the EMI current components and increases with increase in the amplitude of the EMI current components.

### 3. SIMULATION RESULTS

In order to validate the procedure described in this paper, the circuit of Fig. 1 was simulated using 0.18  $\mu\text{m}$  RFCMOS process technology with  $\mu C_{ox} = 355 \mu\text{A}/\text{V}^2$  and using the harmonic balance simulator controller in the advanced design system (ADS) design automation software under different scenarios of DC input current  $I_{DC}$ , EMI amplitudes and frequencies. As an illustrative example, the simulated results obtained with DC supply voltage = 1.8 V,  $W = 5 \mu\text{m}$ ,  $L = 0.18 \mu\text{m}$ ,  $Nf = 5$ ,  $k = 24.65 \text{ mA}/\text{V}^2$ ,  $I_{DC} = 1.0 \text{ mA}$  and a two-tone ( $N = 2$ ) equal-amplitude EMI with

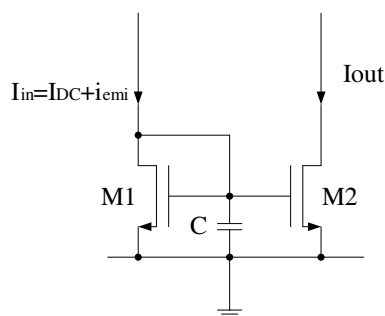


Figure 1: Basic current-mirror with a capacitor between mirror node and ground.

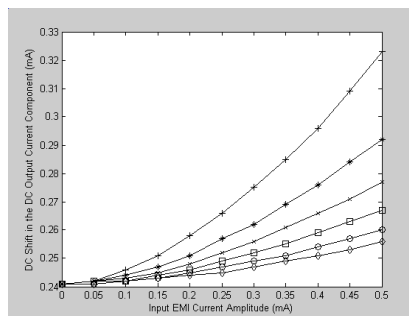


Figure 2: Variation of the DC shift in the output DC current component with the EMI input current amplitude. +:  $C = 0.0$  pF; \*:  $C = 100$  pF; ×:  $C = 150$  pF; □:  $C = 200$  pF; o:  $C = 250$  pF; ◇:  $C = 300$  pF.

$I_r = I_s = I = 0.01$ – $0.5$  mA and frequencies  $f_r = \omega_r/2\pi = 10$  MHz and  $f_s = \omega_s/2\pi = 11$  MHz are shown in Fig. 2. Inspection of Fig. 2 clearly shows that the shift in the DC shift of the output DC current component is increasing with the increase in the input EMI current amplitude. However, with increasing the value of the capacitance  $C$ , the rate of change in the output DC shift in the output DC current component tends to be less.

In order to check the accuracy of Equation (21), calculations were made using  $I_{DC} = 1.0$  mA,  $C = 100$  pF,  $I_r = I_s = 0.4$  mA,  $k = 24.65$  mA/V<sup>2</sup>,  $f_r = \omega_r/2\pi = 10$  MHz, and  $f_s = \omega_s/2\pi = 11$  MHz. The results show that the magnitude of the DC shift in the DC output current component will be 0.028 mA. From Fig. 2, the simulated value is 0.0275 mA. These figures are in fairly good agreement with the calculated results keeping in mind that these calculated results are obtained from a first approximation for solving the nonlinear differential equation of Equation (9). Nevertheless the trends of the calculated and simulated results are in a fairly good agreement.

#### 4. CONCLUSION

In this paper, a new procedure has been presented for predicting the performance of an NMOSFET current-mirror, with a capacitor connected between the mirror node and the ground, excited by an input DC biasing current plus a superimposed multisinusoidal EMI. Using this procedure, a closed-form approximate expression was obtained for the DC component of the output current. Contrary to the available analysis; based on Taylor-series expansion, by virtue of their derivation, these approximate expressions are valid for relatively large amplitudes of the EMI and can provide better insight into the performance of the NMOSFET current mirror, with capacitor between the mirror-node and the ground, under large EMI. The results obtained clearly shows that the DC shift of the output current are almost monotonically increasing with the amplitudes of the EMI and monotonically decreasing with the increase in the value of the capacitor connected between the mirror-node and the ground.

#### ACKNOWLEDGMENT

The authors acknowledge with thanks the support of King Fand University of Petroleum and Minerals.

#### REFERENCES

- Blamford, R. A. H. and W. Redman-White, "New high-compliance CMOS current mirror with low harmonic distortion for high-frequency circuits," *Electronics Letters*, Vol. 29, 1738–1739, 1993.
- Aldea, C., J. Sabadell, S. Celma, and P. A. Martinez, "Optimized design for the high-swing cascade mirror," *Proceedings of the Midwest Symposium on Circuits and Systems*, 4 pages, 1998.
- Redoute, J.-M. and M. Steyart, "Current mirror structure insensitive to conducted EMI," *Electronics Letters*, Vol. 41, 1145–1146, 2005.
- Wang, Q., "Design of a current mirror immune to EMI," *Proceedings of the Chinese Decision and Control Conference*, 4036–4038, 2010.
- Redoute, J.-M. and M. Steyart, *EMC of Analog Integrated Circuits*, Dordrecht, Springer, 2010.
- Koli, K., "CMOS current amplifiers: Speed versus nonlinearity," Doctoral Dissertation, Helsinki University of Technology, 2000.

# Behavioral Modeling of a 12-bit 500-MS/s Multi-stage ADC

Wen Wei He and Qiao Meng

Institution of RF- & OE-ICs, Southeast University, Sipailou 2, Nanjing 210096, China

**Abstract**— In this paper, a behavioral model of 12-bit@500 MS/s pipeline A/D converters (ADCs) and its non-ideal parameters is presented. The proposed model requires 3 stages, the resolution of former two stages is 4.5 bit and the last stage is 4 bit flash architecture. By simulation, the optimum performance is SNDR = 73.2 dB, SFDR = 102.3 dB, ENOB = 11.88 bit when the input signal is 117.7 MHz and the sampling clock rate is 500 MHz. The proposed model can provide a reference for the error and dynamic analysis for pipeline ADC system.

## 1. INTRODUCTION

High speed and high resolution ADCs are most suitable for wireless communication receiver, ultrasound systems and front-end of video capture system. But the complexity of these higher resolution and conversion speed ADCs become higher and higher. To ensure correctness of design and reduce time-to-market for a product, it is crucial to perform behavioral modeling at the functional level.

The behavioral model of circuit is the mathematical expression of the circuit internal physical characteristics, consist of abstract expression of input, output and internal state. Behavioral simulation does not consider the implementation details of the circuit. It describes the circuit behavior based on input-output relationship between circuit architecture and model composition.

Behavioral description can be achieved by the use of different high-level languages [1]. This paper employs the Matlab and Simulink environment which is flexible enough to design the high resolution ADC and simulate its nonidealities. In most pipeline ADC circuits, the 1.5-bit MDAC [2] is the most commonly used stage because of its simple analog integrated circuit design, but in this case, we consider 4.5-bit MDAC, that is 5-bit quantization output and the effective bits is 4.5. Thus, the 4.5-bit MDAC is equivalent to four stages of 1.5-bit MDAC, and three stages (5 + 5 + 4) can achieve the ADC of 12-bit resolution.

Figure 1 shows the block diagram of a generic pipeline ADC, consisting of 3 stages and a Sampled-and-Hold (S/H) circuit at the front [3, 4]. A sample and hold amplifier precedes the pipeline chain. Each of the pipe stages comprises four main blocks: a sub-ADC, sub-DAC, residue amplifier and subtractor. Generally an MDAC realizes the last three. The accuracy of the converter critically depends on the non-idealities of the actual components used. Such non-idealities come from the limited matching of components, clock jitter and offset errors.

## 2. BEHAVIORAL MODELING OF PIPELINE ADC

### 2.1. Sample/Hold Amplifier

A Sample and Hold (S&H) block is a critical part of an ADC. Its function is to sample and then retain the input signal long enough for the A/D converter to complete a conversion [6]. Fig. 2 is the basic Sample and Hold circuit.

When the switch controlled by clock is closed, the sampling capacitor is charged by input signal. This process is called sample, also known as track. After the switch disconnect, the sampling capacitor voltage is keep in the instantaneous value. This process is called Hold.

In Fig. 4, we assume that the conduction resistance is  $R_s$ . The voltage transfer function and

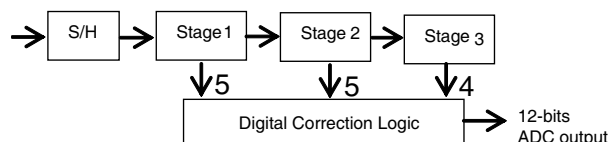


Figure 1: Pipeline ADC block diagram.

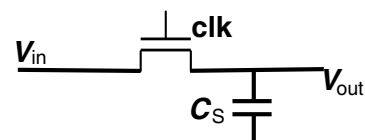


Figure 2: Basic sample and hold circuit.

bandwidth of Sample and Hold Circuit meet the condition:

$$|H(j\omega)| = \left| \frac{1}{j\omega R_s C_s + 1} \right| \tag{1}$$

$$BW = \frac{1}{R_s C_s} \tag{2}$$

We have modeled an S&H block considering the non-idealities of offset errors shown in Fig. 3. The thermal noise is the main noise of high speed S&H circuit. The noise source density is:

$$v_n^2 = 4kTR_S \tag{3}$$

Combination of the transfer function (1), the output noise is:

$$\overline{v_o^2} = \int_0^\infty v_n^2 |H(j\omega)|^2 df = 4kTR_S \int_0^\infty \frac{1}{1 + (2\pi f R_s C_s)^2} df = \frac{kT}{C_S} \tag{4}$$

Therefore, in order to reduce the noise impact, we need to increase the  $C_S$ , but formula (2) shows that the increasing of sample capacitor will lead to a decline in bandwidth. For ensure bandwidth, we need to increase the size of switch transistor to reduce conduction resistance.

### 2.2. Clock Jitter

Clock jitter is the difference of time from its ideal rising clock edge. This difference occurs randomly before or after its ideal rising edge. The magnitude of this error is a function of both the statistical properties of the jitter and the input signal. The error introduced when a sinusoidal signal  $x(t)$  with amplitude  $A$  and frequency  $f_{in}$  is sampled at an instant which is in error by an amount  $\delta$  is given by

$$x(t + \delta) - x(t) \approx 2\pi f_{in} \delta A \cos(\pi f_{in} t) = \delta \frac{d}{dt} x(t) \tag{5}$$

This effect can be simulated at behavioral level by using the model shown in Fig. 4.

The input signal  $x(t)$  and its derivative ( $du/dt$ ) are continuous-time signals. They are sampled with sampling period  $T_S$  by a zero-order hold. In the model, the signal  $n(t)$  is implemented starting from a sequence of random numbers with Gaussian distribution, zero mean, and unity standard deviation [7].

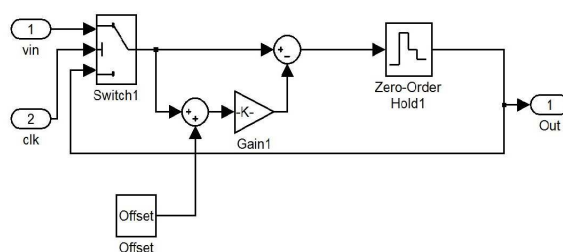


Figure 3: Sample and hold circuit model.

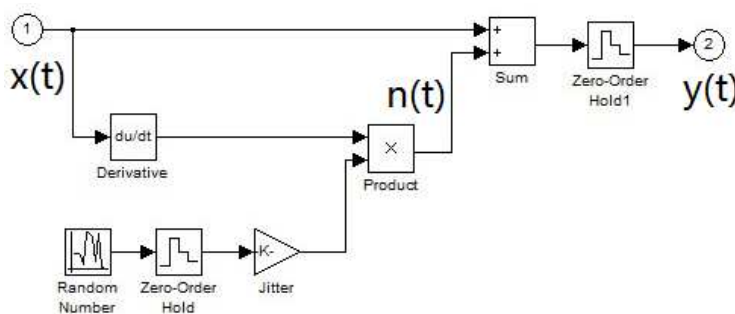


Figure 4: Modeling a random sampling jitter.

Assume that the input signal is:

$$V = 0.5 \times V_{FS} \sin(2\pi f_{in} \times t) \tag{6}$$

$V_{FS}$  is the full-scale range of ADC, and  $f_{in}$  is the frequency of the input signal. When the non-ideality clock jitter is  $\Delta t$ , the maximum offset of input signal is:

$$\Delta V = \pi f_{in} \times V_{FS} \times \cos(2\pi f_{in} t) \Delta t \tag{7}$$

In order to meet the overall accuracy of the N-bit ADC,  $\Delta V$  must be limited in the range of (8):

$$\Delta V_{\max} < 1LSB = \frac{V_{FS}}{2^N} \tag{8}$$

By the formula (7) and (8), the clock jitter  $\Delta t$  can be determined by the following formula:

$$\Delta t < \frac{1}{\pi f_{in} \times 2^N} \tag{9}$$

In this behavioral model,  $N = 5$ .

**2.3. 4.5-bit/stage MDAC Model**

MDAC circuit is consisted of S&H, sub-DAC, subtractor and Residual amplifier circuit. The transfer accuracy depends on the accuracy of residual signal, and the speed is determined by the set-up time of residual amplifier [8].

To 4.5 bit MDAC, the overall accuracy and the inhibit ability of conversion error stage to stage are improved. It has the following advantages: (1) It is not very strict to the gain of amplifier and the set-up time, which means we can achieve this structure with low power consumption amplifier architecture [5]. (2) Due to the low  $KT/C$  noise, capacitance matching errors are relatively small; this architecture can effectively reduce the size of capacitor, also reduce the power consumption; (3) the noise from feedback is isolated by the high gain amplifier, so the input noise will be decreased, and the impact to this stage will be greatly reduced.

4.5-bit/stage MDAC divide the input range into 31 intervals, and the gain of residual signal is 16 times. The transfer function is as below and shown in Fig. 5.

According to the 4.5-bit MDAC transfer curve, we can get the 4.5-bit MDAC model shown in Fig. 6.

The output of all stages circuit is sent into delay unit, and the signals of delay units will arrive to the digital correct circuit at the same time.

**2.4. Delay Unit and Digital Correction Model**

The delay unit consists of  $D$  flip-flop, and the delay of all stages is different. The model is shown in Fig. 7.

According to the principle of Digital correction algorithm, the offset error and redundant code is eliminated by the way of Fig. 8.

The behavioral model of redundant correction in Simulink is shown as Fig. 9.

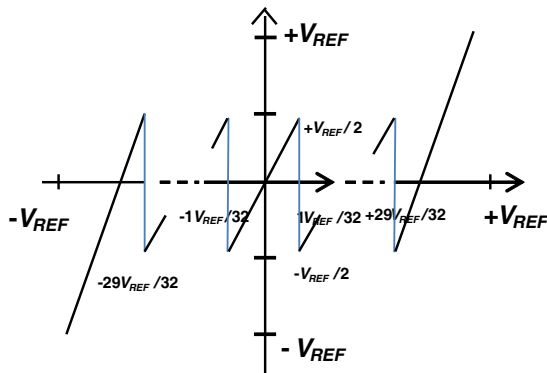


Figure 5: 4.5-bit MDAC transfer curve.

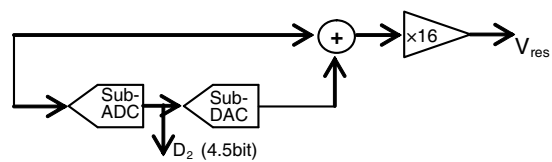


Figure 6: 4.5-bit MDAC Block diagram.

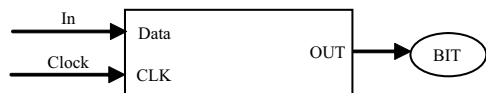


Figure 7: Delay unit.

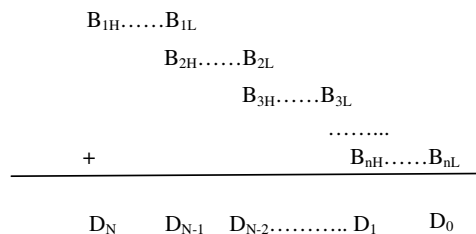


Figure 8: Principle of Redundant Correction algorithm.

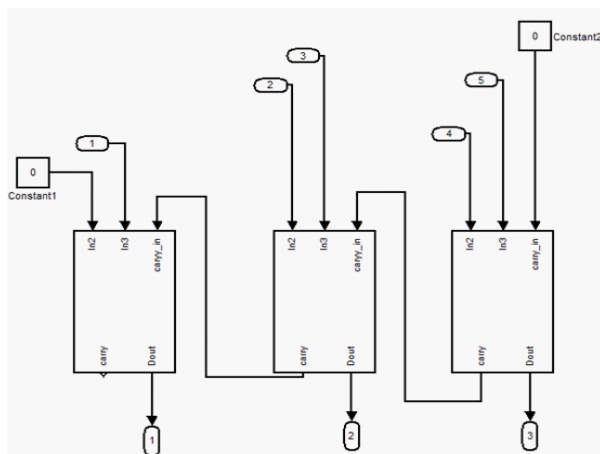


Figure 9: Behavioral model of digital redundant correction.

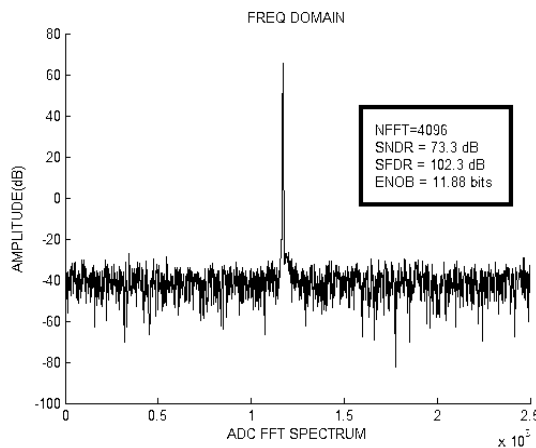


Figure 10: Ideal model dynamic characteristic.

### 3. SIMULATION AND RESULTS

The proposed model above was used to simulate a 4.5-bit/stage 12-bit pipeline ADC at 500 MHz with digital correction and the reference voltage is 2.5 V.

#### 3.1. Simulation on Ideal Condition

Several simulations were performed considering variation of a non-ideal parameter while the rest of the blocks were considered ideal. Fig. 10 shows the pipeline ADC dynamic characteristic in the ideal condition and input signal frequency is 117.7 MHz.

The Fig. 10 shows that the SNDR is 73.3 dB and ENOB is 11.88 bits which is very close with theoretical value in ideal condition.

#### 3.2. Simulation with Offset Errors

Then, we can analysis he dynamic performance of the circuit by increasing offset errors and keeping the frequency of sampling and input signal unchanged. In fact, for convenience the offset errors can be considered as the sum of  $KT/C$  noise, comparator offset, amplifier offset and reference voltage offset. When the offset is 100 mv, the simulation is shown in Fig. 11.

Table 1 shows that the system performance under specified offset errors.

Simulations performed under the specified conditions show that the offset should be below in  $V_{ref}/2^N$ , in this case,  $N = 5$ . As is shown in Table 1, there is a significant decrease of SNDR and SFDR when offset is above 80 mv.

#### 3.3. Simulation with Clock Jitter

Figure 12 shows the dynamic performance of model with clock jitter is 1ns which is 50% of Clock frequency.

Table 2 shows the dynamic performance under specified clock jitter.

The simulation shows that the SNDR will decrease rapidly when the clock jitter is above 10% of clock jitter.

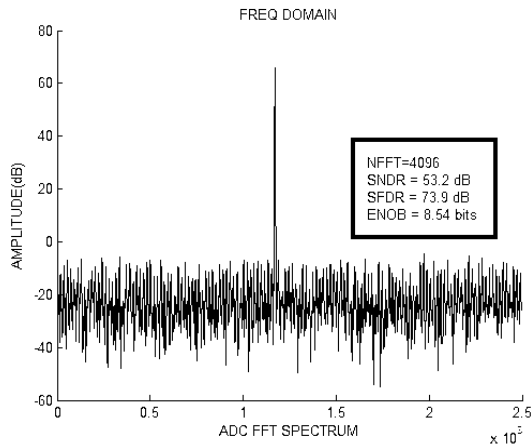


Figure 11: Dynamic performance with offset errors is 100 mv.

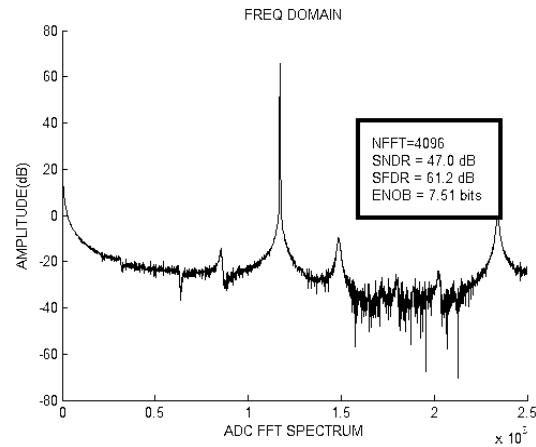


Figure 12: Dynamic performance with clock jitter is 1 ns.

Table 1: Effect of offset errors.

Offset (v)	SNDR (dB)	SFDR (dB)	ENOB (bit)
0	73.2	102.3	11.88
0.08	72.6	91.3	11.77
0.1	52.3	71.5	8.39

Table 2: Effect of clock jitter.

clock (ns)	SNDR (dB)	SFDR (dB)	ENOB (bit)
0	73.2	102.3	11.88
0.2	72.13	91.3	11.69
1	47	71.5	7.51

#### 4. CONCLUSION

In this paper, we presented a set of behavioral models implemented in the MATLAB SIMULINK environment for a 12-bit pipeline ADC. Simulation shows that the SNDR is 73.3 dB and SNDR is 102.3 dB in ideal condition which proved that the model is suitable for the high resolution ADC. Meanwhile, we simulate the behavioral model considered the offset errors and clock jitter, and give the relationship between the system performance and non-idealities. The proposed model can provide an effective reference for the 12-bit pipeline ADC design.

#### REFERENCES

- Maloberti, F., P. Estrada, A. Valero, and P. Malcovati, "Behavioral modeling and simulation of data converters," *IMEKO 2000*, Vienna, Austria, Sep. 2000.
- Yoo, S.-M., J.-B. Park, S.-H. Lee, et al., "A 2.5-V 120-M sample/s CMOS pipelined ADC based on merged-capacitor switching," *IEEE Transactions on Circuits and System*, Vol. 51, No. 5, 269–275, May 2004.
- Rodríguez-Vázquez, A., F. Medeiro, and E. Janssens, *CMOS Telecom Data Converters*, Kluwer Academic Publishers, 2003.
- Gustavsson, M., J. J. Wikner, and N. N. Tan, *CMOS Data Converters for Communications*, Kluwer Academic Publishers, 2000.
- Cho, C.-H., "A power optimized pipeline analog-to-digital converter design in deep sub-micron cmos technology," *UMI*, No. 3198520, 2005.
- Bilhan, E. and P. C. Estrada, "Behavioral model of pipeline ADC by using Simulink," *South-west Symposium on Mixed-signal Design*, 147–151, 2001.
- Malcovati, P., "Behavioral modeling of switched-capacitor sigma-delta modulators," *IEEE Transactions on Circuits and Systems — I: Fundamental Theory and Applications*, Vol. 50, No. 3, Mar. 2003.
- Phillip, E. A. and D. R. Holberg, *CMOS Analog Circuit Design*, Publishing House of Electronic Industry, Beijing, 2007.

# The Impact of USB 3.0 Module on Wireless Communication with Improved Solution for EMI Problem of High Speed Connectors

Han-Nien Lin<sup>1</sup>, Wei-Hua Huang<sup>2</sup>, and Wei-Jr Lai<sup>1</sup>

<sup>1</sup>Department of Communications Engineering, Feng-Chia University, Taiwan, R.O.C.

<sup>2</sup>Training Research Co., LTD

6F.-1, No. 3-1, Park St., Nangang Dist., Taipei City 115, Taiwan, R.O.C.

**Abstract**— With the development of Ultrabook in recent years, the main and auxiliary antennas for WLAN are moved down to PC base because the LCD panel is too thin to install antennas inside. On top of that, there are also more and more laptops equipped with super high-speed USB 3.0 ports. Unfortunately, the USB 3.0 modules will usually radiate the EMI noise to affect the receiving performance of WLAN in the Ultrabook if USB dongle is inserted or the USB cable is plugged in. To analyze and quantify the effect of the USB 3.0 EMI noise on the WLAN performance of Ultrabook, several experiments have been conducted for relationship between throughput rate and EMI noise power received by the antennas. Some equipment utilized will be presented in this paper, which have been developed to help trouble-shooting and identifying the root cause of EMI problem relevant to the radiated EMI noise from various IC chips, modules, devices, and so on. In addition, the EMI diagnosis procedure also applies to other high speed modules such as HDMI, LVDS, SATA, PCI Express, Display Port, and EDP. Finally, the possible solution to USB 3.0 EMI problem will also be discussed.

## 1. INTRODUCTION

With the development of Ultrabook in recent years, the two wireless LAN antennas are moved down to the position beside the keyboard and mother-board as shown in Fig. 1 because the panel is too thin for the antennas to be installed, which is different from the traditional laptop that the wireless LAN antennas are built in the upper left and right corners of the panel. On top of that, with the development of the USB 3.0 super-speed technology, there are more and more NB computer installed the USB 3.0 ports. Unfortunately, if the USB 3.0 pen drive is inserted or the USB cable is plugged in to a notebook computer, the USB 3.0 module will radiate the noise power to affect the receiving performance of the WLAN antennas in Ultrabook.

For instance, once the USB 3.0 pen drive is plugged in, the lagging, or disconnection of the wireless network system in Ultrabook happens. Therefore, all of the computer system manufacturers and USB 3.0 module manufacturers should do something to solve or mitigate the USB 3.0 EMI problem. Otherwise, with the coming of the Windows To Go function built in Microsoft Windows 8 as shown in Fig. 2, the WLAN antennas in Ultrabook won't always work properly if the Windows 8 pen drive is used to boot the Ultrabook.

Several papers, including Intel White Paper [1], mention that the USB 3.0 high speed module will give rise to the lagging or disconnection of the wireless PC mouse. Besides, some author mentions that the common mode filter can be designed to control the EMI in 3G wireless communication systems [2].

In this paper, the impact of the USB 3.0 high speed module on various RF wireless communication bands is investigated first. This paper will then come with the approach for the mitigation of the USB 3.0 EMI, together with some RF measurement systems that will be applied to solving the USB 3.0 EMI further such as SNA (System Noise Analyzer), PNS (Platform Noise Scanner), and Microwave Power Clamp, and so on.

## 2. THE USB 3.0 IMPACT ON RF WIRELESS COMMUNICATIONS

To investigate how much impact the USB 3.0 modules have on various RF wireless communication bands, several experiments have been conducted, including the throughput rate measurement, WWAN sensitivity test, and so forth. In this section, we first describe the throughput rate of the WLAN antennas in Ultrabook degraded by the USB 3.0 high speed modules.

The test setup for WLAN throughput rate is shown in Fig. 3. Fig. 4 shows the measured WLAN throughput rate in different receiving power level which is used to simulate the different distances from Access Point (AP) to the notebook computer.



Figure 1: The locations of the WLAN antennas and USB 3.0 port in Ultrabook.



Figure 2: The windows to go pen drive for booting the computer.



Figure 3: The test setup for the WLAN throughput rate.

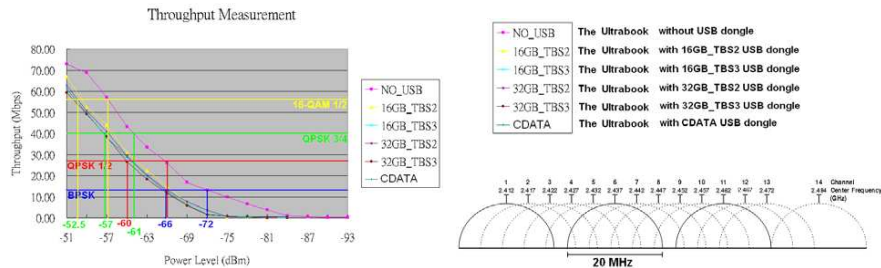


Figure 4: The WLAN throughput rate measurement with different USB 3.0 drive, and the 11 channels for WLAN operation. (Note that the throughput rates of 11 channels are tested and taken average).

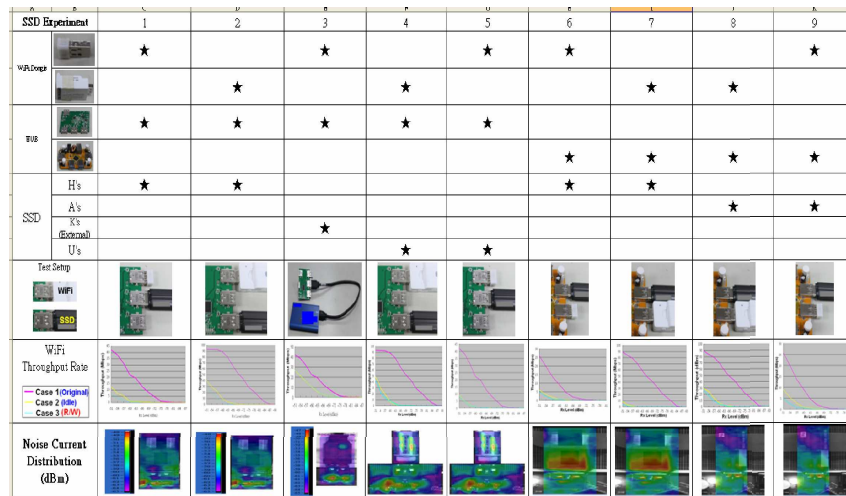


Figure 5: WiFi throughput rate measurement with the corresponding test setups and noise current distributions. (Two kinds of WiFi dongles, USB 3.0 hubs, and four kinds of USB 3.0 SSDs are chosen).

It can be discovered that in BPSK modulation scheme, if the USB dongle is not inserted into Ultrabook, the receiving power level is  $-72$  dBm; if the USB dongle is inserted, the receiving power level shifts to  $-66$  dBm. That is, the USB 3.0 module generates 6 dB noise power, which affects the WLAN antennas that are about 10 ~ 15 cm away from the USB dongle in Ultrabook.

Figure 5 shows the throughput rate of WiFi dongles themselves, WiFi dongles beside the USB 3.0 pen drive, and WiFi dongles beside the USB 3.0 pen drive reading and writing data. Two kinds of USB 3.0 hubs and four kinds of SSDs are chosen to conduct the experiment.

It can be inferred from Fig. 5 that different combinations of USB 3.0 hub and USB 3.0 SSD cause different degradation level of WiFi throughput rate, and note that different USB 3.0 hubs means different designs for USB 3.0 connectors. Moreover, from the noise current distributions shown in Fig. 5, it can be inferred that the more noise power the USB 3.0 radiates, the poorer the WiFi throughput rate is.

Besides the degradation of WLAN throughput rate, the USB 3.0 modules can also cause the

degradation of WWAN sensitivity. Fig. 6 shows if the mobile phone is put beside the USB 3.0 module, the reception of cell phone gets worse. The WWAN test includes sensitivity and RSSI levels.

From Fig. 6, it clearly shows that the degradation of WiFi throughput rate is relevant to the USB 3.0 noise power distribution. Therefore, the next section deals with how to use the RF measurement systems to find out the noise source in the whole USB 3.0 module.

### 3. RF MEASUREMENT SYSTEM FOR USB 3.0 EMI

In the past few years, TRC (Training Research Corporation, Ltd.) developed a variety of equipments related to the noise power measurement such as PNS (Platform Noise Scanner), NFS (Noise Floor Measurement System), SNA (System Noise Analyzer), and so on. Additionally, “Microwave Power Clamp” is also developed for noise power measurement at USB receptacle and plug, and even along the cable of the USB, LVDS, HDMI, SATA, and so forth. Compared with the conventional absorbing clamps using ferrite ring cores, the TRC’s Microwave Power Clamp is small, power-saving, and user-friendly.

#### 3.1. Microwave Power Clamp with SNA (System Noise Analyzer)

Firstly, the measurement for the noise power of the USB 3.0 cable is taken as an example for the application of the Microwave Power Clamp, and Fig. 7 is the measurement setup for the noise power of the USB 3.0 cable with various kinds of HDDs.

The Microwave Power Clamp shown in Fig. 8 is connected to its auxiliary device, SNA (System Noise Analyzer), to show the noise power detected by the clamp.

Figure 9 shows the measurement results for the noise power of the USB 3.0 cable. Note that if the SNA is used as an auxiliary device to measure the noise power, the unit of the noise power density is (dBm/200 kHz). Furthermore, the calibration method of the Microwave Power Clamp is referred to CISPR 16-1 [3].

There are many different test cases and the corresponding test results shown in Fig. 9. For instance, “Sample 1” stands for the fact that the Ultrabook is connected with the HDD from X Company using the USB 3.0 cable from Y Company, and “Sample 2” stands for the fact that the Ultrabook is connected with the HDD from Z Company using the T Company’s USB 3.0 cable. In total, there are 8 test cases for two kinds of HDDs and four kinds of USB 3.0 cables.

From Fig. 9, it shows that “Sample 2” is the best case because the noise power density of sample 2 is the lowest among all samples.

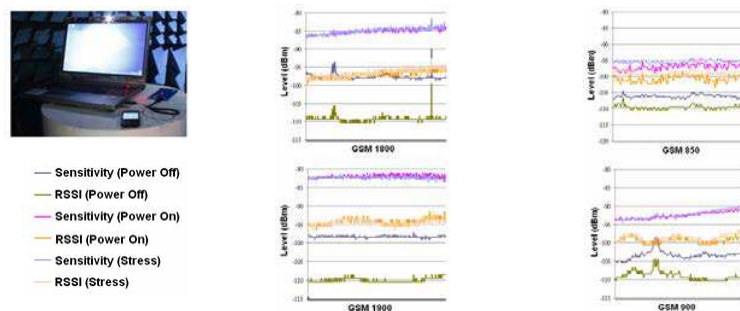


Figure 6: WWAN sensitivity test, including power off, on, and stress modes for the notebook computer.



Figure 7: The measurement setup for the noise power.



Figure 8: The auxiliary device of the microwave power clamp, SNA.

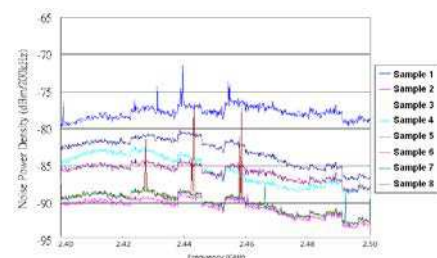


Figure 9: The measured noise power by the microwave power clamp.

### 3.2. NFS (Antenna Noise Floor Measurement System)

In the previous section, since the USB 3.0 port tends to radiate the noise power to the nearby wireless LAN antennas, the measurement of the USB 3.0 noise power received by wireless LAN antennas can be carried out to prove the effect of the USB 3.0 noise power on RF wireless communication.

The test setup is shown in Fig. 10, and note that NFS (Noise Floor Measurement System) is applied to measure the noise power received by the WLAN antennas.

The experiment for the antenna noise power measurement can be divided into two parts. The first part is to measure the noise power received by the wireless LAN antennas using NFS with various kinds of the USB dongles working, and compare with the measured noise power without the insertion of the USB dongle into the Ultrabook. In addition, the second one is to measure the amount of the noise power radiated from the USB 3.0 dongle by the Microwave Power Clamp along with NFS.

Figure 11 shows the test setup for the Microwave Power Clamp utilized to carry out the noise power measurement.

Figure 12 shows the results of the USB 3.0 noise power measurement using the Microwave Power Clamp along with NFS. The USB pen drive is plugged into the Ultrabook to measure the noise power received by the WLAN main antenna and measure the amount of the noise power radiated from the USB 3.0.

From Fig. 12, it is worthy of being noted that the main antenna still receives the noise power when the dongle isn't plugged into the Ultrabook, and such noise power comes from other modules of the Ultrabook, such as motherboard, and LVDS port, etc..

### 3.3. PNS (Platform Noise Scanner)

To understand how the USB 3.0 noise power generates, radiates, and affects the wireless LAN antennas, it is necessary to use PNS to scan the noise power distribution around or on the USB receptacle. Fig. 13 shows the overview of PNS developed by TRC, and Fig. 14 shows the test results of the noise power distribution on the USB receptacles from A and B companies, respectively.

Figure 14 shows the hot spot image, and it clearly show that the USB 3.0 receptacle radiates noise power in Ultrabook. As discussed previously, such noise power shown in Fig. 14 stems from the discontinuities of the connections in the USB receptacle and PCB. Note that the amount of the measured noise power in Figs. 14(a) and (b) are different due to the difference of the structure between these two USB receptacles.

## 4. THE POSSIBLE MITIGATION METHODS TO USB 3.0 EMI PROBLEM

Some solutions to mitigating USB 3.0 EMI problem have been worked out by TRC with USB 3.0 modules' manufacturers. For instance, Fig. 15 shows the structure of improved design for USB 3.0 receptacle. Note that three pairs of the transmission lines (SSTX, SSRX, and D) are isolated by VBUS and GND, and the test setup and test result for the receptacle in Fig. 15 is shown in Fig. 16.

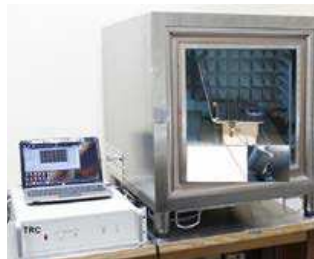


Figure 10: The test setup for the measurement of the noise power received by the WLAN antennas.

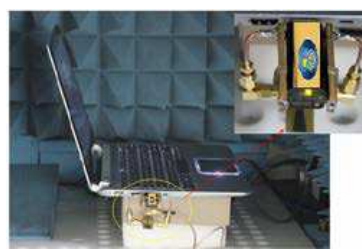


Figure 11: The test setup for the measurement of the amount of the noise power radiated from the USB 3.0 dongle.

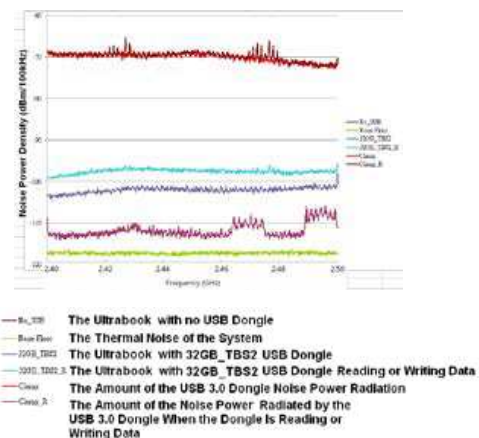


Figure 12: The results of the main antenna noise power measurement using the Microwave Power Clamp (The EUT is connected with the 32GB\_TBS2 dongle).



Figure 13: The overview of TRC's PNS.

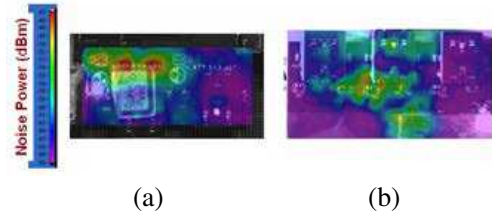


Figure 14: The test results for the USB receptacles from A and B companies.

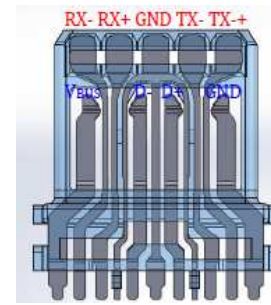


Figure 15: The improved design for USB 3.0 receptacle.

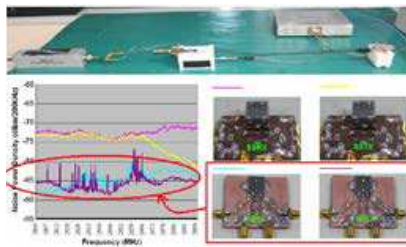


Figure 16: The test setup and test results for the typical receptacle and the receptacle shown in Fig. 15.



Figure 17: The improved termination scheme for mitigating USB 3.0 EMI problem.

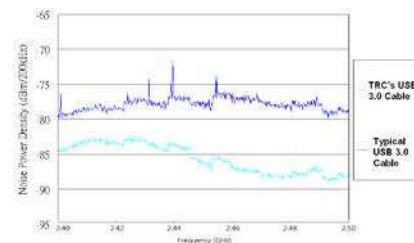


Figure 18: The test results for the typical USB 3.0 cable and the cable with improved termination scheme as shown in Fig. 17.

Besides, to control the USB 3.0 EMI, the power lines must keep on outer layers, and the signal lines must go through the inner layers. In addition, Fig. 17 shows the improved termination scheme for mitigating USB 3.0 EMI problem. The plugs are shielded tightly using copper foil, and Fig. 18 shows the test results for the typical USB 3.0 cable and the cable with improved termination scheme as shown in Fig. 17.

## 5. CONCLUSION

The issue of the USB 3.0 noise power radiation and its impact on wireless communication cannot be neglected for brand-new Ultrabook design owing to the short distance between the WLAN antennas and USB 3.0 ports. If the issue cannot be solved, the WLAN of Ultrabook may be cut off once the USB dongle is plugged in to operate the Windows To Go system, as discussed in this paper. Besides, several equipments for the USB 3.0 noise power measurement have been introduced. Those equipments can provide customers the directions for modification and optimization of their ICs, and products. Finally, the possible solutions for controlling USB 3.0 EMI are also covered in this paper.

## REFERENCES

1. White Paper, "USB 3.0 radio frequency interference impact on 2.4 GHz wireless devices," Intel Document: 327216-001,1–22, Apr. 2012.
2. Jeong, I.-I. A., C.-H. Tsai, and T.-L. Wu, "An ultra compact common-mode filter for RF interference control in 3G wireless communication systems," *IEEE International Symposium on Electromagnetic Compatibility*, 776–779, 2010.
3. Schaefer, W., "Radio-interference measurements and statistical techniques," *CISPR A*, CISPR 16-1 Amd. 1 f3 Ed. 2.0, Nov. 2001.

# Verification Analysis of Electromagnetic Coupling between Display Module and Antenna of Mobile Devices for Wireless Communications

Han-Nien Lin<sup>1</sup>, Allen Laio<sup>2</sup>, Yen-Lin Tseng<sup>1</sup>, and Ming-Shan Lin<sup>3</sup>

<sup>1</sup>Department of Communications Engineering, Feng-Chia University  
No. 100, Wenhua Rd., Xitun Dist., Taichung City 407, Taiwan, R.O.C.

<sup>2</sup>Training Research Co., LTD, 6F.-1, No. 3-1, Park St.  
Nangang Dist., Taipei City 115, Taiwan, R.O.C.

<sup>3</sup>Bureau of Standards, Metrology and Inspection, MOEA  
No. 4, Sec. 1, Jinan Rd., Zhongzheng Dist., Taipei City 100, Taiwan, R.O.C.

**Abstract**— In this paper, we showed the verification of electromagnetic coupling between display module and antenna. We will analyze here the RF tests needed to be performed by vendors for those display modules before they are to be integrated into smart phones with accepted performance. There are 3 tests needed to be verified, the near field EMC surface scan, the  $S$ -parameter test and RF immunity test. After these tests, we can tell the quality for different display modules and prove that the module performance works well with De-sense test.

## 1. INTRODUCTION

Since the display modules occupy the largest area of various smart phones nowadays, they may either act as an EMI noise radiators or a noise receivers. The EMI noise on mobile platform may couple with display module via traces of PCB, FPC, or the panel ICs. Because the antenna of a smart phone is usually located around the display module, the EMI noise generated from display module would strongly couple with nearby antenna and cause sensitivity degradation of communications. On the other hand, the antenna will radiate a higher level power to keep the link effectively when the phone initiates a call connection, and it may thus affect the function of display module due to electromagnetic coupling. The coupling relationship is showed in Figure 1.

We will analyze here the RF tests needed to be performed by vendors for those display modules before they are to be integrated into smart phones with accepted performance. The 1st test is near field emission test of display module measured with an EMC surface scanner. The test is to scan the operating display module with horizontal near field probe, and to limit the radiated power from the whole display module (including control Panel ICs and FPC connectors) in the designated communication bands. The test also has to ensure that the EMI noise is from the display module itself by filtering power supplier or other PCB traces. The 2nd test is the  $S$ -parameter test for radiated emission by performing with microstrip. The test is to measure electromagnetic coupling between the selected dominant noisy lines and microstrip line. Evaluate the EMC performance of display module under test in terms of emissions from the dominant lines. The 3rd test is

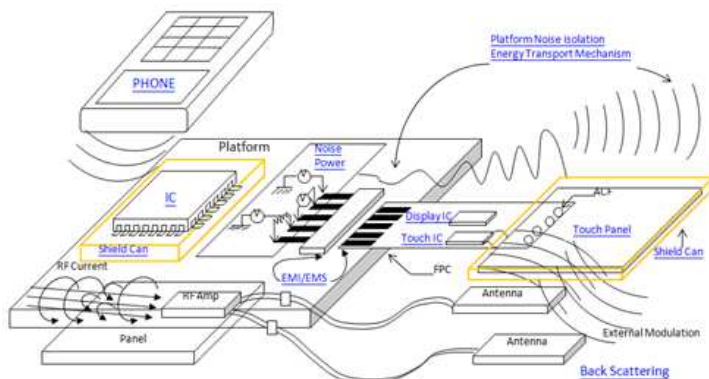


Figure 1: The coupling between display module and antenna.

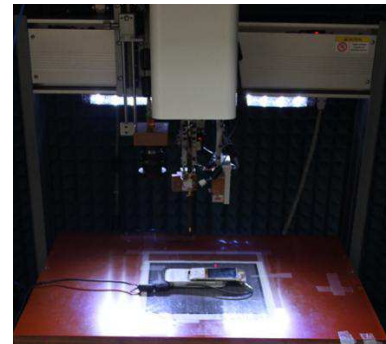


Figure 2: The setup of near field emission test of display module.

RF immunity test by performing with display module against the high level power transmitted from mobile phone without any specific image degraded. The base station simulator will make a connection to mobile phone to control the radiated power during the test, and the quality of image (including display module state, image color, and tone) should not be degraded under RF interference. To achieve better performance of wireless communications, we will summarize the principle and applications of various RF test for display modules to be integrated in mobile devices.

## 2. DISPLAY MODULE NEAR-FIELD EMI

The 1st test is near field emission test of display module measured with an EMC surface scanner. The setup of measurement is showed in Figure 2.

We measured the near field power by a horizontal probe and its diameter is 2 mm. The distance between probe and display module and the step of probe movement are 1 mm. The spectrum analyzer we used here is Agilent N9030A. We chose GSM850 band for following tests. Figures 3 and 4 are showed the test result in spectrum type and hot zone type.

We can tell that the strongest power is about  $-62.7$  dBm at 885 MHz, and the average noise level is about  $-66$  dBm on display module area.

We will process the 2nd test, *S*-parameter test for radiated emission. The network analyzer is R&S ZVB8, the probe is Agilent A1818. The setup of the test is showed in Figure 5. The one end of microstrip line was connecting to port 1 of network analyzer and the other was terminated. The display module is placed on the spacer and under the microstrip line. We measure the coupling between the selected dominant noisy lines and microstrip line with an activity probe.

The coupling is  $-22$  to  $-22.6$  dBm over the GSM 850 band in Figure 6. It means the noise radiated by the display module will be reduced about 22 dB.

We want to proof the relationship between the noise radiated by the display module and cell phone TIS, so we will compare the TIS of two display module types. We placed a steel plate between the display module and antenna area, and the TIS was improved about 1.5 dB over the GSM 850 band, showed in Figure 7. It can be said that the steel plate played a shielding material isolate the noise from display module to antenna.

The TIS test usually takes much time (about few hours) to confirm the effect of solution. So, the 1st and 2nd test can help us to confirm in shorter time. Figure 8 is showed the near field emission test of display module with steel plate.

The strongest power is about  $-63.7$  dBm at 883 MHz and the average level on the module is smaller the before in Figure 8.

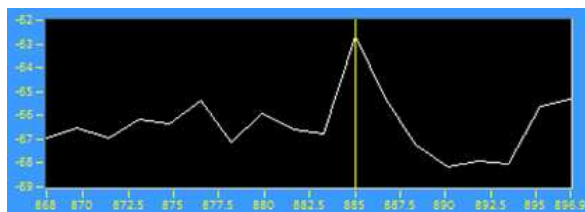


Figure 3: The test result of display module in spectrum type.

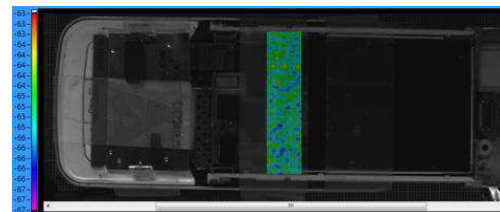


Figure 4: The test result of display module in hot zone type.

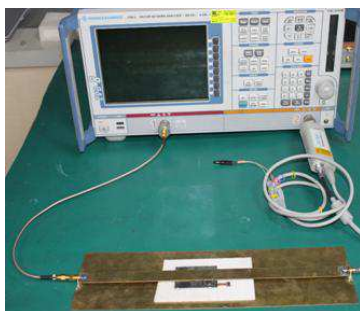


Figure 5: The setup of *S*-parameter test.

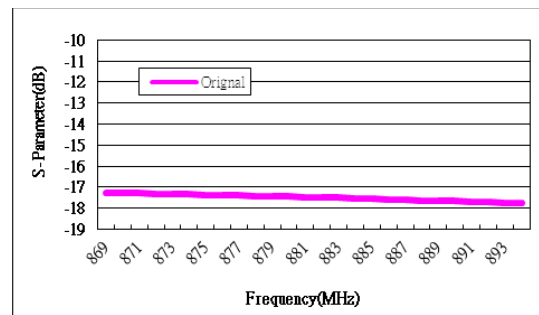


Figure 6: The coupling between dominant line and microstrip line.

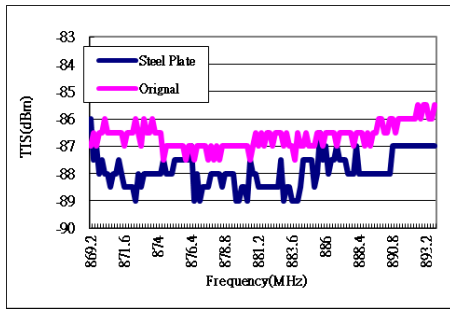


Figure 7: The measured TIS of two state display module.

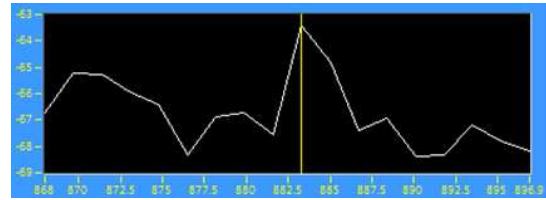


Figure 8: The test result of display module in spectrum type.

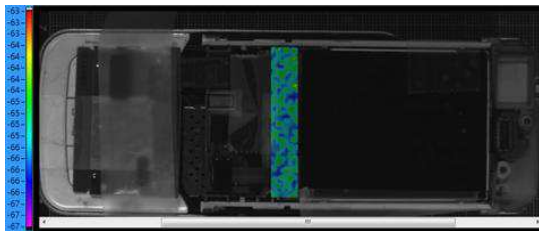


Figure 9: The test result of display module in hot zone type.

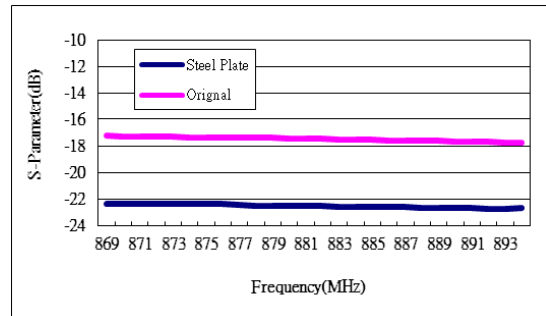


Figure 10: The test result of display module in hot zone type.



Figure 11: The test setup of display module near field EMS.

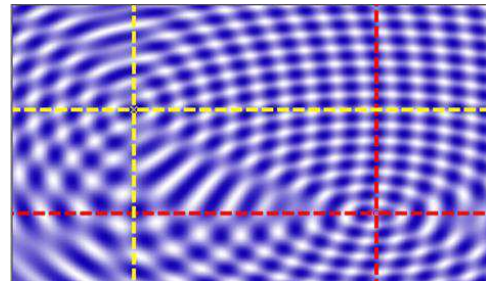


Figure 12: The EMS interference on display module.

The *S*-parameter is showed the isolation could be improved about 5dB in Figure 10. The Figures 8 to 10 are showed that how near field EMI can interference over the air (OTA) performance TIS.

### 3. DISPLAY MODULE NEAR FIELD EMS

The 3rd test setup is showed in Figure 11. The radio communication station is Anritsu MT8820A, and the antenna in the figure is played a connecting antenna. We will make a call to the mobile phone and keep the communication during EMS test. The distance between mobile phone and display module is 1 mm. The test channel is ch. 190 in GSM 850 band, and the TX level is 33 dBm.

The mobile phone should be placed around the display module both side.

In this case, the quality of image (including display module state, image color, and tone) did not be degraded under RF interference. We can't expect which channels or which communication protocols will cause the quality of image degraded, so the EMS test should be process all bands and all channels in WWAN. Figure 12 is showed a type of EMS fail result, called "Wave Interference".

#### 4. CONCLUSION

We showed the verification of electromagnetic coupling between display module and antenna. The near coupling does actually affect the OTA performance, was showed in Section 2 and EMS test setup in Section 3. Vendors should verify those display modules before they are to be integrated into smart phones with accepted performance with. Vendors may collect the test result and make a report to show the performance of they own modules.

#### ACKNOWLEDGMENT

The authors would like to thank research group from BSMI (Bureau of Standards, Metrology and Inspection) for their technical support and measurement assistance. The original research work presented in this paper was made possible in part by the BSMI under Contract grant from BSMI Taiwan.

#### REFERENCES

1. Helttula, J., “Display and touch module electromagnetic verification specification,” *Nokia SD NWP Product Quality*, 6–15, Feb. 2012.
2. Pankinaho, I., “RF emission measurement calibration report template,” Nokia/TP/PT/AV Entities/ Display unit, 7–11, Jan. 2006.

# Resonant Capability of Multilayer Spheroidal Nanoparticles as Plasmonic Nanoantennas

M. Khosravi, R. A. Sadeghzadeh, and M. S. Abrishamian

Department of Electrical and Computer Engineering, K. N. Toosi University of Technology  
Shariati Street, P. O. Box 16314, Tehran, Iran

**Abstract**— In this paper, we study the effect of changing different parameters on the resonant behavior of a single element nanoantenna in the form of multilayer nanosphere. Thickness and number of layers are parameters that their variations have been focused. As final step, the gradual transformation from sphere to ellipsoid has been considered. This alteration in symmetry has interesting results on outputs.

## 1. INTRODUCTION

Guiding light in nanostructures are important challenges for current research and development. A proper solution to these kinds of nanoscale problems is applying metallic nanoantennas [1]. In recent years, a variety of schemes taking advantage of localized optical near-fields generated by metallic nanoparticles have been proposed to use them as optical nanoantennas [2]. Optical antennas consisting of nanometer size metallic particles can be used to improve the size mismatch between the diffraction limited spot of the excitation light and fluorescent molecules that are much smaller than the excitation wavelength. Such antennas which act in optical regime support a localized surface plasmon resonance. In certain condition, light excited plasmons lead to strong light scattering and absorption, and also an enhancement of the local field. Plasmon modes exist in a number of geometries and in various metals especially in noble metals such as gold and silver [3, 4].

Here, we study the effect of changing different parameters on the resonant behavior of a single element nanoantenna in the form of multilayer nanosphere. Thickness and number of layers are parameters which their variations have been focused. As final step, the gradual transformation from sphere to both oblate and prolate spheroids has been considered. This alteration in symmetry has interesting results on outputs. In this paper, we discuss extinction cross section (ECS) as special output which its consideration is essential in studying parameters variation. The CST Microwave Studio (full-wave 3D software) is applied as main tool for simulations. Moreover, it is good to know that the dielectric response of noble metal modeled by Drude function.

## 2. THEORY AND IDEAS

**Scattering from nanosphere.** Energy may be removed from a beam of light incident on a particle embedded within a homogeneous, non-absorbing medium by two processes. Firstly light may be *scattered* whereby a photon is redirected along a path that is no longer parallel to the incident beam. Secondly light may be *absorbed* by the particle whereby energy is converted into another form, for instance heat. In almost all cases both scattering and absorption are present and the combined effect is referred to as extinction. Extinction is a measure of the attenuation of a beam of light traversing a medium from which the energy is removed by scattering and absorption. The amount of light absorbed and the amount of light scattered depends on the *nature of the particle*, its *composition*, *size* and *shape*.

**Optical properties of noble metals.** The design of optical antennas has been widely inspired by their analogs in the radio frequency range. It is noticeable that metals are no longer a perfect electric conductor at optical frequencies but have certain, yet high, conductivity. At radio frequencies, metals behave very similarly to a perfect conductor that can instantaneously cancel out time-varying fields by generating a surface current. In optical frequency range many materials, especially metals, have strong dispersions, i.e., their dielectric constants change significantly with light frequency. To model devices accurately, the permittivity can be described by the Drude model [4]. Considering the epsilon infinity ( $\epsilon_\infty$ ), plasma frequency ( $\omega_p$ ), and collision frequency ( $\nu_c$ ) the correspondent relative permittivity is given as

$$\epsilon_r(\omega) = \epsilon_\infty - \frac{\omega_p^2}{\omega(\omega - i\nu_c)} \quad (1)$$

### 3. SIMULATION AND RESULTS

The basic model used for the studies presented in this work is a spherical nanoparticle as a simple example of an optical antenna. One clear benefit of this geometry is the possibility of straightforward analytical solutions. Initial model contains a metal coated silica sphere at optical frequencies. The silica material is defined as simple “normal” material with a relative permittivity of  $\epsilon_2 = 2.08$ . As mentioned above, the metal material properties are modeled by using Drude dispersion model. The

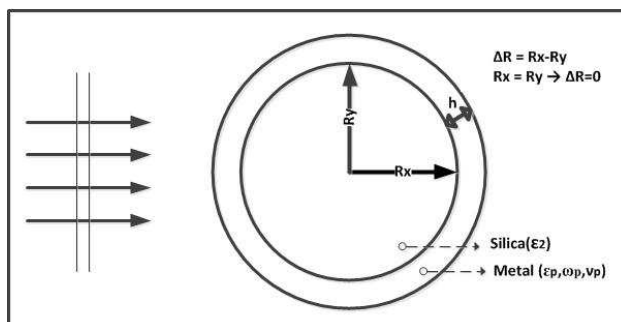


Figure 1: Silica nanoparticle coated by a noble metal (basic model).

Table 1: ECS vs. frequency as metallic cover thickness ( $h$ ) changing gradually.

Curve No.	Rtotal	R <sub>Si</sub>	h	f (TH)	ECS (nm <sup>2</sup> )
1	43	38	5	468.75	7.126e-014
2	48	38	10	572.92	8.184e-014
3	53	38	15	625	8.568e-014

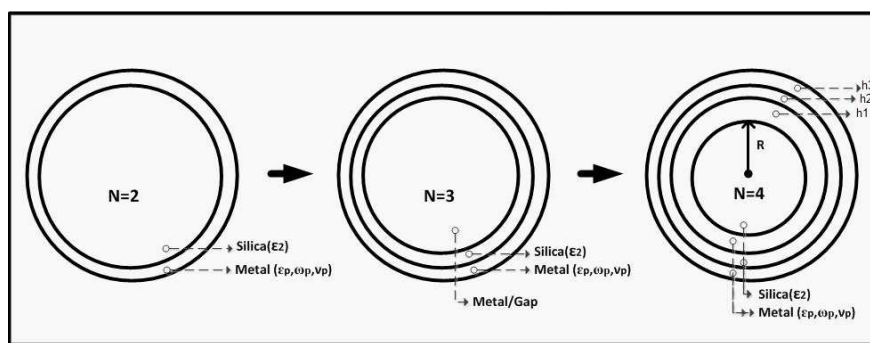


Figure 2: Modeling the effect of layer's numbers (from  $N = 2$  to  $N = 4$ ).

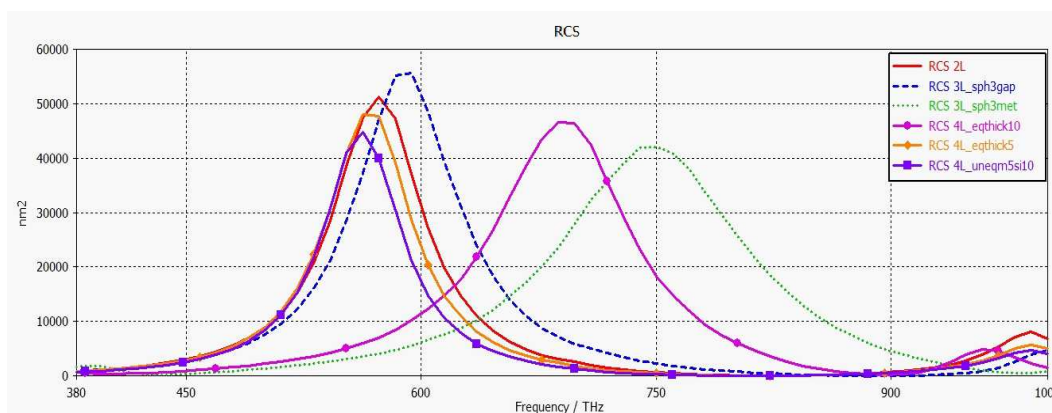


Figure 3: RCS vs. frequency for different number of layers.

corresponding Drude parameters are  $\varepsilon_\infty = 5$ ,  $\omega_p = 1.4418e + 016$  [rad/s],  $\nu_p = 1.56996e + 014$  [1/s].

As incident light (Figure 1), a plane wave is used to excite the structure. For direct extraction of the Extinction Cross Section (ECS) the broadband scattering response is extracted. The ECS of antenna element peaks at its resonance frequency, since an increase in antenna current result in greater scattering and absorption.

### 3.1. Metal Shell Thickness

At first, we try to study the effect of changing metallic cover thickness ( $h$ ). Based on final results (Table 1), an increase in  $h$  (while internal dielectric radius ( $R_{Si}$ ) is constant) will cause an increase in resonant frequency and ECS.

### 3.2. Number of Layers

Number of layers is another important parameter which its effect has been considered. But, in this section we deal with multilayer nano-sphere (Figure 2). For  $N = 2$ , silica is covered by metal. When  $N = 3$ , silica is sandwiched among outer metal layer and inner metal/gap one. Finally, for

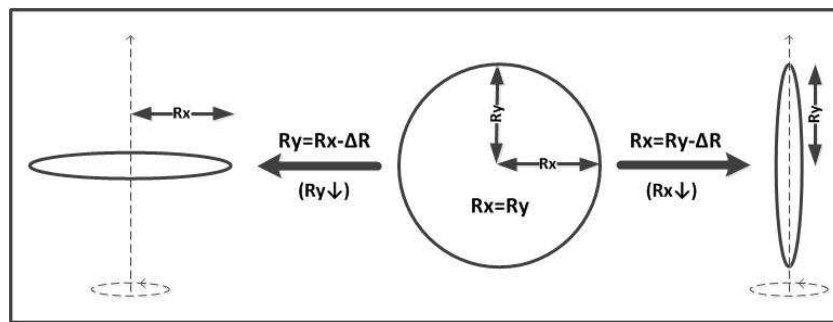


Figure 4: Transform from sphere to spheroid by a gradual increase in  $\Delta R$ .

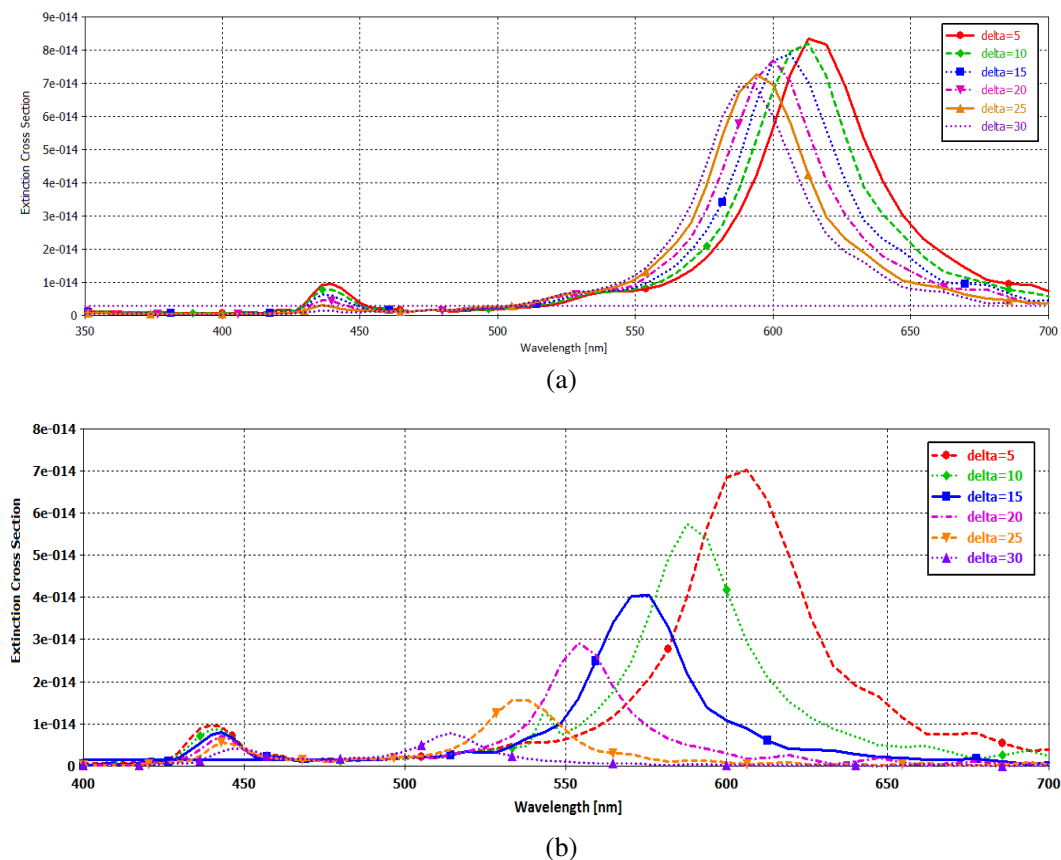


Figure 5: Extinction cross section (ECS) vs. wavelength, (a) oblate, (b) prolate spheroid.

$N = 4$ , 2 silica layers are separated by an inner metallic layer among them and the whole set is also covered by metal as outer layer.

As it is shown in Figure 3, one can see for  $N = 3$ , the added inner layer will cause increase in resonant frequency for both case of gap or metal. Of course, when silica shell is sandwiched by metal in both sides, a considerable enhancement occurs. When  $N$  is 4, frequency increased and ECS decreased for the case of  $\Delta h = 10$  (equal thickness of 10), but there is a small difference among the results of two other cases (equal thickness of 5, and unequal thickness) with what we see in  $N = 2$ . It is clear that size has higher effect than number of layers.

### 3.3. Gradual Transformation from Sphere to Ellipsoid

Ellipsoidal particles with two principal axes of the same length are known as spheroids. Based on Figure 4, rotation of the ellipse about the major axis generates a prolate spheroid (cigar-shaped) and rotation about the minor axis generates an oblate spheroid (disk-shaped).

As shown by Figure 5, a gradual increase in  $\Delta R$  and transforming from sphere to ellipsoid will cause an increase in resonant frequency (or a decrease in resonant wavelength) and also a reduction in ECS, for both oblate and prolate configurations. By a comparison among these two, we can see that reduction in resonant wavelength and ECS for transforming to prolate spheroid (Figure 5(a)) is more considerable than oblate one (Figure 5(b)). Also, the difference among two continuous steps is very greater in the case of prolate spheroid.

## 4. CONCLUSIONS

A judicious combination of dielectric and metallic materials can produce highly tunable compact optical antenna. These investigations give new insight into the number of layers and their thickness, and also change in symmetry. As an important result, one can see that introducing gradual asymmetry in nanoparticle shape from sphere to spheroid causes an improvement in response. Also, results show that how the thickness of metallic cover could change ECS and resonant frequency, which are two important outputs under study in this work.

## ACKNOWLEDGMENT

The authors have special thanks to Faculty of Micro-Electronic (FME) for financial support.

## REFERENCES

1. Novotny, L., "Optical antennas for enhanced light-matter interactions," Report, The Institute of Optics, University of Rochester, 2010.
2. Thomas, R., J. Kumar, R. S. Swathi, and K. G. Thomas, "Optical effects near metal nanostructures: Towards surface-enhanced spectroscopy," *Current Science*, Vol. 102, No. 1, Jan. 2012.
3. Brongersma, M., "Plasmonics engineering optical nanoantennas," *Nature Photonics*, Vol. 2, 2008.
4. Maier, S. A., *Plasmonics: Fundamentals and Applications*, Springer, 2007.

# Electromagnetic Equations in Curved Octonion Compounding Spaces

Zi-Hua Weng

School of Physics and Mechanical & Electrical Engineering  
Xiamen University, Xiamen 361005, China

**Abstract**— J. C. Maxwell adopted the quaternion to describe the electromagnetic theory, while A. Einstein introduced the curved 4-dimensional space-time to depict the gravitational field. Those methods inspire the scholars to bring into use the curved octonion space to study the physical features of electromagnetic and gravitational fields simultaneously. In the octonion space, the radius vector and the integral of field potential can be combined together to become the compounding radius vector. The latter can be considered as the radius vector of the octonion compounding space. In the octonion compounding space, the paper discusses the impact of the velocity and velocity curl on the movement of charged particles. In the curved octonion compounding space, the connection coefficient and curvature have the influence on the field strength, field source, angular momentum, and force etc.. It means that the space bending will exert directly an influence on the features of electromagnetic and gravitational fields.

## 1. INTRODUCTION

J. C. Maxwell was the first to adopt the two methods, the quaternion and vectorial terminology, to describe the electromagnetic theory. It leads the subsequent scholars to introduce the quaternion and octonion to depict the electromagnetic and gravitational fields [1]. Adopting the octonion enables the subsequent scholars to describe simultaneously the features of electromagnetic and gravitational fields, and to draw out the gravitational field equations as well as the electromagnetic field equations. The gravitational field equations are able to include the law of gravitation of Newton. And the electromagnetic field equations can cover the Maxwell's equations, although the direction of displacement current and the gauge equation both are different.

In the octonion space, the integral of field potential and the radius vector can be combined together to become the compounding radius vector, which can be considered as the radius vector of the octonion compounding space (one kind of function space). A. Einstein studied the some features of gravitational fields with the curved 4-dimensional space-time [2]. It spires the scholars to apply the curved octonion compounding space to depict simultaneously some features of the electromagnetic and gravitational fields [3].

The connection coefficient has an influence on the field potential, field strength, field source, power, and force etc. directly. From the definition of field source, the paper will obtain the field equations of electromagnetic and gravitational fields. The above means that the connection coefficient and the space curvature can impact the field equations directly.

## 2. QUATERNION COMPOUNDING SPACE

### 2.1. Flat Quaternion Compounding Space

The quaternion is suitable to describe the features of gravitational fields. In the quaternion space for gravitational fields, the quaternion basis vector is  $\{\mathbf{i}_i\}$ , with  $\mathbf{i}_0 = 1$ . The quaternion radius vector is  $\mathbb{R}_g(r^i) = \mathbf{i}_i r^i$ , the quaternion velocity is  $\mathbb{V}_g(v^i) = c \diamond \circ \mathbb{R}_g$ , the quaternion angular velocity is  $\mathbb{Y}_g(y^i) = \diamond \circ \mathbb{V}_g$ , and the quaternion angular acceleration is  $\mathbb{Z}_g(z^i) = -\diamond^* \circ \mathbb{Y}_g$ . Herein  $\circ$  denotes the quaternion multiplication.  $\diamond = \mathbf{i}_i(\partial/\partial r^i)$ .  $c = v^0$  is the speed of light.  $i, j, k, m = 0, 1, 2, 3$ .

In the gravitational field, there is one quaternion quantity  $\mathbb{X}_g(x^i)$ , which is the integral of field potential,  $\mathbb{A}_g(a^i) = \diamond \circ \mathbb{X}_g$ . The quaternion strength is  $\mathbb{B}_g(h^i) = \diamond \circ \mathbb{A}_g$ , and the quaternion source is  $\mathbb{S}_g(s^i) = -\diamond^* \circ \mathbb{B}_g/\mu_g$ . Herein the gravitational constant is  $\mu_g < 0$ . By Comparison with the Newtonian gravitational theory, it finds that,  $\mathbb{S}_g = m\mathbb{V}_g$ , with  $m$  being the mass density.

In the quaternion space for gravitational fields, the quaternion radius vector  $\mathbb{R}_g$  and the quaternion physical quantity  $\mathbb{X}_g$  can be combined together to become the quaternion compounding radius vector,  $\mathbb{R}_g = \mathbb{R}_g + k_{rx}\mathbb{X}_g$ , or the quaternion compounding physical quantity,  $\mathbb{X}_g = \mathbb{X}_g + K_{rx}\mathbb{R}_g$ . The quaternion compounding radius vector  $\mathbb{R}_g$  can be considered as the radius vector in the quaternion compounding space (function space). In the quaternion compounding space, the quaternion

compounding field potential is  $\bar{\mathbb{A}}_g = \diamond \circ \bar{\mathbb{X}}_g = \mathbb{A}_g + (K_{rx}/c)\nabla_g$ , the quaternion compounding field strength is  $\bar{\mathbb{B}}_g = \diamond \circ \bar{\mathbb{A}}_g = \mathbb{B}_g + (K_{rx}/c)\mathbb{Y}_g$ , and the quaternion compounding field source is  $\bar{\mathbb{S}}_g = -\diamond^* \circ \bar{\mathbb{B}}_g/\mu_g$ . Herein  $\bar{\mathbb{S}}_g = m\nabla_g$ .  $\bar{\mathbb{S}}_g = \mathbb{S}_g + \mathbb{Z}_g/(\mu_g k_{rx})$ .  $\mathbb{Z}_g = (\mu_g k_{rx}^2 mc)\mathbb{A}_g$ .  $K_{rx} = 1/k_{rx}$ .

### 2.2. Curved Quaternion Compounding Space

In the curved space, the quaternion compounding radius vector is  $\bar{\mathbb{R}}_g(\bar{u}^i)$ , the coordinate is  $\bar{u}^i$ , and the tangent frame quaternion is  $\{\mathbf{e}_i\}$ . And its space-time interval is defined as,

$$d\bar{R}^2 = d\bar{\mathbb{R}}_g \odot d\bar{\mathbb{R}}_g = g_{ij}d\bar{u}^i d\bar{u}^j, \tag{1}$$

where the metric coefficient is  $g_{ij} = \mathbf{e}_i \odot \mathbf{e}_j$ . The tangent frame quaternion is  $\mathbf{e}_j = \partial\bar{\mathbb{R}}_g/\partial\bar{u}^j$ , with  $\mathbf{e}_0$  being the scalar.  $\odot$  denotes the scalar product of quaternions.  $u^0 = ct$ , and  $t$  is the time.

In the flat quaternion compounding space, the quaternion product  $\bar{\mathbb{G}} \circ \bar{\mathbb{H}}$  of two quaternions,  $\bar{\mathbb{G}}(\bar{g}^i)$  and  $\bar{\mathbb{H}}(\bar{h}^j)$ , consists of the scalar part  $\bar{\mathbb{G}} \odot \bar{\mathbb{H}}$  and the vector part  $\bar{\mathbb{G}} \otimes \bar{\mathbb{H}}$ . According to the definition of quaternion orthogonality, when  $\bar{\mathbb{G}} \odot \bar{\mathbb{H}} = 0$ ,  $\bar{\mathbb{G}}$  and  $\bar{\mathbb{H}}$  are on an orthogonal state.

In the curved space, the quaternion compounding physical quantity  $\bar{\mathbb{A}}_1$  in the tangent space  $\mathbb{T}_1$  of one point  $\mathbb{M}_1$  on the quaternion manifold can be decomposed in the tangent space  $\mathbb{T}_2$  of the point  $\mathbb{M}_2$  around  $\mathbb{M}_1$ . According to the definition of quaternion orthogonality,  $\bar{\mathbb{A}}_1$  can be decomposed as the projection part  $\bar{\mathbb{A}}_2$  in  $\mathbb{T}_2$  of  $\mathbb{M}_2$ , and the orthogonal part  $\bar{\mathbb{N}}_2$  being perpendicular to  $\mathbb{T}_2$ . On the basis of the quaternion parallel transport,  $\bar{\mathbb{A}}_2$  is parallel transported from  $\bar{\mathbb{A}}_1$ . For 1 rank contravariant tensor  $\bar{Y}^i(\mathbb{P})$  of one point  $\mathbb{P}$ , the component of the quaternion covariant derivation with respect to  $\bar{u}^k$  is,  $\nabla_k \bar{Y}^i = \partial\bar{Y}^i/\partial\bar{u}^k + \Gamma_{jk}^i \bar{Y}^j$ , and  $\Gamma_{jk}^i$  being the connection coefficient.

### 3. EQUATIONS IN THE GRAVITATIONAL FIELD

In the curved quaternion compounding space, the gravitational strength and gravitational source can be derived from the gravitational potential and quaternion operator. Expanding the definition of gravitational source will infer the field equations, including the law of gravitation.

The compounding gravitational potential  $\bar{\mathbb{A}}_g(\bar{a}^0, \bar{a}^1, \bar{a}^2, \bar{a}^3)$  is defined as,

$$\bar{\mathbb{A}}_g = \diamond \circ \bar{\mathbb{X}}_g = \diamond \odot \bar{\mathbb{X}}_g + \diamond \otimes \bar{\mathbb{X}}_g, \tag{2}$$

where  $\bar{\mathbb{X}}_g = \bar{x}^j \mathbf{e}_j$ .  $\diamond \bar{x}^i = \mathbf{e}^k \nabla_k \bar{x}^i$ , with  $\mathbf{e}^j = g^{ij} \mathbf{e}_j$  and  $g^{ij} = (g_{ij})^{-1}$ . The scalar part  $\diamond \odot \bar{\mathbb{X}}_g$  of  $\bar{\mathbb{A}}_g$  is  $\bar{a}^0 \mathbf{e}_0 = \bar{a}$ , while the vector part  $\diamond \otimes \bar{\mathbb{X}}_g$  of  $\bar{\mathbb{A}}_g$  is  $\bar{a}^p \mathbf{e}_p = \bar{\mathbf{a}}$ .  $p, q = 1, 2, 3$ .

The compounding gravitational strength  $\bar{\mathbb{B}}_g(\bar{k}^0, \bar{k}^1, \bar{k}^2, \bar{k}^3)$  is written as,

$$\bar{\mathbb{B}}_g = \diamond \circ \bar{\mathbb{A}}_g = \diamond \odot \bar{\mathbb{A}}_g + \diamond \otimes \bar{\mathbb{A}}_g, \tag{3}$$

where the scalar part of  $\bar{\mathbb{B}}_g$  is  $\diamond \odot \bar{\mathbb{A}}_g = \bar{k}^0 \mathbf{e}_0$ , and the vector part of  $\bar{\mathbb{B}}_g$  is  $\diamond \otimes \bar{\mathbb{A}}_g = \bar{k}^p \mathbf{e}_p$ . The gauge equation is chosen as,  $\bar{k}^0 = 0$ , in the gravitational field. The vector part of the gravitational strength can be rewritten as two parts,  $\bar{k}^p \mathbf{e}_p = \bar{\mathbf{g}}/c + \bar{\mathbf{b}}$ . The first part,  $\bar{\mathbf{g}}/c = \nabla_0 \bar{\mathbf{a}} + \nabla \bar{a}$ , is related with the acceleration, while the second part,  $\bar{\mathbf{b}} = \nabla \times \bar{\mathbf{a}}$ , is relevant to the angular velocity of rotation.  $\nabla \bar{a} = (\mathbf{e}^q \nabla_q) \circ (\bar{a}^0 \mathbf{e}_0)$ .  $\nabla \times \bar{\mathbf{a}} = (\mathbf{e}^q \nabla_q) \otimes (\bar{a}^p \mathbf{e}_p)$ .  $\nabla_0 \bar{\mathbf{a}} = \nabla_0 (\bar{a}^p \mathbf{e}_p)$ .  $\nabla = \mathbf{e}^q \nabla_q$ .

The compounding gravitational source  $\bar{\mathbb{S}}_g(\bar{s}^0, \bar{s}^1, \bar{s}^2, \bar{s}^3)$  is written as,

$$-\mu \bar{\mathbb{S}} = -(\mu_g \bar{\mathbb{S}}_g - \bar{\mathbb{B}}_g^* \circ \bar{\mathbb{B}}_g/c) = (\diamond + \bar{\mathbb{B}}_g/c)^* \circ \bar{\mathbb{B}}_g, \tag{4}$$

where  $-\mu_g \bar{\mathbb{S}}_g = \diamond^* \circ \bar{\mathbb{B}}_g = \diamond^* \odot \bar{\mathbb{B}}_g + \diamond^* \otimes \bar{\mathbb{B}}_g$ . The scalar part of  $\bar{\mathbb{S}}_g$  is  $-\diamond^* \odot \bar{\mathbb{B}}_g/\mu_g = \bar{s}^0 \mathbf{e}_0$ , and the vector part of  $\bar{\mathbb{S}}_g$  is  $-\diamond^* \otimes \bar{\mathbb{B}}_g/\mu_g = \bar{s}^p \mathbf{e}_p$ .  $\mu$  and  $\mu_g$  are the coefficients. Expanding the above will conclude the gravitational field equations.

The angular momentum, energy-torque, and power-force can be defined from the linear momentum and the quaternion operator  $\diamond$ . The force includes the inertial force, gravity, and extra force term caused by the space bending etc..

The quaternion compounding angular momentum  $\bar{\mathbb{L}}_g(\bar{l}^0, \bar{l}^1, \bar{l}^2, \bar{l}^3)$  can be defined as,

$$\bar{\mathbb{L}}_g = \bar{\mathbb{R}}_g \circ \bar{\mathbb{P}}_g = \bar{\mathbb{R}}_g \odot \bar{\mathbb{P}}_g + \bar{\mathbb{R}}_g \otimes \bar{\mathbb{P}}_g, \tag{5}$$

where the compounding linear momentum of field source is  $\bar{\mathbb{P}}_g = \mu \bar{\mathbb{S}}/\mu_g$ . The scalar part of  $\bar{\mathbb{L}}_g$  is  $\bar{\mathbb{R}}_g \odot \bar{\mathbb{P}}_g = \bar{l}^0 \mathbf{e}_0$ , and the vector part of  $\bar{\mathbb{L}}_g$  is  $\bar{\mathbb{R}}_g \otimes \bar{\mathbb{P}}_g = \bar{l}^p \mathbf{e}_p$ . For the case of many field sources, the angular momentum may be complicated because of the accumulation.

The quaternion compounding energy-torque  $\bar{\mathbb{W}}_g(\bar{w}^0, \bar{w}^1, \bar{w}^2, \bar{w}^3)$  is defined as

$$\bar{\mathbb{W}}_g = c(\diamond + \bar{\mathbb{B}}_g/c) \circ \bar{\mathbb{L}}_g = c(\diamond + \bar{\mathbb{B}}_g/c) \odot \bar{\mathbb{L}}_g + c(\diamond + \bar{\mathbb{B}}_g/c) \otimes \bar{\mathbb{L}}_g, \quad (6)$$

where the scalar part of  $\bar{\mathbb{W}}_g$  is  $c(\diamond + \bar{\mathbb{B}}_g/c) \odot \bar{\mathbb{L}}_g = \bar{w}^0 \mathbf{e}_0$ , and is relevant to the energy. The vector part of  $\bar{\mathbb{W}}_g$  is  $c(\diamond + \bar{\mathbb{B}}_g/c) \otimes \bar{\mathbb{L}}_g = \bar{w}^p \mathbf{e}_p$ , and is related with the torque.

The quaternion compounding power-force  $\bar{\mathbb{N}}_g(\bar{n}^0, \bar{n}^1, \bar{n}^2, \bar{n}^3)$  is written as

$$\bar{\mathbb{N}}_g = c(\diamond + \bar{\mathbb{B}}_g/c)^* \circ \bar{\mathbb{W}}_g = c(\diamond + \bar{\mathbb{B}}_g/c)^* \odot \bar{\mathbb{W}}_g + c(\diamond + \bar{\mathbb{B}}_g/c)^* \otimes \bar{\mathbb{W}}_g, \quad (7)$$

where the scalar part of  $\bar{\mathbb{N}}_g$  is  $c(\diamond + \bar{\mathbb{B}}_g/c)^* \odot \bar{\mathbb{W}}_g = \bar{n}^0 \mathbf{e}_0$ , and is relevant to the power as well as the mass continuity equation. The vector part of  $\bar{\mathbb{N}}_g$  is  $c(\diamond + \bar{\mathbb{B}}_g/c)^* \otimes \bar{\mathbb{W}}_g = \bar{n}^p \mathbf{e}_p$ , and is related with the force in the gravitational field.

In the curved quaternion compounding space for gravitational fields, the compounding force is,  $\bar{\mathbf{f}} = -(\bar{n}^p \mathbf{e}_p)/(2c)$ . Herein the force  $\bar{\mathbf{f}}$  includes the inertial force, gravity, gradient of energy, and extra force term caused by the space bending etc.. The force  $\bar{\mathbf{f}}$  can be impacted by the gravitational potential  $\bar{\mathbb{A}}_g$  etc.. And the extra force term is related with the connection coefficient etc..

## 4. OCTONION COMPOUNDING SPACE

### 4.1. Flat Octonion Compounding Space

The octonion can be separated into two components, the quaternion and the  $S$ -quaternion. The quaternion is suitable to describe the feature of gravitational fields, while the  $S$ -quaternion is applied to depict the property of electromagnetic fields.

In the  $S$ -quaternion space for electromagnetic fields, the vector basis is  $\{\mathbf{I}_i\}$ . The  $S$ -quaternion radius vector is  $\mathbb{R}_e(R^i) = \mathbf{I}_i R^i$ , the  $S$ -quaternion velocity is  $\mathbb{V}_e(V^i) = c \diamond \circ \mathbb{R}_e$ , the  $S$ -quaternion angular velocity is  $\mathbb{Y}_e(Y^i) = \diamond \circ \mathbb{V}_e$ , and the  $S$ -quaternion angular acceleration is  $\mathbb{Z}_e(Z^i) = -\diamond^* \circ \mathbb{Y}_e$ . In the electromagnetic field, the  $S$ -quaternion physical quantity is  $\mathbb{X}_e(X^i)$ , which is the integral of  $S$ -quaternion field potential, that is  $\mathbb{A}_e(A^i) = \diamond \circ \mathbb{X}_e$ . The  $S$ -quaternion field strength is  $\mathbb{B}_e(H^i) = \diamond \circ \mathbb{A}_e$ , and  $S$ -quaternion field source is  $\mathbb{S}_e(S^i) = -\diamond^* \circ \mathbb{B}_e/\mu_e$ . Herein the electromagnetic constant is  $\mu_e > 0$ .  $\circ$  denotes the octonion multiplication. By comparison with the classical electromagnetic theory, there is  $\mathbb{S}_e = q \mathbb{V}_e$ , with  $q$  being the density of electric charge.

In the octonion space, the octonion radius vector is,  $\mathbb{R} = \mathbb{R}_g + k_{eg} \mathbb{R}_e = \mathbf{i}_0 \circ (r^i + k_{eg} R^i \mathbf{I}_0)$ , with  $k_{eg}$  being the coefficient. The radius vector  $\mathbb{R}_g$  in the quaternion space is independent of the radius vector  $\mathbb{R}_e$  in the  $S$ -quaternion space. In the  $S$ -quaternion space for the electromagnetic field, the  $S$ -quaternion radius vector  $\mathbb{R}_e$  and the  $S$ -quaternion physical quantity  $\mathbb{X}_e$  can be combined together to become the  $S$ -quaternion compounding radius vector  $\bar{\mathbb{R}}_e = \mathbb{R}_e + k_{rx} \mathbb{X}_e$ , or the  $S$ -quaternion compounding physical quantity  $\bar{\mathbb{X}}_e = \mathbb{X}_e + K_{rx} \mathbb{R}_e$ . The  $S$ -quaternion compounding radius vector can be considered as the radius vector of the  $S$ -quaternion compounding space (function space). In the  $S$ -quaternion compounding space for the electromagnetic field, the  $S$ -quaternion compounding field potential is  $\bar{\mathbb{A}}_e = \diamond \circ \bar{\mathbb{X}}_e = \mathbb{A}_e + (K_{rx}/c) \mathbb{V}_e$ , the  $S$ -quaternion compounding field strength is  $\bar{\mathbb{B}}_e = \diamond \circ \bar{\mathbb{A}}_e = \mathbb{B}_e + (K_{rx}/c) \mathbb{Y}_e$ , and  $S$ -quaternion compounding field source is  $\bar{\mathbb{S}}_e = -\diamond^* \circ \bar{\mathbb{B}}_e/\mu_e$ . Herein  $\bar{\mathbb{S}}_e = q \bar{\mathbb{V}}_e$ .  $\bar{\mathbb{S}}_e = \mathbb{S}_e + \mathbb{Z}_e/(\mu_e k_{rx})$ .  $\mathbb{Z}_e = (\mu_e k_{rx}^2 q c) \mathbb{A}_e$ .

Further the octonion radius vector  $\mathbb{R}$  and the octonion physical quantity  $\mathbb{X}$  can be combined together to become the octonion compounding radius vector,  $\bar{\mathbb{R}} = \mathbb{R} + k_{rx} \mathbb{X} = \bar{\mathbb{R}}_g + k_{eg} \bar{\mathbb{R}}_e$ , or the octonion compounding physical quantity,  $\bar{\mathbb{X}} = \mathbb{X} + K_{rx} \mathbb{R} = \bar{\mathbb{X}}_g + k_{eg} \bar{\mathbb{X}}_e$ .

### 4.2. Curved Octonion Compounding Space

In the curved octonion compounding space, the octonion compounding radius vector is  $\bar{\mathbb{R}}(\bar{u}^i, \bar{U}^j) = \bar{\mathbb{R}}_g(\bar{u}^i) + k_{eg} \bar{\mathbb{R}}_e(\bar{U}^j)$ . In the quaternion compounding space, the radius vector is  $\mathbb{R}_g(\bar{u}^i)$ , and the tangent frame quaternion is  $\{\mathbf{e}_i\}$ . In the  $S$ -quaternion compounding space, the radius vector is  $\mathbb{R}_e(\bar{U}^j)$ , and the tangent frame  $S$ -quaternion is  $\{\mathbf{E}_i\}$ . The radius vectors in the quaternion and  $S$ -quaternion compounding spaces can be combined together to become the octonion compounding radius vector  $\bar{\mathbb{R}}$ . The latter can be written as,  $\bar{\mathbb{R}} = \bar{u}^s \mathbf{e}_s$ . Herein  $\bar{u}^{j+4} = k_{eg} \bar{U}^j$  and  $\mathbf{e}_{j+4} = \mathbf{E}_j$ .  $u^0 = ct$ ,  $c$  is the speed of light, and  $t$  is the time.  $r, s, t, u = 0, 1, 2, 3, 4, 5, 6, 7$ .

The space-time interval of the octonion compounding space is,

$$d\bar{R}^2 = d\bar{\mathbb{R}} \odot d\bar{\mathbb{R}} = g_{rs} d\bar{u}^r d\bar{u}^s, \quad (8)$$

where the metric coefficient is  $g_{rs} = \mathbf{e}_r \odot \mathbf{e}_s$ . The tangent frame octonion is  $\mathbf{e}_r = \partial \bar{\mathbb{R}} / \partial \bar{u}^r$ , with  $\mathbf{e}_0$  being the scalar.  $\odot$  denotes the scalar product of octonions.

In the curved octonion compounding space, the octonion product  $\bar{\mathbb{G}} \circ \bar{\mathbb{H}}$  of two octonions,  $\bar{\mathbb{G}}(\bar{g}^r)$  and  $\bar{\mathbb{H}}(\bar{h}^s)$ , consists of the scalar part  $\bar{\mathbb{G}} \odot \bar{\mathbb{H}}$  and the vector part  $\bar{\mathbb{G}} \otimes \bar{\mathbb{H}}$ . According to the definition of octonion orthogonality, when  $\bar{\mathbb{G}} \odot \bar{\mathbb{H}} = 0$ ,  $\bar{\mathbb{G}}$  and  $\bar{\mathbb{H}}$  are on an orthogonal state.

The octonion compounding quantity  $\bar{\mathbb{A}}_1$  in the tangent space  $\mathbb{T}_1$  of one point  $\mathbb{M}_1$  on the octonion manifold can be disassembled in the tangent space  $\mathbb{T}_2$  of the point  $\mathbb{M}_2$  near  $\mathbb{M}_1$ . According to the definition of octonion orthogonality,  $\bar{\mathbb{A}}_1$  can be separated into the projection part  $\bar{\mathbb{A}}_2$  in  $\mathbb{T}_2$  of  $\mathbb{M}_2$ , and the orthogonal part  $\bar{\mathbb{N}}_2$  being perpendicular to  $\mathbb{T}_2$ . On the basis of the definition of octonion parallel transport,  $\bar{\mathbb{A}}_2$  is parallel transported from  $\bar{\mathbb{A}}_1$ . For 1 rank contravariant tensor  $\bar{Y}^s(\mathbb{Q})$  of one point  $\mathbb{Q}$ , the octonion covariant derivation is,  $\nabla_t \bar{Y}^s = \partial \bar{Y}^s / \partial \bar{u}^t + \Gamma_{rt}^s \bar{Y}^r$ , and  $\Gamma_{rt}^s$  being the connection coefficient.

### 5. EQUATIONS IN THE ELECTROMAGNETIC FIELD

In the curved octonion compounding space, the electromagnetic strength and the electromagnetic source can be defined from the electromagnetic potential and quaternion operator. Expanding the definition of field source deduces the field equations, including Maxwell's equations.

The octonion compounding field potential,  $\bar{\mathbb{A}} = \bar{\mathbb{A}}_g + k_{eg} \bar{\mathbb{A}}_e$ , is defined as,

$$\bar{\mathbb{A}} = \diamond \circ \bar{\mathbb{X}} = \diamond \odot \bar{\mathbb{X}} + \diamond \otimes \bar{\mathbb{X}}, \tag{9}$$

where the compounding electromagnetic potential is  $\bar{\mathbb{A}}_e(\bar{A}^0, \bar{A}^1, \bar{A}^2, \bar{A}^3)$ . The octonion compounding physical quantity is  $\bar{\mathbb{X}} = \bar{\mathbb{X}}_g + k_{eg} \bar{\mathbb{X}}_e$ . The  $S$ -quaternion compounding physical quantity is  $\bar{\mathbb{X}}_e = \bar{X}^j \mathbf{E}_j$ . The ‘scalar’ part  $\diamond \odot \bar{\mathbb{X}}_e$  of  $\bar{\mathbb{A}}_e$  is  $\bar{\mathbb{A}}_q = \bar{A}^0 \mathbf{E}_0$ , and the ‘vector’ part  $\diamond \otimes \bar{\mathbb{X}}_e$  of  $\bar{\mathbb{A}}_e$  is  $\bar{\mathbb{A}} = \bar{A}^p \mathbf{E}_p$ .  $\diamond \bar{X}^p = \mathbf{e}^k \nabla_k \bar{X}^p$ , with  $\mathbf{e}^i = g^{ij} \mathbf{e}_j$  and  $g^{us} = (g_{us})^{-1}$ .

The octonion compounding field strength,  $\bar{\mathbb{B}} = \bar{\mathbb{B}}_g + k_{eg} \bar{\mathbb{B}}_e$ , is written as,

$$\bar{\mathbb{B}} = \diamond \circ \bar{\mathbb{A}} = \diamond \odot \bar{\mathbb{A}} + \diamond \otimes \bar{\mathbb{A}}, \tag{10}$$

where the compounding electromagnetic strength is  $\bar{\mathbb{B}}_e(\bar{K}^i)$ . The ‘scalar’ part of  $\bar{\mathbb{B}}_e$  is  $\diamond \odot \bar{\mathbb{A}}_e = \bar{K}^0 \mathbf{E}_0$ , while the ‘vector’ part of  $\bar{\mathbb{B}}_e$  is  $\diamond \otimes \bar{\mathbb{A}}_e = \bar{K}^p \mathbf{E}_p$ . The gauge equation for the electromagnetic field is chosen as,  $\bar{K}^0 = 0$ . The ‘vector’ part of electromagnetic strength can be separated into two components, that is,  $\bar{K}^p \mathbf{E}_p = \bar{\mathbf{E}}/c + \bar{\mathbf{B}}$ . The first component,  $\bar{\mathbf{E}}/c = \nabla_0 \bar{\mathbf{A}} + \nabla \circ \bar{\mathbf{A}}_q$ , is the electric field intensity, while the second component,  $\bar{\mathbf{B}} = \nabla \times \bar{\mathbf{A}}$ , is the magnetic flux density.  $\nabla \circ \bar{\mathbf{A}}_q = (\mathbf{e}^p \nabla_p) \circ (\bar{A}^0 \mathbf{E}_0)$ .  $\nabla \times \bar{\mathbf{A}} = (\mathbf{e}^q \nabla_q) \otimes (\bar{A}^p \mathbf{E}_p)$ .  $\nabla_0 \bar{\mathbf{A}} = \nabla_0 (\bar{A}^p \mathbf{E}_p)$ .

The octonion compounding field source,  $\mu \bar{\mathbb{S}} = \mu_g \bar{\mathbb{S}}_g + k_{eg} \mu_e \bar{\mathbb{S}}_e$ , is written as,

$$-\mu \bar{\mathbb{S}} = -(\mu_g \bar{\mathbb{S}}_g + k_{eg} \mu_e \bar{\mathbb{S}}_e - \bar{\mathbb{B}}^* \circ \bar{\mathbb{B}}/c) = (\diamond + \bar{\mathbb{B}}/c)^* \circ \bar{\mathbb{B}}, \tag{11}$$

where  $-\mu_g \bar{\mathbb{S}}_g = \diamond^* \circ \bar{\mathbb{B}}_g = \diamond^* \odot \bar{\mathbb{B}}_g + \diamond^* \otimes \bar{\mathbb{B}}_g$ , and  $-\mu_e \bar{\mathbb{S}}_e = \diamond^* \circ \bar{\mathbb{B}}_e = \diamond^* \odot \bar{\mathbb{B}}_e + \diamond^* \otimes \bar{\mathbb{B}}_e$ . The compounding electromagnetic field source is  $\bar{\mathbb{S}}_e(\bar{S}^i)$ . The ‘scalar’ part of  $\bar{\mathbb{S}}_e$  is,  $-\diamond^* \odot \bar{\mathbb{B}}_e/\mu_e = \bar{S}^0 \mathbf{E}_0$ , while the ‘vector’ part of  $\bar{\mathbb{S}}_e$  is,  $-\diamond^* \otimes \bar{\mathbb{B}}_e/\mu_e = \bar{S}^p \mathbf{E}_p$ .  $\mu$  and  $\mu_e$  are the coefficients. Expanding the above yields the electromagnetic field equations and the gravitational field equations.

The angular momentum, energy-torque, and power-force can be defined from the linear momentum and the quaternion operator  $\diamond$ . The force includes the inertial force, gravity, Lorentz force, Coulomb force, and extra force term caused by the space bending etc..

The octonion compounding angular momentum  $\bar{\mathbb{L}}_g(\bar{l}^i, \bar{L}^j)$  is written as,

$$\bar{\mathbb{L}} = \bar{\mathbb{R}} \circ \bar{\mathbb{P}} = \bar{\mathbb{R}} \odot \bar{\mathbb{P}} + \bar{\mathbb{R}} \otimes \bar{\mathbb{P}}, \tag{12}$$

where the linear momentum of field source is  $\bar{\mathbb{P}} = \mu \bar{\mathbb{S}}/\mu_g$ . The scalar part of  $\bar{\mathbb{L}}$  is  $\bar{\mathbb{R}} \odot \bar{\mathbb{P}} = \bar{l}^0 \mathbf{e}_0$ , while the vector part of  $\bar{\mathbb{L}}$  is  $\bar{\mathbb{R}} \otimes \bar{\mathbb{P}} = \bar{l}^p \mathbf{e}_p + \bar{L}^0 \mathbf{E}_0 + \bar{L}^p \mathbf{E}_p$ . For the case of many field sources, the angular momentum may be complicated because of the accumulation.

The octonion compounding energy-torque  $\bar{\mathbb{W}}(\bar{w}^i, \bar{W}^j)$  is defined as,

$$\bar{\mathbb{W}} = c(\diamond + \bar{\mathbb{B}}/c) \circ \bar{\mathbb{L}} = c(\diamond + \bar{\mathbb{B}}/c) \odot \bar{\mathbb{L}} + c(\diamond + \bar{\mathbb{B}}/c) \otimes \bar{\mathbb{L}}, \tag{13}$$

where the scalar part of  $\bar{\mathbb{W}}$  is  $c(\diamond + \bar{\mathbb{B}}/c) \odot \bar{\mathbb{L}} = \bar{w}^0 \mathbf{e}_0$ , and is relevant to the energy. The vector part is  $c(\diamond + \bar{\mathbb{B}}/c) \otimes \bar{\mathbb{L}} = \bar{w}^p \mathbf{e}_p + \bar{W}^0 \mathbf{E}_0 + \bar{W}^p \mathbf{E}_p$ . The term  $\bar{w}^p \mathbf{e}_p$  is related with the torque.

The octonion compounding power-force  $\bar{N}_g(\bar{n}^i, \bar{N}^j)$  is,

$$\bar{N} = c(\diamond + \bar{\mathbb{B}}/c)^* \circ \bar{W} = c(\diamond + \bar{\mathbb{B}}/c)^* \odot \bar{W} + c(\diamond + \bar{\mathbb{B}}/c)^* \otimes \bar{W}, \quad (14)$$

where the scalar part of  $\bar{N}$  is  $c(\diamond + \bar{\mathbb{B}}/c)^* \odot \bar{W} = \bar{n}^0 \mathbf{e}_0$ , and the vector part is  $c(\diamond + \bar{\mathbb{B}}/c)^* \otimes \bar{W} = \bar{n}^p \mathbf{e}_p + \bar{N}^0 \mathbf{E}_0 + \bar{N}^p \mathbf{E}_p$ . The term  $\bar{n}^0 \mathbf{e}_0$  is relevant to the power, and the term  $\bar{n}^p \mathbf{e}_p$  is dealt with the force. The scalar term  $\bar{n}^0 \mathbf{e}_0$  and ‘scalar’ term  $\bar{N}^0 \mathbf{E}_0$  are related with the mass continuity equation and the current continuity equation respectively.

In the curved octonion compounding space, the force in the gravitational and electromagnetic fields is,  $\bar{\mathbf{f}} = -(\bar{n}^p \mathbf{e}_p)/(2c)$ . Herein the force  $\bar{\mathbf{f}}$  includes the inertial force, gravity, Lorentz force, Coulomb force, gradient of energy, and extra force term caused by the space bending etc.. The force  $\bar{\mathbf{f}}$  can be impacted by the gravitational potential  $\mathbb{A}_g$  and the electromagnetic potential  $\mathbb{A}_e$ . And the extra force term is related with the connection coefficient and curvature etc..

Further referring to the process of Einstein’s General Relativity, the above equations in the curved octonion compounding space can be transferred similarly. In one equation, the physical quantity  $\mathbb{X}$  and its diverse derivations terms can be gathered to one side of the equal mark, while the radius vector  $\mathbb{R}$  and its diverse derivations terms to the other side. And the results reveal that the matter has an influence on the space bending.

## 6. CONCLUSIONS

In the curved octonion compounding space, there may exist many kinds of geometric structures and their connections. One or several of them should be suitable to describe the physical features of gravitational and electromagnetic fields.

The octonion space is able to depict simultaneously the physical features of gravitational and electromagnetic fields. By means of the concept of octonion orthogonality, the paper defines the octonion parallel transport in the curved octonion compounding space, which can be applied to depict the curvature and connection coefficient. The curved octonion compounding space will impact the physical quantities in the gravitational and electromagnetic fields, including the field potential, field strength, field source, angular momentum, energy, torque, power, and force etc..

## ACKNOWLEDGMENT

This project was supported partially by the National Natural Science Foundation of China under grant number 60677039.

## REFERENCES

1. Weng, Z.-H., “Electromagnetic and gravitational fields in the curved octonion spaces,” *PIERS Proceedings*, 1372–1376, Moscow, Russia, Aug. 19–23, 2012.
2. Beckwith, A., “Octonionic gravity formation, its connections to micro physics,” *Open Journal of Microphysics*, Vol. 1, No. 1, 13–18, 2011.
3. Tsagas, C. G., “Electromagnetic fields in curved spacetimes,” *Classical and Quantum Gravity*, Vol. 22, No. 2, 393–407, 2005.

# Design of Three-coupled Finline Bandpass Filter Using Full Wave Analysis

V. Madhusudana Rao<sup>1</sup> and B. Prabhakara Rao<sup>2</sup>

<sup>1</sup>Jawaharlal Nehru Technological University, Kakinada 533003, India

<sup>2</sup>Electronics and Communication Engineering Department

Jawaharlal Nehru Technological University, Kakinada 533003, India

**Abstract**— This paper presents a systematic procedure for designing a bandpass filter with wide bandwidth based on parallel coupled three finline structures. Normal mode parameters like propagation constants, characteristic impedance and equivalent voltage eigenvector of multiple coupled unilateral finlines are evaluated by using full wave modal analysis. A design graph for symmetric three unilateral finline structure is presented for the design of bandpass filter. A bandpass filter of order 3 having center frequency of 10 GHz with fractional bandwidth of 20% is designed and simulated in HFSS (High Frequency Structure Simulator).

## 1. INTRODUCTION

THE finline is a wave guiding structure which is increasingly used as millimeter wave component due to various advantages such as reducing size, weight and cost. At millimeter wave frequency the finline filter has been implemented in [1–3] which are mostly based on ladder/cascaded shape. Limited analysis is available on finline filter, which is based on coupled finline. This paper presents the design of bandpass filter using three coupled unilateral finlines. The advantage of present filter is low loss and wider bandwidth over the ladder/cascaded type filter. The unilateral coupled finline structures have been analyzed by many authors [4–8]. The full wave modal analysis for unilateral finline coupling section and an admittance inverter circuit are derived in [9, 10].

In this paper, a Chebyshev filter of order 3 with fractional bandwidth 20% has been designed on RT-duroid 5880<sup>TM</sup> substrate using unilateral three finlines. In Section 2, the numerical procedure based on the full wave modal analysis is formulated to compute all the frequency-dependent normal mode parameters for symmetric unilateral finlines. A bandpass filter is designed using full wave modal analysis is presented in Section 3.

## 2. ANALYSIS OF THREE COUPLED UNILATERAL FINLINES

The simulated 3 dimension model of three finline filter structure is shown in Figure 1. The cross-section of the symmetric unilateral finlines structure is assumed to be uniform in  $z$ -direction is shown in Figure 2. The enclosure is ridged metal waveguide.

### 2.1. Normal Mode Parameters

The propagation constants are evaluated by applying the Galerkin's method to the transformed Green's function matrix relating the voltage and electric fields at various boundaries of the structure

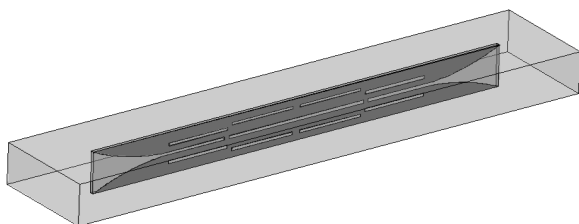


Figure 1. Model of three finline filter structure in HFSS software.

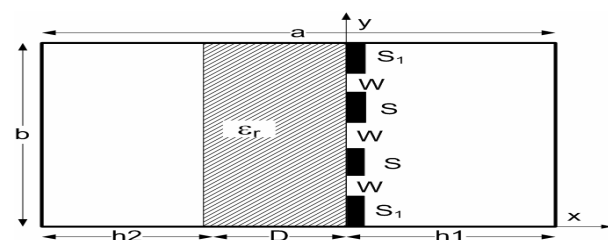


Figure 2. Cross section of three-finline structure.

and solving for the roots of the determinant of the Eq. (1) in [7].

$$\begin{aligned} \sum_{k=1}^{\infty} c_k \sum_{n=0}^{\infty} p_n G_{11} L_{2n}^k L_{2n}^m + \sum_{k=1}^{\infty} d_k \sum_{n=0}^{\infty} q_n G_{12} L_{1n}^k L_{2n}^m &= 0 \\ \sum_{k=1}^{\infty} c_k \sum_{n=1}^{\infty} p_n G_{21} L_{2n}^k L_{1n}^m + \sum_{k=1}^{\infty} d_k \sum_{n=1}^{\infty} q_n G_{22} L_{1n}^k L_{1n}^m &= 0 \end{aligned} \quad (1)$$

The set of basis functions used in this analysis are sinusoidal and expressed as follows:

$$V_z(y) = \frac{\cos \left[ 2(n-1)\pi \frac{(y-y_i)}{w_i} \right]}{\sqrt{1 - \left[ \frac{2(y-y_i)}{w_i} \right]^2}}, \quad V_y(y) = \frac{\sin \left[ 2n\pi \frac{(y-y_i)}{w_i} \right]}{\sqrt{1 - \left[ \frac{2(y-y_i)}{w_i} \right]^2}}.$$

where  $w_i$  being the width of the  $i$ th fin,  $y_i$  is the distance from origin to the center of  $i$ th fin.

## 2.2. Characteristics Impedances

Mode characteristics impedance of the coupled unilateral finlines lines are evaluated for all hybrid modes in a straight forward manner by calculating the power associated with a given finline for a given mode and the corresponding finline voltage as shown in [7]. The finline mode impedance is given by

$$Z_{lm} = \frac{(V_{lm})^2}{P_{lm}} \quad (2)$$

where  $V_{lm}$  is the modal voltage of the  $l$ th slot given by the integral of the electric field across the slot and  $P_{lm}$  is the partial modal power associated with the same slot when the  $m$ th normal mode is excited.

## 3. FILTER DESIGN

Figure 2 shows the port convention and connections of a resonator used to realize the band pass filter structure. The resonator consists of three parallel-coupled unilateral finlines approximately quarter wavelength long. In this paper, multi resonators are cascaded to achieve high rejections. The six port impedance matrix parameters for a section of three coupled finlines of length  $l$  are found from mode characteristic impedances, phase velocities and voltage ratios [7–11].

This three-coupled finline structure supports three dominant modes as OE, EE, and OO, which correspond to 1, 2 and 3, respectively [7–11]. Each mode has its own modal phase constant, eigenvoltage vector and characteristic impedance. The eigenvoltage matrix for symmetrical three line which have equal fin-width and spacing are given by

$$[Mv] = \begin{bmatrix} 1 & 1 & 1 \\ m_1 & 0 & m_3 \\ 1 & -1 & 1 \end{bmatrix}$$

Each vector of  $[M_v]$  is the eigenvoltage vector of the matrix product  $[L][C]$ . The matrix  $[M_v]$  can be used to derive the relation between port voltages and port currents.

$$\begin{bmatrix} V_A \\ V_B \end{bmatrix} = \begin{bmatrix} Z_A & Z_B \\ Z_B & Z_A \end{bmatrix} \begin{bmatrix} I_A \\ I_B \end{bmatrix}$$

where

$$\begin{aligned} [V_A] &= [V_1, V_2, V_3]^T, & [V_B] &= [V_4, V_5, V_6]^T, \\ [I_A] &= [I_1, I_2, I_3]^T, & [I_B] &= [I_4, I_5, I_6]^T \end{aligned}$$

And the impedance matrix  $[Z_A]$  and  $[Z_B]$  can be derived as

$$\begin{aligned} [Z_A] &= [M_V] \text{diag}[-jZ_{mi} \cot \theta_i] [M_V]^T \\ [Z_B] &= [M_V] \text{diag}[-jZ_{mi} \csc \theta_i] [M_V]^T \end{aligned}$$

Now  $\theta_i = \beta_i l$  with  $\beta_i$  is the phase constant of the  $i$ th mode,  $l$  the length of the coupled section, and  $Z_{mi}$  given by

$$Z_{mi} = \frac{Z_{oi}}{m_i^2 + 2} \quad (3)$$

where  $Z_{oi}$  is the characteristic impedance of  $i$ th mode. In Eq. (3),  $m_2 = 0$ . Comparing the two port  $Z$ -parameters of the circuit in Figure 3(b) with Figure 3(c), we obtain Eqs. (4), (5), (6).

$$m_1 Z_{m1} - m_3 Z_{m3} = J Z_A Z_B \quad (4)$$

$$m_1^2 Z_{m1} - m_3^2 Z_{m3} = Z_A (J^2 Z_A Z_B + 1) \quad (5)$$

$$Z_{m1} + Z_{m3} = Z_B (J^2 Z_A Z_B + 1) \quad (6)$$

According to [9] boundary conditions shown in Figure 3(a)

$$m_1 Z_{m1} \approx \left[ \frac{2 + \mu^2}{2\mu} \right] (Z_0/2) (J^2 Z_0^2 + J Z_0 + 1) \quad (7)$$

$$Z_{m3} \approx \left[ \frac{2 + \mu^2}{2\mu} \right] (Z_0/2) (J^2 Z_0^2 - J Z_0 + 1) \quad (8)$$

where

$$\mu = \frac{\sqrt{2 \left[ 2 (Z_{ee} - Z_{oo})^2 - Z_{oe} (Z_{oe} - Z_{ee} - Z_{oo}) - Z_{ee} Z_{oo} \right]}}{2Z_{ee} - Z_{oe} - Z_{oo}}$$

The value of  $JZ_O$  for each admittance inverter can be determined from the values of lumped circuit elements of the low pass prototype.

$$J_1 = \frac{1}{Z_0} \sqrt{\frac{\pi \Delta}{2g_1}} \quad (9)$$

$$J_n = \frac{1}{Z_0} \sqrt{\frac{\pi \Delta}{2g_{n-1}g_n}}, \quad \text{for } n = 2, 3, \dots, N, \quad (10)$$

$$J_{N+1} = \frac{1}{Z_0} \sqrt{\frac{\pi \Delta}{2g_N g_{N+1}}} \quad (11)$$

where  $\Delta = \frac{\omega_2 - \omega_1}{\omega_0}$ .

For  $N = 3$ , the values of  $g_1$  to  $g_{N+1}$  are given below using [12].

$$g_1 = 1.5963, \quad g_2 = 1.0967, \quad g_3 = 1.5963, \quad g_4 = 1.0000.$$

Once  $JZ_O$  is known the values of  $m_1 Z_{m1}$  and  $m_3 Z_{m3}$  for each coupled section can be known. The values of  $m_1 Z_{m1}$  and  $m_3 Z_{m3}$  for Section 1 are  $82.02 \Omega$  and  $64.69 \Omega$  respectively and for the Section 2 are  $37.65 \Omega$  and  $40.94 \Omega$  respectively. The designed data from the above is calculated and finally the filter is optimized. Both the data are shown in Table 1.

The design graph in Figure 4 for  $\epsilon_r = 2.2$  is used to determine the line width and line spacing of three coupled unilateral finlines at 10 GHz. Due to symmetry of filter only the width, spacing and

Table 1.

Dimensions	Designed Data		Optimized Data	
	Section 1	Section 2	Section 1	Section 2
$W$	0.650	0.680	0.750	0.750
$S$	1.320	2.370	1.400	2.400
$L$	9.592	10.164	12.970	13.413
$G$	1.975	2.033	1.076	1.633

All the dimensions are in mm.

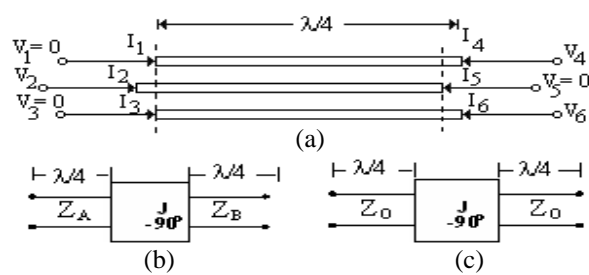


Figure 3. Reduction of a coupled three-finline section to a two-port network. (a) Coupled three-line section as a six-port network. (b) Equivalent admittance inverter. (c) Further approximated admittance inverter.

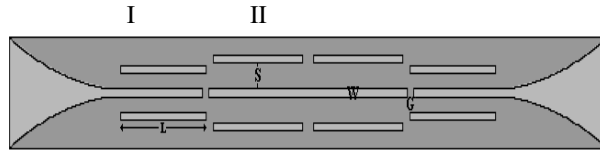


Figure 5. PCB layout of the three finline filter of order 3.

length of two sections has been mentioned here. Simulated model of three finline filter structure in HFSS Software is shown in Figure 4. The pattern of the designed filter has been shown in Figure 5.

The designed filter dimension has been simulated in HFSS. The return loss  $S_{11}$  and insertion loss  $S_{21}$  over a frequency band have been given in Figure 6. The insertion loss in passband is 0.5 dB and return loss is less than  $-10$  dB and stop band attenuation is 20 dB at 11.5 GHz frequency. If desired a tradeoff between the bandwidth and return losses can be achieved by further optimization of the filter dimensions. The above simulated results are not been compared with fabricated results due to lack of fabrication facilities in university.

#### 4. CONCLUSION

The most important advantage of three finline filter presented here is that it can be widely used in microwave and millimeter wave applications. Another advantage of this three coupled finline filter design is that the tight line spacing for designing wideband bandpass filter can be greatly relaxed. The design presented here, provides a relatively compact ultra wideband filter using coupled finline structure.

#### REFERENCES

1. Vahldieck, R. and W. J. R. Hofer, "Finline and metal insert filters with improved passband separation and increased stopband attenuation," *IEEE Trans. Microwave Theory & Tech.*, Vol. 33, No. 12, 1333–1339, Dec. 1985.
2. Vahldieck, R., "Quasi planar filters for millimeter-wave applications," *IEEE Trans. Microwave Theory & Tech.*, Vol. 37, No. 2, 324–334, Feb. 1989.
3. Bhat, B. and S. K. Koul, *Analysis, Design and Application of Finline*, Artech House, 1987.
4. Meier, P. J., "Integrated finline millimeter components," *IEEE Trans. Microwave Theory & Tech.*, Vol. 22, No. 12, 1209–1216, Dec. 1974.

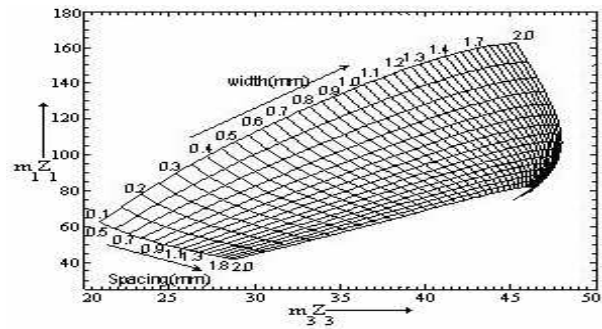


Figure 4. The bandpass filter design graph for a symmetric three unilateral finline structure. [Substrate dielectric constant  $\epsilon_r = 2.2$ , substrate thickness ( $D$ ) = 0.8 mm, frequency = 10 GHz].

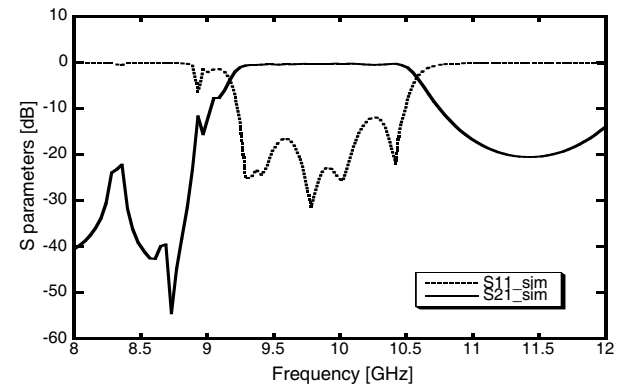


Figure 6. The simulated  $S$ -parameters response of three finline filter.

5. Syahkal, D. M. and J. B. Davies, “An accurate, unified solution to various finline structures, of phase constant, characteristic impedance and attenuation,” *IEEE Trans. Microwave Theory & Tech.*, Vol. 30, No. 11, 1854–1861, Nov. 1982.
6. Schmidt, L. P., C. Chang, and T. Itoh, “Spectral domain analysis of dominant and higher order modes in finlines,” *IEEE Trans. Microwave Theory & Tech.*, Vol. 28, No. 9, 981–985, Sep. 1980.
7. Luo, S., A. Biswas, and V. K. Tripathi, “Finline mutiport couplers,” *IEEE Trans. Microwave Theory & Tech.*, Vol. 42, No. 12, 2208–2215, Dec. 1994.
8. Biswas, A. and V. K. Tripathi, “Analysis and design of symmetric and multiple coupled finline couplers and filters,” *IEEE MTT-S Int. Microwave Symp. Dig.*, 403–406, 1990.
9. Kuo, J.-T. and E. Shih, “Wideband band-pass filter design with three line microstrip structures,” *IEEE MTT-S Int. Microwave Symposium Digest*, 1593–1596, 2001.
10. Awasthi, S., A. Biswas, and K. V. Srivastava, “Realization of broadband band-pass filter structure in suspended substrate using multi-conductor lines,” *Asia Pacific Microwave Conference’04*, New Delhi, Dec. 2004.
11. Srivastava, K. V., S. Awasthi, and A. Biswas, “Effect of anisotropy on effective dielectric constant and characteristic impedance of multi-port finlines,” *36th European Microwave Conference*, 107–110, Manchester, UK, Sep. 2006.
12. Pozar, D. M., *Microwave Engineering*, John Wiley & Sons, Inc., 2011.

# Perturbation Influence Analysis on the RCS of Dynamic Targets

Jia Liu, Min Su, Ning Fang, and Bao Fa Wang

Department of Electronic and Information Engineering  
Beijing University of Aeronautics and Astronautics, Beijing 100191, China

**Abstract**— The computation of the electromagnetic scattering for flying target usually has more practical meanings in stealth performance evaluation and weapon design. As a fast RCS prediction method with acceptable error, GRECO (Graphical Electromagnetic Computing) provides the possibility of broad-scale RCS computation for electrically large dynamic targets. In the actual environment, flying target (like aircraft) is influenced by the unpredictable factors, like atmospheric interference, fuselage shake and flying operation, etc.. These factors usually bring perturbation in both flight and radar view point, which are commonly not considered in the simulation. The high sensitivity of the target’s RCS in high frequency region indicates the potential influence on radar target characteristic simulated from the simulation results without perturbation consideration. In this paper, the perturbation of the aircraft is modeled as the uniformly distributed random variables on pitch, yaw and roll planes individually. The application of the Monte-Carlo simulation in GRECO is used for analyzing the perturbation effects on the aircraft’s RCS. Gaussian model is proposed as the description of the RCS difference, whose sensitivity on frequency, polarization and turbulence extents are also studied. The conclusion could be used as the consultation on the comparison of RCS between measurement and simulation.

## 1. INTRODUCTION

The importance of RCS (radar cross section) in electromagnetic research and radar application is evident. Traditional method of collecting RCS data from target is mainly based on the indoor and outdoor measurements, which cost great manpower, money and time. The development of computational electromagnetic (CEM) makes it possible to get the RCS of target through computer simulation with acceptable error and low cost, both in manpower and time. Improvements on the algorithm and hardware performance of computer also achieve the function that calculates the radar target’s RCS in the practical dynamic scene. However, the issue on the error (or difference) between measurement and simulation was always a controversy and have been challenging the computation method in EM simulation. One of the error sources comes from the perturbation in target’s movement. The unpredictable air turbulence, bump of the earth, sea surface’s undulation and the pilot’s operation offset are all the possible factors lead to the perturbation in target attitude. That always result in the confusion on the comparison between measurement and simulation results, the latter usually does not take perturbation into account and achieve perfect control in attitude during movement. This paper proposes a method to simulate target’s dynamic RCS considering the unpredictable perturbation. The characteristic of the difference in RCS between “static” and “dynamic” situation is analyzed, the credibility curve of the RCS also provides the reference in practical measurements.

## 2. DYNAMIC SIMULATION USING GRECO

The RCS simulation results presented in this paper come from the GRECO method [1, 2]. GRECO is a fast RCS prediction method with the function of target visibility on the screen, which gives a more explicit demonstration on radar target’s attitude in radar view. It takes high frequency approximation method to calculate the far scattering field with the advantage of fast calculation with acceptable error for electrically large targets. For large scale objects, the total far-field RCS is the summation of the scattering field from these independent scattering sources. PO (physical optics) and PTD (physical theory of diffraction) method is used to calculate the scattering from facet and wedge respectively according to the position of the pixel. It usually takes formula (1) to calculate the back scattering contribution from the pixel on the facet using PO theory [3].

$$S_{\text{PO}} = \sum_{\text{PIXELS}} \text{sinc} \left( \frac{kl}{\cos \theta} \sin \theta \right) e^{i2kz} \Delta s' \quad (1)$$

$k$  is the wave number,  $\cos \theta = n_z$ ,  $l = \sqrt{\Delta s'}$  is the size of the pixel on the screen (the same scale in both  $X$  and  $Y$  direction),  $z$  is the direction of backscattering,  $\theta$  is the angle between  $z$  direction and

the pixel's norm. As for the contribution from diffraction field of the edge, the discrete formula (2) is used, which also takes

$$L_{\text{PTD}}^{xx} = \sum_{\text{PIXELS}} \frac{1}{t_x^2 + t_y^2} [-ft_x^2 + gt_y^2] \Delta l \text{sinc}(kt_z \Delta l) e^{2jkz} \quad (2)$$

pixel as the basic unit. In (2),  $t_x$ ,  $t_y$  and  $t_z$  are the unit vector of the edge,  $\Delta l$  is the length of the edge.  $f$  and  $g$  are diffraction coefficient [4]. The contribution from facets and edges could be combined to calculate the total RCS

$$\sigma = 4\pi R^2 \frac{|E_s|^2}{|E_0|^2} = \frac{1}{\pi} |jkS_{\text{PO}} + L_{\text{PTD}}|^2 \quad (3)$$

SBR (Shooting and Bouncing Ray) method [5] is also applied in the code for the field calculation which involves multi-scattering of the EM wave. In most of the practical cases, GRECO method could give the results of electrically large objects with acceptable error in engineering application. Its time-efficiency also provides the possibility in the target's dynamic simulation considering the perturbation influence.

The dynamic simulation of target's RCS usually takes "quasi-static" method, which discrete the movement trace into the composition of several static positions. In each static position, target's electromagnetic scattering characteristic is calculated and time-axis is used as the coordinate to represent the moving series. Building the target coordinate and radar coordinate is the first step of the dynamic simulation. In radar coordinate, the radar locates at the origin and target's position is interpreted by three parameters as illustrated in Figure 1. The target's geometry center locates at the origin of target's coordinates. As for an aircraft, it usually defines the  $XOY$  plane on its azimuth plane, where  $X$ -axis is along the fuselage direction. The attitude of the aircraft is usually described by the pitch, yaw and roll angle. Matrix transformation between two coordinates is necessary for calculating the target's attitude information in radar view [6, 7].

### 3. MONTE-CARLO SIMULATION FOR DYNAMIC PERTURBATION

In this paper, the flying aircraft is taken as the model to illustrate the dynamic RCS simulation considering the perturbation effect. The attitude of the aircraft is described by pitch, yaw and roll angles in radar view by the transformation from target coordinate to radar coordinate. Therefore, the perturbation of the aircraft could be seen as the composition of perturbations in pitch, yaw and roll plane respectively. Seldom report and literature gives the exact mathematical interpretation of the unpredictable perturbation [8]. For generalization, we treat the perturbation as the random process that evenly distributes within the specified range. Define the perturbation angle in pitch, yaw and roll plane to be  $\Delta\varphi(t)$ ,  $\Delta\theta(t)$  and  $\Delta\gamma(t)$ , the aircraft's attitude in radar view could be described as  $\varphi(t) + \Delta\varphi(t)$ ,  $\theta(t) + \Delta\theta(t)$  and  $\gamma(t) + \Delta\gamma(t)$ . Monte-Carlo simulation method is necessary for this kind of problem since  $\Delta\varphi(t)$ ,  $\Delta\theta(t)$  and  $\Delta\gamma(t)$  are all random variables. Large amount of simulations is needed to collect results with good credibility. The flow chart of the dynamic RCS simulation with perturbation effect is demonstrated in Figure 2.

The aircraft model used in the simulation is the combination of several simple geometry objects such as flat plate and right cylinder. It could be seen as the representation of the typical object. The radar locates at the origin of the coordinate, the model takes a straight line flying from  $(-10000, 700, 700)$  to  $(10000, 700, 700)$ , all units are meter. The perturbation in pitch, yaw

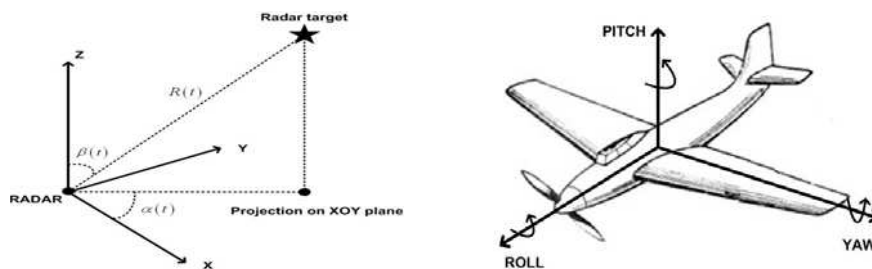


Figure 1: Target and radar coordinate definition.

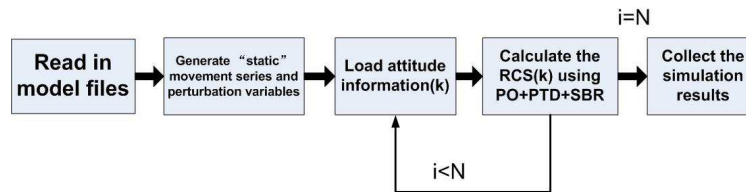


Figure 2: Flow chart of Monte Carlo simulation for perturbation RCS calculation.

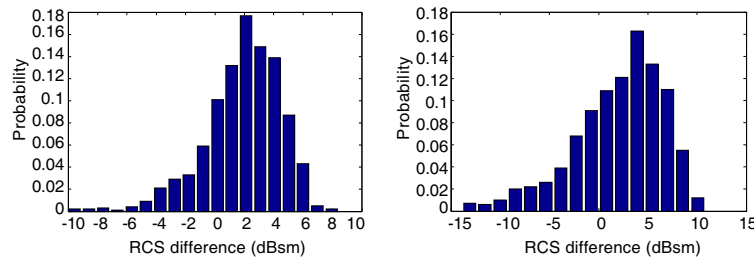


Figure 3: Histogram of RCS difference of any two samples from the movement series — 3 GHz.

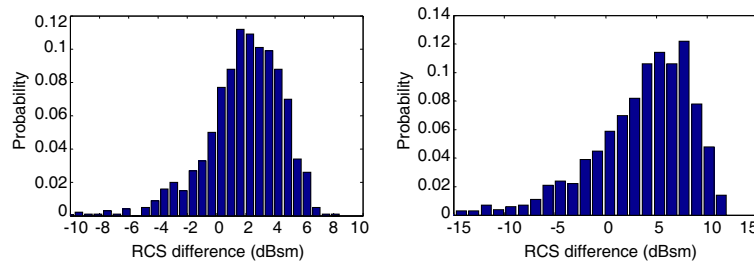


Figure 4: Histogram of RCS difference of any two samples from the movement series — 10 GHz.

and roll angle are evenly distributed random variables in  $(-1^\circ, 1^\circ)$ . Radar wave frequencies are 3 GHz and 10 GHz respectively with  $VV$  polarization. The sample number over the entire trace is 1000. Simulation programs generate 100 evenly distributed numbers for each perturbation variable. Therefore, at least  $10^6$  simulations are necessary for the comprehensive consideration.

#### 4. RESULTS

Direct comparison of RCS on the entire trace usually could hardly get any meaningful conclusion. Since Monte-Carlo simulation method is utilized and large amounts of results are available, it is reasonable to use the statistical method to analysis the perturbation influence on RCS. Figures 3 and 4 are the probability histograms of RCS difference sampled randomly from the entire moving trace. The horizontal axis represents the RCS difference in dBsm units. All histograms have the high similarity to Gaussian distribution. This phenomenon also satisfies the requirement of central limit theory since in high frequency region RCS could be seen as the composition of independent scattering sources, which makes the RCS difference the summation of independent scatters.

The Gaussian like probability distribution of the RCS difference also provides the opportunity to demonstrate the perturbation effect on dynamic RCS in a more explicit and comprehensive way. People from different research fields may wonder how much influence that the attitude perturbation could cause on the RCS. In another word, there should be a range of RCS changing in attitude perturbation. We use the word credibility zone to describe the possible RCS distribution range while considering the attitude perturbation. The quasi-symmetric property of the RCS difference histogram makes it easy to find the upper and lower limit of the RCS range under the specified probability threshold. The initial point locates at the one with maximum probability and moves to two directions with the same step. When the integration within the range between lower and upper limit reach the specified threshold, the RCS perturbation range is determined, which means there is a possibility of specified value that the RCS is within the region bounded by the lower and upper value. Figure 5 is the dynamic RCS credibility zone of 80%. It should be noted that the

upper boundary is not always having a larger value than that of the static one, neither is the lower boundary.

This kind of credibility zone description could also be used in the target RCS data base construction, in which the full-aspect angle RCS in one plane is always preferred. Perturbation influence on RCS from Pitch, Yaw and Roll plane respectively could provide useful information in the target’s dynamic EM scattering characteristic, as illustrated in Figure 6. The credibility zone are collected under 10 GHz with perturbation amplitude of  $1^\circ$ . The RCS in the  $0^\circ$  and  $180^\circ$  zone are usually more sensitive to the perturbation in Pitch plane. The perturbation in three planes lead to changes in aircraft’s broadside back scattering to different extent. Figure 7 demonstrates the jet’s perturbation RCS of full-aspect angle on azimuth plane with probability threshold of 80%. For the more explicit illustration, RCS data are smoothed due to the high scintillation characteristic of the original data.

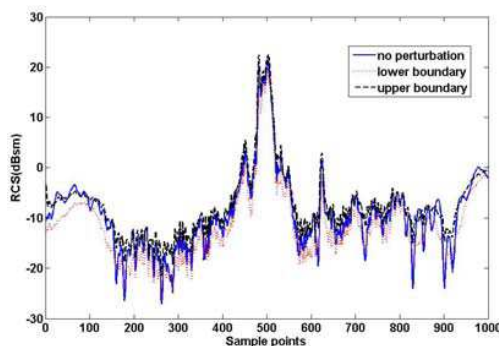


Figure 5: Credibility zone of perturbation dynamic RCS with probability of 80%.

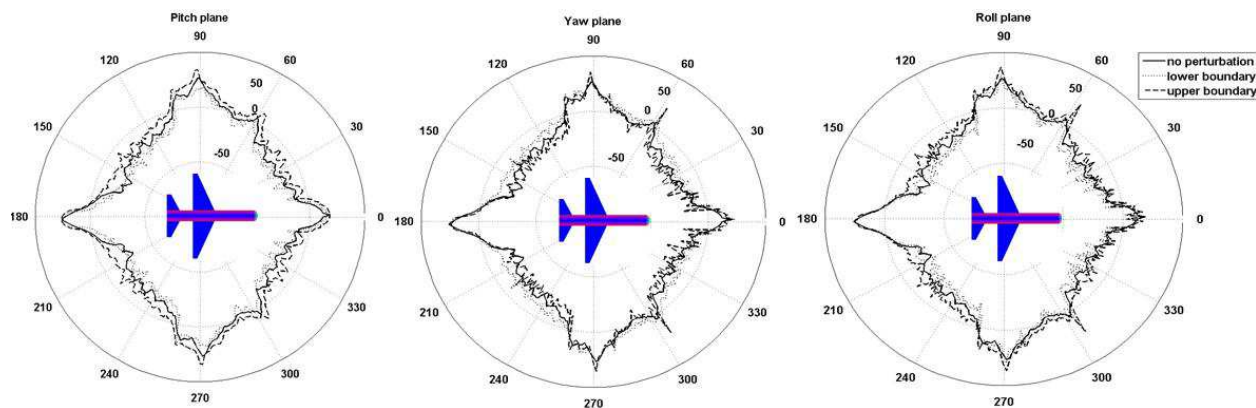


Figure 6: Perturbation influence on RCS from different planes — 10 GHz.

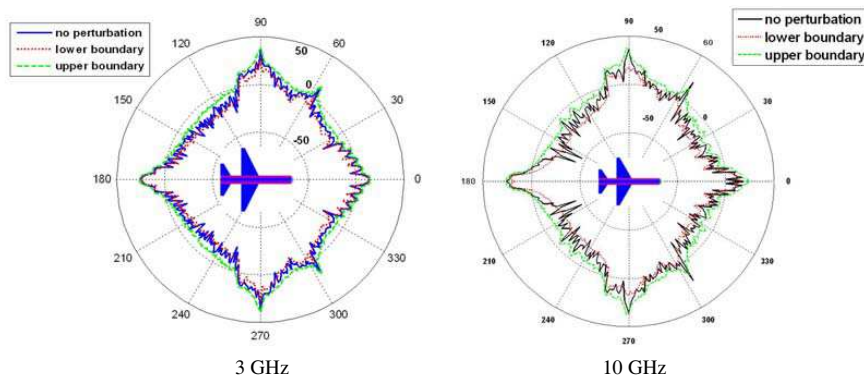


Figure 7: Credibility zone of perturbation RCS in full aspect azimuth angle.

## 5. CONCLUSIONS

The attitude perturbation of dynamic radar target in practical situation usually leads to controversy while comparing results from measurement and simulation. The uncertainty and unpredictable property of perturbation requires the statistical method for its simulation. The combination of GRECO and Monte-Carlo simulation methods achieves the simulation of dynamic radar target's RCS considering attitude perturbation. Gaussian like probability distribution of RCS difference makes it easy to find the credibility zone of dynamic RCS, which also provides reference on the comparison of simulation and measurement results.

## ACKNOWLEDGMENT

This paper is supported by the National Science Fund for Distinguished Young Scholars of NFSC. No. 61001003.

## REFERENCES

1. Rius, J. M., M. Ferrando, and L. Jofre, "High-frequency RCS of complex radar targets in real-time," *IEEE Transactions on Antennas and Propagation*, Vol. 41, No. 9, 1308–1319, 1993.
2. Rius, J. M., M. Ferrando, and L. Jofre, "GRECO: Graphical electromagnetic computing for RCS prediction in real time," *IEEE Antennas and Propagation Magazine*, Vol. 35, No. 2, Apr. 1993.
3. Balanis, C. A., *Advanced Engineering Electromagnetics*, Wiley, New York, 1989.
4. Shaeffer, J. F., M. T. Tuley, and E. F. Knott, *Radar Cross Section*, SciTech Publishing, 2004.
5. Weinmann, F., "Ray tracing with PO/PTD for RCS modeling of large complex objects," *IEEE Transactions on Antennas and Propagation*, Vol. 54, No. 6, Jun. 2006.
6. Keen, K. M., "New technique for the evaluation of the scattering cross-sections of radar corner reflectors," *Microwaves, Optics and Antennas*, Vol. 130, No. 5, 322–326, 1983.
7. Huang, P., X. Xu, et al., *Radar Target Characteristic*, Publishing House of Electronics Industry, BeiJing, 2005.
8. Shirman, Y. D., et al., "Aerial target backscattering simulation and study of radar recognition, detection and tracking," *IEEE International Radar Conference*, 521–526, 2000.

# Efficient Characterization of Fabry-Perot Resonator Antennas

Yuehe Ge<sup>1,2</sup> and Wang Can<sup>1</sup>

<sup>1</sup>College of Information Science and Engineering, Huaqiao University  
Xiamen, Fujian 361021, China

<sup>2</sup>State Key Laboratory of Millimeter Waves, Nanjing 210096, China

**Abstract**— In this paper, an extended transmission line method is applied to characterize high-performance Fabry-Perot resonator antennas, showing its effectiveness and efficiency. In this method, ABCD network is used to represent electromagnetic band-gap (EBG) structures or partially reflective surfaces (PRSs) and reciprocity is used together with the extended model to characterize the radiation properties of Fabry-Perot resonator antennas. An 1D wideband dielectric Fabry-Perot resonator antenna, an 1D dual-band dielectric Fabry-Perot resonator antenna and a 2D wideband Fabry-Perot resonator antenna, which have clear wideband or dual-band design principles. were successfully analyzed using the extended method.

## 1. INTRODUCTION

Dielectric leaky-wave antennas (DLWAs) have been studied in the past decades [1], as a means to enhance the directivity of small antennas. In recent ten years, electromagnetic band-gap (EBG) materials and other partially reflective surfaces (PRSs) based on frequency selective surfaces (FSS) have been developed and applied to leaky-wave antennas [2–5] for the same purpose.

The transmission line method was successfully applied to the analysis of DLWAs [1], where the size of the dielectric superstrate is considered infinite. In [6], antenna superstrate is equivalent to a shunt admittance in the transmission line model, making it possible the analysis of 2D and 3D Fabry-Perot resonator antennas using the transmission line method. However, the method is not reliable when the superstrate of Fabry-Perot resonator antennas is thick and radiation properties concerned is far from the broadside of the antenna. An extended Transmission line method [7, 8], where ABCD network is applied to represent the EBG superstrate, was developed to accurately characterize Fabry-Perot resonator antennas. In this paper, the extended method is applied to characterize 1D and 2D Fabry-Perot resonator antennas to demonstrate its advantages including simplicity, versatility, efficiency and occupying less computer resource.

## 2. THE EXTENDED TRANSMISSION LINE METHOD

As demonstrated in [1], the analysis of dielectric Fabry-Perot resonator antennas can be performed with the aid of the transmission line method, by reciprocity. To extend the method to accurately characterize 2D or 3D Fabry-Perot resonator antennas, the ABCD network can be applied to characterize the performance of the EBG superstrate forming the Fabry-Perot cavity. Other dielectric layers and the PEC ground are still modeled by transmission line model. The details of the method and the related calculation of the radiation field are given in [7, 8], and not provided in this paper. According to the method, as well as the ABCD network parameters of the EBG/PRS periodic superstrate are obtained, other radiation properties, such as directivity, beamwidth, etc., can be calculated correspondingly.

## 3. WIDEBAND DIELECTRIC FABRY-PEROT RESONATOR ANTENNAS

A wideband Fabry-Perot resonator antenna, presented in [9], has a configuration shown in Fig. 1. Based on the design principle in [10], the antenna has two resonant cavities, which resonate at two close frequencies, resulting in a wider transmission bandwidth. Here this antenna is taken advantage of to demonstrate the effectiveness of the design principle in [9, 10] using the extended transmission line method. It can be seen from Fig. 1 that the antenna is composed of three dielectric slabs  $N_1$ ,  $N_3$ ,  $N_5$  and a PEC ground. A horizontal electric dipole (HED) is considered to excite the antenna. The magnitude and phase of the reflection from the bottom surface of slab  $N_5$ , obtained from the commercial software CST Microwave Studio, are plotted in Fig. 2(a). As can be seen, the reflection phase from the three-layer-slab superstrate increases with frequency from 11.5 GHz to 12.3 GHz but decreases at other frequencies. Based on the antenna design principle in [10], a wideband Fabry-Perot resonator antenna is expected.

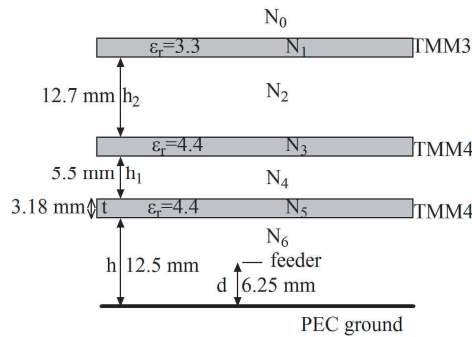


Figure 1: A wideband 1D Fabry-Perot resonator antenna.

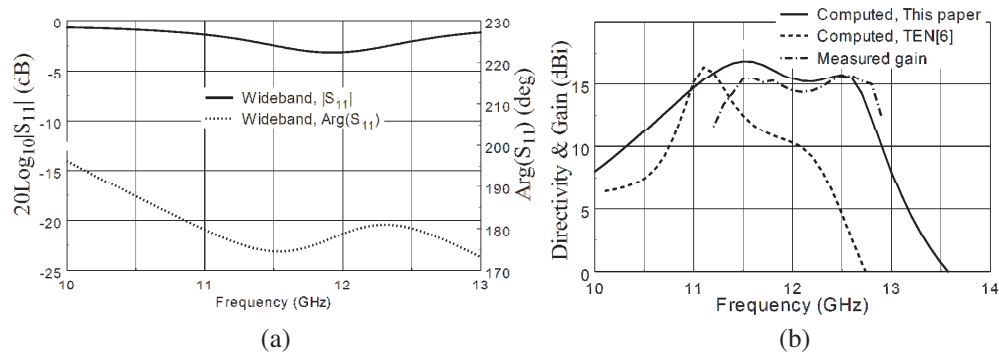


Figure 2: (a) Magnitude and phase of reflection coefficients; (b) Computed and measured directivity and gain.

Applying the antennas parameters to the extended transmission line method,  $S$  parameters of the three dielectric-layer superstrate can be analytically obtained. These  $S$  parameters can be easily converted to ABCD network parameters. Then the performance of the antenna can be estimated using the extended transmission line method [7, 8].

The directivity of the antenna was calculated and is plotted in Fig. 2(b). For comparison, the same antenna was also analyzed using the transmission line method presented in [6] and the directivity result is also plotted in Fig. 2(b). It can be seen that the extended method gives two peak gains, perfectly verifying the wide-band design principle for wide-band Fabry-Perot resonator antennas presented in [10]. This antenna has been fabricated and measured. As can be seen from Fig. 2(b), a good agreement between the computed and measured results is obtained.

#### 4. DUAL-BAND DIELECTRIC FABRY-PEROT RESONATOR ANTENNAS

The design principle of dual-band Fabry-Perot resonator antennas have been introduced in [11] and demonstrated using an 2-D EBG/PRS superstrates with strong resonant inclusion. Dual-band 1D dielectric Fabry-Perot resonator antennas can also be designed using this method [12].

The configuration of the 1D dielectric Fabry-Perot resonator antenna is shown in Fig. 3. Two FR4 dielectric slabs and a PEC ground form the antenna that is excited by a HED. The reflection magnitude and phase from the bottom surface of the lower slab, obtained from CST Microwave Studio, are plotted in Fig. 4(a). The reflection phase, which is required to maintain the cavity resonance condition at the entire concerned frequency band, is also plotted in Fig. 4(a). It can be seen that there are three cross points between the PRS reflection phase and the ideal phase, however, as detailed in [11] the antenna can only operate at two cross points, around 10.7 GHz and 13.2 GHz.

Using the extended transmission line method, the directivity of the antenna is calculated and plotted in Fig. 4(b). It can be seen that two peak directivities, 16 dBi and 14.3 dBi, appear at about 10.5 GHz and 13.2 GHz, respectively. This antenna has also been fabricated and tested. The measured gain is also plotted in Fig. 4(b), for comparison. It can be seen that a good agreement between the theoretical and measured results is obtained.

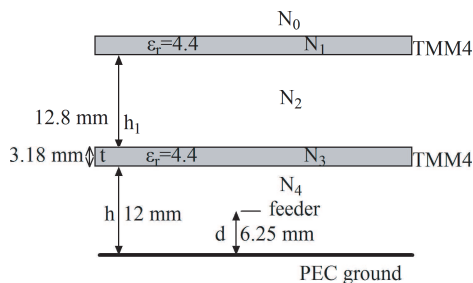


Figure 3: A 1D dual-band Fabry-Perot resonator antenna.

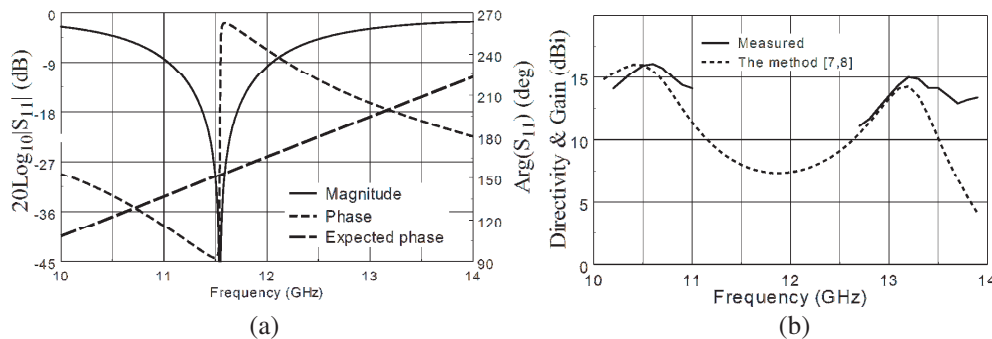


Figure 4: (a) Computed reflection magnitude and phase and the expected phase of the superstrate; (b) Computed directivity and measured gain.

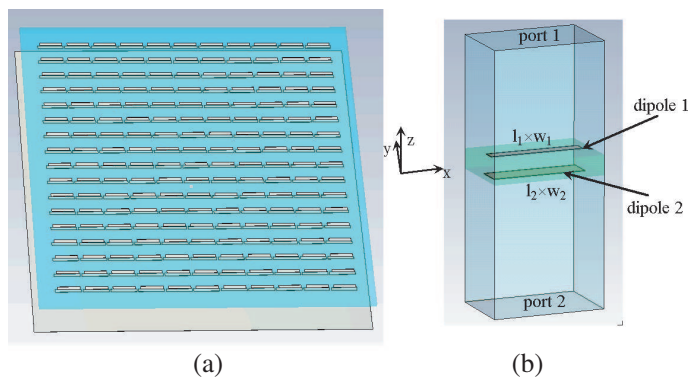


Figure 5: (a) Configuration of the concerned wideband 2D Fabry-Perot resonator antenna; (b) Characterization model of the PRS for the calculation of ABCD parameters.

### 5. WIDEBAND 2D FABRY-PEROT RESONATOR ANTENNAS

The configuration of the wideband 2D Fabry-Perot resonator antenna concerned here is shown in Fig. 5(a). It is composed of a feed antenna, a single-layer PRS and a PEC ground plane. The PRS is made out of Rogers RT/Duriod 5880 material, which has a thickness of 1.5 mm and a dielectric constant of 2.2, with two dipole arrays printed on its two surfaces. The details of the PRS can be found in [10]. This periodic PRS can be characterized using a single unit cell, as shown in Fig. 5(b), with the aid of the periodic boundary condition [11]. The reflection from the surfaces of the PRS, obtained from commercial software CST Microwave Studio, are plotted in Fig. 6(a). It can be seen that the reflection phase from the top surface (port 1) of the PRS decreases with frequency, while that from the bottom surface (port 2) increases with frequency within the frequency band of 12.1 Hz–13.15 GHz. As described in [10], the increasing reflection phase is helpful to maintain the resonance condition within the Fabry-Parot cavity over a wide operating frequency band, resulting in a wideband Fabry-Perot resonator antenna.

In this work, CST Microwave Studio is applied to obtain the  $S$  parameters of the 2D PRS. ABCD network parameters are then evaluated. Applying the obtained ABCD network parameters and the extended transmission line method [7, 8], the wideband 2D Fabry-Perot resonator antenna

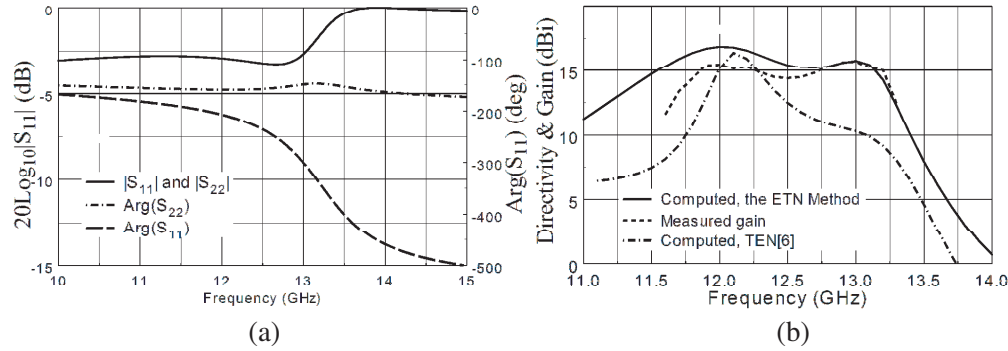


Figure 6: (a) Reflection magnitude and phase from the top and bottom surface of the PRS; (b) Calculated directivities and the measured gain.

can be characterized. Fig. 6(b) shows the calculated directivity. The 3-dB directivity bandwidth is 11.3 GHz–13.2 GHz, up to 15.5%. The prototype of the antenna was also fabricated and measured. The measured gain is also plotted in Fig. 6(b). One can see that a wide bandwidth, up to 13.2%, is obtained, and a good agreement with the theoretical result is achieved. For comparison, the same antenna was also analyzed using the TEN method [6] and the result is also plotted in Fig. 6(b). It can be seen that the wide bandwidth that should be achieved by the antenna is not obtained using the TEN method [6].

## 6. CONCLUSIONS

It is demonstrated that the extended transmission line method, based on the reciprocity and the modeling of EBG/PRS structures using ABCD network, can be used to efficiently determine the radiation properties of Fabry-Perot resonator antennas. For 1D dielectric Fabry-Perot resonator antennas, the ABCD parameters of the superstrate and the radiation properties of the antenna can be determined analytically. For 2D and 3D Fabry-Perot resonator antennas, full-wave numerical methods have to be used to determine ABCD network parameters of the EBG/PRS structures, and then radiation properties of these antennas can be calculated analytically.

The method has been successfully applied to the characterization of wideband and dual-band 1D dielectric Fabry-Perot resonator antennas and a 2D wideband Fabry-Perot resonator antenna. The wideband [10] and dual-band design principles [11, 12], used to design these antennas, have been confirmed. This in turn verifies the effectiveness of the method. Compared to other full-wave numerical methods, this method has the advantages of versatility, simplicity and efficiency.

## ACKNOWLEDGMENT

This research was supported by the start-up grant (11BS301) of Huaqiao University, Xiamen 361021, China, and Open Research Program (K201212) from State Key Laboratory of Millimeter Waves, Nanjing 210096, China.

## REFERENCES

1. Jackson, D. R. and N. Alexopoulos, "Gain enhancement methods for printed circuits antennas," *IEEE Trans. Antennas Propag.*, Vol. 33, No. 9, 976–987, Sept. 1985.
2. Thevenot, M., C. Cheype, A. Reineix, and B. Jecko, "Directive photonic-bandgap antennas," *IEEE Trans. Microw. Theory Tech.*, Vol. 47, No. 11, 2115–2122, Nov. 1999.
3. Pirhadi, A., F. Keshmiri, M. Hakkak, and M. Tayarani, "Analysis and design of dual band high directive EBG resonator antenna using square loop FSS as superstrate layer," *Progress In Electromagnetics Research*, Vol. 70, 1–20, 2007.
4. Boutayeb, H., T. A. Denidni, and M. Nedil, "Bandwidth widening techniques for directive antennas based on partially reflecting surfaces," *Progress In Electromagnetics Research*, Vol. 74, 407–419, 2007.
5. Ge, Y., K. P. Esselle, and Y. Hao, "Design of low-profile high-gain EBG resonator antennas using a genetic algorithm," *IEEE Antennas Wireless Propag. Lett.*, No. 6, 480–483, 2007.

6. Zhao, T., D. R. Jackson, J. T. Williams, and A. A. Oliner, “Simple CAD model for a dielectric leaky-wave antenna,” *IEEE Antennas Wireless Propag. Lett.*, Vol. 3, 243–245, Dec. 2004.
7. Costa, F. and A. Monorchio, “Design of subwavelength tunable and steerable fabry-perot/leaky wave antennas,” *Progress In Electromagnetics Research*, Vol. 111, 467–481, 2011.
8. Ge, Y., “Equivalent transmission network method for the characterization of fabry-perot resonator antennas,” *2012 5th Global Symposium on Millimeter-Waves*, Harbin, China, May 27–30, 2012.
9. Weily, A., K. P. Esselle, T. S. Bird, and B. C. Sanders, “Dual resonator 1-D EBG antenna with slot array feed for improved radiation bandwidth,” *IET Proc. Microw., Antennas Propag.*, Vol. 1, No. 1, 198–203, Feb. 2007.
10. Ge, Y., K. P. Esselle, and T. S. Bird, “The use of simple thin partially reflective surfaces with positive reflection phase gradients to design wideband, low-profile EBG resonator antennas,” *IEEE Trans. Antennas Propag.*, Vol. 64, No. 2, 743–750, Feb. 2012.
11. Ge, Y., K. P. Esselle, and T. S. Bird, “A method to design dual-band, high-directivity EBG resonator antennas using single-resonant, single-layer partially reflective surfaces,” *Progress In Electromagnetics Research C*, Vol. 13, 245–257, 2010.
12. Zeb, B. A., Y. Ge, K. P. Esselle, and M. E. Tobar, “A simple dual-band electromagnetic band gap resonator antenna based on inverted reflection phase gradient,” *IEEE Trans. Antennas Propag.*, Vol. 64, No. 10, 4522–4529, Oct. 2012.

# Transparent Antenna Design for Wireless Access Point Application

A. S. Azini, M. R. Kamarudin, T. A. Rahman, S. K. A. Rahim, and M. S. A. Rani  
 Wireless Communication Centre (WCC), Faculty of Electrical Engineering  
 Universiti Teknologi Malaysia, UTM Skudai, Johor 81310, Malaysia

**Abstract**— In this paper, transparent monopole antenna using AgHT-4 film has been presented. The radiating element and ground plane are both designed using AgHT-4 while the substrate is made of glass. By having a suitable arc-shape slot on the ground plane, a wide impedance bandwidth of 41.89% (2.00 GHz to 3.06 GHz) that cover WLAN system in the 2.4 GHz has been obtained. The transparent antenna provides gain of 3.16 dBi.

## 1. INTRODUCTION

At present there are many researchers keen to explore new types of antenna which use transparent materials. First reports on transparent antennas have been published in the early 90s [1, 2]. Due to its transparent characteristics it is suitable to be implemented with clear substrates such as window glass for security, aesthetics [1, 3], vehicles [4] or can be integrated with solar cells to save surface area of small satellites [5]. Transparent conductive films allows the transmission of electric currents and retain the optically transparency [6]. There are three types of transparent conductive films namely indium tin oxide (ITO), fluorine-doped tin oxide (FTO) and silver coated polyester film (AgHT) [7] used by researcher for antenna developments.

There are many slot shape introduced to enhance the antenna bandwidth particularly in monopole antenna design such as elliptical slot [8, 9], inverted-U shaped slot [10], circular slot [11] and pentagonal-shaped slot [12]. All these antennas have complicated design and make the fabrication difficult. As the transparent antenna is manually made by cutting out the patch and the feed from the coated polyester sheet of AgHT-4, a simple shape is preferred and a wide bandwidth can be obtained by proper designing suitable slot shaped on the ground plane. The antenna has been fabricated using AgHT-4 and it is designed at frequency 2.4 GHz for WiFi access point. The measured and simulated return loss and simulated radiation result are presented in this paper.

## 2. ANTENNA DESIGN

Figure 1 shows the dimensions of wideband transparent monopole antenna. The radiating element and ground plane are both designed using AgHT-4 film which is 0.175 mm thickness and has conductivity of ( $\sigma = 2.2 \times 10^5$  S/m) [7]. The transparent antenna is mounted on 2 mm thick glass substrate which has dielectric permittivity of 7. The size of the glass substrate is designed large enough ( $90 \times 60$  mm<sup>2</sup>) so that the antenna properties, including gain could be stabilized and not change after increasing the dimension of the glass substrate [13, 14]. The width of the feedline,  $g$  which is 2 mm were obtained for leading to a characteristic impedance of  $50 \Omega$ . A ground frame ( $50 \times 40$  mm<sup>2</sup>) is necessary in order to have bi-directional radiation pattern. In addition, the wide slot on the ground plane helps the antenna to achieve wider bandwidth. The proposed transparent monopole antenna is designed and optimized using the CST Microwave Studio, simulation tool. As shown in Figure 2, the UTM logo can be seen which indicate the antenna is transparent.

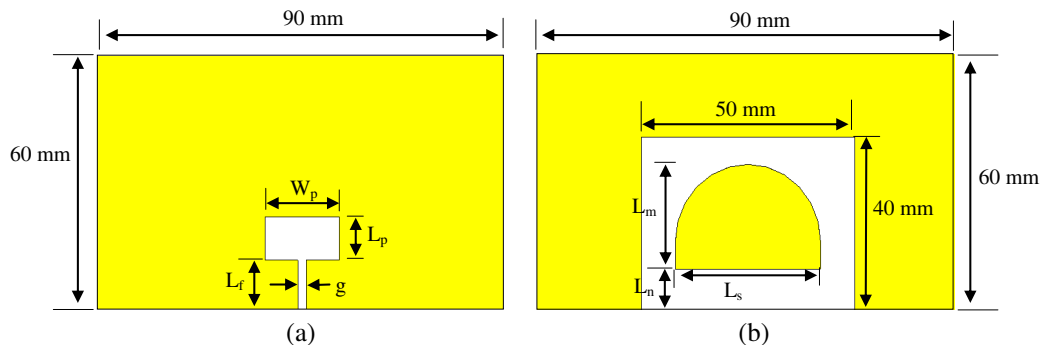


Figure 1: Layout of wideband transparent antenna. (a) Front view. (b) Back view.

The dimensions of the proposed antenna as follows:  $W_p = 18$  mm,  $L_p = 10$  mm,  $L_f = 12$  mm,  $g = 2$  mm,  $L_m = 23$  mm,  $L_n = 11$  mm and  $L_s = 34$  mm.

### 3. RESULTS AND DISCUSSION

Figure 3 shows the comparisons of the return loss between arc-shaped slot and without arc-shaped slot on the ground plane. It can be seen that by introducing a suitable arc-shape slot on the ground plane, a wide impedance bandwidth of 41.89% (2.00 GHz to 3.06 GHz) that cover WLAN system in the 2.4 GHz has been obtained. This is due to the fact that the arc-shape slot helps the current flows much longer and consequently makes the antenna tuned at lower frequency of 2.4 GHz. Figure 4 shows the variation of the various radius of the arc-shaped slot. The radius of the arc varies from 11 mm to 17 mm. It can be seen from the graph that the wider the arc slot of the antenna, the higher is the frequency and hence, the optimized value of 17 mm is used in this design.



Figure 2: Antenna prototype.

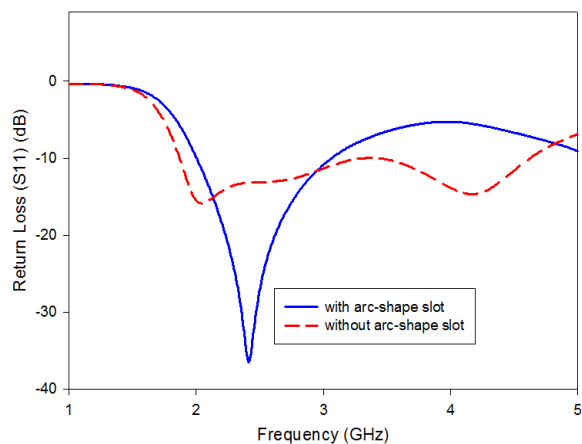


Figure 3: With and without arc-shaped slot.

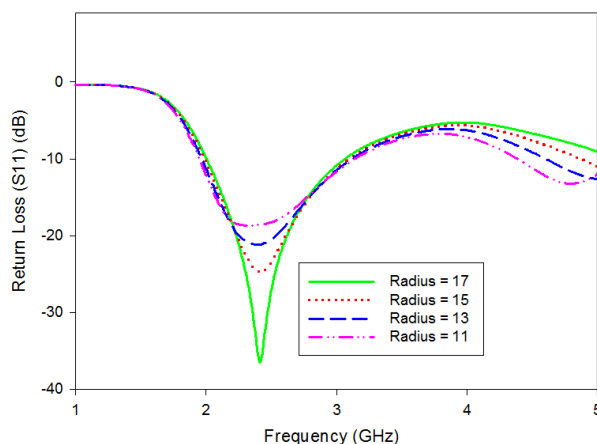


Figure 4: Radius slot variation.

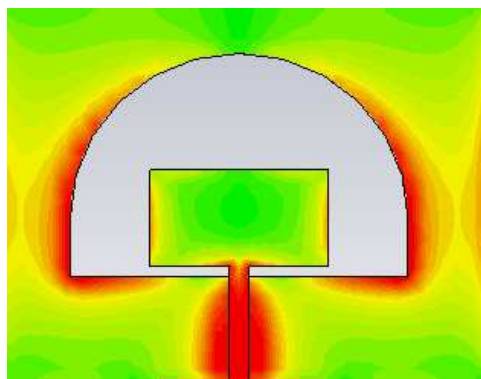


Figure 5: Current distribution.

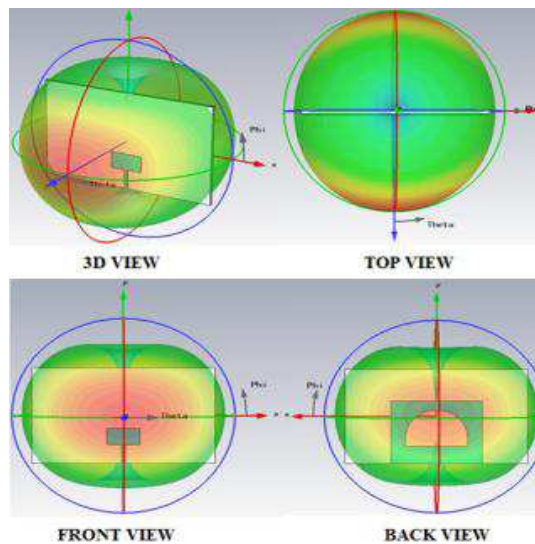


Figure 6: Radiation pattern.

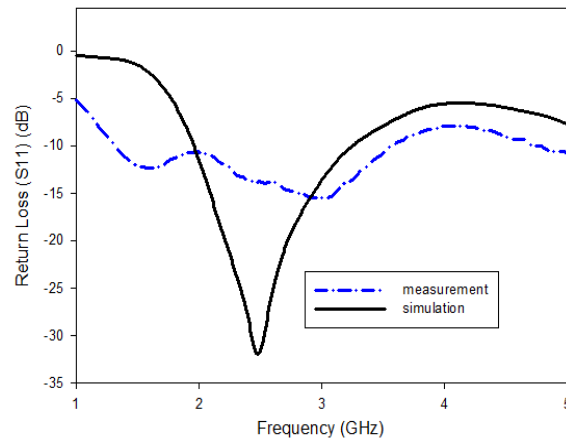


Figure 7: Measured and simulated return loss.

Figure 5 shows the surface current distribution at frequency 2.4 GHz. As seen from Figure 5, the surface currents concentrated more along the arc-shape slot of the antenna. This shows that the arc-shape slots acts as a resonator to generate the resonance frequency of 2.4 GHz. Figure 6 shows the radiation pattern of the transparent antenna. The transparent antenna have bi-directional radiation pattern which proved that the antenna is suitable for indoor access points application and can easily mounted against glass in order to have a signal on both sides. The directivity of this transparent antenna is 3.4 dBi. Figure 7 shows the measured and simulated return loss result of the proposed antenna. It is observed that the measured and simulated result have close agreement.

#### 4. CONCLUSION

In this paper, a wideband monopole transparent antenna for WiFi access point application has been designed, fabricated and measured. The transparent antenna has bi-directional radiation pattern and a wide impedance bandwidth of 41.89% (2.00 GHz to 3.06 GHz) that cover WLAN system in the 2.4 GHz operation band. The transparent antenna provides gain of 3.16 dBi. The transparent antenna is suitable to be used for WiFi access point application.

#### ACKNOWLEDGMENT

The authors would like to thank to Ministry of Higher Education (MOHE) and UTM GUP (vote 01H00 and vote 00G36) for sponsoring this work. Besides, thanks to the members of Wireless Communication Center (WCC), UTM for helping and providing resources to enable this work to be completed.

#### REFERENCES

1. Ito, K. and M. Wu, "See-through microstrip antennas constructed on a transparent substrate," *Seventh International Conference on (IEE) Antennas and Propagation, ICAP 91*, Vol. 1. 133–136, 1991.
2. Meng-Shien, W. and K. Ito, "Basic study on see-through microstrip antennas constructed on a window glass," *Antennas and Propagation Society International Symposium, AP-S Digest, Held in Conjunction with: IEEE URSI Radio Science Meeting and Nuclear EMP Meeting*, Vol. 1, 499–502, 1992.
3. Simons, R. N. and R. Q. Lee, "Feasibility study of optically transparent microstrip patch antenna," *IEEE Antennas and Propagation Society International Symposium, 1997 Digest*, Vol. 4, 2100–2103, 1997.
4. Song, H. J., "Challenges in glass integrated optically transparent antennas," *International Symposium on Antennas and Propagation (ISAP)*, Jeju, Korea, 2011.
5. Turpin, T. W. and R. Baktur, "Meshed patch antennas integrated on solar cells," *IEEE Antennas and Wireless Propagation Letters*, Vol. 8, 693–696, 2009.
6. Kawashima, T., H. Matsui, and N. Tanabe, "New transparent conductive films: FTO coated ITO," *Thin Solid Films*, Vol. 445, 241–244, 2003.

7. Song, H. J., T. Y. Hsu, D. F. Sievenpiper, H. P. Hsu, J. Schaffner, and E. Yasan, “A method for improving the efficiency of transparent film antennas,” *IEEE Antennas and Wireless Propagation Letters*, Vol. 7, 753–756, 2008.
8. Wang, X. M., L. Zhang, J. P. Xiong, and Y. C. Jiao, “Printed microstrip-line-fed elliptical slot antenna with very wide bandwidth,” *Journal of Electromagnetic Waves and Applications*, Vol. 22, Nos. 14–15, 1865–1871, 2008.
9. Liu, Z. Y., Y. Z. Yin, L. H. Wen, W. C. Xiao, Y. Wang, and S. L. Zuo, “A Y-shaped tri-band monopole antenna with a parasitic M-strip for PCS and wlan applications,” *Journal of Electromagnetic Waves and Applications*, Vol. 24, Nos. 8–9, 1219–1227, 2010.
10. Xiong, L. and P. Gao, “A compact triple-band wide-slot antenna for WLAN/WiMAX applications,” *Journal of Electromagnetic Waves and Applications*, Vol. 26, No. 7, 895–903, 2012.
11. Habib, M. A., T. A. Denidni, and G. Y. Delisle, “Design of a new wide-band CPW-fed circular slot antenna,” *IEEE Antennas and Propagation Society International Symposium*, Vol. 1B, 565–568, 2005.
12. Foudazi, A., H. R. Hassani, and S. M. A. Nezhad, “A dual-band WLAN/UWB printed wide slot antenna,” *Loughborough Antennas and Propagation Conference (LAPC)*, 1–3, 2011.
13. Yasin, T., R. Baktur, and C. Furse, “A study on the efficiency of transparent patch antennas designed from conductive oxide films,” *IEEE International Symposium on Antennas and Propagation (APSURSI)*, 3085–3087, 2011.
14. Yasin, T., R. Baktur, and C. Furse, “A comparative study on two types of transparent patch antennas,” *XXXth URSI General Assembly and Scientific Symposium*, 1–4, 2011.

# Design of a Programmable Low-pass Filter for UHF RFID ZIF Receivers

C. C. Zhang<sup>1,2</sup>, C. Wang<sup>1</sup>, Y. F. Guo<sup>1</sup>, Y. M. Fang<sup>1</sup>, L. L. Liu<sup>1</sup>,  
D. Y. Chen<sup>1</sup>, and W. Li<sup>1</sup>

<sup>1</sup>Power and RF Microelectronic Research Centre

Nanjing University of Posts and Telecommunications, Nanjing 210046, China

<sup>2</sup>Nanjing Research Institute of Electronics Technology, Nanjing 210013, China

**Abstract**— A programmable low-pass filter for 860 ~ 960 MHz UHF RFID ZIF (zero IF) receivers was designed in 0.18  $\mu\text{m}$  CMOS process. Taking into account the high linearity requirements, the Active-RC filter was selected. Moreover, a fully differential operational amplifier with common-mode feedback (CMFB) was employed as a critical building block. With a 4th-order Butterworth low-pass-type topology, based on the tow-thomas biquad, the filter was synthesized. Its bandwidth can be programmed to 480/600/700/900/1100/1680 kHz with an attenuation greater than 50 dB at frequencies of  $10 \times f_c$  (cutoff frequency). The filter exhibits many advantages, such as low order, low power consumption, small size, wide cutoff frequency selection range and high linearity. From a single 1.8 V power supply, simulations show that the filter has an input referred noise of 98.95 nV/ $\sqrt{\text{Hz}}$ , a third-order intercept point (IIP3) of 24.25 dBm, and a power consumption of 12.42 mW.

## 1. INTRODUCTION

RFID (radio frequency identification) systems can be classified, according to their operation frequency bands, into the low-frequency, high-frequency, ultra-high-frequency (UHF) and microwave ones. Among them, the UHF RFID systems possess a lot of advantages, e.g., long recognition distance, fast communication velocity, large information capacity, small size and widespread applications, and so on, so they become the current research hot-spots, nowadays.

Due to both multiple stages of mixers and off-chip filters, a superheterodyne receiver has many shortcomings, such as high cost, low integration and high power consumption [1]. As for a near-zero IF receiver, just like the superheterodyne counterpart, image frequency suppression problems still exist [2]. Whereas, a ZIF receiver is characterized by no image-reject filter, high integration, small size, low power consumption, etc., therefore the ZIF architecture is chosen for the UHF RFID reader.

A low-pass filter design for a single-chip UHF RFID reader with the operation frequency range of 860 ~ 960 MHz is focused on in this paper. The filter aims to filter out noise and interferences on the image frequencies of the subsequent ADC in order not to distort the required signals by aliasing [3].

## 2. FILTER STRUCTURE SELECTION AND CIRCUIT DESIGN

Continuous-time analog filters can be divided into three types: Active-RC, MOSFET-C, and Gm-C. The MOSFET-C filter has advantages, such as a small chip area, low power consumption, low noise and insensitive to parasitic capacitance; however, due to its usage of operational amplifiers (op amps), its operating frequency is limited, so, usually this type of filter is only used in audio frequency bands [4]. The Gm-C filter works in an open-loop topology to avoid the problem of the stability of the op amp, which leads to a wider bandwidth and a larger dynamic range; however, its linearity is poor, so, the power consumption has to be increased to improve its linearity [5]. Compared to the Gm-C one, the active resistor-capacitor (Active-RC) filter operates in a closed-loop topology, thereby it has a higher linearity [6], and the operating frequency and power consumption are mainly determined by the used op amps. Taking into account the special requirements of higher receiver linearity, the Active-RC filter is selected. According to the agreements, the return signal data rate from a tag ranges from 40 kHz to 640 kHz. Without considering the limitations from the channel bandwidth, the highest rate is 640 kHz, so a 1.28 M bandwidth is occupied. Furthermore, if a signal frequency offset of 20% is taken into account, the maximum bandwidth turns into 1.54 MHz. According to the operation rates, the low-pass filter cutoff frequency should be able to be programmable to 480 kHz, 600 kHz, 700 kHz, 900 kHz, 1.1 MHz and 1.68 MHz.

Since the rejection requirement on the baseband analog filter is greater than 15 dB at the frequency of twice channel bandwidth, equivalent to 50 dB/dec, at least a third-order low-pass filter is required. The higher the order is, the bigger the occupied area is. Therefore, a 4th-order fully differential butterworth low-pass active RC filter is chosen, which consists of two second-order filter cells. During synthesis, the Tow-Thomas biquad, shown in Figure 1, is used. This kind of filter owns many excellent characteristics, similar to a passive RLC filter, for example, insensitive to parasitic parameters and strong tolerance to the non-idealities from op amps, which makes the design and tuning easier [7].

The transfer function of the Tow-Thomas biquad is as follows:

$$H(s) = \frac{V_{OUT}(s)}{V_{IN}(s)} = -\frac{\frac{1}{R_1 R_2 C_1 C_2}}{s^2 + \frac{s}{R_3 C_1} + \frac{1}{R_2 R_4 C_1 C_2}} \quad (1)$$

From (1),  $-3$  dB frequency ( $\omega_0$ ), quality factor ( $Q$ ), and gain ( $A_0$ ) of the biquad can be obtained:

$$\omega_0 = \frac{1}{\sqrt{R_2 R_4 C_1 C_2}}; \quad Q = R_3 \sqrt{\frac{C_1}{R_2 R_4 C_2}}; \quad A_0 = \frac{R_4}{R_1} \quad (2)$$

If  $R_1 = R_2 = R_4 = R$ , and  $C_1 = C_2 = C$ , according to (2),  $\omega_0$  and  $Q$  can be simplified to  $1/RC$ , and  $R_3/R$ , respectively.

It can also be seen from (2), the  $\omega_0$  and  $Q$  can be adjusted independently. The  $R_3$  in the Tow-Thomas biquad is mainly used to prevent oscillation, so it needs to be adjusted to achieve the stability of the whole loop.

Within the 4th-order Butterworth topology, two biquads, shown in Figure 1, are in series. For the differential one, the inverter can be omitted [8], and, eventually, the LPF is given in Figure 2.

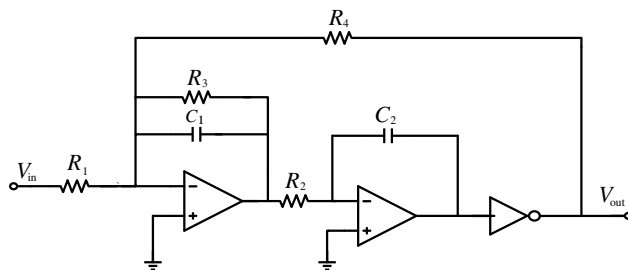


Figure 1: Tow-Thomas biquad.

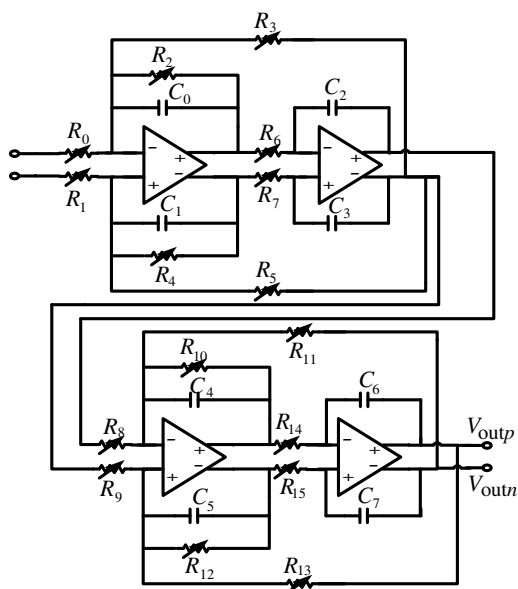


Figure 2: Schematic diagram of the designed LPF.

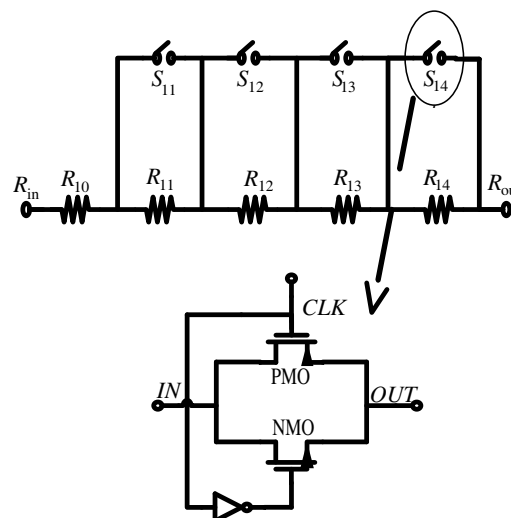


Figure 3: Schematic diagram of the programmable resistor circuit.

In order to achieve an adjustable cutoff frequency and also prevent frequency deviation due to errors of the manufacturing process and temperature/voltage variations, as shown in Figure 3, a 4-bit programmable resistor is selected. Also, from Figure 3, it can be found that a CMOS complementary switch is used, due to its excellent performance [9]. According to the relationship table shown in Table 1, the desired cutoff frequency of the filter can be easily selected by the 4-bit control word.

A 2-stage fully differential op amp is chosen. The phase margin of the op amp is compensated and then its stability is assured [10]. The first stage of the op amp is the input differential pair consisting mainly of NMOS transistors. The NMOS transistors are chosen over the PMOS ones, because, under the same premise as the compensation capacitance and the aspect ratio, they can achieve a larger transconductance, and then a greater bandwidth. Also, from another view, a smaller compensation capacitor can be used to reduce the area of the op amp [11]. The PMOS common-source stage amplifier is used as the second stage to increase the gain and improve the swing of the op amp. A common-mode feedback technique is used to stabilize the output DC level [12].

### 3. SIMULATION RESULTS

The programmable low-pass filter is designed and simulated in a standard 0.18  $\mu\text{m}$  CMOS process. The supply voltage is 1.8 V. Figures 4 and 5 show the AC response and the input-referred noise

Table 1: Relationship between control signals and cut-off frequencies.

$A_0$	$A_1$	$A_2$	$A_3$	Cut-off frequency
1	1	1	1	480 kHz
1	1	0	1	600 kHz
1	0	1	1	700 kHz
1	0	0	1	900 kHz
0	0	1	1	1.1 MHz
0	0	0	1	1.68 MHz

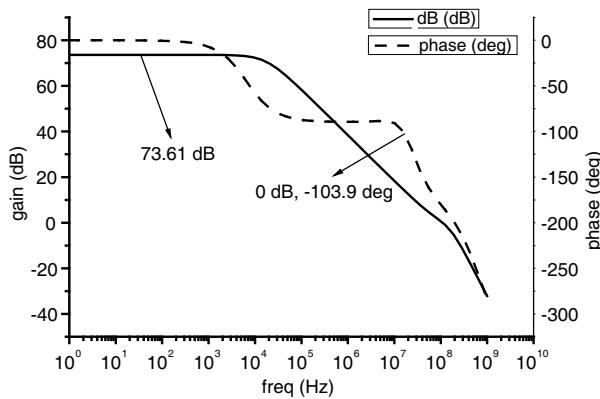


Figure 4: AC response of the op amp.

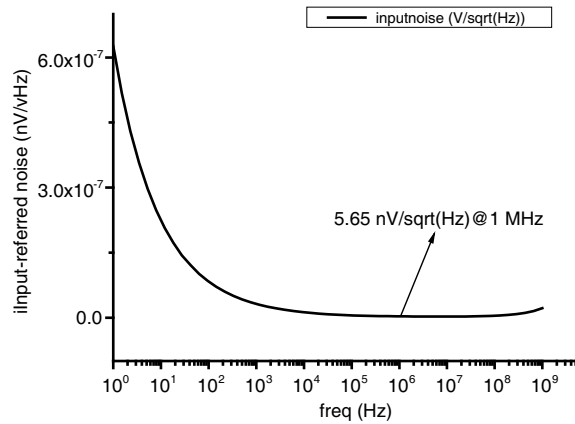


Figure 5: Noise response of the op amp.

Table 2: Simulation results of the two-stage full differential op amp.

Parameter	Measured Results
Supply Voltage	1.8 V
Open-loop Gain	73.61 dB
Phase Margin	76.1°
-3 dB Bandwidth	15.1 kHz
Input-referred noise @1 MHz	5.65 nV/ $\sqrt{\text{Hz}}$
Power Consumption	3.092 mW

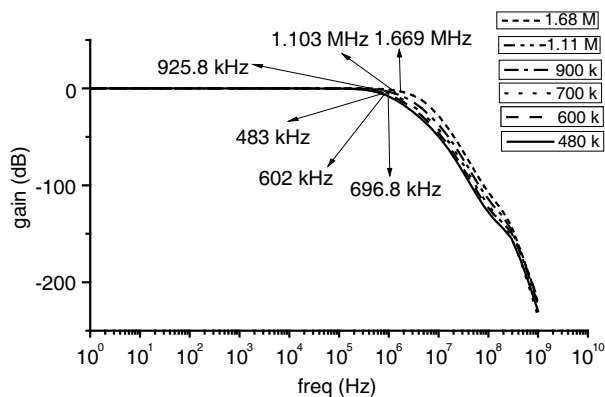


Figure 6: AC response of the low-pass filter with six different cut-off frequencies.

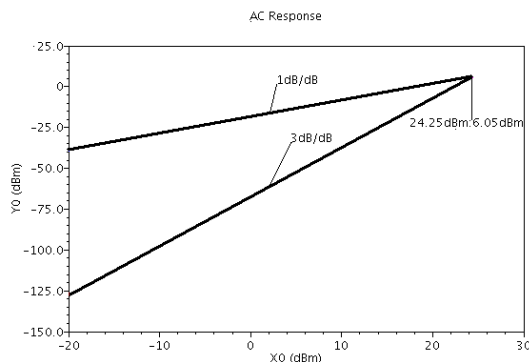


Figure 7: In-band IIP3 of the filter.

Table 3: Performance comparison with other recently published works.

Parameter	Ref. [13]	Ref. [14]	Ref. [3]	This work
Order	4th/7th-order	7th-order	4th-order	4th-order
Process	0.18 $\mu\text{m}$	90 nm	0.18 $\mu\text{m}$	0.18 $\mu\text{m}$
Supply Voltage	1.8 V	1.2 V	1.8 V	1.8 V
Power Consumption	/	16 mW	2.952 mW	12.42 mW
-3 dB Bandwidth	0.33/1.5 MHz	3/3.5/4 MHz	3 MHz	0.483 ~ 1.67 MHz
Pass-band Ripple	0.5 dB	< 0.15 dB	1.5 dB	< 0.05 dB
Attenuation	/	56 dB@4 MHz	79.7 dB@30 MHz	> 50 dB/dec
In-band IIP3	2 dBm	26 dBm	/	24.25 dB
Input-referred noise	/	48 nV/ $\sqrt{\text{Hz}}$	137 nV/ $\sqrt{\text{Hz}}$	98.95 nV/ $\sqrt{\text{Hz}}$

of the fully differential two-stage op amp, respectively. It can be seen that a 105.8 MHz unity-gain bandwidth and 5.65 nV/ $\sqrt{\text{Hz}}$ @1 MHz input-referred noise are achieved. Table 2 shows the simulation results of the fully differential two-stage op amp.

The amplitude-frequency response characteristics of this low-pass filter is shown in Figure 6, which shows that the cutoff frequencies can be programmable to 483 kHz, 602 kHz, 697 kHz, 926 kHz, 1.1 MHz and 1.67 MHz, and the out-band attenuation also meets design goals. At the frequency of  $10 \times f_c$ , over 50 dB attenuation can be achieved. Figure 7 shows the simulation plot of the third-order input intermodulation distortion at 483 kHz cutoff frequency, from which, it can be found that 24.25 dBm IIP3 is achieved when two single tones of 300 kHz and 400 kHz are applied.

The presented low-pass filter is compared with other recently published works and summarized in Table 3. From this table, it can be found that this work achieves a better performance, for example, broader selection of programmable bandwidth, smaller pass-band ripple, moderate power consumption, good linearity, > 50 dB/dec attenuation.

#### 4. CONCLUSIONS

A fourth-order low-pass Butterworth programmable fully differential filter for ZIF UHF RFID readers is designed in a standard 0.18  $\mu\text{m}$  CMOS mixed-signal technology. In order to achieve an adjustable bandwidth required by system and also to correct frequency deviation due to errors of the manufacturing process and voltage/temperature variations, the filter can be programmed. Compared with other recently published works, this work achieves a better performance, for example, broader selection of programmable bandwidth, smaller pass-band ripple, moderate power consumption, good linearity, > 50 dB/dec attenuation, and so on. Simulation results show that it can meet the requirements of UHF RFID ZIF receivers.

#### ACKNOWLEDGMENT

This work was supported by the National Natural Science Foundation of China (No. 61076073), the Research Funds of Nanjing University of Posts and Telecommunications (No. NY211016, No. 211058),

and the China Postdoctoral Science Foundation (No. 2012M521126).

#### REFERENCES

1. Yi, J. T., “Research on a 2 ~ 6 GHz universal receiver and design and experiment on its critical circuits,” Master’s Thesis, University of Electronic Technology, 2007.
2. Zhang, L. and B. M. Luo, “Discussion on a solution to a near-zero IF mirror interference,” *Popular Science & Technology*, No. 2, 13–14, 2009.
3. Han, Y. F., “Research and realization on key techniques of the UHF RFID reader chip,” Doctoral Dissertation, Fudan University, 2008.
4. Wang, W. L. and P. Wang, “New technologies of continuous-time filters and their application,” *Electronic Design Engineering*, Vol. 18, No. 1, 110–112, 2010.
5. Chang, Z. Y., D. Haspelagh, and J. Verfaillie, “A highly linear CMOS  $G_m$ -C bandpass filter with on-chip frequency tuning,” *IEEE J. Sol. Sta. Circ.*, Vol. 32, No. 3, 388–397, 1997.
6. Fu, W. Y., “Research and design on high-speed analog low-pass filters,” Master’s Thesis, University of Electronic Science and Technology, 2005.
7. Zheng, H. and H. C. Luong, “A 36/44 MHz switched-capacitor bandpass filter for cable-TV tuner application,” *IEEE Asian Solid-State Circuits Conf.*, 235–238, Nov. 2006.
8. Le, Y., H. L. Liao, F. Song, et al., “A single-chip CMOS UHF RFID reader transceiver for chinese mobile applications,” *IEEE J. Sol. Sta. Circ.*, Vol. 45, No. 7, 1316–1329, 2010.
9. He, L. N. and Y. Wang, *Analog Integrated Circuit Design and Simulation*, Science Press, Beijing, 2010.
10. Allen, P. E. and D. R. Holberg, *CMOS Analog Circuit Design*, Oxford University Press, New York, 2002.
11. Zhou, Z. J. and N. Li, “A dual-mode active RC lowpass filter for GSM and WCDMA,” *Microelectronics*, Vol. 36, No. 6, 825–829, 2006.
12. Razavi, B., *Design of Analog CMOS Integrated Circuits*, McGraw-Hill, New York, 2001.
13. Khannur, P. B., X. S. Chen, D. L. Yan, et al., “A universal UHF RFID reader IC in 0.18- $\mu$ m CMOS technology,” *IEEE J. Sol. Sta. Circ.*, Vol. 43, No. 5, 1146–1155, 2008.
14. Qi, J. Y. and X. L. Wang, “Design of channel-select filter for ZIF DVB-H tuner,” *Microelectronics*, Vol. 38, No. 2, 289–293, 2008.

# Experimental Evaluation of Cytotoxicity Effects in Cancer and Normal Cells Exposed to Far Infrared Radiation

P. Peidaee<sup>1</sup>, T. Istivan<sup>2</sup>, R. Shukla<sup>3,4</sup>, and E. Pirogova<sup>1,4</sup>

<sup>1</sup>School of Electrical and Computer Engineering, RMIT University, Melbourne, Australia

<sup>2</sup>Department of Biotechnology and Environmental Biology, School of Applied Sciences  
RMIT University, Bundoora, Victoria, Australia

<sup>3</sup>Department of Applied Chemistry, School of Applied Sciences  
RMIT University, Bundoora, Victoria, Australia

<sup>4</sup>Health Innovation Research Institute, RMIT University, Australia

**Abstract**— It has been proven that many of biological processes are frequency selective processes that relate to quantum energy state of photosensitive molecules. It was shown that light-activated changes in protein energy states can induce or modulate biological processes. Various up-to-date methodologies that incorporate low-intensity light into therapeutic procedures have been integrated into modern medicine. Here we have studied experimentally the hypothesis of the Resonant Recognition Model (RRM) that selectivity of protein activities is based on specific resonant electromagnetic interactions [1]. The RRM theory proposes that an external electromagnetic field at a particular activation frequency would produce resonant effects on protein biological activity, and this activation frequency can be determined computationally [1].

In our previous study [2] it was proposed that the wavelengths of the applied electromagnetic radiation (EMR) in a range of 3500–6400 nm are expected to affect biological activity of oncogene and proto-oncogene proteins [2,3]. Thus, in this study we designed an exposure system based on IR-LED to irradiate the selected cancer and normal cells in the wavelength range predicted computationally by the RRM. The experimental evaluation of the attained far infrared wavelengths of 3400 nm, 3600 nm, 3800 nm, 3900 nm, 4100 nm and 4300 nm was conducted on a mouse melanoma (B16F0) and Chinese Hamster Ovary (CHO) cell lines. CHO cells are normal cells and used here as a control and B16F0 is cancer cell line.

A comprehensive quantitative analysis of the exposed and sham-exposed B16F0 and CHO cells has been carried out. The results obtained from LDH cytotoxicity test of B16F0 and CHO cells exposed to the computationally predicted wavelengths of far IR light presented and discussed here. In addition qualitative analysis of the effects of applied radiation on cancer and normal cells was performed using the light microscopy. The significance of the findings obtained from the cytotoxicity effects measured by LDH test as well as light microscopy's results is discussed and compared with the computational predictions.

## 1. INTRODUCTION

Cancer is one of the top ten disease with the highest mortality rate according to World Health Organization, and has a second highest death rate in the developed countries [4]. Cancer develops due to permutations in DNA of a somatic cell resulted from the functional changes in some of its genes. Genes are small coding sequences along a strand of DNA, which control the functionality of cells and human body in general. The functionality of a gene depends on the combination of amino acids present and active in the cell structure. Low intensity light therapy is an external irradiation exposure method which showed to be able to affect biological processes. The effects of low intensity light radiation on cells and molecules have been extensively studied recently.

Amongst different modelling approaches proposed in previous years, we found that the Resonant Recognition Model (RRM) presents an efficient tool for computation of frequencies which have resonant effects on proteins biological activity [5,6]. Protein interactions are highly selective, and this selectivity is defined within a protein's structure. In our previous work [2] a relationship between the RRM spectra of some protein groups and their interaction with visible light has been established.

In this study, the RRM approach was used to predict the activation frequency of EMR that would modulate the function of proto-oncogene proteins. We have designed and presented the exposure system that can emit light at the selected frequencies [2]. This study investigates the effect of non-coherent low intensity light exposures on B16F0 mouse melanoma cancer cells and CHO, normal Chinese Hamster Ovarian cell line.

## 2. MATERIAL AND METHODS

### 2.1. Determination of the RRM Characteristic Frequency

It was shown in our previous studies that all protein sequences with a common biological function have a common frequency component in the free energy distribution of electrons along the protein backbone. This characteristic frequency was shown to be related to protein biological function [2, 3]. It was also shown that proteins and their targets share a characteristic frequency. Thus, it can be postulated that RRM frequencies characterize not only a general function but also a recognition/interaction between the particular proteins and their target at a distance. Thus, protein interactions can be viewed as a resonant energy transfer between the interacting molecules. This energy can be transferred through oscillations of a physical field, possibly electromagnetic in nature [2]. Since there is evidence that proteins have certain conducting or semi-conducting properties, a charge moving through the protein backbone and passing different energy stages caused by different amino acid side groups can produce sufficient conditions for a specific electromagnetic radiation or absorption [2]. A strong linear correlation exists between the predicted and experimentally determined frequencies corresponding to the absorption of electromagnetic radiation of such proteins [2]. It is inferred that approximate wavelengths in real frequency space can be calculated from the RRM characteristic frequencies for each biologically related group of sequences. These calculations can be used to predict the wavelength of the light irradiation, which might affect the biological activity of exposed proteins. The frequency range predicted for protein interactions is from  $10^{13}$  Hz to  $10^{15}$  Hz. This estimated range includes IR, visible and UV light. These computational predictions were confirmed by comparison of: (i) absorption characteristics of light absorbing proteins and their characteristic RRM frequencies [2]; (ii) frequency selective light effects on cell growth and characteristic RRM frequencies of growth factors [2]; and (iii) activation of enzymes by laser radiation [2]. These results indicate that the specificity of protein interaction is based on a resonant electromagnetic energy transfer at the frequency specific for each interaction. A linear correlation between the absorption spectra of proteins and their RRM spectra with a regression coefficient of  $K = 201$  was established. Using RRM postulates, a computationally identified characteristic frequency for a protein functional group can be used to calculate the wavelength of applied irradiation,  $\lambda$ , defined as  $\lambda = 201/f_{RRM}$ , which could activate this protein sequence and modify its bioactivity [2, 3].

Here we employed the RRM for analysis of 28 proto-oncogene proteins. The RRM characteristic frequency was determined at  $f_{RRM} = 0.0576$ . This frequency is then converted into the wavelength of the applied irradiation using the scaling factor  $K = 201$  to define the range of activation frequency,  $\lambda$ , that would modulate the activity of the proto-oncogene proteins. The predicted wavelength is defined at  $\lambda = 3489$  nm. The exposure LED-based system was developed and the experimental evaluation of the attained far infrared wavelengths of 3400 nm, 3600 nm, 3800 nm, 3900 nm, 4100 nm and 4300 nm was conducted on B16F0 and CHO cell lines.

### 2.2. Materials and Cell Lines

LDH diagnosis kit (Roche Australia). The culture media: clear DMEM (Invitrogen Australia). Each bottle of 500 ml had 10ml of HEPES (buffer for Media) with 10% of Fetal Bovine Serum and 1% of Antibiotics (streptomycin). Three different patches of B16F0 and CHO have been used for the experiments.

### 2.3. Experimental Procedures

In our experimental set up, exposure and post exposure conducted inside incubator with constant intensity for a better comparison factor. All experiments were done three times in triplicate for the accuracy of the results.

All the cell lines were seeded in the plate for 24 hrs before the start of experiments. Three types of experiments were conducted: (i) 1.5 hrs of exposure +0 hrs of post exposure; (ii) 1.5 hrs of exposure +24 hrs of post exposure; and (iii) 1.5 hrs of exposure +24 hrs of post exposure.

In addition, to eliminate any effect induced by the heat generated by the LEDs used, we have used a heat shield gel purchased from Inventables, USA. More importantly, we have eliminated any cross talk between the LED frequencies and effect of two frequencies on the same well by having empty wells around each well that we are running the experiments.

### 3. RESULTS AND DISCUSSION

Irradiation of the selected cancer and normal cells was conducted with the results shown in Figure 1 which presents the cell viability tests conducted on B16F0 and CHO cells.

It can be clearly seen from Figure 1 that the cell viability of murine cancer cells B16F0 is reduced when the time of exposure and the time of post exposure are increased. The difference between the cell viability of exposed and non-exposed (untreated) cells is increased by increasing the post

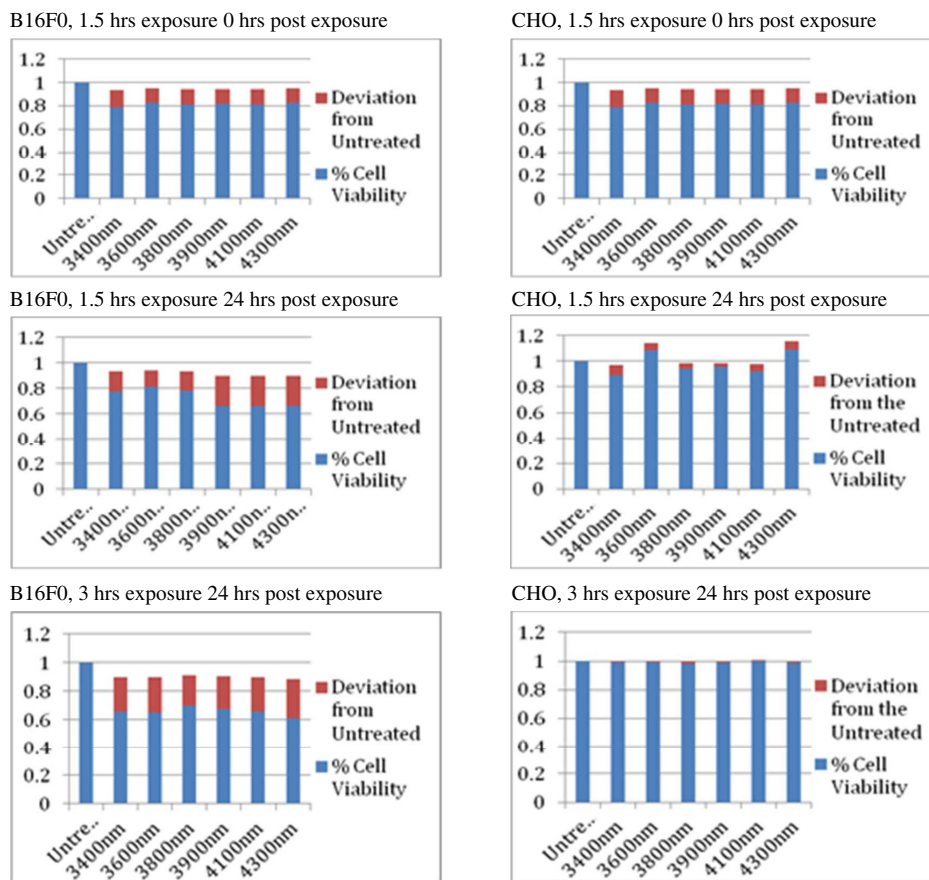


Figure 1: Cell viability of B16F0 and CHO cells for different exposure and post exposure times.

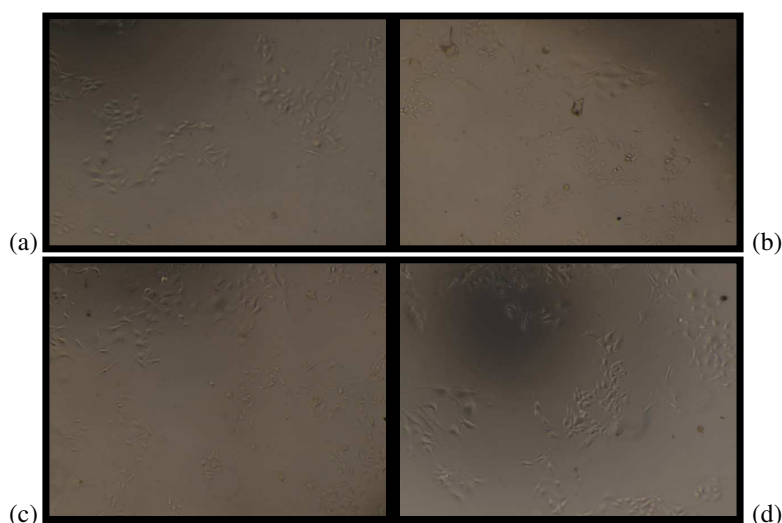


Figure 2: Light microscopy images of B16F0, murine melanoma cells, before and after the far infrared light exposures: (a) before 1.5 hr of exposure, (b) before 3 hrs of exposure, (c) after 1.5 hr of exposure, and (d) after 3 hrs of exposure.

exposure duration. However, in the case of CHO cells, the difference in cell viability for exposed vs. non-exposed cells is not significant. Irradiation of CHO cells at all studied wavelengths has not induced any effects on their viability.

Figure 2 shows the images obtained by light microscopy which do not indicate any changes in the morphology of the cells while LDH results clearly demonstrate reduction in the cell viability upon irradiation.

#### 4. CONCLUSIONS

The experiments conducted in this study showed that far infrared light at the specific frequencies predicted computationally can induce changes in cell viability of the selected murine melanoma cells B16F0. These results support the hypothesis that external electromagnetic radiation can modulate biological process. The exposure system based on LEDs was developed and its efficiency was evaluated experimentally. Quantitative analysis of the experimental data with LDH cytotoxicity test showed the reduced cell viability observed for cancerous cell line while the normal cells were not affected by light exposures. However, light microscopy images of cancer cells taken before and after the exposures to far infrared light do not show any changes in the cells morphology.

#### REFERENCES

1. Vojisavljevic, V., E. Pirogova, and I. Cosic, "The effect of electromagnetic radiation (550 nm–850 nm) on L-Lactate dehydrogenase kinetics," *Journal of Radiation Biology*, 2007.
2. Peidaee, P., I. Cosic, and E. Pirogova, "Low intensity light therapy exposure system," *World Congress of Medical Physics and Biomedical Engineering*, Beijing, China, 2012.
3. Pirogova, E., J. Fang, M. Akay, and I. Cosic, "Investigation of the structural and functional relationships of oncogene proteins," *IEEE Proceedings*, Vol. 90, No. 1, 1859–1867, 2002.
4. (WHO) W.H.O., "The top 10 causes of death," 2011.
5. Pirogova, E., V. Vojisavljevic, and I. Cosic, "Biological effects of electromagnetic radiation," Review Report, Melbourne, Australia.
6. Pirogova, E., V. Vojisavljevic, T. Istivan, P. Coloe, and I. Cosic, "Review study: Influence of electromagnetic radiation on enzyme activity and effects of synthetic peptides on cell transformation," *Medical Data*, Vol. 2, No. 4, Dec. 2010.

# The Effect of Pulse Parameters and Medium Information on the Temporal Coherence Length of a Partially Coherent Pulse on Scattering

Chaoliang Ding\* and Liuzhan Pan

College of Physics and Electronic Information, Luoyang Normal University, Luoyang 471022, China

**Abstract**— The changes of the temporal coherence length of partially coherent plane-wave pulse produced by scattering from quasi-homogeneous random medium are studied with the accuracy of the first Born approximation. It is shown that the temporal coherence length of scattered partially coherent plane-wave pulse, depending on the medium properties and incident pulse parameters, varies non-monotonously with increasing scattering angle. The numerical calculation results are given.

## 1. INTRODUCTION

Scattering of a light wave is of considerable importance in many areas such as medical diagnostics and imaging, remote sensing in the atmosphere and ocean, and so on, because one can obtain information about properties of the object from the knowledge of the scattered field [1]. In the past two decades, many papers were published about scattering, both for deterministic and random media [2–6]. And the incident field was spatially fully coherent monochromatic or polychromatic light wave. Very recently, Van Dijk et al. studied the degree of coherence of the incident field on the radiant intensity of the scattered field [7]. However, all the above investigations mentioned have been restricted to the stationary light wave.

Recently, a model of spectrally partially coherent plane-wave pulse, in which the correlation between different frequency components was taken into consideration, was introduced by Pääkkönen et al. [8, 9]. The propagation property of partially coherent plane-wave pulse in space-time domain was investigated by using tensor method [10]. And some methods to generate partially coherent plane-wave pulse have been proposed [11, 12]. The propagation of partially coherent pulses through various systems has been studied widely [13–16]. Most recently, we consider the scattering of partially coherent plane-wave pulse that is incident to the quasi-homogeneous random medium. And we have pointed that the temporal coherence length of the scattered field depends on the effective radius and correlation length of medium and the incident pulse parameters [17]. In the present paper, we present the detailed numerical calculation results to illustrate the dependence of temporal coherence length of scattered field on the effective radius  $\sigma_R$  and the correlation length  $\sigma_r$  of the medium, and the pulse duration  $T_0$ , the temporal coherence length  $T_c$  of the incident pulse.

## 2. THEORY

Let us consider a spectrally partially coherent plane-wave pulse, propagating in a direction specified by a unit vector  $\mathbf{s}_0$ , incident on a random medium occupying a finite volume  $D$  (see Fig. 1 in Ref. [17]). The cross-spectral density function of the incident pulse at a pair of points specified by the position vectors  $(\mathbf{r}_1, \omega_1)$  and  $(\mathbf{r}_2, \omega_2)$  can be expressed as in the form

$$\begin{aligned} W^{(i)}(\mathbf{r}'_1, \mathbf{r}'_2, \omega_1, \omega_2) &= \langle U^{(i)*}(\mathbf{r}'_1, \omega_1) U^{(i)}(\mathbf{r}'_2, \omega_2) \rangle \\ &= W_0 \exp \left[ -\frac{(\omega_1 - \omega_0)^2 + (\omega_2 - \omega_0)^2}{2\Omega_0^2} - \frac{(\omega_1 - \omega_2)^2}{2\Omega_c^2} \right] \exp [i(k_2 \mathbf{s}_0 \cdot \mathbf{r}'_2 - k_1 \mathbf{s}_0 \cdot \mathbf{r}'_1)], \end{aligned} \quad (1)$$

where  $W_0 = \frac{T_0}{2\pi\Omega_0} \Gamma_0$ ,  $\Omega_0 = \sqrt{\frac{1}{T_0^2} + \frac{2}{T_c^2}}$ ,  $\Omega_c = \frac{T_c}{T_0} \Omega_0$ .  $T_0$  characterizes the pulse duration.  $T_c$  is the temporal coherence length, which denotes the temporal correlation of the pulse.  $\omega_0$  is the center frequency of the pulse.

Let  $F(\mathbf{r}, \omega)$  be the scattering potential of the medium and assume that the scattering medium is so weak that the scattering can be analyzed within the accuracy of the first-order Born approximation [18]. The correlation function of the scattering potential can be defined as [19]

$$C_F(\mathbf{r}'_1, \mathbf{r}'_2, \omega_0) = \langle F^*(\mathbf{r}'_1, \omega_0) F(\mathbf{r}'_2, \omega_0) \rangle_m, \quad (2)$$

\*Corresponding author: Chaoliang Ding (dingchaoliang2006@126.com).

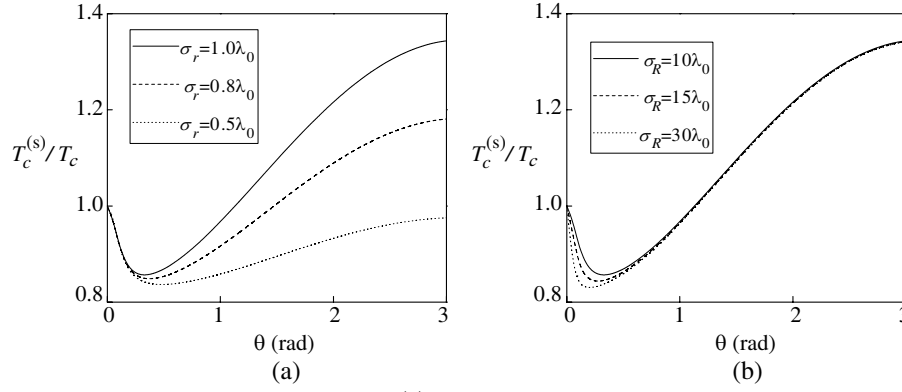


Figure 1: Relative temporal coherence length  $T_c^{(s)}/T_c$  as a function of scattering angle  $\theta$ . The parameters (a)  $\sigma_R = 10\lambda_0$ , (b)  $\sigma_r = \lambda_0$ ,  $T_0 = 5$  fs,  $T_c = 5$  fs,  $\omega_0 = 2.36$  rad/fs.

where the asterisk denotes the complex conjugate and the angular brackets denote the average taken over the ensemble of the random medium. The cross-spectral density function of the scattered field in the far zone, at two points specified by position vectors  $r\mathbf{s}_1$  and  $r\mathbf{s}_2$  ( $\mathbf{s}_1^2 = \mathbf{s}_2^2 = 1$ ), can be expressed as [19]

$$W^{(s)}(r\mathbf{s}_1, r\mathbf{s}_2, \omega_1, \omega_2) = W_0 \exp \left[ -\frac{(\omega_1 - \omega_0)^2 + (\omega_2 - \omega_0)^2}{2\Omega_0^2} - \frac{(\omega_1 - \omega_2)^2}{2\Omega_c^2} \right] \frac{\exp [ir(k_2 - k_1)]}{r^2} \\ \times \int_D \int_D C_F(\mathbf{r}'_1, \mathbf{r}'_2, \omega_0) \exp \{-i[\mathbf{K}_1 \cdot \mathbf{r}'_1 + \mathbf{K}_2 \cdot \mathbf{r}'_2]\} d^3r'_1 d^3r'_2, \quad (3)$$

where  $\mathbf{K}_1 = -k_1(\mathbf{s}_1 - \mathbf{s}_0)$ , and  $\mathbf{K}_2 = k_2(\mathbf{s}_2 - \mathbf{s}_0)$  are analogous to the momentum transfer vector of quantum mechanical theory of potential scattering.  $k_i = \omega/c$  ( $i = 1, 2$ ),  $c$  being the speed of light *in vacuo*.

Suppose that the scatterer is a Gaussian-correlated, quasi-homogeneous isotropic medium. We assume that the macroscopic properties of the medium do not changes in time, i.e., that we are dealing with static scattering. The correlation function of the scattering potential has been given by the expression [4, 6]

$$C_F(\mathbf{r}'_1, \mathbf{r}'_2, \omega_0) = C_0 \exp \left[ -\frac{|\mathbf{r}'_1 + \mathbf{r}'_2|^2}{8\sigma_R^2} \right] \exp \left[ -\frac{|\mathbf{r}'_1 - \mathbf{r}'_2|^2}{2\sigma_r^2} \right], \quad (4)$$

where  $C_0$  is a positive constants.  $\sigma_R$  denotes the effective radius and  $\sigma_r$  denotes the correlation length of the scatterer,  $\sigma_R \gg \sigma_r$ . On substituting from Eq. (4) into Eq. (3), one can obtain the cross-spectral density function of the scattered field

$$W^{(s)}(r\mathbf{s}_1, r\mathbf{s}_2, \omega_1, \omega_2) = W_0 \exp \left[ -\frac{(\omega_1 - \omega_0)^2 + (\omega_2 - \omega_0)^2}{2\Omega_0^2} - \frac{(\omega_1 - \omega_2)^2}{2\Omega_c^2} \right] \frac{\exp [ir(k_2 - k_1)]}{r^2} \\ \times (2\pi\sigma_R\sigma_r)^3 C_0 \exp \left[ -\frac{1}{2}\sigma_R^2 |\mathbf{K}_1 + \mathbf{K}_2|^2 \right] \exp \left[ -\frac{1}{2}\sigma_r^2 \left| \frac{\mathbf{K}_2 - \mathbf{K}_1}{2} \right|^2 \right], \quad (5)$$

Using the inverse Fourier transform of the cross-spectral density function, the mutual coherence function of the scattered field is

$$\Gamma^{(s)}(r\mathbf{s}_1, r\mathbf{s}_2, t_1, t_2) = \int \int_{-\infty}^{\infty} W^{(s)}(r\mathbf{s}_1, r\mathbf{s}_2, \omega_1, \omega_2) \exp [i(\omega_1 t_1 - \omega_2 t_2)] d\omega_1 d\omega_2. \quad (6)$$

where the mutual coherence function  $\Gamma$  is the basic quantity of the so-called second-order coherence theory, the term “second-order” indicating that  $\Gamma$  is a correlation function involving a product of the field variable at two points.

After a tedious calculation, degree of temporal coherence of the scattered field, when the observation positions coincide ( $\mathbf{s}_1 = \mathbf{s}_2 = \mathbf{s}$ ), can be expressed as

$$\left| \mu^{(s)}(r\mathbf{s}, r\mathbf{s}, t_1, t_2) \right| = \left| \frac{\Gamma^{(s)}(r\mathbf{s}, r\mathbf{s}, t_1, t_2)}{\sqrt{\Gamma^{(s)}(r\mathbf{s}, r\mathbf{s}, t_1, t_1)} \sqrt{\Gamma^{(s)}(r\mathbf{s}, r\mathbf{s}, t_2, t_2)}} \right| = \exp \left[ -\frac{(t_1 - t_2)^2}{2(T_c^{(s)})^2} \right], \quad (7)$$

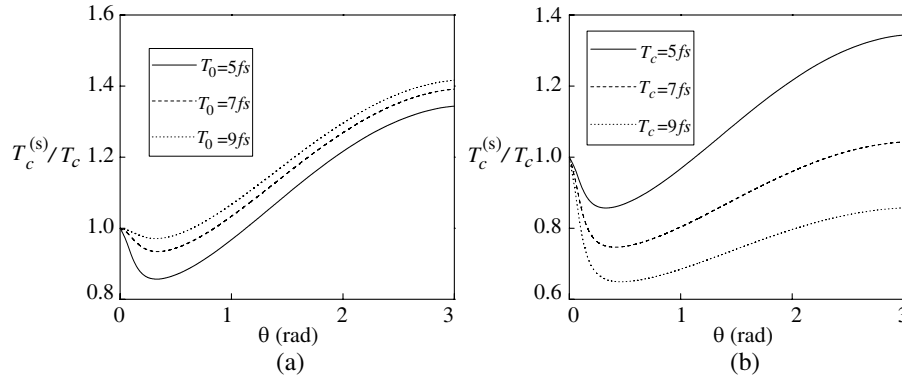


Figure 2: Relative temporal coherence length  $T_c^{(s)}/T_c$  as a function of scattering angle  $\theta$ . The parameters (a)  $T_c = 5$  fs, (b)  $T_0 = 5$  fs,  $\sigma_R = 10\lambda_0$ ,  $\sigma_r = \lambda_0$ .

where

$$\left(T_c^{(s)}\right)^2 = \frac{\left(\frac{T_0^2 T_c^2}{T_c^2 + 2T_0^2} + 2 \sin^2 \frac{\theta}{2} \frac{\sigma_r^2}{c^2}\right) \left(T_0^2 + 8 \sin^2 \frac{\theta}{2} \frac{\sigma_R^2}{c^2}\right)}{\left[\frac{T_0^4}{T_c^2 + 2T_0^2} + 4 \sin^2 \frac{\theta}{2} \left(\frac{\sigma_R^2}{c^2} - \frac{\sigma_r^2}{4c^2}\right)\right]}. \quad (8)$$

Equation (8) describes the changes in the temporal coherence length  $T_c^{(s)}$  of spectrally partially coherent plane-wave pulses scattered by a random medium. From Eq. (8), we can see that the temporal coherence length  $T_c^{(s)}$  of scattered field depends on the effective radius  $\sigma_R$  and the correlation length  $\sigma_r$  of the medium, and the pulse duration  $T_0$ , the temporal coherence length  $T_c$  of the incident pulse. In the following section, we will present the detailed numerical results.

### 3. NUMERICAL CALCULATION RESULTS AND ANALYSES

The relative temporal coherence length  $T_c^{(s)}/T_c$  of scattered field for different medium properties and incident pulse parameters is given in Figs. 1 and 2, respectively. As is shown that the relative temporal coherence length  $T_c^{(s)}/T_c$ , depending on the medium properties ( $\sigma_R$ ,  $\sigma_r$ ) and incident pulse parameters ( $T_0$ ,  $T_c$ ), varies non-monotonously with increasing scattering angle  $\theta$ . And there is a minimum of temporal coherence length  $T_c^{(s)}/T_c$  in the region  $0 \leq \theta \leq 3$ . From Figs. 1(a) and (b), the effective radius  $\sigma_R$  and correlation length  $\sigma_r$  of medium play an important role on the  $T_c^{(s)}/T_c$  in the region  $0.3 \leq \theta \leq 3$  and  $0 \leq \theta \leq 0.6$ , respectively. And  $\sigma_R$  and  $\sigma_r$  affect the minimum and corresponding scattering angle  $\theta_{\min}$ . As can be see from Fig. 2 that the temporal coherence length  $T_c^{(s)}/T_c$  increases with increasing pulse duration  $T_0$  and decreasing temporal coherence length  $T_c$  of incident pulse. And the temporal coherence length  $T_c$  of incident pulse affects the minimum and corresponding scattering angle  $\theta_{\min}$ . However, the pulse duration  $T_0$  of incident pulse affects the minimum of temporal coherence length only, the corresponding scattering angle  $\theta_{\min}$  is a constant for different  $T_0$ .

### 4. CONCLUSIONS

In conclusion, with the accuracy of the first Born approximation, the changes of the temporal coherence length of partially coherent plane-wave pulse produced by scattering from quasi-homogeneous random medium have been investigated. Numerical calculation results are given to illustrate the dependence of temporal coherence length of scattered field on the effective radius and correlation length of medium and the incident pulse parameters. It has been shown that the relative temporal coherence length  $T_c^{(s)}/T_c$ , depending on the medium properties ( $\sigma_R$ ,  $\sigma_r$ ) and incident pulse parameters ( $T_0$ ,  $T_c$ ), varies non-monotonously with increasing scattering angle  $\theta$ . The medium parameters  $\sigma_R$  and  $\sigma_r$  play an important role on the  $T_c^{(s)}/T_c$  in the region  $0.3 \leq \theta \leq 3$  and  $0 \leq \theta \leq 0.6$ , respectively. And the  $T_c^{(s)}/T_c$  increases with increasing pulse duration  $T_0$  and decreasing temporal coherence length  $T_c$  of incident pulse.

### ACKNOWLEDGMENT

This work was supported by the National Natural Science Foundation of China under Grant Nos. 61275150, 61108090, and 61078077, and Natural Science Foundation of Henan Province under

Grant Nos. 112300410062 and 13A140797.

#### REFERENCES

1. Tsang, L., J. A. Kong, and K. H. Ding, *Scattering of Electromagnetic Waves: Theories and Applications*, 1st Edition, Wiley, 2000.
2. Wolf, E., J. T. Foley, and F. Gori, “Frequency shifts of spectral lines produced by scattering from spatially random media,” *J. Opt. Soc. Am. A*, Vol. 6, No. 8, 1142–1149, 1989.
3. Sahin, S. and O. Korotkova, “Scattering of scalar light fields from collections of particles,” *Phys. Rev. A*, Vol. 78, No. 6, 063815, 2008.
4. Lahiri, M., E. Wolf, D. G. Fischer, and T. Shirai, “Determination of correlation functions of scattering potentials of stochastic media from scattering experiments,” *Phys. Rev. Lett.*, Vol. 102, No. 12, 123901, 2009.
5. Sahin, S. and O. Korotkova, “Effect of the pair-structure factor of a particulate medium on scalar wave scattering in the first born approximation,” *Opt. Lett.*, Vol. 34, No. 12, 1762–1764, 2009.
6. Du, X. Y. and D. M. Zhao, “Scattering of light by Gaussian-correlated quasi-homogeneous anisotropic media,” *Opt. Lett.*, Vol. 35, No. 3, 384–386, 2010.
7. Van Dijk, T., D. G. Fischer, T. D. Visser, and E. Wolf, “Effects of spatial coherence on the angular distribution of radiant intensity generated by scattering on a sphere,” *Phys. Rev. Lett.*, Vol. 104, No. 17, 173902, 2010.
8. Pääkkönen, P., J. Turunen, P. Vahimaa, A. T. Friberg, and F. Wyrowski, “Partially coherent Gaussian pulses,” *Opt. Commun.*, Vol. 204, Nos. 1–6, 53–58, 2002.
9. Lajunen, H., J. Tervo, and P. Vahimaa, “Overall coherence and coherent-mode expansion of spectrally partially coherent plane-wave pulses,” *J. Opt. Soc. Am. A*, Vol. 21, No. 11, 2117–2123, 2004.
10. Lin, Q., L. G. Wang, and S. Y. Zhu, “Partially coherent light pulse and its propagation,” *Opt. Commun.*, Vol. 219, Nos. 1–6, 65–70, 2003.
11. Lajunen, H., J. Tervo, J. Turunen, P. Vahimaa, and F. Wyrowski, “Spectral coherence properties of temporally modulated stationary light sources,” *Opt. Express*, Vol. 11, No. 16, 1894–1899, 2003.
12. Torres-Company, V., G. Mínguez-Vega, J. Lancis, and A. T. Friberg, “Controllable generation of partially coherent light pulses with direct space-to-time pulse shaper,” *Opt. Lett.*, Vol. 32, No. 12, 1608–1610, 2007.
13. Friberg, A. T., H. Lajunen, and V. Torres-Company, “Spectral elementary-coherence-function representation for partially coherent light pulses,” *Opt. Express*, Vol. 15, No. 8, 5160–5165, 2007.
14. Torres-Company, V., H. Lajunen, J. Lancis, and A. T. Friberg, “Ghost interference with classical partially coherent light pulses,” *Phys. Rev. A*, Vol. 77, No. 4, 043811, 2008.
15. Ding, C. L., L. Z. Pan, and B. D. Lü, “Characterization of stochastic spatially and spectrally partially coherent electromagnetic pulsed beams,” *New J. Phys.*, Vol. 11, No. 8, 083001, 2009.
16. Lajunen, H., V. Torres-Company, J. Lancis, E. Silvestre, and P. Andrés, “Pulse-by-pulse method to characterize partially coherent pulse propagation in instantaneous nonlinear media,” *Opt. Express*, Vol. 18, No. 14, 14979–14991, 2010.
17. Ding, C. L., Y. J. Cai, O. Korotkova, Y. T. Zhang, and L. Z. Pan, “Scattering-induced changes in the temporal coherence length and the pulse duration of a partially coherent plane-wave pulse,” *Opt. Lett.*, Vol. 36, No. 4, 517–519, 2011.
18. Born, M. and E. Wolf, *Principles of Optics*, 7th Edition, Cambridge University Press, Cambridge, 1999.
19. Wolf, E., *Introduction to the Theory of Coherence and Polarization of Light*, 1st Edition, Cambridge University Press, Cambridge, 2007.

# Analysis of Transmission Characteristics and Multiple Resonances in Plasmonic Gratings Coated with Homogeneous Dielectrics

P. Arora and A. Krishnan

Department of Electrical Engineering, Indian Institute of Technology Madras, Chennai, India

**Abstract**— We analyze the broadband transverse magnetic transmission characteristics of two very low aspect ratio plasmonic nanograting structures under normal incidence, using rigorous coupled wave analysis and full wave Maxwell’s equations solver. A binary metallic grating with narrow fundamental surface plasmon resonance mode was obtained by systematic variation of geometrical parameters. The binary grating had an aspect ratio of 0.2 and exhibited a sensitivity of 560 nm/RIU. Our analysis of another structure consisting of a metallic grating with a very small aspect ratio of 0.1, patterned on a thin homogeneous metal interspacer layer on a dielectric substrate shows  $\sim 50\%$  reduction in full width at half maximum of fundamental surface plasmon resonance with a sensitivity of 590 nm/RIU. This plasmonic nanograting structure exhibits a strong potential to be used as refractive index sensor due to very high sensitivity, higher localization of the fields, possibly higher signal to noise ratio and very low aspect ratios that are needed to maintain laminar flow of analyte.

## 1. INTRODUCTION

Grating coupled surface plasmon resonances have received tremendous interest in the recent past due to the possibility of coupling to surface plasmon modes at near normal incidences and avoidance of complicated mechanical angular scanning instrumentation needed as in the case of Kretschmann’s geometry [1]. However, they have also been shown to exhibit lower sensitivities compared to Kretschmann arrangement due to distribution of incident light across multiple diffraction orders [2]. Recently, there have been a few reports on extremely high aspect ratio plasmonic nanostructures like tall sub 10 nanometer grooves that exhibit improved sensitivity due to extreme localization of the fields, but the nanofabrication requirements to manufacture these structures are extremely high and secondly, the adsorption of analytes to be sensed in these extremely narrow width and high aspect ratio structures may be very difficult [3].

In this paper we describe the transmission characteristics of very low aspect ratio plasmonic nanograting structure based on a grating patterned on a thin homogeneous metal interspacer layer, that exhibits sensitivity of 590 nm/RIU with a reduction of Full Width at Half Maximum (FWHM) of the fundamental surface plasmon mode by  $\sim 50\%$  when compared to an optimized binary metallic grating structure.

## 2. ANALYSIS OF TRANSMISSION CHARACTERISTICS OF PLASMONIC GRATINGS COATED WITH A HOMOGENEOUS DIELECTRIC

The schematic of the geometrical structures of Binary Metal Grating (BMG) and Metal Grating on Metal interspacer (MGM) are shown in Figs. 1(a) and (b) respectively. The substrate of both these structures is assumed to be BK-7 glass with a refractive index of 1.542. The metal considered in all our simulations is gold with a permittivity defined by the Drude-Lorentz model in Equation (1), the parameters were obtained from [4]

$$\varepsilon_r(\omega) = \varepsilon_\infty - \left( \frac{\omega_p^2}{\omega^2 + j\omega\Gamma_p} \right) - \left( \frac{\Delta\varepsilon\Omega_L^2}{(\omega^2 - \Omega_L^2) + j\omega\Gamma_L} \right) \quad (1)$$

where,  $\varepsilon_\infty = 5.9673$ ,  $\omega_p = 2\pi * 2113.6$  rad/s,  $\Gamma_p = 2\pi * 15.92$  rad/s,  $\Omega_L = 2\pi * 650.07$  rad/s,  $\Gamma_L = 2\pi * 104.86$  rad/s and  $\Delta\varepsilon = 1.09$ .

The dielectric superstrate is assumed to be 400 nm thick ( $t_d$ ) with a refractive index of 1.33 for both structures. In the case of BMG structure [Fig. 1(a)], a gold nanograting is assumed to be patterned on top of the BK-7 substrate directly, however, in the case of the MGM structure [Fig. 1(b)], a homogeneous thin metal film layer in between the substrate and the grating is considered. Such structures can easily be fabricated using conventional semiconductor processing techniques involving a photolithography or electron beam lithography, a metal evaporation step followed by a lift-off

process. Alternately, such structures may also be fabricated using Focused Ion Beam milling of the top metal layer deposited on the glass substrate.

Broadband simulations were performed for normal incidence from the top of the structures using a homemade Rigorous Coupled Wave Analysis (RCWA) program [5] and the field distributions were obtained using a commercial finite elements full wave solver. The geometrical parameters of the BMG structure namely the period of the grating ' $\Lambda$ ', the width of the metal stripe ' $w$ ', the thickness of the metal stripes ' $t_m$ ' and the thickness of the dielectric superstrate ' $t_d$ ' were changed systematically and the transmittivity was measured from the bottom of the substrate for Transverse Magnetic (TM) polarization for a range of wavelengths from 500 nm to 1500 nm. It was observed that for a  $t_d$  of 400 nm,  $\Lambda$  of 600 nm,  $w_m$  of 300 nm and  $t_m$  of 60 nm and for a superstrate refractive index of 1.33, the BMG structure exhibited three distinct absorption dips at 630.8 nm, 794.3 nm and 938.2 nm as shown in the black curve of Fig. 2(a). The shift of the resonances with a change in the dielectric superstrate's refractive index by  $\pm 0.01$  RIU is shown in Fig. 2(a) as blue and red curves respectively and the inset of Fig. 2(a) shows a zoomed in region around the resonance at 794.3 nm. The Electric field ( $E_y$ ) distributions for this geometry with superstrate refractive index of 1.33, at wavelengths 630.8 nm, 794.3 nm and 938.2 nm are shown in Figs. 2(b), 2(c) and 2(d) respectively. It is observed that the resonant dip in transmission at wavelength of 630.8 nm is due to a dielectric mode wherein the field in Fig. 2(b) resembles a conventional waveguide mode. The occurrence of these higher order modes have been reported earlier and have been attributed to the interface of metal and thicker dielectrics that can support multiple modes, wherein the plasmons with lower momentum propagate with majority of the field away from the metal dielectric interface [4], resulting in lower propagation losses due to weaker interaction with the metal. It was also observed that as the thickness of the dielectric superstrate increased, a number of high quality factor dielectric modes were excited (not shown here) and the spectral position of the dielectric modes varied with thickness of the superstrate considered, which is consistent with earlier reports [6]. The resonance at 794.3 nm is attributed the fundamental surface plasmon resonance at the metal and dielectric superstrate interface. The third broad resonance at 938.2 nm is due to excitation of the surface plasmons at the metal substrate interface. It is seen that this mode is very broad due to two reasons, first, the absorption of the metal in the grating causes a significant loss of energy prior to the light arriving at the substrate metal interface resulting in lower quality factor resonance and second, the higher refractive index of the substrate results in weaker excitation of the plasmons at this interface due to higher momentum mismatch. The choice of the these geometrical parameters for the BMG structure were from a number of simulations carried out with systematic variation of the geometry and these values of geometrical parameters resulted in narrowest FWHM for the fundamental resonance at the metal and dielectric superstrate interface, since this is the most important resonance for sensing applications. The FWHM for the fundamental mode at metal and dielectric superstrate was extracted as 78.9 nm and the sensitivity of this mode to a change in refractive index was 560 nm/RIU. Even though the dielectric waveguide higher order mode has lower FWHM of 37.8 nm, the sensitivity of this mode was found to be 290 nm/RIU which is significantly lower than the sensitivity of the fundamental surface plasmon mode at metal dielectric superstrate interface. The position of the waveguide mode also shifts with thickness of the superstrate of constant refractive index which is not suitable for refractive index sensing, however the number of higher order modes excited may be used as a coarse method for detecting the thickness of the dielectric superstrate, provided the refractive index is extracted using

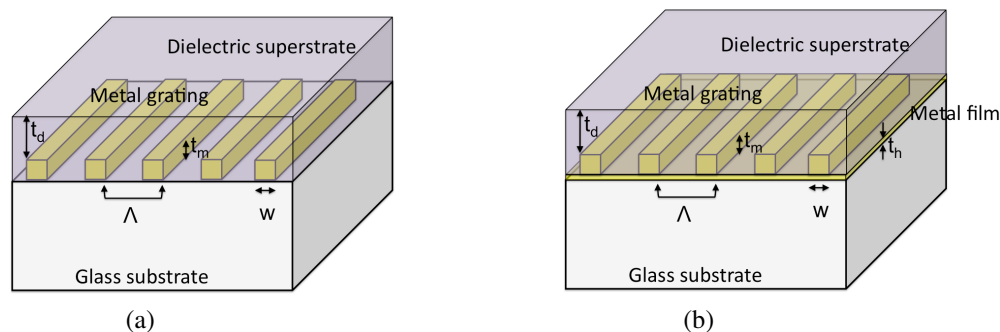


Figure 1: (a) and (b) schematic diagram (not to scale) of the BMG and MGM plasmonic nanogratings.

the position of the fundamental plasmon resonance at the metal and dielectric superstrate interface.

The transmission characteristics of the MGM structure for a  $t_d$  of 400 nm,  $\Lambda$  of 600 nm,  $w_m$  of 300 nm,  $t_m$  of 30 nm and for a homogeneous thin metal film interspacer thickness  $t_h$  of 30 nm, with a superstrate refractive index of 1.33, is shown in Fig. 3(a). The MGM structure also exhibited three resonances at 654.1 nm, 841.6 nm and 970.9 nm as shown in black curve of Fig. 3(a). The shift of the resonance peaks with a change in the dielectric superstrate's refractive index by  $\pm 0.01$  RIU is shown in Fig. 3(a) as blue and red curves respectively and the inset of Fig. 3(a) shows a zoomed in region around the resonance at 841.6 nm. The resonances now occur as transmission peaks instead of transmission dips observed in BMG structure. The transmission peaks occur since under most conditions almost all of the incident light is reflected back to the top except for momentum matching conditions for different resonances wherein surface plasmon modes are excited at the metal dielectric superstrate interface. When the surface plasmon modes are excited on the metal dielectric superstrate interface, due to the very small thickness of the homogeneous metal film ( $t_h = 30$  nm), a radiative decay of the surface plasmons occurs through the substrate and the light leaks through the substrate at specific angles depending on refractive indices of substrate and superstrate. Such radiative decay of surface plasmon modes have been used in the recent past in leakage radiation microscopy based experiments [7].

The electric field ( $E_y$ ) distribution for the three resonances at 654.1 nm, 841.6 nm and 970.9 nm are shown in Figs. 3(b), 3(c) and 3(d) respectively. From the field distribution in Fig. 3(b), it is clear that the resonance at 654.1 nm corresponds to a dielectric waveguide mode. The FWHM of this peak was calculated to be 14.8 nm, exhibited a sensitivity of 320 nm/RIU. The transmission peak at 841.6 nm of black curve in Fig. 3(a) was attributed to the fundamental surface plasmon resonance at the metal and dielectric superstrate interface. The electric field distribution for this mode (Fig. 3(c)) shows a strongly confined mode at the metal grating dielectric superstrate interface. The FWHM of this peak was 41.1 nm as opposed to FWHM of 78.9 nm for BMG structure in

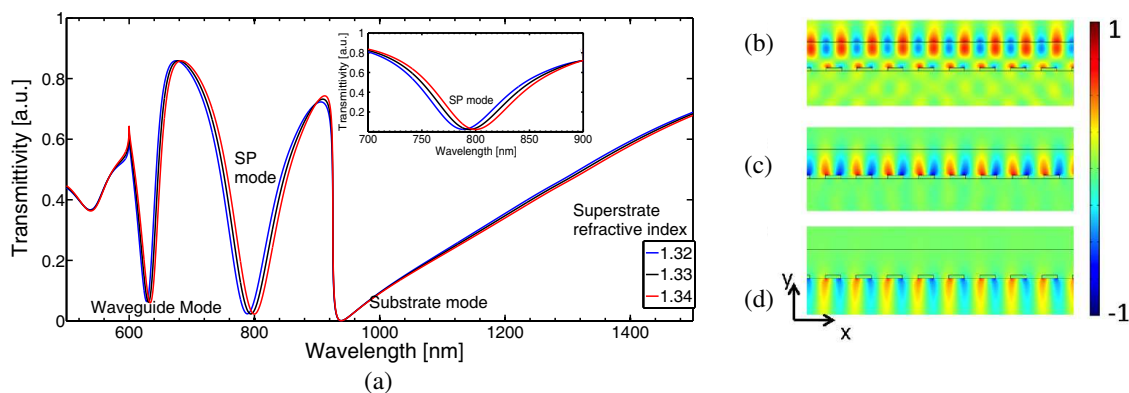


Figure 2: (a) Transmission spectrum for the BMG configuration (inset: zoomed in region corresponding to the SP mode). (b), (c) and (d)  $E_y$  distribution at waveguide mode, SP mode and substrate mode respectively.

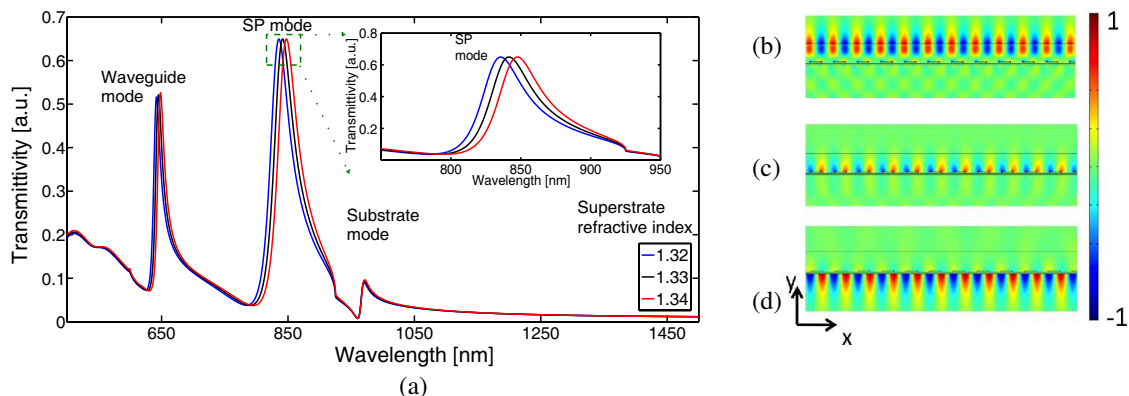


Figure 3: (a) Transmission spectrum for the MGM configuration (inset: zoomed in region corresponding to the SP mode). (b), (c) and (d)  $E_y$  distribution at waveguide mode, SP mode and substrate mode respectively.

Fig. 2(a). The sensitivity to a change of refractive index of the dielectric superstrate was measured to be 590 nm/RIU for identical thickness and refractive index of superstrate in BMG structure.

The reduction in the FWHM of fundamental surface plasmon resonance at metal and dielectric superstrate interface by  $\sim 50\%$  accompanied by an increase in sensitivity was further studied. The field distribution of this mode in Fig. 3(c) corresponded to a  $1/e$  field decay length in the  $y$ -direction of 190 nm, as opposed to 251 nm for the BMG structure. The peak value of the electric field at the grating region of the MGM structure for the fundamental surface plasmon mode at the metal superstrate interface was three times the peak value observed in BMG structure. The stronger localization of the field in  $y$ -direction in the case of the MGM structure is attributed to the homogeneous metal film interspacer and very low aspect ratio of the grating structure, due to which the interaction of the field on top of the metallic grating region with the homogeneous metal film is enhanced. This results in a stronger localization of the field in  $y$ -direction, which directly results in lower propagation losses for the mode and translates as a significant decrease of about  $\sim 50\%$  in the FWHM of the resonance. As  $t_m$  was increased to 50 nm, the maximum transmissivity reduced to 0.24, due to absorption of the metal layer preventing a lot of light from reaching the bottom of the substrate. When  $t_m$  was lower than 30 nm, the interaction of the field between the top of the grating and the homogeneous metal film reduced due to increased transmission through very thin metal layer. As a consequence, the peak transmissivity was higher but with increased FWHM, while all other geometrical parameters were maintained constant. Hence, a careful choice of the thickness of the homogeneous metal interspacer results in lower FWHM with no compromise in sensitivity. It should also be noted that the transmissivity corresponding to the substrate mode (Fig. 3(a) and Fig. 3(d)) at 970.9 nm is significantly reduced due to the absorption of the homogeneous metal film interspacer.

For sensing applications, we claim that the MGM structure may be a better choice over BMG structure because of lower FWHM of resonances resulting from stronger localization of the field in the vicinity of the grating region. In the case of refractive index estimation of dielectric superstrate materials, an experiment involving shining a TM polarized broadband light from the top normal to the surface and collection of the transmitted light from the bottom of the substrate using high Numerical Aperture (NA) objectives may be performed. Refractive index sensing can be achieved by analyzing the spectral content of the collected light. In case, this is done using a CCD camera arrangement at the back focal plane, the resonances of BMG structure will show up as black circular rings in bright field and in the case of MGM structure, the resonances will appear as bright colored rings in dark field. The signal to noise ratio in the case of BMG structures in such arrangements may be lower since detecting the absence of a spectral content in a bright field may be tedious due to coupling of signals from adjacent pixels of the CCD camera. In the case of MGM structure, since the imaging will be in dark field, one may expect a higher signal to noise ratio.

### 3. CONCLUSION

We demonstrate that, by carefully choosing a thin homogeneous metal interspacer layer between a dielectric substrate and an ultra low aspect ratio plasmonic nanograting, a refractive index sensor with sensitivity of 590 nm/RIU and reduced FWHM is possible. The reduction in the FWHM is caused by enhanced field localization between the grating surface and the metal interspacer layer. This structure may be used in experiments involving transmission based refractive index sensors employing normal incidence schemes.

### REFERENCES

1. Homola, J., S. S. Yee, and G. Gauglitz, "Surface plasmon resonance sensors: Review," *Sensors and Actuators B.*, Vol. 54, 3–15, 1999.
2. Roh, S., T. Chung, and B. Lee, "Overview of the characteristics of micro- and nano-structured surface plasmon resonance sensors," *Sensors*, Vol. 11, 1565–1588, 2011.
3. Dhawan, A., M. Canva, and T. Vo-Dinh, "Narrow groove plasmonic nano-gratings for surface plasmon resonance sensing," *Opt. Express*, Vol. 19, No. 2, 787–813, 2011.
4. Vial, A., A. Grimault, D. Macias, D. Barchiesi, and M. Chapell, "Improved analytical fit of gold dispersion: Application to the modeling of extinction spectra with a finite difference time domain method," *Phys. Rev. B*, Vol. 71, No. 085416, 1–7, 2005.
5. Moharam, M. G., E. B. Grann, and D. A. Pommet, "Formulation for stable and efficient implementation of the rigorous coupled wave analysis of binary gratings," *J. Opt. Soc. Am. A*, Vol. 12, No. 5, 1068–1076, 1995.

6. Frisbie, S. P., A. Krishnan, X. Xu, L. G. De Peralta, S. A. Nikishin, M. W. Holtz, and A. A. Bernussi, “Optical reflectivity of asymmetric dielectric-metal-dielectric planar structures,” *J. Lightw. Technol.*, Vol. 27, No. 15, 2964–2969, 2009.
7. Krishnan, A., S. P. Frisbie, L. G. De Peralta, and A. A. Bernussi, “Plasmon stimulated emission in arrays of bimetallic structures coated with dye-doped dielectric,” *Appl. Phys. Lett.*, Vol. 96, 111104-1–111104-3, 2010.

# The Design and Implementation of a MISO Fuzzy Logic Controller Based on CPLD

Chien-Nan Lee and Kai-Teng Jheng

Department of Electronic Engineering, Oriental Institute of Technology  
New Taipei City, Taiwan

**Abstract**— The main purpose of this approach is designing and realizing a MISO (Multi-Input Single-Output) fuzzy logic controller based on CPLD. The power control system for a mobile radio channel that was regarded as the example, two input variables are signal error and error-change, output variable is the signal power increment. The main component of a fuzzy logic controller include the fuzzification interface, knowledge base, decision-making logic and defuzzification interface. This approach design the fuzzification interface with the truth table, design the database and decision logic with decoder, ROM and comparator, etc., design the defuzzification interface with multiplier, adder, divider and truth table, etc.. According to the design method may realize a fuzzy logic controller very much easily.

## 1. INTRODUCTION

Advances in the manufacturing of semi-conductors have resulted in the prevalence of employing application-specific integrated circuits (ASICs) in circuit design. Specifically, the complex programmable logic device (CPLD), a logic device programmable into ASIC, is known for its high speed, large capacity, low costs, fast time to market, high modifiability, and ease for prototyping circuit tests. In addition, CPLDs are characterized by their reprogrammability and fixed delays, as well as their ease of use and design, which facilitates the understanding and learning of applications. Therefore, CPLDs are highly effective tools for circuit design [1].

A fuzzy logic control system is a specific expert system that models human experiences and human decision-making behavior [2]. The fuzzy control system employs a knowledge base, that is, fuzzy inference rules, and an appropriate inference engine to solve a given control problem. The topic of fuzzy logic control has provided substantial results when in applied research on fuzzy set theory. The primary features of fuzzy logic control research are as follows: (1) employ linguistic variables to describe system properties; and (2) employ the method of fuzzy approximate reasoning to manipulate the plant.

## 2. FUZZY PRODUCTION RULES

Let  $\mathbf{R}$  be a set of fuzzy production rules consisting of  $R_1, R_2, \dots, R_{n-1}, R_n$ , and  $\mathbf{R} = \{R_1, R_2, \dots, R_{n-1}, R_n\}$ . Consequently, the fuzzy production rule  $R_i$  is denoted by  $R_i \in R$ . The standard form is written as follows:

$$R_i: \text{ IF } X \text{ is } A_i \text{ THEN } Y \text{ is } B_i \quad (1)$$

This statement is interpreted as follows: (a)  $X$  is  $A_i$  forms the premise of rule  $R_i$  and  $Y$  is  $B_i$  is the conclusion of rule  $R_i$ , which are both expressed as propositions; (b)  $X$  and  $Y$  are fuzzy variables, that is,  $X$  denotes the system input variable, and  $Y$  denotes the system output variable; and (c)  $A_i$  and  $B_i$  are linguistic variables that express the fuzzy concepts of the linguistic property. Furthermore, these concepts employ the fuzzy set definition to further describe the membership function. For example,

$$\text{IF Temperature is High THEN the Pressure is Big} \quad (2)$$

which is a fuzzy production rule.

## 3. BASIC STRUCTURE OF A FUZZY LOGIC CONTROLLER

The basic structure of a fuzzy logic controller (FLC) comprises the following four primary components [3]: a fuzzification interface, knowledge base, decision logic, and defuzzification interface.

a. The fuzzification interface performs the following functions:

(a) Measures the value of the input variable, (b) conducts scale mapping, and (c) converts data into linguistic values that can be denoted using fuzzy sets according to the fuzzification function.

- b. The knowledge base includes a database and a linguistic control rule base.
  - (a) The database provides the required definitions to define linguistic control rules and to facilitate the FLC's processing of fuzzy data; and (b) the rule base describes the control target and control strategies of domain experts according to linguistic control rules.
- c. Decision logic is essentially a fuzzy inference engine with the FLC at its core. Decision logic is based on the fuzzy concept; it employs fuzzy inference to obtain fuzzy-control actions, and is, thus, capable of simulating human inference and decision-making.
- d. The defuzzification interface performs the following functions:
  - (a) Scale mapping and (b) defuzzification by computing solutions based on the inferred fuzzy-control actions, thereby obtaining crisp control actions.

#### 4. DESIGN OF A FUZZY LOGIC CONTROLLER INCORPORATING A CPLD

The main objective of this study was to design a multiple-input single-output (MISO) fuzzy logic controller with a CPLD as the control core (CPLD/FLC). An automatic sprinkler system was adopted as an example for modeling experiential rules that regulate the professional operation of automatic sprinkling in a flowerbed. This model was presented in the form of a CLPD circuit. Figure 1 shows the structure of an automatic sprinkler system.

Periodically, the automatic sprinkler system monitored the temperature and humidity in the flowerbed soil using the temperature and humidity sensor. The sprinkler system then compared the values and converted them into numbers before transmitting the results to the CPLD/FLC. After fuzzification, inference, and defuzzification, the crisp sprinkling time was obtained (because the amount of water during a time unit was fixed by the valve employed in this study, controlling the sprinkling time corresponded to controlling the sprinkling amount). The controller was designed using the following steps [2, 4, 5].

##### 4.1. Designing Fuzzification and Defuzzification Interfaces

###### 4.1.1. Define the Input and Output Variables

The automatic sprinkler system routinely detected the temperature and humidity in the flowerbed soil and controlled the sprinkling time accordingly. Therefore, temperature and humidity were defined as the input variables, and the sprinkling time was the output variable.

###### 4.1.2. Conduct Scale Mapping

Considering Taiwan's climate, the reference value for temperature in this study was set as 25°C, and the universal set for temperature variations was defined as  $-17^{\circ}\text{C}$  to  $+17^{\circ}\text{C}$ . Regarding humidity, the reference value was set as 60%, and the universal set for humidity variations was defined as  $+29\%$  to  $-29\%$ . The sprinkling time was set between 1 and 7 min. In addition, the closed interval  $[-3, +3]$  was defined as the discrete universal set, in which the seven integers between  $-3$  and  $+3$  were regarded as discrete quantitative ranks that quantified the temperature, humidity, and sprinkling time.

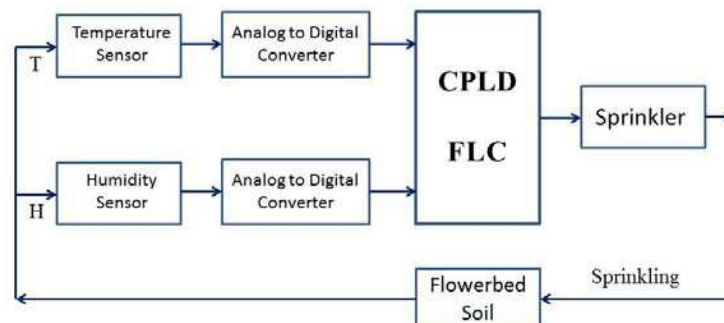


Figure 1: The structure of an automatic sprinkling system.

### 4.2. Designing the Knowledge Base

#### 4.2.1. Define the Linguistic Variable and the Membership Function

In this sprinkler system, seven linguistic conditions were adopted to describe the input and output variables. These linguistic conditions are commonly employed by standard fuzzy controllers to describe fuzzy sets of the input and output variables. The range spanned the largest negative error value, approximately zero, to the largest negative error value.

- NL — Negative Large      PL — Positive Large
- NM — Negative Medium    PM — Positive Medium
- NS — Negative Small      PS — Positive Small
- AZ — Approximately Zero

#### 4.2.2. Design the Rule Base

The automatic sprinkling system was a MISO system. Because the two input variables temperature ( $T$ ) and humidity ( $H$ ) were categorized into four linguistic conditions each, the maximum number of rules in the rule base  $N$  was 16. However, the actual number of rules was smaller because some combinations of linguistic conditions did not appear. Let  $R_i$  be the  $i$ th rule in the rule base ( $1 \leq i \leq N$ ),  $T$  be the temperature,  $H$  the humidity, and  $W$  the sprinkling time;  $R_i$  is then written as follows:

$$R_i: \text{ IF } T = A \text{ and } H = B \text{ THEN } W = C \tag{3}$$

In this equation,  $A$  and  $B$  were among the fuzzy conditions NL, NM, AZ, PM, and PL, whereas  $C$  was among the fuzzy conditions NL, NM, NS, AZ, PS, PM, and PL. The rule base can be expressed in the form of a matrix, as shown in Table 1.

### 4.3. Designing the Decision Logic

Decision logic is essentially a fuzzy inference engine with a fuzzy control system as its core. To simplify the computation, this example employed Eq. (3), Mamdani’s mini-fuzzy implication relationship, and Eq. (4) to make inferences. Designing a fuzzy inference engine involves establishing a fuzzy implication relationship between all rules in the rule base. When a universal set is a finite set, using a relationship matrix to denote the fuzzy implication relationship can simplify the fuzzy inference computation and relationship matrix composition.

Table 1: Rule base of an automatic sprinkling system.

		H			
	W	NL	NM	PM	PL
T	NL	NL	NM	NS	AZ
	NM	NM	NS	AZ	PS
	PM	NS	AZ	PS	PM
	PL	AZ	PS	PM	PL

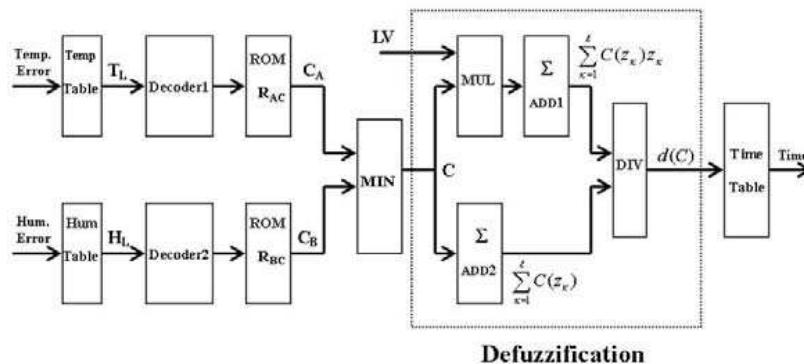


Figure 2: The core block diagram of the an automatic sprinkling system.

#### 4.4. Selecting an Equation for Defuzzification

To conduct defuzzification, the automatic sprinkling system selected the center-of-area method, which is commonly employed in the selection of fuzzy controls. Assuming that the inferred conclusion was fuzzy set  $C$ , let  $d(C)$  be its crisp conclusion, which was the actual control action. If  $C$  was defined beyond a finite discrete universal set  $\{Z_1, Z_2, \dots, Z_\ell\}$ , then  $d(C)$  can solve [3, 6] using the following equation:

$$d(C) = \frac{\sum_{\kappa=1}^{\ell} C(z_\kappa)z_\kappa}{\sum_{\kappa=1}^{\ell} C(z_\kappa)} \quad (4)$$

#### 4.5. A Summary of the CPLD Circuit

The block diagram indicating the core of the automatic sprinkling system is shown in Fig. 2. This study employed the following for the controller design: (1) a truth table to design the fuzzification interface; (2) a decoder, read-only memory (ROM), and comparator (MIN) to design the database and fuzzy inference engine; and (3) a multiplier, adder, divider, and truth table to design the defuzzification interface.

### 5. CONCLUSIONS

CLPDs are characterized by various advantages including high speed, large capacity, fast time to market, and high modifiability. This study constructed a fuzzy logic controller with a CPLD circuit as the control core by designing a fuzzification interface, knowledge base, decision logic, and defuzzification interface. The core circuit of this controller comprised various fundamental components of a digital system, including a truth table, decoder, ROM, comparator, multiplier, adder, divider, and register. The design methods recommended in this study can increase the simplicity and feasibility of controller implementation.

### REFERENCES

1. Hsiao, J. H., *Personal Computer-aided Digital Circuit Design*, 1st Edition, 10–13, Scholars Book, Taipei, Taiwan, 1996.
2. Zimmermann, H. J., *Fuzzy Set Theory and Its Applications*, 2nd Edition, 201–209, Kluwer Academic Publishers, Boston, 1991.
3. Lee, C. C., “Fuzzy logic in control systems: Fuzzy logic controller, Part I & II,” *IEEE Transactions on Systems, Man, and Cybernetics*, Vol. 20, No. 2, 404–435, Mar./Apr. 1990.
4. Sun, T. Y. and Y. K. Yang, *Fuzzy Control: Theory, Implementation, and Application*, 1st Edition, 174–203, Chuan Hwa Science & Technology Book Co., Taipei, Taiwan, 1994.
5. Klir, G. J. and B. Yuan, *Fuzzy Sets and Fuzzy Logic: Theory and Applications*, 330–347, Prentice-Hall, New Jersey, 1995.
6. Ester, V. B. and D. B. Bernard, “Fast and accurate center of gravity defuzzification of fuzzy system outputs defined on trapezoidal fuzzy partitions,” *Journal of Fuzzy Sets and Systems*, Vol. 157, No. 7, 904–918, 2006.

# Mobile Mouse Pad

Li-Lin Chen

Electronic Engineering Department, Oriental Institute of Technology  
New Taipei City, Taiwan, R.O.C.

**Abstract**— Carpal tunnel syndrome is a common modern occupational disease, which is often diagnosed among people whose work requires their wrists repeating the same action or exerting excess strength over a long period. For example, personnel who use the computer for long periods employ the mouse for hours every day, inducing repeated and excess movements of the wrist joints. This may compress or damage the median nerve that travels through the wrist and block nerve conduction, thereby numbing the hand and obstructing hand movements [1, 2].

To prevent suffering resulting from carpal tunnel syndrome caused by the long-term use of computers, a mobile mouse pad is developed in this study, which can detect the amount of time people use the mouse. The air-pump motor in the mobile mouse pad can charge and release air regularly to repeat the up-down and left-right movements of the pad, thereby relieving and stretching the median nerve in the wrist. This product also initiates voice alarms periodically to remind users to stop operating the mouse and rest their hands appropriately. If a user continues to use the mouse, the voice reminder repeats. Consequently, this product can be used to prevent diseases and conditions related to an excess burden on the wrists.

## 1. INTRODUCTION

Because of the popularization of computers, numerous people use computers for long periods. Work, education, and recreational or entertainment activities are all related to computers. However, using computers for long periods may pose a significant burden on the median nerve of the wrists, thereby eventually inducing the occupational disease carpal tunnel syndrome, which is also known as “mouse hand” [3].

Patients with carpal tunnel syndrome feel numbness or abnormalities in their thumbs, index, and middle fingers, and those with severe carpal tunnel syndrome tend to bend their wrists when sleeping, thereby prompting a narrowed carpal tunnel, aggravated soreness, and disturbed sleep. The users’ finger strength and dexterity are also influenced, frequently resulting in hand numbness and reflective pain in the arm [4]. Current rehabilitation treatment for carpal tunnel syndrome consists mostly of thermotherapy and electrotherapy, which are used to relieve pain, alleviate the stress inside the carpal tunnel, activate each articular surface of the wrist, and reduce the development of febleness, pain, and other symptoms [5]. However, the key to avoiding carpal tunnel syndrome is to prevent the upper extremities from executing fixed, mechanical, and frequent motions or working situations, such as using a mouse. After working for an hour, computer users should stand and perform upper-extremity exercises to relax their fingers, such as clenching their fists and kneading their fingers [5].

To prevent carpal tunnel syndrome from becoming a common “disease of civilization,” we hope to use the proposed device to detect the overall time people spend using computers, which compress and employ their wrists, thereby determining whether mouse-usage time is excessive. When excess mouse-usage time is determined, an air-pump motor is activated to effectuate up-down and left-right movements to alleviate the compression of the median nerve. In addition, a voice reminder function can provide a timely notification to the user to stand and perform stretching exercises that relax the extremities and provide rest. If the user continues to use the computer, the voice reminder plays repeatedly until the user’s hand leaves the mouse. Thus, this proposed device can achieve the effect of preventing wrist conditions. As a result, modern people, including employees and online gamers, can balance their health during work and leisure.

## 2. SYSTEM STRUCTURE

This product uses AT89S52 as the core microprocessor, which comprises functions, such as pressure-sensor signal control, timing control, reminder signal control. The peripheral devices include the pressure sensor, FSR\_406, analog-to-digital driver IC, ADC0932, air-pump motor SC3701PM, and SunPlusPCE061A [6] with voice functions. This mobile mouse-pad system integrates the core microprocessor controls and peripheral devices to realize functions such as reminding users to take

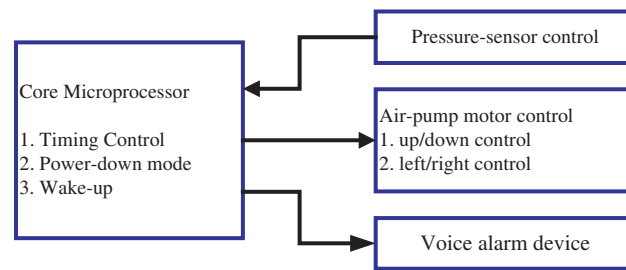


Figure 1: System structure.

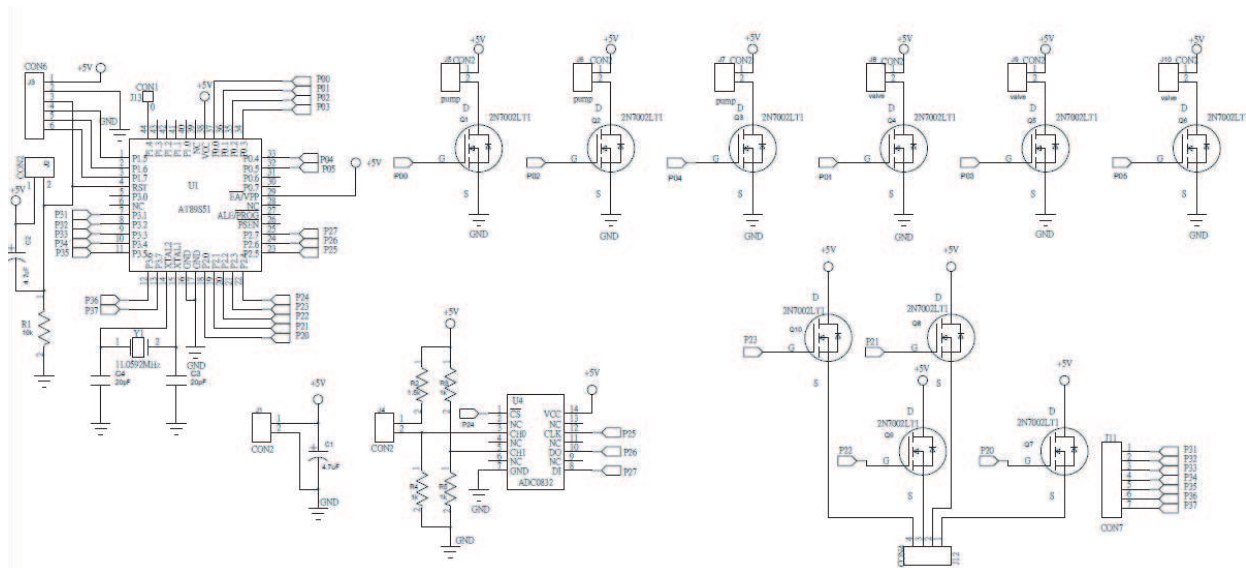


Figure 2: System circuit.

adequate rest, reducing long-term compression in fixed positions, and encouraging users to stop operating the mouse. The system structure of this product is shown in Figure 1.

AT89S52 is adopted as the core microprocessor to receive the signals transmitted by the pressure sensor, and determines whether the user is using the developed product. If activation signals of the developed product are not received within a default settime of 10 minutes, the system enters the power-down mode to conserve energy. In the power-down mode, the system enters the general mode when it receives an activation signal from the pressure sensor. From the general mode, the system can enter the usage mode and can detect signals from the pressure sensor to calculate usage time. If the user operates the mouse for more than 10 minutes continuously, the system activates an air-pump motor to repeatedly move the mouse pad in up-down and left-right directions. If the user operates the mouse for more than 50 minutes, the system issues a voice reminder and sends a warning signal.

### 3. SYSTEM IMPLEMENTATION

When the developed product is on, the system enters power-down mode (standby mode) if the microprocessor AT89S52 does not detect a signal from the pressure sensor that the system is in use. After the user begins to use the mouse, the pressure sensor in the mouse pad detects the user condition and sends signals to the core microprocessor AT89S52, which subsequently activates the timer and the air-pump motor. When activated, the internal timer begins to monitor usage time and determines whether the user's usage time exceeds the set period or is excessive. If the usage time is within the set period, timing continues; by contrast, if the usage time exceeds the set period, the timer sends a signal to the SunPlusSPCE061A to issue a warning signal. System circuit.

Figure 2 shows the system circuit which includes the main control circuit of the core microprocessor AT89S52, peripheral control circuits of the pressure sensor, and the control circuit of the air-pump motor. Each of these circuits is described below:

#### (1) Core Microprocessor

When the power is on, the core microprocessor AT89S52 enters the power-down mode until the pressure sensor sends a signal to activate the system. The system activates timing control, air-pump motor control and voice alarm control. In this product, the air-pump motor is activated to generate repeated movements, including rising, descending, and leftward and rightward rotations, to enable the effects of reducing compression on a fixed point or position of the median nerve.

(2) Pressure-sensor Control

FSR\_406 is similar to a variable resistor that can be used to detect whether the user is using the proposed product. This circuit can convert the pressure placed on its surface into voltage values, which are further converted from analog signals into digital signals and sent to the core microprocessor through the A/D converter IC, thereby identifying whether the user is using this product. FSR\_406 can be operated under a 10 kg load, which is suitable for application as a pressure sensing component in the mouse pad.

(3) Air-pump Motor Control

To integrate user comfort and reduce noise, the developed mobile mouse pad uses the air-pump motor SC3701PM as a component to control the rise and descent of the mouse pad. The peripheral circuits of the air-pump motor mainly consist of three air-pump motors and air valves that control the motor, causing it to pump and release air into an air cushion for up-down controls in the mouse pad. Two air-pump motors are used to control the left-right movement of the mouse pad. When the left motor pumps and the right motor releases air, the mouse pad moves right and vice versa. These repeated controls of left and right movements can change the compression point of the user's median nerve.

(4) Voice Alarm Device

The alarm device provides voice reminders. When the user operates the system for an excessive time, the core microprocessor transmits a signal to the SunPlusSPCE061A, which subsequently issues a warning signal. If the user operates the mouse continuously for more than 50 min, the system continuously issues voice reminders to notify the user to rest. The voice reminder device will not stop until the user's hand leaves the mouse. This system can detect the time that the pressure sensor is not used. The user must stop using the mouse for approximately 10 minutes to confirm stoppage for the voice reminder system and return the timer to zero. If the user operates the mouse again within the 10-minute rest break, the timer adds the usage time and continues to send voice reminders. This function ensures that the user rests adequately.

(5) Software Flowchart

The system software flowchart is shown in Figure 3. The system enters the power-down mode until the pressure sensor interrupts to wake-up the core microprocessor. The system activates air-pump motor to puff up and off the mouse pad to move it up and down repeatedly. The

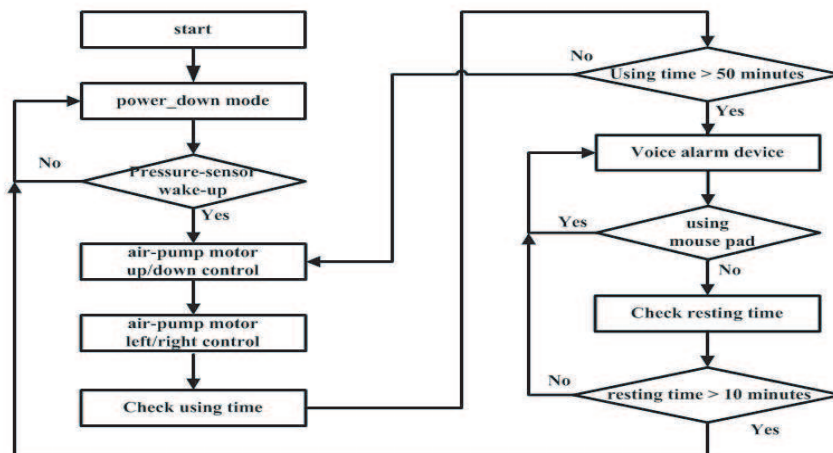


Figure 3: Software flowchart.

mouse pad will be moved left and right by two air-pump motors. The timing control is enacted to measure the time that the user uses the product, and determines whether the usage time is excessive. This product is set to immediately transmit voice signals that notify the user to rest after using the system continuously for over 50 consecutive minutes. Rest time is set for 10 minutes. The system will be back to the power-down mode after resting 10 minutes and it will remain asleep until it is awoken.

#### 4. CONCLUSIONS

A mobile mouse pad was implemented in this study. Invention patents were applied for regarding this product [7, 8] and it won the silver medal in the ITEX 2012 23rd International Invention, Innovation & Technology Exhibition and the bronze medal in the 8th Taipei International Invention Show & Technomart. Using this mobile mouse pad can relieve the compression on the median nerve in the wrist and provide timely reminders to users to rest, thereby reducing the user's risk of contracting conditions such as carpal tunnel syndrome, and decreasing the damage to patients who already suffer from carpal tunnel syndrome when using a mouse.

To increase the usability and reduce the cost of the product, future studies should investigate downsized mobile mouse pads or reducing the size of mobile mouse pads. In addition to selecting SMD components, compact or smaller parts that can replace the air-pump motor SC3701PM can be identified to achieve usability. Consequently, the modified mobile mouse pad will be more suitable for use in offices and households.

#### ACKNOWLEDGMENT

Thanks to Dr. Yiu-Tong Chu and Nurse Ling Cheng of Far Eastern Memorial Hospital for their help.

#### REFERENCES

1. Horng, Y., S. Hsieh, Y. Horng, and M. C. Lin, "Occupational carpal tunnel syndrome," *Taiwan Journal of Public Health*, 85–92, 2009.
2. Lin, J., "Chinese new year syndromes: Beware of video-game and cell-phone elbows," *Consumer Reports of Taiwan*, Vol. 385, 21–23, 2011.
3. Cai, Q., "Carpal tunnel syndrome," *Journal of Blood Purification Society*, 65–73, 2010.
4. Lin, C., P. Chao, and H. Liang, "Job-related carpal tunnel syndrome," *Primary Medical Care & Family Medicine*, 214–218, 2006.
5. Su, Z., "The effects of mouse positions on arm, neck-shoulder muscles and wrist postures," Master's Thesis, Department of Industrial Engineering, Chung Yuan Christian University, 1998.
6. Tu, Y., J. Guo, C. Lin, and M. Lin, "Principles of microprocessors: SPCE061A," Chirkal Technology Co., Ltd, 2007.
7. Chen, L., C. Chen, Y. Chu, L. Cheng, Z. Chen, Y. Zhong, C. Tsai, and S. Liu, "Mobile mouse pad structure," Patent applied number 100142195, September 23, 2011.
8. Chen, L., Z. Chen, and L. Wu, "A device for preventing mouse overuse," Patent number M 410913, September 1, 2011–January 5, 2021.

# An ECG Signal Enhancement Based on Improved EMD

Mei-Lin Su<sup>1</sup> and Keh-Shih Chuang<sup>2</sup>

<sup>1</sup>Department of Communication Engineering  
Oriental Institute of Technology, Taiwan

<sup>2</sup>Department of Biomedical Engineering & Environmental Sciences  
National Tsing-Hua University, Taiwan

**Abstract**— Electrocardiogram (ECG) is an important biological signal to diagnose cardiac arrhythmia. The P wave is the combined result of the action potentials of the atrial muscle units, while the QRS and T waves are formed by the spatio-temporal summation of the action potentials of the ventricular muscle units. However, ECG signals are often corrupted by various noise, such as muscle noise, baselines wander and power-line interference. Therefore, ECG noise reduction is an important issue and has been studied for many years. A common encountered in ECG de-noising systems is the removal of unwanted disturbances, i.e., a low-pass filter was designed to remove the high-frequency noise, and a high-pass filter was designed to remove the low-frequency noise. These filter banks based denoising process smooth the *P* and *R* amplitude of ECG signal and it is less robust to different levels of noise. Comparatively, the empirical mode decomposition (EMD) based on the decomposition of data into a collection of intrinsic mode function (IMF) was investigated to improve the ECG signals. In this study, we proposed an adaptive method to select the IMF index for separating the noise components from the ECG signal. The performance of the proposed method is evaluated in terms of standard metrics by performing extensive simulations using the MIT-BIH arrhythmia database. The results show improvements of ECG signals at different levels of SNR. Moreover, the low frequency noise components are separated by a partial reconstruction from the IMFs and still preserve the QRS complex.

## 1. INTRODUCTION

The empirical mode decomposition (EMD) algorithm is an adaptive method to analyze non-linear and non-stationary signals [1]. In EMD, a given time signal is decomposed into a set of oscillatory functions, known as intrinsic mode functions (IMFs). It is a fully data-driven separation of a signal into fast and low oscillations. However, EMD exists the mode mixing and the mode-misalignment problems for analyzing multivariate time series. The mode-mixing occurs when a single IMF contains multiple oscillatory modes or a single mode resides in multiple IMFs. Ensemble EMD (EEMD) was introduced to remove the mode-mixing effect [2]. It performs the EMD over many ensembles of the signal plus different Gaussian white noise. Then the added noise solves the mode mixing problem if the number of trials is sufficient. The mode-misalignment corresponds to a problem where the same-index IMFs across multivariate data contain the different frequency modes so that the IMFs are not match either in scale or in the number. During the ECG measurement, various types of noises, such as muscle noise, baseline wander, and power-line interferences, are recorded in the ECG signals. The Multivariate EMD (MEMD) has been proposed to extend the application of EMD to multivariate time series and deal with the mode-misalignment issue in multivariate data [3].

In this paper, we adopted MSE parameters to decide major IMFs which can be combined to get the enhanced ECG signals.

## 2. MATERIALS AND METHODS

### 2.1. EMD and EEMD

The decomposition of EMD can be processed with the following steps [1]:

1. Identify the extrema of the data set  $x(t)$ , and generate the upper and lower envelopes defined by the cubic spline interpolation of the extrema point.
2. Compute the mean function  $m(t)$  by averaging the upper envelop and lower envelop, and make the difference between the data and the mean values to get the first component  $h_1(t) = x(t) - m_1(t)$ .
3. If the first component is not an IMF, let  $h_1(t)$  be the new data set. Continue the steps 1 and 2 until the first component is an IMF.

4. The first IMF component is called as  $c_1(t)$ . Let  $r_1(t) = x(t) - c_1(t)$ . Continue the steps 1–3 until the final signal  $r_N(t)$  is obtained as a monotonic function.

At the process, a decomposition of the data into  $n$ -empirical modes  $c_j(t)$  is achieved, named IMFs.

$$x(t) = \sum_{j=1}^N c_j + r_N \quad (1)$$

According to [2], EEMD algorithm can be described as:

1. Generate  $x^i(t) = x(t) + w^i(t)$ , where  $w^i(t)$  ( $i = 1, \dots, I$ ) are different realizations of white Gaussian noise.
2. Each ensemble signal  $x^i(t)$  ( $i = 1, \dots, I$ ) is fully decomposed by EMD getting its IMFs.
3. Assigned  $\text{EEMD-}c_j(t)$  as the  $j$ -th mode of  $x(t)$ , obtained as the average of the  $c_j(t)$ .

$$\text{EEMD-}c_j(t) = \frac{1}{I} \sum_{i=1}^I c_{ij} \quad (2)$$

## 2.2. MEMD

MEMD projects the multivariate signal along different directions to generate the multiple multi-dimensional envelopes averaged to obtain the local mean. The MEMD effectively deals with the mode-misalignment issue [3].

## 2.3. MSE

Multiscale Entropy is developed to measure the complexity over the different scales of time series [4]. Given a time series with  $N$  samples,  $x = \{x_1, x_2, \dots, x_N\}$ ,

1. The original time series  $x$  is divided into non-overlapping windows of length  $\tau$ , defined as the scale factor. The data points inside each window are then averaged.

$$y_\tau(j) = \frac{1}{\tau} \sum_{i=(j-1)\tau+1}^{j\tau} x_i, \quad 1 \leq j \leq \frac{N}{\tau} \quad (3)$$

2. Compute the sample entropy [5] of each-grained time series.

Sample entropy provided a quantification of irregularity of a temporal series. In our study, we according to the MSE curve to select the probable IMFs which can be combined to a denoising ECG signal.

## 2.4. DATA

Synthetic and real signals were analyzed in the present paper. High frequency ECG noise types, such as muscle contraction and 50 Hz power line interference, and low frequency ECG, baseline wander were simulated in the following session [6]. A second example, using real data: Electrocardiogram (ECG) signals and real noise were extracted from the MIT-BIH normal sinus rhythm and noise stress test database [7].

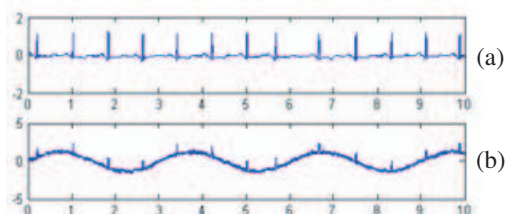


Figure 1: (a) Clean ECG. (b) Synthetic noisy ECG.

### 3. RESULTS

In Fig. 1, a simulated arrhythmia was added noises, including EMG, 50 Hz power line and baseline wanders. Fig. 2 shows IMFs by EEMD and MEMD decomposition. From Fig. 3, we observed the first IMF works like the white noise and its MSE curve decades as the scale increasing and the MSE of low level IMFs tend to zeros. Therefore, we accorded to the MSE curves to reconstructed

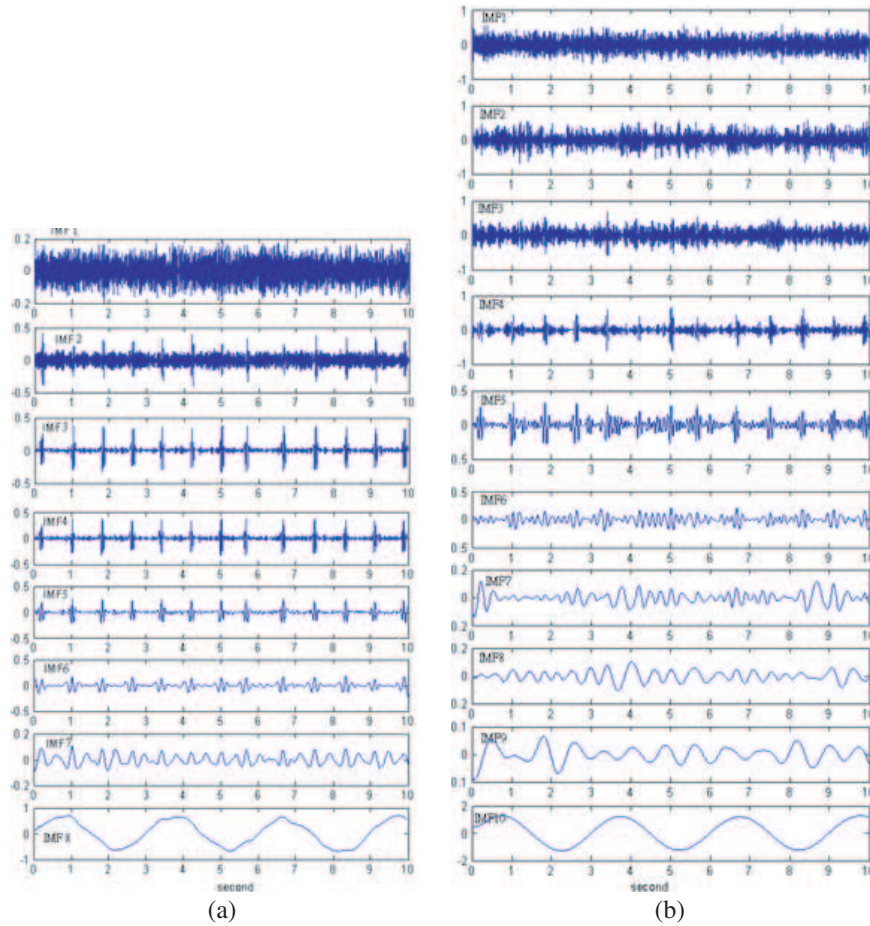


Figure 2: (a) IMFs of EEMD (trials = 200). (b) IMFs of MEMD.

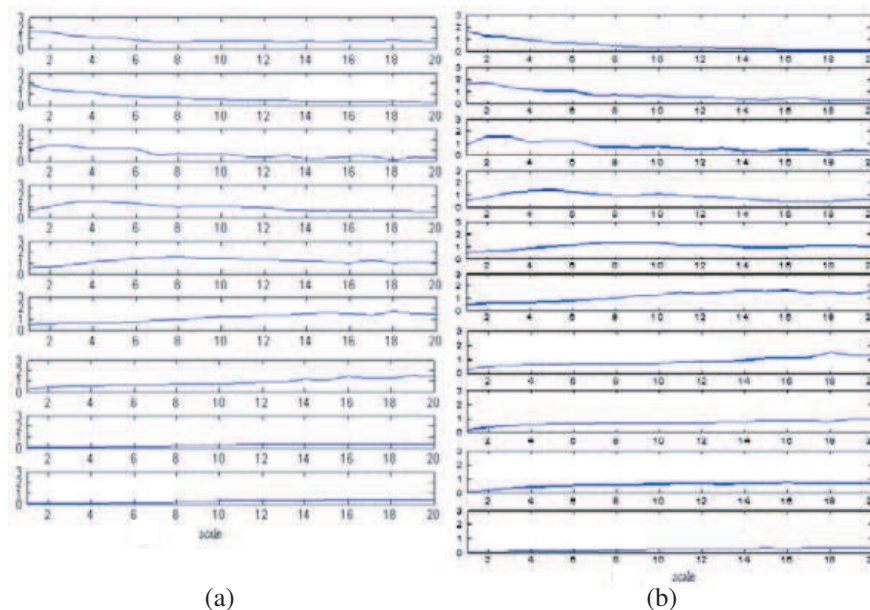


Figure 3: (a) MSE of IMFs by EEMD. (b) MSE of IMFs by MEMD.

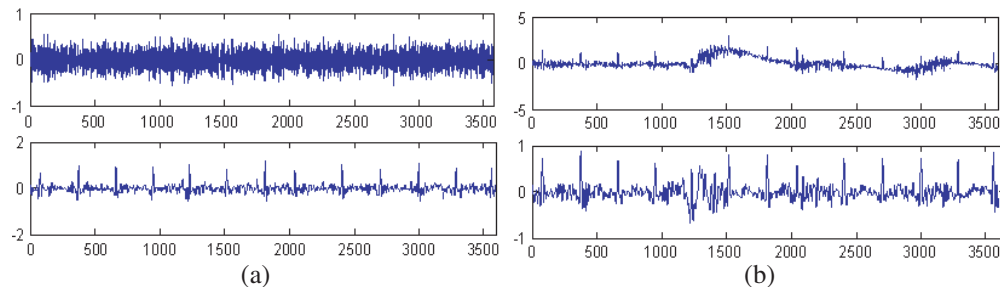


Figure 4: (a) Composition of level 4, 5, 6, 7 IMF of EEMD for Synthetic signal at SNR =  $-10$  dB. (b) Composition of level 4, 5, 6, 7 IMF of EEMD for real signal at SNR =  $-10$  dB.

enhanced ECG signals.

For real noise, baseline wander, muscle contraction and motion artifact, MSE is still a good tool to select the IMFs to reconstruct enhanced ECG signals. Fig. 4 indicated that the proposed method can be applied to the synthetic and real ECG signals even at low SNR values.

#### 4. CONCLUSIONS

In this work, we have presented a new method to select the IMF. MSE makes EEMD can more adaptively for analyzing and processing non-linear signals. The new method was successfully tested on synthetic and real ECG signals. Moreover, we applied multivariate EMD algorithm to decompose the signal of IMFs and it works well as EEMD.

#### REFERENCES

1. Huang, N. E., Z. Shen, S. Long, M. Wu, H. Shih, Q. Zheng, N. Yen, C. Tung, and H. Liu, "The empirical mode decomposition and Hilbert spectrum for non-linear and non-stationary time series analysis," *Proc. Roy. Soc. A*, Vol. 454, 903–995, 1998.
2. Wu, Z. and N. E. Huang, "Ensemble empirical mode decomposition: A noise-assisted data analysis method," *Advances in Adaptive Data Analysis*, Vol. 1, No. 1, 1–41, 2009.
3. Rehman, N. and D. P. Mandic, "Multivariate empirical mode decomposition," *P. R. Soc. Amer.*, Vol. 446A, 1291–1302, 2010.
4. Costa, M., A. L. Goldberger, and C. K. Peng, "Multiscale entropy analysis of complex physiologic time series," *Phys. Rev. Lett.*, Vol. 89, 068102, 2002.
5. Costa, M., A. L. Goldberger, and C. K. Peng, "Multiscale entropy analysis of biological signals," *Phys. Rev. E*, Vol. 71, 021906, 2005.
6. Blanco-Velasco, M., B. Weng, and K. E. Barner, "ECG signal denoising and baseline wander correction based on the empirical mode decomposition," *Comput. Biol. Med.*, Vol. 38, 1–13, 2008.
7. Goldberger, A. L., L. A. N., L. Glass, J. M. Hausdorff, P. C. Ivano, R. G. Mark, J. E. Mietus, G. B. Moody, C. K. Peng, and H. E. Stanley, "PhysioBank, PhysioToolkit, and PhysioNet: Components of a new research resource for complex physiologic signals," *Circulation 2000*, Vol. 101, e215–e220, 2000.

# A Rehabilitation Device for the Patients of Carpal Tunnel Syndrome

Li-Lin Chen

Electronic Engineering Department

Oriental Institute of Technology, New Taipei City, Taiwan, R.O.C.

**Abstract**— People who move their wrist repetitively or under excessive force are prone to developing carpal tunnel syndrome (CTS). Cooks, pianists, and computer operators are among the people most likely to experience this condition. In modern society, people use computers not only for work but also for leisure and recreation activities. Thus, the incidence of CTS has risen, with the affected patients becoming increasingly younger. The primary symptom of carpal tunnel syndrome is numbness and paresthesia of the thumb, index, and third fingers [1, 2]. The impact of the condition for patients includes disturbed sleep because of severe wrist pain and to danger the future functions of their wrists. Thus, we have developed a rehabilitation device for the patients of CTS.

The CTS rehabilitation device developed in this study offers the following functions: (1) the patient's wrist is held at a fixed angle and then repeatedly rotated clockwise and counterclockwise for a specific period; (2) the lifted angles can be adjusted according to doctor recommendations and the situation of each patient; (3) the device rotation time and duration can be adjusted according to the specific stage of rehabilitation; (4) heat can be applied to the wrist to relieve pain; and (5) the small size of the device enable use at any time and place. Furthermore, the device can be employed for both the rehabilitation and prevention of CTS.

## 1. INTRODUCTION

Nowadays lots of people use computers for long periods. Work, education, and recreational or entertainment activities are all related to computers. It may pose a significant burden on the median nerve of the wrists because of using computers for long periods, thereby eventually inducing the occupational disease carpal tunnel syndrome [3]. People who move their wrist repetitively or under excessive force are prone to developing CTS. Currently, the physical treatment most commonly employed for CTS is the use of wrist splints [4]. Splints are worn to immobilize the wrist at an angle of approximately  $15^\circ$ , preventing excessive stretching and flexing of the wrist and reducing total wrist activity. The disadvantage of splints is that they may restrict wrist movement excessively. Patients with acute CTS may require surgical intervention, where the transverse carpal ligament is released to decompress the median nerve and relieve pain. The rehabilitation devices currently developed for the wrist are generally mechanical and relatively large [5]. Thus, this study developed an adaptive rehabilitation device for the wrist.

The study researchers had previously developed the healthy mobile mouse pad and the mobile mouse pad for computer users [6, 7]. The healthy mobile mouse pad periodically reminds or forces computer users to rest, and the mobile mouse pad relieves compression of the median nerve. However, the development of these two designs focused on computer users and were ineffective for patients already experiencing CTS. Thus, this study developed an adaptive rehabilitation device for the wrist. By controlling the internal motor rotation, the rehabilitation device can maintain clockwise or counterclockwise rotations, and rehabilitation of the wrist can be achieved with the inclusion of a temperature control function. The compact body of the proposed device enables patients to easily comply with physicians' rehabilitation instructions at home, thereby alleviating symptoms and reducing the likelihood of surgery for CTS. The device developed in this study is an electronic medical prototype with preventive functions to promote health.

## 2. FUNCTIONALITY

The primary function of the device is to facilitate wrist rehabilitation among CTS patients. The device comprises three functional modes, that is, normal, free, and adaptive. In normal mode, the device manipulates the wrist in clockwise rotations followed by counterclockwise rotations at fixed intervals. In the free mode, patients can adjust the direction and speed of the rotations according to their preferences. In the adaptive mode, the device automatically adjusts the direction and speed of the rotations according to the patient's rehabilitation condition. The functionalities and operation modes are explained below.

- A. Rotation speed adjustment: Rotation speed can be adjusted according to the patient's degree of injury and rehabilitation conditions.
- B. Rotation angle adjustment: The rotation angle can be adjusted to ensure the device fits comfortably on the patient's wrist.
- C. Infrared heating: Infrared heating functions are incorporated into the device to simultaneously apply 30°C heat to the wrist area.
- D. Mode settings

1. Normal mode

In this mode, rehabilitation is set at fixed times. The motor within the device initially rotates clockwise for a fixed time followed by counterclockwise for a fixed time, and the device simultaneously activates infrared heating. At fixed intervals, the rotation pattern changes. When the timer reaches an appropriate rehabilitation duration, the device automatically deactivates. The fixed rotation times for rehabilitation should be determined by a physician or physical therapist.

2. Free mode

The user can randomly and freely set the rotation direction, angle, and speed of the device based on their wrist condition or level of pain. This mode should only be applied with the consent of a physician.

3. Adaptive mode

In this mode, users must record and input their rehabilitation conditions into the device after each session. The system then compares the user's rehabilitation data with their operation results and automatically adjusts the rotation modes using a neural network algorithm.

### 3. SYSTEM IMPLEMENTATION

This study adopted HT46RU232 as the core processor of the rehabilitation device. This main processing unit calculates the timing, displays the duration, controls the DC motor rotation, provides control settings, and determines and interrupts mode changes. Subsequently, the peripheral device controls the operation of the DC motor, scanning and display of the seven-phase display unit, and heating of the wrist area.

During operation, the rehabilitation device activates motor rotation according to mode settings. For example, in the normal mode, the motor operates according to the fixed times suggested by the patient's physician or physical therapist; the rotation angle, speed, and duration of rehabilitation are set based on recommendation from health care personnel. When operating in the free mode, the timing control unit is deactivated to allow users to freely alter the rotation direction. In the adaptive mode, the system determines the optimal operation condition for the user based on previous operations and rehabilitation condition data, considering factors such as rotation speed, angle, and time.

#### 3.1. Hardware Structure

The hardware structure of the device is shown in Fig. 1. During system activation, the HT46RU232 core processor activates the DC motor, heat controller, and timer when receiving mode selection signals. For example, when the user adjusts the rotation knob, the core processor inputs differing voltage values using a variable resistor and related circuitry, and obtains related settings using an internal A/D converter. The rotation speed of the DC motor is then modified according to the settings.

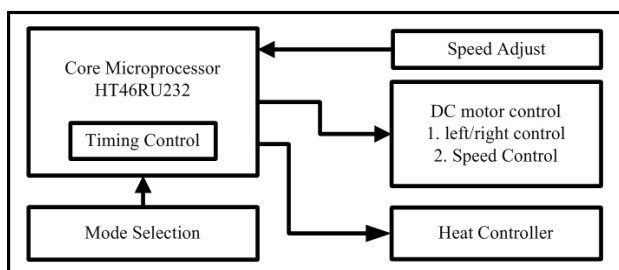


Figure 1: Hardware structure.

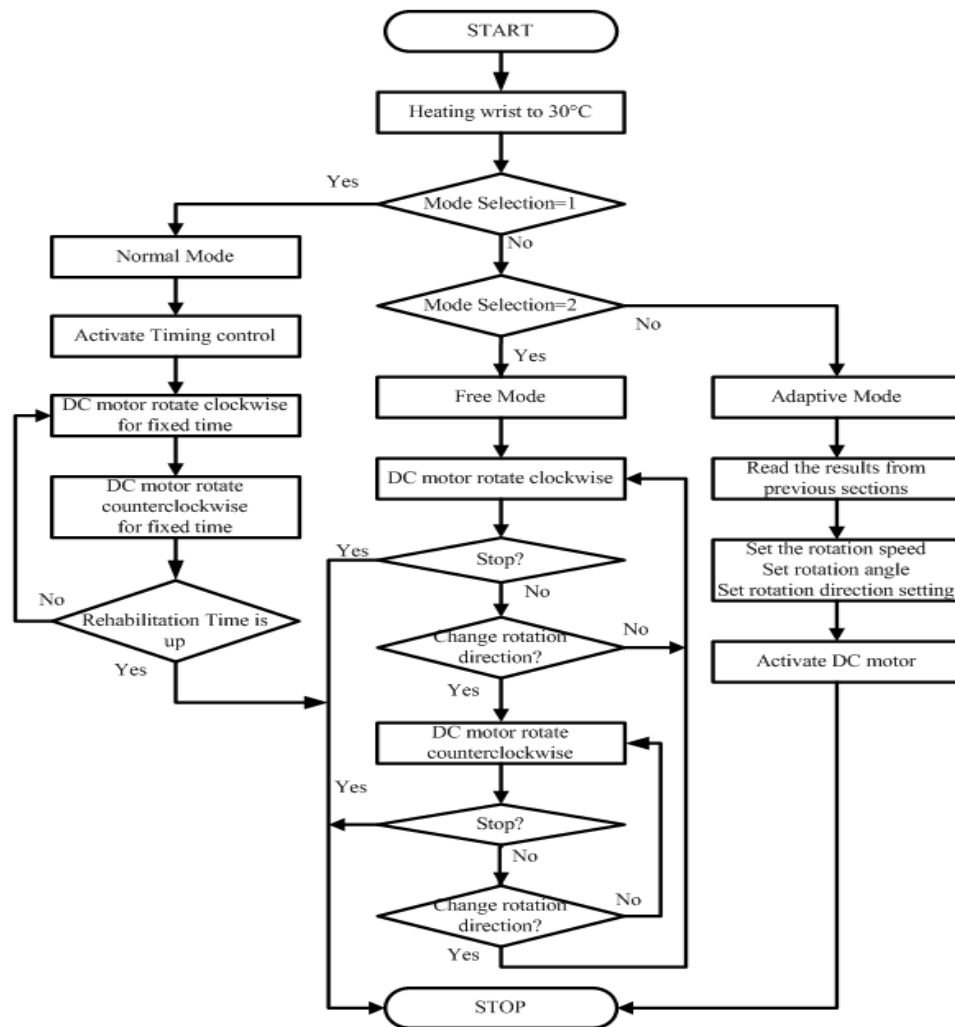


Figure 2: Software flowchart.

### 3.2. Software Structure

A flowchart of the system software is shown in Fig. 2. After the core processor is activated, the infrared heating and temperature control program is initiated to heat the patient's wrist to 30°C. Then, the mode selection is determined, where '1' represents the normal mode, '2' represents the free mode, and '3' represents the adaptive mode.

In the normal mode, the rotation speed is first determined. Clockwise rotation is then initiated according to the settings. Subsequently, the timer for rotation activation and deactivation is activated. When the timed clockwise rotation period expires, the system activates counterclockwise rotation, and the timer for activation and deactivation is reset. This process is repeated until the end of a rehabilitation session. In the free mode, the system activates clockwise rotation based on the rotation speed settings. When a setting for rotation change is received, the system adjusts the rotation direction and simultaneously reads the adjusted speed settings. This process is used to control the rotation speed throughout a rehabilitation session. In the adaptive mode, the system first reads user settings data from the previous five sessions, including the rotation speed, angle, and duration. Furthermore, by using the rehabilitation condition data inputted by the user after each session, excellent, good, moderate, and poor conditions can be set. Based on the provided data, the optimal rotation speed, angle, and duration for each session can be established.

## 4. CONCLUSIONS

An adaptive rehabilitation device is implemented. To achieve wrist rehabilitation, this device guides wrist rotation by controlling the internal motor of the device. Additional functionalities

such as clockwise and counterclockwise rotation and heating are also employed to relieve pain. An application for an invention patent of this device has been submitted under the description “rehabilitation device for the hand.” This device supports CTS rehabilitation and prevents the occurrence of CTS. The advantages of the device include a compact size, versatile applications, and customizable functions. In addition, because the device is easy to carry, use is not restricted to hospitals, further enhancing rehabilitation for people with busy lifestyles.

This research will continue with the cooperation with the neurology department of far eastern memorial hospital. The developed device will be enhanced with two modifications. The first involves incorporating an electrode function in the device to treat patients’ tender spots and assess the treatment effectiveness, thereby enabling patients to avoid surgery. The second modification involves providing support points for the arm, where the angle of the support can be adjusted based on the patient’s arm length. This enables the device to be placed on a surface, which reduces the burden placed on the patient’s arm.

#### ACKNOWLEDGMENT

Thanks to Dr. Yiu-Tong Chu and Nurse Ling Cheng of Far Eastern Memorial Hospital for their help.

#### REFERENCES

1. Horng, Y., S. Hsieh, Y. Horng, and M. C. Lin, “Occupational carpal tunnel syndrome,” *Taiwan Journal of Public Health*, 85–92, 2009.
2. Lin, J., “Chinese new year syndromes: Beware of video-game and cell-phone elbows,” *Consumer Reports of Taiwan*, Vol. 385, 21–23, 2011.
3. Cai, Q., “Carpal tunnel syndrome,” *Journal of Blood Purification Society*, 65–73, 2010.
4. Katz, J. N. and B. P. Simmons, “Carpal tunnel syndrome,” *New England Journal of Medicine*, Vol. 346, 1807–1812, 2002.
5. Huang, P., “The research and development of a continuous passive motion machine for wrist and hand,” Master Thesis, 2004.
6. Chen, L., Z. Chen, and L. Wu, “A device for preventing mouse overuse,” Patent Number M 410913, Sep. 1–Jan. 5. 2021.
7. Chen, L., C. Chen, Y. Chu, L. Cheng, Z. Chen, Y. Zhong, C. Tsai, and S. Liu, “Mobile mouse pad structure,” Patent Applied Number 100142195, Sep. 23, 2011.